Lecture Notes in Physics 874

M. Yu. Kagan

Modern Trends in Superconductivity and Superfluidity

Springer

Lecture Notes in Physics

Volume 874

For further volumes:
http://www.springer.com/series/5304

The Lecture Notes in Physics

The series Lecture Notes in Physics (LNP), founded in 1969, reports new developments in physics research and teaching—quickly and informally, but with a high quality and the explicit aim to summarize and communicate current knowledge in an accessible way. Books published in this series are conceived as bridging material between advanced graduate textbooks and the forefront of research and to serve three purposes:

- to be a compact and modern up-to-date source of reference on a well-defined topic
- to serve as an accessible introduction to the field to postgraduate students and nonspecialist researchers from related areas
- to be a source of advanced teaching material for specialized seminars, courses and schools

Both monographs and multi-author volumes will be considered for publication. Edited volumes should, however, consist of a very limited number of contributions only. Proceedings will not be considered for LNP.

Volumes published in LNP are disseminated both in print and in electronic formats, the electronic archive being available at springerlink.com. The series content is indexed, abstracted and referenced by many abstracting and information services, bibliographic networks, subscription agencies, library networks, and consortia.

Proposals should be sent to a member of the Editorial Board, or directly to the managing editor at Springer:

Christian Caron
Springer Heidelberg
Physics Editorial Department I
Tiergartenstrasse 17
69121 Heidelberg/Germany
christian.caron@springer.com

M. Yu. Kagan

Modern Trends in Superconductivity and Superfluidity

Springer

M. Yu. Kagan
Theoretical Department
P.L. Kapitza Institute for Physical Problems
of Russian Academy of Sciences
and Moscow State Institute of Electronics
and Mathematics
National Research University
Higher School of Economics
Moscow
Russia

ISSN 0075-8450 ISSN 1616-6361 (electronic)
ISBN 978-94-007-6960-1 ISBN 978-94-007-6961-8 (eBook)
DOI 10.1007/978-94-007-6961-8
Springer Dordrecht Heidelberg New York London

Library of Congress Control Number: 2013943720

Printed on acid-free paper

Springer is part of Springer Science+Business Media (www.springer.com)

Preface

The idea to write this book came to my mind after two advanced lecture courses which I have read in summer semesters of the year 2010 as Leverhulme visiting professor in Loughborough University UK and of the year 2011 as a visiting professor in LTPMS-Orsay (associated with the University Paris-Sud).

The first Chapters of this book had the approbation during 16 years of my pedagogical work as a Professor on Galitskii chair of Theoretical Nuclear Physics in Moscow Engineering Physical Institute and during autumn semester of the year 1994 in the University of Amsterdam.

The course is based on the original research work where I actively participated and contributed as a principal scientist and a group leader in P.L. Kapitza Institute for Physical Problems in Moscow during 30 years of my scientific career. It includes the set of eight lectures and eight seminars which cover several important topics of the modern condensed matter physics, namely:

- Quantum hydrodynamics of fermionic and bosonic superfluids and supersolids;
- BCS-BEC crossover in ultracold quantum gases;
- Non-phonon mechanisms of superconductivity in high-T_C materials and other unconventional superconductors;
- Nanoscale phase separation in CMR-materials, heavy-fermions, and other strongly correlated electron systems;
- Mesoscopic electron transport in multi-band and phase-separated metallic and oxide compounds.

I hope the book will be useful for undergraduate students of the senior courses, postgraduate students, and postdocs specializing in solid-state and low-temperature physics.

I am very grateful to my teachers, colleagues and pupils, first of all to A. S. Alexandrov, A. F. Andreev, A. G. Aronov, S. Balibar, M. A. Baranov, H. Beck, J. G. Bednorz, I. V. Brodsky, P. Brussard, H. W. Capel, H. Capellman, M. Capezzalli, R. Combescot, A. V. Chubukov, V. N. Devyatko, D. V. Efremov, M. A. Efremov, I. A. Fomin, R. Fresard, G. Frossati, P. Fulde, B. Halperin, Yu. A. Izumov, V. V. Kabanov, Yu. Kagan, L. V. Keldysh, A. V. Klaptsov, Yu. V. Kopaev, K. I. Kugel, D. I. Khomskii, Yu. A. Kosevich, F. V. Kusmartsev, A.V. Kuznetsov, A. I. Larkin, N. P. Laverov, Yu. E. Lozovik, I. M. Lifshitz,

S. Maekawa, M. S. Mar′enko, B. E. Meierovich, A. P. Menushenkov, M. Mezard, P. Nozieres, S. L. Ogarkov, V. M. Osadchiev, A. V. Ozharovskii, A. Ya. Parshin, L. P. Pitaevskii, N. M. Plakida, F. Pobell, N. V. Prokof'ev, A. M. M. Pruisken, A. L. Rakhmanov, T. M. Rice, G. Sawatzky, A. O. Sboychakov, T. Schneider, G. V. Shlyapnikov, S. Stringari, V. V. Val′kov, C. M. Varma, D. Vollhardt, G. E. Volovik, J. T. M. Walraven, G. Wendin, Ch. van Weert, P. Wölfle, and Ya. B. Zeldovich, who encouraged me to start writing this book and greatly improved its quality during our intensive scientific collaboration, numerous and sometimes very hot discussions both in Moscow and abroad. I am also very grateful to my family for their patience during the work on this book and acknowledge very important technical support from my assistants M. M. Markina and A. M. Padokhin.

Moscow, November 2013 M. Yu. Kagan
Corresponding Member of Russian Academy of Sciences
Principal scientist in P.L. Kapitza Institute for Physical Problems

and

Professor of Physics in Moscow
State Institute of Electronics and Mathematics,
National Research University
Higher School of Economics

Contents

Part I

Introduction

The subjects of superconductivity and magnetism, superfluidity and BCS-BEC crossover are very dynamically developing fields of condensed matter physics with very intensive exchange of ideas between them.

The main idea of the present manuscript is to consider these closely related phenomena in a coherent fashion and to show how the achievements in one of the fields enrich the other and vice versa. I would also like to demonstrate the results obtained in these fields both in Moscow and at the West during last 30 years.

The book is based on the results of my group at Theoretical Department of Kapitza Institute as well as other groups and on advanced lecture courses which I have read in Moscow Engineering Physical Institute, in the Amsterdam University, Loughborough University, and LPTMS-Orsay associated with the University Paris Sud in the period of 1994–2011.

I tried to include in the book space of the most interesting ideas worked out in the end of twentieth century and very recently and thus bridge different communities working in solid state and low-temperature physics.

The book consists of 4 Parts and 16 Chapters. In the first part, I describe the recent developments in superfluid hydrodynamics of quantum fluids and solids including a very hot subject of possible supersolidity in quantum crystals of ^{4}He. There are several other interesting topics considered in this part. Among them is the nature of the roughening transition on the phase-interface between quantum crystal and a superfluid, as well as a spectrum of weakly damped melting-crystallization waves, which can exist and were experimentally measured on a mobile rough phase-interface between solid and superfluid ^{4}He in the conditions of thermodynamic equilibrium on the phase boundary.

In Chap. 1, we start with general Landau scheme of the conservation laws for the hydrodynamics of classical liquids and of the superfluids. On the basis of Landau scheme, we consider the hydrodynamics of rotating superfluids with large number of quantized vortices. We study different regimes of rotations in the presence of Feynman-Onsager triangular vortex lattice, which we call hydrodynamics of slow and fast rotations, respectively. In connection with dilute Bose gases in rotating magnetic traps, we also consider the situation when the vortex

lattice is melted or almost melted and we have a transition from a vortex lattice phase to a phase of vortex liquid.

The subjects of possible supersolidity in quantum crystals and melting-crystallization waves on the mobile phase-interface between quantum crystall and quantum liquid are presented in Chaps. 2 and 3, respectively. We discuss here also the Andreev–Lifshitz theory for quantum crystals, which is based on the large values of Lindemann and de Boer parameters, as well as recent experimental results of Chan et al., on the possible observation of the non-classical moment of inertia in rotating experimental cell loaded with solid ^{4}He.

Discussing in these chapters the surface science, we present the ideas of Nozieres on the Berezinskii–Kosterlitz–Thouless type of roughening transition in solid ^{4}He as well as Andreev–Parshin ideas of quantum roughening due to delocalization of the 2D gas of kinks on the rough interface at low temperatures.

In Chap. 4, we consider a complicated and yet unresolved problem of chiral anomaly in superfluid ^{3}He-A and present two competing approaches for this interesting topic. The first one is based on the inclusion of a fermionic goldstone mode connected with zeroes of superfluid gap in the hydrodynamical scheme in the framework of the superhydrodynamics. Another one is based on a formal analogy between Bogoliubov-De Gennes equations for quasiparticles in ^{3}He-A and Dirac equation in quantum electrodynamics. We invite experimentalists to measure the spectrum and damping of orbital waves in ^{3}He-A at low temperatures and in this way to help theorists to improve their understanding of the complicated subject of orbital hydrodynamics.

The second part of the book also contains the four Chaps. 5–8. In this part, I review the recent progress in the field of BCS-BEC crossover in quantum Fermi-Bose gases and mixtures and show the analogy between the mechanism of BCS-BEC crossover in gases and in underdoped high-T_C superconductors.

In Chap. 5, I present the introduction to the subject of Bose–Einstein condensation in ultracold bosonic gases in the restricted geometry of the magnetic traps. In the second part of the chapter, I discuss the Feshbach effect which yields experimental possibilities to study BCS-BEC crossover between extended Cooper pairs and local pairs (or molecules) in ultracold fermionic gases.

In Chap. 6, I study composed fermions and bosons which correspond to the different bound states (molecules) consisting of two fermions, two bosons, and fermion and boson in ultracold quantum gases and mixtures. I also elucidate the exact solutions of the Skorniakov-Ter Martirosian integral equations for the binding energies of the more sophisticated complexes consisting of three and four resonantly interacting particles. We determine as well the atom-molecule and the molecule–molecule scattering amplitudes in the resonance Fermi-gas.

In Chap. 7, I present the basic ideas of Nozieres–Schmitt-Rink and Leggett theory on BCS-BEC crossover and construct the phase-diagrams for the s-wave and p-wave resonance Fermi gases in 3D and 2D case. In the last case, we discuss also the point of the possible topological quantum phase transition which appears on the phase diagram of p-wave superfluid with the symmetry of A1-phase. I also illustrate the Bogoliubov-Anderson and Galitskii-Vaks-Larkin schemes for

studying the spectrum of collective excitations in superfluid resonance Fermi gases with s-wave and p-wave pairing and determine the spectrums of sound waves and orbital waves both in BCS and BEC regimes.

In Chap. 8, we study the models with short-range attraction between fermions and discuss the interesting physics of the pseudogap actual for high-T_C superconductivity as well as a new interesting phase of a normal bosonic metal which arises in these models. We also discuss the scenario of Fermi-Bose mixture to explain superconducting and normal properties in another interesting superconducting family of plumbates-bismuthates where the local pairing is established due to the requirements of "valence skipping" in these compounds.

The third part of the manuscript is devoted to non-phonon mechanisms of superconductivity and first of all to the famous Kohn-Luttinger mechanism of superconductivity in purely repulsive Fermi-systems. It contains the five Chaps. 9–13.

In Chap. 9, I present the basic ideas of Kohn-Luttinger. I show that the presence of Kohn's anomaly (of the Friedel oscillations) in the effective interaction between two fermions via the polarization of the fermionic background leads to superconductive p-wave pairing in purely repulsive Fermi-gas or Hubbard model at low electron density both in 3D and 2D cases.

In Chap. 10, we show that the critical temperature of superconductive pairing can be strongly increased already at low electron density in the presence of the external magnetic field or in the two-band situation.

In Chaps. 11 and 12, we apply the ideas of Kohn–Luttinger to the problem of the search of fermionic superfluidity in ^{3}He–^{4}He and ^{6}Li–^{7}Li mixtures, as well as in the gas of neutral particles (such as fermionic ^{6}Li) in the magnetic traps at low and ultralow temperatures. We also search for the new phase of superfluid ^{3}He different from traditional A and B phases in non-polarized and strongly spin-polarized case.

In Chap. 13, we discuss the ideas of spin-charge separation and spin-charge confinement in quasi-1D ladder materials and in quasi-2D high-T_C superconductors. We discuss the superconducting phase-diagram of high-T_C superconductors in the framework of the popular nowaday t-J model and show that in the optimally doped case, we can have d-wave superconducting pairing with a high T_C of the order of 100 K. We also propose a possible scenario of BCS-BEC crossover in the d-wave channel for pairing of two composite holes (two strings or two spin polarons) in the underdoped high-T_C materials.

Finally in the last part of the manuscript, I search for marginal non-Fermi-liquid behavior and anomalous temperature dependence of the resistivity in the normal state of low density superconductors. I reveal here also the tendency toward nanoscale phase separation in the normal state of cuprates and CMR systems. Effectively this part serves as a bridge between the physics of strongly correlated electron systems and magnetism from one hand and the physics of mesoscopic quantum phenomena and localization from the other. Part 4 contains three Chaps. 14–16.

In Chap. 14, I search for marginal non-Fermi liquid behavior in the normal state of low density Fermi-systems in 3D and 2D case. I also discuss electron polaron effect and anomalous resistivity in the two band model with one narrow band due to strong heavy-mass enhancement and localization corrections for scattering of light particles on the heavy ones.

In Chap. 15, I reveal the similarities between high-T_C cuprates and manganites, which exhibit the phenomenon of colossal magnetoresistance. Both families of strongly correlated materials have a pronounced tendency to the formation of inhomogeneous states and in particular to nanoscale phase-separation corresponding to the state with small ferromagnetic or paramagnetic metallic droplets inside antiferromagnetic or charge-ordered insulating matrices.

Finally in Chap. 16, I discuss anomalous tunneling conductivity, tunneling magnetoresistance, and the spectrum of 1/*f*-noise in the non-metallic phase-separated state which are connected with the electron tunneling from one metallic cluster (or droplet) to a neighboring one via an insulating barrier. I present here the experimental results of several groups confirming the proposed tunneling model.

In conclusion, I discuss the interesting unresolved problems which still exist in the modern condensed matter physics and encourage the young researchers to continue their careers in this fascinating field.

I hope this book will be useful for undergraduate students of senior courses as well as for postgraduate students, postdocs, and active researchers specializing in a solid state and low-temperature physics.

Part I

Chapter 1
Hydrodynamics of Rotating Superfluids with Quantized Vortices

While many forthcoming Chapters of the present manuscript deal with the microscopical models for the description of Quantum Gases, Fluids and Solids, as well as strongly correlated electron systems, the first four Chapters are devoted to a purely phenomenological (macroscopic) description of hydrodynamic phenomena in anisotropic and inhomogeneous superfluids and superconductors.

The presentation in these Chapters is based on Landaus' ideas. Let us stress that Landau theory of hydrodynamics [1–5] based on the conservation laws in the differential form (together with Quantum Mechanics [6] and Statistical Physics [7]) is one of the masterpieces of Landau-Lifshitz course of the Theoretical Physics. While the essence of this theory is well known (serves as a mother's milk) to Russian researchers from the first steps of their scientific career, in the West many young physicists, specializing on microscopic models, do not have a deep background in this subject. A good style meanwhile is to know fluently both microscopics and phenomenology from our point of view.

That is why from the pedagogical reasons we decided to start the present Chapter with brief description (in Sect. 1.1) of the Landau theory for hydrodynamics in classical [1–5] and superfluid [1–5, 8, 9] liquids. We present Landau scheme of the conservation laws for the description of slowly varying in space and time Goldstone (gapless) collective modes.

We will discuss Landau [1–5] (or Landau-Tisza [1–5, 10–13], as often referred to in the West) two-velocity superfluid hydrodynamics for ^{4}He [1–5, 8–13] which contains normal and superfluid velocities $\vec{v}_n$ and $\vec{v}_s$, as well as normal and superfluid densities ρ_{n} and ρ_{s}, thus describing both the normal and superfluid motion in helium [14–16]. We will derive the spectrum and damping of first and second sound in superfluid helium (in He-II). We will obtain $\omega = c_{\mathrm{I}}k$ and $\omega = c_{\mathrm{II}}k$ (the spectrum is linear for both waves) and compare the velocities c_{I} and c_{II} of these sound waves. We will stress that while in first sound total mass-current $\vec{j} = \rho_s\vec{v}_s + \rho_n\vec{v}_n \neq 0$, in the second sound wave $\vec{j} = 0$ but the relative velocity $\vec{W} = \vec{v}_n - \vec{v}_s \neq 0$.

In Sect. 1.2 we proceed to the hydrodynamics of rotating superfluids with a large number of quantized vortices. We start this Section with famous

M. Yu. Kagan, *Modern Trends in Superconductivity and Superfluidity*,
Lecture Notes in Physics 874, DOI: 10.1007/978-94-007-6961-8_1,

Andronikashvili experiments (on non-classical moment of inertia in rotating He-II) [17, 18] and discuss Feynmann-Onsager quantization of the vortex lines in superfluid helium [19–22]. We introduce the notion of first and second critical angular velocities of rotation Ω_{C1} and Ω_{C2} in helium and stress their correspondence with first and second critical magnetic fields H_{C1} and H_{C2} in type—II superconductors [23–26]. Than we will present the scheme of macroscopic averaging [27–30] for a large number of vortices and construct nonlinear elasticity theory for a 2D (triangular) vortex lattice in helium [31]. The linearization of this theory yields well-known Tkachenko modes [32–34] (which describe longitudinal and transverse oscillations of the vortex lattice), as well as Lord Kelvin (Thomson) bending oscillations of the vortex lines [35, 36]. We include dissipation in the system and discuss Hall-Vinen friction coefficients β and β' [37–41] for the scattering of normal component on the vortex lattice. In the end of Sect. 1.2 we will construct the complete system of equations (which describe hydrodynamics of slow rotations [31, 42]) based on the Landau scheme of the conservation laws. We will discuss briefly another elegant method to derive a system of hydrodynamic equations based on Poisson brackets [43] and emphasize, nevertheless, the advantages of Landau method especially in nonlinear regime.

In the Sect. 1.3 we consider the different limit for hydrodynamics of fast rotating superfluid. In this case due to Umklapp processes [23, 44] the normal excitations are bound to vortex lattice, and hence the normal and superfluid velocities perpendicular to the vortex lines coincide $\vec{v}_{n\perp} = \vec{v}_{s\perp}$. In the same time in the direction parallel to the vortex lines due to translational invariance $\vec{v}_{n||} \neq \vec{v}_{s||}$. Thus we have one-velocity motion in the plane of the vortex lattice $\vec{v}_{\perp} = \vec{j}_{\perp}/\rho$ and two-velocity motion parallel to the vortex lines. Hence we are in a strongly anisotropic situation where we have a crystal in the plane of the vortex lattice and a standard superfluid in the direction perpendicular to the lattice and parallel to the vortex lines. We will construct the full system of hydrodynamic equations for a regime of rapid rotations and analyze the spectrum and damping of collective excitations (first of all of a second sound mode) in this regime. We will get that the spectrum is linear and sound wave can freely propagate only along the vortex lines where $\vec{W}_{\parallel} = \vec{v}_{n\parallel} - \vec{v}_{s\parallel} \neq 0$, while the spectrum is overdamped in the perpendicular direction. More specifically for $k_{\perp} = 0$ the spectrum reads $\omega^2 = c_{II}^2 k_z^2$, while for $k_z = 0$: $\omega = -\frac{i\kappa_{\perp} k_{\perp}^2}{C_p}$ [31], where $\kappa_{\perp}$ is heat conductivity in the direction perpendicular to the vortex lines, C_p is a specific heat and k_z, $k_{\perp}$ are the components of the $\vec{k}$-vector along and perpendicular to the vortex lines, respectively.

In the Sect. 1.4 we consider an opposite case of a single bended line. Here, as shown by Lord Kelvin, the spectrum for the bending oscillations is almost quadratic $\omega = \frac{k_z^2}{2m} \ln \frac{1}{dk_z}$ [23, 35, 36] (d is a normal vortex core, which in the case of superfluid ^{4}He is of the order of the interatomic distance). Naive considerations show that such quasi 1D system (as a bended vortex line) should be completely destroyed by the thermal fluctuations and experience in analogy with the biophysical systems a phase-transition to the state of a globule [23]. We show,

however, that in fact [31] the bending oscillations correspond to rotation: $\vec{u} \times \dot{\vec{u}} \neq 0$, where $\vec{u}$ and $\dot{\vec{u}}$ are respectively a local displacement of the bended vortex from a nondeformed position and its time derivative (local velocity). Thus the quanta of the bending oscillations in fact have the rotation moment $(-\hbar)$ (diamagnetic situation) and hence the gap $\hbar\Omega$ appears in their spectrum. This gap stabilizes the fluctuations of this 1D system providing a finite ratio $\sqrt{\langle \vec{u}^2 \rangle / R^2} \ll 1$ of a mean square displacement $\langle \vec{u}^2 \rangle$ to the radius squared R^2 of the rotating vessel with helium. It is a reason why a regular (triangular) vortex lattice can be directly visualized (the photograph of the lattice with small vortex displacements can be obtained) in the experiments of Packard et al. [86–88].

We conclude the Chapter with the discussion in Sect. 1.5 how we can realize the hydrodynamics of fast rotations at not very high frequencies $\Omega \ll \Omega_{C2}$ (note that the second critical angular velocity Ω_{C2} is very high in superfluid ^{4}He). We propose to use for that regime ^{4}He-^{3}He mixtures, where ^{4}He is superfluid and has a large number of vortices. In this case according to the Bernoulli law [1–5] $\mu + \frac{v_s^2}{2} = const$ all the ^{3}He impurities will be driven by the gradient of the pressure (∇p) to the vortex core and organize inside the core the quasi 1D normal component with a free motion only along the vortex lines. This is just a desirable regime of rapid rotations which we discuss in Sect. 1.2. Another possibility is to use an isotropic triplet phase (B-phase) of superfluid ^{3}He [45, 46] where we can make the Umklapp processes very effective already at moderate rotation frequencies [31]. We stress that a recent revival of interest to the rotating superfluids with large number of vortices is connected with the intensive experimental and theoretical studies of rotating Bose-condensates in the restricted geometry of magnetic traps in ultracold gases and mixtures [47]. We will discuss the most important results in this field especially those connected with the possible melting of the vortex lattice [27–30, 47–62] in Sect. 1.2.6.

1.1 The Foundation of Landau Theory for Superfluid Hydrodynamics

We will start this Section with a brief description of Landau approach to the hydrodynamics of the classical liquid.

1.1.1 The Essence of the Hydrodynamics. Description of the Goldstone Modes

Generally speaking, hydrodynamics is a science which describes all *slowly-varying* in space and time processes in the liquid (the elasticity theory does the same in

the solid [63]). For these processes in momentum space a frequency $\omega \to 0$ when the wave-vector $\vec{k} \to 0$. Thus hydrodynamics describes all low-lying gapless (*Goldstone*) modes.

Moreover, hydrodynamics assumes local thermodynamic equilibrium (equilibrium in small volume), so we can adopt reduced description of the system [7] and introduce finite number of local variables. For ordinary liquid (with one velocity $\vec{v}$) the canonical variables in Landau scheme are $\rho(\vec{r},t)$—density; $\vec{j}(\vec{r},t)$—density of linear momentum, and $S(\vec{r},t)$—entropy of the unit volume.

1.1.2 Landau Scheme of the Conservation Laws. Euler Equation

According to Landau the system of equations for classical liquid contains an equation for mass-conservation:

$$\frac{\partial \rho}{\partial t} + \vec{\nabla} \cdot \vec{j} = 0, \ \vec{j} = \rho \vec{v}, \tag{1.1.1}$$

an equation for linear momentum conservation:

$$\frac{\partial j_i}{\partial t} + \frac{\partial}{\partial x_k}(\Pi_{ik}) = 0, \tag{1.1.2}$$

Π_{ik} is momentum flux (in ideal dissipationless liquid $\Pi_{ik} = \rho v_i v_k + p\delta_{ik}$; p—is pressure), and an equation for entropy increase:

$$\frac{\partial S}{\partial t} + \vec{\nabla} \cdot \left(S\vec{v} + \frac{\vec{q}}{T} \right) = \frac{R}{T}, \tag{1.1.3}$$

where $R \geq 0$ is positively defined dissipative function, $\vec{q}$ is dissipative entropy flux, T is temperature (in ideal liquid $R = 0$ and $\vec{q} = 0$). Note that if we take into account only one source of dissipation connected with the heat flux, then $\vec{q} = -\kappa \vec{\nabla} T$ (κ is heat conductivity) and correspondingly the dissipative function $R \sim \kappa \frac{(\vec{\nabla} T)^2}{T} > 0$ is quadratic in gradients. In general case in Eqs. (1.1.2) and (1.1.3) in the expression for Π_{ik} and R enter also viscous contributions $\pi_{ik} = \Pi_{ik}^{dis} = \eta\left(\frac{\partial v_i}{\partial x_k} + \frac{\partial v_k}{\partial x_i} - \frac{2}{3}\delta_{ik}\vec{\nabla} \cdot \vec{v}\right) + \xi \delta_{ik} \vec{\nabla} \cdot \vec{v}$, where η and ξ are viscosity coefficients (ξ is often called second viscosity) and accordingly $R \sim \pi_{ik} \frac{\partial v_i}{\partial x_k}$.

The system of 3 equations for $\partial\rho/\partial t, \partial j_i/\partial t$ and $\partial S/\partial t$ (1.1.1–1.1.3) are consistent with an equation of total energy conservation:

$$\frac{\partial E}{\partial t} + \vec{\nabla} \cdot \vec{Q} = 0. \tag{1.1.4}$$

While deriving (1.1.4) we can use the Galilean invariance and introduce the internal energy E_0 in the reference frame K_0 (where the liquid is at a rest) according to:

$$E = E_0 + \rho\frac{\vec{v}^2}{2} = E_0 + \frac{\vec{j}^2}{2\rho}\,. \tag{1.1.5}$$

In Eq. (1.1.4) $\vec{Q}$ is an energy flux. In an ideal dissipationless liquid:

$$\vec{Q} = \left(W + \rho\frac{v^2}{2}\right)\vec{v}, \tag{1.1.6}$$

where $W = E_0 + P$ is the density of the enthalpy (the enthalpy of the unit volume). To get (1.1.4) with $\vec{Q}$ from (1.1.6) we should utilize the thermodynamic identity for internal energy:

$$dE_0 = TdS + \mu d\rho, \tag{1.1.7}$$

where μ is the chemical potential, and use the expression for pressure:

$$P = TS + \mu\rho - E_0 = W - E_0. \tag{1.1.8}$$

From the expression (1.1.8) we get:

$$dP = SdT + \rho d\mu \tag{1.1.9}$$

1.1.2.1 Euler Equation

From Eq. (1.1.2) for linear momentum conservation and Eq. (1.1.1) for mass-conservation we can get for an ideal dissipationless liquid:

$$\frac{\partial\vec{v}}{\partial t} + \left(\vec{v}\cdot\vec{\nabla}\right)\vec{v} + \frac{1}{\rho}\vec{\nabla}p = 0\,. \tag{1.1.10}$$

It is a famous Euler equation for an ideal classical liquid. At zero temperature ($T = 0$) we can rewrite (1.1.10) as:

$$\frac{\partial\vec{v}}{\partial t} + \vec{\nabla}\left(\mu + \frac{v^2}{2}\right) = \vec{v}\ \times\left(\vec{\nabla}\times v\right), \tag{1.1.11}$$

1.1.2.2 Potential Irrotational Flows

Note that for $\vec{\nabla}\times\vec{v} = 0$ we have so-called potential (irrotational) flows. In this case:

$$\frac{\partial\vec{v}}{\partial t} + \vec{\nabla}\left(\mu + \frac{v^2}{2}\right) = 0, \tag{1.1.12}$$

Correspondingly we can represent velocity as a gradient of some scalar potential $\vec{v} = \vec{\nabla}\varphi$.

For stationary potential flows $\frac{\partial \vec{v}}{\partial t} = 0$ and $\vec{\nabla}\left(\mu + \frac{v^2}{2}\right) = 0$. Thus

$$\mu + \frac{v^2}{2} = const, \tag{1.1.13}$$

This equation is often called Bernoulli equation (see [1–5]).

1.1.3 Sound Waves in Classical Liquid. Damping of Sound Waves

Linearizing the system of Eqs. (1.1.1–1.1.3) for an ideal (dissipationless) liquid we get the following set of equations:

$$\frac{\partial \delta\rho}{\partial t} + \rho_0 \vec{\nabla} \cdot \vec{v} = 0,]] > \tag{1.1.14}$$

$$\rho_0 \frac{\partial \vec{v}}{\partial t} + \vec{\nabla}\delta P = 0, \tag{1.1.15}$$

$$\frac{\partial \delta S}{\partial t} + S_0 \vec{\nabla} \cdot \vec{v} = 0, \tag{1.1.16}$$

where $\delta\rho$, δP and δS are slowly varying and small (in amplitude) deviations of density, pressure and entropy from equilibrium values in the sound wave. Thus $\rho(\vec{r}, t) = \rho_0 + \delta\rho(\vec{r}, t)$ with $|\delta\rho| \ll \rho_0$ and so on. We also assume that the velocity $\vec{v}$ in the sound wave is small $\vec{v} = \delta\vec{v}(\vec{r}, t)$. In fact it is a condition $v \ll c$, where c is sound velocity, which is required.

In ideal liquid all the motions are adiabatic. It means that the entropy of unit mass $S_M = S/\rho =$ const (where S is an entropy of unit volume). Thus δS in Eq. (1.1.16) yields $\delta S = S_M \delta\rho$ and Eq. (1.1.16) for entropy becomes equivalent to Eq. (1.1.14) for density. Moreover the pressure $P = TS + \mu\rho - E_0 = T\rho S_M + \mu\rho - E_0$ (which in general case is the function of S_M and ρ) for adiabatic sound wave is a function only of ρ. Thus for small deviations of pressure from equilibrium values $\delta P = \left(\frac{\partial P}{\partial \rho}\right)_{S_M} \delta\rho$, where by its definition we can introduce the sound velocity squared as:

$$c^2 = \left(\frac{\partial P}{\partial \rho}\right)_{S_M} \text{ and } \delta P = c^2 \delta\rho \tag{1.1.17}$$

Correspondingly we can rewrite Eq. (1.1.15) as:

$$\rho_0 \frac{\partial \vec{v}}{\partial t} + c^2 \vec{\nabla}\delta\rho = 0 \tag{1.1.18}$$

If we take the time derivative $(\partial/\partial t)$ from Eq. (1.1.14) for density and space derivative $(\vec{\nabla})$ from Eq. (1.1.15) for linear momentum, we will get:

$$\frac{\partial^2 \delta\rho}{\partial t^2} + \rho_0 \vec{\nabla} \cdot \dot{\vec{v}} = 0, \tag{1.1.19}$$

$$\rho_0 \vec{\nabla} \cdot \dot{\vec{v}} + c^2 \Delta \delta\rho = 0, \tag{1.1.20}$$

where Δ is an operator of Laplacian.

Substitution of (1.1.20) into (1.1.19) finally yields:

$$\frac{\partial^2 \delta\rho}{\partial t^2} - c^2 \Delta \delta\rho = 0. \tag{1.1.21}$$

If we assume that $\delta\rho$ varies in a monochromatic sound wave $\delta\rho \sim e^{-i\omega t + i\vec{k}\vec{r}}$ we will get for the spectrum:

$$\omega^2 = c^2 k^2. \tag{1.1.22}$$

Thus the sound spectrum is linear as expected. It corresponds to compressible liquid where $\delta\rho \neq 0$ and $\vec{j} \neq 0$.

1.1.3.1 Damping of the Sound Waves

The damping of sound in hydrodynamic theory is given by higher gradients connected with dissipative terms in the system of Eqs. (1.1.1–1.1.3). The spectrum with an account of damping reads [1–5]:

$$\omega = ck + i\gamma, \tag{1.1.23}$$

where

$$\gamma = \frac{\omega^2}{2\rho c^2}\left\{\left(\frac{4}{3}\eta + \xi\right) + \kappa\left(\frac{1}{C_V} - \frac{1}{C_P}\right)\right\}, \tag{1.1.24}$$

η and ξ are coefficients of first and second viscosity, κ is heat conductivity, C_P and C_V are specific heat at constant pressure and constant volume [7]. We can see that the damping $\gamma \sim \omega^2$ and thus it is small for $\omega \to 0$. Moreover in hydrodynamics (collisional) theory we can write $\gamma \approx \omega^2\tau = c^2k^2\tau$ and

$$\gamma/\omega \approx \omega\tau \ll 1, \tag{1.1.25}$$

where we introduced a characteristic (scattering) time τ. Note that if we consider the damping due to the presence of the first viscosity η and take into account a simple estimate from the kinetic theory [64] $\eta \sim \rho l\bar{v} \sim \rho\bar{v}^2\tau$, than $\gamma \sim \frac{\omega^2\eta}{\rho c^2} \sim \frac{\bar{v}^2}{c^2}\omega^2\tau$ and indeed $\gamma/\omega \sim \frac{\bar{v}^2}{c^2}\omega\tau$, where $\tau = l/\bar{v}$ is a scattering time, l is a length of the

mean-free path and $\bar{v}$ is the thermal (average) velocity (in Boltzman molecular gas, for example). Note that in Boltzman gas $c^2 \sim \bar{v}^2$ and hence $\gamma \sim \omega^2 \tau$.

We can conclude that hydrodynamic description (with the small damping and the propagating sound waves) is valid for small frequencies $\omega\tau \ll 1$ or, correspondingly, for small wave-vectors $kl \ll 1$. For larger frequencies $\omega\tau \gg 1$ we are in a ballistic (or Knudsen) regime (see for example Physical Kinetics [64]). In this regime we should start our theoretical analysis with a good kinetic equation in classical or degenerate case (see Chap. 16) and derive the dynamic equations in the collisionless (ballistic) regime.

1.1.3.2 Equation for Heat Conductivity. Overdamped Temperature Waves

Let us analyze now Eq. (1.1.3) for the entropy increase. In the absence of the drift velocity (for the liquid at a rest) $\vec{v} = 0$ and Eq. (1.1.3) reads:

$$\frac{\partial S}{\partial t} + \vec{\nabla} \cdot \left(\frac{\vec{q}}{T} \right) = \frac{R}{T}, \tag{1.1.26}$$

where $\vec{q} = -\kappa \vec{\nabla} T$ is a heat flux, κ is heat conductivity, T is temperature, and R is dissipative function.

If we are interested in small entropy and temperature deviations from the equilibrium values, having in mind temperature waves, we can linearize (1.1.22). After linearization we get:

$$\frac{\partial \delta S}{\partial t} - \frac{\kappa}{T_0} \Delta \delta T = 0, \tag{1.1.27}$$

where the entropy S and temperature T are given by: $S = S_0 + \delta S(\vec{r}, t)$ and $T = T_0 + \delta T(\vec{r}, t)$. To find the spectrum of the temperature waves (which will be overdamped as we will see soon) we should express $\frac{\partial \delta S}{\partial t}$ in (1.1.23) via the time derivative of the temperature $\frac{\partial \delta T}{\partial t}$.

For almost incompressible fluid (which is a legitimate approximation in this case) $\delta S = \rho \delta S_M$, where S_M is an entropy of a unit mass. Assuming that correct thermodynamic variables for mass entropy S_M are p—pressure and T—temperature, and, moreover that we can put $p = \text{const}$ in temperature waves (see Ref. [1], Sect. 1.3, and Chap. 3), we can represent the time derivative:

$$\frac{\partial \delta S}{\partial t} \approx \rho \frac{\partial \delta S_M}{\partial t} \approx \rho \left(\frac{\partial S_M}{\partial T} \right)_P \frac{\partial \delta T}{\partial t} = \frac{\rho C_P}{T_0} \frac{\partial \delta T}{\partial t}, \tag{1.1.28}$$

where $C_p = T_0 \left(\frac{\partial S_M}{\partial T} \right)_p$ is specific heat at constant pressure (see Refs. [1, 7], Sect. 1.3, and Chap. 3).

Correspondingly Eq. (1.1.23) reads:

$$\frac{\rho C_P}{T_0} \frac{\partial \delta T}{\partial t} - \frac{\kappa}{T_0} \Delta \delta T = 0. \tag{1.1.29}$$

Equation (1.1.25) is a famous equation for the heat conductivity (or a Fourier equation as mathematicians often call it). For the monochromatic temperature wave $\delta T \sim e^{-i\omega t + i\vec{q}\vec{r}}$ we get:

$$i\omega = \frac{\kappa}{\rho C_P} q^2 \text{ or } \omega = -i\frac{\kappa}{\rho C_P} q^2. \tag{1.1.30}$$

Thus we conclude that the spectrum of the temperature waves in a classical liquid is overdamped and quadratic in the wave-vector q.

1.1.4 Rotational Fluid. Vorticity Conservation. Inertial Mode

If $\vec{\nabla} \times \vec{v} \neq 0$ we can take curl from l.h.s and r.h.s. of the Euler equation (1.1.11). Then we get:

$$\frac{\partial\left(\vec{\nabla} \times \vec{v}\right)}{\partial t} = \vec{\nabla} \times \left(\vec{v} \times \left(\vec{\nabla} \times \vec{v}\right)\right), \text{ or } \frac{\partial \vec{\omega}}{\partial t} = \vec{\nabla} \times (\vec{v} \times \vec{\omega}), \tag{1.1.31}$$

where $\vec{\omega} = \vec{\nabla} \times \vec{v}$. This equation is an equation for vorticity conservation. Note that for solid-state rotation $\vec{v} = \vec{\Omega} \times \vec{r}$ and hence $\vec{\omega} = \vec{\nabla} \times \vec{v} = 2\vec{\Omega}$, where $\vec{\Omega}$ is an angular frequency of rotation.

1.1.4.1 Inertial Mode in Classical Fluid

Let us consider uniformly rotating liquid with an angular velocity $\vec{\Omega}$ and find the spectrum $\omega(k)$ in rotation frame for small variations of the velocity field $\vec{v} = \vec{\Omega} \times \vec{r} + \delta\vec{v}(\vec{r}, t)$ on top of solid-state rotation. Let us consider an incompressible fluid. Then $\vec{\nabla} \cdot \vec{v} = \vec{\nabla} \cdot \delta\vec{v}(\vec{r}, t) = 0$. Correspondingly $\vec{\nabla} \times \vec{v} = 2\vec{\Omega} + \vec{\nabla} \times \delta\vec{v}(\vec{r}, t)$. The linearization of Euler equation with an account of the thermodynamic identity $\frac{1}{\rho}\vec{\nabla}P = \vec{\nabla}\mu$ reads:

$$\left\{\frac{\partial}{\partial t} + \left(\vec{v}_0 \cdot \vec{\nabla}\right) - \vec{\Omega}x\right\}\delta\vec{v} + \frac{1}{\rho_0}\vec{\nabla}\left(P - \rho\frac{\left(\vec{\Omega} \times \vec{r}\right)^2}{2}\right) + 2\vec{\Omega} \times \delta\vec{v} = 0 \tag{1.1.32}$$

where $\vec{v}_0 = \vec{\Omega} \times \vec{r}$ is a linear velocity of solid-state rotation. Note that in curly brackets in the l.h.s. of Eq. (1.1.32) stands the operator which transforms the time derivative of the vector $\delta\vec{v}$ to the rotation frame. Thus

$$\frac{\partial\delta\vec{v}}{\partial t'} + \frac{1}{\rho_0}\vec{\nabla}\left(P - \rho\frac{\left(\vec{\Omega} \times \vec{r}\right)^2}{2}\right) + 2\,\vec{\Omega} \times \delta\vec{v} = 0, \tag{1.1.33}$$

where operator $\partial/\partial t'$ refers to the rotation frame. In Eq. (1.1.33) we recognize a Coriolis force $2\vec{\Omega} \times \delta\vec{v}$ and a centrifugal force $\vec{\nabla}\left(\frac{(\vec{\Omega}\times\vec{r})^2}{2}\right)$ which are always present in the rotation frame. We can also introduce an effective pressure $P_{eff} = P - \rho\frac{(\vec{\Omega}\times\vec{r})^2}{2}$. Then

$$\frac{\partial\delta\vec{v}}{\partial t'} + \frac{1}{\rho_0}\vec{\nabla}P_{eff} + 2\vec{\Omega} \times \delta\vec{v} = 0 \tag{1.1.34}$$

Representing $P_{eff} = P_{0\,eff} + \delta P$ we get:

$$\frac{\partial\delta\vec{v}}{\partial t'} + \frac{1}{\rho_0}\vec{\nabla}\delta P + 2\vec{\Omega} \times \delta\vec{v} = 0. \tag{1.1.35}$$

Applying operator of curl to l.h.s. of (1.1.34) we get:

$$\frac{\partial}{\gamma}(\vec{\nabla} \times \delta\vec{v}) + 2\vec{\nabla} \times (\vec{\Omega} \times \delta\vec{v}) = 0. \tag{1.1.36}$$

If $\vec{\Omega} = \Omega\vec{e}_z$ than for $\vec{\nabla} \cdot \delta\vec{v} = 0$ we get $2\vec{\nabla} \times \left(\vec{\Omega} \times \delta\vec{v}\right) = -2\Omega\frac{\partial\delta\vec{v}}{\partial z}$ and

$$\frac{\partial}{\partial t'}\left(\vec{\nabla} \times \delta\vec{v}\right) - 2\Omega\frac{\partial\delta\vec{v}}{\partial z} = 0 \tag{1.1.37}$$

For the monochromatic wave $\delta\vec{v} \sim e^{-i\omega t + i\vec{k}\vec{r}}$

$$-i\omega\left(\vec{k} \times \delta\vec{v}\right) = ik_z 2\Omega\delta\vec{v}. \tag{1.1.38}$$

If we take a vector product with $\vec{k}$ of the l.h.s and the r.h.s. of (1.1.38) we get with an account of incompressibility condition $\vec{k}\,\delta\vec{v} = 0$

$$-i\omega k^2\delta\vec{v} = ik_z 2\Omega\left(\vec{k} \times \delta\vec{v}\right). \tag{1.1.39}$$

Comparing (1.1.38) and (1.1.39) we conclude that $-i\omega\left(\vec{k} \times \delta\vec{v}\right) = ik_z 2\Omega\frac{ik_z 2\Omega}{-i\omega k^2}\left(\vec{k} \times \delta\vec{v}\right)$ and correspondingly

$$\omega^2 k^2 = k_z^2 4\Omega^2. \tag{1.1.40}$$

Finally

$$\omega^2 = 4\Omega^2\frac{k_z^2}{k^2}, \text{ or } \omega = \frac{2(\vec{\Omega}\vec{k})}{k}. \tag{1.1.41}$$

This is a well-known inertial mode in an uncompressible ideal fluid. Note that it is a Goldstone mode for $k_z/k \to 0$ where $k^2 = k_z^2 + k_\perp^2$ and $\vec{k}_\perp = (k_x, k_y)$. Note also that the spectrum $\omega(k)$ in (1.1.41) is a spectrum in rotation frame.

Let us discuss compressible rotating fluid now. According to Sonin [39, 40] the spectrum in this case reads:

$$\omega^2 = 4\Omega^2 \frac{\omega^2 - c^2 k_z^2}{\omega^2 - c^2 k^2}. \tag{1.1.42}$$

The solution of this equation yields two branches for the spectrum:

$$\omega^2 = \frac{1}{2}\left(4\Omega^2 + c^2 k^2\right) \pm \left[\frac{1}{4}\left(4\Omega^2 + c^2 k^2\right)^2 - (2\Omega c k_z)^2\right]^{1/2}. \tag{1.1.43}$$

In a fluid at a rest (for $\Omega = 0$) $\omega_1 = ck$ and $\omega_2 = 0$. Thus we see that rotation adds a second mode with non-zero frequency to the sound mode. The reason for that according to Sonin is a Coriolis force: rotation makes the fluid rigid in the direction perpendicular to rotation axis.

We can distinguish two regimes in Eq. (1.1.43): the regime of large k-vectors $k > \frac{2\Omega}{c}$ (or almost incompressible liquid $c \to \infty$) and the regime of small k-vectors $k < \frac{2\Omega}{c}$.

In the regime of largez k-vectors the solution of (1.1.43) yields $\omega_1^2 = \frac{4\Omega^2 k_z^2}{k^2}$ for the inertial mode and

$$\omega_2^2 = c^2 k^2 + \left(\frac{2\Omega k_\perp}{k}\right)^2 \tag{1.1.44}$$

for the modified sound wave.

In the opposite limit of small k-vectors $k < \frac{2\Omega}{c}$ (compressible liquid, c is finite):

$$\omega_1^2 = 4\Omega^2 + c^2 k^2 \text{ and } \omega_2^2 = c^2 k_z^2. \tag{1.1.45}$$

Note that usually the space scale c/Ω in a liquid (like ^{4}He) is extremely large (of the order of hundreds of meters) and is not relevant to any real laboratory experiment where typical size of the container with rotating liquid is $0.1 \div 1$ cm. Thus the regime of small k-vectors where incompressibility condition fails is very difficult to realize experimentally.

1.1.5 Two-Velocity Hydrodynamics for Superfluid Helium. $\vec{v}_n$ and $\vec{v}_s$, ρ_n and ρ_s

Switching our considerations now to the hydrodynamics of a superfluid helium we should start from the well-known phase diagram of ^{4}He (see [1–5, 8–13, 19, 21, 65, 66, 67] and Fig. 1.1).

According to Kapitza at zero (and small) pressures and temperatures $T \approx 2.2$ K ^{4}He becomes superfluid. It has zero viscosity $\eta = 0$ and according to Landau [1–5] and Tisza [10–13] can be described by two-velocity hydrodynamics.

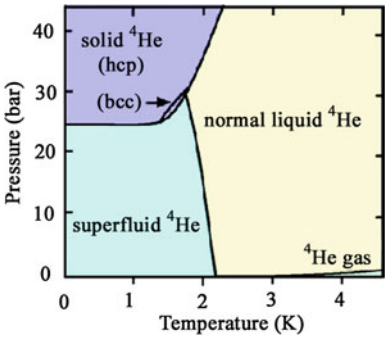

Fig. 1.1 Phase diagram of ^{4}He [21]. There is no triple point where the liquid, solid and gas phases would meet. At $P = 0$ ^{4}He becomes superfluid for $T < 2.2$ K (see [1–5]). For pressures $P > 26$ Bar and low temperatures we have solid phase (with hcp and bcc crystalline structures). There is a shallow minimum on the P–T curve for solid-superfluid phase-boundary at $T \sim (0.5 - 0.6)$ K

Note that for pressures $P > 26$ Bar and low temperatures ^{4}He becomes solid [95–97] and is either in hcp or bcc crystalline phases (see Chap. 2 for more details). At low pressures and high temperatures we have normal ^{4}He which is in a phase of a normal bosonic liquid or in a gas phase (see Fig. 1.1).

For temperatures $0 < T < T_C$ Landau and Tisza proposed to describe superfluid ^{4}He (or He-II in terminology of Kapitza) in terms of superfluid and normal densities ρ_n and ρ_s, and superfluid and normal velocities $\vec{v}_n$ and $\vec{v}_s$ respectively, where

$$\rho = \rho_s + \rho_n \tag{1.1.46}$$

is a total density, and a total mass current (total density of linear momentum) is given by:

$$\vec{j} = \rho_s \vec{v}_s + \rho_n \vec{v}_n = \vec{j}_0 + \rho \vec{v}_s. \tag{1.1.47}$$

In Eq. (1.1.47)

$$\vec{j}_0 = \rho_n (\vec{v}_n - \vec{v}_s) = \rho_n \vec{W} \tag{1.1.48}$$

(where $\vec{W} = \vec{v}_n - \vec{v}_s$ is relative velocity) describes the motion of normal component in the reference frame where a superfluid component is at a rest ($\vec{v}_s = 0$).

According to Landau the normal density in 3D case is given by:

$$\rho_n = -\frac{1}{3} \int \frac{\partial n_B(\varepsilon/T)}{\partial \varepsilon} p^2 \frac{d^3 \vec{p}}{(2\pi)^3}, \tag{1.1.49}$$

where $n_B(\varepsilon/T)$ is bosonic distribution function of the quasiparticles and correspondingly $n_B(\varepsilon/T) = \frac{1}{e^{\varepsilon/T}-1}$. Thus the normal density is closely connected with the spectrum of elementary excitations [1–5, 19] in superfluid helium (see Fig. 1.2).

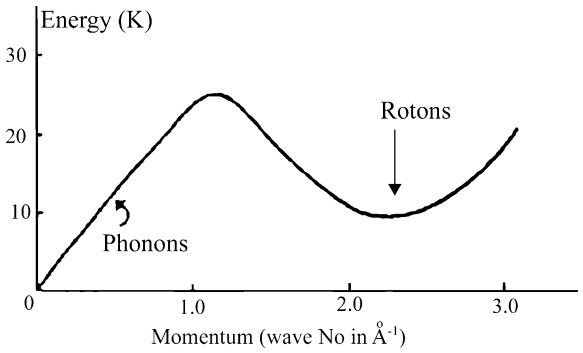

Fig. 1.2 The spectrum of elementary excitations in superfluid ^{4}He [14, 15, 21, 23, 94]. At small wave numbers the spectrum is almost linear and corresponds to phonons, while at larger wave numbers there is a minimum in $E(k)$ which corresponds to rotons

There are two main branches of the elementary excitations according to Landau, Feynman theory—phonons with almost linear spectrum $\varepsilon = cp$ at small p and rotons $\varepsilon = \Delta + \frac{(p-p_0)^2}{2m^*}$. The sound velocity in ^{4}He at zero pressure $c = 2.4 \cdot 10^4$ cm/s. The roton spectrum is described by the parameters $\Delta = 8.7$ K; $p_0/\hbar = 1.9 \cdot 10^8$ cm^{-1} and $m^* = 0.16$ m of ^{4}He. Correspondingly the phonon contribution to ρ_n reads (see [23]):

$$(\rho_n)_{ph} = \frac{2\pi^2 T^2}{45c^5}, \quad (\hbar = 1) \tag{1.1.50}$$

while the roton contribution $(\rho_n)_r \sim e^{-\Delta/T}$.

The simple estimates show that the phonon contribution to ρ_n is dominant for low temperatures $T \leq 0.6$ K, while for higher temperatures rotons are more important. Note that the condition $(\rho_n(T = T_C))_r = \rho$ yields a rough estimate for $T_C \approx 2.2$ K in superfluid helium (^{4}He) (see Fig. 1.3).

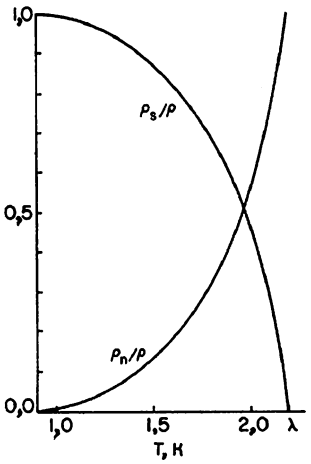

Fig. 1.3 The temperature dependence of ρ_s/ρ and ρ_n/ρ in superfluid ^{4}He from Superfluid Hydrodynamics by S. Putterman [16]. For $T = 0$ $\rho_s/\rho = 1$ and $\rho_n/\rho = 0$ while in the λ-point (at $T_C = 2.2$ K) vice a versa $\rho_s/\rho = 0$ and $\rho_n/\rho = 1$

Note also that the spectrum of elementary excitations on Fig. 1.2 according to Landau defines the critical velocity $v_C = \min(\varepsilon/p)$ for the destruction of the superfluid flow.

1.1.5.1 The System of Hydrodynamic Equations

To derive the system of hydrodynamic equations for superfluid ^{4}He we should use again the Galilean invariance for the total energy:

$$E = E_0 + \vec{j}_0\vec{v}_s + \rho\frac{\vec{v}_s^2}{2}, \tag{1.1.51}$$

where E_0 is an internal energy in the reference frame K_0 where $\vec{v}_s = 0, \vec{j} = \vec{j}_0 + \rho\vec{v}_s$ (see Eq. (1.1.47)). Moreover the internal energy E_0 satisfies the thermodynamic identity [1–5, 14, 15]:

$$dE_0 = TdS + \mu d\rho + \vec{W}d\vec{j}_0, \tag{1.1.52}$$

where $\vec{j}_0 = \rho_n\vec{W}$ and $\vec{W} = \vec{v}_n - \vec{v}_s$ is relative velocity.

Applying again Landau scheme of the conservation laws after some simple algebra we get the following system of equations:

$$\frac{\partial\rho}{\partial t} + \vec{\nabla}\cdot\vec{j} = 0, \tag{1.1.53}$$

$$\frac{\partial\vec{v}_s}{\partial t} + \vec{\nabla}\cdot\left(\frac{v_s^2}{2} + \mu + \Psi\right) = \vec{v}_s \times \left(\vec{\nabla}\times\vec{v}_s\right), \tag{1.1.54}$$

$$\frac{\partial S}{\partial t} + \vec{\nabla}\cdot\left(S\vec{v}_n + \frac{\vec{q}}{T}\right) = \frac{R}{T}, \tag{1.1.55}$$

$$\frac{\partial j_i}{\partial t} + \frac{\partial\Pi_{ik}}{\partial x_k} = 0. \tag{1.1.56}$$

The first Eq. (1.1.53) yields the conservation of mass, the second Eq. (1.1.54) is Euler equation for superfluid velocity $\vec{v}_s$, the third Eq. (1.1.55) is an increase of entropy due to normal motion only [superfluid component does not carry an entropy and thus we have $S\vec{v}_n$ in (1.1.55)]. Finally fourth Eq. (1.1.55) corresponds to the conservation of total mass current $\vec{j}$ in Eq. (1.1.47). In Eq. (1.1.55) the momentum flux:

$$\begin{aligned}\Pi_{ik} &= \rho_n v_{ni}v_{nk} + \rho_s v_{si}v_{sk} + P\delta_{ik} + \pi_{ik}\\ &= v_{si}j_k + v_{nk}j_{0i} + P\delta_{ik} + \pi_{ik}\end{aligned} \tag{1.1.57}$$

is a natural generalization of the expression for ordinary classical fluid, π_{ik} is dissipative momentum flux corresponding to viscous contribution, $P = TS + \mu\rho + \rho_n(\vec{v}_n - \vec{v}_s)^2 - E_0$ is the pressure and accordingly:

$$dP = SdT + \rho d\mu + \vec{j}_0 d\vec{W} \tag{1.1.58}$$

These 4 equations (2 of them have 3 Cartesian projections, so in total we have 8 equations) are consistent with the energy-conservation law (see [1–5]):

$$\frac{\partial E}{\partial t} + \vec{\nabla} \cdot \vec{Q} = 0, \tag{1.1.59}$$

where the energy flux

$$\vec{Q} = TS\vec{v}_n + \left(\mu + \frac{v_s^2}{2}\right)\vec{j} + \vec{v}_n(\vec{v}_n\vec{j}_0) + \vec{Q}_{dis} \tag{1.1.60}$$

and dissipative part of the energy flux:

$$Q^i_{dis} = q_i + \pi_{ik}v_{nk} + \Psi(j_i - \rho v_{ni}). \tag{1.1.61}$$

Correspondingly the dissipative function R in the equation for entropy increase (1.1.55) reads:

$$R = -\frac{\vec{q}\vec{\nabla}T}{T} - \pi_{ik}\frac{\partial v_{ni}}{\partial x_k} - \Psi\vec{\nabla} \cdot (\vec{j} - \rho\vec{v}_n) > 0. \tag{1.1.62}$$

Note that R should be positively defined, quadratic in gradients function.

1.1.6 First and Second Sound Modes in Superfluid Liquid

Two-fluid hydrodynamics describes not only a standard first sound wave, but also a second sound wave. First sound mode as usual demands finite compressibility of the system $\delta\rho \neq 0$; $\delta P \neq 0$ and is governed by the relation (see Sect. 1.1.3):

$$\omega^2 = c_I^2 k^2;\ c_I^2 = \left(\frac{\partial P}{\partial \rho}\right)_s \tag{1.1.63}$$

For the second sound we can consider an incompressible superfluid where $\delta\rho = 0$. Thus from the continuity equation we get $\vec{\nabla} \cdot \delta\vec{j} = 0$ and can safely put:

$$\delta\vec{j} = \rho_s\delta\vec{v}_s + \rho_n\delta\vec{v}_n = 0 \tag{1.1.64}$$

Hence

$$\delta\vec{v}_s = -\frac{\rho_n}{\rho_s}\delta\vec{v}_n \tag{1.1.65}$$

in a second sound wave.

From the conservation of linear momentum we have $\frac{\partial\delta j_i}{\partial t} + \nabla_i\delta P = 0$ and correspondingly for $\delta j_{\mathrm{i}} = 0$ we get $\delta P = 0$. On the other hand we know that

$$dP = SdT + \rho d\mu \tag{1.1.66}$$

Hence if $\delta P = 0$ then

$$d\mu = -S\frac{dT}{\rho} \tag{1.1.67}$$

in a second sound wave.

Now we can consider the linearized Euler equation for superfluid motion $\frac{\partial \delta v_{si}}{\partial t} + \nabla_i \delta\mu = 0$ and rewrite it via δv_{ni} and δT as follows:

$$-\frac{\rho_n}{\rho_s}\frac{\partial \delta v_{ni}}{\partial t} - \frac{S_0}{\rho}\nabla_i \delta T = 0\,. \tag{1.1.68}$$

Note that the relative velocity in the second sound wave $\delta\vec{W} = \delta\vec{v}_n - \delta\vec{v}_s = \left(1 + \frac{\rho_n}{\rho_s}\right)\delta\vec{v}_n = \frac{\rho}{\rho_s}\delta\vec{v}_n$. Finally we can use the equation for entropy increase. In the absence of dissipation it is given by:

$$\frac{\partial \delta S}{\partial t} + S_0\ \vec{\nabla}\cdot\delta\vec{v}_n = 0 \tag{1.1.69}$$

Expressing again δS via δT: $\delta S = \left(\frac{\partial S}{\partial T}\right)_P \delta T = \frac{C_P}{T_0}\delta T$ we get

$$\frac{\partial \delta T}{\partial t} + \frac{S_0 T}{C_P}\ \vec{\nabla}\cdot\delta\vec{v}_n = 0, \tag{1.1.70}$$

where C_P is specific heat per unit mass at constant pressure, S_0 is entropy in equilibrium. The system of Eqs. (1.1.68) and (1.1.70) allows us to find the spectrum of the second sound wave. Differentiation of Eq. (1.1.70) with respect to $\partial/\partial t$ and of Eq. (1.1.68) with respect to $\partial/\partial x_i$, and after that the substitution of (1.1.68–1.1.70) yields:

$$\frac{S_0}{\rho_n}\frac{\rho_s}{\rho}\Delta T - \frac{C_P}{S_0 T}\ddot{T} = 0\,. \tag{1.1.71}$$

Thus for the spectrum we get

$$\omega^2 = c_{II}^2 k^2, \tag{1.1.72}$$

where

$$c_{II}^2 = \frac{TS^2\rho_s}{C_P\rho_n\rho} \tag{1.1.73}$$

is a velocity of a second sound squared and we skipped the subscript for the equlibrium entropy ($S = S_0$). It is a second sound Goldstone mode which distinguishes superfluid liquid from a normal one where we only have overdamped temperature waves. We can say that a second sound is a sound in the subsystem of thermal normal excitations (phonons and rotons). For low temperatures $T \leq 0.6$ K in superfluid ^{4}He the normal density ρ_n as well as entropy S and specific heat C_P

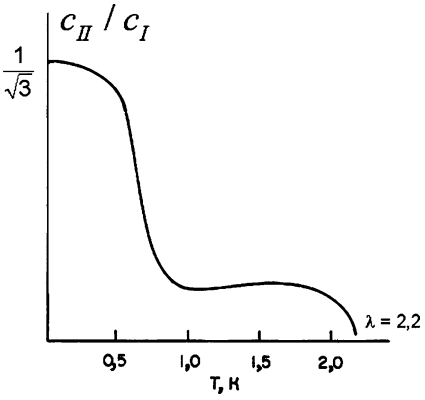

Fig. 1.4 The temperature dependence of the ratio c_{II}/c_I in superfluid ^{4}He from Putterman [16]. For $T \leq 0.5$ K $c_{II}/c_I \to 1/\sqrt{3}$. In the λ-point (at $T = 2.2$ K) $c_{II}/c_I = 0$

are mostly governed by phonons with linear spectrum. In this region in 3D system $c_{II} = c_I/\sqrt{3}$ (In 2D $c_{II} = c_I/\sqrt{2}$) (see Fig. 1.4). At higher temperatures c_{II} is governed mostly by rotons. For $T = T_C$ (λ-point) $c_{II} = 0$ (see Fig. 1.4).

1.1.7 Gross-Pitaevskii Equation for Dilute Bose-Gas. Connection Between Superfluid Hydrodynamics and Microscopic Theory

For weakly non-ideal repulsive (Bogoliubov) Bose-gas we can establish the connection between the microscopic equations for superfluid hydrodynamics for irrotational liquid $\left(\vec{\nabla} \times \vec{v}_s = 0\right)$ at $T = 0$ and gradients and time derivatives of the order parameter:

$$\Psi(\vec{r}, t) = \sqrt{n_s(\vec{r}, t)} e^{i\varphi(\vec{r}, t)} \tag{1.1.74}$$

where $\rho_s(\vec{r}, t) = m n_s(\vec{r}, t) = m|\Psi|^2$.

To establish this connection we should use Gross-Pitaevskii (GP) equation for the order parameter Ψ [68–71]:

$$i\hbar \frac{\partial \Psi}{\partial t} = \left(-\frac{\hbar^2 \Delta}{2m} + V_{ext}(\vec{r}) + g|\Psi(\vec{r}, t)|^2 \right) \Psi(\vec{r}, t), \tag{1.1.75}$$

where $V_{ext}(\vec{r})$—is an external potential (confinement potential of a magnetic trap, for example, see Chap. 4), $g = \frac{4\pi\hbar^2 a}{m}$ is a coupling constant and a is an s-wave scattering length. GP equation is valid if the Bose-gas is dilute $na^3 \ll 1$ and the number of particles in the trap is much larger than 1. As usual we can introduce $\vec{v}_s = \frac{\hbar}{m}\vec{\nabla}\varphi$ for superfluid velocity and $\rho_s = m|\Psi(\vec{r}, t)|^2$ for superfluid density. Substituting (1.1.74) into (1.1.75) and separating real and imaginary parts in

(1.1.75) we obtain 2 equations for superfluid hydrodynamics at $T = 0$ and in the absence of vortices $\left(\vec{\nabla} \times \vec{v}_s = 0\right)$:

$$\begin{aligned} \frac{\partial \rho}{\partial t} + \vec{\nabla} \cdot (\rho \vec{v}_s) = 0, \\ \frac{\partial \vec{v}_s}{\partial t} + \vec{\nabla}\left(\mu + \frac{v_s^2}{2}\right) = 0. \end{aligned} \tag{1.1.76}$$

In (1.1.76) we introduce a chemical potential:

$$m\mu = V_{ext}(\vec{r}) + gn \tag{1.1.77}$$

assuming that the phase of the order parameter φ in (1.1.74) varies more rapidly in space and time than $|\Psi| = \sqrt{n_s}$ (quasicalssical or eikonal approximation [6]). Note that $\delta\mu = \frac{1}{\rho}\delta P$ in (1.1.77) and hence the pressure P contains the term $gn^2/2$ [68, 69].

1.2 Hydrodynamics of Rotating Superfluids

In this Section we provide the basic notion for the standard hydrodynamics of a superfluid liquid with large number of quantized vortices, which includes the elasticity of the vortex lattice and the scattering of normal excitations on the vortices [14, 15, 27–31]. We will start the presentation with the short description of the famous Andronikashvili experiments which measure the ratio of ρ_n/ρ or, more precisely, non-classical moment of inertia in slowly rotating superfluid ^{4}He [17, 18].

1.2.1 Andronikashvili Experiments in Rotating Helium

If we rotate a cylindrical vessel with an ordinary normal (classical) liquid (see Fig. 1.5), than due to the boundary conditions in the viscous liquid on the container wall the tangential component of the velocity $\vec{v}_\tau = \vec{V}_{wall} = \vec{\Omega} \times \vec{R}$, where $\vec{\Omega}$

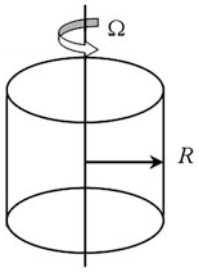

Fig. 1.5 Cylindrical vessel with superfluid ^{4}He rotates with an angular velocity $\vec{\Omega}$. R is the radius of the vessel

is an angular velocity of the rotation, R is the radius of a cylindrical vessel which contains the liquid. Thus in this case all the liquid participates in solid-state rotation. In contrast to this in superfluid liquid only normal component follows the walls of the container $\vec{v}_n = \vec{\Omega} \times \vec{R}$, while frictionless superfluid component stays at a rest at slow rotations.

As a result at small angular frequencies the response of a superfluid on rotation is governed not by the total moment of inertia $I \sim MR^2$ (M—is the total mass of the liquid in the container), but only by its normal fraction $\frac{\rho_n}{\rho} I \equiv \left(1 - \frac{\rho_s}{\rho}\right) I$. It is non-classical moment of inertia. This fact was used in Andronikashvili experiments to measure ρ_n/ρ [17, 18]. In his first experiments he used a sequence of parallel disks with small distance (smaller than the viscous penetration length $\delta_\eta = \left(\frac{2\eta}{\omega\rho_n}\right)^{1/2}$ see[1–5, 17, 18] and Fig. 1.6) between them. Then he can consider that all the normal part of the volume of liquid ^{4}He between the rotating disks participates in rotation.

The scheme of updated experiments on the measurements of non-classical moment of inertia is presented on Fig. 1.7a. In updated Andronikashvili-type of

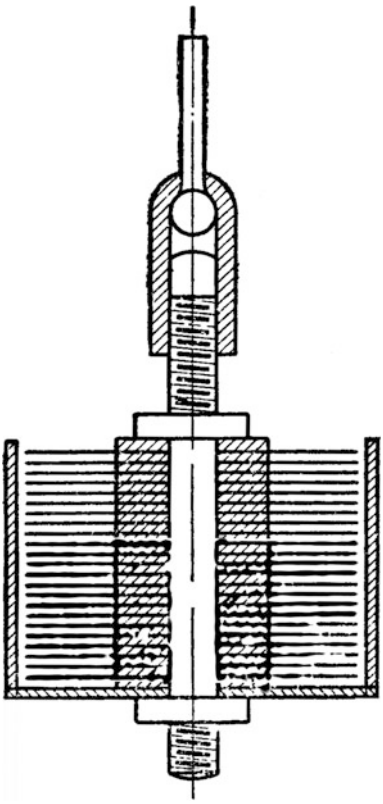

Fig. 1.6 First experiments of Andronikashvili [17, 18] with a sequence of parallel disks for measurements of the non-classical moment of inertia. The viscous penetration length $\delta_\eta = \left(\frac{2\eta}{\omega\rho_n}\right)^{1/2}$ is smaller than the distance between the disks [17]

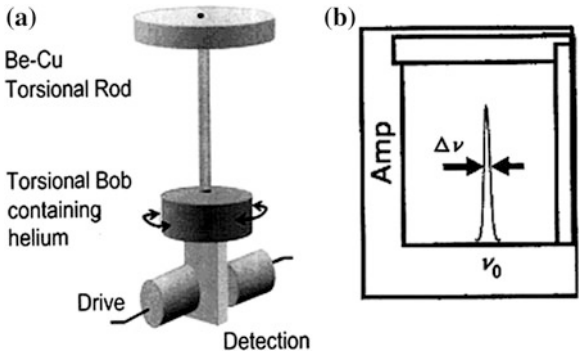

Fig. 1.7 A qualitative scheme of updated Andronikashvili-type of experiments on torsional oscillator by Chan et al. [72, 73] for the search of supersolidity in solid ^{4}He. On Fig. 1.7a we present a sketch of the experimental setup with torsional bob containing helium. On Fig. 1.7b we show the amplitude of the oscillations and the quality factor of the measurements $Q = \nu_0/\Delta\nu$ for the resonance frequency$\nu_0 = 1/\tau_0$, where $\tau_0 = 2\pi\sqrt{I/K}$ is the resonance period, I is the moment of inertia and K is rotating rigidity of the rode

experiments torsional oscillator is used. It is an ideal method for measuring of the non-classical moment of inertia (and thus of a transition to a superfluid state $\rho_s/\rho \neq 0$) especially in solid ^{4}He (see Chap. 2 and [72, 73]). In these experiments the time-period τ_0 for the returning of the rode (of the string) in the initial position is measured using a torsional oscillator with a resonance frequency $\nu_0 = 1/\tau_0$. More specifically experimentalists measure the period $\tau_0 = 2\pi\sqrt{I/K}$ for the container with Helium which is attached to a torsional rode. Note that I is the moment of inertia and K is rotating rigidity of the rode.

This scheme was used in recent experiments of Kim and Chan [72, 73] on the search of supersolidity [74, 75] in solid crystalline ^{4}He. The typical resonant period in this type of experiments $\tau_0 \sim 1$ ms, stability in τ is given: $\delta\tau \sim \frac{\delta K}{K}\tau_0 \sim 5 \cdot 10^{-7}$, and the quality factor $Q = \nu_0/\Delta\nu \sim 2 \cdot 10^6$ (see Fig. 1.7b), where $\nu_0 = 1/\tau_0 \sim 1000$ Hz is the resonance frequency.

1.2.2 Feynman-Onsager Quantized Vortices. Critical Angular Velocities Ω_{C1} and Ω_{C2}

The situation with non-classical moment of inertia occurs at low angular velocities $\Omega < \Omega_{C1}$. For $\Omega < \Omega_{C1}$ (Ω_{C1} is the first critical angular velocity) the first Feynman-Onsager [19, 20] quantized vortex line appears in the center of cylindrical vessel. According to Feynman and Onsager the velocity field of single quantized vortex can be found from the quantization of the circulation of a superfluid velocity:

$$\Gamma_v = \oint\limits_C \vec{v}_s d\vec{l} = 2\pi \frac{\hbar}{m}, \tag{1.2.1}$$

where $\hbar$ is Planck constant, m is the mass of ^{4}He atom.

In fact $\Gamma_v = \Delta\varphi\hbar/m$ where $\Delta\varphi = 2\pi$ is the phase change on the contour. Note that in the absence of vortices we can introduce a scalar complex order-parameter $\Psi = \sqrt{n_s}e^{i\varphi}$ which describes a superfluid state of ^{4}He [23]. Correspondingly $|\Psi|^2 = n_s$ and $mn_s = \rho_s$—superfluid density, while $\vec{v}_s = \hbar/m\,\vec{\nabla}\varphi$ is superfluid velocity. Thus $2\pi\hbar/m$ is a natural unit to measure the circulation of a superfluid velocity in (1.2.1). It is often called as a circulation quanta. Note that, in principle, the vortices with larger amount of circulation quanta $\Gamma_v = 2\pi n\hbar/m \;\; (n > 1)$can be also stabilized in superfluid ^{4}He. When the first vortex appears at $\vec{r} = 0$ (in the center of cylindrical vessel) the superfluid velocity still can be represented as $\vec{v}_s = \hbar/m\,\vec{\nabla}\varphi$ for all distances $\vec{r} \neq 0$. Hence it immediately follows that $\Gamma_v = \oint\limits_C \vec{v}_s d\vec{l} = \frac{\hbar}{m}\Delta\varphi$. In the absence of vortex the phase change $\triangle\varphi = 0$. In the presence of a first quantized vortex $\triangle\varphi = 2\pi$ and we get (1.2.1).

Correspondingly from the Gauss theorem $\iint_S \left(\vec{\nabla} \times \vec{v}_s\right) d\vec{s} = \oint\limits_C \vec{v}_s d\vec{l} = 2\pi\frac{\hbar}{m}$ we easily obtain that:

$$\vec{\nabla} \times \vec{v}_s = \frac{2\pi\hbar}{m}\delta(\vec{r})\vec{e}_z \tag{1.2.2}$$

The solution for $\vec{v}_s$ which satisfies (1.2.1) [and also (1.2.2)] reads:

$$\vec{v}_s = \frac{\hbar}{m}\frac{\vec{e}_\varphi}{r}, \tag{1.2.3}$$

where $\vec{e}_\varphi$ is a tangential unit vector [remind that in cylindrical coordinates $(r,\ \varphi,\ z)$ we have the triade of mutually perpendicular unit vectors $\vec{e}_\varphi, \vec{e}_r, \vec{e}_z$ and thus $d\vec{l} = r\,d\varphi\,\vec{e}_\varphi$ in (1.2.1)].

1.2.2.1 Critical Angular Velocity Ω_{C1}

The first critical angular velocity Ω_{C1} can be found according to [23] from the minimization of the Free-energy in the rotating frame:

$$\Delta F = E_v - (\vec{M}_v\vec{\Omega}) \leq 0 \;\text{ for }\; \Omega \geq \Omega_{C1}, \tag{1.2.4}$$

where $\Delta E = E_v$ is the kinetic energy of the vortex line

$$E_v = \int \rho_s \frac{v_s^2}{2} dV = \frac{\rho_s}{2}\frac{\hbar^2}{m^2}\ln(R/d), \tag{1.2.5}$$

where L is the height of the container and d is the vortex-core, which is normal due to the violation of Landau criteria of superfluidity ($v_s = \frac{\hbar}{md} \geq c_I$—exceeds the first sound velocity for d of the order of interatomic distance). Note that from the spectrum of quasiparticle excitations in superfluid ^{4}He (see Fig. 1.2) we get $v_c = \min(\varepsilon/p) = c_I$ for the critical velocity of a destruction of the superfluid flow. In superfluid ^{4}He $d \sim (3 \div 4)$ Å, $R \sim 0.1$ cm for a typical radius of the container with helium.

In the same time M_v in (1.2.4) is an angular momentum associated with a vortex line:

$$M_v = \rho_s \int r v_s dV = \pi \rho_s L \frac{\hbar}{m} \frac{R^2}{2}. \tag{1.2.6}$$

Correspondingly the first critical angular velocity:

$$\Omega_{C1} = \frac{E_v}{M_v} = \frac{\hbar}{mR^2} \ln \frac{R}{d} \tag{1.2.7}$$

can reach 0.1 rotations/s in ^{4}He.

1.2.2.2 Critical Angular Velocity Ω_{C2}

At very large angular velocities the normal cores of the vortex lines start to overlap. As a result all the volume of a superfluid helium becomes normal. It is evident that

$$\Omega_{C2} = \frac{\hbar}{m\pi d^2} \sim 10^{11} s^{-1}, \tag{1.2.8}$$

where $S = \pi d^2$ is an area of one vortex core. Thus Ω_{C2} in dense superfluid helium is very high and practically unachievable. Note that in dilute weakly non-ideal Bose-gases in a confined geometry of magnetic traps from the solution of Gross-Pitaevskii equation [23, 68–71] the vortex core $\xi_0 = \frac{1}{\sqrt{na}}$, where a is an s-wave scattering length (see [23, 75, 76] and Chap. 6). Thus in dilute case $na^3 < 1$: $\xi_0 \gg a$ and the condition $\Omega_{C2} = \frac{\hbar}{m\pi\xi_0^2}$ is easier to fulfill (note that often $a \sim d$ in a dilute repulsive gas).

Of course from the definitions (1.2.7, 1.2.8) we have very direct correspondence between critical angular velocities Ω_{C1} and Ω_{C2} in superfluid ^{4}He and critical magnetic fields in type-II superconductors.

1.2.2.3 Macroscopic Averaging for a Large Number of Vortices

In between Ω_{C1} and Ω_{C2} we have a system of quantized linear vortices. Their velocity circulations Γ_v [see (1.2.1) and Fig. 1.8] cancel each other inside the vortex region and enhance each other outside the vortex region—thus the vortices

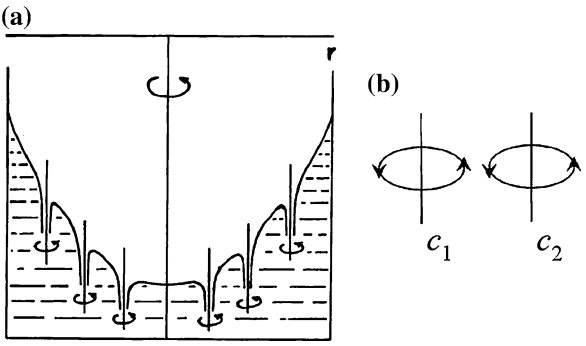

Fig. 1.8 **a** Rotating superfluid helium with large number of vortices for angular velocities $\Omega_{C1} \ll \Omega \ll \Omega_{C2}$. **b** The vortex circulations cancel each other inside the vortex region and enhance each other outside the vortex region. Thus the superfluid component mimics the *solid-state* rotation [22]

of the same "charge" (same circulation) mimic solid-state rotation for superfluid component effectively performing macroscopic averaging (see [14, 15, 27–30]) over an area containing a large number of vortices (but still much smaller than a container area πR^2). We can introduce an averaged vorticity $\vec{\omega} = \vec{\nabla} \times \vec{v}_s \approx 2\vec{\Omega}$ (thus an averaged superfluid vorticity $\vec{v}_s \neq \frac{\hbar}{m}\vec{\nabla}\varphi$). The average vorticity is connected with the number of vortices in 1 cm^2 (with the 2D vortex density):

$$n_v \frac{\hbar}{m} = |\vec{\omega}| \approx 2\Omega, \tag{1.2.9}$$

where $n_v = 1/\pi b^2$ and b is the mean distance between the vortices. The unit vector $\vec{v} = \frac{\vec{\omega}}{|\vec{\omega}|}$ defines the average orientation of vortex lines. We can say that the macroscopic averaging is valid in the long wavelength-limit $\lambda \gg b$ or equivalently when $kb \ll 1$.

1.2.3 Vortex Lattice. Nonlinear Elasticity Theory. Vorticity Conservation Law

For $\Omega_{C1} \ll \Omega \ll \Omega_{C2}$ the developed structure of the vortices form a triangular lattice similar to Abrikosov lattice in type-II superconductors in a magnetic field (see [24] and Fig. 1.9). The state of the vortex lattice, whose parameters vary slowly in space and time, in the non-linear elasticity theory [31] is convenient to describe by the vectors the $\vec{e}_a(\vec{r}, t)$, $a = 1, 2$ which are equal to the local values of the vectors of elementary translations of the lattice in the 2D plane perpendicular to the vortex lines.

We can also define the vectors of the reciprocal lattice: $\vec{e}^a = -\frac{1}{s}\varepsilon^{ab}[\vec{v} \times \vec{e}_b]$ where s—is the area of elementary cell in real lattice, $\varepsilon^{12} = -\varepsilon^{21} = 1$; $\varepsilon_{11} = \varepsilon_{22} = 0$, $\vec{v} = \frac{1}{s}[\vec{e}_1 \times \vec{e}_2]$ is a unit vector parallel to the vortex lines (we will see that $\vec{v} = \frac{\vec{\omega}}{|\vec{\omega}|}$, where $\vec{\omega} = \vec{\nabla} \times \vec{v}_s$ is vorticity—see Fig. 1.9). Note that $|\vec{e}^a| \neq 1$—vectors

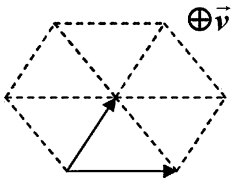

Fig. 1.9 2D triangular vortex lattice for $\Omega_{C1} \ll \Omega \ll \Omega_{C2}$ in the plane perpendicular to the vortex lines (to the unit vector $\vec{v} = \frac{\vec{\omega}}{|\vec{\omega}|}$, where $\vec{\omega} = \vec{\nabla} \times \vec{v}_s$). The lattice is convenient to describe in terms of the vectors $\vec{e}_1(\vec{r}, t), \vec{e}_2(\vec{r}, t)$, which are equal to the local values of the vectors of elementary translations of the 2D lattice

of the reciprocal lattice $\vec{e}^1$ and $\vec{e}^2$ are not the unit vectors. There are evident equalities:

$$\vec{e}^a \vec{e}_b = \delta^a_b; \quad e_{ai} e^a_k = \delta_{ik} - v_i v_k \tag{1.2.10}$$

between real and reciprocal lattices, where $\{i, k\} = \{x, y, z\}$ are Cartesian coordinates. Nonlinear elasticity is described similar to General Theory of Relativity by metric tensors [77]:

$$g_{ab} = \vec{e}_a \vec{e}_b; \quad g^{ab} = \vec{e}^a \vec{e}^b; \quad g_{ac} g^{cb} = \delta^b_a. \tag{1.2.11}$$

We can also introduce a local velocity of the vortex lattice $\vec{v}_L(\vec{r}, t)$ in the direction perpendicular to the vortex lines. Thus $(\vec{v}_L \vec{v}) = 0$ by definition. If $\vec{v}_L$ is known and the functions $\vec{e}^a(\vec{r})$ at the initial time moment are specified, we can determine $\vec{e}^a$ at the nearby time moment, i.e. the derivative $\frac{\partial \vec{e}^a}{\partial t}$ via $\vec{v}_L(\vec{r}, t)$. To establish this connection we express the physically infinitely small differential of the coordinates $d\vec{r}$ (which is large compared with the lattice period, but small compared with the distance over which the vortex configuration varies) in the form (see [31] for more details):

$$d\vec{r} = \vec{e}_a dN^a. \tag{1.2.12}$$

The quantities dN^a for two lattice points separated by a distance $d\vec{r}$ are the two projections of $d\vec{r}$ measured in units of the corresponding lattice periods. These quantities, obviously, are not altered by an arbitrary elastic deformation (in the absence of dislocations).

From (1.2.12) we get:

$$dN^a = \vec{e}^a d\vec{r} = \vec{e}^a_0 d\vec{r}_0, \tag{1.2.13}$$

where $\vec{e}^a_0$ and $d\vec{r}_0$ are respectively the period of the reciprocal lattice and the difference between the coordinates of the undeformed state. From (1.2.13) we see that:

$$\vec{e}^a = \vec{\nabla} N^a. \tag{1.2.14}$$

Correspondingly

$$\vec{\nabla} \times \vec{e}^a = \vec{\nabla} \times \left(\vec{\nabla} N^a \right) = 0. \tag{1.2.15}$$

Thus the specified functions $N^a(\vec{r}, t)$ determine completely the configuration of the vortex lines. We can say that $N^a(\vec{r}, t)$ defines the number of sites (or nodes) of the vortex lattice in the direction of an elementary vector $\vec{e}^a$. Moreover if we consider the vortex lattice without vacancies or dislocations, than each site of the lattice is singly occupied and the number of sites (or nodes) is conserved. We can conclude that N^a is a topological invariant (see Andreev and Kagan [31]) and we have a very convenient technique for all the problems of the non-linear theory of elasticity.

To establish the relation between $\frac{\partial \vec{e}^a}{\partial t}$ and $\vec{v}_L(\vec{r}, t)$ we note that the unit vector $\vec{n} = \vec{e}^1/e^1$ is the normal to the corresponding crystallographic plane (to the plane defined by the vectors $\vec{e}_2$ and $\vec{v}$) and $d = 1/e^1$ is proportional to the local value of the interplanar distance. From simple geometric considerations we get:

$$\begin{aligned} &\dot{\vec{n}} + V(\vec{n} \cdot \vec{\nabla})\vec{n} = -\vec{\nabla} V + \vec{n}(\vec{n} \cdot \vec{\nabla} V); \\ &\dot{d} + V(\vec{n} \cdot \vec{\nabla}) d = d(\vec{n} \cdot \vec{\nabla}) V, \end{aligned} \tag{1.2.16}$$

where $V = (\vec{v}_L \vec{n}) = (\vec{v}_L \vec{e}^1)/e^1$ is the projection of the velocity normal to the considered crystallographic plane.

From (1.2.16) we obtain:

$$\dot{\vec{e}}^1 + \vec{\nabla}(\vec{e}^1 \vec{v}_L) = V\left(\vec{n} \times \left(\vec{\nabla} \times \vec{e}^1 \right) \right). \tag{1.2.17}$$

A similar relation holds also for $\vec{e}^2$.

Taking into account that $\vec{\nabla} \times \vec{e}^a = 0$ we finally get:

$$\frac{\partial \vec{e}^a}{\partial t} + \vec{\nabla}(\vec{e}^a \vec{v}_L) = 0. \tag{1.2.18}$$

Thus comparing (1.2.18) and (1.2.14) we obtain:

$$\vec{v}_L = -\vec{e}_a N^a \tag{1.2.19}$$

Note that the variables analogous to N^a were considered for the vortex lattice by Volovik and Dotsenko [78].

In macroscopic hydrodynamics of a rotating superfluid liquid one introduces an averaged velocity $\vec{v}_S$ of the superfluid component, whose *curl* is determined by the direction and the density of the vortex lines, as well as the circulation quantum $2\pi\hbar/m$. Since the unit area s of the real lattice is equal to $g^{1/2}$, where g is determinant of the metric tensor g_{ab}, we have:

$$\vec{\nabla} \times \vec{v}_s = \frac{2\pi\hbar}{ms} \vec{v} = \frac{2\pi\hbar}{mg} (\vec{e}_1 \times \vec{e}_2) = \frac{2\pi\hbar}{m} \left(\vec{e}^1 \times \vec{e}^2 \right). \tag{1.2.20}$$

By differentiating (1.2.20) with respect to time and using (1.2.18) we obtain the equation of the vorticity conservation:

$$\dot{\vec{\omega}} = \vec{\nabla} \times \dot{\vec{v}}_s = \vec{\nabla} \times (\vec{v}_L \times \vec{\omega}). \tag{1.2.21}$$

1.2.4 Hydrodynamics of Slow Rotations. Hall-Vinen Friction Coefficients β and β'

In accord with the general Landau method of deriving the hydrodynamic equations from the conservation laws [1–5], we introduce in the case of slow rotations two velocities $\vec{v}_s$ and $\vec{v}_n$ and search for the system of equations in the form of the conservation laws [similar to the system of Eqs. (1.1.53–1.1.56)]:

$$\begin{aligned} &\dot{\rho} + \vec{\nabla} \cdot \vec{j} = 0; \quad \frac{\partial j_i}{\partial t} + \frac{\partial}{\partial x_k} \Pi_{ik} = 0 \\ &\dot{S} + \vec{\nabla} \cdot (S\vec{v}_n + \vec{q}/T) = \frac{R}{T}; \quad \dot{\vec{v}}_s = \vec{v}_L \times \left(\vec{\nabla} \times \vec{v}_s \right) + \vec{\nabla}\varphi, \end{aligned} \tag{1.2.22}$$

where ρ, S and $\vec{j}$ are the mass, entropy and momentum per unit volume, while Π_{ik}, $\vec{q}$, $R > 0$ and φ are the quantities to be determined. We must also find the connection between the velocities $\vec{v}_s, \vec{v}_n$ and $\vec{v}_L$. The criterion is the requirement that the energy conservation equation should be automatically obtained form the system of Eq. (1.2.22).

The Galilean transformation formulas (similar to Eqs. (1.1.51) and (1.1.47)):

$$E = \rho \frac{v_s^2}{2} + \vec{j}_o \vec{v}_s + E_0; \quad \vec{j} = \vec{j}_o + \rho \vec{v}_s \tag{1.2.23}$$

connect again the energy E per unit volume and the momentum $\vec{j}$ with their values E_0 and $\vec{j}_0$ in a system where $\vec{v}_s = 0$. The energy E_0 can be regarded as a function of ρ, S, $\vec{j}_0$, and the metric tensor g^{ab}, so that:

$$dE_0 = TdS + \mu d\rho + (\vec{v}_n - \vec{v}_s, d\vec{j}_o) + \frac{1}{2} h_{ab} dg^{ab}. \tag{1.2.24}$$

Equations (1.2.22–1.2.24) differ from the corresponding equations of Bekarevich, Khalatnikov [14, 15] in that the vortex conservation condition (1.2.21) is taken into account in (1.2.22) in the equation of the superfluid motion, and also in that the dependence of the energy of the deformation of the vortex lattice is fully taken into account in the identity (1.2.24).

Differentiating with respect to time the first equation for energy in (1.2.23) we obtain by using (1.2.23) and (1.2.24):

$$\begin{aligned} &\dot{E} + \vec{\nabla} \cdot \{\vec{Q}_0 + \vec{q} + v_{nk}\pi_{ik} + \Psi(\vec{j} - \rho\vec{v}_n) + v_{Lk} h_{ai} e_i^a e_k^b\} = \\ &= R + \frac{\vec{q}\vec{\nabla}T}{T} + \pi_{ik} \frac{\partial v_{ni}}{\partial x_k} + \Psi\vec{\nabla} \cdot (\vec{j} - \rho\vec{v}_n) + \{\vec{v}_L - \vec{v}_n, \vec{\omega} \times \left(\vec{j} - \rho\vec{v}_n\right) + \vec{e}^a \vec{\nabla} \cdot (h_{ab}\vec{e}^b)\}. \end{aligned} \tag{1.2.25}$$

While deriving Eq. (1.2.25) we used Eq. (1.2.18) for $\frac{\partial \vec{e}^1}{\partial t}$ and $\frac{\partial \vec{e}^2}{\partial t}$ which yield:

$$\frac{\partial g^{ab}}{\partial t} = \frac{\partial}{\partial t}(\vec{e}^a \vec{e}^b) = -\left(\vec{e}^b \cdot \vec{\nabla}\right)(\vec{v}_L \vec{e}^a) - \left(\vec{e}^a \cdot \vec{\nabla}\right)\left(\vec{v}_L \vec{e}^b\right). \tag{1.2.26}$$

In (1.2.25)

$$\begin{aligned} \vec{Q}_0 &= \left(\mu + \frac{v_s^2}{2}\right)\vec{j} + ST\vec{v}_n + \vec{v}_n(\vec{j}_o \vec{v}_n), \\ \pi_{ik} &= \Pi_{ik} - P\delta_{ik} - v_{si} j_k - v_{nk} j_{0i} - h_{ab} e_i^a e_k^b. \\ \Psi &= -\left(\mu + \frac{v_s^2}{2} + \varphi\right); \quad P = -E_0 + TS + \mu\rho + (\vec{v}_n - \vec{v}_s, \vec{j}_o). \end{aligned} \tag{1.2.27}$$

Note that from (1.2.26) it follows the equality

$$\begin{aligned} &\tfrac{1}{2} h_{ab} \dot{g}^{ab} + \tfrac{1}{2} v_{ni} h_{ab} \tfrac{\partial g^{ab}}{\partial x_i} \\ &= -\vec{\nabla} \cdot \{h_{ab} \vec{e}^a (\vec{v}_L - \vec{v}_n, \vec{e}^b)\} - \tfrac{\partial v_{ni}}{\partial x_k}(h_{ab} e_i^a e_k^b) + \{\vec{v}_L - \vec{v}_n, \vec{e}^a \vec{\nabla} \cdot (h_{ab} \vec{e}^b)\} \end{aligned} \tag{1.2.28}$$

The form of (1.2.25, 1.2.27) enables us to determine the energy-flux vector:

$$\vec{Q} = \vec{Q}_0 + \vec{q} + v_{nk}\pi_{ki} + \Psi(\vec{j} - \rho\vec{v}_n) + v_{Lk} h_{ab} e_i^a e_k^b \tag{1.2.29}$$

and the dissipative function:

$$\begin{aligned} R = &-\frac{\vec{q}\vec{\nabla}T}{T} - \pi_{ik}\frac{\partial v_{ni}}{\partial x_k} - \Psi div(\vec{j} - \rho\vec{v}_n) \\ &- \left\{\vec{v}_L - \vec{v}_n, \left(\vec{\nabla} \times \vec{v}_s\right) \times (\vec{j} - \rho\vec{v}_n) + \vec{e}^a \vec{\nabla} \cdot (h_{ab}\vec{e}^b)\right\} \end{aligned} \tag{1.2.30}$$

From the condition that R is positive it follows that the unknown quantities $\vec{q}$, π_{ik}, Ψ and $\vec{v}_L - \vec{v}_{s\perp}$—(the symbol $\perp$ means that we are dealing with the projection of the corresponding vector on a plane perpendicular to $\vec{v}$) can be written in the general case as linear combinations of all conjugated variables $\vec{\nabla}T$, $\frac{\partial v_{ni}}{\partial x_k}$, etc., contained in (1.2.30). We shall not write out the unwieldy general formulas and confine ourselves, as usual, to the mutual friction effects described by the last term in (1.2.30). We have:

$$\begin{aligned} &\vec{v}_L - \vec{v}_{n\perp} = -\alpha\left\{\vec{j}_\perp - \rho\vec{v}_{n\perp} + \tfrac{mg^{1/2}}{2\pi\hbar}(\vec{e}^a \times \vec{v})\vec{\nabla} \cdot (h_{ab}\vec{e}^b)\right\} - \\ &-\beta\left\{\vec{v} \times (\vec{j} - \rho\vec{v}_n) + \tfrac{mg^{1/2}}{2\pi\hbar}\vec{e}^a \vec{\nabla} \cdot (h_{ab}\vec{e}^b)\right\}, \end{aligned} \tag{1.2.31}$$

where α and β are certain coefficients with $\beta > 0$. Since at $T = 0$ there is no normal part, so that $\vec{v}_L$ should be independent of $\vec{v}_n$, it follows that the constant α should be equal to—$1/\rho$. If we put $\alpha = -1/\rho_s + \beta'$, the constants β and β' will vanish at $T \to 0$, that coincide with the friction coefficients introduced by

Bekarevich and Khalatnikov [14, 15] and differ from the constants of Hall and Vinen [37, 38] by a factor $\rho_n/2\rho\rho_s$.

At zero temperature we obtain from (1.2.31):

$$\vec{v}_L - \vec{v}_{s\perp} = \frac{mg^{1/2}}{2\pi\hbar\rho}(\vec{e}^a \times \vec{v})\vec{\nabla}\cdot(h_{ab}\vec{e}^b), \tag{1.2.32}$$

which is the generalization of a known relation [48–50, 78] to the case of arbitrary and not small deformations of the vortex lattice.

1.2.4.1 The Physical Meaning of β, β' Coefficients. Elementary Estimates

The coefficient β is a dissipative coefficient, while β' is a Hall-like dissipationless coefficient. According to Iordansky [41] to get the feeling about coefficients β-s we should consider the elementary excitations with momentum $\vec{p}$ and energy $\varepsilon_0(\vec{p})$ approaching the vortex and thus experiencing the velocity field of the vortex $\vec{v}_s$ (see Fig. 1.10).

According to the requirements of the Galilean invariance $\varepsilon(\vec{p}) = \varepsilon_0(\vec{p}) - \vec{p}\vec{v}_s$ or more rigorously

$$\varepsilon(\vec{p}) = \varepsilon_0(\vec{p}) - \vec{p}(\vec{v}_s - \vec{v}_n) \tag{1.2.33}$$

for the spectrum of quasiparticles (if normal excitations have a drift velocity $\vec{v}_n$). Thus according to Iordansky and Sonin [39–41], an effective interaction:

$$H_{\text{int}} = \vec{p}(\vec{v}_n - \vec{v}_s) \tag{1.2.34}$$

arises in our system. According to the elementary kinetic theory

$$\beta \sim \frac{1}{n_V\sigma l} \sim \frac{1}{n_V\sigma v\tau_U}, \tag{1.2.35}$$

where $v = \frac{\partial\varepsilon_0}{\partial p}$ is a group velocity for elementary excitations, σ is the cross-section, n_V is the density of vortices, τ_U is the scattering time due to Umklapp processes $1/\tau_U \sim \beta\rho_s\Omega$ [37, 38]. Note that we need Umklapp processes [64] connected with the vortex lattice to have the relaxation of the quasiparticle linear momentum. For a rough estimate we can find an impact parameter a ($\sigma = \pi a^2$) from the

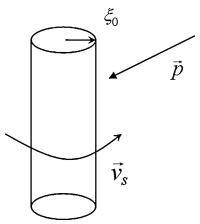

Fig. 1.10 The scattering of the normal excitations with momentum $\vec{p}$ on the vortex line, which creates the velocity field $\vec{v}_s$ (outside the vortex core $\xi_0 \sim d$)

quasiclassical turning point, that is $\varepsilon_0(\vec{p}) - \vec{p}\vec{v}_s(a) = 0$ (for $\vec{v}_n = 0$). For a single vortex line $\vec{v}_s = \frac{\hbar}{mr}\vec{e}_\varphi$ and if we have, for example, a roton with an energy $\varepsilon_0(\vec{p}) = \Delta_0 + \frac{(p-p_0)^2}{2m_*}$ for $p \approx p_0$, then $\Delta_0 = \frac{\hbar p_0}{ma}$ or

$$a = \frac{\hbar p_0}{m\Delta_0} \geq (\xi_0 \sim d) \tag{1.2.36}$$

for the impact parameter. If $a \sim \xi_0 \sim d$ we can say that the normal component scatters on the vortex cores, which are also normal.

1.2.5 Linearization of the Elasticity Theory. Connection Between $\vec{v}_s$ and $\vec{u}$ in Linearized Theory

When we expand the hydrodynamic energy and hydrodynamic equations in powers of deformation it is convenient to put

$$N^a = N_0^a - u^a \tag{1.2.37}$$

for the number of nodes N^a, where $N_0^a = \vec{e}_o^a\vec{r}$ and $\vec{e}_o^a$ is a non-deformed unit vector of a reciprocal lattice. We can also introduce the displacement

$$\vec{u} = \vec{e}_{oa}u^a \tag{1.2.38}$$

which is a 2D vector perpendicular to the axes of undeformed vortices.

1.2.5.1 Shear, Compression and Bending Elastic Modulus

We represent the elastic energy (the energy of vortex repulsion due to the lattice rigidity) E_{el} per unit lattice volume in the form:

$$E_{el} = E_1 + E_2, \tag{1.2.39}$$

where

$$E_1 = \frac{\pi\rho_s}{2}\left(\frac{\hbar}{m}\right)^2 n_V \ln\frac{1}{n_V d^2} \tag{1.2.40}$$

is a compression energy, $n_V = \frac{1}{s} = \frac{1}{\sqrt{g}}$ is the density of vortices per unit area, E_2 is shear energy (which depends on the shape of a deformed unit cell) (see Elasticity theory [63] for the details).

Accordingly

$$h_{ab} = \frac{2\partial E_{el}}{\partial g^{ab}} = h_{ab}^{(1)} + h_{ab}^{(2)}. \tag{1.2.41}$$

Differentiating E_1 with respect to g^{ab} with the allowance for the identity $-\frac{1}{g}dg = g_{ab}dg^{ab}$ and linearizing the result with respect to the deviations δg^{ab} of the metric tensor from its value $g^{\mathrm{ab}}(0)$ in an undeformed triangular lattice, we obtain:

$$h_{ab}^{(1)} = \rho_s \frac{\hbar\Omega}{m}\left\{\ln\frac{b}{d}\left(g_{ab}^{(0)} - \delta g_{ab} + \frac{1}{2}g_{ab}^{(0)}\delta g_c^c\right) - \frac{1}{4}g_{ab}^{(0)}\delta g_c^c\right\}, \tag{1.2.42}$$

where $\pi b^2 \sim \frac{\hbar}{m\Omega} \sim \frac{1}{n_V}$ is the mean distance between the vortex lines, $\Omega = (\pi\hbar/m)g_o^{-1/2}$ is the angular velocity of the rotation, and

$$\delta g_{ab} = g_{ac}^{(0)}g_{bd}^{(0)}\delta g^{cd}; \quad \delta g_c^c = g_{cd}^{(0)}\delta g^{cd}. \tag{1.2.43}$$

The constant term appears in (1.2.42) because at equilibrium the energy that has a minimum is the energy in the rotating coordinate frame. We express the shear part $h_{ab}^{(2)}$ of the full h_{ab} in the form:

$$h_{ab}^{(2)} = \mu_s\left(\delta g_{ab} - \frac{1}{2}g_{ab}^{(0)}\delta g_c^c\right), \tag{1.2.44}$$

where $\mu_s = \rho_s\frac{\hbar\Omega}{4m}$ is the shear modulus calculated by Tkachenko [32–34] for the triangular lattice.

The quantities δg_{ab} and $\vec{e}^a$ can be easily expanded in the displacement $\vec{u}$ by using Eqs. (1.2.11) and (1.2.14). As a result we get the following expression for the elastic terms that enter in Eq. (1.2.25) for $\vec{v}_L$:

$$\vec{F} = \vec{e}^a\vec{\nabla}\cdot(h_{ab}\vec{e}^b) = 2\Omega\lambda\vec{\nabla}_\perp\rho_s + \rho_s\frac{\hbar\Omega}{4m}\left(2\nabla_\perp(\vec{\nabla}\cdot\vec{u}) - \Delta_\perp\vec{u}\right) - \rho_s 2\Omega\lambda\frac{\partial^2\vec{u}}{\partial z^2}, \tag{1.2.45}$$

where

$$\lambda = \frac{\hbar}{2m}\ln\frac{b}{d}. \tag{1.2.46}$$

If according to Tkachenko we introduce the compression modulus $\mu_{\mathrm{c}} = -\mu_{\mathrm{s}} = -\frac{\hbar\Omega}{4m}\rho_s$ (where μ_{s} is the shear modulus), and a bending modulus $\mu_{\mathrm{b}} = \rho_s 2\Omega\lambda$ (see [35, 36]) we can rewrite Eq. (1.2.35) as:

$$\vec{F} = 2\Omega\lambda\nabla_\perp\rho_s + \mu_c\nabla_\perp(\vec{\nabla}\cdot\vec{u}) - \mu_s\Delta_\perp\vec{u} - \mu_b\frac{\partial^2\vec{u}}{\partial z^2}. \tag{1.2.47}$$

Note that it is convenient to introduce the longitudinal (c_{l}) and the transverse sound velocities (c_{t}) in the vortex lattice according to the standard relations of the Elasticity theory [63]:

$$\mu_c = 2\rho_s(c_l^2 - 2c_t^2) \text{ and } \mu_s = 2\rho_s c_t^2. \tag{1.2.48}$$

In our case

$$c_t^2 = c_l^2 = \frac{\hbar\Omega}{8m} = \frac{\mu_s}{2\rho_s}. \tag{1.2.49}$$

As the result for the elastic terms which enter the system of equations for hydrodynamics of slow rotations:

$$\vec{F} = 2\Omega\lambda\vec{\nabla}_\perp\rho_s - 2\rho_s c_t^2\vec{\nabla}_\perp(\vec{\nabla}\cdot\vec{u}) - 2\rho_s c_t^2\Delta_\perp\vec{u} - \mu_b\frac{\partial^2\vec{u}}{\partial z^2}, \tag{1.2.50}$$

$$\frac{\partial}{\partial x_k}(h_{ab}e_i^a e_k^b) = -2\rho_s\Omega\lambda\ \nabla_i(\vec{\nabla}\cdot\vec{u}) + \vec{F}_i \tag{1.2.51}$$

Let us emphasize that the first term in the right-hand side of Eq. (1.2.51) $-2\rho_s\Omega\lambda\vec{\nabla}(\vec{\nabla}\cdot\vec{u})$ can be left out upon the normalization of the pressure in (1.2.38)

$$P \to P - 2\rho_s\Omega\lambda(\vec{\nabla}\cdot\vec{u}) \tag{1.2.52}$$

and a simultaneous replacement of the chemical potential μ in Eq. (1.2.22) for the superfluid motion (for $\partial\vec{v}_s/\partial t$) by the chemical potential of the liquid without allowance for elasticity. Indeed, in the linear approximation we have:

$$\begin{aligned} d\mu &= -\tfrac{S}{\rho}dT + \tfrac{1}{\rho}dP - \tfrac{1}{\rho}\vec{j}_0 d(\vec{v}_n - \vec{v}_s) + \tfrac{1}{2\rho}h_{ab}dg^{ab} \\ &= -\tfrac{S}{\rho}dT - \tfrac{1}{\rho}\vec{j}_0 d(\vec{v}_n - \vec{v}_s) + \tfrac{1}{\rho}d(P - \rho_s 2\Omega\lambda(\vec{\nabla}\cdot\vec{u})). \end{aligned} \tag{1.2.53}$$

Let us point out that when Eq. (1.2.35) for $\vec{F}$ is substituted in Eq. (1.2.26) for $\vec{v}_L$ at $T = 0$, we get the customary employed equation (see [39, 40, 48–50])

$$\vec{v}_L - \vec{v}_{s\perp} = \frac{m}{2\pi\hbar\rho_s n_V}\left(\vec{F}\times\vec{v}\right) \approx \frac{1}{2\rho_s\Omega}\left(\vec{F}\times\vec{e}_z\right), \tag{1.2.54}$$

where $\vec{e}_z = \vec{v}^{(0)}$ is a unit vector in the direction of the undeformed vortex lines and $\rho_s(T = 0) = \rho$.

1.2.5.2 Connection Between $\vec{v}_s$ and $\vec{u}$ in Linearized Theory for $T = 0$

Let us find first the relation between $\vec{v}_s$ and $\vec{u}$. To get this relation in linearized theory we use the Eq. (1.2.19) $\vec{v}_L = -\vec{e}_a\dot{N}^a$ and the Eq. (1.2.27) $N_0^a = N^a - u^a$, where $\vec{u} = \vec{e}_{0a}u^a$. Note also that $\vec{e}_0^a = \vec{\nabla}N_0^a$, where $\vec{e}_0^a$ are the vectors of an undeformed but uniformly rotating lattice. Therefore $\dot{\vec{e}}_0^a = \vec{\Omega}\times\vec{e}_0^a$ and

$$\dot{N}_0^a = \left(\vec{\Omega}\times\vec{e}_0^a\right)\vec{r} = -\vec{v}_0\vec{e}_0^a \tag{1.2.55}$$

where $\vec{v}_0 = \vec{\Omega} \times \vec{r}$ is a linear velocity of a solid state rotation. We should also use the condition $\vec{v}_L \vec{v} = 0$ where $\vec{v}_L = \vec{v}_0 + \delta\vec{v}_L$ and $\vec{v} = \vec{e}_z + \delta\vec{v}$ in linearized theory. Having in mind that $\delta\vec{v} \sim \frac{\partial \vec{u}}{\partial z}$ we finally get:

$$\vec{v}_L = \vec{v}_0 + \dot{\vec{u}} + \left(\vec{v}_0 \cdot \vec{\nabla}\right)\vec{u} - \vec{e}_z\left(\vec{v}_0 \frac{\partial \vec{u}}{\partial z}\right) - \vec{\Omega} \times \vec{u}. \tag{1.2.56}$$

Now we can find the relation between $\vec{v}_s$ and $\vec{u}$ using Eq. (1.2.46). To find this relation it is important to note that in linearized theory $\vec{v}_s = \vec{v}_0 + \delta\vec{v}_s$ and correspondingly $\delta\vec{v}_{s\perp}$ in (1.2.54) reads:

$$\delta\vec{v}_{s\perp} = \delta\vec{v}_s - \delta v_{sz}\vec{e}_z - \vec{e}_z\left(\vec{v}_0 \frac{\partial \vec{u}}{\partial z}\right). \tag{1.2.57}$$

Substituting (1.2.57) in (1.2.56) we get the cancellation of the term $\vec{e}_z\left(\vec{v}_0 \frac{\partial \vec{u}}{\partial z}\right)$ in the relative velocity $\vec{v}_L - \vec{v}_{s\perp}$ and moreover:

$$\vec{v}_L - \vec{v}_{s\perp} = \dot{\vec{u}} + \left(\vec{v}_0 \cdot \vec{\nabla}\right)\vec{u} - \vec{\Omega} \times \vec{u} - (\delta\vec{v}_s - \delta v_{sz}\vec{e}_z) = \frac{1}{2\rho_s \Omega}\left(\vec{F} \times \vec{e}_z\right). \tag{1.2.58}$$

Introducing the two-dimensional projection of $\delta\vec{v}_s$ on the (x,y) plane:

$$\delta\vec{v}_{s2D} = \delta\vec{v}_s - \delta v_{sz}\vec{e}_z \tag{1.2.59}$$

we can rewrite (1.2.63) in the form:

$$\left\{\frac{\partial}{\partial t} + \left(\vec{v}_0 \cdot \vec{\nabla}\right) - \vec{\Omega}\times\right\}\vec{u} - \delta\vec{v}_{s2D} = \frac{1}{2\rho_s \Omega}\left(\vec{F} \times \vec{e}_z\right). \tag{1.2.60}$$

Now we can use that in curly brackets in the l.h.s. of (1.2.60) just stands an operator which is responsible for the transformation of the vector quantity to the rotation frame. Thus we derive an important relation between the time derivative of $\vec{u}$ in the rotation frame $\frac{\partial \vec{u}}{\partial t'}$ and the two dimensional projection of the superfluid velocity $\delta\vec{v}_{s2D}$:

$$\frac{\partial \vec{u}}{\partial t'} = \delta\vec{v}_{s2D} + \frac{1}{2\rho_s \Omega}\left(\vec{F} \times \vec{e}_z\right). \tag{1.2.61}$$

1.2.5.3 Linearized Euler Equation at $T = 0$

Returning back to Euler equation for superfluid velocity $\vec{v}_s$ at $T = 0$ we get in linearized theory:

$$\begin{aligned}\frac{\partial \vec{v}_s}{\partial t} + \vec{\nabla}\left(\mu + \frac{v_s^2}{2}\right) &= \vec{v}_L \times \left(\vec{\nabla} \times \vec{v}_s\right) \\ &\approx \vec{v}_s \times \left(\vec{\nabla} \times \vec{v}_s\right) + \frac{1}{2\rho\Omega}\left(\vec{F} \times \vec{e}_z\right) \times \left(\vec{\nabla} \times \vec{v}_s\right)\end{aligned} \tag{1.2.62}$$

In the rotation frame in direct analogy with the situation in an ideal rotating fluid (see Sect. 1.1.4) we get:

$$\frac{\partial \delta\vec{v}_s}{\partial t'} + \vec{\nabla}\frac{\delta P}{\rho_0} + 2\vec{\Omega} \times \delta\vec{v}_s = \frac{1}{\rho_0}\vec{F}. \tag{1.2.63}$$

Applying an operator of curl to the l.h.s. and to the r.h.s. of this equation we finish with:

$$\frac{\partial}{\partial t'}(\vec{\nabla} \times \delta\vec{v}_s) + \vec{\nabla} \times \left(2\vec{\Omega} \times \delta\vec{v}_s\right)X = \frac{1}{\rho_0}(\vec{\nabla} \times \vec{F}). \tag{1.2.64}$$

This equation together with the relation (1.2.61) (which establishes the connection between $\delta\vec{v}_{s2D}$ and $\frac{\partial\vec{u}}{\partial t'}$) and the continuity equation

$$\frac{\partial \delta\rho}{\partial t} + \rho_0\vec{\nabla} \cdot \delta\vec{v} + (\vec{v}_0 \cdot \vec{\nabla})\delta\rho = \frac{\partial \delta\rho}{\partial t'} + \rho_0\vec{\nabla} \cdot \delta\vec{v} = 0 \tag{1.2.65}$$

(where we used the transformation $\frac{\partial}{\partial t} \to \frac{\partial}{\partial t} + \left(\vec{v}_0 \cdot \vec{\nabla}\right)$ to the rotation frame for a scalar) helps us to find the spectrum of collective excitations in a rotating macroscopically averaged superfluid at long wave-vectors $kb \ll 1$.

1.2.6 Collective Modes of the Lattice. Tkachenko Waves and Kelvin Waves. Melting of the Vortex Lattice

According to Sonin in the general case of compressive rotating superfluid with a triangular vortex lattice the spectrum of collective excitations in the long wavelength limit reads (see [39, 40]):

$$\omega^2 = \left(2\Omega + \lambda k_z^2\right)\left[2\Omega\frac{\omega^2 - c_I^2 k_z^2}{\omega^2 - c_I^2 k^2} + \lambda k_z^2 + \frac{c_t^2 k_\perp^4}{2\Omega}\right], \tag{1.2.66}$$

where $c_t^2 = \frac{\mu_s}{2\rho_s} = \frac{\hbar\Omega}{8m}$ is Tkachenko sound velocity squared, c_I^2 is first sound velocity squared, $\lambda = \frac{\hbar}{2m}\ln\frac{b}{d}$ and k_z and $k_\perp$ are the projections of the wave-vector $\vec{k}$ ($k^2 = k_\perp^2 + k_z^2$) on the undeformed vortex axis (on the z-axis) and on the xy plane perpendicular to undeformed vortex axis. For $k_\perp = 0$ the spectrum (1.2.66) contains 2 modes—a sound mode with a spectrum $\omega_1^2 = c_I^2 k_z^2$ and Kelvin (Thomson) mode for bending oscillations of the vortex lines $\omega_2^2 = \left(2\Omega + \lambda k_z^2\right)^2$.

In the same time for $k_z = 0$ (and thus $k = k_\perp$) there are 2 modes again $\omega_1^2 = 4\Omega^2 + c_I^2 k_\perp^2$ and $\omega_2^2 = \omega_T^2 \approx \frac{c_t^2 c_I^2 k_\perp^4}{4\Omega^2 + c_I^2 k_\perp^2}$ for $c_\mathrm{I} \gg c_\mathrm{t}$. First mode is usually called an inertial mode. It has a gap. Note that the second mode has a nontrivial dispersion in the denominator. Moreover, for $k_\perp > \frac{2\Omega}{c_I} : \omega_T^2 = c_t^2 k_\perp^2$ and we have a linear spectrum for Tkachenko mode, while for very small $k_\perp < \frac{2\Omega}{c_I} : \omega_T^2 = \frac{c_t^2 c_I^2 k_\perp^4}{4\Omega^2}$ and

correspondingly $\omega_T = \frac{c_t c_l k_\perp^2}{2\Omega}$—the spectrum of Tkachenko mode becomes quadratic.

According to Baym [27–30] the quadratic character of the spectrum at very small k-vectors leads to dramatic consequences for purely 2D flows with $k_z = 0$. Namely the mean displacement squared of a single vortex line from equilibrium (due to the excitations of very long wavelength Tkachenko modes) is logarithmically divergent:

$$\frac{\langle \vec{u}^2 \rangle}{b^2} \sim \frac{T}{\Omega} \frac{n_v}{nL} \ln \frac{k_{\max}}{k_{\min}}, \tag{1.2.67}$$

where in dense ^{4}He $k_{\max} \sim \frac{2\Omega}{c_l}$, $k_{\min} \sim \frac{2\pi}{R}$, n and n_v are 3D density of particles and 2D density of vortices, and L is the height of the container (or effective third dimension of a quasi-2D magnetic trap). Thus $\frac{n_v}{nL}$ is dimensionless density ratio. The linear in T dependence of $\langle \vec{u}^2 \rangle / b^2$ requires that $T \gg \omega_{\mathrm{T}}^{\max}$ since in this regime bosonic distribution function for Tkachenko waves $n_B\left(\frac{\omega_T}{T}\right) \sim \frac{T}{\omega_T}$. From (1.2.67) it follows that $\langle \vec{u}^2 \rangle / b^2$ is logarithmically divergent in infrared region of small $k \sim 1/R$. The strong effect of compressibility on the Tkachenko mode in the long wavelength limit $\omega_T = \frac{c_t c_l k_\perp^2}{2\Omega}$ was studied by Reato [79].

Note, however, that in practice it is very difficult to fulfill the condition

$$\frac{2\pi}{R} < k_\perp < \frac{2\Omega}{c_l} \tag{1.2.68}$$

in dense ^{4}He where the typical size of the container $R \sim 0.1$ cm. Usually the transition to quadratic regime requires unachievably high angular velocities in dense liquid. In helium, for example, $c_{\mathrm{I}} \sim 2.4 \cdot 10^4$ cm/s, $\Omega_{C1} = \frac{\hbar}{mR^2} \ln \frac{R}{d} \sim 1$ rot/s and we need to demand $\Omega \geq 10^7 \Omega_{C1}$ to get the quadratic regime, which is practically impossible. We notice again that nL is an effective two-dimensional density of particles (number of particles per unit area). Thus

$$\frac{n_v}{nL} = \frac{N_{vortices}}{N_{particles}} = \frac{1}{p}, \tag{1.2.69}$$

where p is a dimensionless filling factor. In terms of p Eq. (1.2.67) reads:

$$\frac{\langle \vec{u}^2 \rangle}{b^2} \sim \frac{T}{\Omega} \frac{1}{p} \ln(R k_{\max}), \tag{1.2.70}$$

where R is the size of the container.

In dense ^{4}He $mc_{\mathrm{I}}^2 \sim (20 \div 30)$ K, $T \sim 1$ K, $\hbar\Omega/k_B \sim 10^{-11}$ K for $\Omega \sim \Omega_{\mathrm{C1}}$. Thus $mc_{\mathrm{I}}^2 \gg T \gg \Omega$ and the requirement for macroscopic averaging $k_\perp b \ll 1$ is automatically fulfilled for $k_\perp < 2\Omega/c_{\mathrm{I}}$ since $\Omega/mc_{\mathrm{I}}^2 \ll 1$. Correspondingly, $k_\perp < 2\Omega/c_{\mathrm{I}} < 1/b$. The requirement $\omega_{\mathrm{T}}^{\max} \ll T$ is also fulfilled since for $k_\perp^{\max} \sim \frac{2\Omega}{c_l}$: $\omega_T^{\max} \sim c_t k_\perp^{\max} \sim \frac{c_t \Omega}{c_l} \ll \Omega \ll T$ for $c_{\mathrm{t}} \ll c_{\mathrm{I}}$. Finally in dense ^{4}He

we always have $p \gg 1$ for the filling factor since only at $\Omega = \Omega_{C2}$ $N_{\text{particles}} \sim N_{\text{vortices}}$ (for $\Omega = \Omega_{C2}$ the normal cores which in ^{4}He have interatomic size start to overlap). For $\Omega < \Omega_{C2}$: $N_{\text{particles}} \gg N_{\text{vortices}}$ and thus $p \gg 1$.

In dilute Bose-gases $mc_I^2 = \frac{4\pi a}{m} n$, where a is the s-wave scattering length. To get the "inverse ratio" $\Omega/mc_I^2 \gg 1$ we have to consider very small densities $na^3 \ll 1$ and very large angular velocities. Note that in this limit $k_\perp < 1/b < 2\Omega/c_I$ and the spectrum of Tkachenko mode will be always quadratic in $k_\perp$. The filling factor ν in dilute Bose-gases in magnetic traps can be also much smaller than in helium since the vortex cores $\xi_0 \sim 1/\sqrt{na} \gg d$ are much larger than in dense ^{4}He [98, 99].

Note also that in real ^{4}He the situation is always three-dimensional $k_z \neq 0$. The spectrum still has two branches $\omega_1^2(k_z, k_\perp)$ and $\omega_2^2(k_z, k_\perp)$. Moreover for Tkachenko mode according to Williams and Fetter [48] we can use an approximate form $\omega_T^2 = \omega_2^2 \approx 4\Omega^2 \frac{k_z^2}{k^2} + \frac{\hbar\Omega}{4m} k^2 \frac{k_\perp^4}{k^4} + 2\Omega\lambda \frac{k_z^2}{k^2}\left(1 + \frac{k_z^2}{k^2}\right)$, or introducing $\cos\theta = k_z/k$ ($\sin\theta = k_\perp/k$) we get $\omega_T^2 = 4\Omega^2 \cos^2\theta + \frac{\hbar\Omega}{4m} k^2 \sin^4\theta + 2\Omega\lambda \cos^2\theta(1 + \cos^2\theta)$, where $\lambda = \frac{\hbar}{2m} \ln\frac{b}{d}$.

Than according to Baym [27–30] the mean displacement squared $\left\langle \vec{u}^2 \right\rangle = \frac{T}{\rho} \int_0 \frac{d^3\vec{k}}{(2\pi)^3} \frac{1+\cos^2\theta}{\omega_T^2} \sim \frac{T}{\rho} \int_{-1}^{1} \frac{d\cos\theta}{4\pi^2} \int_0 k^2 dk \frac{1+\cos^2\theta}{4\Omega^2\cos^2\theta + \frac{\hbar k^2 \Omega}{4m}\sin^4\theta + 2\Omega\lambda\cos^2\theta(1+\cos^2\theta)}$ becomes finite in the infrared limit $k \to 0$ in 3D case. However, even in this case for the quasi two-dimensional thin film or a slab geometry in z-direction (for the system restricted by the two planes separated by the distance L in z-direction and with a discrete set of $k_z = 2\pi n/L$) Gifford and Baym [27–30] predict the logarithmic divergence of the correlator of the two displacements:

$$\frac{\left\langle \left|\vec{u}(\vec{r}) - \vec{u}(\vec{r}')\right|^2 \right\rangle}{b^2} \sim T \ln R_\perp \tag{1.2.71}$$

at finite temperatures and very large distances $R_\perp^2 \gg Lb$, where $\vec{R} = \vec{r} - \vec{r}' = \left\{\vec{R}_\perp, R_z\right\}$.

1.2.6.1 An approach to Collective Modes Based on Gross-Pitaevskii-Equation

Note that at large filling factors $\nu \gg 1$ there is another more microscopic (but still mean-field) approach to study the spectrum and even the damping of collective modes (see Matvienko et al. [51, 52]). It is based on the mean-field solution for the GP equation for rotating dilute Bose-gas. Note that for a stationary problem $\Psi(\vec{r}, t) = \Psi(\vec{r}) e^{i\mu t}$ and GP equation can be written as a nonlinear Schroedinger equation for the charged particles in strong magnetic field. Namely

$$\hat{H}\Psi(r) = \left\{ \left(\hat{p} - \frac{e}{c}\vec{A} \right)^2 + V_{ext}(\vec{r}) - \frac{m\Omega^2 r^2}{2} + g|\Psi(\vec{r})|^2 \right\} \Psi(\vec{r}) = \mu\Psi(\vec{r}); \quad (1.2.72)$$

where $\vec{A} = m\,\vec{\Omega} \times \vec{r} = \vec{B} \times \vec{r}$ is an effective vector potential in radial (cylindrical) gauge [7], $\vec{B}$ is a magnetic field.

The chemical potential μ in (1.2.72) plays a role of an averaged energy on one particle E in the standard Schroedinger equation. If an external trapping potential in (1.2.72) is also quadratic (confinement potential—see Chap. 4) $V_{ext}(\vec{r}) = \frac{m\omega^2 r^2}{2}$, than neglecting the nonlinear term $g|\Psi|^2\Psi$ we can get from (1.2.72) an equation for Landau levels which is well known from Quantum mechanics. The spectrum of this equation reads for close values of angular velocity and trapping frequency $\Omega \sim \omega$ (more precisely for $|\Omega - \omega|/\Omega \ll 1$)

$$E_{n,l} = \hbar\omega\left(n + \frac{1}{2}\right) + \hbar(\Omega - \omega)l + \frac{p_z^2}{2m}, \quad (1.2.73)$$

where $n = n_r + l$ is a principal quantum number and l is an orbital momentum (n_r is radial quantum number).

For the lowest Landau level (LLL) $n = 0$ and for purely 2D motion ($p_z = 0$) we get:

$$E_{0l} = \frac{\hbar\omega}{2} + \hbar(\Omega - \omega)l. \quad (1.2.74)$$

The corresponding Ψ-function of the LLL

$$\Psi_{0l} = f_l(z)e^{-\frac{\omega|z|^2}{2}} \quad (1.2.75)$$

where $z = x + iy$, $\bar{z} = x - iy$, and $|z|^2 = z\bar{z}$.

To have vortices we should demand that $f_l(z)$ is analytic function of z, which does not have any poles. Moreover $f_l(z = z_i) = 0$ for the vortex solutions centered at the points $z = z_i$. In the most simple case according to Matvienko et al. f_l should behave linearly [proportional to $(z - z_i)$] close to each vortex core. Such mean-field solution corresponding to the triangular lattice can be described by some θ-function of Yakobi (see [51, 52]) similar to Abrikosov solution for type-II superconductors [24]. Note that we can safely neglect the nonlinear term in (1.2.72) if $gn < |\Omega - \omega|$. The authors of [51, 52] also managed to derive the spectrum and damping of collective modes in the same type of formalism.

1.2.6.2 Melting of the Vortex Lattice

If $\langle \vec{u}^2 \rangle / b^2$ exceeds some finite number (which is less that 1), then according to Lindemann criterion [80, 81] the 2D vortex lattice starts to melt. For finite temperatures we have classical melting while for $T = 0$ we can still have quantum melting. The last case is very interesting both for vortex lattices in rotating gases

and for the search of supersolidity in Quantum crystals (see Chap. 2). The quantum melting for the 2D lattice requires $\langle \vec{u}^2 \rangle / b^2 \geq 0.07$ (see Cooper et al. [53–55]).

Note that according to Baym at zero temperature the mean displacement squared for purely 2D flows ($k_z \equiv 0$) reads:

$$\frac{\langle \vec{u}^2 \rangle}{b^2} \sim \frac{n_v}{n_s L} \left(\frac{mc_I^2}{\Omega} \right)^{1/2} \sim \frac{1}{p} \left(\frac{mc_I^2}{\Omega} \right)^{1/2}, \tag{1.2.76}$$

where n_S is a superfluid particle density. In dense ^{4}He the ratio $\left(\frac{mc_I^2}{\Omega} \right)^{1/2}$ as we already discussed is very large. For $\Omega \geq \Omega_{C1} \sim 1$ rot/s : $\left(\frac{mc_I^2}{\Omega} \right)^{1/2} \sim 10^6$. However, v is also very large and thus at $T = 0$ $\frac{\langle \vec{u}^2 \rangle}{b^2} \ll 1$ in ^{4}He.

In weakly non-ideal Bogoliubov Bose gas

$$\left(\frac{mc_I^2}{\Omega} \right)^{1/2} = \left(\frac{4\pi a n_s}{m\Omega} \right)^{1/2} \sim \left(\frac{4}{m\Omega \xi_0^2} \right)^{1/2} \sim \frac{b}{\xi_0} \sim \left(\frac{\Omega_{C2}}{\Omega} \right)^{1/2}, \tag{1.2.77}$$

where $m\Omega = b^2$ and $\xi_0 = 1/\sqrt{na}$. Note that for $\Omega = \Omega_{C2} : n_v = na$ and $p = \frac{nL}{n_v} = \frac{L}{a}$. Hence at $T = 0$ in a dilute Bose gas

$$\frac{\langle \vec{u}^2 \rangle}{b^2} \sim \frac{1}{p} \frac{b}{\xi_0}. \tag{1.2.78}$$

Thus if we have small enough $p \geq 1$ (for that we should have almost 2D trap with $L \geq a$ for z-dimension) we can reach the regime of quantum melting $\langle \vec{u}^2 \rangle / b^2 \geq 0.07$. In this case according to Cooper et al. [53–55] we will have a phase transition form a vortex crystal to a strongly correlated phase of a vortex liquid. The strongly correlated vortex liquid (in contrast with the vortex crystal) is closely related to incompressible liquid states which according to Laughlin [82–85] and Haldane et al. [68, 69] arise in the physics of the Fractional Quantum Hall Effect (FQHE). Note that in practice $v_C \sim (5 \div 6)$ for a phase-transition from vortex crystal to vortex-liquid [53–55] in dilute rotating Bose gases.

Note again that in this Chapter we mostly used Landau scheme of the conservation laws to derive the nonlinear hydrodynamics of slow rotations and to get the spectrum of the collective modes. There are other methods to derive these equations based on Poisson brackets (PB) [43, 78] or on Gross-Pitaevskii (GP) equation [51–55]. These methods are also very elegant ones. However they are not purely phenomenological and use some additional microscopic arguments. The method of PB, for example, utilizes some additional microscopic equation for vortex lines. We can say that the other approaches do not provide the nonlinear fluxes in the system of hydrodynamic equations for slow rotations and do not describe the nonlinear elasticity theory of the vortex lattice in such a straightforward and a single-valued fashion as Landau scheme of the conservation laws. Note that Baym and Chandler [27–30] in their classical paper also considered equations for slow-rotations but only in a form linearized in the lattice deformations.

1.3 Hydrodynamics of Fast Rotations

In connection with dilute quantum gases in rotation the researchers usually understand rapid rotations as a quantum limit when $\frac{n_v}{nL} = \frac{N_{vortices}}{N_{particles}} = \frac{1}{p}$ and we are in the regime of vortex liquid (the vortex lattice is melted). In this Section we will always work in a mean-field hydrodynamic regime (classical limit $p \gg 1$) mostly considering dense superfluid ^{4}He. Thus the vortex lattice is always present in our considerations. Nevertheless even here we can distinguish between slow and rapid rotations, having in mind absolutely different regimes and phenomena in comparison with dilute quantum gases. Namely we will construct strongly anisotropic hydrodynamics with two different velocities of normal and superfluid component $\vec{v}_{n\parallel} \neq \vec{v}_{s\parallel}$ in the direction parallel to the vortex lines and with only one velocity $\vec{v}_{n\perp} = \vec{v}_{s\perp} = \vec{j}_{\perp}/\rho$ in the direction perpendicular to the vortex lines. This hydrodynamics, describing the crystal in perpendicular to the vortex lines direction and a free superfluid in a parallel direction, can be realized at large rotation frequencies with the help of intensive Umklapp processes [64] for the scattering of normal excitations on the 2D vortex lattice. Throughout this Section we will often use a term of fast rotations to distinguish this regime from rapid rotations in quantum gases considered in the end of the Sect. 1.2.

1.3.1 The Foundation of the Hydrodynamics of Fast Rotations. The Role of Umklapp Processes

According to Andreev and Kagan [31] the two different approaches are possible to a hydrodynamic description of rotating systems, i.e. to a description in which the quantities are assumed to vary slowly in space and time and the expansions are in terms of gradients. In the first one the initial state of the system is assumed to be at a rest and the expansion is in all the gradients including the components of the velocity curl connected with the uniform rotation. This is hydrodynamics of slow rotations (in terminology of Andreev and Kagan considered in the previous Section).

In the same time since uniform rotation is always in thermodynamic equilibrium, another approach is possible in which the velocity curl that corresponds to uniform rotation is not assumed small, and the expansion is only in terms of nonequilibrium gradients, in the gradients on top of the uniform rotation. This expansion corresponds to hydrodynamics of fast rotations in the terminology of Andreev and Kagan.

Note that hydrodynamics of slow rotations, considered in Sect. 1.2, contains two independent velocities of normal and superfluid motions. The interaction of the normal excitations with the vortex lines are taken into account as a mutual friction force proportional to the difference between normal and superfluid

velocities. For such a description to be valid it is necessary in any case that the excitations mean free path time τ_N which is connected with their scattering on each other, should be considerably smaller than the analogous time τ_U connected with the scattering of normal excitations on the vortex lattice. Note that otherwise an introduction of the velocity of normal component as an independent thermodynamic variable is meaningless. But even if the condition $\tau_U \gg \tau_N$ is satisfied, the usual equations are valid only for not very low angular velocities of rotation.

Let us clarify this situation, considering for simplicity on the basis of usual equations for hydrodynamics of slow rotations, the temperature oscillations and the related with them oscillations of the relative velocity $\vec{W}_\perp = \vec{v}_{n\perp} - \vec{v}_{s\perp}$ perpendicular to the vortex lines. In this case such oscillations are analogous in many respect to temperature oscillations in crystal under conditions of phonon hydrodynamics (see Gurevich [44]). In this case τ_U and τ_N play the role of the times of phonon relaxation due to normal and Umklapp processes respectively. In both cases there are two oscillation modes, whose frequencies can be expressed as the functions of the wave vectors in the form:

$$\omega_{1,2} = -i\gamma \pm \left(c_{II}^2 k^2 - \gamma^2\right)^{1/2}, \tag{1.3.1}$$

where c_{II} is a second sound velocity and

$$\gamma = 1/\tau_U + c_{II}^2 k^2 \tau_N. \tag{1.3.2}$$

In the case of a rotating superfluid liquid we have (see [37, 38] and Sect. 1.2)

$$1/\tau_U \sim (B\Omega), \tag{1.3.3}$$

where Ω is an angular frequency of rotation and $B = \frac{2\rho\rho_s}{\rho_n}\beta$ is one of the two dimensionless parameters introduced by Hall and Vinen [37, 38] to define the mutual friction force. From the view-point of a hydrodynamics of slow rotations, both modes are hydrodynamic, since both frequencies $\omega_{1,2}$ tend to zero when k and Ω tend simultaneously to zero (for $\Omega \to 0$ the inverse Umklapp time $1/\tau_U \to 0$ and γ also tends to zero for $\Omega \to 0$ and $k \to 0$).

In fast rotation hydrodynamics, however, i.e. as $k \to 0$ and at constant Ω, $\gamma \neq 0$ and only one (heat-conduction) mode is hydrodynamic (gapless) mode.

The usual equations are thus hydrodynamic in the sense of slow rotations. For given Ω, however, their validity is restricted by the condition $\tau_U \gg \tau_N$. If, however, this condition is satisfied and the motion frequency ω satisfies the inequality $\omega\tau_U \ll 1$, we can replace the ordinary equations by the much simpler equations of fast rotations which will be derived in this Section. Note that in the crystals (see [44]) for $\tau_U \gg \tau_N$ and $\omega\tau_U \ll 1$ we can exactly in the same way replace the equations of phonon-hydrodynamics by the usual equations of the elasticity theory [65].

In fast rotation hydrodynamics we introduce for a superfluid liquid with a vortex lattice only one independent velocity of macroscopic motion in the direction perpendicular to the vortex lines, i.e. the system behaves for these directions

as an ordinary crystal. Since the longitudinal total momentum of the excitations (parallel to the vortex lines) is preserved by the demands of the homogeneity of the system in the lines direction, we introduce in this direction two velocities and a system behaves as a standard superfluid liquid. Note that hydrodynamics of fast rotations is valid for given Ω at sufficiently low frequencies $\omega \ll \tau_U^{-1}$ and $\omega \ll \tau_N^{-1}$ no matter what is the ratio of τ_U and τ_N. At temperatures of the order of 1 K in liquid He-II the dimensionless constant B of Hall and Vinen is of the order of unity and the validity of fast rotations hydrodynamics is restricted to frequencies $\omega \ll (\tau_U^{-1} \sim \Omega)$ [see (1.3.3)].

1.3.2 The System of the Nonlinear Equations for the Hydrodynamics of Fast Rotations

In fast rotations hydrodynamics we must introduce one velocity in the direction perpendicular to the vortices and two independent velocities in the longitudinal direction. Under these considerations it is not convenient to use as the hydrodynamic variable the true superfluid velocity which we define as $\vec{V}_s$ in this Section. Instead of it we introduce a single perpendicular velocity $\vec{v}_\perp$ ($\vec{v}_\perp \vec{v} = 0$) defined by the equality:

$$\vec{v}_\perp = \frac{\vec{j}_\perp}{\rho}, \tag{1.3.4}$$

where $\vec{j}_\perp$ is the exact value of the perpendicular momentum. The motion in the longitudinal direction will be described by two velocities $v_{n||}$ and $v_{s||}$, with $v_{s||} = \vec{V}_s \vec{v}$. Thus we put:

$$\vec{v}_s = \vec{v}_\perp + v_{s||}\vec{v}; \quad \vec{v}_n = \vec{v}_\perp + v_{n||}\vec{v}. \tag{1.3.5}$$

We emphasize once more that the velocity $\vec{v}_s$ introduced by us does not coincide, generally speaking, with the true superfluid velocity $\vec{V}_s$. Nevertheless Eq. (1.2.23) for Galilean transformation of the energy and the linear momentum, as well as Eq. (1.2.24) for the differential of an internal energy E_0 (in the frame where $\vec{v}_s = 0$) are still valid in terms of new velocities $\vec{v}_n$ and $\vec{v}_s$ from (1.3.5). Indeed from the definition of $\vec{v}_n$ and $\vec{v}_s$ in (1.3.5) it follows that the relative velocity $\vec{W} = \vec{v}_n - \vec{v}_s = (v_{n||} - v_{s||})\vec{v}$ and $\vec{j}_0 = (\vec{j} - \rho\vec{v}_s) = \vec{j}_{||} - \rho\vec{v}_{s||} = j_{0||}\vec{v}$ have only longitudinal components. Thus the term $\vec{W}d\vec{j}_0$ in dE_0 can be written in the form $(v_{n||} - v_{s||})dj_{0||}$, which corresponds precisely to the correct expression for a system that is superfluid only in the longitudinal direction. We emphasize that the one-dimensional densities of the normal (ρ_n) and superfluid components ($\rho_s = \rho - \rho_n$), defined by the formula $j_{0||} = \rho_n(v_{n||} - v_{s||})$, differ substantially, generally speaking,

from the corresponding "microscopic" three-dimensional quantities which enter in the expressions (1.2.42), (1.2.45) and (1.2.48) for the elastic module (for $\frac{1}{2}h_{ab} = \frac{\partial E_{el}}{\partial g^{ab}}$) of a vortex lattice. Note that all the definitions connected with the kinematics of the vortex lattice, particularly expression (1.2.13) $\vec{v}_L = -\vec{e}_a\dot{N}^a$, remain the same as before. Since the number of the independent velocity components is now smaller by two than in slow rotation hydrodynamics, the number of equations in hydrodynamics of fast rotations should be correspondingly less than in (1.2.22). Specifically the last equation of the system (1.2.22) (the three component equation for the superfluid motion) should be replaced by one component scalar equation for the fast rotations. We derive it by using the formula:

$$\vec{v}_s\vec{v} = \vec{V}_s\vec{v} \tag{1.3.6}$$

and the relation (1.2.21) for the vorticity conservation which in the notation of the present Section can be written in the form:

$$\dot{\vec{V}}_s + \vec{\nabla}\varphi = \vec{v}_L \times \left(\vec{\nabla} \times \vec{V}_s\right), \tag{1.3.7}$$

where φ is a certain scalar.

Differentiating (1.3.6) with respect to time, and taking into account (1.3.7) as well as the relation $\vec{v} = \frac{\vec{\nabla}\times\vec{V}_s}{|\vec{\nabla}\times\vec{V}_s|}$, we obtain:

$$\vec{v}\dot{\vec{v}}_s = -(\vec{v}\cdot\vec{\nabla})\varphi - \dot{\vec{v}}\left(\vec{V}_s - \vec{v}_s\right). \tag{1.3.8}$$

An expression for $\dot{\vec{v}}$ can be easily derived from (1.3.7):

$$\dot{\vec{v}} + (\vec{v}_L\cdot\vec{\nabla})\vec{v} = (\vec{v}\cdot\vec{\nabla})\vec{v}_L - \vec{v}(\vec{v},(\vec{v}\cdot\vec{\nabla})\vec{v}_L). \tag{1.3.9}$$

Substituting it in (1.3.8) we obtain after simple transformations:

$$\vec{v}\left(\dot{\vec{v}}_s + \vec{\nabla}\left(\mu + \frac{v_s^2}{2} + \Psi\right) - \vec{v}_L \times \left(\vec{\nabla}\times\vec{v}_s\right)\right) = 0, \tag{1.3.10}$$

where

$$\Psi = \varphi - \mu - \frac{v_s^2}{2} - \vec{v}_L\left(\vec{V}_s - \vec{v}_s\right). \tag{1.3.11}$$

It is convenient to choose Eq. (1.3.10) with yet undetermined scalar Ψ as a required scalar equation which together with the first three equations of the system (1.2.22) constitute the complete system of equations for the hydrodynamics of fast rotations [31].

Differentiating as usual the first equation of (1.2.23) for total energy with respect to time and using the aforementioned complete system of equations, we reduce the equation for $\dot{E}$ to the form:

$$\dot{E} = -\vec{\nabla}\cdot\{\vec{Q}_0 + \vec{q} + v_{nk}\pi_{ik} + v_{Lk}h_{ab}e_i^a e_k^b + \Psi(\vec{j} - \rho\vec{v}_n)\} + R + \frac{\vec{q}\vec{\nabla}T}{T} + \pi_{ik}\frac{\partial v_{ni}}{\partial x_k}$$
$$+\Psi\vec{\nabla}\cdot(\vec{j} - \rho\vec{v}_n) + \{\vec{v}_L - \vec{v}_\perp, \vec{F} + (\vec{j} - \rho\vec{v}_n, \vec{v})\cdot(\vec{\nabla}\times\vec{v}_s)\times\vec{v}\}, \tag{1.3.12}$$

where the expressions for $\vec{Q}_0$ and π_{ik} formally coincide with those given in Eq. (1.2.27) of the preceding Section. From (1.3.12) we find the dissipation function:

$$R = -\frac{\vec{q}\vec{\nabla}T}{T} - \pi_{ik}\frac{ni}{\partial x_k} - \Psi\vec{\nabla}\cdot(\vec{j} - \rho\vec{v}_n)$$
$$-\{\vec{v}_L - \vec{v}_\perp, \vec{F} + (\vec{j} - \rho\vec{v}_n, \vec{v})\cdot(\vec{\nabla}\times\vec{v}_s)\times\vec{v}\}. \tag{1.3.13}$$

Confining ourselves, as in the preceding Section, to consideration of only the last term in (1.3.13), we write down the expression for the relative velocity of the vortices and of the matter in the following general form:

$$(\vec{v}_L - \vec{v}_\perp)_\alpha = -\hat{B}_{\alpha\beta}G_\beta, \tag{1.3.14}$$

where

$$\vec{G} = \vec{F} + (\vec{j} - \rho\vec{v}_n, \vec{v})\cdot(\vec{\nabla}\times\vec{v}_s)\times\vec{v}, \tag{1.3.15}$$

and α and β are two-dimensional spatial indices in a plane perpendicular to $\vec{v}$. The matrix of the coefficients $\hat{B}_{\alpha\beta}$ satisfies the Onsager relations [64]:

$$\hat{B}_{\alpha\beta}(\vec{v}) = \hat{B}_{\beta\alpha}(-\vec{v}). \tag{1.3.16}$$

Therefore

$$(\vec{v}_L - \vec{v}_\perp)_\alpha = \left(\frac{mg^{1/2}}{2\pi\rho\hbar} - B'\right)\left(\vec{G}\times\vec{v}\right)_\alpha - \hat{B}_{\alpha\beta}G_\beta, \tag{1.3.17}$$

where $B_{\alpha\beta}$ is the symmetric part of $\hat{B}_{\alpha\beta}$, $B_{\alpha\beta}(T=0) = B'(T=0) = 0$. For an arbitrary deformed lattice $B_{\alpha\beta}$ is an arbitrary symmetric tensor. We point out that the second term in the expression for $\vec{G}$, in contrast to the analogous term in the slow-rotation hydrodynamics, is of the second order in the deviations from the state of the uniform rotation. Therefore $B_{\alpha\beta}$ has in fast-rotation hydrodynamics the meaning of the diffusion coefficient of the vortices. The coefficient B' describes an effect of the Hall type in the diffusion. In an undeformed triangular lattice the tensor B reduces to a scalar.

We recall that the complete system of the equations for the hydrodynamics of fast rotations consists of the first three equations of (1.2.22) for $\dot{\rho}$, $\dot{j}$ and $\dot{S}$, and of Eq. (1.3.10) for the superfluid motion.

1.3.3 Linearized System of Equations of Fast Rotations. The Spectrum and the Damping of the Second Sound Mode

Linearizing the equations for $\dot{S},\ \dot{\rho},\ \dot{j}$ and $v_i\dot{v}_{si}$ near the uniform rotation we obtain the following set of the equations that describes the oscillations of the temperature and the associated oscillations of the relative velocity $\delta W_{\|} = \delta v_{n\|} - \delta v_{s\|}$ along the vortices (compare with Eqs. (1.1.65) and (1.1.67) for a second sound wave):

$$\begin{cases} \delta\dot{T} + \left(\vec{v}_o \cdot \vec{\nabla}\right)\delta T + \dfrac{TS\rho_s}{C_p\rho}\nabla_z \delta W_{\|} + \dfrac{\vec{\nabla}\cdot\vec{q}}{\rho C_p} = 0, \\ \delta\dot{W}_{\|} + \left(\vec{v}_o \cdot \vec{\nabla}\right)\delta W_{\|} + \dfrac{S}{\rho_n}\nabla_z \delta T = 0, \end{cases} \tag{1.3.18}$$

where S and C_p are the entropy and heat capacity per unit mass at a constant pressure, and the liquid is assumed incompressible $\delta P = \delta\rho = 0,\ \rho_n \delta v_{n\|} + \rho_s \delta v_{s\|} = 0$. In (1.3.18) $\vec{v}_0 = \vec{\Omega}\times\vec{r}$. Equations (1.3.18) are reduced to the equations with constant coefficients by transforming to a rotation frame. This corresponds to the substitution $\frac{\partial}{\partial t} \to \frac{\partial}{\partial t'} - \vec{v}_o \times \vec{\nabla} - \Omega\times$ for vectors and $\frac{\partial}{\partial t} \to \frac{\partial}{\partial t'} - \vec{v}_o \times \vec{\nabla}$ for scalars (where $\partial/\partial t'$ is the time derivative in the rotation frame). The heat flux in (1.3.18) can be set equal to $\vec{q} = -\kappa_\perp \vec{\nabla}_\perp T$ ($\kappa_\perp$ is the heat conductivity in the direction perpendicular to the vortex axis), since the equations contain other considerably larger terms with $\partial/\partial z$. As the result we get:

$$\begin{cases} \dfrac{\partial\delta T}{\partial t'} + \dfrac{c_{II}^2\rho_n}{S}\dfrac{\partial\delta W_{\|}}{\partial z} - \dfrac{\kappa_\perp}{\rho C_p}\Delta_\perp \delta T = 0 \\ \dfrac{\partial\delta W_{\|}}{\partial t'} + \dfrac{S}{\rho_n}\dfrac{\partial\delta T}{\partial z} = 0, \end{cases} \tag{1.3.19}$$

where $c_{II}^2 = \frac{TS^2\rho_s}{C_p\rho^2\rho_n}$ is the second sound velocity.

The differentiation of the first equation in (1.3.19) with respect to $\partial/\partial t'$ and of a second one with respect to $\partial/\partial z$, and after that the substitution of the second equation in the first one yields:

$$\frac{\partial^2\delta T}{\partial t'^2} - c_{II}^2\frac{\partial^2\delta T}{\partial z^2} - \frac{\kappa_\perp}{\rho C_p}\Delta_\perp\frac{\partial T}{\partial t'} = 0. \tag{1.3.20}$$

Correspondingly $\omega^2 - c_{II}^2 k_z^2 + \frac{\kappa_\perp}{C_p}k_\perp^2 i\omega = 0$ and the spectrum in rotation frame reads:

$$\omega_{1,2} = -i\frac{\kappa_\perp k_\perp^2}{2\rho C_p} \pm \sqrt{c_{II}^2 k_z^2 - \left(\frac{\kappa_\perp k_\perp^2}{2\rho C_p}\right)^2} \tag{1.3.21}$$

For $k_\perp = 0$ $\omega_{1,2} = \pm c_{II}|k_z|$, for $k_z = 0$ $\omega_{1,2} = i(-1 \pm 1)\frac{\kappa_\perp k_\perp^2}{2\rho C_p}$. It is interesting to compare this spectrum with the overdamped temperature waves in ordinary classical liquid with the spectrum $\omega = -i\frac{\kappa_\perp k_\perp^2}{\rho C_p}$ considered in Sect. 1.1 [see Eq. (1.1.30)], and the propagating second sound waves with the spectrum $\omega^2 = c_{II}^2 k^2$ [see Eq. (1.1.69)] for irrotational superfluid (the same propagating spectrum of the second sound $\omega^2 = c_{II}^2 k^2$ we get in the hydrodynamics of slow rotations). From the spectrum (1.3.21) it follows, that in the hydrodynamics of fast rotations the oscillations of the temperature propagate in the form of the second sound only along the axis of the vortices, while in perpendicular direction they are ordinary damped thermal waves (the second root in Eq. (1.3.21) corresponds at small k_z to $\delta T \to 0$ and $\delta W_\parallel = const$).

1.3.3.1 Another Collective Modes in the Hydrodynamics of Fast Rotations

To establish another application of the derived equations we consider the oscillations of the transverse velocity $\delta\vec{v}_\perp$ and of the displacement $\vec{u}$ in a state with simultaneous uniform rotation and a uniform heat flux $Q = TSv_{n\parallel}$ along the vortex lines. This problem is of interest because a substantial role in it is played by the second term of the expression (1.3.15) for $\vec{G}$. Confining ourselves for simplicity to the case of low temperatures $\rho_n \ll \rho$ and neglecting in (1.3.17) the term with $B_{\alpha\beta}$ and B', we rewrite this equation in the rotation frame in the form:

$$\vec{u} - \vec{v}_\perp = \frac{1}{2\Omega\rho}\left(\vec{F} \times \vec{e}_z\right) - iv_{n\parallel}k_z\vec{u} - \frac{i}{2\Omega}v_{n\parallel}\left\{k_z(\vec{e}_z \times \delta\vec{v}_\perp) + (\vec{e}_z \times \vec{k}_\perp)\frac{\vec{k}_\perp \delta\vec{v}_\perp}{k_z}\right\}, \tag{1.3.22}$$

where $\vec{F}$ is defined by (1.2.50) and $v_{n\parallel} = Q/TS$. The second equation that connects $\vec{u}$ with $\vec{v}_\perp$ is obtained by projecting on the $\{xy\}$ plane of the second equation for $\partial j_i/\partial t$ of the system (1.2.22) and excluding from it the pressure using the incompressibility condition at low temperatures $\vec{\nabla} \cdot \vec{v}_s = 0$. We have in the rotation frame:

$$\delta\dot{\vec{v}}_\perp + 2\vec{\Omega} \times \delta\vec{v}_\perp - \frac{\vec{k}_\perp}{k^2}\left(\vec{k}_\perp\left(2\vec{\Omega} \times \delta\vec{v}_\perp\right)\right) + \frac{1}{\rho}\vec{F} - \frac{\vec{k}_\perp}{\rho k^2}\left(\vec{k}_\perp \cdot \vec{F}\right) = 0. \tag{1.3.23}$$

If $\vec{k}$ is small enough, Eqs. (1.3.22, 1.3.23) describe in the principle approximation the independent oscillations of $\delta\vec{v}_\perp$ and $\vec{u}$. The former have a frequency:

$$\omega = \frac{2\left(\vec{\Omega} \cdot \vec{k}\right)}{k} \tag{1.3.24}$$

and are inertial waves in an ordinary (classical) hydrodynamics of the incompressible rotational fluid considered in Sect. 1.1.

The second mode constitutes the oscillations of the displacement $\vec{u}$ and are peculiar to the fast rotations hydrodynamics. The frequency of this mode in the rotation frame:

$$\omega = v_{n\|} k_z; \quad v_{n\|} = Q/TS. \tag{1.3.25}$$

It must be emphasized that this mode exists only at finite temperature. It vanishes at $T = 0$, i.e. in the total absence of the normal component. Here lies an essential difference between hydrodynamics of slow-rotations and fast-rotations at finite temperatures.

In the hydrodynamics of slow rotations the velocity $\vec{v}_s$ and the displacement $\vec{u}$ are not independent variables, but are connected by the additional condition (1.2.20) for $curl\, \vec{v}_s$ and vectors of elementary translations $\vec{e}_a$. In hydrodynamics of fast-rotations the same takes place at $T = 0$, when the difference between $\vec{v}_s$ and $\vec{V}_s$ vanishes. The presence of the root with $\omega = 0$ means here simply compatibility of hydrodynamic equations with the supplementary condition (1.2.20).

We should also make a remark concerning the spectrum (1.3.24). Although the mode (1.3.24) has zero gap, its frequency, generally speaking, does not tend to zero as $\vec{k} \to 0$. This highlights the distinction of the fast-rotations hydrodynamics, for the validity of which the condition $\vec{k} \to 0$ is generally speaking not sufficient and one more condition is required. To determine this condition we note that the frequency in a rotating coordinate frame can be regarded as an eigenvalue of the operator:

$$i\left\{\frac{\partial}{\partial t} + \left(\left(\vec{\Omega} \times \vec{r}\right)\vec{\nabla}\right) - \vec{\Omega}\times\right\} = i\frac{\partial}{\partial t} - \Omega J_z, \tag{1.3.26}$$

where $J_z = S_z + L_z$, $L_z = -i\left(\vec{r} \times \vec{\nabla}_\perp\right)$ is the orbital angular momentum and $S_z = -i\varepsilon_{z\alpha\beta}$ is the spin of the vector field $\delta\vec{v}_\perp$. The derivative $\partial\omega/\partial\Omega$, as can be seen from (1.3.26) is equal to $-\langle J_z \rangle$. For the frequencies of all the modes in the fast-rotations hydrodynamics to tend to zero we must satisfy besides the condition $\vec{k} \to 0$ also $\langle J_z \rangle \to 0$. The latter is equivalent for the spectrum (1.3.24) to the condition $k_z/k \to 0$, where $k^2 = k_z^2 + k_\perp^2$.

1.4 Opposite Case of a Single Bended Vortex Line for Extremely Slow Rotations ($\Omega \sim \Omega_{C1}$)

In the last section of the present chapter we will consider an opposite case of a single bended vortex line aligned with the axis of a cylindrical vessel of radius R. It is known that such a state corresponds to the thermodynamic equilibrium at $\Omega \sim \Omega_{C1} = \frac{\hbar}{mR^2}\ln\frac{R}{d}$. As it was shown by Hall [36, 37], the equation that describes the bending oscillations of the vortex lines is reduced to the Schroedinger equation with an effective mass:

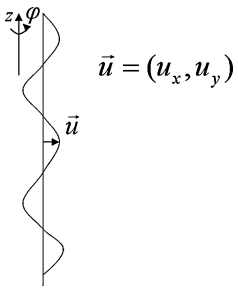

Fig. 1.11 The bended vortex line situated in the center of the cylindrical vessel. $\vec{u}$ is the 2D displacement perpendicular to the vortex line. z is the axis of the vessel, φ is rotation angle

$$m^* = \frac{m}{\ln(\hbar/p_z d)} \tag{1.4.1}$$

(p_z is the momentum of the oscillations parallel to the vortex line) by introducing the wave-function:

$$\Psi = const(u_x + iu_y). \tag{1.4.2}$$

In Eq. (1.4.2) $\vec{u}$ is the two-dimensional vector of the displacement of the vortex line in a plane perpendicular to the rotation axis (see Fig. 1.11). If we choose $const = (\pi\rho_s/m)^{1/2}$ in Eq. (1.4.2) the energy of the oscillations also becomes identical with the energy given by Schroedinger expression:

$$E = \frac{\hbar^2}{2m^*}\int \left|\frac{\partial\Psi}{\partial z}\right|^2 dz. \tag{1.4.3}$$

1.4.1 Stabilization of the Bending Oscillations by Rotation

Note that in our case rotation around z-axis on an angle φ is simultaneously the gauge transformation of the Ψ-function: $\Psi \rightarrow \Psi e^{i\varphi}$. The generator of this gauge transformation is the operator $\hbar\hat{N}$, where $\hat{N}$—is the number of particles operator. In the second quantization technique the operator of the number of particles $\hat{N} = \sum_{p_z} b^+_{p_z} b_{p_z}$ commutes with the Hamiltonian $\hat{H} = \sum_{p_z} \frac{p_z^2}{2m*} b^+_{p_z} b_{p_z}$ of the 1D Bose-gas of the oscillating quanta carrying the momentum p_z.

From the other hand the operator of the z-component of the angular momentum in our case equals to $\hat{J}_z = \hbar\hat{N}$ and hence $\hat{J}_z$ also commutes with the Hamiltonian $\hat{H}$. Thus the quanta of the vortex line oscillations besides a linear momentum p_z possess also an independent quantum number—an intrinsic angular momentum—$\hbar$

("diamagnetic situation" according to Andreev and Kagan [31]). That is why in our case the bended vortex line in reality does not vibrate but rotates around z-axis (we can prove that in second quantization technique $\vec{u} \times \dot{\vec{u}} \neq 0$). Thus the real thermodynamic equilibrium takes place only in the rotating frame and hence the spectrum in this frame reads:

$$\varepsilon(p_z) = \varepsilon_0(p_z) - \Omega \frac{J_z}{N} = \hbar\Omega + \varepsilon_0(p_z) = \hbar\Omega + \frac{p_z^2}{2m} \ln \frac{\hbar}{d\, p_z}. \tag{1.4.4}$$

Thus the spectrum of the bended vortex line acquires a gap $\hbar\Omega$. Note that in the macroscopic hydrodynamics of slow rotations for $\Omega_{C1} \ll \Omega \ll \Omega_{C2}$: $\hbar\omega = 2\hbar\Omega + \frac{\hbar^2 k_z^2}{2m} \ln \frac{b}{a}$ and we have a gap $2\hbar\Omega$ for Lord Kelvin waves (see Sect. 1.2). The difference between the macroscopic gap 2Ω and the "microscopic" gap $\Omega = \Omega_{C1}$ is connected with the fact that for a single bended vortex line we cannot introduce a macroscopic superfluid velocity of the solid state rotations $\vec{v}_0 = \vec{\Omega} \times \vec{r}$ and hence the orbital angular momentum $\hat{L}_z = 0$ (see the discussion in the end of the Sect. 1.3). Correspondingly $\hat{J}_z = \hat{S}_z$ (is purely intrinsic angular momentum) and $\partial\omega/\partial\Omega = \hbar$ (and not $2\hbar$).

1.4.1.1 Thermodynamics of a Bended Vortex Line

The presence of the energy gap $\hbar\Omega$ causes the spectrum (1.3.30) to satisfy the Landau criterion for superfluidity. The critical velocity is:

$$v_C = \min \frac{\varepsilon(p_z)}{p_z} = \left(\frac{\hbar\Omega}{m} \ln \frac{\hbar}{2md^2\Omega} \right)^{1/2}, \tag{1.4.5}$$

where d is the vortex core. For $\Omega \sim \Omega_{C1}$ $v_C \sim \frac{\hbar}{mR}$.

For the same reason, the divergences at small momenta, which are customary for one-dimensional systems, are absent in this case. Indeed, let us calculate again the mean displacement from the equilibrium position of the bended vortex line squared $\langle \vec{u}^2 \rangle$ (see Sect. 1.2) assuming that the condition $T \gg \Omega$ (more rigorously $k_B T \gg \hbar\Omega$) is satisfied. In this case the bosonic distribution function $n_B\left(\frac{\varepsilon(p_z)}{T}\right) \approx \frac{T}{\varepsilon(p_z)}$ and

$$\langle \vec{u}^2 \rangle = \frac{m}{\pi\rho_s} \langle |\Psi|^2 \rangle = \frac{m}{\pi\rho_s} \int \frac{dp_z}{2\pi\hbar} n_B\left(\frac{\varepsilon(p_z)}{T}\right) = \frac{mT}{\pi\hbar\rho_s v_C}, \tag{1.4.6}$$

where the critical velocity v_C is given by (1.4.5).

1.4.2 Visualization of the Vortex Lattice in Rotating Superfluid. Packard Experiments

The ratio of this quantity to the square of the vessel radius is of the order of

$$\frac{\langle \vec{u}^2 \rangle}{R^2} \sim \frac{d}{R}\frac{Tmd^2}{\hbar^2}\frac{1}{\ln\frac{\hbar}{2md^2\Omega}} \sim \frac{d}{R}\frac{Tmd^2}{\hbar^2}\frac{1}{\ln(R^2/d^2)} \tag{1.4.7}$$

for $\Omega \sim \Omega_{C1}$.

In superfluid ^{4}He for $\Omega = \Omega_{C1} = \frac{\hbar}{mR^2}\ln\frac{R}{d} \sim 1\ \frac{\text{rot}}{\text{s}}$, $d \sim 3$ Å and $R \sim 0.1$ cm: $\frac{\langle \vec{u}^2 \rangle}{R^2} \ll 1$. Note that without the gap $\langle \vec{u}^2 \rangle \sim T\int \frac{dp_z}{p_z^2}$ and we have a strong infrared divergence at $p_z \to 0$. Hence without the gap 1D bended vortex will form a globule as in many 1D systems (like in polymers for example). The small value of $\langle \vec{u}^2 \rangle / R^2 \ll 1$ can provide an explanation of Packard experiments [86–88]. He with his colleagues injected electrons in the vortex core, applied the voltage in the direction parallel to the vortex lines and got the photograph of the vortex lattice in ^{4}He on the screen. In his experiments on visualization of the vortex lattice he observed small vortex displacements from equilibrium positions in the triangular lattice (see Fig. 1.12).

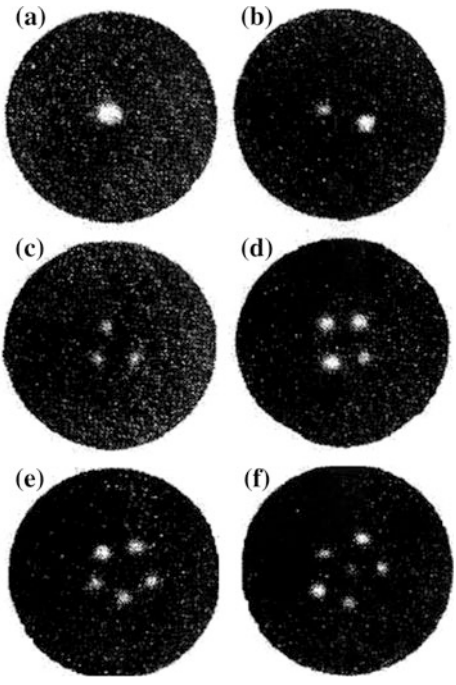

Fig. 1.12 Vortex arrays in superfluid ^{4}He from Yarmchuk, Gordon, Packard [86–88] and Vinen [37, 38]. On Figs. **a**–**f** the number of vortices changes from 1 to 6

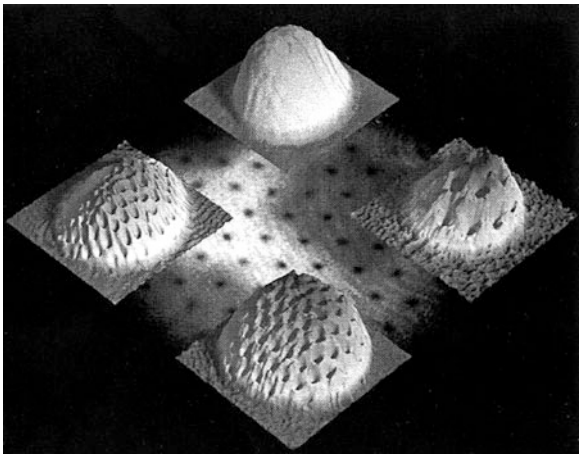

Fig. 1.13 Vortex lattice in rotating dilute Bose gases of alkali elements (^{7}Li, ^{23}Na, ^{87}Rb) [58–61, 92]

Note that in alkali gases in magnetic traps a low-temperature regime of Bose–Einstein condensation (BEC) was achieved in 1995 (see Chap. 4) [89–91]. Quantum vortices, which are the main signature of the superfluidity, are found in rotating condensate [58–61, 92] similar to that in liquid helium (see Sect. 1.2). The snapshot of the vortex lattice in dilute Bose-gases is presented on Fig. 1.13.

Later on the vortex lattice was discovered also in BCS-phase of fermionic gases [47] (^{6}Li and ^{40}K) in the regime of Feshbach resonance (see Chap. 4). From both Figures we can see almost regular distribution of vortices forming triangular lattice both in dense superfluid helium and in dilute gases. Hence the mean displacements squared of the vortex lines are finite and small in comparison with the intervortex distance b in both experimental pictures.

1.4.3 Contribution to Normal Density and Specific Heat from Bended Vortex Lines

Returning back to the thermodynamic contribution from bended vortex lines we can calculate also the one-dimensional density of the normal component ρ_n (see Sect. 1.1):

$$\rho_n = -\int p_z^2 \frac{\partial n_B(\varepsilon(p_z)/T)}{\partial \varepsilon} \frac{dp_z}{2\pi\hbar} = \frac{2T\Omega}{v_c^3} \tag{1.4.8}$$

With decreasing Ω the density ρ_n varies proportionally to $\Omega^{-1/2}$ (note that anyway $\Omega \geq \Omega_{C1}$). We can also write down an expression for the specific heat C_Ω per unit length of the vortex line at constant angular velocity Ω:

$$C_\Omega = C_0(T) + \frac{2\Omega}{v_C}, \tag{1.4.9}$$

where

$$C_0(T) = \frac{3\xi(3/2)}{4\hbar}\left(\frac{mT}{\pi \ln \frac{\pi}{mTd^2}}\right)^{1/2}, \tag{1.4.10}$$

and $\xi(3/2)$ is Riemann function.

In contrast to Eq. (1.4.7) for $\langle \vec{u}^2 \rangle$ and Eq. (1.4.8) for ρ_n, in the case of the specific heat only the second correction term in (1.4.9) depends on the rotation frequency for $T \gg \hbar\Omega$.

The thermal oscillations delocalize the vortex line. As a result, the average velocity curl differs from a δ-function (compare with Eq. (1.2.2) in Sect. 1.2) and is determined by the probability distribution of the values of the distance r of the vortex line from the vessel axis. Since the distribution is obviously Gaussian at $T \gg \hbar\Omega$, we have in accord with (1.4.7):

$$\left\langle \vec{\nabla} \times \vec{v}_s \right\rangle = \frac{2\hbar}{m\langle \vec{u}^2 \rangle} \exp\left\{ -\frac{r^2}{\langle \vec{u}^2 \rangle} \right\} = \frac{2\pi\hbar^2 \rho_s v_C}{m^2 T} \exp\left\{ -\frac{r^2 mT}{\pi\hbar\rho_s v_C} \right\}. \tag{1.4.11}$$

Note that the bending oscillations of the vortex lines as we already mentioned have an intrinsic angular momentum and thus produce an interesting effect of the angular-momentum transport by the heat flux in the absence of the matter flux. The angular momentum flux is:

$$L = -\hbar|\Psi|^2 v_n = -\frac{Tv_n}{v_C} = -\frac{Q}{Sv_C}, \tag{1.4.12}$$

where $Q = TSv_n$ is the heat flux.

The torque carried by the heat flux between solid surfaces perpendicular to the rotation axis at $v_n \sim v_C$ is of the order of $N_v T$, where N_v is the total number of vortices. At $T \sim 1$ K the torque measured in dyn·cm is of the order of 10^{-12} Ω (s^{-1}) S_0 (cm^2), where S_0 is the area of the solid surface. Although this is a small quantity, it seems to be experimentally observable.

1.5 Experimental Situation and Discussion. How to Achieve the Limit of the Fast Rotations at Not Very High Frequencies in He II- ^{3}He Mixtures and in Superfluid ^{3}He-B

Concluding the present Chapter let us stress once more that:

1. We present a hydrodynamic description of the two-velocity hydrodynamics of a superfluid ^{4}He and dilute Bose gases following Landau scheme of the conservation laws.

2. We generalize the hydrodynamic scheme on the presence of the quantized linear vortices and construct nonlinear hydrodynamics of slow and fast rotations with an account of the vortex lattice and the friction forces between normal excitations and vortices.
3. We analyze collective modes of the vortex lattice and in particular the shear (Tkachenko mode) as well as the bending mode of Lord Kelvin. We find out their contribution to the vortex displacements and to the thermodynamics. We also analyze the possibility to melt the vortex lattice in quasi two-dimensional rotating Bose gases due to the contribution of the quadratic in k-vector Tkachenko modes at very low frequencies.

The last topic which should be considered in this Chapter is how to achieve the limit of the hydrodynamics of fast rotations at not very high frequencies.

In the end of Sect. 1.3 we mentioned that when the Hall-Vinen coefficient β becomes of the order of one, the Umklapp relaxation time for the scattering of the normal excitations on the vortices $\tau_U \sim 1/\beta\Omega$ is of the order of $1/\Omega$ and the condition $\omega\tau_U \ll 1$ for the validity of the hydrodynamics of fast rotations require the condition $\omega < \Omega$ for the frequencies. With decreasing temperature, however, the situation changes since the bending oscillations of the vortex lines begin to produce a substantial contribution to the density of the normal component. This contribution $\rho_{n\Omega} = 2T\Omega/v_C^3$ exceeds the phonon contribution $\rho_n^{ph} = T^4/c_I^5$ [see Eq. (1.1.50)] for $T \leq 0.1$ K in a very clean superfluid ^{4}He thus creating the possibility for the hydrodynamics of rapid rotations for $\Omega \sim \Omega_{C1}$. Note that the quasiparticles which correspond to the quanta of the bended oscillations, are localized on the vortex lines and can move easily only along them. Correspondingly we have only one component of the normal velocity $v_{n\|}$ and can speak only about highly anisotropic hydrodynamics of fast rotations.

A similar but even more clearly pronounced situation arises at low temperatures in the solutions of ^{3}He in He-II (see Chap. 15), owing to the absorption of the impurities by the vortex cores (see [93]). In other words in the rotating solution all the ^{3}He-impurities (which serve as the normal excitations in this system) are localized in the vortex core due to the gradient of Bernoulli integral $\vec{\nabla}\left(\mu + \frac{v_s^2}{2}\right)$ [see Eq. (1.1.13)]. Note that $\vec{v}_s$ increases when we approach the vortex core thus the pressure gradient causes the localization of the impurities inside the core. From the other hand they can again move freely along the vortex lines. We again have only one $v_{n\|}$ and can speak only about the hydrodynamics of fast rotations.

Finally in superfluid ^{3}He-B, in which as in He-II, the orbital hydrodynamics is isotopic the condition $\tau_U \sim \tau_N$ starts to be satisfied at temperatures $T \leq (T_C \sim 1$ mK) for $\Omega \leq 1$ s^{-1} because of the rather large τ_N for the scattering of (fermionic) quasiparticles on each other in ^{3}He-B. The higher angular velocities in ^{3}He-B should be described by the fast-rotations hydrodynamics.

We can repeat once more that for the dilute Bose gases we should distinguish between the slow rotations with vortex lattice and rapid rotations when the vortex lattice is melted. In the same time in dense superfluids (He-II, ^{3}He-B, ^{3}He- He-II

solutions) we should distinguish between the isotropic hydrodynamics of the slow rotations and the anisotropic hydrodynamic of the fast rotations. However, the vortex lattice is present in both types of the hydrodynamic descriptions in dense superfluids.

We should like also to clarify more detaily the similarity between the hydrodynamics of rotating superfluids in the presence of the vortex lattice and the second sound regime in alkali crystals briefly mentioned in the Introduction to the Sect. 1.3.

Note that in the alkali crystals the second sound as a propagating mode with a drift velocity $\vec{v} \neq \dot{\vec{u}}$ ($\dot{\vec{u}}$ is the lattice velocity) exists only in the frequency window $\gamma_U = \frac{1}{\tau_U} < \omega < \gamma_N = \frac{1}{\tau_N}$ for weak Umklapp processes with $\gamma_U < \gamma_N$ (see Gurevich [44] for a review). In the same time for small frequencies $\omega < \gamma_U < \gamma_N$ the second sound is overdamped.

The same estimates distinguish hydrodynamics of slow and fast rotations. Namely, the total damping of a second sound $\frac{\mathrm{Im}\omega}{\omega} = \frac{\gamma_U}{\omega} + \frac{\omega}{\gamma_N}$ is a sum of the damping due to Umklapp process and $\mathrm{Im}\omega \sim \gamma_U$ and a standard hydrodynamic damping $\mathrm{Im}\omega \sim \omega^2 \tau_N \sim \frac{\omega^2}{\gamma_N}$ [see Eq. (1.1.25)]. For $\gamma_U < \omega < \gamma_N$, $\frac{\mathrm{Im}\omega}{\omega} \ll 1$—the second sound wave is propagating and we have the hydrodynamics of the slow rotations. In the same time for $\omega < \gamma_U < \gamma_N$, $\frac{\mathrm{Im}\omega}{\omega} \gg 1$ (due to the contribution of γ_U/ω) and we have an overdamped second sound in the direction perpendicular to the vortex lines. Thus we restore the hydrodynamics of the fast rotations.

References

1. Landau, L.D., Lifshitz, E.M.: Fluid Mechanics, vol. 6 (Course of Theoretical Physics). Butterworth-Heinemann, Oxford (1987)
2. Landau, L.D.: J. Phys. (USSR) **5**, 71 (1941)
3. Landau, L.D.: Phys. Rev. **75**, 884–885 (1949)
4. Kapitza, P.L.: J. Phys. (USSR) **5**, 59 (1941)
5. Kapitza, P.L.: Phys. Rev. **60**, 354–355 (1941)
6. Landau, L.D., Lifshitz, E.M.: Quantum Mechanics. Non-Relativistic Theory. Pergamon Press, New York (1977)
7. Landau, L.D., Lifshitz, E.M.: Statistical Physics, Part I. Butterworth-Heinemann, Oxford (1999)
8. Allen, J.F., Misner, A.D.: Nature **141**, 75(1938)
9. Allen, J.F., Misner, A.D.: Proc. Roy. Soc. A **172**, 467 (1939)
10. Tisza, L.: Nature **141**, 913 (1938)
11. Tisza, L.: Compt. Rend. **207**, 1035, 1186 (1938)
12. Tisza, L.: J. Phys. Rad. **1**, 164, 350 (1940)
13. Tisza, L.: Phys. Rev. **72**, 838–854 (1947)
14. Khalatnikov, I.M.: An Introduction to the Theory of Superfluidity. Perseus Publishing, Cambridge (2000)
15. Bekarevich, I.L., Khalatnikov, I.M.: JETP **13**, 643 (1962)
16. Putterman, S.J.: Superfluid Hydrodynamics (North-Holland series in low temperature physics). North-Holland, New York (1974). (and the reference therein)

17. Andronikashvili, E.L., Mamaladze, Y.G.: Rev. Mod. Phys. **38**, 567–625 (1966)
18. Andronikashvili, E.L.: JETP **18**, 424 (1948)
19. Feynman, R.P.: Progr. Low Temp. Phys. **1**, Chap. 2, 17–53 (1955)
20. Onsager, L.: Nuovo Cimento **6**(Suppl. 2), 249 (1949)
21. Feynman, R.P.: Statistical Mechanics: A Set of Lectures (Advanced Books Classics). Westview Press, Boulder (1998)
22. Tilley, D.R., Tilley, J.: Superfluidity and Superconductivity (Graduate Student Series in Physics). Institute of Physics Publishing, Bristol (1990)
23. Lifshitz, E.M., Pitaevskii, L.P.: Statistical Physics, Part 2. Pergamon, New York (1980)
24. Abrikosov, A.A.: JETP **5**, 1174–1183 (1957)
25. Schrieffer, J.R.: Theory of Superconductivity. Benjamin, New York (1964)
26. Bardeen, J., Cooper, L.N., Schrieffer, J.R.: Phys. Rev. **108**, 1175–1204 (1957)
27. Baym, G., Chandler, E.: J. Low. Temp. Phys. **50**, 57–87 (1983)
28. Baym, G.: Phys. Rev. B **51**, 11697–11703 (1995)
29. Baym, G.: Phys. Rev. A **69**, 043618 (2004)
30. Gifford, S.A., Baym, G.: Phys. Rev. A **70**, 033602 (2004)
31. Andreev, A.F., Kagan, M.Yu.: JETP **59**, 318 (1984)
32. Tkachenko, V.K.: JETP **22**, 1282 (1965)
33. Tkachenko, V.K.: JETP **23**, 1049 (1966)
34. Tkachenko, V.K.: JETP **29**, 245 (1969)
35. Thomson W. (Lord Kelvin).: Phil. Mag. **10**, 155–168 (1880)
36. Hall, E.: Proc. Roy. Soc. A **245**, 546–561 (1958)
37. Hall, E., Vinen, W.F.: Proc. Roy. Soc. A **238**, 215–234 (1956)
38. Hall, E.: Adv. Phys. **9**, 89–146 (1960)
39. Sonin, E.B.: Rev. Mod. Phys. **59**, 87–155 (1987)
40. Sonin, E.B.: Doctoral Dissertation. Lebedev Physical Institute, Moscow (1981)
41. Iordanskii, S.V.: JETP **22**, 160 (1960)
42. Lebedev, V.V., Khalatnikov, I.M.: JETP **48**, 1167 (1978)
43. Dzyaloshinskii, I.E., Volovik, G.E.: Ann. Phys. **125**, 67–97 (1980)
44. Gurevich, V.L.: Transport in Phonon Systems (Modern Problems in Condensed Matter Sciences). Elsevier Science Ltd., Oxford, 1988, Kinetics of Phonon Systems, Moscow, Nauka, 1980
45. Vollhardt, D., Wölfle, P.: The Superfluid Phases of Helium 3. Taylor and Francis, London (1990)
46. Leggett, A.J.: Rev. Mod. Phys. **47**, 331–414 (1975)
47. Zwierlein, M.W., Abo-Shaeer, J.R., Schirotzek, A., Schunck, C.H., Ketterle, W.:Nature **435**, 1047–1051 (2005)
48. Williams, M.R., Fetter, A.L.: Phys. Rev. B **16**, 4846–4852 (1977)
49. Fetter, A.L.: Phys. Rev. **162**, 143–153 (1967)
50. Fetter, A.L.: Rev. Mod. Phys. **81**, 647–691 (2009)
51. Matvienko, S.I., Kovrizhin, D., Ouvry, S., Shlyapnikov, G.V.: Phys. Rev. A **80**, 063621 (2009)
52. Matvienko, S.I., Shlyapnikov, G.V.: Phys. Rev. A **83**, 033604 (2011)
53. Cooper, N.R., Wilkins, N.K., Gunn, J.M.F.: Phys. Rev. Lett. **87**, 120405 (2001)
54. Cooper, N.R.: Adv. Phys. **57**, 539–616 (2008)
55. Cooper, N.R., Komineas, S., Read, N.: Phys. Rev. A **70**, 033604 (2004)
56. Rezayi, E.H., Haldane, F.D.M.: Phys. Rev. B **50**, 17199–17207 (1994)
57. Rezayi, E.H., Haldane, F.D.M., Yang, K.: Phys. Rev. Lett. **83**, 1219–1222 (1999)
58. Bretin, V., Stock, S., Seurin, Y., Dalibard, J.: Phys. Rev. Lett. **92**, 050403 (2004)
59. Madison, K.W., Chevy, F., Wohlleben, W., Dalibard, J.: Phys. Rev. Lett. **84**, 806–809 (2000)
60. Chevy, F., Madison, K.W., Dalibard, J.: Phys. Rev. Lett. **85**, 2223–2227 (2000)
61. Madison, K.W., Chevy, F., Bretin, V., Dalibard, J.: Phys. Rev. Lett. **86**, 4443–4446 (2001)
62. Ho, T.-L.: Phys. Rev. Lett. **87**, 060403 (2001)

63. Landau, L.D., Lifshitz, E.M.: Theory of Elasticity (Course of Theoretical Physics). Pergamon Press, Oxford (1959)
64. Lifshitz, E.M., Pitaevskii, L.P.: Physical Kinetics: Course of Theoretical Physics, vol. 10. Butterworth-Heinemann, Oxford (1981)
65. Kamerlingh Onnes, H.: Proc. Roy. Acad. (Amsterdam), **13**, 1903 (1911)
66. Kamerlingh Onnes, H.: Trans. Faraday Soc. **18**, 145–174 (1922)
67. Shalnikov, A.I.: JETP **14**, 753 (1962)
68. Pitaevskii, L.P.: JETP **13**, 451 (1961)
69. Dalfovo, F., Giorgini, S., Pitaevskii, L.P., Stringari, S.: Rev. Mod. Phys. **71**, 463–512 (1999)
70. Gross, E.P.: Nuovo Cimento **20**, 454 (1961)
71. Gross, E.P.: J. Math. Phys. **4**, 195 (1963)
72. Kim, E., Chan, M.H.W.: Nature **427**, 225–227 (2004)
73. Kim, E., Chan, M.H.W.: Science 305, 1941–1944 (2004)
74. Andreev, A.F., Lifshitz, I.M.: JETP **56**, 2057 (1969)
75. Leggett, A.J.: Phys. Rev. Lett. **25**, 1543–1546 (1970)
76. Hugenholtz, N.M., Pines, D.: Phys. Rev. **116**, 489–506 (1959)
77. Landau, L.D., Lifshitz, E.M.: The Classical Theory of Fields: Course of Theoretical Physics, vol. 2. Butterworth-Heinemann, Oxford (1980)
78. Volovik, G.E., Dotsenko, V.S.: JETP **51**, 65–73 (1980)
79. Reatto, L.: Phys. Rev. **167**, 191–202 (1968)
80. Kittel, C.: Quantum Theory of Solids. Wiley, New York (1963)
81. Kittel, C.: Introduction to Solid State Physics. Wiley, New York (1986)
82. Laughlin, R.B.: Rev. Mod. Phys. **71**, 863–874 (1999)
83. Laughlin, R.B.: Phys. Rev. B **23**, 5632–5633 (1981)
84. Laughlin, R.B.: Phys. Rev. Lett. **50**, 1395–1398 (1983)
85. Laughlin, R.B.: Phys. Rev. B **27**, 3383–3389 (1983). In: Prange, R.E., Girvin, S.M. (eds.) The Quantum Hall Effect, 2nd edn. Springer, New York (1990)
86. Packard, R.E.: XVI international conference on low temperature physics. Physica B+C **109**, **110**, 1474 (1982)
87. Yarmchuk, E.J., Gordon, M.J.V., Packard, R.E.: Phys. Rev. Lett. **43**, 214–217 (1979)
88. Yarmchuk, E.J., Packard, R.E.: J. Low Temp. Phys. **46**, 479 (1982)
89. Anderson, M.H., Ensher, J.R., Matthews, M.R., Wieman, C.E., Cornell, E.A.: Science **269**, 198–201 (1995)
90. Bradley, C.C., Sackett, C.A., Tollett, J.J., Hulet, R.G.: Phys. Rev. Lett. **75**, 1687–1690 (1995)
91. Davis, K.B., Mewes, M.-O., Andrews, M.R., van Druten, N.J., Durfee, D.S., Kurn, D.M., Ketterle, W.: Phys. Rev. Lett. **75**, 3969–3973 (1995)
92. Abo-Shaeer, J.R., Raman, C., Vogels, J.M., Ketterle, W.: Science **292**, 476–479 (2001)
93. Reut, L.S., Fisher, I.Z.: JETP **28**, 375 (1969)
94. Abrikosov, A.A., Gor'kov, L.P., Dzyaloshinskii, I.E.: Quantum Field Theoretical Methods in Statistical Physics. Pergamon, New York (1965)
95. Keesom, W.H., Macwood, G.E.: Physica **5**, 737 (1938)
96. Keesom, W.H., Keesom, A.P.: Physica **2**, 557 (1935)
97. Keesom, W.H.: Helium. Elsevier, Amsterdam (1942)
98. Lee, T.D., Yang, C.N.: Phys. Rev. **105**, 1119–1120 (1957)
99. Lee, T.D., Huang, K., Yang, C.N.: Phys. Rev. **106**, 1135–1145 (1957)

Chapter 2
Quantum Crystals. The Search for Supersolidity

The present chapter will consist of the two main parts devoted correspondingly to bulk and surface phenomena in quantum crystals. In the first part of the chapter we will discuss a notion of quantum crystals and their distinction from ordinary classical crystals from the point of view of Lindemann criterion [1, 2] for crystal melting. We will also use de Boer parameter to describe the quantum crystals. Note that it measures the degree of quantumness or the ratio of kinetic delocalization energy of zero vibrations to the potential energy [3]. We will discuss Andreev, Lifshitz theory [4] for the hydrodynamics of superfluid quantum crystals and the flow of zero vacancies [5–7] as well as recent Andronikashvili type of rotating experiments of Chan et al. [8–13] on non-classical moment of inertia [14, 15] and the search of supersolidity in the crystals of ^{4}He [16–21]. We will provide a short review of the important experimental and theoretical articles on this fascinating subject [22–36] published during last several years by several groups in Moscow and by other groups in the West. We will discuss the overall pessimism of the community with respect to the possible discovery of supersolidity in [8–12] and provide the alternative explanations connected with the mass flow of defects (impurities, dislocations, two-level systems, thermal vacancies and so on) relative to the crystalline lattice in the non-perfect crystals of solid ^{4}He [36–38]. Very convincing results belong here to Rittner and Reppy who showed the disappearance of the supersolid fraction in rotating experiments after good annealing of the quantum crystal [36]. We will start the second part of the present chapter with the brief discussion of classical [39–42] and quantum roughening [43, 44] for different crystal surfaces of solid ^{4}He and present the estimates for roughening transition in the framework of Nozieres [39] theory of Berezinskii-Kosterlitz-Thouless type [45, 46] as well as mean-field arguments of Andreev and Parshin [47]. We will also briefly consider the two branches of surface waves on the mobile rough interface—the melting-crystallization waves (predicted and experimentally discovered in Kapitza Institute in Moscow [47–49]) and the more standard Rayleigh waves typical for the free surfaces of the crystals [5].

M. Yu. Kagan, *Modern Trends in Superconductivity and Superfluidity*,
Lecture Notes in Physics 874, DOI: 10.1007/978-94-007-6961-8_2,

2.1 Quantum Crystals. Phase-Diagram. The Search for Supersolidity

In the introduction to the Landau Theory of Superfluidity in Chap. 1 we presented the phase-diagram of ^{4}He (see Fig. 1.1) and briefly discuss it. The phase-diagram contains superfluid and normal liquid phases as well as gas and solid phases. Moreover there is no triple point where the liquid, solid and gas phases would coexist. For pressures $P > 26$ bar ^{4}He becomes solid. On the melting curve at low temperatures solid ^{4}He has hexagonal (hcp) structure. Between 1.46 and 1.76 K it has a cubic (bcc) structure. Note that there is a shallow minimum on the pressure versus temperature (P–T) curve for solid-superfluid phase-boundary at $T \sim$ (0.5–0.6) K (see [40] and Fig. 1.1). Close to the melting curve the density of a solid phase is very close to the density of a superfluid phase and thus $\frac{\Delta\rho}{\rho} \sim 0.1$, where $\Delta\rho = (\rho_S - \rho_L)$. It means that the interparticle distance (as well as other parameters) of solid ^{4}He are very close to superfluid ^{4}He. Moreover close to the minimum on the P–T curve the latent heat Q corresponding to liquid–solid phase-transition is small and thus first order phase-transition from superfluid to solid phase could be considered to be close with some degree of precaution to a second order phase transition. The only essential difference between liquid and solid phases is a translational invariance in solid phase connected with the elementary translations of the crystal lattice and the change of the short range order when we go from liquid to solid phase. This change is connected with an appearance of elementary cell in solid ^{4}He and thus with a shape energy a shape energy defined by a shear modulus (see Chap. 1). This "proximity" effect [50] between solid and superfluid phases was a main motivation to search for some type of quantumness in crystalline ^{4}He at low temperatures.

2.1.1 Lindemann and de Boer Parameters

Additional support for these ideas came from the estimates of Lindemann [1, 2] and de Boer [3] parameters for solid ^{4}He.

2.1.1.1 Lindemann Parameters in Solid ^{4}He

As we already mentioned in Chap. 1, Lindemann parameter [1, 2] is essential for melting of the crystal. It is the ratio of the root mean square of the displacement of atoms to the interatomic distance d:

$$\gamma_L \sim \frac{\sqrt{\langle \vec{u}^2 \rangle}}{d}. \tag{2.1.1}$$

The classical solid will melt if the Lindemann's parameter exceeds the critical value of the order of 0.1 in 3D. However, the X-ray measurement of Debye-Waller factor of solid ^{4}He at $T \sim 0.7$ K and near melting curve shows this ratio to be 0.262 [51]. Thus, γ_L in ^{4}He strongly exceeds γ_L in classical crystal and hence the solid ^{4}He can be named a Quantum crystal.

According to Andreev, Lifshitz considerations [4] a solid ^{4}He also possesses a large de Boer parameter.

2.1.1.2 de Boer Parameter for Solid ^{4}He

de Boer parameter Λ measures the ratio of kinetic delocalization energy and potential energy of the system:

$$\Lambda = \left(\frac{E_{kin}}{E_{pot}}\right)^{1/2}, \tag{2.1.2}$$

where total energy of the system $E_{tot} = E_{kin} + E_{pot}$. In solid ^{4}He the potential energy is connected with the standard 6–12 potential with hard-core repulsion and van der Waals attractive tail:

$$U(r) = 4\varepsilon\left[\left(\frac{d}{r}\right)^{12} - \left(\frac{d}{r}\right)^{6}\right], \tag{2.1.3}$$

where ε is a characteristic energy of the two atom interaction and d is the inter-particle distance. Thus E_{pot} in (2.1.2) is of the order of ε close to the minimum (see Fig. 2.1.) where $r \sim d$. Correspondingly kinetic energy or zero-vibrations is given by:

$$E_{kin} \sim \frac{\hbar^2}{m\langle r^2\rangle} \sim \frac{\hbar^2}{md^2}, \tag{2.1.4}$$

where m is a mass of ^{4}He atom. Hence:

$$\Lambda \sim \frac{\hbar}{d}\frac{1}{\sqrt{m\varepsilon}}. \tag{2.1.5}$$

On Fig. 2.1 we present interatomic potential and zero-point energy in solid ^{4}He as the functions of the distance r between the atoms.

In ordinary crystals de Boer parameter Λ determined by Eq. (2.1.5) is small. It becomes larger for inert gases. For instance $\Lambda = 0.6$ for Ne. However, for ^{4}He $\Lambda = 2.7$ is large (it is even larger for ^{3}He crystals $\Lambda = 3.1$ since the atomic mass m_3 is smaller than m_4). For $\Lambda > 1$ it means that the kinetic energy prevails over potential energy and we have the conditions for the delocalization of the atoms (for the large zero-vibration energy). In principal the number of atoms in such crystal should not necessary coincide with the number of the lattice cites. Moreover the

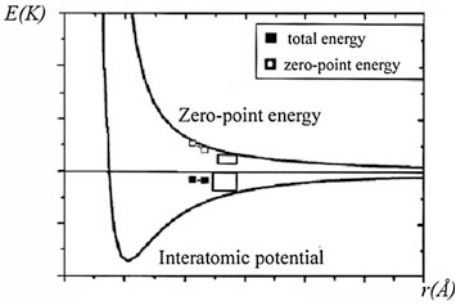

Fig. 2.1 Interatomic potential $U(r)$ and zero-point energy $E_{kin} = \frac{\hbar^2}{2md^2}$ in solid ^{4}He as the functions of the distance r between the atoms [8–13]

motion of the atoms (more precisely of the elementary excitations such as vacancions and defectons see [4]) should resemble the motion in ideal liquid i.e. should be without binding to the equilibrium position of the atom in the lattice. Thus it is appealing to describe such a system in analogy with liquid ^{4}He by a macroscopic Ψ-function of Jastrow type (see the papers by Chester and Reatto [17, 18]). The mutual permutations of the atoms in such a crystal could lead to the delocalization, or in the other words to the motion of vacancies in crystal (see Yang [19–21]).

2.1.1.3 Formal Theoretical Remark on off Diagonal Long Range Order (ODLRO) and Superfluidity

Note that Penrose and Onsager [19–21] emphasized that in a perfect solid each atom is localized at a specific lattice site and only lattice translational symmetry is present. Thus there is no Bose–Einstein condensation (BEC) [52] at $T = 0$ (when the thermal vacancies are absent and thus there is no band motion in the crystal). Moreover, according to Yang, the Off Diagonal Long Range Order (ODLRO), or superfluidity, which is directly related to Bose–Einstein condensation [53], may occur in a solid phase only if the particles are delocalized. In other words to have superfluidity in Quantum crystals we should have according to Matsuda and Tsuneto [16] the coexistence of DLRO (diagonal long range order) connected with translational symmetry and ODLRO, connected with superfluidity in the crystals.

These considerations are often used nowadays especially when the theorists investigate with respect to superfluidity (or supersolidity) the Bosonic models on the lattice [27–31]. More specifically they often consider Bose-Hubbard model or extended Bose-Hubbard model with short-range repulsion between bosons on one site and additional repulsion between them on the neighboring sites of the lattice (see Chap. 5 for more details). The main goal here is to find the region of parameters on the phase-diagram where a new phase with a superstructure (with an incommensurate density wave) can be stabilized on top of a crystalline lattice. This additional superstructure or superlattice (or density wave) will just correspond to ODLRO, while the initial lattice—to a standard translational long range order (DLRO). Thus such a new phase can be considered with some degree of precaution as a supersolid phase.

Note that these arguments are supported by the old idea to increase the pressure and thus to reduce the roton gap Δ to zero near the melting curve (see Fig. 1.2 for the spectrum of elementary excitations in the superfluid ^{4}He) and thus to create a superstructure or a superlattice with a period proportional to $1/p_0$ (where $\varepsilon(p_0) = \Delta$ for roton's minimum).

Note also that thermodynamics of an incommensurate quantum crystal was considered recently by Anderson, Brinkman and Huse [22, 23]. The authors of [22, 23] derived an effective Ginzburg–Landau (GL) functional for the incommensurate case when the number of vacancies ($N_{\rm vac}$) does not coincide with the number of the interstitials ($N_{\rm interst}$). The GL-functional is constructed in terms of the parameter of incommensurability δ which measures the difference between the ratio of $\frac{N_{vac}}{N_{sites}}$ at finite temperature and at temperature zero:$\delta = \frac{N_{vac}(T)}{N_{sites}} - \frac{N_{vac}(T=0)}{N_{sites}}$.

The vacancies and interstitials according to Anderson et al. are in strongly-correlated state and provide a small contribution to the entropy of the incommensurate crystal $\Delta S_{cryst} = \beta T^7$ [22]. The main contribution to the entropy is still due to phonons $\Delta S_{cryst} = \beta T^3$. In the next article [23] Anderson also proposed a model wave-function for a superfluid solid which accounts for the vacancy component [51] and Gutzwiller constraint [81]. The constraint prohibits the double occupancy of one site in quantum Bose solid.

2.1.1.4 Quantum Permutations

In the absence of vacancies the permutations between particles are complicated in the perfect quantum crystal by large short-range Hubbard (or contact) repulsion between them (see Fig. 2.2).

2.1.2 Flow of Zero Vacancies. Andreev-Lifshitz Theory

However, usually there are vacancies, defects and impurities in the quantum crystals which make the permutations easier.

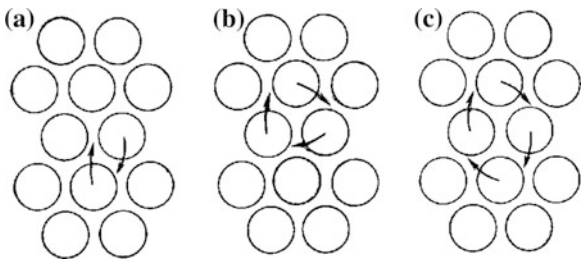

Fig. 2.2 Quantum permutations of two (**a**), three (**b**), and four (**c**) particles in a perfect quantum crystal without defects (from review-article of Andreev [43])

2.1.2.1 Vacancions, Defectons and Impuritons

In other words in quantum crystals besides a standard phonon branch of the elementary excitations should be an additional branch with a band character of motion. The most difficult logical point here is that the number of atoms can be different from the number of lattice sites in the quantum crystal. To realize this idea we need vacancies, dislocations, interstitials or other defects in the crystalline lattice. Another possibility to realize this scenario is to consider the system of impurities (^{3}He for example) in the crystalline matrix of ^{4}He. In this case the band character of impurity atoms (impuritons) leads to the phenomena of quantum diffusion (Andreev and Lifshitz [4], Y. Kagan and Maksimov [54–57]). Note that in ordinary crystals the spectrum of vacancions has a large energy gap and so their number and their contribution to specific heat are exponentially small. Andreev and Lifshitz assumed that in quantum crystal of ^{4}He the number of vacancions is of the order of 1 per site that is there are *zero vacancies* in the system. In definite conditions then (in particular in the absence of Mott–Hubbard localization—see Chap. 4, 5, 9 for more details) the vacancies could Bose-condense [52] and all the crystal will undergo the transition to the superfluid state. On the macroscopical language this state will be described by the many component superfluid hydrodynamics similar to Landau hydrodynamics [58] for superfluid liquid helium which was detaily considered in Chap. 1. To be more precise the hydrodynamics of a supersolid is even a bit closer to the hydrodynamics of rotating superfluid in a presence of the vortex lattice since it also contains three independent velocities.

One of them is $\vec{v}_S$—the velocity for the superfluid motion of zero vacancies (or other zero quantum defects). Another one $\dot{\vec{u}}$ stands for the lattice velocity. The third one $\vec{v}_n$ is governed by the normal motion of elementary excitations such as thermal vacancies and phonons. Note that the two relative velocities $\vec{w}_1 = \vec{v}_s - \dot{\vec{u}}$ and $\vec{w}_2 = \vec{v}_n - \dot{\vec{u}}$ are nonzero in our case. Correspondingly besides the standard transverse and longitudinal sound in the phonon subsystem, we have an additional sound mode in the subsystem of vacancies (defectons) in a supersolid. The last mode a bit resembles the second sound in a superfluid liquid ^{4}He but does not exactly coincide with a second sound since a fraction of vacancies is superfluid. Nevertheless in analogy with a second sound the phase velocity of this mode depends upon the ratio ρ_n/ρ_S between the densities of thermal and superfluid vacancies. Note that since at $T = 0$ there is a finite difference $\Delta\rho/\rho \sim 0.1$ between the densities of solid and liquid phase we can expect the same amount of spatial disorder (or 10 % of surface vacancies) on the phase-interface between quantum crystal of ^{4}He and quantum superfluid He-II (see the next chapter). If we can organize the diffusive flow [80] of vacancies from the surface to the bulk of the crystal, we can probably create the sufficient amount of zero vacancies in the bulk solid ^{4}He and thus promote non-equilibrium superfluidity. If, vice versa, we believe that there is a lot of equilibrium zero vacancies in the bulk, than we can create the diffusive flow of vacancies in the opposite direction—from the bulk to the surface and in this way to measure the spatial distribution of vacancies (or defectons) and the gradients of their density.

2.1.2.2 Zero Vacancies. Theoretical Background

Andreev and Lifshitz assumed the following bare spectrum of vacancies in solid ^{4}He:

$$\varepsilon(p) = \varepsilon_0 + \frac{p^2}{2M}, \tag{2.1.6}$$

where $\varepsilon_0 < 0$ is negative at low temperatures and M is an effective mass of vacancion (which in principle can be different from the mass of ^{4}He atom m_4). In solid ^{4}He vacancies are bosons, as well as ^{4}He atoms themselves. In general we have weakly non-ideal low-density Bogoliubov Bose-gas with repulsive interaction between vacancies [53]. In this case the chemical potential μ is negative for low density of vacancies $n_V d^3 \ll 1$. Indeed in the Hartee-Fock approximation the chemical potential reads [4, 43]:

$$\mu = -|\varepsilon_0| + \frac{4\pi\hbar^2}{M} f_0 n_V < 0, \tag{2.1.7}$$

where $f_0 > 0$ is repulsive scattering amplitude and $\frac{4\pi\hbar^2}{M} f_0$ is pseudo potential for the vacancies interaction (see Chap. 6). Of course, in this situation the vacancies will be Bose-condensed at the temperature given by Einstein formula $T_C^{BEC} \sim \frac{3.31\, n_V^{2/3}}{M}$ [52]. Moreover after diagonalization of the Bogoliubov Hamiltonian for vacancies (after Bogoliubov u-v transformation [53]) their transformed spectrum will read:

$$E(p) = \sqrt{c^2 p^2 + \left(\frac{p^2}{2M}\right)^2}. \tag{2.1.8}$$

It will become linear at small momenta $E(p) = cp$, where

$$c^2 = \frac{4\pi\hbar^2}{M^2} f_0 n_V \tag{2.1.9}$$

is a sound velocity squared (see Chap. 6 for more details). Thus the Bogoliubov spectrum of vacancions (2.1.8) will satisfy Landau criterion for superfluidity (see Chap. 1).

2.1.2.3 Zero Vacancies. Experimental Search

The attempts to find experimentally zero vacancies were based on three main ideas:

1. To perform an analog of Josephson experiment in a ring where a thin peace of solid ^{4}He serves as a cork to superfluid ^{4}He (see Fig. 2.3) and to find the manifestation of the macroscopic wave-function Ψ which penetrates in the solid and connects left and right branches of the superfluid ^{4}He via the small cork [59] of atomic size.

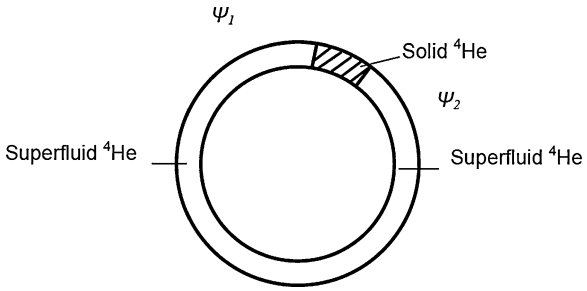

Fig. 2.3 The principal scheme of the gedanken Josephson-type of experiment in a ring where a piece of solid ^{4}He serves as a cork to superfluid ^{4}He

2. To measure the low-temperature specific heat in solid ^{4}He [6, 7, 13, 60, 61] and to subtract a phonon contribution proportional to T^3 thus finding (if it exists) the contribution of zero-vacancies $C_V \sim \exp\{|\varepsilon_0|/T\}$. Another possibility is to measure the temperature dependence of the melting pressure $P(T)$ at low temperatures and to subtract T^4 contribution due to phonons (Parshin et al. [38]).
3. To perform an analog of Andronikashvili experiment [14] with rotation of solid ^{4}He and to extract a non-zero superfluid fraction $(1 - \rho_n/\rho) = \rho_S/\rho$ from the non-classical moment of inertia (Leggett's idea [15], experiments of Chan et al. [8–12]) if supersolidity exists.

Unfortunately until now numerous measurements do not confirm the existence of zero vacancies. Namely in NMR, X-ray and acoustic measurements experimentalists observe only the contribution of thermo-activated vacancies. In the same time in the measurements of specific heat and heat conductance as well as of the temperature dependence of the melting pressure all the results can be explained only by phonon contribution without vacancies at all. If there is some small vacancy contribution in these experiments, it is connected with bosonic (and not Boltzman) vacancies with a broad band and a complicated spectrum. Finally in the experiments on thermal expansion in solid ^{4}He at high temperatures the researchers observe Anderson's type of the corrections to the specific heat $\delta C_V \sim bT^7$. These corrections can be possibly explained by some degree of incommensurability according to Anderson et al. [22, 23], but not by the thermoactivative vacancies.

Thus the problem of the experimental search of zero vacancies is opened for future investigations in different quantum solid systems with large Lindemann and de Boer parameters. Maybe the better conditions for supersolidity can be experimentally achieved in excitonic systems (Balatsky et al. [24–26]) and in ultracold Bose-gases on optical lattices where it is easier experimentally to tune the parameters of the system.

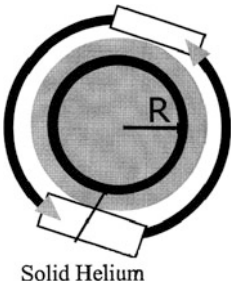

Fig. 2.4 The principal scheme of the gedanken Leggett's type of experiment to measure the non-classical rotation inertia in rotating solid ^{4}He [15]

2.1.2.4 Leggett's Idea

The ideal method to detect superflow according to Leggett [15] would be to subject solid ^{4}He to undergo dc or ac rotation and to look (in similarity with Andronikashvili experiments in superfluid ^{4}He) for the evidence of Non-Classical Rotation Inertia (NCRI—see Chap. 1).

Quantum exchange of particles arranged in an annulus under rotation leads to a measured moment of inertia that is smaller than the classical value (see Fig. 2.4 and [8–13, 61]). Namely the moment of inertia $I(T) = I_{classic}(1 - f_s(T))$, where $f_S(T) = \rho_S/\rho$ is the supersolid fraction.

2.1.3 Chan Experiments with Rotating Cryostat. The Search for Supersolidity in Solid ^{4}He

Recently an attempt to realize the Leggett's idea was made by the group of Chan [8–13, 61] in Penn State University, USA (see Fig. 1.7 in Chap. 1 for the principal scheme of the experimental setup used by Chan's group). In the first paper Kim and Chan filled the pores of Vycor glass (of aerogel, see Chap. 3) with solid ^{4}He and studied the rotation of this solid system. They observed that effective moment of inertia was smaller than the total one at low temperatures $T < 0.125$ K. The authors interpreted their result as a transition of solid ^{4}He in pores in a superfluid state. This result produced a huge interest in the low temperature community and casts doubts connected with the side effect of porous medium. Trying to reduce the skepticism Kim and Chan published two more articles where they have studied the moment of inertia of solid ^{4}He in the absence of aerogel and at small concentration of ^{3}He impurities (clean situation). They worked close to the melting line on the phase diagram of ^{4}He and carefully studied thermodynamics close to its minimum at $T \sim (0.5 \div 0.6)$ K where nontrivial quantum effects cannot be excluded in principle. They claimed that $\rho_S \leq 0.01\,\rho$ in these experiments (1 % of superfluid fraction). However, scientific community again was not convinced even by these results. Rittner and Reppy [36] challenging Chan's results showed experimentally that, when all the defects like grain boundaries, dislocations etc. are carefully

annealed and when we have a very pure crystal, the effect of non-classical moment of inertia disappears. So now the most part of the low temperature community (see papers by Andreev [33–35], Balatsky et al. [24–26], Prokof'ev et al. [27–31], Parshin et al. [38], Balibar et al. [32]) does not believe in the real supersolidity but more in some glassy state with a superflow of defects (grain boundaries etc.) relative to the lattice [59]. Note that in glasses (like SiO_2 for example) the number of equivalent sites under deformation is larger than the number of atoms. Therefore two types of motion are possible in a glassy state: oscillations near the equilibrium positions (analogous to phonon modes in regular solids) and sudden "jumps" of diffusive types from initial state to the neighboring equivalent positions.

Equivalently upon deformation of a quantum crystal there arises a self-consistent motion of lattice sites and a flow of defectons, accompanied by a transport of mass. According to the recent discussion of Andreev-Lifshitz theory in Kavli Institute [62] with some degree of precaution we can speak about possible "superplasticity" of a quantum crystal.

The important recent observation should be mentioned here in this context, namely the increase of a shear modulus in ^{4}He crystal at low temperatures $T \sim 0.1$ K instead of a decrease typical for superfluid or "superplastic" quantum crystal. The increase of the shear modulus K can produce a drop in the resonant period $T = 2\pi\sqrt{I/K}$ without a decrease of the moment of inertia I [83, 84], and thus without a real supersolidity. In their recent experiments [83] Kim and Chan confirmed the increase of the shear modulus at low temperatures due to solidification of one ^{4}He layer and the absence of the superfliud fraction. These results according to Kim and Chan [83] prove the absence of supersolidity in solid helium in porous vycor glass. Another interesting aspect to be mentioned is an idea of Y. Kagan [63] about the possibility of the choc-ice model for the explanation of the rotating experiments of Chan et al. Namely due to a small difference of densities between solid and liquid phases it could be probably easier to have a surface melting of the crystal instead of melting in the bulk. Then it is possible to create a surface layer of superfluid ^{4}He between the crystal and the walls of rotating experimental container similar to the surface melting of ice-cream in a glass. This melted surface layer becomes superfluid and can in principle explain the difference between a measured moment of inertia connected with rotation and a total moment of inertia of a solid in the absence of aerogel.

2.2 The Surface Physics of Quantum Crystals. Atomically Smooth and Atomically Rough Surfaces

We proceed now to the second part of the chapter where we will concentrate mainly on the surface physics for the different phase-interfaces of the solid ^{4}He in contact with superfluid helium. It is also a subject of a hot debate today especially concerning the problem of quantum and classical roughening and the correlation between microscopic models of roughening and macroscopic hydrodynamics on

atomically (or even quantum) rough surfaces where the spectrum of weakly damped melting-crystallization waves $\omega \sim k^{3/2}$ was measured. These measurements were performed not only for relatively high (roton) temperatures $T \sim (0.7 \div 1.2)$ K but also for much lower (phonon) temperatures $T \sim (0.3 \div 0.6)$ K. In this section we will try to present a now-a-day understanding of the problem and emphasize the unresolved questions which still, according to our point of view, do nor allow to construct the coherent microscopic physical picture of a mobile phase-interface between quantum solid and quantum liquid.

2.2.1 The Concept of the Mobile Rough Interface Between Solid ^{4}He and Superfluid He-II

As we understood in the Introduction to Sect. 2.1, the ^{4}He atoms in quantum crystals have large zero-vibration energy of quantum oscillations and can be considered as delocalized or almost delocalized quasiparticles. The atoms of superfluid helium are also delocalized and participate (even in the absence of a drift flow) in a coherent oscillating motion of the Bose-condensate. Thus with some degree of precaution it is appealing to talk about the joint macroscopic Ψ-function which connects solid and liquid subsystems via a coherent phase-interface (see [50]). In fact the situation is more complicated especially at zero temperature (at $T = 0$) (see [40]).

In the series of the pioneering papers Castaing and Nozieres [64], Andreev and Parshin [47], Marchenko and Parshin [65] developed the ideas of *delocalized atomically* (or even quantum) *rough* state of the interface (see Fig. 2.5) and the

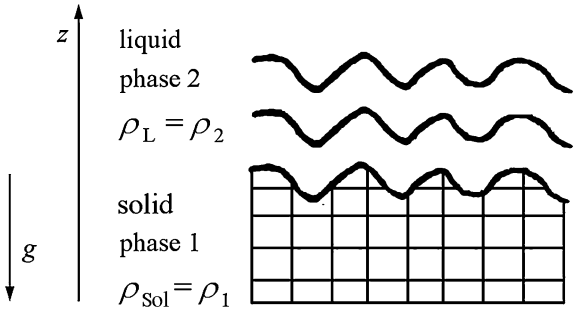

Fig. 2.5 The qualitative picture of the surface hydrodynamic waves on the mobile rough interface between solid and superfluid ^{4}He. At low frequencies these waves are melting-crystallization waves (see the next section). For these waves we can introduce $z = \varsigma + u_s$ for a total displacement of the surface point from equilibrium position (see explanation below). $\vec{g}$ is gravitational acceleration, ρ_{sol}, ρ_L are the densities of solid and liquid phase

roughening transition (Nozieres [39], Andreev [43]) between atomically rough (or quantum rough) and atomically smooth states of the interface.

2.2.2 Growth and Melting Shape of a Crystal

On Fig. 2.6 we present growth and melting shapes of ^{4}He crystal following a nice review-article of Balibar et al. [40]. We can see the rectangular parts on Fig. 2.6 corresponding to atomically smooth surfaces (or facets) and rounded corners corresponding to atomically rough surfaces. An important observation is that facets grow and melt more slowly then atomically rough rounded corners. Thus atomically rough interfaces are more mobile. Remind that a crystal grows from a liquid phase when we increase a pressure a little bit (create an overpressure) working near the melting curve. Note also that the classical crystals at low temperatures always have characteristic faceting and melting-crystallization processes on them are very slow (see review-article of Chernov [66] for example). The quantum crystals in contrast to the classical ones have extended atomically rough regions (see Fig. 2.6) with rapid melting-crystallization processes on the rough surfaces.

2.2.3 Melting-Crystallization Waves and Phase Equilibrium on the Mobile Rough Surface

The atomically rough surface state together with the small difference between the densities of bulk solid and superfluid phases $\Delta\rho/\rho \sim 0.1$ and between zero-vibration energies of liquid and solid phases promote rapid and practically dissipationless character of melting-crystallization processes on the phase boundary. In fact it is possible to incorporate the atom from the liquid rather rapidly and over a small potential barrier in the surface atomic row in the crystal. The rapidness and practically dissipationless character of melting-crystallization waves on the rough surface [47–49, 76, 77, 82] in macroscopic language can be expressed in the

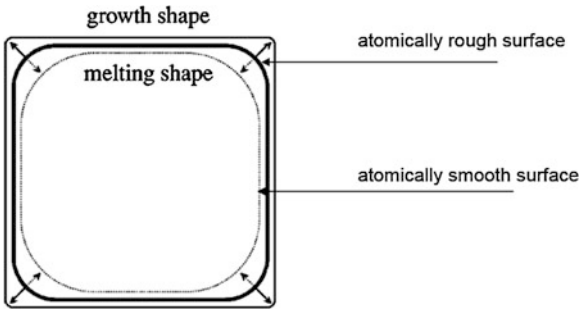

Fig. 2.6 Growth and melting shapes of a crystal from [40]. Facets grow and melt more slowly than atomically rough rounded corners

condition of the thermodynamic equilibrium on the boundary $\mu_1 = \mu_2$ for chemical potentials of solid and liquid phases (see Fig. 2.5). Together with the standard boundary condition for the mechanical equilibrium $P_1 = P_2$ for the pressures (see [5]) and thermodynamic identities at $T = 0$ $\delta P_1 = \rho_1 \delta\mu_1$ and $\delta P_2 = \rho_2 \delta\mu_2$ for small pressure deviations, we can use the equation $\delta\mu_1 = \delta\mu_2$ for the deviations of the chemical potentials from equilibrium to get:

$$(\rho_1 - \rho_2)\delta\mu_2 = 0. \tag{2.2.1}$$

Hence $\delta\mu_2 = 0$ and $\delta P_2 = 0$ for the liquid phase, where δP_2 is the difference between local pressure in the liquid and the equilibrium one $P_0 = 26$ bar. Thus the atomically rough interface between solid and superfluid ^{4}He becomes equivalent to the free interface between liquid and vacuum. Note that in more rigorous considerations there are surface (capillary) terms [58] of the Laplace type in the right-hand side of (2.2.1) (see the next section). As a result the melting-crystallization waves on the rough surface resemble according to Andreev and Parshin [47] the standard capillary waves on the free surface of the liquid [58]. These waves are sometimes called riplons and for liquid-vacuum interface have the spectrum $\omega^2 \sim (\alpha/\rho)k_{||}^3$. where α is the surface tension coefficient and $k_{||}$ is a projection of the wave-vector parallel to the free surface (see also Chaps. 3 and 15). Correspondingly for the mobile rough interface between solid and superfluid ^{4}He $\omega^2 \sim \frac{\alpha\rho}{(\Delta\rho)^2}k_{||}^3$ where $\rho/(\Delta\rho)^2$ is a specific density factor for this interface. The spectrum and damping of melting-crystallization waves will be derived more rigorously from the linearization of the equations of the surface hydrodynamics in the Chap. 3. Note that for melting-crystallization waves the growth velocity $V_b = \dot{\varsigma}$ of the boundary does not coincide with the lattice velocity $\dot{u}_z$ (see Fig. 2.5). Note also that more rigorously in the spectrum of melting-crystallization waves instead of a surface tension coefficient α enters the surface rigidity $\tilde{\alpha}$ (see Chap. 3).

2.2.4 Rayleigh Waves on Rough and Smooth Surfaces

Another branch of the surface waves which usually corresponds to higher frequencies on mobile solid—superfluid interface is a more standard one. In this branch we neglect melting-crystallization processes and get for the rough surface:

$$\delta P_1 = \delta\sigma_{zz} = 0;\ \delta\sigma_{z\alpha} = 0;\ \rho_2\delta\mu_2 = \delta P_2 = 0 \tag{2.2.2}$$

for the oscillating parts of the pressures P_1 and P_2 and the stress-tensor components σ_{zz} and $\sigma_{z\alpha}$, $\alpha = \{x, y\}$ (note that z-axis corresponds to the normal to the surface).

In other words while for melting-crystallization waves the total growth velocity of the boundary $V_b = \dot{\varsigma} + \dot{u}_z \approx \dot{\varsigma}$ (and correspondingly the lattice velocity $\dot{u}_z \approx 0$), for Rayleigh waves we have vice a versa $V_b \approx \dot{u}_z$ and $\dot{\varsigma} = 0$ for the recrystallization rate. Hence the rough interface between solid and liquid becomes equivalent at high frequencies to the interface between solid and vacuum. On this interface

the standard Rayleigh waves can propagate (see Landau, Lifshitz Elasticity Theory [5]) in similarity with the surface of the crystal with vacuum. The spectrum of the Rayleigh waves is linear:

$$\omega = \eta c_t k_{||}, \tag{2.2.3}$$

where c_t is transverse sound velocity in solid (see also Chap. 1) and in isotropic approximation the coefficient $\eta = \eta(c_t/c_l)$ depends upon the ratio between transverse (c_t) and longitudinal (c_l) sound velocities in solid phase. In solid ^{4}He $\eta \sim 0.8 \div 0.9$. Note that as we discussed there are different interfaces of solid ^{4}He. Their character (atomically smooth or atomically rough) depends on their orientation to the main crystallographic axis of the crystal (we consider mostly hexagonal hcp structure of the ^{4}He crystal). Some of the interfaces are atomically rough at low temperatures. They are rapidly growing mobile surfaces. On these surfaces we have two branches of the surface waves: melting-crystallization waves at low frequencies and Rayleigh waves at higher frequencies (see the more precise derivations in the next chapter).

The other interfaces grow much slower. They are atomically smooth and obey more standard laws of growth. They have characteristic faceting (see Fig. 2.7) and only Rayleigh waves (more precisely Rayleigh-Stonely waves) propagate on their surface in the linear regime. The spectrum of melting-crystallization waves on them is strongly modified and becomes non-linear (amplitude-dependent) see Parshin and Gusev [67].

2.2.5 Roughening Transition

There are two main competing approaches to the roughening transition in solid ^{4}He which belong to Nozieres [39] and Andreev and Parshin [47] respectively (see also quantum models of Iordanskii and Korshunov [44]). Note that the roughening transition takes place, generally speaking, in the 2D gas of steps and kinks on the surface. Thus, steps and kinks serve as elementary excitations in surface science which define the kinetics and thermodynamics of surface growth as well as the roughening transition from atomically smooth to atomically rough state of the surface. Let us remind that a step is an additional row of atoms which joins already exciting terrace for a flat part of the surface (see Fig. 2.8). It is important to emphasize that besides straight "bare" steps there are also steps with kinks, where the kink is an additional atom (adatom) on a straight "bare" step (see Fig. 2.8).

According to Andreev and Parshin there are surfaces which can be in atomically (or quantum) rough state till very low temperatures due to delocalization of quantum kinks on the steps. In this case Andreev and Parshin assume that the energy of a step with kinks reads (see [47]):

$$\beta = \beta_0 + d\left(-\frac{\Delta}{2} + \varepsilon\right), \tag{2.2.4}$$

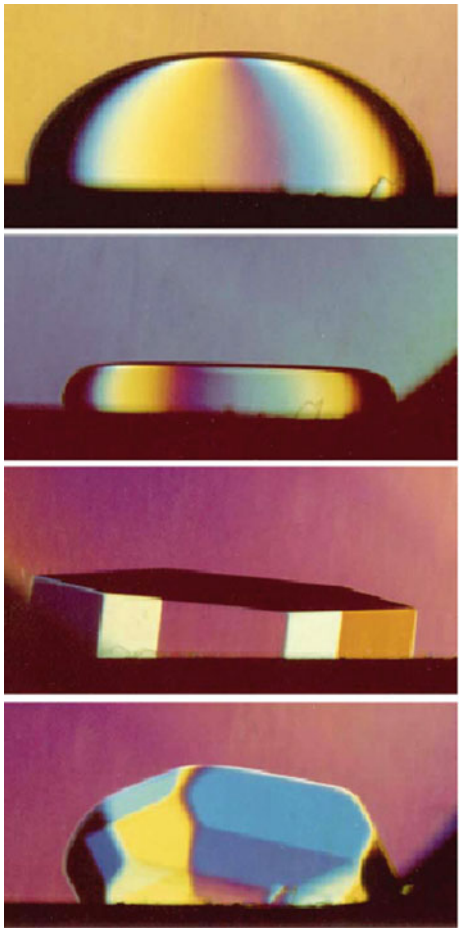

Fig. 2.7 Faceting of ^{4}He crystals from Balibar, Guthmann and Rolley [71]. As temperature goes down, more and more facets appear at the surface of ^{4}He crystals. From *top* to *bottom*, the temperature is successively 1.4, 1, 0.4, and 0.1 K. When we decrease the temperature more surfaces become atomically smooth

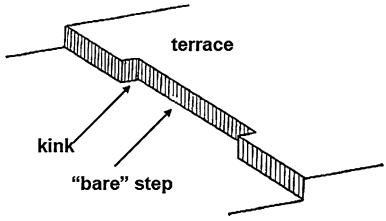

Fig. 2.8 A step with kinks on the growing surface (from [43])

where β_0 is an energy of a straight "bare" step without kinks, d is intersite distance, Δ is the bandwidth for delocalized kinks and ε is the kinks quasiparticle energy counted from the bottom of the band (from $-\frac{\Delta}{2}$). For highly delocalized ensemble of kinks the second term in the r.h.s of (2.2.4) can coincide by the order of magnitude with the first one $\left(\frac{\Delta}{2} - \varepsilon\right) \sim \frac{\beta_0}{d}$.

It means that the kinks quasiparticle energy coincides by the order of magnitude with a step energy per unit length. Correspondingly β in (2.2.4) can tend to zero or even becomes negative for the bottom of the band for zero vacancies. So we can have a quantum rough state with no steps (or highly delocalized "zero-point" steps) and with only rounded parts of the surface already at low temperatures. At some finite temperature T_R Andreev and Parshin predicted a mean-field (second order) phase transition from quantum rough state to a classical rough state. Nozieres [39] has quite different point of view. According to Nozieres [39] (see also [40] for an extended review) the roughening transition between low temperature atomically smooth phase and high-temperature atomically rough phase takes place at a finite temperature T_R and is governed by Berezinskii—Kosterlitz—Thouless (BKT)—type [45, 46] of the transition in 2D gas of steps. In the approach of Nozieres for high temperatures $T > T_R$ the steps are delocalized and highly fluctuating and thus we can put a step energy $\beta = 0$ for $T > T_R$. In the same time for $T < T_R$ the macroscopically large steps are formed. As a result the typical size of the terrace on Fig. 2.8 (effectively the coherence length) should diverge and all the surface becomes flat. Thus, we are in atomically smooth state at $T < T_R$. The atomically smooth surface is faceted and very slowly growing. Its growth velocity $V_b \to 0$. Note that the step energy β in Nozieres theory plays a role of a superfluid density ρ_s in BKT-theory for 2D ^{4}He-films. Thus, it should be a finite jump in β at T_R. Correspondingly we can estimate the roughening transition temperature T_R in the same way as T_{BKT} for a 2D superfluid film. Namely:

$$T_R \sim d\beta(T_R), \tag{2.2.5}$$

where βd is a step energy calculated for one atom at $T = T_R$.

In surface science it is convenient to introduce also the angular dependent surface energy $\alpha(\varphi)$. For the atomically smooth surface with steps of the atomic height the surface energy reads for small angles $\varphi \ll 1$ (see Fig. 2.9):

$$\alpha(\varphi) = \alpha_0 + \frac{\beta}{d}|\varphi| + \gamma|\varphi|^3, \tag{2.2.6}$$

where $\frac{\beta}{d}$ is a step energy of unit height, γ is an interaction energy between the steps.

Note that in solid ^{4}He $\alpha_0 \sim 0.127\ \frac{\text{erg}}{\text{cm}^2}$, $\frac{\beta}{d} \sim 1.3 \cdot 10^{-2}\ \frac{\text{erg}}{\text{cm}^2}$, $d \sim 3$ Å. The coefficient γ is a subject of a debate and is different in the estimates of different groups.

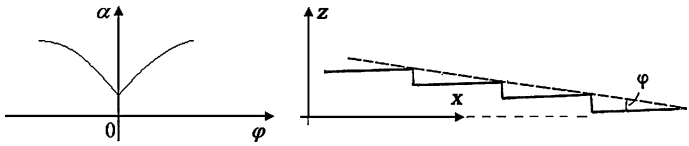

Fig. 2.9 The angular dependence of the surface energy $\alpha(\varphi)$ for $\varphi \ll 1$ for the surface with steps of the atomic height, d is interatomic distance

Note also that according to Landau [42] the derivative $\frac{\partial\alpha}{\partial\phi}$ has a finite jump $\frac{2\beta}{d}$ at $\phi = 0$ for atomically smooth surfaces.

Another important and widely used quantity is the so-called surface stiffness (or surface rigidity):

$$\tilde{\alpha} = \alpha + \frac{\partial^2\alpha}{\partial\phi^2}. \tag{2.2.7}$$

For small angles $\phi \ll 1$ on the smooth surface:

$$\tilde{\alpha} = \alpha_0 + \left(\frac{\beta}{d} + 6\gamma\right)|\phi| + \gamma|\phi|^3. \tag{2.2.8}$$

From (2.2.8) we see that $\tilde{\alpha}$ is different from α with respect to the surface anisotropy $\frac{\partial^2\alpha}{\partial\phi^2}$. For small β, the surface rigidity $\tilde{\alpha}$ is governed by the coefficient γ (by the interaction energy between the steps).

If vice versa β is finite and γ is small then $\tilde{\alpha}$ is governed by β on the smooth surfaces.

For the rough surfaces with only rounded parts it is difficult to define $\tilde{\alpha}$ via the angles φ and usually another definition is used:

$$\tilde{\alpha}_{\mu\nu} = \alpha\delta_{\mu\nu} + \frac{\partial^2\alpha}{\partial\varsigma_\mu\partial\varsigma_\nu}, \tag{2.2.9}$$

where $\varsigma_\mu = \nabla_\mu\varsigma$ is a gradient of the displacement of the surface ς from the initial point. Note that precisely this quantity enters into the spectrum of melting-crystallization waves on rough surfaces (see the next chapter).

Correspondingly we can also express T_R via the surface rigidity $\tilde{\alpha}(T_R)$ in Nozieres theory. Namely according to the universal roughening relation (see Fisher and Weeks [68] and Jayprakash et al. [69]):

$$k_B T_R = \frac{2\tilde{\alpha}(T_R)}{\pi} d^2, \tag{2.2.10}$$

where $\tilde{\alpha}\, d^2$ is a surface rigidity calculated on one atom for $T = T_R$. Note that the estimates (2.2.5) and (2.2.10) for T_R can be obtained also from the minimization of the Free-energy of the step:

$$\Delta F = \Delta E - T_R \Delta S = 0, \tag{2.2.11}$$

where $\Delta E \sim \beta d$ is an increase of the energy due to the creation of a step at $T = T_R$ and ΔS is a configurational entropy connected with different "charges" of the steps which are situated above or below the averaged surface position. Note also that the exact value of T_R and the behavior of β for $T < T_R$ in Nozieres approach can be extracted from the renorm-group (RG) equations. The renorm-group equations are explicitly derived in [39] and we will not present them here. We just mention that

close to T_R on the smooth side of the transition ($T \leq T_R$) the step-energy β diverges according to the law:

$$\beta(T) \sim \exp\left\{-\frac{\pi/2 \cdot const}{\sqrt{1 - T/T_R}}\right\}. \tag{2.2.12}$$

Correspondingly the correlation length $\varsigma(T)$, which enters as a scale in RG-equations, is also exponentially divergent near T_R :

$\varsigma(T) \sim \frac{k_B T_R}{\pi\beta(T)} \to \infty$ signaling the formation of the macroscopically large step or a flat terrace of the infinite size $\varsigma(T)$. Finally for $T \leq T_R$ the surface rigidity $\tilde{\alpha}(T) \sim \tilde{\alpha}(T_R)\left(1 - \sqrt{1 - T/T_R}\right)$ does not show a critical behavior. Note that the theory of Nozieres considers the periodic pinning surface potential $V(z) = V\cos(2\pi z/d)$ where $z(x)$ is the local height of the surface at the point x. Effectively his RG-approach is based on the Hamiltonian $H = \iint d^2\vec{r}\left[\frac{1}{2}\tilde{\alpha}(\nabla z)^2 + V\cos\frac{2\pi z}{d}\right]$ and is equivalent to the solution of the sine–Gordon equation $\tilde{\alpha}\frac{d^2 z}{dx^2} + \frac{2\pi}{d}V\sin\left(\frac{2\pi z}{d}\right) = 0$ in the weak coupling limit $V/\tilde{\alpha} \ll 1$. Close to T_R it predicts the formation of the macroscopic step with atomic height given by the expression: $z(x) = \frac{2d}{\pi} arctg\left(\exp\frac{x}{\varsigma(T)}\right)$, where $\varsigma(T)$ is the coherence length. Note that the limiting values of the height are given by $z(x = -\infty) = 0$ and $z(x = +\infty) = d$ for this solution. Thus, Nozieres theory effectively starts from atomically smooth side and describes the temperature evolution of the system towards the transition to atomically rough state.

It is interesting to compare the analytical renorm-group approach of Nozieres with the results of the numerical simulations by Leamy et al. (see [70] and Fig. 2.10). The roughening transition in these simulations $T_R \sim \beta d \cdot 0.632$ corresponds, crudely speaking, to the estimate (2.2.11) $T_R \sim \frac{\beta d}{\Delta S}$ with configurational entropy ΔS approximately equals to $ln3$ (see [40]. From the other hand numerical simulations (see Fig. 2.10) are in favor of an important role of kinks or adatoms for the understanding of the roughening transition. Note that delocalized kinks or adatoms serve as a cornerstone of Andreev, Parshin scenario of quantum roughening, while in Nozieres theory (which is a more classical one) only linear surface defects—the steps are introduced and deeply investigated. We have a feeling that a complete quantum picture of roughening transition is far from understanding and requires the consideration of 2D gas of steps and kinks on equal grounds. In this context we should mention the $T = 0$ predictions of the exactly solvable quantum models considered by Iordansky and Korshunov [44].

From the experimental side the different groups (Balibar et al. [71], Andreeva et al. [72, 73], Babkin et al. [74], Wolf et al. [75], Rolley et al. [76–78]) measured the angular dependence of the surface rigidity $\tilde{\alpha}(\varphi)$ and linear contribution to $\tilde{\alpha}(\varphi)$ for small φ (corresponding to the step formation). The experiments were performed at different temperatures and lead to the observation of the roughening

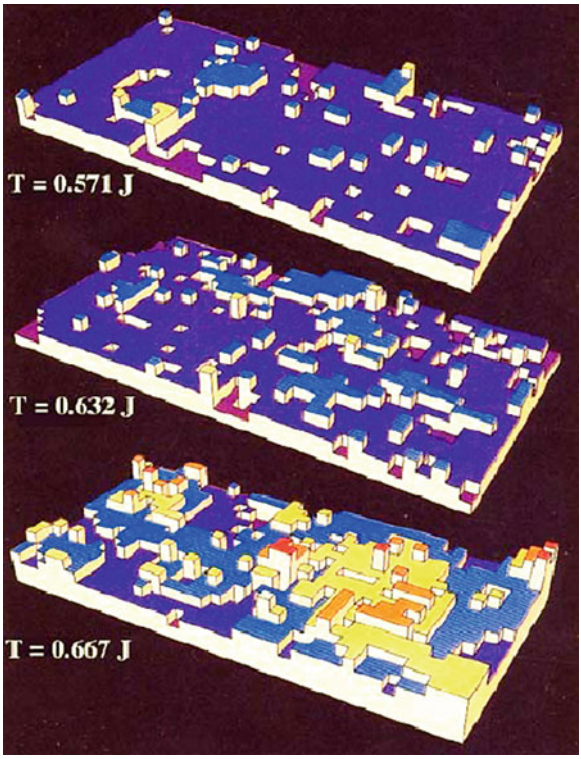

Fig. 2.10 Numerical simulations by Leamy et al. [70] illustrating the basic physics of a roughening transition. The crystal has a simple cubic lattice and each atom is represented by a cube. At low temperature, there are very few defects such as adatoms, surface vacancies, steps and terraces. As temperature increases, steps proliferate and the crystal surface looses reference to the lattice. The temperature is expressed as a function of the bond energy J. The roughening transition occurs at $T_R \sim 0.632\, J\, d^2$ (from Leamy et al. [70], where $J \sim \beta/d$ is the step energy per unit length)

transitions for three particular atomically smooth surfaces at the temperatures $T_{R1} = 1.28$ K, $T_{R2} = 0.9$ K and $T_{R3} = 0.35$ K correspondingly. They also show the increase of the faceted area fraction (in comparison with the total area of the crystal surface) when we decrease the temperature. In the same time many surfaces remain atomically rough till low temperatures. In particular for some crystallographic directions (which are described by large Miller indices and can be obtained by tilting on a small angle of the main crystallographic surface) there are families of the so-called vicinal surfaces staying in atomically rough state till very low temperatures. These temperatures are less then typical phonon temperatures $T_{ph} \sim (0.4 \div 0.5)$ K in liquid He-II.

Thus the very interesting question whether we can have atomically (or quantum) rough surface precisely at $T = 0$ is still a subject of a debate today.

In the next chapter we will detaily consider the hydrodynamic aspect of this discussion, namely a spectrum of weakly damped melting-crystallization waves. The existence of the weakly damped low frequency branch of the spectrum and its hydrodynamic derivation based on the condition of thermodynamic equilibrium serve as a good proof of a mobile character of many phase-interfaces till relatively low temperatures. Experiments of Keshishev et al. and Balibar et al. on melting-crystallization waves were done until the temperature as low as 0.25 K, which is a

direct proof that even at these temperatures many surfaces are still atomically rough. Moreover the melting-crystallization waves were observed on the surface of solid ^{3}He even at much lower temperatures in Helsinki [40, 79]. In the last case, however, the spectrum was not detaily measured. So we cannot say a priori whether these waves are linear melting-crystallization waves predicted by Andreev, Parshin for rough surfaces or nonlinear waves (which exist even on smooth surface) predicted recently by Gusev and Parshin [67].

Concluding this chapter let us emphasize again that in the first part of it we provide an introduction to the concept of quantum crystals and to the interesting problem of possible supersolidity in them. In the second part of this chapter we started to discuss the interesting surface physics on the phase interface between quantum crystals and quantum liquids. We provided an introduction to the problem of roughening transition on the crystal surfaces of solid ^{4}He and briefly considered the spectrum of melting-crystallization waves on rough surface as well as Rayleigh waves, which exist both on rough and smooth surfaces. The next chapter will be devoted to the construction of quantum hydrodynamics on the mobile rough surfaces at low temperatures.

References

1. Kittel, C.: Quantum Theory of Solids. Wiley, New York (1963)
2. Kittel, C.: Introduction to Solid State Physics, 6th edn. Wiley, New York (1986)
3. de Boer, J.: Physica **14**, 139 (1948)
4. Andreev, A.F., Lifshitz, I.M.: JETP **29**, 1107 (1969)
5. Landau, L.D., Lifshitz, E.M.: Elasticity Theory. Pergamon, Oxford (1959)
6. Burns, C.A., Goodkind, J.M.: J. Low Temp. Phys. **95**, 695 (1994)
7. Gardner, W.R., Hoffer, J.K., Phillips, N.E.: Phys. Rev. A **7**, 1029 (1973)
8. Kim, E., Chan, M.H.W.: Science **305**, 1941 (2004)
9. Kim, E., Chan, M.H.W.: Nature **427**, 225 (2004)
10. Kim, E., Chan, M.H.W.: J. Low Temp. Phys. **138**, 859 (2005)
11. Kim, E., Chan, M.H.W.: Phys. Rev. Lett. **97**, 115302 (2006)
12. Kim, E., Chan, M.H.W.: The Plenary Talk at LT-24 Conference. Orlando, USA (2005)
13. Clark, A.C., Lin, X., West, J. Chan, M.H.W.: The Plenary Talk on the Conference on Quantum Fluids and Solids (QFS2007), Kazan, Russian Federation (2007)
14. Andronikashvili, E.L.: JETP **18**, 424 (1948)
15. Leggett, A.J.: Phys. Rev. Lett. **25**, 1543 (1970)
16. Matsuda, H., Tsuneto, T.: Suppl. Progr. Theor. Phys. **46**, 411 (1970)
17. Chester, G.V.: Phys. Rev. A **2**, 256 (1970)
18. Reatto, L.: Phys. Rev. **183**, 334–338 (1969)
19. Penrose, O., Onsager, L.: Phys. Rev. **104**, 576 (1956)
20. Yang, S.N.: Rev. Mod. Phys. **34**, 694 (1962)
21. Penrose, O.: Phil. Mag. **42**, 1373 (1951)
22. Anderson, P.W., Brinkman, W.F., Huse, D.A.: Science **310**, 1164–1166 (2005)
23. Anderson, P.W.: arXiv:cond-mat/0603726 (2006)
24. Balatsky, A.V., Abrahams, E.: J. Supercond. Novel Magn. **19**, 395 (2006)
25. Nussinov, Z., Balatsky, A.V., Graf, M.J., Trugman, S.A.: Phys. Rev. B **76**, 014530 (2007)
26. Balatsky, A.V., Graf, M.J., Nussinov, Z., Trugman, S.A.: Phys. Rev. B **75**, 094201 (2007)

27. Pollet, L., Boninsegni, M., Kuklov, A.B., Prokof'ev, N.V., Svistunov, B.V., Troyer, M.: Phys. Rev. Lett. **98**, 135301 (2007)
28. Boninsegni, M., Prokof'ev, N., Svistunov, B.: Phys. Rev. Lett. **96**, 105301 (2006)
29. Capogrosso-Sansone, B., Prokof'ev, N.V., Svistunov, B.V.: Phys. Rev. B **75**, 134302 (2007)
30. Prokof'ev, N., Svistunov, B.: Phys. Rev. Lett. **94**, 155302 (2005)
31. Prokof'ev, N.V.: Adv. Phys. **56**, 301 (2007)
32. Sasaki, S., Ishiguro, R., Caupin, F., Maris, H.J., Balibar, S.: Science **313**, 1098–1100 (2006)
33. Andreev, A.F.: JETP Lett. **85**, 585 (2007)
34. Andreev, A.F.: JETP **108**, 1157 (2009)
35. Andreev, A.F.: JETP Lett. **94**, 129 (2011)
36. Rittner, A.S.C., Reppy, J.D.: Phys. Rev. Lett. **98**, 175302 (2007)
37. Day, J., Beamish, J.: Phys. Rev. Lett. **96**, 105304 (2006). Nature **450**, 853 (2007)
38. Todoshenko, L.A., Alles, H., Parshin, A.Y., Tsepelin, V.: JETP Lett. **85**, 454 (2007)
39. Nozieres, P.: Shape and growth of crystals. In: Godreche, C. (ed.) Solids far from Equilibrium, p. 1. Cambridge University, UK (1991)
40. Balibar, S., Alles, H., Parshin, A.Y.: Rev. Mod. Phys. **77**, 317 (2005)
41. Avron, J.E., Balfour, L.S., Kuper, C.G., Landau, J., Lipson, S.G., Schulman, L.S.: Phys. Rev. Lett. **45**, 814 (1980)
42. Landau, L.D.: The Equilibrium Form of Crystals, in Collected Papers. Pergamon, Oxford (1965)
43. Andreev, A.F.: Defects and surface phenomena in quantum crystals. In: Lifshitz, I.M. (ed.) Quantum Theory of Solids. Mir Publishers, Moscow (1982)
44. Iordanskii, S.V., Korshunov, S.E.: JETP **60**, 528 (1984)
45. Kosterlitz, J.M., Thouless, D.J.: J. Phys. C **6**, 1181 (1973)
46. Berezinskii, V.L.: JETP Lett. **34**, 610 (1972)
47. Andreev, A.F., Parshin, A.Y.: JETP **48**, 763 (1978)
48. Keshishev, K.O., Parshin, A.Y., Babkin, A.V.: JETP Lett. **30**, 56 (1980)
49. Keshishev, K.O., Parshin, A.Y., Babkin, A.V.: JETP **53**, 362 (1981)
50. Kagan, M.Yu.: Superfluid Properties of the Systems with Anisotropic and Inhomogeneous Ordering, Ph.D Thesis. Kapitza Institute (1989)
51. Burns, C.A., Isaak, E.D.: Phys. Rev. B **55**, 5767 (1997)
52. Landau, L.D., Lifshitz, E.M.: Statistical Physics, Part I. Butterworth-Heinemann, Oxford (1999)
53. Lifshitz, E.M., Pitaevskii, L.P.: Statistical Physics, Part II. Pergamon Press, Oxford (1988)
54. Kagan, Y., Maksimov, L.A.: JETP **57**, 459 (1983)
55. Kagan, Y., Maksimov, L.A.: JETP **38**, 307 (1974)
56. Kagan, Y., Maksimov, L.A.: JETP **61**, 583 (1985)
57. Kagan, Y., Klinger, M.I.: Phys. C **7**, 2791 (1974)
58. Landau, L.D., Lifshitz, E.M.: Fluid Mechanics, vol. 6. Butterworth-Heinemann, Oxford (1987). (Course of Theoretical Physics)
59. Kagan, M.Yu.: Superfluidity of quantum crystals: new life of a beautiful idea, in a book commemorated to the 90-th anniversary of Prof. Lifshitz, I.M. (in Russian). In: Baklay, A.C., Volobyev, A.V., Gredeskul, S.A., et al. (eds.) Kharkov, Syntex LTD (2006)
60. Fraas, B.A., Granfors, P.R., Simmons, R.O.: Phys. Rev. B **39**, 124 (1989)
61. Clark, A.C., Chan, M.H.W.: J. Low Temp. Phys. **138**, 853 (2005)
62. Discussion of Andreev-Lifshitz Theory in Kavli Institute of Theoretical Physics, Santa-Barbara, USA (2006)
63. Kagan, Y.: Private communication to the author, unpublished
64. Castaing, B., Nozieres, P.: J. Phys. **41**, 701 (1980). (France)
65. Marchenko, V.I., Parshin, A.Y.: JETP Lett. **31**, 724 (1980)
66. Chernov, A.V.: Sov. Phys. Uspekhi. **13**, 101 (1970)
67. Gusev, R.B., Parshin, A.Y.: JETP Lett. **85**, 588 (2007)
68. Fisher, D.S., Weeks, J.D.: Phys. Rev. Lett. **50**, 1077 (1983)
69. Jayaprakash, C., Saam, W.F., Teitel, S.: Phys. Rev. Lett. **50**, 2017 (1983)

70. Leamy, H.J., Gilmer, G.H., Jackson, K.A.: In: Blakeley, J.B. (ed.) Surface Physics of Materials, p. 121. Academic Press, New York (1975)
71. Balibar, S., Guthmann, C., Rolley, E.: J. Phys. **13**, 1475 (1993)
72. Andreeva, O.A., Keshishev, K.O., Osip'yan, S.Y.: JETP Lett. **49**, 759 (1989)
73. Keshishev, K.O., Andreeva, O.A.: In: Wyatt, A.F.G., Lauter, H.J. (ed.) Excitations in Two-Dimensional and Three-Dimensional Quantum Fluids, p. 387. Plenum, New York (1991)
74. Babkin, A.V., Kopeliovich, D.B., Parshin, A.Y.: JETP **62**, 1322 (1985)
75. Wolf, P.E., Gallet, F., Balibar, S., Rolley, E., Nozieres, P.: J. Phys. **46**, 1987 (1985). (Paris)
76. Rolley, E., Balibar, S., Graner, F.: Phys. Rev. E **49**, 1500–1506 (1994)
77. Rolley, E., Guthmann, C., Chevalier, E., Balibar, S.: J. Low Temp. Phys. **99**, 851 (1995)
78. Rolley, E., Chevalier, E., Guthmann, C., Balibar, S.: Phys. Rev. Lett. **72**, 872 (1994)
79. Parshin, A.Y.: Private communication to the author, unpublished
80. Lifshitz, E.M., Pitaevskii, L.P.: Physical Kinetics. Butterworth-Heinemann, Oxford (1981)
81. Gutzwiller, M.C.: Phys. Rev. Lett. **10**, 159 (1963)
82. Bodensohn, J., Nicolai, K., Leiderer, P.: Zeit. Phys. B: Cond. Mat. **64**, 55 (1986)
83. Kim, D. Y., Chan, M. H. W.: Phys. Rev. Lett., **109**, 155301 (2012)
84. Schwarzschild, B. M.: Physics Today, **65**, 11 (2012)

Chapter 3
Melting-Crystallization Waves on the Phase-Interface Between Quantum Crystal and Superfluid

We will start this chapter by providing an introduction to the surface hydrodynamics of the mobile rough surfaces based on Andreev-Parshin theory [1]. The most important is a condition of thermodynamic equilibrium or continuity of chemical potentials $\mu_1 = \mu_2$ on this surface. We will construct the linear hydrodynamics of the rough interface with an account of all important capillary terms, such as surface tension coefficient α or more rigorously surface anisotropy $\tilde{\alpha} = \alpha + \frac{\partial^2 \alpha}{\partial \varphi^2}$, surface stress λ_{ik} and surface effective mass M_{eff} [2–9].

From the system of the equations of the surface hydrodynamics we will determine the spectrum of the melting-crystallization waves as well as Rayleigh waves on the rough surface (see Ref. [47] in Chap. 2). We will present pioneering experimental results of Keshishev et al. [10, 11] in Kapitza Institute on the discovery of the melting-crystallization waves on the rough surface of solid ^{4}He. In the end of the Chapter we will generalize the hydrodynamic equations for the rough interface on the presence of ^{3}He impurities [18] and for the case of non-zero temperatures. We will also consider a stationary tangential flow of superfluid liquid parallel to the surface. The system of hydrodynamic equations will be compatible again (according to Landau scheme–see Chap. 1 [1, 2]) with the conservation law for the surface energy. We will consider briefly the surface dissipative function and define the surface kinetic coefficients such as Kapitza thermal resistance R_K and growth coefficient K_{gr} [13, 14–16] On the basis of this analysis we will determine the damping of the melting-crystallization waves and compare it with the experiment [10, 11]. We will show that tangential flows of superfluid liquid parallel to the rough surface of solid ^{4}He lead to the positive (growing) increment $\mathrm{Im}\,\omega > 0$ for the imaginary part of the spectrum of the melting-crystallization waves. This instability was independently predicted in the papers of Kagan [17] and Uwaha and Nozieres [19, 20] and experimentally confirmed by Tsymbolenko in Kurchatov Institute [21, 22]. It resembles the instability of tangential flow on the surface between two liquid layers in the classical hydrodynamics (Kelvin-Helmholtz instability). We also analyze the acoustic properties of the rough interface and find that the sound transmission from the superfluid to a quantum crystal is possible only due to the presence of the capillary

M. Yu. Kagan, *Modern Trends in Superconductivity and Superfluidity*,
Lecture Notes in Physics 874, DOI: 10.1007/978-94-007-6961-8_3,

terms in the equations of surface hydrodynamics [6, 7, 17, 18]. We predict the phenomena of the Cherenkov emissions of second sound quanta by the thermal surface waves as well as the inverse effect of the resonance excitement of the surface Rayleigh or Rayleigh-Stonley waves by the bulk second sound [17, 18] incident on the interface from the liquid over the transcritical angle corresponding to total internal reflection [13, 23–26] with respect to the normal of the surface.

3.1 The Surface Hydrodynamics for Rough Interface at Low Temperatures

In the previous sections we argued that the large energy scale of zero-point particle vibrations at a rough quantum liquid-quantum crystal phase interface as well as the closeness of the solid- and liquid phase densities, allows us to assume that thermodynamic equilibrium can be established in the system over fairly short periods of time. Consequently the melting-crystallization processes on the rough interface are nondissipative (or at least weakly dissipative) at low temperatures. The correctness of this assumption is confirmed by the existence at the rough interface of weakly damped melting-crystallization waves which were theoretically predicted by Andreev and Parshin [1] and experimentally observed by Keshishev et al. [10].

The rapid establishment of thermodynamic equilibrium at a mobile quantum liquid—quantum crystal interface also manifests itself in the effect, discovered by Castaing et al. [2, 4, 5], of anomalously weak low-frequency sound transmission across the interface. Indeed if the period of the incident wave is longer than the time required for the establishment of thermodynamic equilibrium, then, as we briefly discussed in Chap. 2, besides the normally required continuity of the pressure across the interface, we must also have equality of the chemical potentials $\mu_1 = \mu_2$ at the interface. In this case the variable part of the pressure is equal to zero, and the incident acoustic wave should be totally reflected from the boundary, as happens at a boundary with vacuum.

But allowance for the purely surface effects in the boundary conditions gives rise to a small but finite sound-transmission coefficient D. Correspondingly, we obtain a finite, though anomalously large, Kapitza thermal resistance R_K. As will be shown below, of greatest importance for the sound-transmission problem is the allowance for three main types of surface effects in the boundary conditions. The first type is described by the terms connected with the surface-tension coefficient α and with the surface anisotropy $\frac{\partial^2 \alpha}{\partial \varphi^2}$ (see Chap. 2). The second type is described by a term connected with the additional surface kinetic energy. This term was introduced by Castaing and Puech [4, 5]. It is quadratic in the difference between solid- and liquid-phase velocities perpendicular to the boundary. This term is derived in [27] on the basis of model arguments. The effect is due to the fact, that when the matter flows over from the solid into the liquid phase, its short-range order must be substantially reconstructed at the phase interface. Finally, the third

type of effects is described by the terms introduced by Marchenko and Parshin [3]. They are connected with the surface stresses (surface elasticity). Allowance for the surface stresses leads to a situation in which the surface of a crystal is elastically deformed even in the state of total thermodynamic equilibrium.

3.1.1 Linear Equations of Surface Hydrodynamics in the Absence of Stationary Surface Flows

In this subsection we derive linear equations of surface-hydrodynamics (generalized boundary conditions) at $T = 0$ which are consistent with the surface energy conservation law and take into account simultaneously all the important surface effects. Using these equations, we will determine the spectrum of the melting-crystallization waves. We will also establish a general expression for the frequency and angular dependences of the sound-transmission coefficient in the two opposite limiting cases of the near-normal incidence and the incidence at glancing angles. Using two small parameters of the problem, namely $\frac{\rho_{sol}-\rho_L}{\rho_{sol}} \simeq \frac{\rho_{sol}-\rho_L}{\rho_L} \simeq \frac{\Delta\rho}{\rho} \ll 1$ and $kd \ll 1$ (k is the wave-vector) we will show that in both cases the nonvanishing amplitude of the transmitted wave is largely due to the effects of the reconstruction of the short-range order at the phase-interface and the effect of the surface tension. At the same time, when the acoustic waves are incident at the angles close to the critical angles for total internal reflection, the dominant contribution to the transmission coefficient is due to the surface stress (surface elasticity).

3.1.1.1 Generalized Boundary Conditions

The surface hydrodynamics represents the generalized boundary conditions and is governed again by Landau conservation laws together with the requirements of the Galilean invariance. For $T = 0$ according to Castaing and Nozieres [2] it reads:

$$\nabla_\alpha p^s_\alpha = \left(j^{(1)}_k - j^{(2)}_k\right) n_k - (\rho_1 - \rho_2) V_b, \tag{3.1.1}$$

$$\dot{p}^s_\alpha + \nabla_\beta \pi^s_{\alpha\beta} = \left(\Pi^{(1)}_{\alpha k} - \Pi^{(2)}_{\alpha k}\right) n_k - \left(j^{(1)}_k - j^{(2)}_k\right) V_b, \tag{3.1.2}$$

$$\dot{p}^s_z + \nabla_\beta \pi^s_{z\beta} = \left(\Pi^{(1)}_{zk} - \Pi^{(2)}_{zk}\right) n_k - \left(j^{(1)}_z - j^{(2)}_z\right) V_b, \tag{3.1.3}$$

where p^s_z, p^s_α are surface momenta ($\alpha = x, y$); $\pi^s_{\alpha\beta}$, $\pi^s_{z\beta}$ are surface momentum fluxes, V_b is a velocity of the interface boundary.

In the system of Eqs. (3.1.1), (3.1.2), (3.1.3) $j^{(1)}_k$ and $j^{(2)}_k$ are the bulk momenta in solid and liquid phases respectively, $\Pi^{(1)}_{\alpha k}$ and $\Pi^{(2)}_{\alpha k}$ are the bulk momentum fluxes, $\vec{n}$ is the vector normal to the deformed surface, ρ_1 and ρ_2 are the densities

of the solid and liquid phases. For undeformed surface $\vec{n} = \vec{e}_z$ and $\vec{V}_b$ is parallel to the z-axis. In general case $\vec{V}_b$ is directed normal to the deformed surface and $\vec{n}$ is different from $\vec{e}_z$ (see below). These three Eqs (3.1.1), (3.1.2), (3.1.3) are consistent with the surface energy conservation law:

$$\dot{E}_s + \nabla_\alpha \theta^s_\alpha = \left(Q^{(1)}_k - Q^{(2)}_k\right) n_k - (E_1 - E_2) V_b, \tag{3.1.4}$$

where E_s is the density of a surface energy, θ^s_α is the surface energy flux, $Q^{(1)}_k$ and $Q^{(2)}_k$ are the bulk energy fluxes, E_1 and E_2 are the bulk energy densities.

Note that in the linear theory $V_b = \dot{u}_z + \dot{\varsigma}$, where $\dot{u}_z$ is a z-component of a solid state velocity $\dot{\vec{u}}$, $\dot{\varsigma}$ is a velocity (a rate) of recrystalization.

3.1.1.2 The Bulk Fluxes at $T = 0$

In the system of Eqs. (3.1.1–3.1.3)

$$\Pi^{(2)}_{ik} = \rho_2 v_{2i} v_{2k} + P_2 \delta_{ik} \tag{3.1.5}$$

is a bulk momentum flux for superfluid at $T = 0$. Correspondingly $\vec{v}_2 = \vec{v}_s$ is a superfluid velocity, P_2 is a pressure in the liquid phase.

In linear theory

$$\Pi^{(1)}_{ik} = \rho_1 v_{1i} v_{1k} + P\delta_{ik} - \sigma^*_{ik} \tag{3.1.6}$$

is a momentum flux for solid, where

$$\sigma^*_{ik} = \sigma_{ik} - \frac{1}{3}\sigma_{ll}\delta_{ik} \tag{3.1.7}$$

is a shear part of the stress tensor.

In (3.1.7) as we already discussed in Chap. 1 a stress tensor reads

$$\sigma_{ik} = 2\rho_1 c_t^2 u_{ik} + \rho_1 \left(c_l^2 - 2c_t^2\right) u_{ll}\delta_{ik}, \tag{3.1.8}$$

where c_t and c_l are transverse and longitudinal sound velocities in solid, u_{ik} is a deformation tensor.

In the absence of dislocations and disclinations in solid $\vec{v}_1 = \dot{\vec{u}}$. Note that we consider solid ^{4}He to be a quantum crystal but not a supersolid. That is why there is no drift velocity relative to the lattice in it at $T = 0$. Correspondingly the bulk momenta in solid and liquid phase read:

$$j_{1i} = \rho_1 v_{1i} \quad \text{and} \quad j_{2i} = \rho_2 v_{2i}. \tag{3.1.9}$$

Finally the bulk energy fluxes in (3.1.4) for the surface energy conservation are given by:

$$Q_k^{(1)} = \left(\mu_1 + \frac{v_1^2}{2}\right) j_k^{(1)} - \sigma_{ik}^{(*)} v_{1i},$$
$$Q_k^{(2)} = \left(\mu_2 + \frac{v_2^2}{2}\right) j_k^{(2)}. \tag{3.1.10}$$

In the same time the bulk energy densities in (3.1.4)

$$E_1 = (\mu_1 \rho_1 - P_1) + \sigma_{ik}^* \frac{u_{ik}}{2} + \rho_1 \frac{v_1^2}{2} \quad \text{and} \quad E_2 = (\mu_2 \rho_2 - P_2) + \rho_2 \frac{v_2^2}{2}. \tag{3.1.11}$$

In the linearized theory for the solid phase

$$P_1 = P_0 - \frac{1}{3}\sigma_{ll}, \tag{3.1.12}$$

where $P_0 = 26$ bar is an equilibrium melting pressure.

Correspondingly for the chemical potential in the solid phase we have:

$$\mu_1 = \mu_0 - \frac{\sigma_{ll}}{3\rho_1}. \tag{3.1.13}$$

According to the thermodynamic identities at $T = 0$ the deviations from the equilibrium of the pressures and chemical potentials are related by:

$$dP_1 = \rho_1 d\mu_1 \quad \text{and} \quad dP_2 = \rho_2 d\mu_2. \tag{3.1.14}$$

Hence momentum flux in the solid phase can be represented as:

$$\Pi_{ik}^{(1)} = \rho_1 v_{1i} v_{1k} + P_0 \delta_{ik} - \sigma_{ik}. \tag{3.1.15}$$

3.1.1.3 The Surface Energy and Surface Fluxes

The total surface energy consists of three terms.

$$E_s = E_s^{el} + E_s^{inert} + E_s^{kin}, \tag{3.1.16}$$

where $E_s^{el}(u_{ik}^t, \nabla_x \varsigma, \nabla_y \varsigma)$ is the elastic surface energy, which depends on the gradients of the elastic and crystallization-induced displacements $\vec{u}$ and ς and u_{ik}^t is the tangential component of the displacement tensor which we will define below.

In (3.1.16) $E_s^{inert}(\dot{\varsigma})$ is the energy due to the necessity of the reconstruction of the short-range order when the matter flows over from phase to phase. It is quadratic in the recrystallization rate $\dot{\varsigma}$. Finally E_s^{kin} is the surface kinetic energy, which depends on the surface momentum density $\vec{p}^s = \left(\vec{p}_\alpha^s, p_z^s\right)$ $(\alpha = 1.2)$ and the surface mass v, as well as the velocities of the liquid $\vec{v}_2$, crystal $\vec{v}_1 = \dot{\vec{u}}$ and the phase interface V_b. Let us go over into a reference frame K_0 in which, first, the phase interface is at a rest $(V_b = 0)$ and, second, the velocity of the liquid has no tangential component $(\vec{v}_{2\alpha} = 0)$. Then the Galilean transformation formulas

$$\vec{p}^{s}_{\alpha} = \vec{p}^{s}_{0\alpha} + v\vec{v}_{2\alpha}; \quad p^{s}_{z} = p^{s}_{0z} + vV_b \tag{3.1.17}$$

$$E_s = E_{s0} + p^{s}_{0\alpha}v_{2\alpha} + p^{s}_{0z}V_b + \frac{1}{2}vV_b^2 + \frac{1}{2}vv_{2\alpha}^2 \tag{3.1.18}$$

relate the surface energy density E_s and the surface momentum density $\vec{p}^{s}$ in the laboratory reference frame K to the corresponding quantities in the K_0 reference frame. Therefore, taking into account that the kinetic part of the surface energy in the reference frame K_0 can depend only on the Galilean invariant combinations of the velocities $\dot{\vec{u}}$, $\vec{v}_2$ and V_b, we have

$$dE_{s0} = \lambda_{ik}du^{t}_{ik} + F_{\alpha}d\nabla_{\alpha}\varsigma + dE^{inert}_{s} + (v_{1\alpha} - v_{2\alpha})dp^{s}_{0\alpha} + (v_{1z} - V_b)dp^{s}_{0z}. \tag{3.1.19}$$

In (3.1.17)

$$dE^{inert}_{s} = \dot{\varsigma}d\left(M_{eff}\dot{\varsigma}\right), \tag{3.1.20}$$

where $M_{eff} \sim \rho d$ is the coefficient of the proportionality between E^{inert}_{s} and $\dot{\varsigma}^2/2$, and has the dimensions of the surface density. In the same time u^{t}_{ik} in dE_{s0} is the tangential displacement (strain) tensor, which is connected with the standard displacement tensor of the bulk elasticity theory by the relation (see [28]):

$$u^{t}_{ik} = \Lambda_{ip}\Lambda_{kl}u_{pl}; \quad \Lambda_{ip} = \delta_{ip} - \frac{n_i n_p}{1 + (\nabla_{\alpha}z)^2}. \tag{3.1.21}$$

In (3.1.19) $z = u_z + \varsigma$ is the total displacement of the surface points which is the sum of the elastic (u_z) and the recrystallization induced (ς) displacements, $\vec{n} = (1, -\nabla_{\alpha}z)$ is the normal to the deformed surface which enters in the system of Eqs. (3.1.1), (3.1.2), (3.1.3). Note that while in undeformed case $\vec{n} = \vec{e}_z$ and $|\vec{n}|^2 = 1$, in the deformed situation

$$|\vec{n}|^2 = 1 + (\nabla_{\alpha}z)^2 \neq 1. \tag{3.1.22}$$

The right-hand side of the identity (3.1.19) is a total differential, therefore the cross derivatives for the elastic part of the surface energy should be equal to each other:

$$\frac{\partial^2 E_{s0}}{\partial\varsigma_{\alpha}\partial u^{t}_{ik}} = \frac{\partial\lambda_{ik}}{\partial\varsigma_{\alpha}} = \frac{\partial F_{\alpha}}{\partial u^{t}_{ik}}. \tag{3.1.23}$$

In the relation (3.1.19) $p^{s}_{0\alpha} = \rho_b(v_{1\alpha} - v_{2\alpha})$ where $\rho_b \sim \rho d$ is the effective surface density. The expression (3.1.18) is the most general expression for the surface-energy differential at $T = 0$. It must be emphasized that the Eqs. (3.1.2), (3.1.3), expressing the conservation law of the surface momentum, are consistent with the conservation law of the surface angular momentum (see [29]) if the following conditions are fulfilled:

$$\pi_{\alpha\beta} = \pi_{\beta\alpha} \quad \text{and} \quad \pi_{\alpha z} = \pi_{\alpha\beta}\nabla_{\beta}z + p_{\alpha}V_b. \tag{3.1.24}$$

Furthermore, since the momentum and the mass flux coincide in the nonrelativistic hydrodynamics, Eq. (3.1.1) expresses in fact the equality of the bulk-momentum components perpendicular to the surface in the reference frame K_0 of the phase interface where $V_b = 0$. Owing to the continuity of the bulk momentum density $j_{0z}^{(1,2)} = \rho_{(1,2)}(v_z^{(1,2)} - V_b)$, there is no need to introduce the surface momentum p_{0z} into the hydrodynamics. Note that there is, generally speaking, no reason why $p_{0\alpha}$ should also vanish. But in the linear equations of the surface hydrodynamics the contribution of the terms containing $p_{0\alpha}$ always turns out to be small.

Note also that while deriving the system of Eqs. (3.1.1–3.1.3) we, as usual, define the boundary as the place where the surface particle density ν, which enters in (3.1.17), (3.1.18) is equal to zero (see [2]).

Let us remind that λ_{ik} in (3.1.19) is a surface stress tensor introduced firstly by Marchenko and Parshin [3]. Physically the surface stress exists even on a free undeformed solid surface because the surface row of atoms on Fig. 2.5 in Chap. 2 have the neighbors below but does not have the neighbors above. So there are gradients of the van der Waals potential acting on the surface row of atoms which correspond to nonzero λ_{ik}.

3.1.1.4 Lowest in Gradients Expansion of the Surface Energy

In the absence of the external stationary flows (for $v_{1\alpha} = v_{2\alpha}$ and $v_{1z} = V_b$) we have $p_{0\alpha}^s = 0$ and $p_{0z}^s = 0$. Than for $\nu = 0$ the surface energy $E_s = E_{s0}$ and

$$dE_s = dE_{s0} = \lambda_{ik} du_{ik}^t + F_\alpha d\nabla_\alpha \varsigma + \dot{\varsigma} d\left(M_{eff}\dot{\varsigma}\right). \tag{3.1.25}$$

Than, using the relation (3.1.23) for the cross derivatives, we obtain for E_s in the lowest (quadratic) order of the gradients expansion:

$$E_s = \left(\alpha_0 \delta_{\mu\nu} + \alpha_{\mu\nu}^{an}\right)\frac{\varsigma_\mu \varsigma_\nu}{2} + \lambda_{1\alpha\beta\gamma}\varsigma_\gamma u_{\alpha\beta} + M_{eff}\frac{\dot{\varsigma}^2}{2}, \tag{3.1.26}$$

where

$$\alpha_{\mu\nu}^{an} = \frac{\partial F_\mu}{\partial \varsigma_\nu}; \quad \lambda_{1\alpha\beta\gamma} = \frac{\partial F_\gamma}{\partial u_{\alpha\beta}} = \frac{\partial \lambda_{\alpha\beta}}{\partial \varsigma_\gamma}. \tag{3.1.27}$$

In (3.1.23) α_0 is the surface energy density in the absence of the deformation (the coefficient of the surface tension), $\alpha_{\mu\nu}^{an}$ is the surface-anisotropy coefficient, $\lambda_{1\alpha\beta\gamma}$ is the coefficient of the off-diagonal term in the expansion of the elastic part of the surface energy: $\lambda_{1\alpha\beta\gamma} = \lambda_{1\beta\alpha\gamma}$. In the expression (3.1.23) we have discarded all the terms of the order of $u^2/\varsigma^2 \ll 1$ which can be shown to be small at not too high frequencies ω with the help of the small parameters of the problem $\frac{\Delta\rho}{\rho} \ll 1$ and $kd \ll 1$. From the small terms of the order of u/ς we have retained only one,

namely, $\lambda_{1\alpha\beta\gamma}u_{\alpha\beta}\varsigma_\gamma$, which, as will be shown below, is important for the acoustic problem when the angle of incidence of the acoustic wave is close to the critical angle for the total internal reflection.

3.1.1.5 Surface Energy Flux and Surface Momentum Fluxes

Differentiating (3.1.25) with respect to the time, and using the forms (3.1.1–3.1.3) of the conservation laws of the surface mass and momentum under conditions when there are no stationary surface flows and $v = p_{0\alpha} = p_{0z} = 0$, we obtain for the energy in the quadratic in gradients approximation

$$\begin{aligned}\dot{E}_s+\nabla_\beta\theta^s_\beta - (Q_{1k} - Q_{2k})n_k + (E_1 - E_2)V_b \\ = -v_{1z}\nabla_\alpha\pi_{z\alpha} - v_{1\beta}\nabla_\beta\left(\pi_{\alpha\beta} + \lambda_{1\alpha\beta\gamma}\varsigma_\gamma\right) \\ - \dot{\varsigma}\left[\rho_1(\mu_2 - \mu_1) + P_1 - P_2 + \nabla_\beta\left(\tilde{\alpha}_{\mu\beta}\varsigma_\mu + \lambda_{1\alpha\gamma\beta}u_{\alpha\gamma}\right) - M_{eff}\ddot{\varsigma}\right],\end{aligned} \tag{3.1.28}$$

where the surface energy flux reads

$$\theta^s_\beta = -\tilde{\alpha}_{\mu\beta}\varsigma_\mu\dot{\varsigma} - \lambda_{1\alpha\gamma\beta}\dot{\varsigma}u_{\alpha\gamma} - \lambda_{1\beta\alpha\gamma}v_{1\alpha}\varsigma_\gamma. \tag{3.1.29}$$

Let us remind that $\tilde{\alpha}_{\mu\beta} = \alpha_0\delta_{\mu\beta} + \alpha^{an}_{\mu\beta}$.

We should demand that (3.1.28) has a form of the surface energy conservation law (3.1.4). Than the following conditions must be fulfilled:

$$\pi_{\alpha\beta} = -\lambda_{1\beta\alpha\gamma}\varsigma_\gamma; \quad \pi_{\alpha z} = 0 \tag{3.1.30}$$

$$\dot{\varsigma}\left[\rho_1(\mu_2 - \mu_1) + P_1 - P_2 + \nabla_\beta(\tilde{\alpha}_{\mu\beta}\varsigma_\mu + \lambda_{1\alpha\gamma\beta}u_{\alpha\gamma}) - M_{eff}\ddot{\varsigma}\right] = 0. \tag{3.1.31}$$

Let us emphasize that the expression $\pi_{\alpha\beta}\nabla_\beta z + p_\alpha V_b = -\lambda_{1\beta\alpha\gamma}\varsigma_\gamma\nabla_\beta z + p_\alpha V_b$ is of the second order in smallness. Therefore, the condition $\pi_{\alpha z} = 0$ in (3.1.27) is consistent with the conservation law of the surface angular momentum.

If the melting-crystallization processes occur in the system, then $\dot{\varsigma} \neq 0$. Therefore, from (3.1.31) follows: $\rho_1(\mu_2 - \mu_1) + P_1 - P_2 + \nabla_\beta(\tilde{\alpha}_{\mu\beta}\varsigma_\mu + \lambda_{1\alpha\gamma\beta}u_{\alpha\gamma}) - M_{eff}\ddot{\varsigma} = 0$. Finally, in the absence of external stationary flows, the linear boundary conditions have the form:

$$\begin{aligned}&\rho_2(v_{2z} - V_b) = \rho_1(v_{1z} - V_b); \quad \sigma_{z\alpha} = \nabla_\beta\left(\lambda_{1\beta\alpha\gamma}\varsigma_\gamma\right); \quad \sigma_{zz} + P_2 - P_0 = 0 \\ &\rho_1(\mu_2 - \mu_1) + P_1 - P_2 + \nabla_\beta\left(\tilde{\alpha}_{\mu\beta}\varsigma_\mu + \lambda_{1\alpha\gamma\beta}u_{\alpha\gamma}\right) - M_{eff}\ddot{\varsigma} = 0,\end{aligned} \tag{3.1.32}$$

where $P_0 = 26$ bar is equilibrium pressure.

The first equation in the system (3.1.32) is a matter-balance equation; the second and third equations constitute the conditions for the mechanical equilibrium at the boundary. Finally the last equation constitutes a generalized condition for the phase equilibrium. This last equation can also be regarded as the equation of the motion of the boundary relative to the solid. In the zeroth approximation the system (3.1.32) is consistent with the conditions for total phase equilibrium:

$$P_{01} = P_{02} = P_0; \quad \mu_{01} = \mu_{02} = \mu_0. \tag{3.1.33}$$

In the approximation linear in the deviations from the equilibrium and with an account of the thermodynamic identities $\delta P_1 = \rho_1 \delta\mu_1$ and $\delta P_2 = \rho_2 \delta\mu_2$ at $T = 0$ for the variable parts of the pressures and the chemical potentials we get:

$$\begin{aligned} &\Delta\rho\delta\mu_2 + \nabla_\beta\left(\tilde{\alpha}_{\mu\beta}\delta\varsigma_\mu + \lambda_{1\alpha\gamma\beta}\delta u_{\alpha\gamma}\right) - M_{eff}\delta\ddot{\varsigma} = 0 \\ &\delta\sigma_{z\alpha} = \nabla_\beta\left(\lambda_{1\beta\alpha\gamma}\delta\varsigma_\gamma\right); \quad \delta\sigma_{zz} + \rho\delta\mu_2 = 0 \\ &\rho\delta v_{1z} - \rho\delta v_{2z} - \Delta\rho\delta\dot{\varsigma} = 0 \end{aligned} \tag{3.1.34}$$

Let us emphasize that in the absence of the stationary surface flows the velocities, the displacements and the stress-tensor components coincide with their variable parts, and the symbol δ in front of them can be dropped. In (3.1.34) $\Delta\rho = \rho_1 - \rho_2$; $\rho \simeq \rho_1 \simeq \rho_2$ $(\Delta\rho/\rho \ll 1)$. In the balance equation, as in the expression (3.1.26) for the surface energy, we have discarded the small terms of the order of u/ς.

3.1.1.6 The Role of Capillary Terms. Anomalous Transmission of the Sound Waves

From the system of Eq. (3.1.34) it follows that for the sound wave incident on the phase-interface, the amplitude of the wave transmitted into the other medium is nonzero only because of the capillary effects.

Indeed, setting $\tilde{\alpha}_{\mu\beta} = \lambda_{1\alpha\gamma\beta} = M_{eff} = 0$ in (3.1.34) we get:

$$\delta\mu_2 = 0 \quad \text{and} \quad \delta\sigma_{zz} = \delta\sigma_{z\alpha} = 0. \tag{3.1.35}$$

Therefore, the liquid and the solid phases become completely decoupled and, for the acoustic waves incident at the boundary from any one of the media, this boundary is equivalent to a boundary with vacuum. As a result the sound wave is not transmitted into the other medium.

3.1.2 The Spectrum of Melting-Crystallization Waves

We briefly discussed the melting-crystallization waves and their spectrum in Chap. 2. In the present subsection we will present the more detailed derivation of their spectrum based on the system of the equations for the generalized boundary conditions (3.1.34).

As we mentioned previously at low frequencies the spectrum of melting-crystallization waves $\omega \sim k^{3/2}$ resembles the spectrum of the capillary waves. Hence they are more soft (they correspond to lower frequencies) than the spectrum of the more standard Rayleigh waves $\omega \sim c_t k$ briefly considered in Chap. 2. That is

why we can decouple the equations for $\vec{u}$ and ς and put $\vec{u} = 0$ in the equations for the melting-crystallization waves. Correspondingly the system of the Eq. (3.1.34) can be reduced to the system of two equations—the balance equation

$$\rho\delta v_{2z} + \Delta\rho\delta\dot{\varsigma} = 0 \tag{3.1.36}$$

and the equation for the thermodynamic equilibrium

$$\Delta\rho\delta\mu_2 + \tilde{\alpha}_{\mu\beta}\nabla_\beta\delta\varsigma_\mu = M_{eff}\delta\ddot{\varsigma}, \tag{3.1.37}$$

where we can safely neglect the small term with $\lambda_{1\alpha\gamma\beta}$ in (3.1.37).

We can also use the bulk Josephson equation for the superfluid velocity:

$$\delta\dot{\vec{v}}_2 + \vec{\nabla}\delta\mu_2 = 0 \tag{3.1.38}$$

and the incompressibility equation

$$\vec{\nabla}\cdot\delta\vec{v}_2 = 0. \tag{3.1.39}$$

The Josephson equation allows us to represent the superfluid velocity as $\delta\vec{v}_2 = \vec{\nabla}\delta\varphi_2$. Then the incompressibility equation will read $\Delta\delta\varphi_2 = 0$, where Δ is Laplasian here. For the surface wave $\delta\varphi_2 = Ae^{i\vec{k}_x\vec{r}_x - k_z z - i\omega t}$, where z is a normal axis to the undeformed surface. Thus, from $\Delta\delta\varphi_2 = 0$ follows that $k_\parallel^2 = k_z^2$ or $k_z = |k_\parallel|$ where $k_\parallel = (k_x^2 + k_y^2)^{1/2}$ is a projection of $\vec{k}$ vector on the (x, y)-plane.

Now we can take the time derivatives from the balance equation (3.1.33) and the ∇_z derivative from the thermodynamic equilibrium equation. Then we will finish with:

$$\rho\delta\dot{v}_{2z} = -\Delta\rho\delta\ddot{\varsigma} = -\rho\nabla_z\delta\mu_2 \tag{3.1.40}$$

$$\Delta\rho\nabla_z\delta\mu_2 + \tilde{\alpha}_{\mu\beta}\nabla_z\delta\varsigma_{\mu\beta} = M_{eff}\nabla_z\delta\ddot{\varsigma}, \tag{3.1.41}$$

where $\delta\varsigma_{\mu\beta} = \nabla_\mu\nabla_\beta\delta\varsigma$.

Substituting the first Eq. (3.1.40) to the second one we finally get from (3.1.41):

$$\frac{(\Delta\rho)^2}{\rho}\delta\ddot{\varsigma} = \nabla_z\left(M_{eff}\delta\ddot{\varsigma} - \tilde{\alpha}_{\mu\beta}\delta\varsigma_{\mu\beta}\right), \tag{3.1.42}$$

or correspondingly:

$$\left[\frac{(\Delta\rho)^2}{\rho}\omega^2 + \omega^2 k_z M_{eff}\right]\delta\varsigma = \tilde{\alpha}_{\mu\beta}k_z k_\mu k_\beta\delta\varsigma. \tag{3.1.43}$$

Hence using the condition $k_z = |k_\parallel|$ we obtain for the spectrum:

$$\omega^2\left[\frac{(\Delta\rho)^2}{\rho} + |k_\parallel|M_{eff}\right] = \tilde{\alpha}_{\mu\beta}k_\mu k_\beta|k_\parallel|. \tag{3.1.44}$$

Let us choose $\delta\varphi_2 = Ae^{ik_x x - k_z z - i\omega t}$. It means that we choose k_x-propagation for the wave-vector of the melting-crystallization waves. Then we get the following remarkable spectrum:

$$\omega^2 = \frac{\tilde{\alpha}_{xx}k_x^2|k_x|}{(\Delta\rho)^2/\rho + |k_x|M_{eff}} = \frac{\rho\tilde{\alpha}_{xx}k_x^2|k_x|}{(\Delta\rho)^2\left(1 + \rho|k_x|M_{eff}/(\Delta\rho)^2\right)}, \tag{3.1.45}$$

where $M_{eff} \sim \rho d$ is an effective surface mass.

At small wave-vectors $kd < \frac{(\Delta\rho)^2}{\rho^2}$ (or $\varepsilon = \frac{\rho^2}{(\Delta\rho)^2}kd < 1$) we can neglect the second term in the brackets in the denominator of (3.1.45) and get

$$\omega^2 = \frac{\rho\tilde{\alpha}_{xx}k_x^2|k_x|}{(\Delta\rho)^2}. \tag{3.1.46}$$

The spectrum (3.1.46) differs from the spectrum of ordinary capillary waves on the surface between liquid and vacuum only in the factor $(\Delta\rho)^2\Big/\rho^2$ and in the difference between the surface tension coefficient α and the surface stiffness $\tilde{\alpha}_{xx} = \alpha + \frac{\partial^2\alpha}{\partial\varsigma_x\partial\varsigma_x}$.

At large wave-vectors $\varepsilon \geq 1$ the spectrum (3.1.45) is linear $\omega^2 = \frac{\tilde{\alpha}_{xx}k_x^2}{M_{eff}}$.

3.1.2.1 Measurements of Melting-Crystallization Waves

The melting-crystallization waves were measured in Kapitza Institute by Keshishev, Parshin and Babkin in 1979 (see [10]).

The authors of [10] made a series of photographs of the surface growth and surface melting after the surface was suddenly perturbed by shaking of the cryostat at the time zero. The photographs (see Fig. 3.1) show the consequence of the states of the solid–liquid interface.

Keshishev, Parshin and Babkin also plotted the spectrum of the melting-crystallization waves which was well described by $\omega \sim k^{3/2}$ law (see Fig. 3.2). They also measured the decay rate of the waves which was several seconds for the temperatures $T \neq 0.5$ K. Effectively the rough interface responds in the same way as a free liquid surface with slowly decaying capillary waves.

3.1.3 The Growth Coefficient: Damping of the Melting-Crystallization Waves

For $T \neq 0$ the melting-crystallization waves are slowly decaying. The simplest way to get their damping according to Andreev and Knizhnik [30] is to introduce

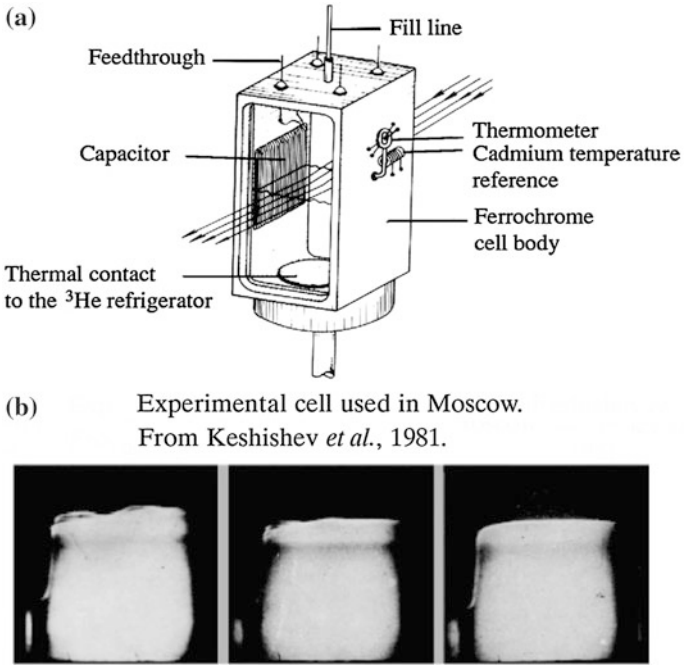

Fig. 3.1 **a** Crystallization waves in ^{4}He. Keshishev et al. [10, 11] discovered crystallization waves in 1979 by shaking the cryostat: the interface between a ^{4}He crystal and superfluid ^{4}He moves so easily by growth and melting that it looks like a free liquid surface. From Keshishev et al. [10, 11]. **b** Experimental cell used in Moscow [10, 11]

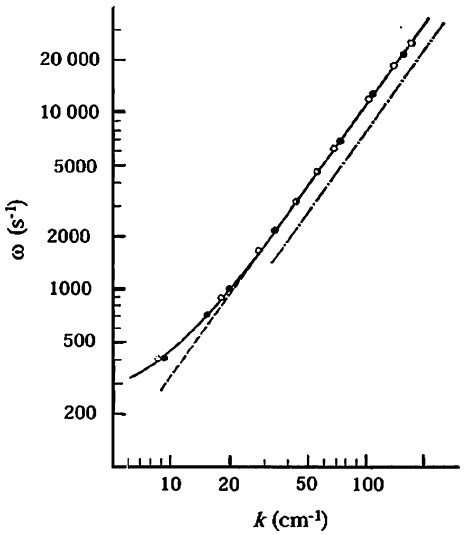

Fig. 3.2 The spectrum of melting-crystallization waves $\omega \sim k^{3/2}$ at small wave-vectors (from Keshishev et al. [10, 11])

the growth coefficient in the equation for the thermodynamic equilibrium. Namely we add in (3.1.41) a term linear in the recrystallization rate $\delta\dot{\zeta}$. As a result:

$$\Delta\rho\delta\mu_2 + \tilde{\alpha}_{\mu\beta}\nabla_\beta\delta\zeta_\mu - M_{eff}\delta\ddot{\zeta} = -\rho\delta\dot{\zeta}\frac{1}{K_{gr}}, \tag{3.1.47}$$

where K_{gr} is the growth coefficient of the crystal connected with the friction of the phase-interface on the normal excitations of superfluid and solid ^{4}He (phonons and rotons). Assuming $1/K_{gr}$ to be a small quantity for a mobile surface (a rapid growth of the rough surfaces) and solving the system of Eqs. (3.1.33) and (3.1.44) perturbatively we get for the spectrum:

$$\omega \simeq \omega_0 - \frac{i}{2}\frac{\rho^2}{(\Delta\rho)^2}\frac{|k_x|}{K_{gr}}, \tag{3.1.48}$$

where $\omega_0 = \frac{\rho\tilde{\alpha}_{xx}k_x^2|k_x|}{(\Delta\rho)^2\left[1+\frac{\rho M_{eff}|k_x|}{(\Delta\rho)^2}\right]}$ (see Eq. (3.1.45)).

In the phonon region $T \leq 0.5$ K we just get the decay rate of the order of the several seconds as in the measurements of Keshishev, Parshin, Babkin. Note that according to Andreev-Knizhnik in the phonon region $T \leq 0.5$ K the inverse growth coefficient $1/K_{gr} \sim T^4$. In the roton region $1/K_{gr} \sim \exp\left(-\frac{\Delta}{T}\right)$, where Δ is the energy of a roton minimum ($\varepsilon(p) = \Delta + \frac{(p-p_0)^2}{2M^*}$ and $\min\varepsilon = \Delta$). The measurements of the growth coefficient in the roton region by different groups are presented on Fig. 3.3. The effective damping is small both in the roton and the phonon region so we can see several oscillations before the amplitude of the wave becomes small. The profile of melting-crystallization waves is shown on Fig. 3.4 for the particular case of the vicinal surface and temperature $T = 0.28$ K.

Note that for atomically smooth surface according to the usual theory of the first-order phase-transition the growth is very slow and has a thermoactivative behavior:

$$\frac{1}{K_{gr}} \sim \exp\left(-\frac{\pi\beta^2\rho}{3d\delta\mu_2 k_\beta T\Delta\rho}\right) \to 0 \quad \text{for} \quad T \to 0, \tag{3.1.49}$$

where β is a step energy and $\delta\mu_2$ is the deviation from the equilibrium of the chemical potential of the liquid phase. Note that due to the continuity of pressures $\rho_1\delta\mu_1 = \rho_2\delta\mu_2$ the difference between the chemical potentials of the liquid and solid phases $\Delta\mu = \mu_2 - \mu_1 = \frac{\Delta\rho}{\rho}\delta\mu_2$. Note also that according to the theory of Lifshitz and Y. Kagan [31] due to the possibility of the quantum nucleation even at $T = 0$ it can still be a tunneling growth of a smooth surface (see [32]) though it is even more slow than one given by Eq. (3.1.49). The inverse growth coefficient at $T = 0$ is given by:

$$\frac{1}{K_{gr}} \sim \exp\left(-\frac{const}{(\Delta\mu)^2}\right). \tag{3.1.50}$$

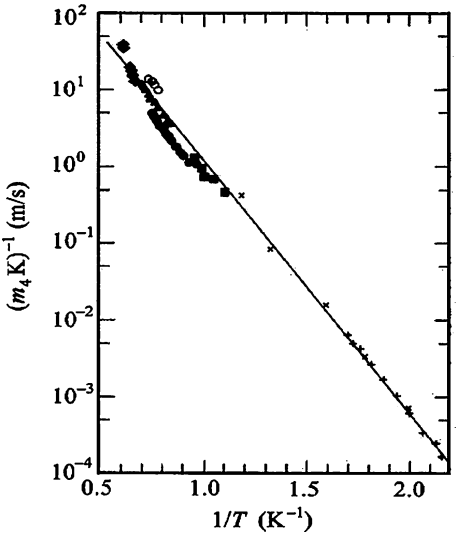

Fig. 3.3 Contribution of rotons to the growth coefficient K_{gr}^{-1} of solid ^{4}He labeled $(m_4 K_{gr})^{-1}$, as calculated by Bodensohn et al. [47]. *Plus symbol* Experiments of Keshishev et al. [10, 11], *Multiplication symbol* Experiments of Castaing et al. [46], *Circle with center dot, Square, Diamond* Experiments of Bodensohn et al. [47], *solid line*, best fit with a simple exponential function. The phonon contribution has been subtracted in the case of Keshishev's measurements. From Bodensohn et al. [47]

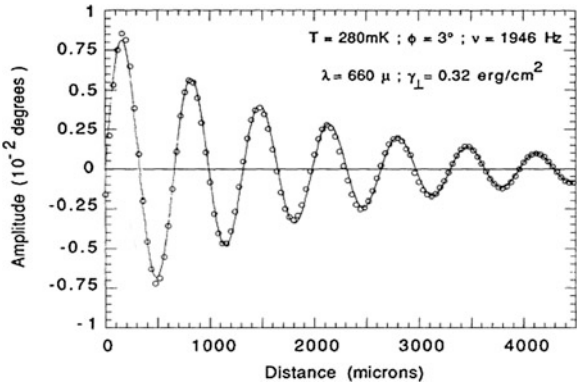

Fig. 3.4 Profile of melting-crystallization wave propagating at the surface of a ^{4}He crystal, as measured by Rolley et al. [48, 49]. In this particular case, $T = 280$ mK, the surface was oriented 3^o away from the (0001) plane, and the frequency was 1,946 Hz, so that the wavelength was 0.660 mm. The recorded quantity is the local tilt angle of the crystal surface with respect to the horizontal plane. From Rolley [48, 49]

The formulae (3.1.46) and (3.1.47) for the inverse growth coefficients of smooth surface which are exponential ($\exp\left(-\frac{1}{\Delta\mu T}\right)$ for the classical theory and $\exp\left(-\frac{1}{(\Delta\mu)^2}\right)$ for the quantum theory) are in sharp distinction with the rough surface where the inverse growth coefficient is linearly proportional to $\Delta\mu$: $\Delta\mu \sim \frac{\Delta\rho}{\rho}\delta\mu_2 \sim \frac{1}{K_{gr}}\dot{\varsigma}$.

3.1.4 *The Instability of Superfluid Tangential Flows on the Mobile Phase-Interface*

In the normal liquid the tangential flows parallel to the phase-interface with solid are prohibited by the boundary condition $\vec{v}_\tau = \dot{\vec{u}}_\tau$ due to the viscous friction on the surface. However, in superfluid helium we can create a frictionless superfluid component with the velocity $\vec{v}_{s0} = \vec{v}_0$ parallel to the surface. Let us consider the problem of the development in time of the surface oscillations (of the melting-crystallization waves) excited in the presence of a uniform "slipping" of a superfluid liquid along the mobile surface of initially undeformed stationary crystal.

The derivation of the equations of the surface hydrodynamics in the presence of a stationary flow of a superfluid liquid parallel to the boundary is carried out on the basis of the same formulas (3.1.1–3.1.13), (3.1.15–3.1.20), that are used in the derivation of the equations in the absence of the surface flows. Let us limit ourselves to the case of the sliding velocities that are small compared with the sound velocities. Then it is easy to show that we again can ignore in the problem the dependence of the surface energy (3.1.19) on the surface momentum $p_{0\alpha}$. We retain as before only the leading terms in the small parameters $\Delta\rho/\rho \ll 1$, $kd \ll 1$, and $v_0/c \ll 1$, where v_0 is the sliding velocity of the liquid and c is the sound velocity. Note that in helium $c_t < c_L < c_l$ for sound velocities in solid phase c_t and c_l and sound velocity of liquid phase. We assume that v_0 is much less than all the sound velocities. As a result for not too high frequencies $\omega < \frac{\Delta\rho}{\rho} c/d$ we get the following linear boundary conditions:

$$\begin{aligned}
&\rho_2(\vec{v}_2\vec{n} - V_b) = \rho_1(\vec{v}_1\vec{n} - V_b),\\
&\nabla_\beta\left(\lambda_{1\beta\alpha\gamma}\varsigma_\gamma\right) = \sigma_{z\alpha} + \rho_1 v_{2\alpha}(\vec{v}_1\vec{n} - V_b),\\
&\sigma_{zz} + P_2 - P_0 = 0,\\
&\rho_1\left(\mu_2 + \frac{v_2^2}{2} - v_{1\alpha}v_{2\alpha} - \mu_1\right) + P_1 - P_2 + \nabla_\beta\left(\tilde{\alpha}_{\mu\beta}\varsigma_\mu + \lambda_{1\alpha\gamma\beta}u_{\alpha\gamma}\right) - M_{eff}\ddot{\varsigma} = 0
\end{aligned} \tag{3.1.51}$$

The system of Eq. (3.1.51) differs from (3.1.34) by the presence of the terms quadratic in the velocities in the generalized phase equilibrium equation and in one of the mechanical equilibrium equations. Let us moreover note that the liquid velocity component along the normal to the deformed surface, $\vec{v}_2\vec{n}$, does not even

in the first approximation in the deviation from equilibrium, coincide with v_{2z}. Namely $\vec{v}_2\vec{n} = v_{2z} - v_{0\alpha}\varsigma_\alpha$. In the zeroth approximation the system of equations (3.1.51) yields the relations:

$$P_{01} = P_{02} = P_0; \quad \mu_{01} = \mu_{02} + \frac{v_0^2}{2} = \mu_0. \tag{3.1.52}$$

Notice that the chemical potentials of the solid and liquid do not coincide in the presence of a stationary flow parallel to the surface even in zeroth approximation (in the absence of small oscillations in the system). In the first approximation in the deviations of the quantities from their equilibrium values using the thermodynamic identities $\delta P_1 = \rho_1 \delta\mu_1$ and $\delta P_2 = \rho_2 \delta\mu_2$ we obtain:

$$\begin{aligned}
&\Delta\rho\delta\mu_2 + \nabla_\beta\left(\tilde{\alpha}_{\mu\beta}\delta\varsigma_\mu + \lambda_{1\alpha\gamma\beta}\delta u_{\alpha\gamma}\right) - M_{eff}\delta\ddot{\varsigma} + \rho v_{0\alpha}(\delta v_{2\alpha} - \delta v_{1\alpha}) = 0,\\
&\delta\sigma_{z\alpha} + \rho v_{0\alpha}\delta\dot{\varsigma} = \nabla_\beta\left(\lambda_{1\beta\alpha\gamma}\delta\varsigma_\gamma\right),\\
&\delta\sigma_{zz} + \rho\delta\mu_2 = 0,\\
&\rho\delta v_{1z} - \rho\delta v_{2z} + \rho v_{0x}\delta\varsigma_\alpha - \Delta\rho\delta\dot{\varsigma} = 0.
\end{aligned} \tag{3.1.53}$$

Let us analyze the spectrum of the surface oscillations (of the melting-crystallization waves) generated in the presence of the uniform slipping of the liquid for small vectors k, that is for $\varepsilon = \left(\frac{\rho}{\Delta\rho}\right)^2 kd \ll 1$. In this case it can be shown that $\left|\dot{\vec{u}}\right| < |\vec{v}_2|$. Therefore, if we are interested only in the low-lying branch of the spectrum, i.e. in the melting-crystallization waves, then we can discard the two mechanical-equilibrium equations in the system (3.1.53) and set, as it is done in [1] $\vec{u} = \dot{\vec{u}} = 0$ in the phase-equilibrium and balance equations. Then (3.1.53) is reduced to (see [17, 18, 33])

$$\begin{aligned}
\Delta\rho\delta\mu_2 + \tilde{\alpha}_{\mu\beta}\nabla_\beta\delta\varsigma_\mu - M_{eff}\delta\ddot{\varsigma} + \rho v_{0\alpha}\delta v_{2\alpha} = 0,\\
-\rho\delta v_{2z} + \rho v_{0\alpha}\delta\varsigma_\alpha - \Delta\rho\delta\dot{\varsigma} = 0.
\end{aligned} \tag{3.1.54}$$

The system (3.1.54) together with the bulk equations for the incompressible superfluid $\vec{\nabla}\cdot\delta\vec{v}_2 = 0$ and $\delta\dot{\vec{v}}_2 + \vec{\nabla}(\delta\mu_2 + v_{0\alpha}\delta v_{2\alpha}) = 0$ is valid at the temperature $T = 0$. In a real experiment $T \neq 0$ and it is important for us to determine both the real and the imaginary parts of the spectrum of the melting-crystallization waves. Therefore, we should again include the dissipation due to the growth coefficient $1/K_{gr}$ (connected with the friction of the phase-interface on the normal excitations of the liquid and the crystal). The solution for the spectrum of the melting-crystallization waves yield now

$$\omega \simeq \left(\omega_0 - \frac{\rho}{\Delta\rho}v_0 k_x\right) - \frac{i}{2}\frac{\rho^2}{(\Delta\rho)^2}\frac{|k_x|}{K_{gr}}\frac{\left(\omega_0 - \left(\frac{\rho}{\Delta\rho}\right)v_0 k_x\right)}{\omega_0}. \tag{3.1.55}$$

This result in the presence of the dissipation was firstly obtained by Kagan [17], Uwaga and Nozieres [19, 20]. For $K_{gr} \to \infty$ it coincides with the results of Parshin

[33]. In deriving (3.1.55), we considered the two-dimensional problem, i.e. $\vec{k} = (k_x, k_z)$ case and assumed the velocity $\vec{v}_0$ to be parallel to x-axis. In (3.1.55) $\omega_0^2 = \frac{\rho\tilde{\alpha}_{xx}k_x^2|k_x|}{(\Delta\rho)^2\left[1+\frac{\rho M_{eff}|k_x|}{(\Delta\rho)^2}\right]}$ is the spectrum of the melting-crystallization waves in the absence of a stationary flow. When $|v_0|k_x > 0$ and $(\rho/\Delta\rho)|v_0||k_x| > \omega_0$, we have Im $\omega > 0$, and, consequently the instability of the tangential flow sets in.

3.1.4.1 The Physical Reasons for the Instability

Physically we should remember that solid state is at a rest. Thus, the corrections $-(\rho/\Delta\rho)v_0k_x$ to Re ω is not just a Galilean shift. We can say that this instability is very similar to the instability of the superfluid flow with respect to the creation of normal excitations at superfluid velocities higher than the critical velocity $v_s > v_c$.

Let us consider the region $\varepsilon < 1$. Then $\omega_0^2 \simeq \frac{\tilde{\alpha}_{xx}k_x^2|k_x|\rho}{(\Delta\rho)^2}$ and $(\rho/\Delta\rho)|v_0||k_x| > \omega_0$ for $|v_0| > (\tilde{\alpha}_{xx}|k_x|/\rho)^{1/2} \to 0$ if $k_x \to 0$. Hence in this case there is no threshold for instability (the limitation on v_0 is only due to the fact that $|k_x| > 2\pi/L$, where L is the size of the crystal). But when we take the gravity into account (see Fig. 2.6) we have for the spectrum [17] (in analogy with the capillary waves in the presence of gravitation):

$$\omega_0^2 = \tilde{\alpha}_{xx}\frac{\rho k_x^2|k_x|}{(\Delta\rho)^2} + \frac{\rho g|k_x|}{\Delta\rho}. \tag{3.1.56}$$

As a result a threshold of the instability appears $\frac{\rho}{\Delta\rho}v_{0c} = \min\left(\frac{\omega_0}{|k_x|}\right)$ and

$$v_{0c} = \left(4g\tilde{\alpha}_{xx}\frac{\Delta\rho}{\rho^2}\right)^{1/4} \sim 4 \text{ cm/ sec} \ll c. \tag{3.1.57}$$

Nevertheless the critical velocity at which the instability sets in is low compared to the sound velocity $v_{0C} \ll c$, so the limitations on the incompressibility of the liquid and the solid phases together with the other assumptions under which we derived the system of Eq. (3.1.51) are still valid. Note that the predicted instability resembles a bit the Kelvin-Helmholtz tangential instability on the surface between two liquid layers in classical hydrodynamics. The theoretical predictions of Kagan [17], Uwaha and Nozieres [19, 20] were confirmed in the experiments of Tsymbalenko in Kurchatov Institute in Moscow (see [21, 22] and Fig. 3.5).

In these experiments the behavior of the atomically rough surface of solid helium was investigated in a jet of fluid for the temperature range 1–1.4 K. After some critical value of the velocity of a tangential flow is exceeded, the surface clearly becomes unstable. Below the roughening transition temperature T_R the same surface is stable in a jet of a fluid.

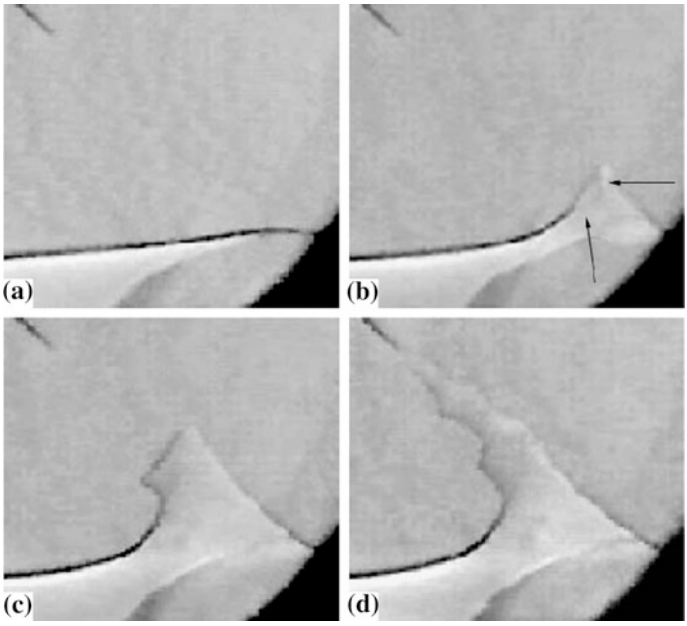

Fig. 3.5 The development of the instability above the roughening transition from Tsymbalenko et al. [21, 22]. At the moment of time $t = 0$ (**a**) the emission from the needle points begins. The field of vision is 5.5×4.9 mm^2, $t = 1.25$ s (**b**), $t = 2$ s (**c**) $t = 2.3$ s (**d**). The *arrows in frame* (**b**) indicate the recess formed on the growing crystal "stalagmite". On the frame (**d**) one can see the development of cylindrical instability. Waists are formed on the surface, which break the crystal "stalagmite"

3.1.5 The Spectrum of the Rayleigh Waves on the Rough Surface

In this subsection we will analyze a bit more detaily the spectrum of the Rayleigh waves. This branch of surface oscillations exists both on atomically rough and atomically smooth surfaces. For mobile atomically rough surface the Rayleigh waves are important at high frequencies.

As we already discussed in Sect. 2.2.4 for Rayleigh waves the recrystallization rate $\dot{\varsigma} = 0$ and a velocity of the boundary $V_b = \dot{u}_z$. From the balance equation in the system (3.1.32) we have then: $\rho_1(\dot{u}_z - V_b) = \rho_2(v_{sz} - V_b) = 0$ and $v_{sz} = V_b = \dot{u}_z$. In the equations for mechanical and thermodynamic equilibrium in (3.1.32) we can safely neglect the surface capillary terms ($\lambda_{1\alpha\beta\gamma} = M_{eff} = \tilde{\alpha}_{\mu\beta} = 0$) and get:

$$\begin{aligned} \sigma_{zx} = 0; \quad \sigma_{zz} + \rho_2 \delta\mu_2 = 0; \\ \Delta\rho\delta\mu_2 = 0; \quad \dot{u}_z = v_{sz} = V_b. \end{aligned} \tag{3.1.58}$$

Correspondingly on the surface $\delta\mu_2 = 0$ and $\sigma_{zx} = \sigma_{zz} = 0$ [see Eq. (2.2.2)].

The boundary conditions (3.1.58) should be considered together with the bulk equations

$$\rho_1 \ddot{u}_i = \nabla_k \sigma_{ik} \tag{3.1.59}$$

in the solid phase and

$$\ddot{\varphi} = c_I^2 \Delta\varphi \tag{3.1.60}$$

in the liquid phase for the compressible potential liquid.

Note that in (3.1.60)

$$\vec{v}_2 = \vec{v}_s = \vec{\nabla}\varphi; \delta P_2 = \rho_2 \delta\mu_2 \tag{3.1.61}$$

and from the Josephson equation $\dot{\vec{v}}_s + \vec{\nabla}\delta\mu_2 = 0$ it follows

$$\delta\mu_2 = -\dot{\varphi} \tag{3.1.62}$$

for potential φ.

In the solid phase in the isotropic approximation as usual in elasticity theory we should represent a total lattice displacement and lattice velocity

$$\vec{u} = \vec{u}_t + \vec{u}_l; \dot{\vec{u}} = \dot{\vec{u}}_t + \dot{\vec{u}}_l \tag{3.1.63}$$

as a sum of transverse and longitudinal parts. In (3.1.63) $\vec{\nabla} \cdot \vec{u}_l = 0$ and thus $\vec{u}_l = \vec{\nabla}\Phi$. In the same time $\vec{\nabla} \cdot \vec{u}_t = 0$ and $\vec{u}_t = \vec{\nabla} \times \vec{\Psi}$. Correspondingly in the bulk for the two-dimensional situation $\vec{u} = (u_x, u_z); u_y = 0, u_x = u_x(x,z), u_z = u_z(x,z)$ we can represent $\vec{\Psi} = \Psi\vec{e}_y$ and get for Φ and Ψ the equations:

$$\ddot{\Phi} = c_l^2 \left(\frac{\partial^2}{\partial x^2} + \frac{\partial^2}{\partial z^2} \right) \Phi, \tag{3.1.64}$$

$$\ddot{\Psi} = c_t^2 \left(\frac{\partial^2}{\partial x^2} + \frac{\partial^2}{\partial z^2} \right) \Psi, \tag{3.1.65}$$

where c_l and c_t are the velocities of the longitudinal and the transverse sounds in the solid phase.

Note that in this geometry $u_x = \frac{\partial\Phi}{\partial x} - \frac{\partial\Psi}{\partial z}$ and $u_z = \frac{\partial\Phi}{\partial z} + \frac{\partial\Psi}{\partial x}$. Correspondingly the boundary conditions demand

$$\ddot{\varphi} = c_I^2 \left(\frac{\partial^2}{\partial x^2} + \frac{\partial^2}{\partial z^2} \right) \varphi \tag{3.1.66}$$

for the liquid potential φ.

Using the system of Eq. (3.1.58) for the boundary conditions together with the bulk Eqs. (3.1.60–3.1.65) we get for the compressible liquid and solid phases:

$$\left(\omega^2 - 2c_t^2 k_x^2\right)^2 - 4c_t^4 k_x^2 \left|k_z^t\right| \left|k_z^l\right| = 0, \tag{3.1.67}$$

where $\left|k_z^t\right|^2 = k_x^2 - \frac{\omega^2}{c_t^2}$ and $\left|k_z^l\right|^2 = k_x^2 - \frac{\omega^2}{c_l^2}$ in compressible case for the surface wave. Taking into account the numerical values of the sound velocities in liquid and solid ^{4}He (remind that $c_t < c_I < c_l$) we finally get (see [17, 18] for example) $\omega \approx \eta c_t |k_x|$, where $\eta(c_t/c_l) \simeq 0.8$. For $\varepsilon \sim \frac{\rho^2}{(\Delta\rho)^2} kd \ll 1$ the group velocity of the melting-crystallization waves $v_M = \frac{d\omega}{dk} \sim k^{1/2}$ is much smaller then the velocity of the Rayleigh waves $c_R \sim 0.8\, c_t$. The two branches of the spectrum begin to interact with each other only for $\varepsilon \geq 1$.

3.1.6 The Angles of the Total Internal Reflection: Excitation of the Surface Wave by the Bulk Second Sound Wave

We have the following hierarchy of different sound velocities $v = \frac{\omega}{k}$ on the rough surface:

$$v_M < c_R < c_t < c_I < c_l, \tag{3.1.68}$$

where c_t and c_l are transverse and longitudinal sound velocities, $c_R \sim 0.8 c_t$ is the velocity of the Rayleigh wave, $v_M \sim k^{1/2}$ is the phase velocity of the melting-crystallization waves at small frequencies and c_I is the first sound velocity in superfluid liquid.

At $T \neq 0$ we also have a second sound wave in the liquid phase. The second sound velocity in the phonon region of low temperatures $T \leq$ (0.5–0.6) K $c_{II} = \frac{c_I}{\sqrt{3}}$ in 3D case but it becomes smaller in the roton region $T \geq 0.6$ K (see Figs. 1.3 and 1.4). Thus, $v_M < c_{II} < c_R < c_t < c_I < c_l$.

At $T = 0$ for the first sound incident from the liquid we can introduce the angle of total internal reflection (or a Brewster angle) for the longitudinal sound in liquid $\sin\theta_L^{cr} = \frac{c_t}{c_l}$ with $\sin\theta_l = 1$ and $\cos\theta_l = 0$. When the first sound is incident from the liquid at an angle greater than a critical angle $\theta > \theta_L^{cr}$, only a transverse acoustic wave is generated in the solid. Note that the phenomenon of the total internal reflection manifests itself in the sharply nonmonotonic character of the angular dependence of the sound-transmission coefficient $D(\theta) = 1 - R(\theta)$. Let us emphasize that at the angle of the incidence which is exactly equal to the Breuster angle the transmission coefficient is nonzero only because of the allowance for the surface capillary terms.

3.1.6.1 The Basic Formalism at $T = 0$

Let us consider a first sound plane acoustic wave incident at the rough phase interface from the liquid at zero temperature. Taking into account (3.1.64), (3.1.65), (3.1.66) which give for the plane waves the relation between the frequency and wave vectors in longitudinal and transverse sound in solid and first sound in liquid, we have for the incident, reflected and two (longitudinal and transverse) transmitted waves the expressions:

$$\begin{aligned}
\varphi &= \varphi_{10}\exp\left[-i\omega t + i\frac{\omega}{c_I}\sin\theta_{1L}x + i\frac{\omega}{c_I}\cos\theta_{1L}z\right] \\
&\quad + \varphi_{20}\exp\left[-i\omega t + i\frac{\omega}{c_I}\sin\theta_{2L}x + i\frac{\omega}{c_I}\cos\theta_{2L}z\right]; \\
\Phi &= \Phi_0\exp\left[-i\omega t + i\frac{\omega}{c_l}\sin\theta_l x + i\frac{\omega}{c_l}\cos\theta_l z\right]; \\
\Psi &= \Psi_0\exp\left[-i\omega t + i\frac{\omega}{c_t}\sin\theta_t x + i\frac{\omega}{c_t}\cos\theta_t z\right],
\end{aligned} \tag{3.1.69}$$

where we again choose 2D geometry for $\vec{u} = (u_x, u_z); u_y = 0; u_x = u_x(x,z)$, $u_z = u_z(x,z)$.

In (3.1.69) φ_{10} and φ_{20} are the amplitudes of the incident and reflected first sound waves in the liquid, Φ_0 and Ψ_0 are the amplitudes of the longitudinal and transverse sound waves generated in the solid and θ_{1L}, θ_{2L}, θ_l, θ_t are the angles between the wave-vectors of the corresponding waves and the normal to the surface. The problem is homogeneous in the coordinate x. Therefore:

$$\frac{\sin\theta_t}{c_t} = \frac{\sin\theta_l}{c_l} = \frac{\sin\theta_{1L}}{c_I} = \frac{\sin\theta_{2L}}{c_I}. \tag{3.1.70}$$

In particular, we have a priori the obvious equalities (see Fig. 3.6)

$$\sin\theta_{1L} = \sin\theta_{2L} = \sin\theta_L \tag{3.1.71}$$

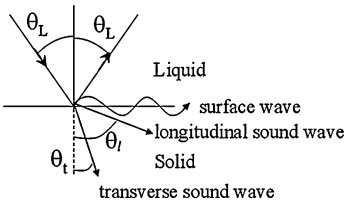

Fig. 3.6 The mirror reflection of the first sound wave incident from the liquid. For the angle smaller than the Brewster angle $\theta_L < \theta_L^{cr} = \arcsin\frac{c_l}{c_l}$ there are two transmitted waves for the longitudinal and transverse sound in the solid phase

For $\theta_L < \theta_L^{cr}$

$$D(\theta) = 1 - R(\theta) = D_l(\theta) + D_t(\theta) \tag{3.1.72}$$

since we have two transmitted waves in the solid phase. In (3.1.72):

$$R = \frac{|\varphi_{20}|^2}{|\varphi_{10}|^2} \tag{3.1.73}$$

is the reflection coefficient,

$$D_l = \frac{\left|\dot{\vec{u}}_l\right|^2 c_l \cos\theta_l}{|\vec{v}_{2in}|^2 c_l \cos\theta_L};\ D_t = \frac{\left|\dot{\vec{u}}_t\right|^2 c_t \cos\theta_t}{|\vec{v}_{2in}|^2 c_I \cos\theta_L} \tag{3.1.74}$$

are the transmission coefficients for longitudinal and the transverse sound waves, $\vec{v}_{2in} = \vec{\nabla}\varphi_1$ is the superfluid velocity field in the incident wave of the first sound. Note that for $\theta_L > \theta_L^{cr}$ $D_l(\theta) = 0$ and $D = D_t(\theta)$. In the same time for the normal incidence $\theta_L = 0$ we get $\theta_t = \theta_L = 0$. In this case $D_t(0) = 0$ and $D = D_l(0)$.

The recrystallization displacement ς for the acoustic problem which we consider is governed by (see [17, 18]):

$$\varsigma = \varsigma_0 \exp\left[-i\omega t + i\frac{\omega}{c_t}\sin\theta_t x\right]. \tag{3.1.75}$$

The frequency dependence of the transmission coefficient D is governed by the value of the characteristic dimensionless parameter $\varepsilon = \omega \frac{d}{c}\left(\frac{\rho}{\Delta\rho}\right)^2$ of the problem (here and below in this paragraph we assume that the sound velocities, though are different, have the same order of magnitude). This parameter can be written also in the form $\varepsilon = \omega\tau$, where $\tau = \frac{d}{c}\left(\frac{\rho}{\Delta\rho}\right)^2$ is the hydrodynamic surface reconstruction time. For normal incidence according to Castraing and Puech [4, 5]:

$$D = 1 - R = \frac{4\varepsilon^2 c_I/c_l}{1 + \varepsilon^2\left(\frac{c_I + c_l}{c_l^2}\right)^2}, \tag{3.1.76}$$

where to be more specific $\varepsilon = \frac{\rho M_{eff}}{(\Delta\rho)^2}\frac{\omega}{c_I}$.

For the small values of the parameter $\varepsilon < 1$ we have $D \approx 4\varepsilon^2 \frac{c_I}{c_l} \sim \omega^2\tau^2 \ll 1$—the transmission coefficient is quadratic in frequency and is nonzero only due to the account of the effective surface mass $M_{\text{eff}} \neq 0$.

For $\varepsilon \geq 1$ the transmission coefficient $D \sim 1$. We can say that for $\omega\tau \geq 1$ the quantum mobile boundary becomes a classical one, and D increases significantly.

The investigation of the transmission coefficient for $\omega\tau \ll 1$ and at different angles (smaller and larger than θ_L^{cr}) helps us to establish the connection between $D(\theta)$ and different surface coefficients ($\tilde{\alpha}$, M_{eff}, $\lambda_{1\alpha\beta\gamma}$) due to which account $D(\theta)$ is nonzero. Note that for all the angles $D(\theta) \sim \omega^2$ for small $\omega\tau < 1$. For $\theta = 0$ $D(0)$

is governed by M_{eff}. For the Brewster angle $\theta_L^{cr} = \arcsin\left(\frac{c_t}{c_l}\right)$ $D(\theta)$ is governed by the surface elasticity $\lambda_{1\alpha\beta\gamma}$. Then from the behavior of $D(\theta)$ for $0 < \theta < \theta_L^{cr}$ we can also independently extract the value of the surface rigidity $\tilde{\alpha}_{xx}$.

3.1.6.2 The Case of Nonzero Temperature $T \neq 0$

If we consider nonzero temperatures $T \neq 0$ and small frequencies then $v_M < c_{II} < c_R < c_t < c_I < c_l$ and for the second sound incident from the liquid there are two critical angles of the total internal reflection. First one is found from the condition $\frac{\sin\theta_{II}}{c_{II}} = \frac{\sin\theta_t}{c_t}$. If $\theta_t = \frac{\pi}{2}$, then $\theta_{II}^{cr} = \arcsin\frac{u_{II}}{c_t} < 1$. For this angle there is no transmission of the transverse and the longitudinal sound waves in the bulk and thus $D = D_{\text{l}} + D_{\text{t}} = 0$ for the transmission coefficient. In the same time there is no reflection of the first sound wave in the superfluid. Hence the total reflection coefficient $R = R_{\text{I}} + R_{\text{II}} = R_{\text{II}}$, where R_{II} is the reflection coefficient of the second sound wave. Thus, for $\theta_{II} > \theta_{II}^{c1}$ we have the phenomenon of the total internal reflection and $R_{\text{II}} = 1$.

However, there is a second critical angle θ_{II}^{c2} already in the region of total internal reflection (Kagan, Kosevich [13]). Namely $\theta_{II}^{c2} = \arcsin\left(\frac{c_{II}}{c_R}\right) > \left(\theta_{II}^{c1} = \arcsin\frac{c_{II}}{c_t}\right)$.

3.1.6.3 The Reflection Coefficient

The second critical angle inside the region of the total internal reflection corresponds to the resonance excitation by the bulk second sound wave (by rotons for $T \geq 0.6$ K) of the surface Rayleigh wave.

If we take the dissipative processes into account, then close to θ_{II}^{c2} the reflection coefficient R_{II} will have a pronounced minimum. The estimates show (Kagan,

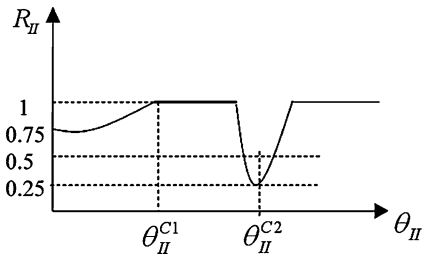

Fig. 3.7 The angular dependence of the reflection coefficient R_{II} for the second sound wave incident on the mobile surface at the angle close to the second critical angle $\theta_{II}^{c2} = \arcsin\frac{c_{II}}{c_R}$. A large fraction of the energy is transferred to a surface Rayleigh wave at $\theta = \theta_{II}^{c2}$

Kosevich [13]) that for $T \geq 0.6$ K the fraction of the energy transferred to a surface wave for $\theta = \theta_{II}^{c2}$ can reach 0.75 (see Fig. 3.7).

Note that if we take into account for example a surface dissipation $R_{\text{sur}} > 0$ (see the expression (3.2.18) for R_{sur} in the next subsection 3.1.4) than for $\theta_{II} > \theta_{II}^{c1}$: $R_{II} \neq 1$. More specifically: $1 - R_{II} = R_{sur}/\rho_n c_{II} \cos\theta_{II} \left|\vec{v}_{n_{II}}^{inc}\right|^2$, where $R_{II} = \frac{\left|\vec{v}_{n_{II}}^{ref}\right|^2}{\left|\vec{v}_{n_{II}}^{inc}\right|^2}$ is the reflection coefficient with respect to the second sound. Let us emphasize again that at high temperatures $T \sim (0.8 \div 1)$ K in the roton region $c_{\text{II}} < c_{\text{R}}$ and we can excite the surface Rayleigh waves by the bulk second sound.

Note also that since $c_{\text{I}} > c_{\text{R}}$ on the interface between solid and liquid ^{4}He we cannot excite the Rayleigh waves by the first sound wave incident from the liquid. This is in contrast to He-II-metal surface where this phenomenon for the first sound wave was predicted by Andreev and measured by Zinov'eva in Kapitza Institute (see [23–25]).

Finally let us mention that when we increase a frequency we can also satisfy the inequality $c_{II} < v_M = \left(\frac{\tilde{\alpha}_{xx}\rho\omega}{(\Delta\rho)^2}\right)^{1/3}$ and get another transcritical angle $\theta_M = \arcsin(c_{II}/v_M)$.

Hence in principle it is also possible to excite thermal melting-crystallization waves by the roton second sound on the mobile (rough) phase-interface between solid and liquid ^{4}He. However, quite often for $T \sim (0.8 \div 1)$ K the melting-crystallization waves can be overdamped at these frequencies.

On the atomically smooth interface between solid and liquid ^{4}He the role of the Rayleigh waves plays the Rayleigh-Stonley surface waves (Kagan and Kosevich [13]). It is also possible to excite them resonantly by the bulk second sound incident from the liquid phase.

3.2 Surface Hydrodynamics on the Mobile Interface at $T \neq 0$ and in the Presence of ^{3}He Impurities

Maris and Huber [6, 7], Wolf et al. [9, 50], Puech et al. [34] measured the Kapitza thermal resistance on the rough interface between solid and superfluid ^{4}He. Graf et al. [15, 16] were among the first who investigated the influence of a small amount of ^{3}He impurity on the mobility of the rough interface and on its thermal resistance R_{K}. Note that Kapitza thermal resistance R_{K} is determined by the energy transfer from the interface to the quasiparticle gas. The theory for Kapitza resistance on the standard atomically smooth interface of the solid and the superfluid ^{4}He or the superfluid ^{4}He and metal was constructed by Khalatnikov [35] and is known as "phonon mismatch theory".

In the experiments of Graf, Bowley and Maris [15, 16] the rough surface of solid ^{4}He was considered being in contact with dilute superfluid solution (with respect to ^{3}He component) of ^{3}He in ^{4}He.

Let us remind that from the experiments of Anufriev, Lopatik and Sebedash in Kapitza Institute [36, 37] as well as from the stratification curves for the solid and liquid solutions at the pressure $P_0 \approx 26$ bar [38–40, 51] it can be deduced, that the equilibrium concentration in the solid solution is negligible compared with the equilibrium concentration in the liquid solution at the temperatures $T < 0.3$ K. Note that the maximal solubility of ^{3}He in ^{4}He at $P = 0$ bar and low temperatures is 6.4 % (see [35]), while for nonzero pressures it can even reach the values of 9.5 % for $P = 10$ bar (see also Chap. 15). In the same time the maximal solubility of ^{3}He in the solid phase at low temperatures is exponentially small for $T \leq 0.3$ K (see [36, 37]). At $T \sim (0.4 \div 0.5)$ K, however, the equilibrium impurity concentrations in the solid and liquid phases become comparable by the order of magnitude.

In the experiments [15, 16] it was in particular established that at low temperatures and the dimensions L of the crystals larger than the capillary constant $a_0 = (2\alpha/g)^{1/2} = 0.14$ cm, the rough interface remains highly mobile up to the impurity concentrations of the order of 10^{-3} (0.1 %). This may seem to contradict the results of Landau et al. [14] who observed visually an increase of the relative flat surface fraction on small ($L \sim a_0$) crystals when a low concentration of impurity (10^{-4}) is added. Qualitative arguments by Castaing et al. [41], however, attribute this phenomenon to the fact that the absorption of the ^{3}He impurity on the surface lowers the surface rigidity $\tilde{\alpha} = \alpha + \frac{\partial^2 \alpha}{\partial \varphi^2}$ and thereby also the sizes of the rounded sections. For large crystals ($L \gg a_0$), however, the role of the surface energy in the establishment of the equilibrium shape is small compared with that of the gravity. So when a low concentration of impurity is added, an appreciable fraction of the boundary remains highly mobile. In [15, 16] the authors have also proposed for the interaction of ^{3}He with the interface a theoretical model involving a macroscopical wave function of the impurity being localized close to the interface. This assumption is in fact equivalent to the neglecting of the equilibrium "freezing-in" (penetration) of the impurity in the solid phase.

Experiments of Anufriev, Lopatik and Sebedach confirm the correctness of this assumption for $T \leq 0.3$ K. From the other hand for higher temperatures we cannot neglect "freezing-in" of the impurity, since the equilibrium solubility of the impurity in the solid phase is comparable with that in the liquid phase.

In [17, 18] a complete system of the generalized boundary conditions with an account of the most important surface dissipative effects as well as with an account of the finite ^{3}He concentration in both the solid and liquid phases is derived.

3.2.1 *Equations of the Surface Hydrodynamics at $T \neq 0$ and in the Presence of the Impurities*

The system contains four more equations that in the case of the interface of the pure solid and liquid ^{4}He at $T = 0$. First one corresponds to the impurity balance equation:

$$j_{3z}^{(1)} - \rho_1 c_1 V_b = j_{3z}^{(2)} - \rho_2 c_2 V_b, \tag{3.2.1}$$

where $V_b = \dot{u}_z + \dot{\varsigma}$ is the velocity of the boundary and the impurity flux in the solid phase:

$$\vec{j}_3^{(1)} = \rho_1 c_1 \dot{\vec{u}} - \rho_1 D_1 \vec{\nabla} c_1, \tag{3.2.2}$$

c_1 is an equilibrium concentration of impurity in the solid phase, D_1 is the diffusion coefficient for the impurity in the solid phase. In the same time $\vec{j}_3^{(2)} = \rho_2 c_2 \vec{v}_n$ is the impurity flux in the liquid phase, c_2 is the equilibrium impurity concentration in the liquid.

Note that the hydrodynamic description is valid in the liquid phase for the frequencies lower than all the characteristic reciprocal relaxation times in the system. In the temperature and the concentration range under consideration we have the following hierarchy of the relaxation frequencies ($\gamma = 1/\tau$) $1\Big/\tau_{ph-ph}^{(2)} \ll 1\Big/\tau_{ph-i}^{(2)} \ll 1\Big/\tau_{i-i}^{(2)}$ for the phonon–phonon, phonon-impurity and impurity–impurity relaxation, respectively. At $T \leq 0.5$ K and $c_2 \sim 10^{-4} \div 10^{-3}$ the hydrodynamics is valid up to quite high frequencies $\omega \sim 1\Big/\tau_{i-i}^{(2)} \sim (10^7 \div 10^8)\ \mathrm{s}^{-1}$. Note that in the considered region the impurities and their scattering by one another are of the principal significance for the thermodynamics and the formation of the second sound waves in the liquid phase (the second sound here is in fact a thermal wave in the impurity subsystem and $c_{II}^2 \sim T$).

Note that for $\omega\tau_{i-i}^{(2)} \leq 1$ the impurity component has the same drift velocity $\vec{v}_i = \vec{v}_n$ as roton and phonon normal excitations in the superfluid solution.

A second equation is an additional equation for the thermal equilibrium with respect to ^{3}He-component:

$$\mu_3^{(1)} - \mu_3^{(2)} = \left(j_{3z}^{(1)} - \rho_1 c_1 V_b\right) 1/K_3, \tag{3.2.3}$$

where the coefficient $1/K_3$ has the meaning of the inverse growth coefficient with respect to the ^{3}He-component.

In (3.2.3) according to Anufriev, Sebedach and Lopatik [36]:

$$\mu_3^{(2)} = \Psi^{(2)}(P, T=0) + \frac{T}{m_4} \ln c_2 - \frac{T}{m_4} \ln \left[\frac{2m_4}{\rho_2} \left(\frac{m^* T}{2\pi\hbar^2} \right)^{3/2} \right] \tag{3.2.4}$$

for the liquid phase and

$$\mu_3^{(1)} = \Psi^{(1)}(P, T=0) + \frac{T}{m_4} \ln c_1 \tag{3.2.5}$$

for the solid phase.

We have neglected here the small contribution to the thermodynamics from the slow band motion of the impurity in the solid phase (the effective band velocity

$v_{band} \sim \frac{\Delta d}{\hbar} \ll (T/m^*)^{1/2}$ for $\Delta \ll T$ where d is interatomic distance, m^* is the effective mass of ^{3}He atom in the solution, and Δ is the impurity bandwidth). Note that a band motion of impurities is absent in the superfluid phase.

The balance equation with respect to ^{4}He component reads again:

$$j_z^{(1)} - \rho_1 V_b = j_z^{(2)} - \rho_2 V_b, \tag{3.2.6}$$

where the mass fluxes in solid and liquid phases yield:

$$\vec{j}^{(1)} = \rho_1 \dot{\vec{u}};\ \vec{j}^{(2)} = \rho_s \vec{v}_s + \rho_n \vec{v}_n. \tag{3.2.7}$$

For $T \sim (0.1 \div 0.5)$ K and $c_2 \sim 10^{-3} \div 10^{-4}$, the influence of diffusion, including heat and mass diffusion, is negligible in the liquid phase compared with the thermal conductivity and will be neglected. The normal density $\rho_n = \rho_n^{ph} + \rho_2 c_2 \frac{m^*}{m_4}$ has the phonon and impurity contributions in the hydrodynamic regime $\omega\tau \ll 1$. The conditions of the mechanical equilibrium if we neglect the surface stress $\lambda_{1\alpha\beta\gamma}$ read:

$$\Pi_{zz}^{(1)} = \Pi_{zz}^{(2)}; \Pi_{z\beta}^{(1)} = 0, \tag{3.2.8}$$

where $\Pi_{ik}^{(1)} = P_1 \delta_{ik} - \sigma_{ik}^*; \mathrm{P}_1 = P_0 - \frac{1}{3}\sigma_{ll}$ as for the pure case at $T = 0$, $\sigma_{ik}^* = \sigma_{ik} - \frac{1}{3}\delta_{ik}\sigma_{ll}$ is a shear part of the stress tensor; $\Pi_{ik}^{(2)} = P_2 \delta_{ik}$ in linear theory. Thus again $\sigma_{zz} + P_2 - P_0 = 0$, where $P_0 = 26$ bar is the equilibrium pressure. To complete the system of equations for $T \neq 0$ and in the presence of the impurity we should add to (3.2.1), (3.2.3), (3.2.6), (3.2.8) the conditions for the thermodynamic equilibrium at $T \neq 0$ and the equation for the surface entropy increase. The first one

$$\mu_4^{(1)} - \mu_4^{(2)} + \left(M_{eff}\ddot{\varsigma} - \tilde{\alpha}_{\gamma\beta}\nabla_\gamma\nabla_\beta\varsigma\right)\frac{1}{\rho_1} = \left(j_z^{(1)} - \rho_1 V_b\right)\frac{1}{K_{gr}} \tag{3.2.9}$$

connects as usual the difference between the chemical potentials of ^{4}He component with the growth coefficient K_{gr} (M_{eff} and $\tilde{\alpha}_{\gamma\beta}$ are again an effective surface density and the surface stiffness).

In (3.2.5) the chemical potential with respect to the ^{4}He component in the liquid phase for a weak nondegenerate solution reads (see [35]):

$$\mu_4^{(2)}(P, T, c_2) = \mu_4^{(2)}(P, T) - \frac{T}{m_4}c_2, \tag{3.2.10}$$

where $\mu_4^{(2)}(P, T)$ is the chemical potential of pure liquid ^{4}He. Analogously in the solid phase

$$\mu_4^{(1)}(P, T, c_1) = \mu_4^{(1)}(P, T) - \frac{T}{m_4}c_1. \tag{3.2.11}$$

The next equation of the complete system is an equation of the increase of the surface entropy:

$$f_z^{(1)} - \rho_1\sigma_1 V_b - f_z^{(2)} + \rho_2\sigma_2 V_b = R_{sur}/T_0, \tag{3.2.12}$$

where $f_z^{(1)}$ and $f_z^{(2)}$ are the entropy fluxes and $S_1 = \rho_1\sigma_1$ and $S_2 = \rho_2\sigma_2$ are the entropy densities of the solid and liquid phases, R_{sur} is the surface dissipative function, T_0 is equilibrium temperature (see discussion after Eq. (3.2.18)).

In (3.1.63) at low temperatures and the impurity concentrations (see Khalatnikov [35])

$$\sigma_2 = \sigma_2^{ph} - \frac{c_2}{m_4}\ln c_2 + \frac{c_2}{m_4}\ln\left[\frac{2m_4}{\rho_2}\left(\frac{m^*T}{2\pi\hbar^2}\right)^{3/2}\right] \tag{3.2.13}$$

for the entropy of the liquid phase, where σ_2^{ph} is the phonon contribution to the entropy of the unit mass σ. In the same time for the entropy of the unit mass of the solid phase

$$\sigma_1 = \sigma_1^{ph} - \frac{c_1}{m_4}\ln c_1. \tag{3.2.14}$$

The entropy flux in the liquid phase

$$\vec{f}^{(2)} = \rho_2\sigma_2\vec{v}_n - \kappa_2\vec{\nabla}T/T_2, \tag{3.2.15}$$

where κ_2 is the thermal conductivity of the liquid solution. Correspondingly the entropy flux in the solid phase

$$\vec{f}^{(1)} = \rho_1\sigma_1\dot{\vec{u}} - \kappa_1\vec{\nabla}T/T_1 - \left(\frac{\partial\sigma_1}{\partial c_1}\right)\rho_1 D_1\vec{\nabla}c_1, \tag{3.2.16}$$

where σ_1 is given by (3.2.9) and κ_1 is the thermal conductivity of the solid solution. Note that a possibility of a complete thermodynamic description in the solid phase and particularly the possibility to introduce a single temperature T_1 for the impurity and phonon subsystem, implies the satisfaction of the condition $\omega\tau_{i-ph}^{(1)} < 1$ (the thermolization condition for impurities). We emphasize that at the temperatures and concentrations considered the following relation holds between the respective relaxation frequencies [38, 39, 42, 43]: $1\Big/\tau_{i-ph}^{(1)} \ll 1\Big/\tau_{ph-i}^{(1)} \leq 1\Big/\tau_{ph-ph}^{(1)U} \leq 1\Big/\tau_{ph-ph}^{N} \leq 1\Big/\tau_{i-i}^{(1)}$ for an impurity on phonon, a phonon on impurity, a phonon on phonon with Umklapp (see Chap. 1) and normal scattering of a phonon by a phonon with an account of anharmonicity. Finally $1\Big/\tau_{i-i}^{(1)}$ is an inverse scattering time of an impurity by an impurity due to the band motion. At $T \sim 0.5$ K we have $1\Big/\tau_{i-ph}^{(1)} \sim 10^2 \div 10^3\ \text{s}^{-1}$ and $1\Big/\tau_{ph-ph}^{U} \sim 1\Big/\tau_{ph-ph}^{N} \sim 10^6\ \text{s}^{-1}$.

When all these relations between the frequency and the relaxation times are satisfied, the bulk fluxes in the solid phase take the form of (3.2.2), (3.2.7), (3.2.16).

3.2.2 The Surface Dissipative Function and Kapitza Thermal Resistance

To find the surface dissipative function R_{sur} in (3.2.12) we have to write the conservation law for the surface energy:

$$\dot{E}_s + \nabla_\beta \theta_\beta - (Q_{1z} - Q_{2z}) + (E_1 - E_2)V_b = 0, \tag{3.2.17}$$

where the surface energy flux $\theta_\beta = -\tilde{\alpha}_{\mu\beta}\varsigma_\mu\dot{\xi}$ in linear approximation, $E_1 = -P_1 + \rho_1\sigma_1 T_1 + \mu_4^{(1)}\rho_1 + \mu_3^{(1)}\rho_1 c_1 + \sigma_{ik}^* u_{ik}^*/2$ is the bulk energy density for the solid phase, $\vec{Q}_1 = \mu_4^{(1)}\vec{j}^{(1)} + \mu_3^{(1)}\vec{j}_3^{(1)} + T_1\vec{f}_1 + \sigma_{ik}^*\dot{u}_k$ is the bulk energy flux in the liquid phase.

Correspondingly

$$E_2 = -P_2 + \rho_2 T_2\sigma_2 + \mu_4^{(2)}\rho_2 + \mu_3^{(2)}\rho_2 c_2,$$
$$\vec{Q}_2 = \mu_4^{(2)}\vec{j}^{(2)} + \mu_3^{(2)}\vec{j}_3^{(2)} + T_2\vec{f}_2$$

are the bulk energy density and the bulk energy flux in the liquid phase. From (3.2.17) it follows that the surface dissipative function

$$\begin{aligned} R_{sur} = &\left[\mu_4^{(1)} - \mu_4^{(2)} + \left(M_{eff}\ddot{\xi} - \alpha_{\gamma\beta}\nabla_\gamma\nabla_\beta\varsigma\right)\frac{1}{\rho_1}\right]\left[j_z^{(1)} - \rho_1 V_b\right] + \\ &+\left(\mu_3^{(1)} - \mu_3^{(2)}\right)\left(j_{3z}^{(1)} - \rho_1 c_1 V_b\right) + (T_1 - T_2)\left(f_z^{(1)} - \rho_1\sigma_1 V_b\right). \end{aligned} \tag{3.2.18}$$

We have neglected in (3.2.18) the surface fluxes of mass, impurity mass, momentum and entropy, and have set the surface temperature equal to those in the interior. Note that in (3.2.12) for the entropy increase T_0 is the equilibrium temperature on the melting curve. From the requirement that the surface dissipative function should be positive $R_{\text{sur}} > 0$ follows (3.2.3) and (3.2.9) for the thermodynamic equilibrium with respect to ^{4}He and ^{3}He components. Moreover, the last term in the r.h.s. of (3.2.18) implies that:

$$T_1 - T_2 = R_K T_0 (f_z^{(1)} - \rho_1\sigma_1 V_b), \tag{3.2.19}$$

where R_{K} is the thermal Kapitza resistance, and $\Delta T = T_1 - T_2$ is a temperature jump between the solid and liquid phase.

Thus we derived the complete system of equations for the generalized boundary conditions at temperatures $T \neq 0$ and in the presence of ^{3}He impurities. The system includes the balance equations with respect to ^{4}He and ^{3}He components (3.2.1) and (3.2.6), the equations of the mechanical equilibrium (3.2.8), the equations for the thermodynamic equilibrium with respect to ^{4}He and ^{3}He

chemical potentials (3.2.3) and (3.2.9), the equation of the surface entropy increase (3.2.12) and the equation for the temperature jump due to Kapitza thermal resistance (3.2.19). Note that this jump can exist only on the solid-superfluid interface since superfluid helium has an infinite effective thermal conductivity. Due to this fact we can speak about almost uniform temperature distribution in the liquid phase which is established during very short relaxation times.

Note also that when we consider the surface dissipative function (3.2.18) and the generalized thermal equilibrium conditions (3.2.3), (3.2.9), (3.2.19), which follow from its positive definiteness, we disregard for simplicity the off-diagonal elements of the Onsager matrix of the kinetic surface coefficients. In the phenomena under consideration the off-diagonal matrix elements of the kinetic coefficients are smaller than the diagonal once (since $R_{\mathrm{sur}} > 0$) and only renormalize the effects connected with the diagonal elements. Thus, they do not lead to qualitatively new results.

Finally let us emphasize that the total thermal conductivity of the surface $\sigma_s = 1/R_K$ is a sum of the two components σ_{sL} from the phonons and σ_{S3} from the impurities. The phonon contribution $\sigma_{sL} \sim T^5$ is determined at low temperatures ($T \leq 0.2$ K) by the capillary effects, that is by the surface stiffness $\tilde{\alpha}$ and the effective surface mass M_{eff}. It was investigated in [19, 20] and [4, 5]. The impurity contribution to the heat conductance of the interface will be discussed below.

In (3.2.9) for the thermodynamic equilibrium (for $\mu_4^{(1)} - \mu_4^{(2)}$) the coefficient $1/K_{gr}$ is a reciprocal crystal-growth coefficient (relative to ^{4}He component). In quantum crystal it is determined mainly, as we already discussed in Chap. 2, by the momentum transfer from the quasiparticle gas to the interface. If the drift velocities of the impurities and of the phonons do not coincide with the interface velocity (as in the case when the impurity has a finite ability to freeze into the solid phase), then the coefficient $1/K_{gr}$, just like $\sigma_s = 1/R_K$, is a sum of the two contributions—from the impurities and from the phonons. The phonon contribution $1/K_{gr}^{(ph)} \sim \rho_n^{ph} c_I/\rho^2 \sim T^4$ was investigated experimentally by Keshishev, Parshin and Babkin. The impurity contribution $1/K_{gr}^{(i)} \sim \rho_{ni}(T/m^*)^{1/2}/\rho^2 \sim c_2 T^{1/2}$ was estimated in [41].

Lastly, $1/K_3$ has the meaning of the coefficient of the crystal growth with respect to ^{3}He component. A similar coefficient was introduced for the growth of a classical crystal (see for example review-article by Chernov (see Ref. [44] in Chap. 2)). A possible estimate of its value for mobile (rough) interface will be given below. When the viscosity of the liquid is taken into account, one more condition should be met. Namely the tangential component of the velocity of normal excitations should be equal to the tangential component of the lattice velocity $\dot{u}_\beta = v_{n\beta}$. In addition, the equations (3.2.8) and (3.2.18) for mechanical equilibrium and surface dissipative function should acquire the terms connected with the viscous-stress tensors (see Chap. 1). For the phenomena considered below, however, viscosity is insignificant and will be neglected.

We discuss now the system (3.2.1), (3.2.3), (3.2.6), (3.2.8), (3.2.9), (3.2.12) and (3.2.19) which consists of eight equations. We have to check whether the number

of the boundary conditions equals to the number of the independent modes. In the liquid phase there are first and second sounds, and the purely dissipative heat-conduction mode having at $c_2 \sim 10^{-3}$ a spectrum $i\omega_{III} = 3\kappa_2 k^2/5\rho_2 c^{(2)}$, where $c^{(2)}$ is the heat capacity per unit mass of the liquid. In the third mode the temperature and the concentration oscillate. If we take into account the impurity diffusion in the liquid phase then the spectrum of this mode would be determined by the effective thermal conductivity κ_{eff} (see Khalatnikov [35]). There is no such mode in pure He-II, and the heat conduction influences only the damping of a second sound $\mathrm{Im}\omega_{II} = (1/5)\kappa_2 k^2/\rho_2 c^{(2)}$. The presence of an independent heat-conduction mode in the liquid solution is very clearly due to the appearance of an independent variable – the concentration of impurities c_2. The careful analysis shows that for $c_2 \to 0$ and $D_2 = 0$ $\omega_{\mathrm{III}} \to 0$.

Four independent modes exist in the solid phase. These are two first sounds (longitudinal and transverse), a heat conduction mode $i\omega = \kappa_1 k^2/\rho_1 c_{ph}^{(1)}$ (if $\omega\tau_U < 1$—see Chap. 1), and, last, a diffusion mode $i\omega = D_1 k^2$.

We emphasize that in view of the relation $D_1 \ll \kappa_1/\rho_1 c^{(1)}$, the heat-conduction and the diffusion modes in solid interact very weakly even when the thermal diffusion is taken into account. Therefore, the stringent impurity-thermolization condition $\omega\tau_{i-ph}^{(1)} < 1$ is, generally speaking, not mandatory for the hydrodynamic scheme being considered. Hydrodynamic treatment of the diffusion and the heat-conduction in a solid is thus actually valid up to the frequencies $\omega < 1/\tau_{ph-ph}^{N(1)} \le 1/\tau_{i-i}^{(1)}$, i.e., to $\omega \sim 10^6$ s^{-1}. Note that the eighth independent variable is the additional recrystallization displacement ζ of the surface. The number of the independent variables is therefore equal to the number of the boundary conditions. Note also that at $T = 0$ and for the pure case (no impurities) the number of the boundary conditions is 4 [see the system (3.1.32)]. Finally for pure ^{4}He at $T \neq 0$ the number of boundary conditions is 6 and we add two equations for the surface entropy increase and for the temperature jump on the surface to the system (3.1.32) which is valid at $T = 0$.

3.2.3 Damping of Melting-Crystallization Waves

The specific property of a mobile interface boundary at $T \neq 0$ and in the presence of impurities is that three surface modes exist on it: melting-crystallization waves (in which ζ and $\vec{j}^{(2)}$ oscillate), Rayleigh waves (in which $\vec{u}$ and $\vec{j}^{(2)}$ oscillate), and surface second sound, whose velocity is close to c_{II} (to the velocity of the bulk second sound in the superfluid solution). In the last mode we have coupled oscillations of temperature and ^{3}He-concentration [52].

Using the derived boundary conditions, let us examine how a low concentration of ^{3}He impurity influences the damping of the crystallization waves.

The spectrum of the melting-crystallization waves at low frequencies ($\varepsilon \sim \frac{\omega}{c} d \frac{\rho^2}{(\Delta\rho)^2} < 1$) at $T \neq 0$ and in the presence of impurities has the form (see [17, 18] and references therein):

$$\omega^2 = \frac{\tilde{\alpha}_{xx} k^3 (\rho/\Delta\rho)^2}{1 + \frac{\rho\rho_n}{(\Delta\rho)^2}} - i\omega k\rho \left(\frac{\rho}{\Delta\rho}\right)^2 \left[\frac{1}{K_{gr}} + \frac{c_1^2}{K_3} + R_K T\sigma_1^2 + \frac{T\left(\sigma_1 - \sigma_2 \frac{c_1}{c_2}\right)}{(\kappa_1 + \kappa_2)k} \left(\sigma_1^{ph} + \frac{c_1}{m_4} \ln \frac{c_2}{c_1}\right)\right], \tag{3.2.20}$$

where $|k_x| = |k_z| = k$ is the wave number of the surface wave. Note that the real part of the spectrum Reω differs from the expression (3.1.46) for the spectrum at $T = 0$ only in the presence of the factor $\frac{\rho\rho_n}{(\Delta\rho)^2}$ in denominator of (3.2.20). Obviously for $T \to 0$ and $c_2 \to 0$ $\rho_n \to 0$ and the factor $\frac{\rho\rho_n}{(\Delta\rho)^2}$ goes to zero restoring the previous result.

In the same time the imaginary part of the spectrum besides a contribution from the inverse growth coefficient with respect to ^{4}He component [compare with (3.1.48)] contains also the contributions from $1/K_3$, R_K and from the bulk thermal conductivity connected with κ_1 and κ_2. At $T \sim (0.4 \div 0.5)$ K the impurity, in both the liquid and the solid phases, makes a larger contribution to the thermodynamics then the phonons for $c \sim 10^{-3}$. The imaginary part of the wave spectrum can therefore be written in this case in the form:

$$\mathrm{Im}\omega = \frac{\rho k}{2} \left(\frac{\rho}{\Delta\rho}\right)^2 \left\{\frac{1}{K_{gr}} + \frac{c_1^2}{K_3} + R_K T\sigma_1^2 + \frac{Tc_2^2}{m_4^2 k(\kappa_1 + \kappa_2)} \frac{c_1^2}{c_2^2} \ln^2\left(\frac{c_1}{c_2}\right)\right\}. \tag{3.2.21}$$

The first three terms in the right-hand side of (3.2.21) are responsible for the surface dissipation, and the fourth for the bulk dissipation. The estimates show that for

$$kl_U < (c_{II}/c_I)\left(\sigma^i/\sigma^{ph}\right) c_1/c_2 \tag{3.2.22}$$

(where l_U is the mean-free path connected with the Umklapp processes, σ^i is the impurity part of the entropy) the main contribution to the damping is made by the bulk dissipation. Note that from the experimental measurements of the damping of the melting-crystallization waves one can independently extract the impurity distribution coefficient between liquid and solid phases c_1/c_2, which is a function only of temperature and pressure in weak solutions.

We point out that if the impurity concentration is decreased in each of the phases, the contribution of the heat-conduction to the imaginary part of (3.2.20) at a fixed temperature $T \neq 0$ is determined by the phonons and still is different from

zero. If, however, the inequality (3.2.22) is reversed, the damping is determined mainly by the surface dissipation. Note that for $T \sim (0.4 \div 0.5)$ K and starting with a concentration $c_2 \sim 10^{-3}$ the imaginary part of the spectrum becomes of the same order as the real part for the frequencies $\omega \leq 10^5\ \mathrm{s}^{-1}$.

Equation (3.2.20) was obtained by Kagan, Kosevich under assumptions:

$$\begin{gathered} R_K \ll \left(\frac{1}{\kappa_1 k} \sim \frac{1}{\kappa_2 k}\right); \quad R_K \geq \frac{\omega}{k c_{II}^2 \rho c^{(1)}}; \\ \frac{1}{K_3}(D_1\omega)^{1/2} \ll \frac{T}{\rho m c_1}; \quad \frac{c_1^2}{K_3} \leq \frac{T c_2^2}{m_4^2 k(\kappa_1+\kappa_2)} \frac{c_1^2}{c_2^2} \ln^2\left(\frac{c_1}{c_2}\right). \end{gathered} \tag{3.2.23}$$

If the first inequality of (3.2.23) is violated, then there is no flow of entropy through the interface, i.e. $f_{1z} - \rho_1\sigma_1 V_b = f_{2z} - \rho_2\sigma_2 V_b = 0$. We emphasize that in the case of pure He-II, i.e. for $\omega_{III} = 0$, the dissipative term in the entropy flux of a liquid phase turns out to be small and we arrive to the "stringent" hydrodynamic boundary condition $v_{nz} = V_b$ used in [30].

When the third and fourth inequalities in (3.2.23) are violated, there is no impurity flux through the interface, i.e.

$$j_{3z}^{(1)} - \rho_1 c_1 V_b = j_{3z}^{(2)} - \rho_2 c_2 V_b = 0,$$

which is also equivalent, for the liquid phase, to the condition $v_{nz} = V_b$. In this case the imaginary part of the spectrum of the melting-crystallization waves is given by:

$$\mathrm{Im}\omega = \frac{1}{2} k \left(\frac{\rho}{\Delta\rho}\right)^2 \rho \left\{\frac{1}{K_{gr}} + \frac{T c_1}{\rho m_4 (D_1\omega)^{1/2}}\right\}, \tag{3.2.24}$$

i.e. it is determined at very low frequency by the diffusion coefficient D_1 in the solid phase (see experiments of Agnolet et al. [40] in Texas). Namely, this contribution vanishes together with the impurity concentration c_1 in the solid phase. For the inverse growth coefficient with respect to the ^{3}He component we can obtain the estimate $\frac{1}{K_3} \sim \frac{T}{\rho m c_1} \frac{l_{ii}^{(1)}}{D_1 \eta} \sim \frac{T}{\rho m c_1} \frac{1}{v_{band}\eta}$, where the dimensionless parameter $\eta < 1$ plays the role of the effective coefficient of the penetration from the solid into the liquid phase and v_{band} is a band velocity of the impurities in the solid phase. The penetration coefficient η becomes much less than unity at low temperatures $T < 0.3$ K, when the ability of the impurity to freeze into the solid is low. We emphasize that the transition to the situation in which there are no entropy and impurity fluxes through the interface can be described not only kinetically but also thermodynamically. The transition occurs at: $c_1 \ll c_2; \sigma_1^{ph} \ll \left(\sigma_2 \approx \sigma_2^i\right)$.

Estimates show that both inequalities hold at the same temperatures $T \sim (0.1 \div 0.2)$ K. At these temperatures the solid can be regarded as free of impurities and phonons, i.e. it can be described by the elasticity theory equations (see Subsection 3.1.3) for $T = 0$.

We note that at low temperatures (when the impurity concentration c_1 in the solid phase is vanishingly small) the damping of the crystallization waves is

determined mainly by the phonon contribution. In this region, as we discussed already, the inverse growth coefficient $1/K_{gr}$ is proportional to T^4 and small (see [30]). In this case a more important role can be played by the corrections (connected with the impurity concentration in the liquid phase) to the real part of the spectrum, and particularly by the effective decrease of the surface stiffness $\tilde{\alpha}$ in $\mathrm{Re}\omega$ [see (3.2.20)] due to ^{3}He impurity adsorption.

3.2.4 Impurity Contribution to the Kapitza Thermal Resistance at Low Temperatures

Using the complete system of the boundary conditions in the low-temperature limit $T \sim (0.1 \div 0.2)$ K ($c_1 \ll c_2$; $\sigma_1^{ph} \ll \sigma_2^i$; $v_{nz} \approx V_b$), we can solve the acoustic problem again and determine the coefficient of the energy transfer for a longitudinal wave incident from solid phase to first- and second-sound waves in liquid. The solution of this problem helps us to evaluate Kapitza resistance R_K on the mobile interface (see Khalatnikov [35]).

For the simplest case of a normal incidence of a longitudinal wave the total transmission coefficient is equal to

$$D = D_I + D_{II} = 4\left(\frac{c_I}{c_l}\varepsilon^2 + \frac{\rho\rho_n c_{II}}{(\Delta\rho)^2 c_l}\right), \tag{3.2.25}$$

where as usual $\varepsilon = \frac{\rho M_{eff}}{(\Delta\rho)^2}\frac{\omega}{c_l}$; $\rho \approx \rho_1 \approx \rho_2$; $\frac{\Delta\rho}{\rho} = \frac{\rho_1 - \rho_2}{\rho} \ll 1$.

Equation (3.2.25) contains a sum of two contributions. The first D_I describes the energy-flux fraction transferred to the first sound in the liquid, and D_{II}, the fraction transferred to a second sound in the liquid. In the range of the temperatures and concentrations which we are considering ρ_n, c_{II} and $\sigma^{(2)}$ are defined by the impurities, and thus the second sound velocity (see Chap. 1) reads:

$$c_{II}^2 = \frac{T\rho_2^2\left(\sigma^{(2)}\right)^2\rho_s}{C_p^{(2)}\rho_n\rho_2} \approx \frac{T\rho_2^2(\sigma^i)^2}{c_2\rho_{ni}} \sim \frac{T}{m^*}, \tag{3.2.26}$$

where $C_p^{(2)}$ is specific heat at constant pressure in the liquid phase. Correspondingly the coefficient D_{II} is given by:

$$D_{II} = \frac{4\rho}{(\Delta\rho)^2 c_l}\left(\frac{5}{3}m^*T\right)^{1/2}\frac{\rho c_2}{m_4}. \tag{3.2.27}$$

Equation (3.2.27) does not depend on frequency and does not contain the relaxation time τ. The expression for D_{II} can therefore be used to represent (at least in the order of magnitude) the efficiency with which the thermal phonon $\hbar\omega \sim T$ is transferred from the solid phase to the impurity subsystem in the liquid solution. The physical reason is that the Kapitza thermal resistance is determined by the

energy transfer from the wall to the He-II quasiparticles on the interface itself, so that R_K depends little on the excitations mean free path l (on the relaxation time τ). The mean free path l determines only the distance over which the temperature jump is formed (is localized), and not the magnitude of this jump. We thus obtain the following estimate for the impurity contribution to the thermal conductivity σ_{s3} of the interface:

$$\sigma_{s3} \sim c_{ph}^{(1)} \bar{c}_t D_{II} \sim (\rho/\Delta\rho)^2 c_2 T^{7/2}, \tag{3.2.28}$$

where $c_{ph}^{(1)}$ is the phonon part of the heat capacity of the solid ($c_{ph}^{(1)} \sim T^3$) and $\bar{c}_t$ is the average sound velocity in the crystal. We point out that the resulting temperature and concentration dependences of σ_{s3} agree with the result of the model calculation of Graf, Bowley and Maris [15, 16].

Moreover, it is interesting to note that the energy fraction transferred to the impurity subsystem, obtained in [16] within the framework of the quantum–mechanical model (the case $l = \infty$) differs from (3.2.27) by no more than 20–25 %.

We point out that D_I in (3.2.25) determines the phonon contribution to the thermal conductivity of the interface σ_{sL}. The latter due to proportionality of D_I to ω^2 takes the form $\sigma_{sL} \sim (\rho/\Delta\rho)^4 T^5$. The total thermal conductivity $\sigma_s = \sigma_{sL} + \sigma_{s3} = 1/R_K$ of the interface is an additive quantity, a fact reflected in (3.2.25). At the temperatures and concentrations considered, we have $\sigma_{s3} \ll \sigma_{sL}$ in view of the "extra factor" $(\rho/\Delta\rho)^2 \sim 10^2$.

3.2.5 Cherenkov Emission of the Second Sound Quanta by the Thermal Surface Waves

Note also that there is one more mechanism, not accounted for in the theoretical parts of [15, 16], for heat transfer to the impurity subsystem. This mechanism is connected with the Cherenkov emission of the second sound quanta by the thermal crystallization oscillations of the interface and by the thermal Rayleigh waves. This contribution is similar to the contribution considered by Khalatnikov [35] of the Rayleigh waves to the thermal resistance on a He-II- metal interface. In the temperature region considered, the thermal crystallization waves with frequencies $\omega \sim T/\hbar \sim 10^{10}$ s^{-1} are estimated to have an acoustic spectrum $\omega \sim \tilde{v}_M k$, where $\tilde{v}_M = (\tilde{\alpha}/M_{eff})^{1/2}$. The contribution of these waves to σ_{s3} therefore has the same temperature and concentration dependences as the contribution from the bulk phonons of the solid i.e. $\sigma_{s3}^M \sim c_2 T^{7/2} (\rho/\Delta\rho)^2$. The exact expression for this contribution to σ_{s3} for $\tilde{v}_M \gg c_{II}$ is:

$$\sigma_{s3}^M = \frac{\pi^3}{4} \left(\frac{\rho}{\Delta\rho}\right)^2 \left(\frac{3}{5} m^* T\right)^{1/2} c_2 \left(\frac{T}{\hbar \tilde{v}_M}\right)^3, \tag{3.2.29}$$

which is also of the same order as the results of [15, 16].

We note that σ_{s3} also receives a contribution from Cherenkov emission of the second sound quanta by the thermal Rayleigh waves. This contribution $\sigma_{s3}^{R} \sim c_2 T^{7/2} (\rho/\Delta\rho)^2$ has just the same order of magnitude as Cherenkov contribution from the thermal crystallization waves.

Concluding this section let us emphasize again that

1. We derived generalized boundary conditions (the system of equations of the surface hydrodynamics) for atomically rough mobile phase-interface between quantum crystal and a superfluid at low temperatures and with an account of a finite impurity concentration in both solid and liquid phases.
2. We discussed different non-dissipative capillary terms such as surface stiffness, surface stress tensor, and kinetic surface density as well as dissipative growth coefficient and Kapitza thermal resistance which play an important role for the spectrum and damping of melting-crystallization waves and for acoustic (sound transmission and reflection) coefficients.
3. We analyzed the instability of a tangential flow of a superfluid liquid in the direction parallel to the rough surface of a quantum crystal and found the growing increment of melting-crystallization waves which governs the transition to the non-linear regime of the surface development
4. We predicted a possibility of a resonant excitation of the surface (Rayleigh) waves by the bulk (second sound) wave incident from the liquid under the transcritical angle of the total internal reflection. We predicted also an inverse effect of Cherenkov emission of the second sound quanta by the thermal surface waves on the rough interface.

Our results suggest that at phonon-temperatures $T \leq (0.4 \div 0.5)$ K and impurity concentrations $c \leq 10^{-3}$ the damping of melting-crystallization waves is small which is in favor of mobile (atomically rough) character of the surfaces under consideration. Experimentally this family of mobile surfaces could correspond, for example, to the vicinal surfaces which are close to the surface perpendicular to the main axis of the hexagonal ^{4}He crystal.

The equations of the surface hydrodynamics on the slow-growing atomically smooth surfaces are much more simple and support at $T = 0$ only one wave of the surface excitations, namely Rayleigh-Stonley waves. The melting-crystallization waves on these surfaces, if they exist, have a nonlinear character [45].

References

1. Andreev, A.F., Parshin, A.Y.: JETP **48**, 763 (1978)
2. Castaing, B., Nozieres, P.: J. Phys. (France) **41**, 701 (1980)
3. Marchenko, V.I., Parshin, A.Y.: JETP Lett. **31**, 724 (1980)
4. Castaing B., Balibar S., Laroche C.: J. Physique Lett., **41**, 897 (1980)

5. Puech L., Castaing B.: J. Physique Lett., **43**, L601 (1982)
6. Maris H.Y., Huber T.E.: J. Low Temp. Phys., **48**, 99 (1982)
7. Maris H.Y., Huber T.E.: Phys. Rev. Lett., **47**, 1907 (1981)
8. Balibar S., Castaing B.: J. Physique Lett., **41**, 329 (1980)
9. Wolf P.E., Balibar S., Gallet F.: Phys. Rev. Lett., **45**, 1366 (1983)
10. Keshishev K.O., Parshin A.Y, Babkin A.V.: JETP Lett., **30**, 56 (1980)
11. Keshishev K.O., Parshin A.Y, Babkin A.V: JETP **53**, 362 (1981)
12. Landau L.D., Lifshitz E.M.: Fluid Mechanics: vol. 6 (Course of Theoretical Physics), Butterworth-Heinemann, Oxford (1987)
13. Kagan, M.Yu., Kosevich, Y.A.: Sov. Low Temp. Phys. **14**, 787 (1988)
14. Landau, J., Lipson, S.G., Maatanen, L.M., Balfour, L.S., Edwards, D.O.: Phys. Rev. Lett. **45**, 31 (1980)
15. Graf, M.J., Bowley, R.M., Maris, H.J.: J. Low Temp. Phys. **53**, 1176 (1984)
16. Graf, M.J., Bowley, R.M., Maris, H.J.: J. Low Temp. Phys. **58**, 209 (1985)
17. Kagan M.Yu.: JETP **63**, 288 (1986)
18. Kagan M.Yu., Kosevich Y.A.: JETP **64**, 487 (1986)
19. Uwaha M., Nozieres P.: J. Phys. (France), **47**, 263 (1986)
20. Nozieres P.: Lectures at the Colledge de France (1981)
21. Maksimov L.A., Tsymbalenko V.L.: JETP **95**, 455 (2002)
22. Dubovskii L.B., Burmistrov S.N., Tsymbalenko V.L.: JLTP, **162**, 391 (2011)
23. Andreev A.F.: JETP, **16**, 257 (1962)
24. Zinov'eva K.N.: JETP Lett., **28**, 269 (1978)
25. Zinov'eva K.N.: JETP **52**, 996 (1980)
26. Brekhovskikh, L.M.: Waves in Layered Media. Academic Press, New York (1960)
27. Kosevich, A.M., Kosevich, Y.A.: Sov. Low Temp. Phys. **7**, 394 (1981)
28. Iordanskii, S.V., Korshunov, S.E., Larkin, A.I.: JETP **56**, 1224 (1982)
29. Andreev, A.F., Kompaneets, D.A.: JETP **34**, 1316 (1972)
30. Andreev, A.F., Knizhnik, V.G.: JETP **56**, 226 (1982)
31. Lifshitz, I.M., Kagan, Yu.: JETP **35**, 206 (1972)
32. Andreev, A.F.: Defects and surface phenomena in quantum crystals. In: Lifshitz, I.M. (ed.) Quantum Theory of Solids. Mir Publishers, Moscow (1982)
33. Parshin A.Y.: Doctoral Dissertation, Institute for Physical Problems, Moscow (1983)
34. Puech, L., Hebral, B., Thoulouze, D., Castaing, B.: J. Physique Lett. **43**, 809 (1982)
35. Khalatnikov, I.M.: An Introduction to the Theory of Superfluidity. Perseus Book Group, New York (1989)
36. Anufriev Y.D., Lopatik V.N., Sebedash A.P.: JETP Lett., **37**, 45 (1983)
37. Lopatik V.N.: JETP **59**, 284 (1984)
38. Esel'son B.N., Grigor'ev V.N., Ivanov V.G., Rudavskii E.A., Sanikidze D.G., Serbin I.A.: ^{3}He–^{4}He Quantum-Liquid Solutions (in Russian). Nauka, Moscow (1973)
39. Mikheev V.A.: Doctoral Dissertation, Khar'kov (1985)
40. Wang C.L., Agnolet G.: Phys. Rev. Lett., **69**, 2102 (1992)
41. Castaing, B., Greenberg, A.S., Popular, M.: J. Low Temp. Phys. **47**, 191 (1982)
42. Gurevich, V.L.: Kinetics of Phonon Systems (in Russian). Nauka, Moscow (1980)
43. Ziman J.M.: Electrons and Phonons: The Theory of Transport Phenomena in Solids. Oxford University Press, Oxford (1960)
44. Bowley, R.M., Edwards, D.O.: J. Phys. France **44**, 723 (1983)
45. Gusev, R.B., Parshin, A.Y.: JETP Lett. **85**, 588 (2007)
46. Balibar, S., Alles, H., Parshin, A.Y.: Rev. Mod. Phys. **77**, 317 (2005)
47. Bodensohn, J., Nicolai, K., Leiderer, P.: Zeit. Phys. B: Cond. Matt. **64**, 55 (1986)
48. Rolley E., Balibar S., Graner F.: Phys. Rev. Lett., **72**, 872–875 (1994)
49. Rolley E., Guthmann C., Chevalier E., Balibar S.: J. Low Temp. Phys., **99**, 851 (1995)
50. Wolf, P.E., Edwards, D.O., Balibar, S.J.: J. Low Temp. Phys. **51**, 489 (1983)
51. Edwards, D.O., Mc Williams, A.S., Daunt, J.G.: Phys. Rev. Lett. **9**, 195 (1962)
52. Kosevich, Y.A.: JETP **63**, 278 (1986)

Chapter 4
Quantum Hydrodynamics of the P-Wave Superfluids with the Symmetry of ^{3}He-A

In the present chapter we derive the equations of orbital hydrodynamics and analyze the spectrum of collective excitations for bosonic and fermionic p-wave triplet superfluids with the symmetry of A-phase.

We discuss the spectrum of orbital waves, the paradox of the intrinsic angular momentum and the complicated problem of chiral anomaly (mass current non-conservation) in the superfluid hydrodynamics of the fermionic A-phase at $T = 0$.

We present two different approaches to the chiral anomaly, one based on supersymmetric hydrodynamics [1–3] and another one on the formal analogy between Bogoliubov-de Gennes equations for ^{3}He-A [38] and the Dirac equation in quantum electrodynamics (QED, [4–7, 9, 10, 26–28]). We are motivated by the experimental discovery of superfluid and superconductive fermionic systems with nodal (Dirac) points and lines, which exist in the complex order parameter or in the energy spectrum of the superfluid ^{3}He-A (see Chaps. 9 and 12), organic and heavy-fermion superconductors, ruthenates (Sr_2RuO_4) (see Chap. 9) and p-wave Fermi gases in the regime of Feshbach resonance (see Chap. 7). Note that both competing approaches, which we discuss in this Chapter, are very general. An approach, connected with the construction of the supersymmetric hydrodynamics, is based on the inclusion of the fermionic Goldstone mode in the low-frequency hydrodynamic action [1–3, 11]. It can be useful for all nodal fermionic superfluids and superconductors with zeroes of the superconductive gap such as ^{3}He-A, Sr_2RuO_4, UPt_3, UNi_2Al_3 and $U_{1-x}Th_xBe_{13}$ [12]. The second approach is also very nice and general. It is connected with the appearance of the Dirac-like spectrum of fermions with a zero mode [4–10], which also arises in many condensed-matter systems such as ^{3}He-A, chiral superconductor Sr_2RuO_4, organic conductor α-(BEDT-TTF)$_2I_3$, 2D semiconductors, or recently discovered graphene [12–16].

M. Yu. Kagan, *Modern Trends in Superconductivity and Superfluidity*,
Lecture Notes in Physics 874, DOI: 10.1007/978-94-007-6961-8_4,

4.1 Orbital Hydrodynamics of Bosonic and Fermionic Superfluids with the Symmetry of A-phase of ^{3}He

In the previous Chapters we considered mostly hydrodynamics of superfluid ^{4}He [24], which is a hydrodynamics of the isotropic bosonic superfluid. At zero temperatures hydrodynamics of a superfluid ^{4}He is trivial. It is described in terms of the two equations, first one for superfluid velocity $\vec{v}_s$ (or mass current $\vec{j}_s = \rho_s(T=0)\vec{v}_s$, where superfluid density $\rho_s(T=0) = \rho$ – equals to the total density) [21–23, 25, 40]. The second equation is a conservation of mass (see Chap. 1). Note that the order parameter in the superfluid ^{4}He is a scalar complex function $\Psi = \sqrt{\rho_s}e^{i\chi}$, where $\vec{v}_s = \frac{\hbar}{m_4}\vec{\nabla}\chi$ and $\rho_s = |\Psi|^2$ (see [20]). The order parameter in a bosonic or a fermionic superfluid with the symmetry of A-phase (where the role of the order parameter Ψ plays a superfluid gap Δ, see Chap. 7) has a more complicated (tensor) structure. It's orbital part is characterized by three mutually perpendicular unit vectors $\vec{e}_1$, $\vec{e}_2$ and $\vec{l}$, where $\vec{l} = \vec{e}_1 \times \vec{e}_2$ and $\vec{l}^2 = \vec{e}_1^2 = \vec{e}_2^2 = 1$ (see [17, 29, 30, 90] and Chap. 7). In the homogeneous case $\vec{l}$, $\vec{e}_1$, $\vec{e}_2$ coincide with the Cartesian unit vectors $\vec{e}_z$, $\vec{e}_y$, $\vec{e}_x$. However, in general case they are slowly varying functions of $\vec{r}$ and t. The orbital part of the order parameter in the A-phase is a complex vector

$$\vec{\Delta} = \Delta_0 e^{i\chi}(\vec{e}_1 + i\vec{e}_2), \tag{4.1.1}$$

where Δ_0 is the amplitude of the order parameter (of the superfluid gap in case of Fermi-liquids and Fermi-gases). Note that $\vec{\Delta}$ in (4.1.1) corresponds to the spherical function Y_{11} and thus $l = l_z = 1$ for the orbital momentum and its z-projection in the A-phase.

The superfluid velocity $\vec{v}_s$ in case of Fermi-liquid (^{3}He-A) or Fermi gas is given by [17]:

$$\vec{v}_s = \frac{\hbar}{2m_3}\left(e_{1i}\vec{\nabla}e_{2i} + \vec{\nabla}\chi\right), \tag{4.1.2}$$

where a factor $2m_3$ reflects the pairing of two fermions [17, 20] and their subsequent Bose-condensation in superfluid ^{3}He [19]. The additional (with respect to superfluid ^{4}He) variable $\vec{l}$ corresponds to the quantization axis of the angular momentum of the p-wave pairs in the superfluid ^{3}He.

Note that in the next chapters we will consider superfluidity (or superconductivity) in Fermi systems of the two types: strong coupling superfluidity, where we have tightly bound pairs (or difermionic molecules) well separated from each other. In this case the pairing takes place in real space. We will often call the Bose–Einstein condensation of local pairs in this case as a BEC limit of the superfluidity [31, 32]. Another type of superfluidity in Fermi systems corresponds to the creation and simultaneous Bose-condensation of the extended Cooper pairs, which strongly overlap with each other in real space. The phenomenon of pairing

takes place in momentum space in this limit. This is a standard BCS-type of superfluidity or superconductivity [20–23]. Thus, when we are speaking about bosonic superfluid we have in mind either elementary bosons (atoms of ^{4}He), or composed bosons (molecules of $^6Li_2$ and $^{40}K_2$ formed in BEC-limit for p-wave superfluid Fermi-gases, which we will consider in Chap. 6 [33–35]). Correspondingly when we are speaking about fermionic superfluids we have in mind BCS-type of pairing (as in ^{3}He-A and ^{3}He-B for example).

4.1.1 Orbital Hydrodynamics and Collective Modes in Bosonic Regime

In this Subsection we will consider bosonic (BEC) regime having in mind first of all diatomic molecules with p-wave symmetry, which arise in ultracold Fermi-gases of ^{6}Li and ^{40}K in the regime of Feshbach resonance (see Chap. 6). In BEC regime at $T = 0$ we could safely define the density of the orbital momentum of p-wave molecules (local pairs) as $\vec{L} = \frac{\hbar}{2m}\rho\vec{l}$. Correspondingly the total mass-current at $T = 0$ reads:

$$\vec{j}_B = \rho\vec{v}_s + \frac{\hbar}{2m}\vec{\nabla} \times \left(\rho\vec{l}\right) = \rho\vec{v}_s + \vec{\nabla} \times \vec{L}, \tag{4.1.3}$$

where $\vec{\nabla} \times \vec{L}$—term in the r.h.s. of (4.1.3) is analogous to a diamagnetic displacement current well known in the Electrodynamics of Continuous Media [18]. Hydrodynamic energy for molecular A-phase reads:

$$E_B = E_0\left(\rho, \vec{l}, \partial_i\vec{l}\right) + \rho\frac{v_s^2}{2}, \tag{4.1.4}$$

where we used Galilean transformation for E_B to the coordinate frame where the superfluid velocity $\vec{v}_s = 0$. In this frame bosonic energy is E_0. The differential dE_0 in general case reads:

$$dE_0 = \mu d\rho + F_{ik}d\nabla_i l_k + M_k dL_k, \tag{4.1.5}$$

where

$$F_{ik} = \frac{\partial E_0}{\partial\nabla_i l_k}, \tag{4.1.6}$$

and $\vec{L}_B = \frac{\hbar\rho}{2m}\vec{l}$ is the density of the orbital momentum.

The internal energy E_0 is connected with thermodynamic and liquid crystal like orbital energy. The term $F_{ik}d\nabla_i l_k$ provides quadratic in gradients contribution to E_0. It corresponds to the energy of the orbital deformation, which is similar to the deformation energy in the liquid crystals [36, 37]. Finally μ in (4.1.5) is a chemical potential and

$$\vec{M} = \frac{1}{2}\vec{\nabla} \times \vec{v}_s. \tag{4.1.7}$$

The differential of the total energy dE_B in (4.1.4) can be rewritten as:

$$dE_B = \left(\mu + \frac{\hbar}{4m}\,\vec{l}\cdot(\vec{\nabla}\times\vec{v}_s) + \frac{v_s^2}{2}\right)d\rho + F_{ik}d\nabla_i l_k + \frac{\hbar\rho}{4m}\left(\vec{\nabla}\times\vec{v}_s\right)_k dl_k + \rho v_{sk}dv_{sk}, \tag{4.1.8}$$

where $dE_0 = \left(\mu + \frac{\hbar}{4m}\,\vec{l}\cdot(\vec{\nabla}\times\vec{v}_s) + \frac{v_s^2}{2}\right)d\rho + F_{ik}d\nabla_i l_k$.

We use again Landau approach for the superfluid hydrodynamics (see Chap. 1). Then collecting all the terms for the time derivative of the energy $\frac{\partial E_B}{\partial t}$ under the divergence (collecting $\vec{\nabla}\cdot\vec{Q}$), we get the energy conservation law in the form:

$$\frac{\partial E_B}{\partial t} + \nabla_i\left\{\left(\mu + \frac{v_s^2}{2} + \frac{\hbar}{4m}\vec{l}\cdot(\vec{\nabla}\times\vec{v}_s)\right)\rho v_{si} - F_{ik}\frac{\partial l_k}{\partial t}\right\} = 0 \tag{4.1.9}$$

where we can define again an energy flux $Q_i = \left(\mu + \frac{v_s^2}{2} + \frac{\hbar}{4m}\vec{l}\cdot(\vec{\nabla}\times\vec{v}_s)\right)_{si} - F_{ik}\frac{\partial l_k}{\partial t}$. Thus, $\frac{\partial E_B}{\partial t} + \vec{\nabla}\cdot\vec{Q} = 0$, and the energy conservation law (4.1.9) is consistent with a system of three hydrodynamic equations for $\frac{\partial\vec{l}}{\partial t}$, $\frac{\partial\vec{v}_s}{\partial t}$ and $\frac{\partial\rho}{\partial t}$. This system of equations yields [63]:

$$\frac{\partial\rho}{\partial t} + \vec{\nabla}\cdot(\rho\vec{v}_s) = 0, \tag{4.1.10}$$

$$\frac{\partial v_{si}}{\partial t} + \nabla_i\left(\mu + \frac{v_s^2}{2} + \frac{\hbar}{4m}\vec{l}\cdot(\vec{\nabla}\times\vec{v}_s)\right) = \frac{\hbar}{2m}\partial_i\vec{l}\left(\vec{l}\times\dot{\vec{l}}\right), \tag{4.1.11}$$

$$\frac{\partial\vec{l}}{\partial t} + \left(\vec{v}_s\cdot\vec{\nabla}\right)\vec{l} + \vec{l}\times\left(\frac{1}{2}\vec{\nabla}\times\vec{v}_s - \frac{\hbar}{2m}\nabla_i\vec{F}_i\right) = 0, \tag{4.1.12}$$

where we introduced $\vec{F}_i = \frac{\partial E_0}{\partial\nabla_i\vec{l}}$ (see 4.1.6).

The first Eq. (4.1.10) in the system (4.1.10–4.1.12) is a standard continuity equation at $T = 0$. Note that in (4.1.10) we used that $\vec{\nabla}\cdot\left(\vec{\nabla}\times\frac{\rho\vec{l}}{2}\right) = 0$ and thus we can also represent it in the form $\frac{\partial\rho}{\partial t} + \vec{\nabla}\cdot\vec{j}_B = 0$. In other words, the displacement current as usual does not contribute to $\vec{\nabla}\cdot\vec{j}_B$.

Second Eq. (4.1.11) is an equation for superfluid velocity with a non-trivial right-hand side. It corresponds to the well known (in the physics of ^{3}He-A) Mermin-Ho [39] identity for $\vec{\nabla}\times\vec{v}_s$:

$$\nabla_i v_{sj} - \nabla_j v_{si} = \frac{\hbar}{2m}\vec{l}(\partial_i\vec{l} \times \partial_j\vec{l}). \tag{4.1.13}$$

The condition (4.1.13) is based on the definition (4.1.2) and plays an important role in the derivation of the system of equations (4.1.10–4.1.12). Note that we can also define the superfluid velocity in different way. To do that we should introduce three angles $\varphi^a(\vec{r}, t)$ defining the orientation of the trio of the mutually orthogonal unit vectors $\vec{e}_1$, $\vec{e}_2$ and $\vec{l} = \vec{e}_1 \times \vec{e}_2$. Let

$$\delta\vec{\theta} = \vec{\lambda}_a(\varphi)d\varphi^a \tag{4.1.14}$$

be the Cartan form defining the infinitesimal rotation $\delta\theta$ corresponding to two neighboring points φ^a and $\varphi^a + \delta\varphi^a$ in the group space $\{\varphi^a\}$ of the three-dimensional rotation group. Setting $\{\varphi^a\} = \vec{\varphi}$ where the vector $\vec{\varphi}$ is directed along the rotation axis and its magnitude is $tg(\theta/2)$ (where θ is the rotation angle) we get (see Andreev, Marchenko [50]):

$$\lambda_{ai} = \frac{2}{1+\varphi^2}\left(\delta_{ai} + \varepsilon_{iba}\varphi^b\right), \tag{4.1.15}$$

where ε_{iba} is the Levi-Civita tensor. We can easily verify that the quantities $\vec{\lambda}_a$ in (4.1.15) satisfy the "flatness" conditions:

$$\frac{\partial\vec{\lambda}_a}{\partial\varphi^b} - \frac{\partial\vec{\lambda}_b}{\partial\varphi^a} + \left[\vec{\lambda}_a\vec{\lambda}_b\right] = 0. \tag{4.1.16}$$

Since the conditions (4.1.16) are covariant with respect to a change of the coordinates φ^a, they retain their form also for any other parameterization of the rotations.

The superfluid velocity $\vec{v}_s$ in this approach has the components:

$$v_{si} = -\frac{\hbar}{2m}\vec{l}\frac{\delta\vec{\theta}}{\delta x_i} = -\frac{\hbar}{2m}\vec{l}\vec{\lambda}_a\frac{\partial\varphi^a}{\partial x_i}. \tag{4.1.17}$$

We can easily check that this definition coincides with the standard definition (4.1.2) for the superfluid velocity and moreover, the "flatness" condition (4.1.16) automatically guaranties the fulfillment of the Mermin-Ho identity (4.1.13). The Mermin-Ho identity yields non zero vorticity in ^{3}He-A even in the absence of singular vortices (see Chap. 1) and, only with an account of continuous textures of the $\vec{l}$-vector.

Third Eq. (4.1.12) is an equation for vector $\vec{l}$ or for the density of orbital momentum $\vec{L}_B = \frac{\hbar\rho}{2m}\vec{l}$.

First two equations on $\partial\rho/\partial t$ and $\partial\vec{v}_s/\partial t$ after linearization yield the sound spectrum $\omega = c_I q$.

Note that physically the sound Goldstone mode corresponds to the gauge transformation $\vec{\Delta} \to \vec{\Delta}e^{i\chi}$ of the order parameter (similar to the origin of a sound

mode in superfluid ^{4}He). On the level of $\vec{l}$-vector it corresponds to the rotation on angle φ around vector $\vec{l}$.

The equation on $\partial\vec{l}/\partial t$ after linearization yields the spectrum of orbital waves. In bosonic (molecular) superfluid it is quadratic in q: $\omega \sim q^2/m$ at small q. We can say that the A-phase is an orbital ferromagnet [29, 30].

Physically the second (orbital) Goldstone mode is connected with the rotations of the $\vec{l}$-vector on angle γ around the perpendicular (to vector $\vec{l}$) axis (see [41]).

Note that, as usual, the system of hydrodynamic equations (4.1.10–4.1.12) is compatible not only with the energy conservation (4.1.9) but also with the linear momentum conservation laws (see Chap. 1):

$$\frac{\partial j_B^i}{\partial t} + \frac{\partial}{\partial x_k}(\Pi_{ik}) = 0, \tag{4.1.18}$$

where $\Pi_{ik} = \rho v_{si} v_{sk} + (P - F_{mn}\nabla_m l_n)\delta_{ik} + F_{km}\nabla_i l_m - \varepsilon_{ikj}\dot{L}_j$ is a momentum tensor and $P = -E_0 + \mu\rho + F_{ik}\nabla_i l_k + \frac{1}{2}\vec{L}(\vec{\nabla} \times \vec{V}_s)$ is the pressure.

4.1.2 *Orbital Waves: The Paradox of the Intrinsic Angular Momentum and Anomalous Current in Fermionic Superfluids*

In fermionic (BCS-type) superfluids with a symmetry of A-phase we deal with extended Cooper pairs. The pairing takes place in momentum space. The fermionic quasiparticle spectrum in momentum space reads (see [17] and Chap. 7):

$$E_p = \sqrt{\left(\frac{p^2}{2m} - \mu\right)^2 + \frac{\left|\vec{\Delta}\cdot\vec{p}\right|^2}{p_F^2}}, \tag{4.1.19}$$

where $\vec{\Delta} = \Delta_0(\vec{e}_x + i\vec{e}_y)$ is the complex order parameter and Δ_0 is the magnitude of the superfluid gap.

In fact, $\left|\vec{\Delta}\cdot\vec{p}\right|^2 = \Delta_0^2 p^2 \sin^2\theta = \Delta_0^2\left(\vec{p}\times\vec{l}\right)^2$, where $\vec{l} = \vec{e}_x \times \vec{e}_y$ is the unit vector of the orbital momentum (see Fig. 4.1). We note that Fermi momentum p_F is fixed by the fixed density $n = \frac{p_F^3}{3\pi^2}$. The angle θ is between the momentum $\vec{p}$ and the axis $\vec{l} = \vec{e}_z$ of the quantization of the orbital momentum.

Note that for a standard s-wave pairing, the quasiparticle spectrum in BCS fermionic superfluid is given by [19, 21–23] $E_p = \sqrt{\left(\frac{p^2}{2m} - \mu\right)^2 + \Delta^2}$. It has no zeroes (no nodes), and therefore the topology of the s-wave superfluid is trivial in momentum space. But for the triplet A-phase the quasiparticle spectrum in BCS superconductor (or superfluid) has two nodes for $\frac{p^2}{2m} = \mu$ and $\theta = 0, \pi$. Note that in

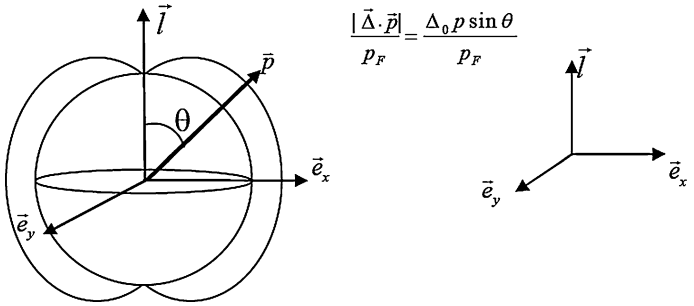

Fig. 4.1 The topology of the superfluid gap in the BCS A-phase. There are two nodes in the quasiparticle spectrum corresponding to the south and north poles [2, 3]

BCS-superfluid $\mu \simeq \varepsilon_F$ and thus for the nodal points $p \simeq p_F$. Hence there are fermionic quasiparticles with practically zero energy in BCS A-phase. They play the role of a fermionic Goldstone mode (additional to Goldstone bosonic modes associated with sound and orbital waves). We will include the fermionic Goldstone mode in the hydrodynamics and construct the supersymmetric hydrodynamic action in Sect. 4.2, which describes both fermionic and bosonic Goldstone modes (see [1–3, 11]) on the equal grounds. In this Subsection we would like to stress that the topological effects, connected with the presence of the nodes in E_p, also are important for the spectrum of the orbital waves in the BCS domain at low temperatures $T \to 0$. Their spectrum is different from the spectrum in bosonic A-phase for small ω and $\vec{q}$. Note that for bosonic superfluid (with p-wave molecules or local pairs) $\mu \simeq -\frac{|E_b|}{2} < 0$ (where E_b is a binding energy of a molecule) and hence the quasiparticle energy $E_p = \sqrt{\left(\frac{p^2}{2m} + |\mu|\right)^2 + \frac{\Delta_0^2 p^2}{p_F^2}\sin^2\theta}$ has no nodes. Thus, its topology in momentum space is trivial just as for the s-wave BCS pairing.

In BCS superfluid A-phase the symmetry requirements also allow us to write an additional anomalous term in the total mass current at $T = 0$:

$$\vec{j}_{tot} = \vec{j}_B + \vec{j}_{an}, \tag{4.1.20}$$

where

$$\vec{j}_{an} = -\frac{\hbar}{4m} C_0 \left(\vec{l}\cdot(\vec{\nabla}\times\vec{l})\right)\vec{l} \tag{4.1.21}$$

is an anomalous current.

In the BEC superfluid the important coefficient $C_0 = 0$, and thus the anomalous current is absent. Formally it is connected with the integral

$$N_{3D}(0)\int d\varsigma_p \left(1 - \frac{\varsigma_p}{|\varsigma_p|}\right), \tag{4.1.22}$$

where $\varsigma_p = \frac{p^2}{2m} - \mu$ is a quasiparticle spectrum in the normal state. In BEC superfluid the chemical potential $\mu < 0$, $\varsigma_p = \frac{p^2}{2m} + |\mu| > 0$ and thus $C_0 = 0$. (Note that $N_{3D}(0) = \frac{mp_F}{2\pi^2}$ is the density of states in 3D Fermi gas).

In BCS superfluid $\mu \simeq \varepsilon_F > 0$ and the integral in (4.1.18) is nonzero. Moreover, in naive estimates it defines the total density in the BCS superfluid ($C_0 \approx \rho$) at least in the weak-coupling case $\Delta_0 \ll \varepsilon_F$.

Thus, it is a difficult question whether $C_0 = 0$ in BCS phase. If $C_0 \neq 0$ the spectrum of orbital waves is strongly modified. Moreover, for nonzero C_0 we cannot get rid of anomalous current in (4.1.16) and (4.1.17). That is very unpleasant since the anomalous current $\vec{j}_{an}$ violates the conservation law (4.1.14) for the total mass current (for the total linear momentum) $\vec{j}_{tot}$. Namely the time derivative of $\vec{j}_{tot}$ cannot be expressed as a divergence of any momentum tensor Π_{ik}(in contrast with a bosonic phase see (4.1.18)):

$$\frac{\partial j^i_{tot}}{\partial t} \neq -\frac{\partial}{\partial x_k}\Pi_{ik}. \tag{4.1.23}$$

Thus, the presence of the anomalous current destroys the superfluid hydrodynamics of the A-phase as $T \to 0$. Its contribution to the equation for the total linear momentum ($\frac{\partial j^i_{tot}}{\partial t}$) can be compensated only by adding a term with the relative normal velocity $\vec{W} = (\vec{v}_n - \vec{v}_s)$ and normal density $\rho_n(T = 0)(\vec{v}_n - \vec{v}_s)$ to the total current $\vec{j}_{tot}$ already at $T = 0$ (see [4–7, 9, 10]). We would like to stress that it is preferable to construct a closed set of the hydrodynamic equations at $T = 0$ only in terms of a superfluid density ρ_s and superfluid velocity $\vec{v}_s$ by putting, as usual, $\rho_s(T = 0) = \rho$. This scenario perfectly works for bosonic A-phase. But it is not clear whether we can describe fermionic (BCS) A-phase only in terms of the condensate oscillations.

Note that, as we already mentioned, the presence of the anomalous current (with $C_0 \neq 0$) also significantly modifies the spectrum of orbital waves.

In Sect. 4.1.1 we mentioned that $\omega \sim q^2$ in bosonic A-phase. More precisely in BEC A-phase for small ω and q,

$$\rho\omega \sim \rho\frac{q_z^2}{m}, \tag{4.1.24}$$

or equivalently $\omega \sim \frac{q_z^2}{m}$, where $\vec{l} || \vec{e}_z$ (see Fig. 4.1) is a quantization axis of the orbital momentum. In the same time we will show in Chap. 7 (see also [2, 3]) that in fermionic (BCS) A-phase

$$(\rho - C_0)\omega \sim \rho\frac{q_z^2}{m}\ln\frac{\Delta_0}{v_F|q_z|}. \tag{4.1.25}$$

We will also show diagrammatically that $C_0 \approx \rho$ and hence $(\rho - C_0) \ll \rho$ in (4.1.25) in the weak-coupling case $\Delta_0 \ll \varepsilon_F$. The most straightforward way to obtain (4.1.25) is to use the diagrammatic technique of Vaks et al. [41] for the

spectrum of collective excitations in p-wave and d-wave superfluids. The technique is based on the solution of the Bethe–Salpeter integral equation in the superfluid state (see Chaps. 5 and 7). The details of the derivation of (4.1.25) will be presented in Sect. 7.4. Here we would like to emphasize that the spectrum (4.1.24) in bosonic A-phase corresponds to the density of angular momentum

$$\vec{L}_B = \frac{\hbar\rho}{2m}\vec{l}, \tag{4.1.26}$$

while the spectrum (4.1.25) in the fermionic A-phase corresponds to the density of intrinsic angular momentum

$$\vec{L}_F = \frac{\hbar}{2m}(\rho - C_0)\vec{l}, \tag{4.1.27}$$

which is different from (4.1.26) for $C_0 \neq 0$ and moreover, $(\rho - C_0) \ll \rho$ for $C_0 \approx \rho$ in the weak-coupling case. We note that there are several competing evaluations of $\vec{L}_F$ which are based not on the spectrum of orbital waves, but on the exact microscopic representation of the static ground-state Hamiltonian of the BCS A-phase. Here different groups provide conflicting results for $\vec{L}_F$. In [42–48] for $\vec{l} = const$ the evaluation of the intrinsic angular momentum yields $\vec{L}_F = \frac{\hbar\rho}{2m}\vec{l}$ in agreement with the bosonic phase, while the inclusion of the inhomogeneous textures of the $\vec{l}$-vector restores the expression (4.1.27).

We note that according to Leggett [49], the total N-particle microscopic Hamiltonian $\hat{H}$ exactly commutes with the z-projection of the angular momentum $\hat{L}_z = \hbar\hat{N}/2$. This fact is in favor of the result $\vec{L}_F = \frac{\hbar\rho}{2m}\vec{l}$ in the BCS A-phase.

Note that rigorously speaking for ^{3}He-A the question about the existence of the superfluid hydrodynamics at $T = 0$ has to some extent a purely academic interest since on the phase-diagram of superfluid ^{3}He at $T = 0$ A-phase does not correspond to a global minimum of the Ginzburg-Landau Free-energy [17], and hence only an isotropic B-phase is realized here (see Fig. 4.2a). To get A-phase as a global minimum of the Free-energy we should switch on a large magnetic field $B_{par} \geq \frac{T_{c1}}{\mu_B}$, where μ_B is Bohr magneton (see Chap. 12). In this case B-phase will be completely paramagnetically suppressed, and the global minima of the Free-energy will correspond to the A1-phase with $S_z^{tot} = 1$ (for z-projection of a total spin $S_{tot} = 1$ of the Cooper pair) and A2-phase with two Bose-condensates and correspondingly with two projections $S_z^{tot} = \pm 1$.

For magnetic fields being smaller than paramagnetic limit $B < B_{par}$, but still sufficiently large the phase-diagram of a superfluid ^{3}He will be given by Fig. 4.2b, and we see that the superfluid A2-phase (which is an analog of A-phase in case of nonzero magnetic field) can exist at $T = 0$ in some interval of pressures P.

For superfluid p-wave Fermi-gases in the regime of Feshbach resonance (see Chaps. 5 and 7) usually only one projection of spin (say $\sigma = \uparrow$) is captured by magnetic trap and thus we have triplet Cooper pairs only with $S_z^{tot} = 1$. We can say that we are dealing with fully-polarized A1-phase here. However, while spin

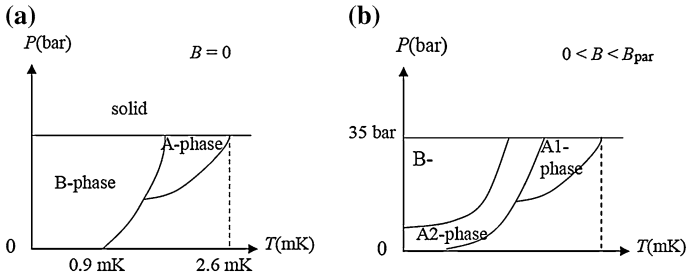

Fig. 4.2 Phase diagram (pressure vs. temperature) in the superfluid ^{3}He in the absence of magnetic field (**a**) and in the presence of magnetic field (**b**), which is sufficient enough but smaller than a paramagnetic limit $B < B_{\rm par}$ (required for total suppression of B-phase). For zero temperatures only isotropic B-phase corresponds to a global minima of Ginzburg-Landau Free-energy [17] at $T = 0$ on **a**. However, on **b** there are regions of pressure where anisotropic A2-phase corresponds to a global minimum of the Free-energy at $T = 0$

sectors of A1 and A2 phases are very different, the orbital (or gauge-orbital sectors [17]) are very similar with respect to the spectrum of collective excitations (sound waves and orbital waves), as well as orbital superfluid hydrodynamics. Thus, in this chapter we will mainly discuss A-phase while in Chap. 7 we will discuss fully polarized A1-phase. Note that the orbital structure of the order parameter both in A1 and A2-phases is governed by the spherical function Y_{11} and thus corresponds to $l = l_z = 1$ for the relative orbital momentum of a triplet pair and its z-projection.

4.2 Two Approaches to a Complicated Problem of Anomalous Current in Fermionic (BCS) A-phase

In this Section we will reconsider two different approaches to the complicated problem of the anomalous current (which is often called the problem of chiral anomaly–see this Section and Sect. 4.2.4). These approaches (see [1, 4–7, 9, 10]) were worked out in the late 1980-s, but are actively discussed till the present time.

4.2.1 Supersymmetric Hydrodynamics of the A-phase

The main idea of [1] (see also [2, 3]) was to check whether an anomalous current $\vec{j}_{an}$ (more precisely, the term $\vec{j}_{an}\vec{v}_s$ in the total energy) is directly related to the zeroes of the superfluid gap (see (4.1.5) and Fig. 4.1). Andreev and Kagan assumed in [1] that in a condensed matter system at low frequencies, the only physical reason for an anomaly (which can produce an anomalous current) can be related to the infrared singularity. We note that the ultraviolet singularities are absent in condensed matter systems [19, 20], in contrast to quantum electrodynamics [26–28]. Strong (critical)

fluctuations are also suppressed in three-dimensional systems. The main idea in [1] was therefore to check the dangerous infrared regions where the gap is practically zero. For that, the authors of [1] considered the total hydrodynamic action of the fermionic (BCS) A phase for low frequencies and small q-vectors as a sum of bosonic and fermionic contributions:

$$S_{tot} = S_B + S_F, \tag{4.2.1}$$

where $S_B(\rho, \vec{l}, \vec{v}_s)$ is the bosonic action related to the zeroes of the superfluid gap (see Fig. 4.3).

Generally speaking, the idea in [1] was to use supersymmetric hydrodynamics to describe all the zero-energy Goldstone modes, including the fermionic Goldstone mode that comes from the zeroes of the gap.

The authors of [1] were motivated by the nice paper of Volkov and Akulov [11], where the massless fermionic neutrino was for the first time included in the effective infrared Lagrangian for the electroweak interactions.

4.2.1.1 Bosonic Part of the Total Action

Bosonic part of the total action S_{B} in (4.2.1) describes sound waves and orbital waves in purely bosonic (molecular) limit and does not contain an anomalous term $\vec{j}_{an}\vec{v}_s$ in the bosonic energy. Formally $S_B = \int L_B d^4x$, where $x = (\vec{r}, t)$ and bosonic Lagrangian reads

$$L_B = \vec{L}\frac{\delta\vec{\theta}}{\delta t} - E_B, \tag{4.2.2}$$

where $\frac{\delta\vec{\theta}}{\delta t}$ is a variational derivative, which defines an angular frequency, connected with the rotation angle θ (see Eqs. (4.1.14, 4.1.15, 4.1.16) and [1, 50] for more details on the parametrization of the three-dimensional rotation group which governs $\delta\vec{\theta}$).

The bosonic Lagrangian L_B corresponds to bosonic energy E_B in (4.1.4). Thus, a bosonic part of the total action describes 3 equations (4.10), (4.11), (4.12) for bosonic hydrodynamics at $T = 0$. They contain the sound waves $\omega = c_l q$ and the orbital waves $\omega \sim \alpha q^2$.

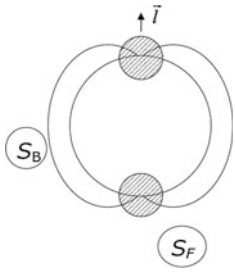

Fig. 4.3 A qualitative illustration of the fermionic (S_{F}) and bosonic (S_{B}) contributions to the total hydrodynamic action S_{tot} of the A phase at $T \to 0$ [2, 3]

4.2.1.2 Fermionic Part of the Total Action

A characteristic peculiarity of ^{3}He-A and fermionic (BCS) phase of a triplet superfluid Fermi gas is the fact that in addition to the usual ground-state degeneracy related to the spontaneous breaking of continuous symmetries, there exists an additional degeneracy related to the vanishing of the quasiparticle energy E_p [see Figs. 4.1 and 4.3 and Eq. (4.1.15)] at the two points of the Fermi surface. It turns out that the states

$$a_1^+|0\rangle \text{ and } a_2^+|0\rangle, \tag{4.2.3}$$

(where $|0\rangle$is the quasiparticle vacuum, and a_1^+ and a_2^+ are the creation operators for quasiparticles with momenta $p_F\vec{l}$ and $-p_F\vec{l}$, respectively) have ground state energy. Similarly to the way in which the usual degeneracy leads in the hydrodynamic description to the appearance of Bose fields, which vary slowly in space and time, this additional degeneracy leads to the appearance of the "Fermionic goldstones", i.e. of the slowly varying anticommuting (Grassman) fields [51–59] $a_1(x)$, $a_2(x)$, $a_1^*(x)$ and $a_2^*(x)$, where $x = (\vec{r}, t)$. In fact, it is more convenient in this case to make use of the certain linear combinations of these fields. The reason for this is that in the systems with Cooper pairing the quantities a_1,a_2,... are the subject to complicated gauge transformation laws. We introduce their linear combinations $\varphi_1(x)$, $\varphi_2(x)$, $\varphi_1^*(x)$, $\varphi_2^*(x)$, so that they satisfy the same anticommutation relations:

$$\{\varphi_1^*, \varphi_1\} = \{\varphi_1, \varphi_2\} = \{\varphi_2^*, \varphi_1\} = \cdots = 0 \tag{4.2.4}$$

as before, but under the gauge transformation $\vec{\Delta} \to \vec{\Delta}e^{i\chi}$ they transform as

$$\varphi_{1,2} \to \varphi_{1,2}e^{i\chi/2}; \quad \varphi_{1,2}^* \to \varphi_{1,2}^* e^{-i\chi/2}. \tag{4.2.5}$$

We note that on account of the known properties of the mentioned linear (Bogoliubov or u-v [20–23]) transformations for spatially homogeneous systems, the subscripts 1, 2 refer, as before, to the states with momenta $p_F\vec{l}$ and $-p_F\vec{l}$.

The presence of the additional degeneracy of the ground state and the related Goldstone character of the fields φ is due to the symmetry properties of the A-phase. We shall convince ourselves below of this independently, by determining the general form of the fermionic part of a Lagrangian L_F satisfying all the necessary symmetry requirements.

We emphasize the following important point: hydrodynamics deals with the slowly varying quantities corresponding to the small statistical volume near the certain points of the momentum space. For the fermionic variables (in contradiction to the bosonic ones) this automatically leads to a small spatial fermionic density. In the Lagrangian L_F ($\int L_F d^4x = S_F$ in (4.2.1)) we can therefore limit ourselves to the consideration of the terms which are quadratic in φ and φ^*.

The Lagrangian L_F of the Fermi subsystem, which together with L_B forms the total Lagrangian of supersymmetric hydrodynamics, must be hermitian, invariant to rotations and gauge transformations, as well as with respect to the reflections

$z \to -z$, $t \to -t$, where the z axis is directed along the vector $\vec{l}$. Moreover, on account of the momentum conservation, the Lagrangian L_{F} must contain the products $\varphi_1^*\varphi_1$, $\varphi_2^*\varphi_2$, $\varphi_1\varphi_2, \ldots$ but not $\varphi_1^*\varphi_2$, $\varphi_2^*\varphi_1, \ldots$. The fields φ, φ^* behave as scalars under rotations. Under reflections they have the transformation properties:

$$\varphi_1^z = \varphi_2; \quad \varphi_2^z = \varphi_1; \quad \varphi_{1,2}^T = \varphi_{1,2}^*; \quad (\varphi_{1,2}^*)^T = \varphi_{1,2}. \tag{4.2.6}$$

Here the subscripts z and T denote respectively the operations $z \to -z$ and $t \to -t$. The operation T is accompanied, as always, by a reversal of the order of factors.

There is a unique expression not containing derivatives and satisfying the abovementioned requirements:

$$g\left(\varphi_1^*\varphi_1 + \varphi_2^*\varphi_2\right). \tag{4.2.7}$$

The coefficient g appearing here is in reality a function of the magnitude of the momentum. This function should vanish at the point $p = p_{\mathrm{F}}$. One may assume that the term (4.2.7) is absent from the Lagrangian L_{F}, since the equation $g(p_{\mathrm{F}}) = 0$ is in fact a definition of the excitation momentum p_{F}. The existence of a zero in the function $g(p)$ is that "topological" property of ^{3}He-A (and other BCS A-phases) which, together with the vector character of the order parameter $\vec{\Delta}$, is responsible for the gapless nature of the fields φ.

There exists a unique hermitian invariant involving the time derivatives:

$$\frac{i}{2}\left(\varphi_1^*\dot{\varphi}_1 + \varphi_2^*\dot{\varphi}_2 - \dot{\varphi}_1^*\varphi_1 - \dot{\varphi}_2^*\varphi_2\right). \tag{4.2.8}$$

In the same time there are two invariants which are linear in the spatial derivatives. One of them contains the vector $\vec{l}$. Owing to the conditions $l^z = l$, $l^T = -l$ it has the form:

$$i\vec{l}\left(\varphi_1^*\vec{\nabla}\varphi_1 - \varphi_2^*\vec{\nabla}\varphi_2\right) - i\vec{l}\left(\vec{\nabla}\varphi_1^* \cdot \varphi_1 - \vec{\nabla}\varphi_2^* \cdot \varphi_2\right). \tag{4.2.9}$$

The second invariant contains order-parameter $\vec{\Delta}$ and on account of the transformation properties $\vec{\Delta}^z = \vec{\Delta}$, $\vec{\Delta}^T = -\vec{\Delta}^*$ it yields:

$$i\vec{\Delta}\left(\varphi_1^*\vec{\nabla}\varphi_2^* + \varphi_2^*\vec{\nabla}\varphi_1^*\right) - i\vec{\Delta}^*\left(\vec{\nabla}\varphi_1 \cdot \varphi_2 + \vec{\nabla}\varphi_2 \cdot \varphi_1\right) \tag{4.2.10}$$

Thus for L_{F} we get:

$$L_F = \frac{i}{2}\left(\varphi_1^*\dot{\varphi}_1 + \varphi_2^*\dot{\varphi}_2 - \dot{\varphi}_1^*\varphi_1 - \dot{\varphi}_2^*\varphi_2\right) + i\frac{v_l}{2}\vec{l}\Big(\varphi_1^*\vec{\nabla}\varphi_1 - \varphi_2^*\vec{\nabla}\varphi_2 - \vec{\nabla}\varphi_1^*\cdot\varphi_1 + \vec{\nabla}\varphi_2^*\cdot\varphi_2\Big) + i\frac{v_t}{2}\frac{\vec{\delta}}{\delta_0}\Big(\varphi_1^*\vec{\nabla}\varphi_2^* + \varphi_2^*\vec{\nabla}\varphi_1^*\Big) - i\frac{v_t}{2}\frac{\vec{\delta}^*}{\delta_0}\Big(\vec{\nabla}\varphi_1\cdot\varphi_2 + \vec{\nabla}\varphi_2\cdot\varphi_1\Big), \tag{4.2.11}$$

where the longitudinal and the transverse velocities v_l and v_t are the functions of the density. In ^{3}He-A, for example, $v_t \sim \left(\frac{T_c}{\varepsilon_F}\right)v_l \ll (v_l \sim v_F)$ since $\frac{T_c}{\varepsilon_F} \sim 10^{-3}$.

The Lagrangian (4.2.11) refers to the spatially homogeneous case, when $\vec{l} = const$ and $\vec{\Delta} = const$. To treat the spatially inhomogeneous case it is necessary to note the following. Since the states 1 and 2 have a finite momentum $\pm p_F\vec{l}$, the "genuine" fields $\Psi_{1,2}$ are related to the slowly varying fields $\varphi_{1,2}$ by the equations:

$$\Psi_1 = \varphi_1 e^{ip_F\vec{l}\vec{r}}; \quad \Psi_2 = \varphi_2 e^{-ip_F\vec{l}\vec{r}}, \tag{4.2.12}$$

and correspondingly for Ψ_1^* and Ψ_2^*.

For $\vec{\nabla}\times\vec{l} \neq 0$ the transformations of the form (4.2.12) do not exist. It is necessary to make use of the fields Ψ and expand not only in terms of gradients, but in terms of the combinations $\vec{\nabla} \pm ip_F\vec{l}$. The corresponding Lagrangian L_{F} is obtained from (4.2.11) by means of the substitution $\varphi \to \Psi$ and $\vec{\nabla} \to \vec{\nabla} \pm ip_F\vec{l}$.

Up to the total derivatives (which appear when the differentiations are transposed either completely to Ψ_1 or completely to Ψ_2^*) we have then:

$$L_F = \psi_1^*\left(i\frac{\partial}{\partial t} + i\frac{v_l}{2}\left\{\vec{l},\left(\vec{\nabla} - ip_F\vec{l}\right)\right\}\right)\psi_1 + \psi_2\left(i\frac{\partial}{\partial t} - i\frac{v_l}{2}\left\{\vec{l},\left(\vec{\nabla} - ip_F\vec{l}\right)\right\}\right)\psi_2^* + i\frac{v_t}{2}\left(\psi_1^*\left\{\frac{\vec{\Delta}}{\Delta_0},\left(\vec{\nabla} - ip_F\vec{l}\right)\right\}\psi_2^* + \psi_2\left\{\frac{\vec{\Delta}^*}{\Delta_0},\left(\vec{\nabla} - ip_F\vec{l}\right)\right\}\psi_1\right), \tag{4.2.13}$$

where the curly brackets stand, as before, for anticommutators.

In addition, it is necessary to add to the Lagrangian independent invariant terms which contain explicitly the spatial derivatives of Δ. The time derivatives may be omitted, since according to the system of Eqs. (4.2.10, 4.2.11, 4.2.12) they are quadratic in the spatial derivatives.

The invariants which are linear in the spatial derivatives $\frac{\partial\Delta_i}{\partial x_k}$ and are at the same time of zero order in the derivatives of the fields Ψ can be of the two types. They may contain expressions obtained by means of the contractions with δ_{ik} or ε_{ikl}, or the terms of the form

$$\underbrace{\Delta_{l_1}^*\Delta_{l_2}^*\ldots}_{n}\underbrace{\Delta_{m_1}\Delta_{m_2}\ldots}_{n}\frac{\partial\Delta_i}{\partial x_k} \tag{4.2.14}$$

and their complex conjugates, or the terms of the form

$$\underbrace{\Delta_{l_1}^{*}\Delta_{l_2}^{*}\dots}_{n}\underbrace{\Delta_{m_1}\Delta_{m_2}\dots}_{n-1}\frac{\partial\Delta_i}{\partial x_k}. \tag{4.2.15}$$

All the terms of the first type are obviously genuine scalars. They are therefore invariant with respect to the transformations $z \to -z$ and consequently they must be multiplied by the combinations of the Ψ fields $\Psi_1^*\Psi_2^* + \Psi_2^*\Psi_1^*$ and $\Psi_1\Psi_2 + \Psi_2\Psi_1$, which vanish on the account of the anticommutation relations. There exist only three independent expressions of the second type which are invariant with respect to the rotation. Namely, these are $\vec{\nabla}\cdot\ \vec{l}, \vec{l}\cdot(\vec{\nabla}\times\vec{l})$ and $\vec{v}_s\cdot\vec{l}$. They are all pseudoscalars, and therefore must be multiplied by $(\Psi_1^*\Psi_1 - \Psi_2^*\Psi_2)$. Moreover, only the last two of them are invariant with respect to the transformation $t \to -t$. Taking all this into account we have:

$$L_F = \Psi^*\Lambda\Psi, \tag{4.2.16}$$

where

$$\Psi = \begin{pmatrix}\Psi_1\\ \Psi_2^*\end{pmatrix}; \quad \Psi^* = \left(\Psi_1^*\,\Psi_2\right), \tag{4.2.17}$$

$$\begin{aligned}\Lambda = i\frac{\partial}{\partial t} + &\begin{pmatrix} iv_l\vec{l}\left(\vec{\nabla} - ip_F\vec{l}\right) & -iv_t\frac{\vec{\Delta}}{\Delta_0}\vec{\nabla}\\ iv_t\frac{\vec{\Delta}^*}{\Delta_0}\vec{\nabla} & -iv_l\vec{l}\left(\vec{\nabla} - ip_F\vec{l}\right)\end{pmatrix}\\ + &\begin{pmatrix} i\frac{v_l}{2}\vec{\nabla}\cdot\vec{l} & i\frac{v_t}{2}\vec{\nabla}\cdot\frac{\vec{\Delta}}{\Delta_0}\\ i\frac{v_t}{2}\vec{\nabla}\cdot\frac{\vec{\Delta}^*}{\Delta_0} & -i\frac{v_l}{2}\vec{\nabla}\cdot\vec{l}\end{pmatrix} + a\,\vec{l}\cdot(\vec{\nabla}\times\vec{l}) + b\,\vec{v}_s\cdot\vec{l},\end{aligned} \tag{4.2.18}$$

and a and b are functions of the density. The function $b(\rho)$ is determined from the requirement of the Galilean invariance of the Lagrangian L_{F}. Under a Galilean transformation $\vec{r} = \vec{r}' + \vec{V}t$, we have $\vec{v}_s = \vec{v}'_s + \vec{V}$ and according to Quantum mechanics [60]:

$$\Psi_{1,2} = \Psi'_{1,2}\exp\left\{im\vec{V}\left(\vec{r'} + \frac{\vec{V}t}{2}\right)\right\}, \tag{4.2.19}$$

$$\vec{\Delta} = \vec{\Delta}'\exp\left\{i2m\vec{V}\left(\vec{r'} + \frac{\vec{V}t}{2}\right)\right\}. \tag{4.2.20}$$

From (4.2.19, 4.2.20) it is clear, that, acting on the quantities which transform like $\Psi_{1,2}$, the invariant operators are

$$i\frac{\partial}{\partial t}+i\vec{v}_s\cdot\vec{\nabla}+\frac{mv_s^2}{2};\quad \vec{\nabla}-im\vec{v}_s \tag{4.2.21}$$

and, correspondingly, their complex conjugated operators acting on the quantities which transform like $\Psi^*_{1,2}$. Since in the adopted approximation one should neglect the terms involving v_s^2, the Galilean-invariant Lagrangian is obtained from the expression for $\vec{v}_s=0$ by means of the substitution

$$\frac{\partial}{\partial t}\to\frac{\partial}{\partial t}+\vec{v}_s\cdot\vec{\nabla};\quad \vec{\nabla}\to\vec{\nabla}\mp im\vec{v}_s, \tag{4.2.22}$$

where the upper sign refers to the operators acting on the quantities which transform like $\Psi_{1,2}$, and the lower sign—to the quantities transforming like $\Psi^*_{1,2}$. As a result of this we find that $b=mv_l-p_F$. In the weak-coupling approximation $v_l=v_F$ and $b=0$. In this approximation the Lagrangian L_F corresponds to the well-known (see Volovik et al. [4–8]) Bogoliubov equations [91–93] for the BCS A-phase, linearized in $\vec{\nabla}\pm ip_F\vec{l}$.

4.2.1.3 The Effective Bosonic Action

We apply the results obtained above to the calculation of the effective action of the bosonic subsystem. For this it is necessary to eliminate the fermionic subsystem by evaluating the functional integral over the fermionic (Grassman) fields. To facilitate the calculations we proceed to the Euclidean formulation by substituting $-\frac{\partial}{\partial\tau}$ for $i\frac{\partial}{\partial t}$ and setting $\tau=it$. The effective action is

$$S_{eff}=S_B+\Delta S_B, \tag{4.2.23}$$

where $S_B=\int L_B d^4x$, L_B is given by (4.2.2) and $x=(\vec{r},\tau)$.

According to general rules (see for example [1] and [56, 57]):

$$\begin{aligned}\Delta S_B&=\ln\int D\Psi D\Psi^*\exp\left(\int d^4x\Psi^*\Lambda\Psi\right)=\ln\left(Det\Lambda\Lambda_0^{-1}\right)\\&=Tr\ln\left(\Lambda\Lambda_0^{-1}\right)=Tr\left(F_1-\frac{1}{2}F_2+\ldots\right),\end{aligned} \tag{4.2.24}$$

where Λ is defined by (4.2.18), Λ_0 is a normalizing operator,

$$F_1=\delta\Lambda\Lambda_0^{-1},\quad F_2=\left(\delta\Lambda\Lambda_0^{-1}\right)^2,\quad \delta\Lambda=\Lambda-\Lambda_0. \tag{4.2.25}$$

The operator Λ_0 is usually chosen equal to the operator Λ in the unperturbed equilibrium state. In an accord with the hydrodynamic character of the theory, which we are developing, we chose Λ_0 in the following manner. In the spatially homogeneous case the operator $\Lambda^{-1}\equiv G$ is an operator, whose matrix elements

$G(x_1, x_2)$ coincide with the fermionic Green's function. It can be easily determined by solving the equation $\Lambda G = \delta(x_1 - x_2)$. Thus, we get for G:

$$G(x) = -\frac{e^{ip_F \vec{l}\vec{r}}}{2\pi^2 v_l v_t^2}\left[\tau^2 + v_t^{-2}\frac{\left|\vec{\Delta}\cdot\vec{r}\right|^2}{\Delta_0^2} + v_l^{-2}\left(\vec{l}\cdot\vec{r}\right)^2\right]^{-2}\begin{pmatrix} \tau + i\frac{\vec{l}\cdot\vec{r}}{v_l} & \frac{i}{v_t}\frac{\vec{\Delta}\cdot\vec{r}}{\Delta_0} \\ \frac{i}{v_t}\frac{\vec{\Delta}^*\cdot\vec{r}}{\Delta_0} & \tau - i\frac{\vec{l}\cdot\vec{r}}{v_l}\end{pmatrix}, \tag{4.2.26}$$

where $x = x_1 - x_2$.

In the general case, when the quantities $\vec{l}$, $\vec{\Delta}$, $p_F(\rho), \ldots$ are slowly varying functions of the coordinates and time, we introduce instead of x_1 and x_2 the "center of mass" variable $X = \frac{x_1+x_2}{2}$ and relative variable $x = x_1 - x_2$. Then we will get the Green's function $G(X, x)$ of the "local-equilibrium", which is obtained from (4.2.26) by setting $\vec{l} = \vec{l}(X)$, $\vec{\Delta} = \vec{\Delta}(X)$, $p_F = p_F(X)$ and so on. We consider as a definition of the operator Λ_0 the requirement that the matrix elements $\left(\Lambda_0^{-1}\right)_{x_1,x_2}$ should be equal to the functions $G(X, x)$.

The product ΛG of Λ and any other operator G (defined by its matrix elements $G(x_1, x_2)$) has the matrix elements which are obtained from $G(x_1, x_2)$ by applying the operator (4.2.18), where all the differential operators act on the first argument x_1 and the arguments in $\vec{l}(x_1)$, $\vec{\Delta}(x_1)$, $p_F(x_1)$ etc. contain also x_1. The action of the operator Λ_0 inverse to $G(X, x)$ is obviously defined by the first two terms in (4.2.18), where the differentiations must be fulfilled with respect to x_1, while X must appear in the arguments $\vec{l}$, $\vec{\Delta}$, p_F etc. Making use of the equalities $x_1 = X + (x/2)$, $\partial/\partial x_1 = \partial/\partial x + \frac{1}{2}\partial/\partial X$ and expanding in terms of the gradients of the slowly varying functions, it is easy to calculate the operator $\delta\Lambda$ in (4.2.24) and (4.2.25). In doing this we should keep in mind that in our theory only the hydrodynamic asymptotic behavior is meaningful, i.e. the asymptotics for large $|x|$. Accordingly one has to retain only the leading terms for $|x| \to \infty$. Moreover, since the original bosonic action S_B contains the density itself, while the quantities $\vec{\Delta}$ and $\vec{l}$ enter in S_B only via derivatives, in the action ΔS_B, as well, the zero-order terms in the derivatives will be absent by definition, and the density may be considered constant. Thus, in ΔS_B one must take into account only the spatial derivatives of $\vec{\Delta}$ and $\vec{l}$. (As noted above, the consideration of the time derivatives would lead to the terms of the higher order of smallness).

We write the formula (4.2.24) for ΔS_B in terms of matrix elements $F_1(X, x)$ of the operator F_1 in the (X, x) representation.

$$\Delta S_B = \int d^4X \lim_{x\to 0} tr\left\{F_1(X, x) + \int d^4x' F_1(X, x - x')F_1(X, x') + \ldots\right\}, \tag{4.2.27}$$

where an operator tr (in distinction from Tr) should be understood as a matrix rather than a complete operator.

We are interested in the part of ΔS_B which contains the terms of the lowest (second) order in the spatial derivatives $\partial/\partial X$. Such terms arise from the first term in the curly brackets in (4.2.27) and in this case they are proportional to $1/|x|$. In addition, the matrix elements F_1 contain also terms which are linear in the derivatives $\partial/\partial X$ and are proportional to $1/|x|^2$. On account of the second term in (4.2.27), which is given by the integral in the curly brackets, they contribute to the expression in the brackets proportional to $(\partial/\partial X)^2$ and $\ln\frac{\lambda}{|x|}$, i.e. it is exactly these terms which determine the hydrodynamic asymptotics. Thus, we can restrict our attention only to the integral term in (4.2.27). The resulting expression for F_1, linear in the derivatives $\ln\frac{\lambda}{|x|}$ (in a reference frame in which the coordinate axes for a given X are respectively along $\vec{e}_1$, $\vec{e}_2$ and $\vec{l}$) has the form:

$$F_1 = -\frac{p_F}{4\pi^2 v_l v_t}\frac{e^{ip_F Z}}{\left(\tau^2+\tau_n^2\right)^2}\sigma_i^{Tr}(\tau\tau_k\omega_{ik} - \varepsilon_{imk}\tau_k\tau_l\omega_{ml}), \tag{4.2.28}$$

where σ_i^{Tr} are the transposed Pauli matrices, $\tau_i = \left(\frac{x}{v_t}, \frac{y}{v_t}, \frac{z}{v_l}\right)$, $T_i = \left(\frac{X}{v_t}, \frac{Y}{v_t}, \frac{Z}{v_l}\right)$ and

$$\omega_{ik} = \left(\frac{\partial l_i}{\partial T_k} - \frac{\partial l_k}{\partial T_i}\right). \tag{4.2.29}$$

Substituting F_1 from (4.2.28) into (4.2.27) we get

$$\Delta S_B = -\int d^4X \frac{p_F^2}{32\pi^2 v_l^2}\omega_{ik}^2 + \int \frac{d|x'|}{|x'|}. \tag{4.2.30}$$

The logarithmically divergent integral must be cut off in the weak-coupling case $\Delta_0 < \varepsilon_F$ at the upper limit (which is the wavelength of the motion λ) and at the lower limit at the mean free-path length l_{MF} (in superfluid Fermi-liquid like ^{3}He-A $l_{MF} \sim d\left(\frac{\varepsilon_F}{T_C}\right)^2$, where d is an interatomic distance. We can also represent l_{MF} as v_F/ω_c, where the hydrodynamic frequencies ω are limited by ω_c). In the chosen coordinate system, in view of $dl_z = 0$, one can represent ω_{ik}^2 in the form:

$$\omega_{ik}^2 = 2v_l^2\left(\frac{\partial l_\alpha}{\partial Z}\right)^2 + v_t^2\left(\frac{\partial l_\alpha}{\partial X_\beta} - \frac{\partial l_\beta}{\partial X_\alpha}\right)^2, \tag{4.2.31}$$

where $\alpha, \beta = 1, 2$.

Therefore (4.2.30) corresponds to the following invariant expression for the fermionic contribution ΔL_B to the effective Lagrangian $L_{eff} = L_B + \Delta L_B$:

$$\Delta L_B = -\frac{p_F^2 v_l}{16\pi^2}\left\{(\vec{l}\times(\vec{\nabla}\times\vec{l}))^2 + \frac{v_t^2}{v_l^2}\left(\vec{l}\cdot(\vec{\nabla}\times\vec{l})\right)^2\right\}\ln\frac{\lambda}{l_{MF}}. \tag{4.2.32}$$

Thus the elimination of the fermionic degrees of freedom leads to the appearance in L_{eff} of nonlocal (albeit weakly logarithmically divergent) terms, similar to the well-known (see [4–8, 61, 62]) terms in the energy of ^{3}He-A in the region $\left(\varsigma_0 \sim \frac{v_F}{T_C}\right) \ll \lambda \ll l_{MF}$.

More specifically these terms lead only to a strong renormalization of the liquid crystal (De Gennes [36, 37]) type coefficients K_2 and K_3 in E_{0B} [61, 62] (and after Fourier transform—to a logarithmic renormalization of the spectrum of orbital waves $\omega \sim \frac{q_z^2}{m} \ln \frac{\Delta_0}{v_F |q_z|}$).

Let us repeat that if we hope to obtain an anomalous term $\vec{j}_{an} = -\frac{\hbar}{4m} C_0 \left(\vec{l} \cdot (\vec{\nabla} \times \vec{l})\right) \vec{l}$ in total current with a large coefficient $C_0 \sim \rho$, we must get the term $\vec{j}_{an} \vec{v}_s$ in ΔL_B. But due to small fermionic density $\rho_F \sim \Psi^* \Psi$ near the south and north poles (small statistical weight of the fermionic pockets on Fig. 4.4 in comparison with the total density ρ) we have to get $C_0 \sim \delta(\vec{p} \pm p_F \vec{l})$ in momentum space or accordingly $C_0 = const$ in real space. That is why in order to obtain an anomalous term in the current we must find very strong delta-functional infra-red divergences in ΔL_B. In our approach we found only weak (logarithmic) infra-red singularities in ΔL_B, but we did not find a strong δ-functional singularity when we accurately evaluated an integral over fermionic (Grassman) variables. Hence even if anomalous current exists in the BCS A-phase, it is not directly connected with the dangerous regions of the momentum space near zeroes of the gap (even if the chiral anomaly exists, in ^{3}He-A it does not have an infra-red character).

4.2.2 A Different Approach Based on the Formal Analogy with Quantum Electrodynamics

The authors of [4–7, 9, 10] proposed a different, and also rather nice approach based on a formal analogy between an anomalous current in ^{3}He-A (and other 3D BCS A-phases) and the chiral anomaly in Quantum Electrodynamics (QED). They assume that the anomalous current in the fermionic A-phase is not directly related

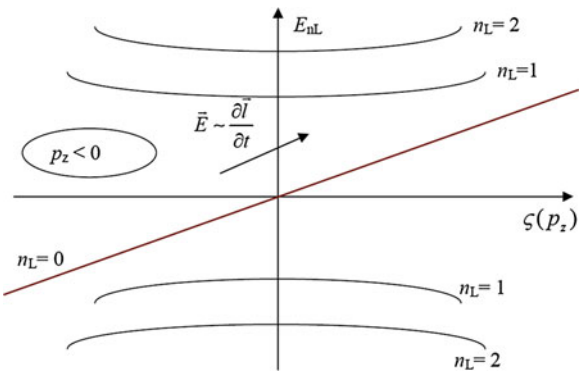

Fig. 4.4 Level structure of the Dirac equation in the magnetic field $B = \left(\vec{l} \cdot (\vec{\nabla} \times \vec{l})\right)$ from [2, 3]. All the levels with $n_L \neq 0$ are doubly degenerate. The zeroth level is chiral. It crosses the origin at $|p_z| = p_F$ in the BCS (fermionic) A-phase. We also illustrate the concept of the spectral flow, which will be discussed in Sect. 4.2.5

to the zeroes of the gap (and hence is not contained even in the supersymmetric hydrodynamics). They believe that it is related to the global topological considerations, and therefore a topological term should be added to supersymmetric hydrodynamics. To illustrate this point, they solve the microscopic Bogoliubov- de Gennes (BdG) [38, 91–93] equations for fermionic quasiparticles in a given inhomogeneous twisted texture ($\vec{l} \parallel \vec{\nabla} \times \vec{l}$) of the $\vec{l}$-vector. To be more specific they consider the case

$$\vec{l} = \vec{l}_0 + \delta\vec{l} \tag{4.2.33}$$

with

$$l_z = l_{0z} = e_z, \quad l_y = \delta l_y = Bx, \quad l_x = 0, \tag{4.2.34}$$

where $\vec{e}_z$ is the direction of a nonperturbed $\vec{l}$ vector. In this case

$$\vec{l} \cdot (\vec{\nabla} \times \vec{l}) = l_z \frac{\partial l_y}{\partial x} = B = const \tag{4.2.35}$$

and, accordingly,

$$\vec{j}_{an} = -\frac{\hbar}{4m} C_0 B \vec{e}_z. \tag{4.2.36}$$

4.2.2.1 Solution of BdG Equation: Analogy with Dirac Equation in Magnetic Field

After linearization BdG equations become equivalent to Dirac equation in homogeneous magnetic field $B = (\vec{l} \cdot (\vec{\nabla} \times \vec{l}))$. Namely after linearization BdG equations read $\hat{H}\chi_F = E\chi_F$, where the doublet χ_F has the form $\chi_F = \begin{pmatrix} u(x) \\ v(x) \end{pmatrix} \exp(ip_z z + ip_y y)$ and for the Hamiltonian we have:

$$\hat{H} = \varsigma(p_z)\hat{\sigma}_3 + v_t\left(\hat{\sigma}_1 \frac{1}{i}\partial_x - \hat{\sigma}_2\left(p_y - eBx\right)\right), \tag{4.2.37}$$

where $\{\hat{\sigma}_1, \hat{\sigma}_2, \hat{\sigma}_3\}$-are Pauli matrices, $\varsigma(p_z) = \frac{p_z^2 - p_F^2}{2m}$, $v_t = v_F \frac{\Delta_0}{\varepsilon_F}$-corresponds to weak-coupling limit ($v_t \ll v_F$), and near the nodes $e = \frac{p_z}{p_F} = \pm 1$ is an electric charge. The solution of BdG equations yields for the doublet $\chi_F(x)$ (see Volovik et al. [4–8]):

$$\chi_{n_L}(x) = \theta(-eB)\begin{pmatrix} \alpha_{n_L} f_{n_L}(\tilde{x}) \\ i\beta_{n_L} f_{n_L-1}(\tilde{x}) \end{pmatrix} + \theta(eB)\begin{pmatrix} \alpha_{n_L} f_{n_L-1}(\tilde{x}) \\ i\beta_{n_L} f_{n_L}(\tilde{x}) \end{pmatrix}, \tag{4.2.38}$$

where θ is a step-function, $f_{n_L}(\tilde{x}) = f_{n_L}\left(x - \frac{p_y}{eB}\right)$ is the ortho-normalized wave-function of the harmonic oscillator [60], $f_{-1} = 0$; $|\alpha_{n_L}|^2 = \frac{E_{n_L} + \varsigma(p_z)}{2E_{n_L}}$ and $|\beta_{n_L}|^2 = \frac{E_{n_L} - \varsigma(p_z)}{2E_{n_L}}$ are Bogoliubov coefficients ($|\alpha_{n_L}|^2 + |\beta_{n_L}|^2 = 1$).

Accordingly for the spectrum

$$E_{n_L}(p_z) = \pm\sqrt{\varsigma^2(p_z) + \tilde{\Delta}^2_{n_L}}, \tag{4.2.39}$$

where $\tilde{\Delta}^2_{n_L} = 2n_L v_t^2 p_F |eB|$ is a gap squared and n_L is a quantum number for the Landau level [60]. The solution for $\chi_{n_L}(x)$ in (4.2.38) contains the level asymmetry.

Namely, for $n_L \neq 0$ (see Fig. 4.4) all the levels are gapped $\tilde{\Delta}^2_{n_L} \neq 0$ and doubly degenerate with respect to $p_z \to -p_z$. Their contribution to the total mass-current is zero for $T \to 0$.

4.2.2.2 Zero Mode and Anomalous Current at $T = 0$

However, for $n_{\mathrm{L}} = 0$ there is no gap $\Delta_0 = 0$ and we have an asymmetric chiral branch which exists only for $p_z < 0$ (only for one sign of eB). The energy spectrum for $n_{\mathrm{L}} = 0$ yields:

$$E_0 = \varsigma(p_z). \tag{4.2.40}$$

We can say that there is no gap for zeroth Landau level. Moreover, in BCS (fermionic) A-phase $E_0 = 0$ for $|p_z| = p_F$–the chiral level crosses the origin in Fig. 4.4, so we have a zero mode.

We note that in the bosonic A-phase the chemical potential $\mu \approx -\frac{|E_b|}{2} < 0$ (as we mentioned already E_b is a molecular binding energy). Thus, $E_0 = \varsigma(p_z) = \frac{p_z^2}{2m} + |\mu| \geq |\mu|$, and the zeroth Landau level does not cross the origin. The absence of a zero mode in molecular A-phase is the physical reason why the coefficient $C_0 = 0$ there.

The zeroth Landau level gives an anomalous contribution to the total current in fermionic A-phase:

$$\vec{j}_{an}(\vec{r} = 0) = -\vec{e}_z(\vec{l} \cdot (\vec{\nabla} \times \vec{l})) \int\limits_{p_z < 0} \frac{p_z}{2\pi^2} d\varsigma(p_z) = -\frac{\hbar C_0}{4m}(\vec{l} \cdot (\vec{\nabla} \times \vec{l}))\vec{l}, \tag{4.2.41}$$

$$\frac{(\vec{l} \cdot (\vec{\nabla} \times \vec{l}))p_z}{2\pi^2 p_F} = \frac{eB}{2\pi^2} = \int |f_0|^2 \frac{dp_y}{2\pi}, \tag{4.2.42}$$

and hence

$$C_0 \sim \frac{mp_F^3}{3\pi^2} \sim \rho \tag{4.2.43}$$

in the fermionic phase (in fully-polarized A1 phase in magnetic traps, which we will consider in Chap. 7, $C_{0\uparrow} \sim \rho_\uparrow = \frac{mp_{F\uparrow}^3}{6\pi^2}$ differs from C_0 in (4.2.43) in factor 2).

We note that $f_0(x - p_y|eB|)$ in (4.2.42) is an eigenfunction of a zeroth Landau level. It is easy to see that the integral for C_0 in (4.2.41) and (4.2.42) is governed by the narrow cylindrical tube inside the Fermi sphere (see Fig. 4.5) with the length p_F parallel to the $\vec{l}$ vector and with the radius of the cylinder squared given by:

$$\left\langle p_y^2 \right\rangle \sim p_F|eB|. \tag{4.2.44}$$

According to the ideas of [4–8, 29, 30], this tube plays the role of a vortex in the momentum space, thus providing a normal core and an anomalous current at $T = 0$.

We note that a key result in [4–7, 9, 10] related to the absence of the gap for the energy of the zeroth Landau level [see (4.2.40)] is pretty stable with respect to small modifications of the texture of the $\vec{l}$-vector in (4.2.33, 4.2.34). Our careful analysis shows that the account of small bending corrections with $(\vec{l} \times (\vec{\nabla} \times \vec{l}))^2$ to the twisted texture (small tilting of the magnetic field with respect to the (x, y) plane $\vec{B} = B_0\vec{e}_z + B_1\vec{e}_x$) as well as an account of small inhomogeneities of a magnetic field $B = B_0 + B_1 x$, which lead to a double-well effective potential, does not suppress the zero mode in the spectrum of the BdG equations. In other words, an account of these corrections does not lead to the appearance of a gap $\tilde{\Delta}_{n_{L=0}}$ for the zeroth Landau level.

4.2.3 How to Reach the Hydrodynamic Regime $\omega\tau \ll 1$

Inspite of the zero mode stability, the authors of [1–3] expressed their doubts regarding the calculation of C_0 based on Dirac equation in the homogeneous magnetic field $B = (\vec{l} \cdot (\vec{\nabla} \times \vec{l}))$. From their standpoint, the calculation of C_0 in

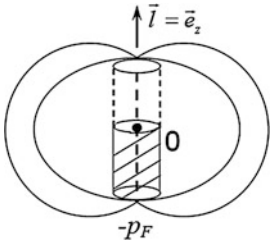

Fig. 4.5 The contribution to the coefficient C_0 is governed by a narrow cylindrical tube of the length p_F and the width $\left\langle p_y^2 \right\rangle = p_F|eB|$ inside the Fermi sphere [2, 3]

(4.2.41, 4.2.42) is an oversimplification of a complicated many-particle problem. In particular, they emphasized the role of the finite damping $\gamma = 1/\tau$ and of the other residual interactions in destroying the chiral anomaly (which is connected with the states inside the Fermi sphere on Fig. 4.5). Thus, they hope to restore the superfluid hydrodynamics at $T = 0$ without the normal velocity $\vec{v}_n$ and the normal density ρ_n. Indeed, if the damping γ is larger than the level spacing of the Dirac equation, we have

$$\omega_0 = v_t p_F \sqrt{\frac{\left|\vec{l} \cdot \left(\vec{\nabla} \times \vec{l}\right)\right|}{p_F}} \tag{4.2.45}$$

in the case where $\varsigma(p_z) = 0$, and then the contribution from the zeroth Landau level should be washed out by the damping (see Fig. 4.6). As a result the hydrodynamic regime will be established.

The damping γ for the chiral fermions (for the fermions living close to the nodes) in a very clean fermionic (BCS) A-phase without impurities is defined at $T = 0$ by the different decay processes (see [20]).

It is natural to assume that the only parameter that determines γ at $T = 0$ for chiral fermions is the gap $\Delta_0\langle\theta\rangle = \Delta_0\langle p_\perp\rangle/p_F$ (where $\sin\theta \approx \theta$ close to the nodes). The leading term in decay processes is given by the emission of an orbital wave (see Fig. 4.7). It is given by (see [2, 3])

$$\gamma \sim \left[\frac{\Delta_0^2 p_\perp^2/p_F^2 + v_F^2 (p_z - p_F)^2}{\varepsilon_F}\right]. \tag{4.2.46}$$

For $p_z = p_F$ ($\varsigma(p_z) = 0$), we have

$$\gamma \sim \frac{\Delta_0^2}{\varepsilon_F}\frac{p_\perp^2}{p_F^2}. \tag{4.2.47}$$

We note that for the chiral fermions on the zeroth Landau level, we have

$$\frac{\langle p_\perp\rangle}{p_F} = \sqrt{\left(\frac{\left|\vec{l} \cdot \left(\vec{\nabla} \times \vec{l}\right)\right|}{p_F}\right)} \tag{4.2.48}$$

and the level spacing for $\varsigma(p_z) = 0$ is

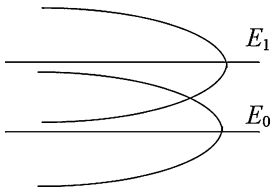

Fig. 4.6 The possible role of damping in reaching the hydrodynamic limit for low frequencies and small $\vec{k}$ vectors for $\gamma > \omega_0$ ($\omega_0 = E_1 - E_0$ is the level spacing) [2, 3]

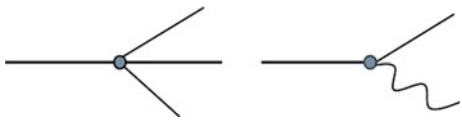

Fig. 4.7 Different decay processes for the damping of chiral fermions at $T = 0$: the standard three-fermion decay process and the decay process with an emission of the orbital wave [2, 3]

$$\omega_0 \sim \Delta_0 \frac{\langle p_\perp \rangle}{p_F}. \tag{4.2.49}$$

Hence, $\gamma/\omega_0 \ll 1$ close to the zero mode for these two decay processes (the second decay process is a standard three-fermion decay, which also yields $\gamma/\omega_0 \ll 1$). Thus, a ballistic regime is established. It is therefore difficult to wash out the contribution from the zeroth Landau level by the different decay processes in superclean ^{3}He-A phase at $T = 0$. We note that the hydrodynamic regime $\omega\tau \ll 1$ could be easily reached in the presence of nonmagnetic impurities or in the presence of aerogel [64–67] (see Sect. 4.2.5).

4.2.4 The Concept of the Spectral Flow and the Exact Anomaly Cancellation

If the anomalous current exists in a superclean fermionic A-phase at $T = 0$ it should be compensated somehow. According to Volovik et al. [4–8], the deficit in the equation for the conservation of the total linear momentum due to the presence of the anomalous current $\vec{j}_{an}$:

$$\frac{\partial j^i_{an}}{\partial t} + \frac{\partial}{\partial x_k}\pi_{ik} = I_l \tag{4.2.50}$$

with a source term

$$\vec{I} = \frac{3\hbar}{4m} C_0 \vec{l}\left((\vec{\nabla} \times \vec{l}) \cdot \frac{\partial \vec{l}}{\partial t}\right) \tag{4.2.51}$$

is exactly compensated by the quasiparticle contribution $\vec{P}_{quasi}$:

$$\frac{\partial P^i_{quasi}}{\partial t} + \frac{\partial \Phi_{ik}}{\partial x_k} = -I_i, \tag{4.2.52}$$

where $\vec{P}_{quasi} = \rho_n(T = 0)(\vec{v}_n - \vec{v}_s)$ in the hydrodynamic regime. Correspondingly the total current in fermionic A-phase

$$\vec{j}_{tot} = \vec{j}_B + \vec{j}_{an} + \vec{P}_{quasi} \tag{4.2.53}$$

is still conserved.

We note that a normal density $\rho_n(T=0) \sim |\vec{l} \cdot (\vec{\nabla} \times \vec{l})|/\Delta_0$ is a non-analytic function in ^{3}He-A and is related to the nonzero bending. The arguments in [4–8] in favor of exact anomaly cancellation are connected with the nonconservation of the axial current j_5 in QED (see [26–28, 97–103]), where the source term $\vec{I}$ is compensated via the Schwinger term [94–96] $\vec{E}\vec{B} \sim \frac{\partial \vec{l}}{\partial t} \cdot (\vec{\nabla} \times \vec{l})$ ($\vec{E} = \frac{\partial \vec{l}}{\partial t}$ is an electric field and $\vec{B} = \vec{\nabla} \times \vec{l}$ is a magnetic field). Physically, according to [4–8, 68, 69], this cancellation is due to the spectral flow from the negative to the positive energy values along the anomalous branch with $n_{\mathrm{L}} = 0$ in Fig. 4.4 and then to the quasiparticle bath in the presence of an electric field $\vec{E} \sim \frac{\partial \vec{l}}{\partial t}$ (of a time-dependent texture of the $\vec{l}$ vector). Considering the tube, which produces $\vec{j}_{an}$ on Fig. 4.5, as a vortex in the momentum space, Volovik et al. [4–8] and Stone et al. [42–47] use the analogies between the physics of bulk ^{3}He-A and the physics of the vortex core. They also consider the role of damping exactly opposite to our considerations. Note that in the physics of a vortex-core in the case of cylindrical symmetry there is again one anomalous level which crosses the zero energy (see Fig. 4.8).

At $T = 0$, as a function of the generalized angular momentum Q, it represents the set of discrete points separated by a minigap $\omega_0 \sim \Delta_0^2/\varepsilon_F$. Therefore, at $T = 0$ and in the superclean case $\gamma = 1/\tau \to 0$, the spectral flow from negative to positive energies is totally suppressed. Thus, in the ballistic regime $\omega\tau \gg 1$ according to Volovik and Stone it is very difficult to transfer momentum to the quasiparticles and in this way to guarantee the conservation of the total current $\vec{j}_{tot}$ in (4.2.53). In the same time in the hydrodynamic regime $\omega\tau \ll 1$ it is easy to transfer momentum along an anomalous branch to quasiparticles and thus to restore a conservation of the total current.

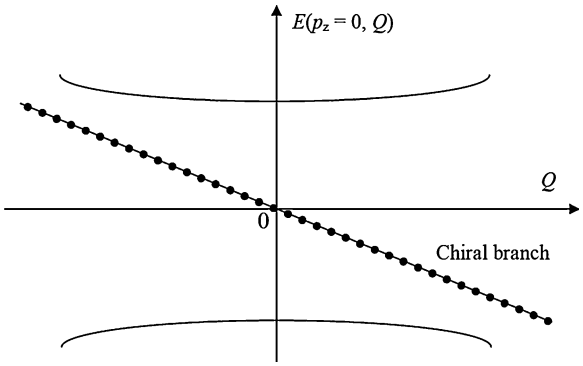

Fig. 4.8 The level structure in the vortex core of ^{3}He-A [2, 3]. All the branches are even in the generalized angular momentum Q, but one branch $E(p_z = 0, Q) = -\omega_0 Q$, which crosses zero energy at $Q = 0$, is chiral (odd in Q). It participates in the momentum exchange between the fermions in the vortex core and the fermions of the heat bath in the hydrodynamic limit $\omega\tau \ll 1$ according to [29, 30]

The authors of [1–3] vice versa think that for $\omega\tau \ll 1$ the coefficient C_0 in front of the anomalous current becomes small $C_0\,(\omega\tau \ll 1) \to 0$. Thus, $\vec{j}_{an} \to 0$ and it is not necessary to add the quasiparticle current in the expression for $\vec{j}_{tot}$ in (4.2.53). In other words, for $\omega\tau \ll 1$: $\vec{j}_{tot} = \vec{j}_B = \rho\vec{v}_s + \vec{\nabla} \times \left(\frac{\hbar\rho\vec{l}}{2m}\right)$- the total current $\vec{j}_{tot}$ coincides with the bosonic current $\vec{j}_B$. Hence the superfluid hydrodynamics is restored (without $\rho_n(T = 0)$ and $\vec{v}_n$) in BCS A-phase at low frequencies and wave-vectors according to the philosophy of [1]. Note that in the physics of the vortex core the analogous discussion about an existence of chiral anomaly and it's possible contribution to one of the Hall-Vinen friction coefficients (see Chap. 1) was started in [70] by Thouless (who believes in a Berry phase [89] without an anomaly) and was thoroughly investigated by Kopnin et al. in [71–74] for different temperature regimes in clean and dirty limits. The authors of [71–74] derived an anomalous contribution to the friction coefficients in the dirty limit $\omega\tau \ll 1$ (large number of impurities) and at finite temperatures. Returning back to the bulk ^{3}He A-phase, we can say that an ideology of Volovik and Stone on exact anomalies cancellation does not work in ballistic (superclean limit) at $T = 0$ (both in bulk and for the vortices). Hence the question of how the total current (total linear momentum) is conserved in this case remains open for an infinite system (without the walls). We note that at very small but finite temperatures $T \ll T_C$ there is a finite number of normal quasiparticles in the system. Hence the damping $\gamma = 1/\tau \sim T^n$ becomes finite and the possibility of the spectral flow and the momentum exchange with the thermal bath restores at low frequencies $\omega < \gamma$ according to Volovik and Stone. However, we would like to stress that at $T \neq 0$ the relative normal velocity $\vec{v}_n - \vec{v}_s = \frac{\partial E_0}{\partial \vec{P}_{quasi}}$ becomes an additional hydrodynamic variable (see Chap. 1 and [25]) and hence the cancellation of the linear momentum deficit in (4.2.50, 4.2.52) will occur automatically.

Thus, the problem of the exact anomaly compensation exists only at $T = 0$. We think that in this case the exact cancellation between the time derivatives of the anomalous and quasiparticle currents should be demonstrated explicitly by deriving and solving the kinetic equations for the nodal quasiparticles both in the ballistic and the hydrodynamic regime. Note that an approach based on the kinetic equation for quasiparticles at different temperatures and the impurity concentrations in a vortex core of the s-wave superconductors and the superfluid ^{3}He was worked out by Kopnin et al. [71–74] in the case of a singular vortex.

In the case of the nonsingular vortex structures in ^{3}He-A (which can be produced by the textures of $\vec{l}$ vector via Mermin-Ho identity, for example) we should mention also papers [68, 69] where the authors consider the scattering of quasiparticles on the walls of the container for a finite system to obtain a finite damping γ at $T = 0$. The importance of the prehistory of the orbital texture for the spectral flow concept was also stressed by Volovik in these papers.

4.2.5 Experimental Situation and Discussion

Concluding this Section we would like to emphasize once more that we discuss a complicated problem of chiral anomaly and mass-current non-conservation in BCS A-phase at $T = 0$. We presented two different approaches to this problem—one based on supersymmetric hydrodynamics, another one—on the formal analogy with Dirac equation in QED-theory. We evaluate the damping $\gamma = 1/\tau$ due to different decay processes in superclean BCS A-phase at $T = 0$ and find that γ is small in comparison with the level spacing ω_0 of the BdG-equation. To reach the hydrodynamic regime $\omega\tau \ll 1$ we need a sufficient amount of aerogel or non-magnetic impurities at $T = 0$. We assume that both in a hydrodynamic and in a ballistic regime at $T = 0$ we have to derive a reliable kinetic equation to demonstrate explicitly an exact cancellation between time-derivatives of anomalous current $\vec{j}_{an} = -\frac{\hbar}{4m} C_0 (\vec{l} \cdot (\vec{\nabla} \times \vec{l}))\vec{l}$ and quasiparticle contribution $\vec{P}_{quasi}$ in the equation for the conservation of the total linear momentum $\vec{j}_{tot}$. Note that for the full theoretical analysis of the problem the other residual interactions different from damping are also important for nodal fermions. To check whether a chiral anomaly has an infra-red manifestation (which was not caught in the approach based on supersymmetric hydrodynamics of [1]) it will be useful to derive a complete set of Ward identities (see [20, 26–28]) between self-energies of chiral fermions $\sum$ and the corresponding vertices Γ. The idea is to find in this approach either a strong infra-red singularity or a powerful reexpansion of the quasiparticle spectrum for $\omega, k \to 0$.

Note that the importance of the residual Fermi-liquid like interactions for the analysis of half-integer vortex in ^{3}He-A was recently emphasized by Leggett et al. [75].

We invite experimentalists to enter this very interesting problem. It will be important to measure a spectrum and damping of orbital waves in superfluid A-phase of ^{3}He at low temperatures $T \ll T_c$. The spectrum is almost quadratic for low frequencies $(\rho - C_0)\omega \sim \rho \frac{q_z^2}{m} \ln \frac{\Delta_0}{v_F |q_z|}$ and contains a density of intrinsic angular momentum $L_F = \frac{\hbar}{2m}(\rho - C_0)$ near the linear in frequency term (see Chap. 7 for more details). Moreover, it is possible to show that in the weak-coupling limit $\Delta_0 \ll \varepsilon_F$: $\frac{(\rho - C_0)}{\rho} \sim \frac{\Delta_0^2}{\varepsilon_F^2} \ll 1$, and thus L_F is very small in comparison with a standard (bosonic) angular momentum $L_B = \frac{\hbar\rho}{2m}$. (In ^{3}He-A we are in a weak-coupling limit $\frac{\Delta_0}{\varepsilon_F} \sim 10^{-3}$ and $\frac{\rho - C_0}{\rho} \sim 10^{-6}$). Note that at higher frequencies $\omega > \Delta_0^2/\varepsilon_F$ the spectrum of orbital waves is almost linear $\omega^2 \ln \frac{\Delta_0}{|\omega|} \sim q_z^2 v_F^2 \ln \frac{\Delta_0}{v_F |q_z|}$, where $\vec{e}_z \parallel \vec{l}$ (see [41]). Note also that in a strong-coupling case $\Delta_0 \geq \varepsilon_F$: $C_0 \ll \rho$ and we restore the hydrodynamics without an anomalous term.

The damping of the orbital waves provides an evaluation of the orbital viscosity in ^{3}He-A at low temperatures $T \ll T_c$. Note that even in this case it is an interesting possibility to get an overdamped (diffusive) character of the spectrum at low

frequencies. This possibility is supported theoretically in [111–113], where Brusov et al. obtained several overdamped modes in the partially polarized A1-phase via the functional integral technique in the hydrodynamic limit of small ω and $\vec{q}$.

Basically we propose to extend the measurements of orbital inertia and orbital viscosity (performed by Bevan et al. [76, 77] in non-singular vortex textures in A-phase) to low temperatures $T \ll T_C$. Of course to have this possibility we need to create a spin-polarization (which according to Fig. 4.1 extends A2-phase to low temperatures on phase-diagram of a superfluid ^{3}He).

Note that another possibility to get an overdamped diffusive spectrum was considered in [78, 79] in the impurity diagrammatic technique [80, 81] for the hydrodynamic regime $\omega\tau \ll 1$ of spin waves in a frustrated two-dimensional AFM, which models strongly underdoped cuprates. We note that in the opposite high-frequency regime, the spectrum of spin waves is linear.

We would like to emphasize that according to the ideology of [1] the overdamped spectrum could serve as a precursor for anomaly-free (bosonic-like) spectrum of orbital waves at very low frequencies (where the superfluid hydrodynamics might be restored).

We also note that a crossover from the ballistic to the hydrodynamic regime $\omega\tau \ll 1$ could occur due to both the aerogel (the nonmagnetic impurities) or at finite temperature $T \neq 0$, which is always present in a real experiment. In the last case, the damping $\gamma \sim T^{\,n}$ is temperature dependent.

In aerogel we can definitely fulfill the inequality $\omega_0 < \gamma$ (where ω_0 is the level spacing in Dirac equation and γ is damping) already at $T = 0$. To fulfill this inequality we should be in a moderately clean ^{3}He-A phase, that is in the presence of a sufficient amount of aerogel. Note that aerogel serves like a non-magnetic impurity for p-wave fermionic superconductor like ^{3}He-A [80, 81]. We can say that effectively the damping γ is an external parameter which depends only upon the concentration of aerogel x. Moderately clean case means that $\omega_0 < \gamma < \Delta_0$, where ω_0 is given by (4.2.45). It can be achieved experimentally since it is possible to have γ as large as $0.1T_C$ in A-phase of ^{3}He [64, 65].

Thus a very interesting experimental proposal is to check our conjecture (that $C_0(\omega_0 \ll \gamma)$ is small) by creating a twisted texture $\vec{l} \parallel (\vec{\nabla} \times \vec{l})$ and varying the aerogel concentration. Then it is interesting to decrease the aerogel concentration drastically and to answer experimentally the question whether $\gamma(x \to 0)$ is larger or smaller than ω_0 in superclean ^{3}He-A.

The similar project with the impurities can be also proposed for the magnetic traps if it will be possible to increase the lifetime of p-wave fermionic A1-phase (see Chap. 7 for more details). Experimentally both in ^{3}He-A and in magnetic traps we can measure either the anomalous current directly or the spectrum of orbital waves, which is usually easier. Anyway, these measurements will allow us to compare C_0 or $(\rho - C_0)$ in moderately clean case and in extremely clean case and thus to check the conjecture of [1–3] about the destruction of the chiral anomaly in the hydrodynamic regime.

Note that in the presence of the sufficient amount of aerogel the phase-diagram of superfluid ^{3}He changes considerably. The global minima now are B-like and A-like phases which differ considerably from B and A-phases in superclean case. Their precise symmetry is a subject of a hot debate today (see discussion in [64–67]).

4.2.5.1 Anomalous Spin Currents in 2D Axial Phase

Let us also consider briefly the spin and orbital hydrodynamics in the axial phase, which is the 2D analog of A-phase (see [17]). The quasiparticle energy in the fermionic 2D phase reads:

$$E_p = \sqrt{\left(\frac{p^2}{2m} - \mu\right)^2 + \frac{\Delta_0^2 p^2}{p_F^2}}. \tag{4.2.54}$$

It has only one nodal point $E_p = 0$ for $\mu = 0$ and $p = 0$ just on the border between BCS and BEC domains.

Note that in this phase the order parameter is given by $\vec{\Delta} = \Delta_0(\vec{e}_x + i\vec{e}_y)$ in similarity with 3D, but $\left|\vec{\Delta}\cdot\vec{p}\right|^2 = \Delta_0^2 p^2$ in two dimensions. An axial phase can be realized in 2D magnetic traps or in thin films or submonolayers of ^{3}He (see also Chap. 12). The most interesting effect for the physics of the ^{3}He 2D films [17, 29, 30, 82, 84–86] is connected with the existence of the topological invariant Q, which comes to the physics of helium from the Quantum Hall Effect (QHE). This invariant is written as

$$Q = \frac{\pi}{2}\varepsilon_{\alpha\beta}\int \frac{d^2\vec{p}}{(2\pi)^2}\vec{n}\cdot\left(\partial_\alpha\vec{n}\times\partial_\beta\vec{n}\right), \tag{4.2.55}$$

where $\varepsilon_{\alpha\beta} = -\varepsilon_{\beta\alpha}$ is asymmetric tensor, the components of the unit vector $\vec{n}$ in the momentum space are given by [82, 84–86]:

$$\vec{n} = \frac{1}{E_p}\left(-\Delta_0 p_x, \Delta_0 p_y, \varsigma_p\right), \tag{4.2.56}$$

and $\varsigma_p = \frac{p^2}{2m} - \mu$, while E_p is given by (4.2.54). In the theory of Quantum Hall Effect the topological invariant Q governs the quantization of the Hall conductivity σ_{xy}. It is also important in the 2D space–time continuum (x, τ) for Haldane effective action, which defines an important difference in the spectrum of collective excitations (gapped or gapless) between the spin chains with integer and half-integer spins S [114, 115].

It is easy to check (see [82, 84–86]) that for 2D axial phase:

$$Q = \int_0^\Lambda dp^2 \frac{d}{dp^2}\left[n_s(p^2)\right] = \frac{1}{2}\left(1 + \frac{\mu}{|\mu|}\right), \tag{4.2.57}$$

where $n_s(p^2) = \frac{1}{2}\left(1 - \frac{\zeta_p}{E_p}\right)$ is a superfluid density.

Thus $Q = 0$ in the BEC phase (where the chemical potential is negative $\mu = -|\mu|$) and $Q = 1$ in the BCS phase. We can say that the BCS phase has a nontrivial topology in contrast to the BEC phase (see [82, 84–86]).

Correspondingly for $\mu \to +0$ $Q = 1$ while for $\mu \to -0$ $Q = 0$. Thus, there is a jump in Q ($\Delta Q = 1$) for a point $\mu = 0$. It is reasonable to assume that a point $\mu = 0$ is a singular point at $T = 0$ [29, 30, 83–86]. In Chap. 7 we will prove that it is a point of a quantum phase-transition (or even a topological phase-transition). To measure the nontrivial topological effects in two dimensions, we propose to perform experiments with a Josephson current (see [2, 3, 20, 116, 117]) between two thin films of ^{3}He or between two magnetic traps containing superfluid Fermi-gases: one with a two-dimensional axial BCS phase and the topological charge $Q = 1$ and another one with the planar 2D phase with $Q = 0$ (see [17, 82]). We hope that it will be possible to measure directly $\Delta Q = 1$ in this type of experiments.

We note that in the 2D axial phase, the $\vec{l}$ vector $\vec{l} = \vec{e}_x \times \vec{e}_y = \vec{e}_z$ is perpendicular to the plane of the 2D film. Hence, the orbital waves, connected, as we discussed in Sect. 4.1, with the rotation of the $\vec{l}$ vector around a perpendicular axis, are gapped. The sound wave is the only Goldstone mode in the gauge-orbital sector. Moreover, $\vec{l} \perp (\vec{\nabla} \times \vec{l})$ and it is impossible to create a twisted texture in two dimensions. Therefore, the anomalous current is absent: $\vec{j}_{an} = -\frac{\hbar}{4m} C_0 (\vec{l} \cdot (\vec{\nabla} \times \vec{l}))\vec{l} = 0$. Hence there is no problem with the mass current nonconservation at $T = 0$ in 2D axial phase [2, 3].

Nontrivial topological effects possibly exist in the spin sector [82] in 2D. Here, the anomalous spin current was predicted by Volovik, Solov'ev and Yakovenko in the presence of an inhomogeneous magnetic field $\vec{B}(\vec{r})$ for 2D ^{3}He-A film (for the axial BCS phase). It reads:

$$j^{spin}_{\alpha,i} \sim Q \varepsilon_{izk} l_z \partial_k B^{\perp}_{\alpha}, \tag{4.2.58}$$

where $\vec{B}_{\perp} \cdot \vec{d} = 0$ and $\vec{d}$ is the spin vector in the 2D ^{3}He film (see [17]).

Another possibility is to measure the contribution of the massless Majorana fermions (see [26, 29, 30, 104]) for the edge states on the surface of superfluid ^{3}He-B and a rough wall (or on the surface of a vibrating wire in the Lancaster experiments) [87, 88].

Note that the physics of Majorana fermions [104] is very popular nowadays in different condensed matter systems including vortex cores of the p-wave superconductors [83, 105], superfluid ^{3}He-B [87, 88], ultracold quantum gases with spin–orbit coupling [106, 107], and hybrid superconductor-semiconductor nanowire devices [108–110].

References

1. Andreev, A.F., Kagan, M.Yu.: JETP **66**, 594 (1987)
2. Kagan, M.Yu., Efremov, D.V.: JLTP **158**, 749 (2010)
3. Kagan, M.Yu., Efremov, D.V.: JETP **110**, 426 (2010)
4. Balatskii, A.V., Volovik, G.E., Konyshev, V.A.: JETP **63**, 1194 (1986)
5. Volovik, G.E.: JETP Lett. **43**, 428 (1986)
6. Volovik, G.E.: JETP Lett. **42**, 363 (1985)
7. Volovik, G.E., Mineev, V.P.: JETP **56**, 579 (1976)
8. Volovik, G.E., Mineev, V.P.: JETP **71**, 1129 (1976)
9. Combescot, R., Dombre, T.: Phys. Rev. B **33**, 79 (1986)
10. Combescot, R., Dombre, T.: Phys. Rev. B **28**, 5140 (1983)
11. Volkov, D.V., Akulov, V.P.: JETP Lett. **16**, 438 (1972)
12. Kee H.-Y., Raghavan A., Maki K.: arXiv:0711.0929 (2007)
13. Roy, R., Kallin, C.: Phys. Rev. B **77**, 174513 (2008)
14. Ivanov, D.A.: Phys. Rev. Lett. **89**, 208 (2001)
15. Novoselov, K.S., Geim, A.K., Morozov, S.V., Jiang, D., Katsnelson, M.I., Grigorieva, I.V., Dubonos, S.V., Firsov, A.A.: Nature **438**, 197 (2005)
16. Tajima, N., Sugawara, S., Tamura, M., Kato, R., Nishio, Y., Kajita, K.: Europhys. Lett. **80**, 47002 (2007)
17. Vollhardt, D., Wölfle, P.: The superfluid phases of Helium 3. Taylor and Francis, London (1990)
18. Landau, L.D., Lifshitz, E.M.: Electrodynamics of Continuous Media. Pergamon Press, New York (1984)
19. Landau, L.D., Lifshitz, E.M.: Statistical Physics. Butterworth-Heinemann, Oxford (1999). Part I
20. Lifshitz, E.M., Pitaevskii, L.P.: Statistical Physics. Pergamon Press, New York (1988). Part II
21. Bardeen, J., Cooper, L.N., Schrieffer, J.R.: Phys. Rev. **108**, 1175 (1957)
22. Cooper, L.N.: Phys. Rev. **104**, 1189 (1956)
23. Schrieffer, J.R.: Theory of Superconductivity. Benjamin, New York (1964)
24. Landau L.D., Lifshitz E.M.: Fluid Mechanics. Butterworth-Heinemann (1987)
25. Khalatnikov, I.M.: An Introduction to the Theory of Superfluidity. Perseus Books Group, New York (1989)
26. Berestetskii V.B., Lifshitz E.M., Pitaevskii L.P.: Quantum Electrodynamics. Butterworth-Heinemann (1982)
27. Bethe, H.A., Salpeter, E.E.: Quantum Mechanics of One and Two Electron Atoms. Springer, Berlin (1957)
28. Ward, J.C.: Phys. Rev. **78**, 182 (1950)
29. Volovik, G.E.: The Universe in Helium Droplet. Oxford University Press, Oxford (2002)
30. Volovik, G.E.: Exotic Properties of Superfluid 3He. World Scientific, Singapore (1992)
31. Leggett, A.J.: Modern Trends in the Theory of Condensed Matter Physics, p. 14. Springer, Berlin (1980)
32. Nozieres, P., Schmitt-Rink, S.: JLTP **59**, 195 (1985)
33. Ticknor, C., Regal, C.A., Jin, D.S., Bohn, J.L.: Phys. Rev. A **69**, 042712 (2004)
34. Regal, C.A., Ticknor, C., Bohn, J.L., Jin, D.S.: Phys. Rev. Lett. **90**, 053201 (2003)
35. Schunck, C.H., Zwierlin, M.W., Stan, C.A., Raupach, S.M.F., Ketterle, W., Simoni, A., Tiesinga, E., Williams, C.J., Julienne, P.S.: Phys. Rev. A **71**, 045601 (2005)
36. de Gennes, P.G.: The Physics of Liquid Crystals. Oxford University Press, London (1974)
37. de Gennes, P.G.: Phys. Lett. A **44**, 271 (1973)
38. de Gennes, P.G.: Superconductivity of Metals and Alloys. Benjamin, New York (1966)
39. Mermin, N.D., Ho, T.L.: Phys. Rev. Lett. **36**, 594 (1977)
40. Putterman, S.J.: Superfluid Hydrodynamics. North-Holland Publishing Company, New York (1974)

41. Vaks, V.G., Galitskii, V.M., Larkin, A.I.: JETP **15**, 914 (1962)
42. Stone M., Anduaga I.: Ann. Phys. (Weinheim), **323**, 2 (2008)
43. Stone M., Gaitan F.: Ann. Phys. (Weinheim), **178**, 89 (1987)
44. Stone, M.: Phys. Rev. B **54**, 13222 (1996)
45. Stone, M.: Physica B **280**, 117 (2000)
46. Stone, M., Roy, R.: Phys. Rev. B **69**, 184511 (2004)
47. Gaitan, F.: Phys. Lett. A **151**, 551 (1990)
48. Mermin, N.D., Muzikar, P.: Phys. Rev. B **21**, 980 (1980)
49. Leggett A.J.: Private communication
50. Andreev, A.F., Marchenko, V.I.: Sov. Phys. Uspekhi **23**, 21 (1977)
51. Tsvelik A.M.: Quantum Field Theory in Condensed Matter Physics. Cambridge University Press, Cambridge (1998)
52. Berezin, F.A.: The Method of Second Quantization. Academic Press, New York and London (1966)
53. Slavnov A., Faddeev L.: Gauge Fields: An Introduction to Quantum Theory. Westview Press (1993)
54. Feynmann, R.P., Hibbs, A.: Quantum Mechanics and Path Integrals. McGraw-Hill Companies, New York (1965)
55. Feynmann, R.P.: The Feynman Lectures on Physics, Addison Wesley Longman (1970)
56. Popov, V.N.: Functional Integrals in Quantum Field Theory and Statistical Physics. Kluwer, Dordrecht (1983)
57. Alonso, V., Popov, V.I.: JETP **46**, 760 (1977)
58. Bogoliubov N.N, Shirkov D.V.: Introduction to the theory of quantized fields. Wiley, New York (1980)
59. Bjorken J.D., Drell S.D.: Relativistic Quantum Mechanics and Relativistic Quantum Fields. McGraw-Hill, New York (1964)
60. Landau, L.D., Lifshitz, E.M.: Quantum Mechanics: Nonrelativistic Theory, 3rd edn. Pergamon Press, Oxford (1977). (problem to paragraph 17, p. 52)
61. Cross, M.C.: JLTP **21**, 525 (1975)
62. Cross, M.C.: JLTP **26**, 165 (1977)
63. Nagai, K.: JLTP **38**, 677 (1980)
64. Dmitriev, V.V., Krasnikhin, D.A., Mulders, N., Zavjalov, V.V., Zmeev, D.E.: JETP Lett. **86**, 594 (2007)
65. Elbs, J., Bunkov, Yu.M, Collin, E., Godfrin, H., Volovik, G.E.: Phys. Rev. Lett. **100**, 215304 (2008)
66. Fomin, I.A.: JETP Lett. **88**, 59 (2008)
67. Fomin, I.A.: JETP Lett. **77**, 240 (2003)
68. Volovik, G.E.: JETP Lett. **61**, 958 (1995)
69. Volovik, G.E.: JETP **75**, 990 (1992)
70. Thouless, D.J., Ao, P., Niu, Q.: Phys. Rev. Lett. **76**, 3758 (1996)
71. Kopnin, N.B., Salomaa, M.M.: Phys. Rev. B **44**, 9667 (1991)
72. Kopnin N.B.: Physica B **210**, 267 (1995)
74. Kopnin, N.B., Soinen, P.S., Salomaa, M.M.: Phys. Rev. B **45**, 5491 (1992)
75. Vakaryuk, V., Leggett, A.J.: Phys. Rev. Lett. **103**, 057003 (2009)
76. Bevan, T.D.C., Mannien, A.J., Cook, J.B., Alles, H., Hook, J.R., Hall, H.E.: JLTP **109**, 423 (1997)
77. Bevan, T.D.C., Mannien, A.J., Cook, J.B., Hook, J.R., Hall, H.E., Vachaspati, T., Volovik, G.E.: Nature **386**, 689 (1997)
78. Chubukov, A.V.: Phys. Rev. B **44**, 12318 (1995)
79. Chubukov A.V: Phys. Rev. B **52**, R3840 (1995)
80. Abrikosov A.A, Gor'kov L.P.: JETP **12**, 1243 (1961)
81. Larkin, A.I.: JETP **31**, 784 (1970)
82. Volovik, G.E., Solov'ev, A., Yakovenko, V.M.: JETP Lett. **49**, 65 (1989)
83. Read, N., Green, D.: Phys. Rev. B **61**, 10267 (2000)

84. Gurarie V., Radzihovsky L.: Ann. Phys. (Weinheim), **322**, 2 (2007)
85. Cheng, C.H., Yip, S.K.: Phys. Rev. Lett. **95**, 070404 (2005)
86. Klinkhamer, F.R., Volovik, G.E.: JETP Lett. **80**, 343 (2004)
87. Volovik, G.E.: JETP Lett. **90**, 398 (2009)
88. Volovik G.E.: JETP Lett., **90**, 587 (2009) and references therein
89. Berry, M.V.: Proc. Roy. Soc. London A **392**, 45 (1984)
90. Leggett, A.J.: Rev. Mod. Phys. **47**, 331 (1975)
91. Bogoliubov, N.N.: JETP **34**, 58 (1958)
92. Bogoliubov, N.N.: JETP **34**, 73 (1958)
93. Bogoliubov, N.N., Tolmachev, N.N., Shirkov, D.V.: A New Method in the Theory of Superconductivity. Consultants Bureau, New York (1959)
94. Schwinger, J.: Phys. Rev. **82**, 664 (1951)
95. Schwinger, J.: Phys. Rev. **128**, 2425 (1962)
96. Schwinger J.: Particles, Sources and Fields, vol. 1,2. Addison Wesley, Reading (1970) and (1973)
97. Adler, S.: Phys. Rev. **177**, 2426 (1969)
98. Adler S: Lectures on Elementary Particles and Quantum Field Theory. In: Desser S., Grissaru M., Pendelton H. (ed.) Cambridge MIT (1970)
99. Adler, S., Dashen, R.: Current Algebras. Benjamin, New York (1968)
100. Itzykson C., Zuber Z.-B.: Quantum Field Theory, vol. 2. Dover Publications (2006)
101. Bell, J.S., Jackiw, R.: Nuovo Cimento, Series A **60**, 47 (1969)
102. Jackiw R.: Lectures on Current Algebra and its Applications. Princeton University Press (1972)
103. Bardeen, W.A.: Phys. Rev. **184**, 1848 (1969)
104. Williams, J.R., Goldhaber-Gordon, D.: Nat. Phys. **8**, 778 (2012)
105. Ivanov, D.A.: Phys. Rev. Lett. **86**, 268 (2001)
106. Gong, M., Tewari, S., Zhang, C.: Phys. Rev. Lett. **107**, 195303 (2011)
107. Gong, M., Chen, G., Jia, S., Zhang, C.: Phys. Rev. Lett. **109**, 105302 (2012)
108. Lutchyn, R.M., Sau, J.D., Das Sarma, S.: Phys. Rev. Lett. **105**, 077001 (2010)
109. Mourik, V., Zuo, K., Frolov, S.M., Plissard, S.R., Bakkers, E.P.A.M., Kouwenhoven, L.P.: Science **336**, 1003 (2012)
110. Oreg, Y., Refael, G., von Oppen, F.: Phys. Rev. Lett. **105**, 177002 (2010)
111. Brusov, P.N., Brusov, P.P.: Collective Excitations in Unconventional Superconductors and Superfluids. World Scientific, New Jersey (2010)
112. Brusov, P.N., Lomakov, M.V., Brusova, N.P.: Sov. Jour. Low. Temp. Phys. **21**, 85 (1995)
113. Brusov, P.N., Lomakov, M.V.: JLTP **85**, 91 (1991)
114. Haldane, F.D.M.: Phys. Lett. **93A**, 464 (1983)
115. Haldane, F.D.M.: Phys. Rev. Lett. **50**, 1153 (1993)
116. Josephson, B.D.: In Superconductivity, ed. Parks, R.D. M. Dekker, New York (1969)
117. Josephson, B.D.: Phys. Lett. **1**, 251 (1962)

Part II

Chapter 5
Bose–Einstein Condensation and Feshbach Resonance in Ultracold Quantum Gases and Mixtures

In this chapter we will start with a brief description of the phenomena of Bose–Einstein condensation (BEC) in ultracold Bose-gases of alkali elements ^{7}Li, ^{23}Na and ^{87}Rb [1–3]. In these systems the experimentalists used evaporative cooling technique in magneto-optical traps and got the critical temperatures of Bose-condensation (BEC) of the order of 10^{-6} K for the densities $10^{12} \div 10^{14}$ cm^{-3} and numbers of particles in the trap (prepared by inhomogeneous dipole or quadrupole magnetic field) on the level of $10^{9} \div 10^{10}$. Note that evaporative cooling technique is based on the release of the potential barrier or sudden lifting of the trap which leads to the escape of the most energetic particles from the trap and thus to the decrease of the temperature. Effectively this technique is based on the "cutting" of Maxwell tails of the most energetic particles in thermal distribution [4, 5].

Soon after the discovery of BEC in Bose systems, the groups of Ketterle and Jin [6–8] in USA as well as the group of Salomon in France [9] and Grimm in Austria [10] began to search for fermionic superfluidity in magneto-optical traps or optical lattices [34].

At first the predictions for the critical temperature were rather pessimistic here, since T_C in the Fermi-systems is usually exponentially smaller than that in bosonic systems (where T_C is of the order of the degeneracy temperature T_0). The experimental progress here was connected with the Feshbach resonance technique [6, 7, 8, 11, 48–50], which gives the possibility to increase the coupling constant (or the scattering length a) greatly in diluted Fermi-systems close to the resonance magnetic field B_0. As a result experimentally feasible critical temperatures ($T_C \sim 10^{-6}$ K) can arise in ultracold Fermi-gases of ^{6}Li and ^{40}K in magneto-optical and dipole traps. The Feshbach resonance technique also provides the possibility for experimental verification of the pioneering ideas of Leggett [12, 13] and Nozieres-Schmitt-Rink [14] on BCS-BEC crossover in the Fermi-systems with attractive interaction between particles. Namely, varying magnetic field (and traversing the resonance from left side $B < B_0$) we can get either tightly bound local pairs $f_{\uparrow}f_{\downarrow}$ of two fermionic atoms (composed bosons or molecules or dimers) $^{6}Li_2$ and $^{40}K_2$ on the BEC side, or extended Cooper pairs on the BCS side [15, 16]. Correspondingly the scattering length a is repulsive ($a > 0$) on the BEC side,

M. Yu. Kagan, *Modern Trends in Superconductivity and Superfluidity*,
Lecture Notes in Physics 874, DOI: 10.1007/978-94-007-6961-8_5,

while it is attractive ($a < 0$) on the BCS side. Thus in a two-particle problem in vacuum close to the resonance we have a shallow bound state on the BEC-side for $a > 0$ and a virtual bound state on the BCS-side for $a < 0$.

In this chapter we provide a brief description of the Feshbach resonance with a special attention on a more sophisticated two-channel description and more simple one-channel description, corresponding to resonance approximation (which we will use in the forthcoming chapters). We will also discuss the experiments of Jin's and Ketterle's groups on molecular BEC in Fermi-gases of ^{6}Li and ^{40}K [48–50].

5.1 BEC in Trapped Bose-Gases

Bose–Einstein condensation (BEC) was discovered in ultracold bosonic gases of alkali elements ^{7}Li, ^{23}Na and ^{87}Rb in confined geometry of magneto-optical traps. There are excellent review articles on this subject [4, 5]. Here we provide only a brief sketch of evaporative and laser cooling technique and discuss the basic designs of magnetic traps. For Bose-gases the parabolic confining potential of the trap (in the case of strong spin-orbital coupling) reads (see Fig. 5.1):

$$U(r) = |\mu|B_0 + \frac{m\omega_0^2 r^2}{2}. \tag{5.1.1}$$

Note that nonzero magnetic field B_0 everytime corresponds to the potential (5.1.1).

Strong spin-orbital coupling means that $|\mu|B_0 < U_{hf}$, where $\mu \approx \mu_{el} < 0$ and $U_{hf}\vec{S}\cdot\vec{I}$ is the hyperfine interaction potential [26] between electron spin $\vec{S}$ and nuclear spin $\vec{I}$. In this case we are dealing with total spin $J = \left|\vec{S}+\vec{I}\right|$ of the atoms. For bosonic isotope ^{7}Li we have $J = 1$ ($S = I = ½$), while for fermionic isotope ^{6}Li we have $J = 3/2$ ($S = ½$, $I = 1$). Thus usually for $\mu_{el} < 0$ only $J_z = 1$ component of the total spin is trapped in case of bosons (for ^{7}Li see Fig. 5.1), while $J_z = 3/2$ component is usually trapped for fermions (for ^{6}Li). The reason for that is Zeeman splitting $\Delta E = B_0 J_z|\mu|$ between different J_z components in the magnetic field B_0 (see Fig. 5.2) and first term in (5.1.1). Magneto-optical traps utilize the combination of laser and evaporative cooling.

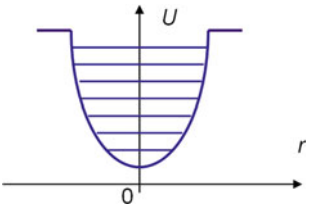

Fig. 5.1 Parabolic confining potential typical for magneto-optical traps. In the case of bosonic isotope ^{7}Li only $J_z = 1$ component of the total spin of the atom is trapped

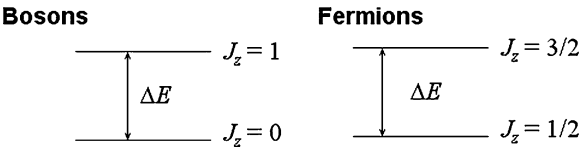

Fig. 5.2 Zeeman splitting in the magnetic field B_0 for different J_z components for bosons and fermions

5.1.1 Foundation of the Laser Cooling Technique

The progress in laser cooling was very important for the subject of ultracold quantum gases. Laser cooling is based on the interaction of quasiresonant radiation pressure with an atom. The principal scheme is the following: we consider an atom as a two-level system (see Fig. 5.2). The additional gradient field $\vec{B}_{grad} = B'z\vec{e}_z(B' > 0)$ is switched on. Then different z-components of the total spin J_z are additionally Zeeman splitted. As a result the total splitting due to the fields $\vec{B}_0$ and $\vec{B}_{grad}$ reads $\Delta E_{Zeeman} = B'zJ_z|\mu| + \Delta E$, where $\Delta E = B_0 J_z|\mu|$.

Now we introduce two laser beams: right-moving R and left-moving L with the frequencies close to but a little bit out of the resonance with the two-level system. The frequencies of the laser beams read $\omega^R = \Delta E - \Gamma/2 < \Delta E$ and $\omega^L = \Delta E + \Gamma/2 > \Delta E$, where Γ is a natural linewidth (see Fig. 5.3).

At $z = 0$ the intensities of the beams are adjusted in the way that the force acting on the atom is zero (see Fig. 5.2).

Consider the atom with trapped $J_z = 1$ component moving in the right-hand side. Then for $z > 0$: ΔE will be increased due to the gradient splitting and will be in a resonance with laser beam L. So the atom will absorb more left-moving photons and hence will feel a restoring force acting antiparallel to the atom velocity $\vec{v}$ (see Fig. 5.4). For $z < 0$: ΔE_{Zeeman} will be decreased and will be in

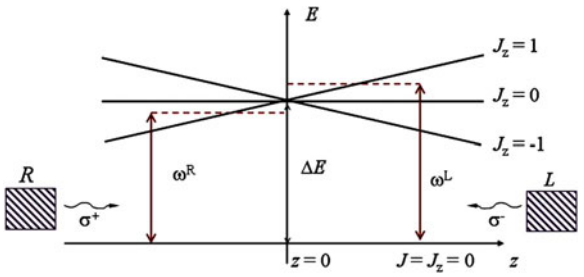

Fig. 5.3 Principal scheme of the laser cooling with left-moving L and right-moving R laser beams and Zeeman splitting of z-components of the total spin $J = 1$ by homogeneous and gradient fields $\vec{B}_0$ and $\vec{B}_{grad}$

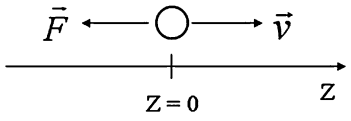

Fig. 5.4 The restoring force of the laser radiation pressure acting on the right-moving atom

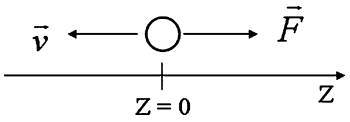

Fig. 5.5 The restoring force acting on the left-moving atom. $J_z = 1$ component of the total spin is trapped

resonance with laser beam R. Thus we again have a restoring force $\vec{F}$ acting antiparallel to $\vec{v}$ (see Fig. 5.5).

The effective force also depends explicitly upon velocity $\vec{v}$ because $\Delta E_{\text{Zeeman}}(\text{for the moving atom}) = \Delta E \pm \Delta\omega_{\text{Doppler}}$. If Doppler shift $\Delta\omega_{\text{Doppler}} > \Gamma/2$ (Γ is natural linewidth), then the atoms are out of the resonance both with laser beams R and L and the force becomes smaller. Finally for small z and $v = \dot{z}$ the resulting force includes restoring (string-like) force and friction force and reads:

$$\vec{F} = -kz\vec{e}_z - \alpha\dot{z}\vec{e}_z. \tag{5.1.2}$$

Thus we have a damped harmonic oscillator governed by an equation of motion:

$$\ddot{z} + 2\beta\dot{z} + \omega_0^2 z = 0, \tag{5.1.3}$$

where $\omega_0^2 = k/m;\ k = dB_{grad}/dz = B';\ \beta = \alpha/2m$.

The most important is that there are limitations on laser cooling, namely it is difficult to get the temperature in atomic system lower than the recoil energy:

$$T < T_{recoil} = \frac{\omega^2}{2mc^2} \sim 10^{-6}\ \text{K} \tag{5.1.4}$$

utilizing this technique only.

5.1.2 Evaporative Cooling Technique

To obtain lower temperatures in ultracold gases we need to load atoms from an optical trap to a static magnetic trap and to use an additional technique of evaporative cooling.

Let us briefly consider this method for a typical example of a static quadrupole trap. In this geometry (see Fig. 5.6 as an illustration) the inhomogeneous field $\vec{B}_{grad}$ reads:

$$\vec{B}_{grad} = B'x\vec{e}_x + B'y\vec{e}_y - 2B'z\vec{e}_z \tag{5.1.5}$$

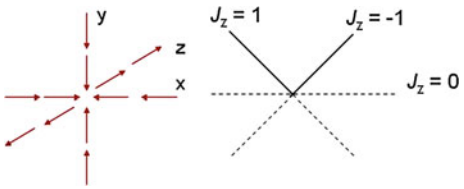

Fig. 5.6 The distribution of the inhomogeneous field $\vec{B}_{grad}$ and the level structure for different J_z components in the quadrupole magnetic trap

This field satisfies Maxwell equations [37] $\vec{\nabla} \times \vec{B}_{grad} = \vec{\nabla} \cdot \vec{B}_{grad} = 0$ and the boundary condition at the trap origin $\vec{B}_{grad}\big|_{r=0} = 0$.

We apply also an additional biased field $\vec{B}_b$ rotating with the frequency:

$$\vec{B}_b = B_0 \cos(\omega_b t)\, \vec{e}_x + B_0 \sin(\omega_b t)\, \vec{e}_y. \tag{5.1.6}$$

The amplitude of this field is constant $B_0 > 0$. We add it to suppress so-called Majorana flops, which constitute the transitions between different Zeeman sublevels close to the origin due to the particle motion. Majorana flops are dangerous since they cause the large decrease of the number of the trapped particles. Then zero of total field $\vec{B}_{tot} = \vec{B}_{grad} + \vec{B}_b$ rotates in the x–y plane with the frequency ω_b. Radius of the orbit reads:

$$R_0 = B_0/B'. \tag{5.1.7}$$

We usually choose the following hierarchy of frequencies in the quadrupole design of the magnetic trap:

$$\omega_0 = \sqrt{\frac{B'}{m}} \ll \omega_b \ll \Omega_L = \frac{B_0|\mu|}{\hbar}, \tag{5.1.8}$$

where Ω_L is Larmor frequency corresponding to the biased field.

It means that:

1. Projection of $\vec{\mu}$ on $\vec{B}_{tot}$ is conserved ($\omega_\mathrm{b} \ll \Omega_\mathrm{L}$);
2. We can average the particle motion over one period of field rotation with the frequency ω_b. As a result we get for the potential energy:

$$U = -\vec{\mu} \cdot \vec{B}_{tot} = -\mu J_z B_{tot} = |\mu||B_{tot}| \tag{5.1.9}$$

for trapped component $J_\mathrm{z} = 1$ and $\mu < 0$.

The total field $\vec{B}_{tot}$ in (5.1.9) is given by:

$$B_{tot} = \sqrt{B_x^2 + B_y^2 + B_z^2}, \tag{5.1.10}$$

where $B_\mathrm{i} = B_\mathrm{igrad} + B_\mathrm{ib}$ for three Cartesian coordinates $i = \{x, y, z\}$. Then the averaged (over one period) potential energy reads in the cylindrical coordinates:

$$U_{eff}(\rho, z) = \frac{\omega_b}{2\pi} \int_0^{2\pi/\omega_b} U dt = |\mu| B_0 + \frac{|\mu|(B')^2}{2B_0}(\rho^2 + 4z^2) \tag{5.1.11}$$

in agreement with (5.1.1). Thus in (5.1.1) $\omega_0 = \sqrt{\frac{B'}{m}}$ and coincides with ω_0 in (5.1.8).

The total magnetic field in (5.1.9) yields:

$$|B_{tot}(\rho, z)| = B_0 + \frac{(B')^2}{2B_0}(\rho^2 + 4z^2) \tag{5.1.12}$$

in cylindrical coordinates $\vec{\rho}$ and z. It is minimal at the origin (for $\rho = z = 0$). The distribution of the particles and magnetic field in the magnetic quadrupole trap is illustrated on Fig. 5.7.

The most important is that evaporative cooling is based on the removal of the most energetic particles from the potential well. The rest of the particles then rethermolize again due to elastic collisions at smaller temperature.

In this scheme the atoms which are moving close to field zero can be lost from the trap due to Majorana flops. The dangerous region corresponds now to small B_{tot} at $z = 0$ and $\rho = R_0 = B_0/B'$ [see Fig. 5.7 and (5.1.12)]. We can say that evaporative cooling is built in this design. Indeed, for $z = 0$ and $\rho = R_0$ an effective radial energy $|\mu| \frac{(B')^2}{2B_0}(\rho^2 + 4z^2)$ is $\frac{B_0|\mu|}{2}$. Hence all the rapid atoms with the effective radial energy higher then $\frac{B_0|\mu|}{2}$ will be removed from the trap by rapidly moving field zero which rotates with the frequency $\omega_{\text{b}} \gg \omega_0$ (see Fig. 5.7 again).

Thus continuous cooling can be achieved by adiabatic decrease of $\vec{B}_{tot}$.

5.1.3 Different Designs of the Magnetic Traps

There can be different designs of the magnetic traps. For instance we can add a bottle-type distribution of the magnetic field:

$$\vec{B}_{bottle-type} = B_0 \frac{k^2}{2}\left(z^2 - \frac{\rho^2}{2}\right)\vec{e}_z + B_0 \frac{k^2}{2} z\rho\, \vec{e}_\rho \tag{5.1.13}$$

to the quadrupole distribution:

$$\vec{B}_{quadrupole} = B_0 k\rho(\cos 2\varphi\, \vec{e}_\rho - \sin 2\varphi\, \vec{e}_\phi), \tag{5.1.14}$$

and consider the total field:

$$\vec{B}_{tot} = B_0\vec{e}_z + \vec{B}_{bottle-type} + \vec{B}_{quadrupole}. \tag{5.1.15}$$

Note that in (5.1.15) the constant field $B_0\vec{e}_z$ does not rotate. Then again we get $\vec{\nabla} \cdot \vec{B}_{tot} = \vec{\nabla} \times \vec{B}_{tot} = 0$ where in cylindrical coordinates (see [18]):

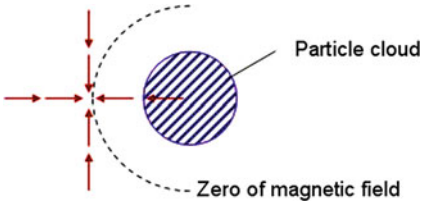

Fig. 5.7 The particle and magnetic field distribution in quadrupole magnetic trap. Zero of magnetic field rapidly rotates with the frequency $\omega_{\text{b}} \gg \omega_0$

$$\vec{\nabla} \cdot \vec{B}_{tot} = \frac{1}{\rho}\frac{\partial}{\partial \rho}(\rho B_{tot\,\rho}) + \frac{tot\,z}{\partial z} + \frac{1}{\rho}\frac{tot\,\varphi}{\partial \varphi}. \tag{5.1.16}$$

The potential energy reads:

$$U = -\vec{\mu} \cdot \vec{B} = -\mu J_z B = |\mu||B| \text{ for } J_z = 1. \tag{5.1.17}$$

In cylindrical coordinates:

$$U = |\mu| B_0 \left[1 + \frac{k^2}{2}\left(z^2 + \frac{\rho^2}{2}\right)\right] \tag{5.1.18}$$

again in agreement with (5.1.1) and magnetic field is minimal at the origin (for $z = \rho = 0$) again.

In this design evaporative cooling can be reached either by adiabatic decrease of k or with the help of rf-pumping (which in the resonance case helps to get the transitions between the Zeeman-splitted levels with different J_z).

Anyway different evaporative cooling technique helps to overcome recoil limit and achieve the temperatures $T \sim 10^{-8}$ K.

Note that in more recent experiments on Feshbach resonance the dipole traps are also used. Namely the system at first can be evaporatively cooled in the magnetic traps and than the system is reloaded to a dipole trap. In a dipole trap the confinement potential reads:

$$U = \vec{d} \cdot \vec{E} + \frac{m\omega^2 r^2}{2}, \tag{5.1.19}$$

where $\vec{E}$ is electric field, $\omega^2 = \frac{(E')^2}{E}$ ($E_{grad} \sim E'r$) and $\vec{d}$ is the dipole moment.

Dipole traps are convenient to switch on than (on top of $\vec{E}$) constant and homogeneous magnetic field $\vec{B}$ in the regime of Feshbach resonance. Finally we can reduce dimensionality of the traps making them highly anisotropic: $U \sim \frac{m\omega_x^2 x^2}{2} + \frac{m\omega_y^2 y^2}{2} + \frac{m\omega_z^2 z^2}{2}$.

5.1.4 BEC in Trapped Ultracold Bosonic Gases

BEC in ^{87}Rb, ^{7}Li, ^{23}Na was observed at $T_C^{BEC} \sim 10^{-6}$ K indirectly by measuring density distribution in the trap. Namely the transition to the superfluid state was measured in [1–3] in the diffraction experiments form the δ-functional density peak of the condensate particles, located in the center of the trap (see Fig. 5.8). Another way to observe the superfluid state is to lift the trap and to study the velocity distribution of the particles, leaving the trap region.

For $T < T_C$ we have the bimodal distribution of the leaving particles instead of the Maxwell one. A normal component is temperature dependent, a superfluid component is temperature independent. Usually for the last one the condensate

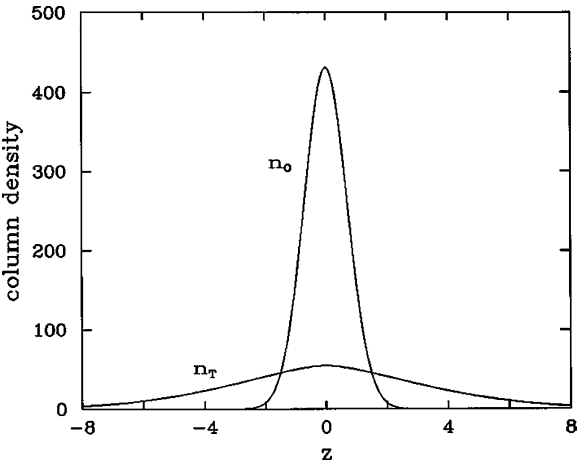

Fig. 5.8 Column density $n(z) = \int \mathrm{d}x n(x, 0, z)$ for noninteracting bosons in a spherical trap at temperature $T = 0.9\, T_C{}^{BEC}$. The central peak is the condensate density n_0 superimposed in the broader thermal distribution with the density n_T from Dalfovo et al. [18]. Distance and density are in units of l_0 and l_0^2 respectively, where $l_0 = \left(\frac{\hbar}{m\omega}\right)^{1/2}$ is the magnetic length

velocity $V_{cond} \sim 1/W$, where W is half-width of the profile of the condensate density (see [3]). In the more recent experiments of Feshbach resonance for the BEC-side of the resonance $W \sim (aN_{\mathrm{cond}})^{1/5}$, where $a > 0$ is repulsive scattering length and N_{cond} is the number of condensate particles. Note that according to Einstein the BEC temperature in 3D Bose-gas reads $T_C = 3.31\frac{n^{2/3}}{m}$, where n is the density of bosons (see [30]) and m is the boson mass. By order of magnitude it coincides with the degeneracy temperature T_0 in an ideal Bose-gas, so the most important for evaporative cooling is to reach the temperatures lower than the degeneracy temperature at a given density.

For the BEC-side of the Feshbach resonance $T_C{}^{BEC} \sim 0.2\varepsilon_F$, where ε_{F} is Fermi energy. For $T < T_{\mathrm{C}}$ there is s macroscopical number of particles which occupy the lowest level in the potential well. For 3D spherically symmetrical well with parabolic potential $U(r) = \frac{m\omega^2 r^2}{2} + U_0$ the solution for the spectrum of harmonic oscillator reads [26]:

$$E - U_0 = \hbar\omega\left(n_x + n_y + n_z + 3/2\right) = \hbar\omega\left(n + 3/2\right), \tag{5.1.20}$$

and thus the lowest level $E_0 = U_0 + 3/2\hbar\omega$ (see Fig. 5.8). The eigenfunction $\Psi_0(r)$ of the lowest level ($n = 0$) is given by (see [30]):

$$\Psi_0(r) = \left(\frac{N_0}{\pi^{3/2} l_0^3}\right)^{1/2} e^{-\frac{r^2}{2l_0^2}}; \tag{5.1.21}$$

where $l_0 = \left(\frac{\hbar}{m\omega}\right)^{1/2}$ is the magnetic length and N_0 is the total number of particles in the condensate. The density of the condensate:

$$n_0(r) = |\Psi_0(r)|^2 \tag{5.1.22}$$

has a maximum at $r = 0$: $n_{0\,\max} = n_0(0) \sim N_0/l_0^3$. The Ψ-function for the next level $E_1 = (U_0 + 5/2\hbar\omega)$ i.e. $\Psi_1(r)$ changes sign and has a node in the origin. In

slightly non-ideal Bogoliubov Bose-gas with repulsive interaction between bosons the scattering length $a > 0$ and we can introduce the pseudopotential $\tilde{U} = \frac{4\pi\hbar^2}{m} a$ following Lifshitz-Pitaevskii book [27]. Then, as it was shown by Yu. Kagan, G. Shlyapnikov and Walraven [24] the convenient parameter which measures the interaction strength is $\eta = \frac{n_0 \tilde{U}}{\hbar\omega}$, where $\hbar\omega$ is the level spacing in the potential well (see Fig. 5.9).

For weakly non-ideal Bose-gas in the trap $\eta \ll 1$ and for low temperatures $T \ll T_C$ almost all the particles occupy the zeroth level. Thus the density in the center of the trap is strongly increased. Just this increase of the density is measured in the diffraction experiments to prove the formation of the Bose-condensate in the trap.

It is interesting that even in strongly-interacting Bose-gas with repulsion (for $\eta \gg 1$) as it was shown in [24] the Ψ-function of the zeroth level:

$$\Psi_0(r) = \sqrt{n_{0\max}} \left(1 - \frac{r^2}{2l_0^2\eta}\right)^{1/2} = \left(\frac{\mu - U(r)}{\tilde{U}}\right)^{1/2}, \tag{5.1.23}$$

and $n_0(r) = |\Psi_0(r)|^2$ is again maximal at $r = 0$.

5.1.5 Typical Densities and Numbers of Particles in the Trap

Usually the total number of particles in the trap $N_{\text{tot}} \sim (10^9 \div 10^{10})$, while the characteristic densities are $n \sim (10^{12} \div 10^{14})$ cm^{-3}. Thus the number of particles in the Bose-condensate for $T \ll T_C^{\text{BEC}}$ is also of the order of 10^9. The lowest characteristic temperatures which we can reach in the evaporative cooling technique are 10^{-8} K. For largest possible densities $n \sim 10^{14}$ cm^{-3} the degeneracy temperatures $T_0 \sim n^{2/3}/m$ are of the order of 10^{-6} K. Note that the large number of particles in the trap $N_{\text{tot}} \gg 1$ guarantees the validity of quasiclassical (or Thomas–Fermi) approximation. Effectively it means that $T_0 \gg \hbar\omega$ where $\hbar\omega$ is the level spacing.

For Bose-gases $T_C^{\text{BEC}} \sim T_0$, while for Fermi-gases $T_C < T_0$ (in the absence of Feshbach effect or far from Feshbach resonance) especially for extended Cooper

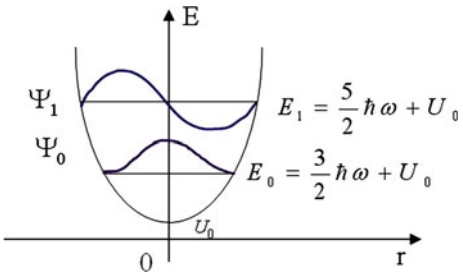

Fig. 5.9 The Ψ-functions $\Psi_0(r)$ and $\Psi_1(r)$ of the lowest $(E_0 = U_0 + 3/2\hbar\omega)$ and first $(E_1 = U_0 + 5/2\hbar\omega)$ levels in the spherically symmetrical parabolic potential well $U(r) = \frac{m\omega^2 r^2}{2} + U_0$

pairs in the BCS-case. Note that for fermions $T_0 = \varepsilon_F$, and due to the Pauli principle the number of particles in the trap for $T \ll T_0$ reads in 3D case:

$$N_{tot} \sim \left(\varepsilon_F/\hbar\omega\right)^3 \gg 1. \tag{5.1.24}$$

Thus $N_{\text{tot}}^{1/3} \sim \varepsilon_F/\hbar\omega$ is the number of the occupied levels in case of fermions, while $\rho(\varepsilon) = \frac{dN_{tot}(\varepsilon)}{d\varepsilon} \sim \frac{\varepsilon^2}{(\hbar\omega)^3}$ is the density of states for a spherical parabolic trap. The quasiclassical criterion for fermions then reads:

$$\varepsilon_F \gg \hbar\omega = \left(\varepsilon_F \Big/ N_{tot}^{1/3}\right) \tag{5.1.25}$$

and coincides with the Migdal criterion [38] well-known in nuclear physics. We will discuss the fermionic superfluidity in the trap for ^{6}Li and ^{40}K isotopes more detaily in this chapter and Chap. 12.

Returning back to bosons, we would like to emphasize that for Rb and Na the scattering length $a > 0$—corresponds to repulsion, and BEC goes along the standard Bogoliubov scenario (hard-core Bose-gas [19, 30]). For ^{7}Li the scattering length $a < 0$—corresponds to attraction, and Bose-condensate exists only for $|\eta| < 1$ due to discrete level structure in the trap (in unrestricted geometry we will have collapse in real space instead of BEC) (see [24]).

Note that for $|\eta| > 1$ levels are effectively smeared by interparticle interactions and there is no BEC in the system of ^{7}Li atoms.

5.1.6 *Recalculation of T_C^{BEC} from the Free Space on the Trap Geometry in Confinement Potential*

It is important to recalculate Einstein formula $T_{\text{C}}^{\text{BEC}} = 3.31\ n^{2/3}/m$ for an ideal Bose-gas from the infinite free space to the confined geometry of magnetic trap using quantum–mechanical solution $E - U_0 = \hbar\omega(n_x + n_y + n_z + 3/2)$ for spherical harmonic oscillator (or in more general anisotropic case using the solution $E - U_0 = \hbar\omega_x(n_x + 1/2) + \hbar\omega_y(n_y + 1/2) + \hbar\omega_z(n_z + 1/2)$.)

To do that according to Dalfovo et al. [18] we should write the total number of particles in the spherical trap:

$$N = \sum_{n_x,n_y,n_z} \frac{1}{\exp\left(\dfrac{\hbar\omega(n_x + n_y + n_z + 3/2) - \mu_B}{k_B T}\right) - 1}. \tag{5.1.26}$$

According to Einstein $\mu_{\text{B}}(T = T_{\text{C}}) = 0$ in free space. For the trap $\mu_B = \frac{3}{2}\hbar\omega$ corresponds to the lowest Landau level. Thus for $T = T_{\text{C}}^{\text{BEC}}$:

$$N = \sum_{n_x,n_y,n_z} \frac{1}{\exp\left(\dfrac{\hbar\omega(n_x + n_y + n_z)}{k_B T_C^{BEC}}\right) - 1}. \tag{5.1.27}$$

In the quasicalssical approximation for $k_B T \gg \hbar\omega$ (when the number of trapped particles is large $N \gg 1$) we can replace the sum by integral in (5.1.27) and get:

$$N = \int_0^\infty \frac{dn_x dn_y dn_z}{\exp\left(\frac{\hbar\omega(n_x+n_y+n_z)}{k_B T_C^{BEC}}\right) - 1} = \xi(3)\left(\frac{k_B T_C^{BEC}}{\hbar\omega}\right)^3, \tag{5.1.28}$$

where $\xi(3)$ is the ξ-function.

Correspondingly

$$k_B T_C^{BEC} = \hbar\omega\left(\frac{N}{\xi(3)}\right)^{1/3} = 0.94\,\hbar\omega\, N^{1/3}. \tag{5.1.29}$$

The proper thermodynamic limit for these systems is obtained by letting $N \to \infty; \omega \to 0$ and keeping $\omega^3 N = \text{const}$. Note that for bosons $T_C^{BEC} \sim T_0$ and $T_0 \gg (\hbar\omega \sim T_0/N^{1/3})$ in similarity with the fermionic case. To get the number of condensed particles N_0 below T_C^{BEC} we can put again $\mu_B = 3\hbar\omega/2$ and write:

$$N - N_0(T) = \sum_{n_x,n_y,n_z \neq 0} \frac{1}{\exp\left(\frac{\hbar\omega(n_x+n_y+n_z)}{k_B T}\right) - 1}. \tag{5.1.30}$$

If we introduce the density of states for the spherical trap $\rho(\varepsilon) = \frac{1}{2}\frac{\varepsilon^2}{(\hbar\omega_0)^3}$, we obtain:

$$N - N_0(T) = \int_0^\infty d\varepsilon \rho(\varepsilon) \frac{1}{\exp\left(\frac{\varepsilon}{k_B T}\right) - 1} = \xi(3)\left(\frac{k_B T}{\hbar\omega}\right)^3, \tag{5.1.31}$$

and using T_C^{BEC} from (5.1.29) we finally get: $\frac{N_0}{N} = 1 - \left(\frac{T}{T_C^{BEC}}\right)^3$, or $N - N_0(T) = N\left(\frac{T}{T_C^{BEC}}\right)^3$ for the noninteracting bosons in 3D spherical traps. Of course we can recalculate T_C^{BEC} on strongly anisotropic case also.

5.1.7 Metastability of Trapped Bose- and Fermi-Gases

It is important to note that the systems like atomic ^{7}Li and ^{6}Li in magnetic traps are inherently metastable. The most effective channels of decay, which define the lifetime of these metastable systems, are three-particle recombination and spin-relaxation processes [23]. The point is that for ^{6}Li–^{6}Li and ^{7}Li–^{7}Li in the two-particle interaction potential exists a virtual quasiresonance level [39, 40] (see Fig. 5.10). It means according to Quantum mechanics [30] that if we make potential well a little bit deeper then a real shallow level appears. Of course there

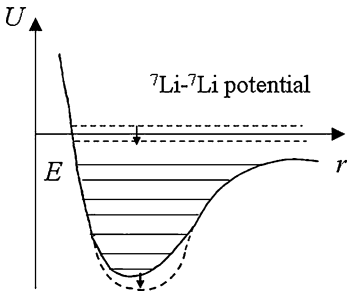

Fig. 5.10 The level-structure for the interaction potential acting between two ^{6}Li or two ^{7}Li atoms. There is a shallow virtual level for this potential well-separated from deep vibrational levels [39, 40]

are deep vibrational levels in the potential, but they are well-separated from a shallow one (from the continuum states).

As it was shown by Yu. Kagan, Shlyapnikov and Glukhov [23] due to three-particle recombination processes the particles leave the shallow quasiresonance levels in a potential well thus loosing their quantum–mechanical identity (they do not participate then in the symmetrization of the BEC or BCS condensate wave-functions). As a result a lifetime of BEC condensate (such as ^{7}Li) for densities $n > 10^{12}$ cm^{-3} is of the order of 40 s. The lifetime of molecular BEC condensate of ^{6}Li is of the order of 10 s in the regime of Feshbach resonance, while the lifetime of the fermionic BCS condensates is much smaller (superfluidity of Cooper pairs is more fragile).

Note that for densities $n \geq 10^{14}$ cm^{-3} the parameter $|\eta|$ becomes usually of the order of 1 and thus in bosonic ^{7}Li with attractive scattering length $a < 0$ the phenomena of BEC disappears. In case of fermionic ^{6}Li in the regime of Feshbach resonance (on the BCS-side of it—see the next section of this Chapter) $|a| \sim (2 \div 3)10^3$ Å and $a < 0$. Here the effective gas parameter of Galitskii, which for fermions reads $\lambda_{eff} = \frac{2|a|p_F}{\pi}$ (see [28] and Chap. 12, where p_F is Fermi-momentum and $\varepsilon_F = p_F^2/2m$) reaches the values of the order of 1 for densities $n \sim 10^{14}$ cm^{-3}. In this case, as we will show in Chap. 12, the compressibility (or the sound velocity squared $\kappa^{-1} = c^2$) of the system becomes negative, and the system of ^{6}Li atoms becomes unstable with respect to phase-separation on several hyperfine components.

Thus the densities $n \sim 10^{14}$ cm^{-3} are usually maximal possible densities of the homogeneous state both for BEC and BCS- condensates in the traps.

5.2 Experiments on Feshbach Resonance in Ultracold Quantum Gases and Mixtures

Molecules or composed bosons $f_\uparrow f_\downarrow$ ($^6Li_2$, $^{40}K_2$) and composed fermions $f_\sigma b$ ($^{40}K + {}^{87}Rb$) were observed in magneto-optical or dipole traps in the experiments on Feshbach resonance by the groups of Jin [6, 7, 48, 49] and Ketterle in USA [8, 21, 50].

In Feshbach resonance we use the abrupt change of the sign and the magnitude of the s-wave scattering length in the external homogeneous magnetic field B:

$$a = a_{bg}\left(1 + \frac{\Delta}{B - B_0}\right), \tag{5.2.1}$$

where a_{bg} is the s-wave scattering length of the quasiresonance origin (see Fig. 5.10 as illustration). For $B \to B_0$ (where B_0 is a resonance magnetic field) $1/a \to 0$ and we are in the so-called unitary limit of the infinite interaction. Usually $|a_{\mathrm{bg}}| \sim (15 \div 20)$ Å, moreover for fermionic ^{6}Li $a_{\mathrm{bg}} < 0$ [39, 40]. Thus not very far from the resonance the typical values of $|a|$ can reach $(2000 \div 3000)$ Å.

Physically Feshbach resonance corresponds to the interception of the singlet and triplet two-particle terms in the resonant magnetic field B_0. The singlet term for ^{6}Li is formed by the one-particle terms $J = 3/2, J_z = ½$ and $J = 3/2, J_z = -½$ and possesses virtual or real shallow bound state (which effectively is a molecule or a composed boson $f_\uparrow f_\downarrow$), while the triplet term is prepared by two one-particle terms $J = ½, J_z = ½$ and $J = ½, J_z = -½$ and does not have it [41–47]. We refer to the singlet term as to a closed channel, while the triplet term corresponds to an open channel. The behavior of the scattering length a in magnetic field B according to (5.2.1) is given by Fig. 5.11.

For $a > 0$ the tightly bound local pairs are created—this side is usually called BEC-side of Feshbach resonance ($\Delta B < 0$ or $B < B_0$). For $a < 0$ ($\Delta B > 0$) there is only virtual level, which excludes the formation of local bound pairs in real space and allows only extended weakly-bound pairs in momentum space. This side of Feshbach resonance corresponds to BCS-side of BEC-BCS crossover. Here only extended Cooper pairs of two fermionic atoms can be formed.

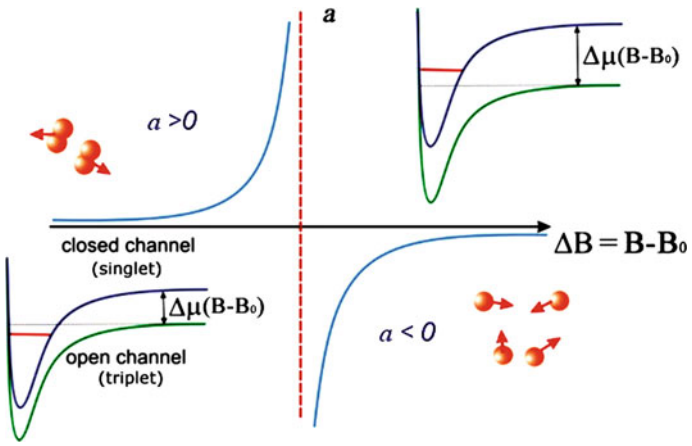

Fig. 5.11 Feshbach resonance for s-wave pairing describing s-wave scattering length a as a function of the relative magnetic field $\Delta B = B - B_0$, where B_0 is a resonance field. On the inserts we show the evolution of singlet and triplet terms when we go from BEC side ($a > 0$) to BCS side ($a < 0$) of the resonance

Note that when we speak about an "open" or "closed channel" (or "singlet" or "triplet" terms) [41–47]we effectively use the terminology of the Heitler-London theory [26] for the molecules of H_2, which are formed in singlet channel (for total electron spin $S_{tot} = 0$ of two hydrogen atoms). In the same time there is no bound state of two hydrogen atoms in the triplet channel (for total electron spin $S_{tot} = 1$ of two hydrogen atoms). Here (for $^6Li_2$ and $^{40}K_2$) the role of effective spin plays J_z^{tot} which is zero both for singlet and triplet channels ($J_z = \pm$ ½ for two one-particle terms in both channels). We can illustrate the behavior of singlet and triplet terms in magnetic field in the following way (see Fig. 5.12).

5.2.1 The General Expression for the s-Wave Scattering Amplitude

Note that according to Landau the general form for the s-wave ($l = 0$) scattering amplitude in resonance approximation reads [26]:

$$f_0(k) = \frac{1}{\frac{1}{a} + ik + k^2 R_*}, \tag{5.2.2}$$

where $W = \frac{\hbar^2}{mR_*^2}$ is the resonance width. In the potential scattering theory $R_* = r_0$ is the range of the potential (kr_0 are the corrections to $1/a$ due to the finite range of

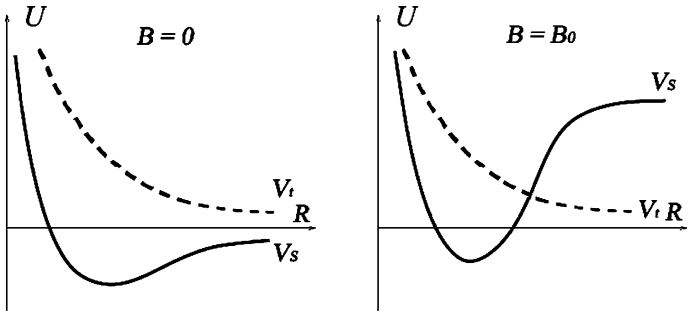

Fig. 5.12 Singlet and triplet terms on Fig. 5.12 do not intercept in the absence of field but intercept in field $B = B_0$ [42] (see also [43–45])

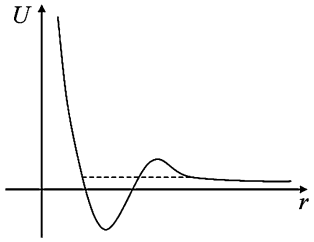

Fig. 5.13 General α-decaying potentials with resonance states $E = E_0 - i\,\Gamma/2$, which have the finite lifetime for $E_0 > 0$ and $\Gamma > 0$

the potential). However in the general case (for α-decaying potentials, see Fig. 5.13 for example) R_* is not connected with r_0.

In the dilute gas limit $kr_0 \ll 1$, but, in principle, kR_* can be larger or smaller than 1. If $kR_* \gg 1$, then we have narrow resonance (with respect to the width $W = \frac{\hbar^2}{mR_*^2}$) [51–53].

5.2.2 Broad Feshbach Resonance

In the opposite limit $kR_* \ll 1$ we have broad resonance [51–53]. Thus for broad resonance we can neglect k^2R_* with respect to ik and get the standard (and with correct analytical properties) quantum–mechanical formula for potential resonance scattering:

$$f(k) = \frac{1}{\frac{1}{a} + ik}. \tag{5.2.3}$$

This situation is well-described by one-channel resonant approximation with one parameter-scattering length a. In the unitary limit $1/a \to 0$ and $f(k) = 1/ik$ according to general quantum–mechanical rules.

5.2.3 Resonant Approximation for Broad Feshbach Resonance

In resonant approximation we change a little bit a depth of potential (see Fig. 5.1). As a result at first we proceed from deep level $E_b \sim -1/mr_0^2$ in potential well with

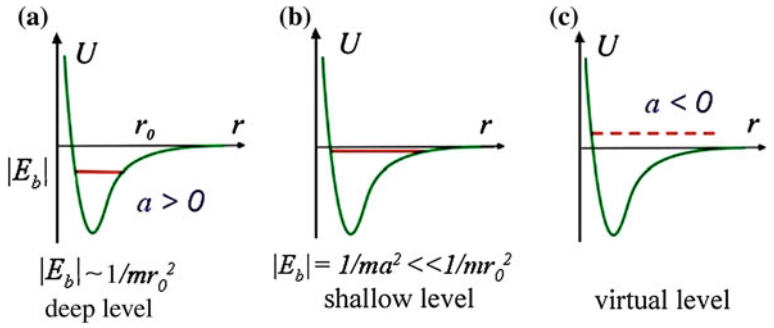

Fig. 5.14 Resonant approximation for typical short-range interatomic potential. **a** Corresponds to deep bound state in potential well. **b** To the shallow bound state for which $a \gg r_0$ and $|E_b| = 1/ma^2 \ll 1/mr_0^2$. Finally Fig. 5.14c corresponds to virtual state with attractive scattering length $a < 0$. When we continually decrease the depth of the potential, we gradually go from **a** to **b**, and than to **c**

radius r_0 (Fig. 5.14a) to a shallow level with $E_b = -1/ma^2$ and $a \gg r_0 > 0$ (Fig. 5.14b), and finally to a shallow virtual level with $E_b = 1/m|a|^2 > 0$ and $|a| > r_0$ (Fig. 5.14c). In the last situation $a < 0$ corresponds to attraction.

Note that the sequence of states on Fig. 5.14a, b, c precisely correspond to the behavior of the scattering length $a = a_{bg}\left(1 + \frac{\Delta}{B-B_0}\right)$ for the closed channel in the regime of Feshbach resonance. Indeed in closed channel for $B < B_0$ and $a_{bg} < 0$ the scattering length $a < 0$, and we have bound pairs, as on Fig. 5.14a and b, which become more and more shallow as we approach a resonance field B_0. Finally for $B > B_0$ and $a_{bg} < 0$ the scattering length a changes sign ($a < 0$) and we have virtual pairs in the closed channel. The only thing which we lose in one-channel (Hubbard-like description [29]) is a possibility to convert molecules in the closed channel to the pairs of free fermions in the open channel and vice a versa (atom-molecule oscillations [41, 42]) very close to the resonance field B_0. Let us emphasize that for $a > 0$ we can independently measure the binding energy $|E_b|$ for the real shallow level by the threshold of the absorption $\omega = |E_b|$ of the soft infrared radiofrequency waves [10, 11]. The same technique yields a possibility to measure a superfluid gap ($\omega = 2\Delta$) in the superfluid state of the resonance Fermi-gas at low temperatures $T \ll T_C$ (see Chap. 7).

5.2.4 Fermi-Gas with Attraction

Note that Fermi-gas with short-range attraction $U(r) = -Ue^{-r/r_0}$ (r_0 is a range of the potential) in momentum space is described by the Hamiltonian:

$$\hat{H} = \sum_{p\sigma} \varepsilon_p f^+_{p\sigma} f_{p\sigma} - \sum_{\substack{pp'q \\ \sigma\sigma'}} U(q) f^+_{p\sigma} f^+_{p'\sigma'} f_{p-q\,\sigma} f_{p'+q\,\sigma}, \tag{5.2.4}$$

where Fourier component of the potential $U(q)$ is given by:

$$U(q) = \begin{cases} U_0 \sim U r_0^3 & \text{for } qr_0 \ll 1, \\ 0, & \text{otherwise.} \end{cases}$$

BCS-domain

The s-wave scattering length in the BCS-domain is given by Lippmann-Schwinger integral equation for the two-particle T-matrix in vacuum [26, 27]. It requires the summation of ladder-type diagrams for vacuum Green-functions G_0 [19, 27, 28] and reads (see Fig. 5.15):

$$T_{vac}(\omega = 0, \vec{q} = 0) = \frac{4\pi a}{m} = -\frac{|U_0|}{1 - |U_0| K_{vac}(0,0)}, \tag{5.2.5}$$

where $K_{vac}(0,0) = \int \frac{d^3\vec{p}}{(2\pi)^3} \frac{d\Omega}{2\pi} G_0(\Omega, \vec{p}) G_0(-\Omega, -\vec{p}) = \int \frac{d^3\vec{p}}{(2\pi)^3} \frac{1}{2\varepsilon_p}$ is a product of the two Green-functions $G_0(\omega, \vec{p}) = \frac{1}{\omega - \frac{p^2}{2m} + io}$ in vacuum for zero total frequency $\omega = 0$

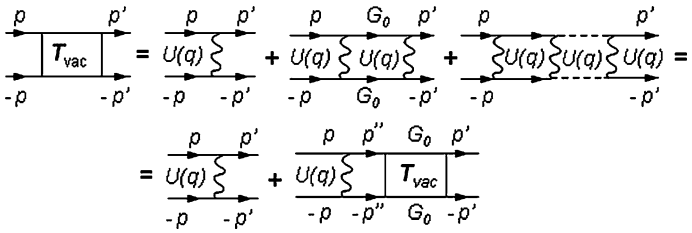

Fig. 5.15 Lippmann-Schwinger integral equation for the vacuum two-particle T-matrix $T_{vac}(\omega = 0, \vec{q} = 0) = \frac{4\pi a}{m}$, which requires the summation of ladder-type diagrams for vacuum Green-functions $G_0(\Omega, \vec{p}) = \frac{1}{\Omega - \frac{\vec{p}^2}{2m} + io}$, p is a four momentum $\{\Omega; \vec{p}\}$ on the figure

and zero total momentum $\vec{q} = 0$, $\varepsilon_p = \frac{p^2}{2m}$ is the free particle spectrum. The scattering length a from (5.2.5) can be represented as:

$$a = \frac{mT_{vac}(\omega = 0, \vec{q} = 0)}{4\pi} = \frac{-\frac{m|U_0|}{4\pi}}{1 - \frac{m|U_0|}{4\pi} \int\limits_0^{\sim 1/r_0} \frac{p^2 dp}{p^2}} \approx \frac{-|\beta| r_0}{1 - |\beta|} < 0, \tag{5.2.6}$$

where $|\beta| = \frac{m|U_0|r_0^2}{4\pi} \approx \frac{m|U_0|}{4\pi r_0}$ is the Born parameter [26, 27].

In this case only extended s-wave Cooper pairing is possible (the BCS-domain [15, 16]).

Note that for the Born parameter close to 1 $\left(\frac{1-|\beta|}{|\beta|} \ll 1\right)$ the scattering length $|a| \gg r_0$ and we have shallow virtual bound state $|E_b| = 1/ma^2 > 0$ [20, 26].

The critical temperature of s-wave Cooper pairing here is given by Gor'kov, Melik-Barkhudarov formula [17]:

$$T_{C0}^{BCS} = 0.28\, \varepsilon_F \exp\left\{-\frac{\pi}{2|a|p_F}\right\}, \tag{5.2.7}$$

which is just BCS-formula but with different preexponential factor 0.28 ε_F (instead of ω_D in the phonon model).

For $|\beta| = 1$ an expression for the scattering length a has a pole. For $|\beta| > 1$ we are in the BEC-domain and formula (5.2.6) for the s-wave scattering length should be modified. For the bound state problem (for the negative energies $E < 0$) we should use the s-wave scattering amplitude $f_0(E)$ which reads [20]:

$$|f_0(E)| = \frac{|\beta| r_0}{1 - |\beta| + |\beta|\sqrt{m|E|r_0^2}}. \tag{5.2.8}$$

Thus $|\beta| = 1$ is a threshold for a bound state of two fermions $f_\uparrow f_\downarrow$. Above the threshold the energy of the bound state yields [20]: $|E_b| \approx \frac{1}{mr_0^2}\left(\frac{|\beta|-1}{|\beta|}\right)^2 = \frac{1}{ma^2}$, where the scattering length $a = \frac{|\beta| r_0}{|\beta|-1} > 0$ corresponds to repulsion for $|\beta| > 1$.

Here the local pairs (molecules or dimers or composed bosons $f_\uparrow f_\downarrow$) are formed, and we are in the BEC-domain [12–14]. For $|\beta| = 1$ the scattering length diverges $1/a \to 0$. We are in the unitary limit. For $\frac{|\beta|-1}{|\beta|} \ll 1 : \ a \gg r_0$ and we have a shallow bound state with an energy $E = -|E_b|$, where $|E_b| = 1/ma^2 \ll 1/mr_0^2$. Note that for positive energies $(E > 0)$ the s-wave scattering amplitude reads: $f_0(E) = \frac{|\beta| r_0}{1-|\beta|+i|\beta|\sqrt{mEr_0^2}} = \frac{1}{1/a+i\sqrt{mE}}$ and in the unitary limit $f_0(E) = \frac{1}{i\sqrt{mE}}$ according to Quantum mechanics [26] $\left(E = k^2/m \ \text{and} \ \sqrt{mE} = k\right)$.

The critical temperature in the BEC-domain according to Einstein reads:

$$T_C^{BEC} = 3.31 \frac{(n/2)^{2/3}}{m_B}, \tag{5.2.9}$$

where in the free space the density of composed bosons $n_\mathrm{B} = n/2$ and bosonic mass $m_\mathrm{B} = 2m$. If we introduce the Fermi-energy $\varepsilon_\mathrm{F} = p_\mathrm{F}^2/2m$, then $T_C^{BEC} \approx 0.22\,\varepsilon_F$ in 3D case (where $n = p_\mathrm{F}^3/3\pi^2$ is the fermion density). In the dilute bosonic limit $|E_b| = 1/ma^2 \gg \varepsilon_\mathrm{F}$ (or $p_\mathrm{F} a \ll 1$) the situation at high temperatures is governed by the dynamical equilibrium between molecules and unbound fermions. This situation is described by the well-known Saha formula (or the law of mass action) (see [30]). In three dimensions it reads:

$$\frac{n_F^2}{n_B} = \frac{1}{2\pi^{3/2}} (mT)^{3/2} \exp\left\{-\frac{|E_b|}{T}\right\}, \tag{5.2.10}$$

where the total particle density $n = n_\mathrm{F} + 2n_\mathrm{B}$ with n_F being the free fermion density and n_B the bosonic molecular density at the temperature T. The crossover temperature T_* is defined from the condition $n_\mathrm{F}(T_*) = 2n_\mathrm{B}(T_*) = n/2$ and yields:

$$T_* = \frac{|E_b|}{3/2 \ln \frac{|E_b|}{\varepsilon_F}}, \tag{5.2.11}$$

where the logarithm in the denominator of (5.2.11) has an entropic character. For high temperatures $T \gg T_*$ one has $n_\mathrm{F}(T) \gg 2n_\mathrm{B}(T)$ which means that most of the fermions are unpaired. For lower temperatures $T \ll T_*$ vice a versa $n_\mathrm{F}(T) \ll 2n_\mathrm{B}(T)$ and most of the fermions are paired. They are Bose-condensed at the critical temperature $T_\mathrm{C}^\mathrm{BEC} < T_*$ given by (5.2.9). Thus for intermediate temperatures $T_\mathrm{C}^\mathrm{BEC} < T < T_*$ we have an interesting phase of normal (non-superfliud) dilute gas of composed bosons (see [14, 31, 32]). In the end of this chapter we will see that composed bosons repel each other. Thus it is a standard weakly repulsive Bogoliubov [27] Bose-gas of the composed bosons $f_\uparrow f_\downarrow$.

Dilute gas of composed bosons in 3D

For $T_\mathrm{C}^\mathrm{BEC} < T < T_*$ the temperature evolution of the attractive Fermi-gas in 3D is described by the two-particle T-matrix $T(i\omega_n, \vec{q})$ in substance (for Matsubara fermionic frequencies $\omega_\mathrm{n} = \pi T(2n+1)$, T is temperature):

$$T(i\omega_n,\vec{q}) = -\frac{|U_0|}{1-|U_0|K(i\omega_n,\vec{q})}, \tag{5.2.12}$$

where

$$K(i\omega_n,\vec{q}) = \sum_{\omega_n}\int \frac{d^3\vec{p}}{(2\pi)^3} G_M(i\Omega_n,\vec{p})G_M(-i\Omega_n+i\omega_n,-\vec{p}+\vec{q}) \tag{5.2.13}$$

is a product of two Matsubara (temperature) Green-functions G_{M} in a Cooper channel for total momentum $\vec{q}$ and total frequency ω_{n}. Sometimes $K(i\omega_n,\vec{q})$ is called a Cooper loop or particle–particle susceptibility. Generally speaking, Green functions G_{M} in (5.2.13) are dressed Green functions (see description of the T-matrix approximation in Chaps. 6 and 8), containing non-trivial self-energies Σ_{M}. Here, however, we will consider only the simplest approximation (which is often called first iteration to the self-consistent T-matrix approximation). In this approximation we can use the bare Matsubara Green functions $G_M(i\Omega_n,\vec{p}) = \frac{1}{i\Omega_n-\frac{\vec{p}^2}{2m}+\mu}$ in (5.2.13). Then graphically the Eq. (5.2.12) for the T-matrix can be represented by Fig. 5.16.

Analytically the Cooper loop $K(i\omega_n,\vec{q})$ in this approximation reads:

$$K(i\omega_n,\vec{q}) = \int \frac{d^3\vec{p}}{(2\pi)^3}\frac{1-n_F(\xi_p)-n_F(\xi_{q-p})}{i\omega_n-\xi(\vec{p})-\xi(\vec{q}-\vec{p})}, \tag{5.2.14}$$

where we performed the summation over the Matsubara frequencies Ω_{n} with the help of Watson transformation $\sum_{\Omega_n} \to \oint_C \frac{dz}{2\pi} n_F(z)$ [27]. In (5.2.14) $\xi(p) = \frac{p^2}{2m} - \mu$ is the quasiparticle spectrum and $n_F(\xi_p) = \frac{1}{e^{\xi_p/T}+1}$ is the Fermi–Dirac distribution function. For $\omega_n = \vec{q} = 0$ we get $1 - n_F(\xi_p) - n_F(\xi_{q-p}) = 1 - 2n_F(\xi_p) = th\frac{\xi_p}{2T}$ and we restore a standard expression for $K(0,0)$ from the textbooks on BCS-theory of superconductivity (see [15, 16, 27]): $K(0,0) = \int \frac{d^3\vec{p}}{(2\pi)^3}\frac{th(\xi_p/2T)}{2\xi_p}$. In the same time for small ω and $\vec{q}$ the T-matrix in substance (5.2.12) has a simple one-pole structure in the BEC-domain. Namely, after analytical continuation $i\omega_n \to \omega + io$,

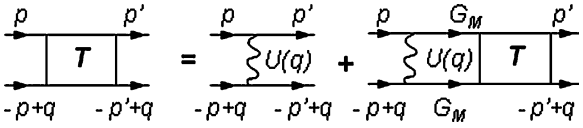

Fig. 5.16 Simplest approximation (first iteration) to the self-consistent T-matrix scheme which requires the summation of ladder-type diagrams for the bare Matsubara Green functions $G_M(i\Omega_n,\vec{p}) = \frac{1}{i\Omega_n-\frac{\vec{p}^2}{2m}+\mu}$, p is a four momentum $\{\Omega_n;\vec{p}\}$ on the figure

the first iteration to the Cooper loop (5.2.14) reads for the BEC-domain $a > 0$ and temperatures $T_C^{\mathrm{BEC}} \ll T \ll T_*$ (see [33]):

$$T(\vec{q}, \omega_n) = \frac{\frac{4\pi a}{m} 4|\mu|}{\left(\omega - \frac{q^2}{2m_B} + \mu_B + io\right)}. \tag{5.2.15}$$

The pole in (5.2.15) corresponds to the spectrum of a molecule (of a composed boson) and reads: $\omega = \frac{q^2}{2m_B} - \mu_B$. Note that in (5.2.15) we introduce a bosonic (molecular) chemical potential [31–33]:

$$\mu_B = 2\mu + |E_b|. \tag{5.2.16}$$

Note also that for $T \ll T_*$ most of the fermions are paired: $n_F(T) \sim \exp\left\{-\frac{|E_b|}{2T}\right\} \ll 2n_B(T)$, and hence $n \approx 2n_{\mathrm{B}}$. The fermionic chemical potential μ acquires a kink and reads for $T \ll T_*$ [33]:

$$\mu \approx -\frac{|E_b|}{2} - \frac{3}{4} T \ln \frac{T}{T_C^{BEC}}. \tag{5.2.17}$$

Accordingly bosonic chemical potential reads:

$$\mu_B \approx -\frac{3}{2} T \ln \frac{T}{T_C^{BEC}}, \tag{5.2.18}$$

and $\mu_{\mathrm{B}}(T_C^{\mathrm{BEC}}) = 0$ just in agreement with Einstein's definition of Bose-condensation critical temperature T_C^{BEC}.

We would like to emphasize that for $\omega = \vec{q} = 0$ the expression for the T-matrix in BEC-regime is reduced to [33]:

$$T(0,0) = \frac{16\pi a n|\mu|}{m} \frac{1}{\mu_B}, \tag{5.2.19}$$

and thus for $\mu_{\mathrm{B}}(T_C^{\mathrm{BEC}}) = 0$: the T-matrix $T(0,0) = 1/\mu_{\mathrm{B}} \to \infty$ diverges in agreement with Landau-Thouless criterion for the second order phase-transitions [19, 27].

Bethe–Salpeter integral equation

To escape confusion note that the equation for the T-matrix in substance, given by Fig. 5.16, is very close to the Bethe–Salpeter (BS) integral equation [22, 25] for the total two-particle vertex Γ. Bethe–Salpeter equation comes to the condensed matter physics from quantum electrodynamics and is widely used do describe superconductive pairing, for example. We will often use it in this book (see this Chapter and Chaps. 9, 10, 12). In general BS integral equation in the Cooper channel has the following graphic form (see Fig. 5.17).

Algebraically the BS integral equation reads:

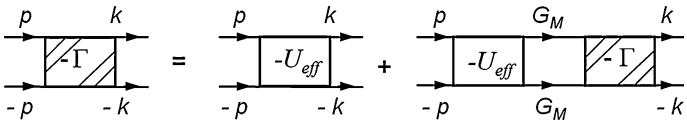

Fig. 5.17 The graphic representation of the Bethe–Salpeter integral equation. Γ stands for total two-particle vertex in the Cooper channel, U_{eff} is irreducible bare vertex with respect to Cooper channel. p and k are four-momenta $p = \{\Omega_n; \vec{p}\}$; $k = \left\{\Omega_m; \vec{k}\right\}$

$$-\Gamma(\vec{p},\vec{k}) = -U_{eff}(\vec{p},\vec{k}) + T\sum_n \int U_{eff}(\vec{p},\vec{q})G_M(\Omega_n,\vec{q})G_M(-\Omega_n,-\vec{q})\cdot\Gamma(\vec{q},\vec{k})\frac{d^3\vec{q}}{(2\pi)^3}, \tag{5.2.20}$$

where Γ is the total vertex in the Cooper channel, $\Omega_{tot} = \Omega_{n1} + \Omega_{n2} = 0$, $\vec{p}_{tot} = \vec{q}_1 + \vec{q}_2 = 0$, $G_M(\Omega_n,\vec{q}) = [i\Omega_n - \xi(q)]^{-1}$—is the Green function in temperature technique, $\Omega_n = \pi T(2n+1)$ is the Matsubara frequency for fermions, T is the temperature, $n = 0, \pm1, \pm2$ is integer, $\xi(q) = \frac{q^2}{2m} - \mu$. In the BCS-domain $\mu = \varepsilon_F$ and $|\vec{p}| = \left|\vec{k}\right| = p_F$ are the incoming and outgoing momenta lying on the Fermi-surface.

In the free space for infinite Fermi gas the reduction of the BS integral equation to the algebraic one can be fulfilled with the help of Legendre polynomials $P_l(\cos\theta)$, where $\theta = \angle\vec{p}\vec{k}$ is the angle between incoming and outgoing momenta $\vec{p}$ and $\vec{k}$, l is the value of the (relative) angular momentum of a pair ($l = 0$ for s-wave pairing, $l = 1$ for p-wave pairing and so on). As a result (see [27]):

$$\Gamma^l = U^l_{eff} - U^l_{eff}K\Gamma^l \tag{5.2.21}$$

and correspondingly

$$\Gamma^l = \frac{U^l_{eff}}{1 + U^l_{eff}K}, \tag{5.2.22}$$

where $K = T\sum\int G_M(\Omega_n,\vec{q})G_M(-\Omega_n,-\vec{q})\frac{d^3\vec{q}}{(2\pi)^3}$—is the Cooper loop. In the BCS-domain it reads[18]:

$$K = \int \frac{d^3\vec{q}}{(2\pi)^3}\frac{th\frac{\xi_q}{2T_C}}{2\xi_q} \approx N_{3D}(0)\ln\frac{2e^C\varepsilon_F}{\pi T_C}, \tag{5.2.23}$$

where $N_{3D}(0) = mp_F/2\pi^2$ is the density of states in 3D, C is the Euler constant [27].

The pole of Γ^l in (5.2.22) yields an equation for T_C according to Landau-Thouless criterion:

$$1 + U^l_{eff} K = 0. \tag{5.2.24}$$

Thus the most important is the sigh of U^l_{eff} for different values of the orbital momentum l. In this chapter we consider mostly $l = 0$. However, in Chaps. 9, 10, 11, 12, 13 we will also consider $l = 1$ (p-wave) and $l = 2$ (d-wave) pairings.

From Fig. 5.17 we see that the main difference between BS integral equation and the equation for the T-matrix in substance (Fig. 5.16) is the replacement of the bare vacuum interaction $U(q)$ by the is irreducible bare vertex $U_{\text{eff}}(q)$. By definition, $U_{\text{eff}}(q)$ in (Fig. 5.17) is a sum of all irreducible diagrams with respect to Cooper channel. These diagrams cannot be cut on two parts along the two solid lines running in the same direction [19, 27].

The difference between irreducible bare vertex (or effective interaction) $U_{\text{eff}}(q)$ from $U(q)$ gives us a possibility to get a superconductive pairing even in purely repulsive Fermi-systems (see Chaps. 9, 10, 11, 12). In the BCS-domain of the 3D attractive Fermi gas this difference also defines preexponential factor 0.28 ε_F in Gor'kov, Melik-Barkhudarov result for T_{C0}^{BCS} in (5.2.7). However, many derived expressions for dilute BEC limit and even for BCS-BEC crossover (see Chap. 6) can be done neglecting a difference between $U_{\text{eff}}(q)$ and $U(q)$ in resonance Fermi-Bose gases and mixtures. Thus if we neglect the vertex corrections for $U_{\text{eff}}(q)$, than the T-matrix equation in substance (in its first iteration) coincides with the Bethe–Salpeter integral equation for the total two-particle vertex Γ in the Cooper channel.

5.2.5 *Attractive-U Hubbard Model*

A detailed investigation of the attractive-U Hubbard model both in 3D and 2D case will be the subject of Chap. 8. Here we would like to note that many formulas obtained in Sect. 5.2.4 are valid also for attractive-U 3D Hubbard model on the lattice:

$$\hat{H} = -t \sum_{\langle ij \rangle \sigma} f^+_{i\sigma} f_{j\sigma} - U \sum_i n_{i\uparrow} n_{i\downarrow}, \tag{5.2.25}$$

where t is the hopping matrix element, $f^+_{i\sigma}$ and $f_{i\sigma}$ are the creation and annihilation fermionic operators on the neighboring sites $<ij>$ of the lattice, $n_{i\uparrow} = f^+_{i\uparrow} f_{i\uparrow}$ is on-site density of fermions with spins "up", U is the Hubbard (short-range) attraction.

After Fourier transform we get in close analogy with (5.2.4):

$$\hat{H} = \sum \varepsilon(p) f^+_{p\sigma} f_{p\sigma} - U \sum_{pp'q} f^+_{p\uparrow} f^+_{p'\downarrow} f_{p-q\downarrow} f_{p'+q\uparrow}, \tag{5.2.26}$$

where $\varepsilon(p) = -2t(\cos p_x d + \cos p_y d + \cos p_z d)$ is a fermionic spectrum for a simple cubic lattice in 3D, d is intersite distance.

At low densities $nd^3 \ll 1$: $\varepsilon(p) \approx -6t + \frac{p^2}{2m}$, and 3D attractive-$U$ Hubbard model becomes equivalent to 3D Fermi gas model with short-range attraction. The role of the range of the potential r_0 in the Hubbard model plays an intersite distance d. Correspondingly Fourier component of the potential $U(q)$ for $q = 0$ reads: $U_0 \sim Ud^3$ in the Hubbard model and the band mass $m = 1/2\, td^2$.

Thus practically all the formulas derived in this Subsection for dilute BEC-domain of the attractive Fermi-gas are valid also for 3D attractive-U Hubbard model. The only difference is the bosonic mass m_B in the expression for $T_\mathrm{C}^\mathrm{BEC}$ (5.2.9) and in the pole of the total vertex Γ: $\omega = \frac{q^2}{2m_B} - \mu_B$. In the absence of the lattice $m_\mathrm{B} = 2m$. On the lattice in the strong-coupling case $U \gg W = 2zt = 12t$ (W is a bandwidth, $z = 6$—the number of nearest neighbors on the simple cubic lattice in 3D) the bosonic mass is additionally enhanced (see [14] and Chap. 8 for more details):

$$m_B^* \sim m_B \frac{|U|}{W}. \tag{5.2.27}$$

The role of the optical lattices

Note that the optical lattices [34] (usually fabricated in the physics of ultracold gases by three or two monochromatic laser beams, which create mutually perpendicular standing waves with the particles in their minima) give us an excellent experimental possibility to study 3D and 2D Hubbard models on the lattice (the 1D optical lattices are also experimentally feasible). Moreover it is possible by changing the periodicity of lasers ($l_i = 2\pi c/\omega_i$) to fabricate the isotropic or anisotropic lattices with different intersite distances d and hopping integrals t (or band masses $m = 1/2\ td^2$). It is also possible to vary (with the help of the amplitudes of the laser beams) the strength of Hubbard interaction U (and thus the ratio U/W), as well as the particle density (or filling factor nd^D). Finally in the case of repulsive-U Hubbard models, the optical lattices provide us an excellent possibility to study Mott- Hubbard localization transition [29, 34] for large values of $U > U_\mathrm{C} \sim W$ (W is a bandwidth) and density $nd^D = 1$ corresponding to one particle per site (see Chap. 9 for more details). Note that currently both fermionic and bosonic Hubbard models are intensively studied on the optical lattices is three-dimensional, two-dimensional and one-dimensional cases.

5.2.6 Narrow Feshbach Resonance

In the opposite limit of narrow Feshbach resonances $kR_* > 1$ [see Eq. (5.2.2)] one-channel theory with contact potential (or resonant approximation) is not sufficient, since it misses an additional possibility to get the quasistationary resonance states

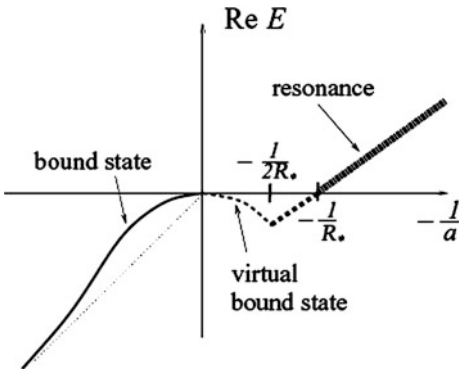

Fig. 5.18 Dependence of the real part of the energy ReE, which defines the dependence of the pole position of the s-wave scattering amplitude (5.2.2) from the inverse scattering length—$1/a$ [36]

with the finite lifetime $E = E_0 - i\Gamma/2$ (see Fig. 5.13) besides real and virtual bound states. A nice illustration of the situation for narrow Feshbach resonance we can find in [36]. On Fig. 5.18 we present the solution for the real part of the pole of the amplitude $f_0(E)$ in terms of the energy $E = k^2/2m$.

For shallow bound states $a \gg R_* > 0$ the pole in energy $E_b = -1/ma^2$ depends quadratic on $1/a$. If $0 < a < R_*$ the dependence of the binding energy from $1/a$ becomes linear $E_b = -1/maR_* < 0$. On the other side of the resonance the scattering length is negative $a < 0$ and large by absolute value $|a| \gg R_*$, and thus we have virtual bound states. However for $|a| < R_*$ we have resonance states with the finite lifetime $E = E_0 - i\Gamma/2$ ($E_0 > 0$, $\Gamma > 0$). It is useful also to show the evolution of the character of the pole of the scattering amplitude $f_0(E)$ in a complex energy plane (see Fig. 5.19).

Thus the conditions to get narrow Feshbach resonance include $kR_* > 1$ and $|a| < R_*$. In degenerate Fermi-gases $k \sim k_F$ and $k_F R_* > 1$ for narrow resonances. Usually in case of ^{40}K the resonance is broad (here the terms $J = 9/2$ and $J = 7/2$ are involved in the formation of singlet and triplet terms). In the same time in case

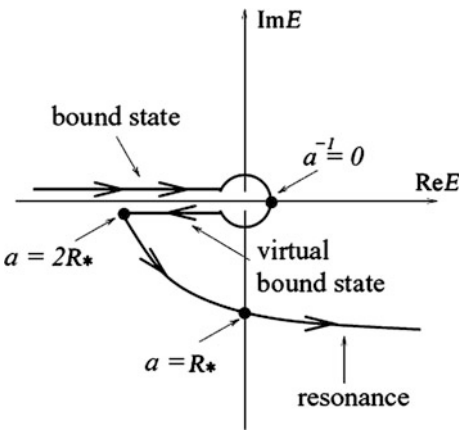

Fig. 5.19 Evolution of the character of the pole of the s-wave scattering amplitude $f_0(E)$ in a complex plane [36]. The arrows indicate the pole's motion as—$1/a$ is increased

of ^{6}Li the resonance is more narrow. Through Chap. 6 we will use one-channel description of the Feshbach resonance concentrating on real and virtual bound states in closed channel and assuming that resonance is broad. Additional argument in favor of one-channel (or resonance approximation) with one parameter $a \gg r_0$ (as for the short-range contact potential) was formulated in [51, 52]. Namely the authors of these papers paid attention on the fact that both singlet and triplet channels in terms of effective spin $J_z = S_z + I_z$ are "singlet" since $J_z^{\mathrm{tot}} = 0$ in both of them ($J_{z1} = ½$, $J_{z2} = -½$ both for singlet and triplet). Moreover both singlet and triplet states have relative angular momentum $l = 0$. Hence in analogy with contact interaction (or attractive Hubbard model [14, 29]) in dilute limit $p_F|a| < 1$ they can be described only in terms of the s-wave scattering length a.

Note that rigorously speaking, very close to the resonance the two-channel character of the Feshbach effect [53–55] can be important and manifests itself in the Feshbach term [53] $g(b_{oq} f^+_{\vec{k}\uparrow} f^+_{-\vec{k}+\vec{q}\uparrow} + h.c.)$, where bosonic operator with momentum q namely b_{0q} corresponds to a molecular bound state ($|E_b|$) in closed channel, while the bilinear combination of the fermionic operators with total momentum $\vec{q}$ corresponds to an open (triplet) channel. For $B \to B_0$ the Feshbach term describes the dissociation of a boson with momentum $\vec{q}$ in singlet channel on two fermions (with total momentum $\vec{q}$) in triplet channel, and the inverse process of the formation of boson in singlet channel from the two fermions in triplet channel. Note that the Feshbach term in atomic physics resembles the Ranninger term in fermion-boson models for high T_C superconductivity [35, 56]. Note also that not very close to the resonance the Feshbach-Ranninger term is not so important both in gases and in superconductive metals.

5.3 Experiments on Molecular BEC in ^{6}Li and ^{40}K

In the first experiments on Feshbach resonance the Fermi-gas of ^{6}Li and ^{40}K was cooled in magneto-optical traps by combination of laser and evaporative cooling till temperatures much lower than the degeneracy temperature T_0. After that the magnetic field B was adiabatically (very slowly) switched on. In the more recent experiments the Fermi-gas was evaporatively cooled till low temperatures, than the system was reloaded in dipole trap [with confinement potential described by (5.1.19)]. After that the homogeneous magnetic field (which is independent of coordinates) was rapidly switched on. Thus in both experiments $T \leq T_0$. The measurements in the first experiments in Ketterle group were performed for magnetic fields B in the interval between 700 and 900 Gauss (the resonance field $B_0 \sim 830$ Gauss). For $a_{bg} < 0$ and $B > B_0$ we are in the BCS-domain. For the fields $B < B_0$ we are in the BEC-domain. Traversing magnetic field from 900 Gauss to 700 Gauss, we go from virtual bound state at $B > B_0$ to real bound state (molecules $^6Li_2$) at $B < B_0$. Since we change magnetic field adiabatically (slowly),

the entropy $S = \text{const}$ and when the molecules are created, the temperature is increased only on 40 %. Hence T is still lower than T_0 even on BEC-side.

In the fields $B < B_0$ ($a > 0$) for temperatures $T_* \sim |E_b| = 1/ma^2 \sim 10^{-5}$K the molecules (composed bosons $f_\uparrow f_\downarrow$) were formed.

They were detected by the threshold of the absorption of the soft infrared electromagnetic waves $\hbar\omega_{thresh} = |E_b|$ [46]. The molecules $f_\uparrow f_\downarrow$ were Bose-condensed at temperatures $T_C^{\text{BEC}} \sim 10^{-6}$ K. The transition to the superfliud state was measured again (as in trapped Bose-gas) in the diffraction experiments form the δ-functional density peak of the condensate particles, located in the center of the trap. Another way to observe the superfliud state is again to measure at $T < T_C^{\text{BEC}}$ the bimodal distribution of the leaving particles (when the trap is lifted) with a temperature independent superfliud component $v_{\text{cond}}^5 a N_{\text{cond}}$. For $B = B_0$: $1/a = N_{\text{cond}}/v_C^5 = 0$ and thus $N_{\text{cond}} = 0$. Note that the critical temperature $T_C^{\text{BEC}} = 3.31\ (n/2)^{2/3}/2m$, in the infinite free space for bosonic density $n_B = n/2$ and $m_B = 2m$ for bosonic mass. If we introduce $n = p_F^3/3\pi^2$ in 3D Fermi-gas and $\varepsilon_F = p_F^2/2m$, than $T_C^{\text{BEC}} \approx 0.2\varepsilon_F$ in free space for composed bosons.

In the trap $k_B T_C^{\text{BEC}} = 0.94\ \omega(N_{\text{tot}}/2)^{1/3}$ and $\varepsilon_F = \omega(3N_{\text{tot}})^{1/3}$. Thus $k_B T_C^{\text{BEC}} = (0.06)^{1/3}\ \varepsilon_F \approx 0.2\varepsilon_F$. In the same time for the Cooper pairing of two fermions in the BCS-domain (for $|a| < 0$) we will get [17] $T_C^{BCS} = 0.28\,\varepsilon_F \exp\left\{-\frac{\pi}{2|a|p_F}\right\}$. Here we should demand that the size of the Cooper pair $\xi_0 = \frac{\hbar v_F}{T_C^{BCS}}$ is smaller than the typical size of the trap R_ε for $\varepsilon \sim \varepsilon_F$. Thus the validity of quasiclassical approximation requires that $\varepsilon_F \gg k_B T_C \gg \omega$ or $\varepsilon_F \gg k_B T_C \gg \varepsilon_F^{1/3}/N_{\text{tot}}$ just in agreement with Migdal criterion in nuclear physics [38]. Note that in strongly-anisotropic case we should replace ω in formulas for T_C and ε_F on $\tilde{\omega} = (\omega_x\omega_y\omega_z)^{1/3}$. Note also that if $\omega_z \gg \{\omega_x, \omega_y\}$ we have effectively quasi one-dimensional trapped gas while for $\{\omega_x, \omega_y\} \gg \omega_z$ the trapped gas is quasi two-dimensional. Thus varying the confinement potential we can change the dimensionality of the trapped gases or mixtures.

References

1. Anderson, M.H., Ensher, J.R., Matthews, M.R., Wieman, C.E., Cornell, E.A.: Science **269**, 198 (1995)
2. Bradley, C.C., Sackett, C.A., Tollett, J.J., Hulet, R.G.: Phys. Rev. Lett. **75**, 1687 (1995)
3. Davis, K.B., Mewes, M.D., Andrews, M.R., van Druten, N.J., Durfee, D.S., Kurn, D.M., Ketterle, W.: Phys. Rev. Lett. **75**, 3969 (1995)
4. Pitaevskii, L.P., Stringari, S.: Bose-Einstein Condensation. Clarendon Press, Oxford (2003)
5. Pethick, C.J., Smith, H.: Bose-Einstein Condensation in Dilute Gases. Cambridge University Press, Cambridge, UK (2008)
6. Regal, C.A., Ticknor, C., Bohn, J.L., Jin, D.S.: Nature **424**, 47 (2003)
7. Greiner, M., Regal, C.A., Jin, D.S.: Nature **426**, 537 (2003)
8. Zwierlein, M.W., Stan, C.A., Schunck, C.H., Raupach, S.M.F., Gupta, S., Hadzibabic, Z., Ketterle, W.: Phys. Rev. Lett. **91**, 250401 (2003)

9. Bourdel, T., Khaykovich, L., Cubizolles, J., Zhang, J., Chevy, F., Teichmann, M., Tarruell, L., Kokkelmans, S.J.J.M.F., Salomon, C.: Phys. Rev. Lett. **93**, 050401 (2004)
10. Jochim, S., Bartenstein, M., Altmeyer, A., Hendl, G., Riedl, S., Chin, C., Denschlag, J.H., Grimm, R.: Science **302**, 2101 (2003)
11. Herbig, J., Kraemer, T., Mark, M., Weber, T., Chin, C., Nägerl, H.-C., Grimm, R.: Science **301**, 1510 (2003)
12. Leggett, A.J.: J. Phys. (Paris) Colloq. **41**, C7 (1980)
13. Leggett, A.J.: Modern trends in the theory of condensed matter (Lecture notes of the XVI Karpacz winter school of theoretical physics). In: Pekalski, A., Przystawa, J. (eds.) Springer, Berlin (1980)
14. Nozieres, P., Schmitt-Rink, S.: Jour. Low Temp. Phys. **59**, 195 (1985)
15. Schrieffer, J.R.: Theory of Superconductivity. Benjamin Cummings, New York (1983)
16. Bardeen, J., Cooper, L.N., Schrieffer, J.R.: Phys. Rev. **108**, 1175 (1957)
17. Gor'kov, L.P., Melik-Barkhudarov, T.K.: JETP **40**, 1452 (1961)
18. Dalfovo, F., Giorgini, S., Pitaevskii, L.P., Stringari, S.: Rev. Mod. Phys. **71**, 463 (1999)
19. Abrikosov, A.A., Gor'kov, L.P., Dzyaloshinskii, I.E.: Quantum Field Theoretical Methods in Statistical Physics. Prentice-Hall, Englewood Cliffs, NY (1963)
20. Kagan, M.Yu., Habilitation thesis, Kapitza Institute, Moscow, (1994)
21. Zwierlein, M.W., Stan, C.A., Schunck, C.H., Raupach, S.M.F., Kerman, A.J., Ketterle, W.: Phys. Rev. Lett. **92**, 120403 (2004)
22. Salpeter, E.E., Bethe, H.A.: Phys. Rev. **84**, 1232 (1951)
23. Kagan, Yu., Shlyapnikov, G.V., Glukhov, N.A.: JETP Lett. **41**, 238 (1995)
24. Kagan, Yu., Shlyapnikov, G.V., Walraven, J.T.M.: Phys. Rev. Lett. **76**, 2670 (1996)
25. Salpeter, E.E.: Phys. Rev. **87**, 328 (1952)
26. Landau, L.D., Lifshitz, E.M.: Quantum Mechanics: Non-Relativistic Theory. Pergamon Press, UK (1977)
27. Lifshitz, E.M., Pitaevskii, L.P.: Statistical Physics, Part II. Pergamon Press, Oxford (1988)
28. Galitskii, V.M.: JETP **34**, 151 (1958)
29. Hubbard, J.: Proc. Roy. Soc. Lond. **A276**, 238 (1963)
30. Landau, L.D., Lifshitz, E.M.: Statistical Physics, Part I. Butterworth-Heinemann, Oxford (1999)
31. Kagan, MYu., Fresard, R., Capezzali, M., Beck, H.: Phys. Rev. B **57**, 5995 (1998)
32. Kagan, MYu., Fresard, R., Capezzali, M., Beck, H.: Phys. B **284–288**, 447 (2000)
33. Combescot, R., Leyronas, X., Kagan, M.Yu.: Phys. Rev. A **73**, 023618 (2006)
34. Greiner, M., Mandel, O., Esslinger, T., Hänsch, T.W., Bloch, I.: Nature **415**, 39 (2002)
35. Ranninger, J., Robaszkiewicz, S.: Phys. B **53**, 468 (1985)
36. Gurarie, V., Radzihovsky, L.: Ann. Phys. (Weinheim) **322**, 2 (2007)
37. Landau, L.D., Lifshitz, E.M.: Electrodynamics of Continuous Media. Pergamon, New York (1984)
38. Migdal, A.B.: Qualitative Methods in Quantum Theory. Westview Press, New York (2000)
39. Ruprecht, P.A., Holland, M.J., Burnett, K., Edwards, M.: Phys. Rev. A **51**, 4704 (1995)
40. Abraham, E.R.I., McAlexander, W.I., Gerton, J.M., Hulet, R.G., Cote, R., Dalgarno, A.: Phys. Rev. A **55**, R3299 (1997)
41. Inouye, S., Andrews, M.R., Stenger, J., Miesner, H.-J., Stamper-Kurn, D.M., Ketterle, W.: Nature **392**, 151 (1998)
42. Timmermans, E., Tommasini, P., Hussein, M., Kerman, A.: Phys. Rep. **315**, 199 (1999)
43. Donley, E.A., Claussen, N.R., Thompson, S.T., Wieman, C.E.: Nature **417**, 529 (2002)
44. Kokkelmans, S.J.J.M.F., Milstein, J.N., Chiofalo, M.L., Walser, R., Holland, M.J.: Phys. Rev. A **65**, 053617 (2002)
45. Kokkelmans, S.J.J.M.F., Holland, M.J.: Phys. Rev. Lett. **89**, 180401 (2002)
46. Takekoshi, T., Debatin, M., Rameshan, R., Ferlaino, F., Grimm, R., Nägerl, H., Ruth Le Sueur, C., Hutson, J.M., Julienne, P.S., Kotochigova, S., Tiemann, E.: Phys. Rev. A **85**, 032506 (2012)
47. Satija, I.I., Zhao, E.: arXiv:1201.1458v1 (2012)

48. Inouye, S., Goldwin, J., Olsen, M.L., Ticknor, C., Bohn, J.L., Jin, D.S.: Phys. Rev. Lett. **93**, 183201 (2004)
49. Regal, C.A., Greiner, M., Jin, D.S.: Phys. Rev. Lett. **92**, 040403 (2004)
50. Stan, C.A., Zwierlein, M.W., Schunck, C.H., Raupach, S.M.F., Ketterle, W.: Phys. Rev. Lett. **93**, 143001 (2004)
51. Parish, M.M., Mihaila, B., Simons, B.D., Littlewood, P.B.: Phys. Rev. Lett. **94**, 240402 (2005)
52. Simonucci, S., Pieri, P., Strinati, G.C.: Europhys. Lett. **69**, 713 (2005)
53. Feshbach, H.: (1962) Ann. Phys. **5**, 357 (1958); ibid **19**, 287 (1962)
54. Fano, U.: Nuovo Cimento **12**, 156 (1935)
55. Fano, U.: Phys. Rev. **124**, 1866 (1961)
56. Ranninger, J., Micnas, R., Robaszkiewicz, S.: Ann. Phys. **13**, 455 (1988)

Chapter 6
Composed Particles, Trios and Quartets in Resonance Quantum Gases and Mixtures

In the beginning of this chapter we consider two-boson pairing for bosons of the same (bb) or different (b_1b_2) sorts. The two-boson pairing was first proposed by Nozieres and Saint James in their famous paper [1]. Here we consider Bose-gas with van der Waals interacting potential between particles and the two-band Hubbard model with attraction between bosons of different sorts [2–4] and repulsion between bosons of the same sort. We also discuss a competing (to two-boson pairing) phenomena of phase-separation in one band and two-band [2–7] bosonic models. In the end of the first section we consider briefly the possibility of two-holon pairing which arises in the 2D underdoped t-J model if we assume the scenario of spin-charge separation between spinons and holons advocated by Anderson [8, 9] and Lee [10].

The second section will be devoted to the model of Fermi-Bose mixture with attractive interaction between fermions and bosons [11–14] and the possibility to get composed fermions $f_\sigma b$ in this model. Note that the attraction between fermions and bosons is opposite to the Fermi-Bose mixtures of ^{3}He and ^{4}He [7, 96, 97] or ^{6}Li and ^{7}Li [15] (which will be considered in more details in Chaps. 11 and 12). In these systems usually the interaction between fermions and bosons is repulsive. The Feshbach resonance effect helps to change the sign of fermion-boson interaction [17].

In the next sections we will consider 3 and 4-particle complexes which can appear in resonance Fermi-Bose-gases and mixtures, where the scattering length a is much larger than the range of the potential r_0. At first we will consider the scattering amplitude a_{2-1} for the scattering of elementary fermion f_σ on the composed boson $f_\uparrow f_\downarrow$. Here we will present exact solution of Skorniakov-Ter-Martirosian integral equation for three particles in resonance approximation and get $a_{2-1} = 1.18|a| > 0$ [18], which corresponds to repulsion between fermion and molecule (dimer). We also consider so-called Efimov effect [16, 90] which predicts a lot of bound states for three bosons bbb in a 3D case with the energies ranging from $|E_3| \approx 1/ma^2$ for shallow levels till $|E_3| \approx 1/mr_0^2$ for deep three-particle levels. The number of levels in the resonance approximation $a \gg r_0$ is governed by $N \sim \frac{1}{\pi}\ln\frac{a}{r_0}$ in 3D [19]. We will show also that Efimov effect is absent in 2D case [20] and thus the number of

M. Yu. Kagan, *Modern Trends in Superconductivity and Superfluidity*,
Lecture Notes in Physics 874, DOI: 10.1007/978-94-007-6961-8_6,

bound states for three bosons bbb [21] or two bosons and one fermion bbf_σ is finite. Moreover all of them have the energies of the order of $|E_b| = 1/ma^2$. Thus all 3-particle levels in 2D case are shallow (or quasiresonance) in origin.

We proceed than to the 4-particle problem. At first we solve Skorniakov-Ter-Martirosian equations 4 fermions [18, 22] and find the scattering length a_{2-2} [23–25] for dimer–dimer scattering (for scattering of one molecule $f_\uparrow f_\downarrow$ on one the other). Here in the resonance approximation we get an exact result $a_{2-2} = 0.6|a| > 0$ which is different from mean-field result $a_{2-2} = 2|a|$ and from the result of the ladder approximation of Pieri and Strinati [26] which predicts $a_{2-2} = 0.75|a|$ if we neglect the dynamics (the possibility for two molecules to form virtual states with 3 and 1 particle [23–25]).

We also discuss the shallow bound states for 4 bosons [27], 3 bosons and 1 fermion and 2 bosons and 2 fermions in 2D case where Efimov effect is absent. Note that all the binding energies of the 4-particle complexes can be expressed in terms of $|E_b| = 1/ma^2$ only in 2D [20, 28].

In the end of the chapter we discuss the importance of the obtained results for the phase diagram and life-time of ultracold Fermi-Bose-gases and mixtures. In particular we use the value of a_{2-1} to estimate the inelastic scattering time in the resonant Fermi-gas [29] and 4-particle binding energies E_4 to complete phase diagram of the resonance Fermi-Bose mixture with attraction between fermions and bosons. Here we pay a special attention on the complexes $(f_\uparrow b, f_\downarrow b)$ formed by two composed fermions $f_\sigma b$ and stress the analogy between ultracold Fermi-Bose mixtures in magnetic traps and strongly-interacting mixture of spinons and holons in underdoped high-T_C compounds in the framework of Laughlin ideas [30–32] on spin-charge confinement. According to Laughlin, the spinons and holons experience the phenomenon of spin-charge confinement in analogy with the confinement [33] in quark-gluon plasma (in quark bags) in QCD-physics [32, 33, 35]. We think [36] that for strongly-correlated quasi-2D (layered) cuprates the philosophy of Laughlin is more adequate that the philosophy of Anderson and Lee [8–10] on spin-charge separation, which is based on the analogy with 1D-physics. We emphasize that due to linear (string-like) confinement potential between spinons $f_{i\sigma}$ and holons b_i [37–39], the composite hole $h_{i\sigma} = f_{i\sigma} b_i$ is formed on the lattice. It represents a compact object (a bag or spin-polaron [40]). The Cooper pairs in this system are formed by the residual (dipole–dipole) interaction [40] between two composite holes and effectively represent 4-particle complex [6, 18, 23, 25, 41], consisting of two spinons and two holons. Thus the superconductive gap reads $\Delta_{ij} = \langle h_{i\sigma} h_{j-\sigma} \rangle = \langle f_{i\sigma} b_i, f_{j-\sigma} b_j \rangle$. It is formed by two composite holes on the lattice with a total spin $S_{tot} = 0$ of a pair. We will consider these ideas more detaily in Chap. 13 on the basis of 2D t-J model and advocate the scenario of BCS-BEC crossover in the d-wave channel for pairing of two composite holes (two strings or two spin polarons) in underdoped cuprates.

We stress also the importance of dimer–dimer amplitude a_{2-2} for the phase-diagram of the BCS-BEC crossover and the spectrum of collective excitations in resonance Fermi-gas. We will consider these properties in detail in Chap. 7.

Note that the creation of three and four particle complexes, as well as the evaluation of different scattering amplitudes, for the two-particle potentials $V(r) = \alpha r^{\delta} + \frac{\beta}{r^{\gamma}}$; $1 \leq \{\delta, \gamma\} \leq 2$, which are the sum of confinement and Coulomb (or dipolar) parts, play an important role in the non-relativistic problem for baryons [43] and in Quantum Chromodynamics [44], especially when the problems of inhomogeneous superconductivity are studied in the QCD theory at zero temperature. Note that the potentials $V(r) = \alpha r^2 + \frac{\beta}{r^2}$ ($\delta = \gamma = 2$) allow also for exact solutions at least on the level of the two-particle problem. The creation of three and four particle complexes was also predicted for the quark-gluon plasma in the high-temperature limit. This limit can be realized experimentally in heavy ion collisions. Here three and four particle complexes can be formed on the way from a gas to a liquid in the hydrodynamic regime for the quark-gluon plasma (see [101] and references therein).

6.1 Two-Particles Pairing and Phase-Separation in Bose-Gas with One or Two Sorts of Bosons

As we already discussed in Chap. 5, in contrast with two-particle Cooper pairing in Fermi-systems (see Chaps. 9–12), the essence of a superfluidity is Bose-systems is one-particle Bose–Einstein condensation (BEC). This asymmetry between Fermi and Bose (two-particle versus one-particle condensation) was challenged in a pioneering paper by Valatin and Butler [45]. They proposed a BCS-like variational function for the description of an attractive Bose-gas. The most difficult problem with the validity of their description is connected with the tendency towards phase separation which arises in attractive Bose systems. Later on Nozieres and Saint-James [1] conjectured that in a Bose-system with a short-range, hard-core repulsion and a van der Waals attractive tail, in principle, it is possible to create a two-particle bosonic bound state and to escape collapse. Unfortunately their calculations in three-dimensional (3D) systems showed that, at least for one sort of structureless boson, either standard one-particle BEC is more energetically beneficial, or that a phase separation takes place earlier than the two-particle condensation. Note that the same result was obtained earlier by Iordanskii [46] for the case of weak van der Waals attraction.

The important development of the ideas of Nozieres and Saint James belongs to Rice and Wang [47]. These authors claimed that in two dimensions (where already an infinitely small attraction leads to the bound state in a symmetrical potential well) it is possible to realize a two-particle boson pairing. Moreover, this two-particle pairing results, for small momenta $q\xi_0 < 1$ (ξ_0 is a coherence length) in a linear, soundlike, dispersion law of quasiparticles at $T = 0$ in an analogy with a standard one-particle Bose-condensation for weakly repulsive Bogoliubov Bose-gas.

To escape a collapse in a 2D attractive Bose-gas, the authors of [47] introduced in their model a Hartree–Fock shift of the chemical potential $\mu_B \sim Un$, connected

with the short-range repulsion U. This shift in the case of $U > 2V$, where V is the magnitude of the van der Waals tail, leads to a positive compressibility in the system $\kappa^{-1} = \mathrm{d}\mu_{\mathrm{B}}/\mathrm{d}n = U - 2V > 0$.

The main goal of this section is to construct a phase diagram of a 2D dilute Bose-gas with the van der Waals interaction between particles, by taking into account on equal grounds the full contribution of a hard-core repulsion U and a van der Waals tail V (see [2–4]). Throughout the paper we will consider the lattice model, and will base our results on the exact solution of the two-particle T-matrix problem presented in [48, 49] in connection with a fermionic t-J model (see Chap. 13). Note that effectively a lattice model with van der Waals interaction between bosons is a bosonic analog of a famous fermionic t-J model considered in Chap. 13 for high-T_{C} systems. We will study the possibility of different two-boson pairings, as well as the possibility of a total phase separation in the system. We will also consider the two sorts of structureless bosons described by the two-band bosonic Hubbard model [50–55] (note that fermionic one-band and two-band Hubbard models [57] are considered in Chaps. 8, 9, 10). In the case of attraction between bosons of two different sorts, we will find a possibility of an s-wave two-boson pairing $\langle b_1 b_2 \rangle \neq 0$.

6.1.1 Lattice Model with van der Waals Interaction Between Bosons

The model under consideration is described by the following Hamiltonian on the 2D square lattice [2–4]:

$$\hat{H} = -t \sum_{<ij>} b_i^{+} b_j + \frac{U}{2} \sum_i n_i^2 - \frac{V}{2} \sum_{\langle ij \rangle} n_i n_j, \tag{6.1.1}$$

where $n_{\mathrm{i}} = b_{\mathrm{i}}^{+} b_{\mathrm{i}}$ is a 2D boson density on site i. We will work in the limit of strong hard-core repulsion $U \gg \{V; t\}$, and restrict ourselves mostly to a low-density limit which in the lattice case yields $n_{\mathrm{B}} d^2 \ll 1$, d being the interatomic distance. In (6.1.1) t is hopping integral for bosons, $\langle ij \rangle$ are nearest lattice sites on the square lattice, V is van der Waals attraction on neighboring sites, U is onsite repulsion, b_{i}^{+} and b_{i} are bosonic creation and annihilation operators on site i of the lattice. Note that in the case of $V = 0$, the model (6.1.1) is just the Bose-Hubbard model, extensively studied in the literature for the case of 2D ^{4}He submonolayers, as well as for the flux lattices and Josephson arrays in the type-II superconductors (see [50–55]). As we already mentioned in the introduction to this section, a model (6.1.1) is, to some extent, a Bose analog of the fermionic t-J model considered by Kagan and Rice in [49]. After Fourier transformation from (6.1.1) we obtain:

$$\hat{H} = \sum_p \varepsilon_p b_p^{+} b_p + \frac{U}{2} \sum_{k_1 k_2 q} b_{k_1}^{+} b_{k_2}^{+} b_{k_2 - q} b_{k_1 + q} - \sum_{k_1 k_2 q} V(q) b_{k_1}^{+} b_{k_1 + q} b_{k_2}^{+} b_{k_2 - q}, \tag{6.1.2}$$

where $\varepsilon_p = -2t(\cos\, p_x d + \cos\, p_y d)$ is an uncorrelated bosonic spectrum on the square lattice, and $V(q) = V[\cos\, q_x d + \cos\, q_y d]$ is a Fourier transform of the van der Waals tail. As a result, a total interaction in the momentum space is given by the formula:

$$V_{eff}(q) = \frac{U}{2} - V(q). \tag{6.1.3}$$

6.1.2 Two-Particle T-Matrix Problem

An instability toward a two-particle boson pairing manifests itself (just as in the case of Cooper pairing of two fermions in Chaps. 5 and 9) in the appearance of a pole at a temperature $T = T_C$ in the solution of the Bethe–Salpeter equation for the two-particle vertex Γ for zero total momentum of the two bosons ($\vec{p}$ and $-\vec{p}$) (see [2–4, 56]). To proceed to the solution of this equation, we must solve at first the T-matrix problem [58] for the two bosonic particles in vacuum. Here we can use the results of [49] (for the T-matrix for two fermions), since the solution of the two-particle problem does not depend upon statistics of colliding particles. For the T-matrix problem it is convenient to expand $V_{\text{eff}}(q)$ in (6.1.3) with the eigenfunctions of the irreducible representation of the lattice symmetry group D_4 (see also Chaps. 9 and 13). This yields:

$$\begin{aligned} V_{eff}(\text{extended s} - \text{wave}) &= \frac{U}{2} - \frac{V}{2}(\cos p_x d + \cos p_y d)(\cos p'_x d + \cos p'_y d); \\ V_{eff}(\text{p} - \text{wave}) &= -\frac{V}{2}(\sin p_x d \sin p'_x d + \sin p_y d \sin p'_y d); \\ V_{eff}(\text{d} - \text{wave}) &= -\frac{V}{2}(\cos p_x d - \cos p_y d)(\cos p'_x d - \cos p'_y d), \end{aligned} \tag{6.1.4}$$

where we use the functions $\varphi_{\text{S}} = (\cos\, p_x d + \cos\, p_y d)$, $\varphi_{\text{p}} = (\sin\, p_x d + i \sin\, p_y d)$ and $\varphi_{\text{d}} = (\cos\, p_x d - \cos\, p_y d)$ respectively for extended s-wave, p-wave and d-wave channels on the square lattice.

Note that, for spinless bosons, which we formally consider in (6.1.1), the total spin of the Bose pair is zero ($S_{\text{tot}} = 0$). Hence only s-wave ($l = 0$ in the absence of lattice) and d-wave ($l = 2$ in the absence of lattice) pairings are allowed by the symmetry of the pair Ψ-function. A p-wave pairing ($l = 1$ in the absence of lattice) is allowed only for an odd total spin ($S_{tot} = 1, 3 \ldots$) of the two bosons (the total pair Ψ-function which is product of orbital part and spin part is symmetric for two bosons). Nevertheless we will conserve the results for the p-wave pairing in our paper because the generalization of (6.1.1) for the case of bosons with internal degrees of freedom is straightforward. The T-matrix problems for p- and d-wave

channels are very simple. Solutions of these problems for the two particles with a total momentum zero and a total energy E yield:

$$T_{d,p}(E) = -\frac{\frac{V}{2}}{1+\frac{V}{2}I_{d,p}}, \tag{6.1.5}$$

where

$$\begin{aligned} I_{d,p} &= \int_0^{2\pi/d}\int_0^{2\pi/d}\frac{dp_x}{2\pi}\frac{dp_y}{2\pi}\frac{\left|\varphi_{d,p}\right|^2}{E+4t(\cos p_x d+\cos p_y d)} \\ &= \int\frac{d\omega}{2\pi}\frac{d^2\vec{p}}{(2\pi)^2}G_0(\omega+E,\vec{p})G_0(-\omega,-\vec{p})\left|\varphi_{d,p}\right|^2, \end{aligned} \tag{6.1.6}$$

$G_0(\omega,\vec{p}) = \frac{1}{\omega-\varepsilon(p)+io}$ is vacuum Green function and $\varphi_{\mathrm{d,p}}$ are the functions for d-wave and p-wave channels.

6.1.3 *Thresholds for Extended S-Wave, P-Wave and D-Wave Two-Bosons Pairings*

Let us find the thresholds for the bound states in the extended s-wave, d-wave and p-wave channels. The appearance of a bound state means that $E = -W + \tilde{E}$ and $\tilde{E} < 0$, where $W = 2zt = 8t$ is a bandwidth for the 2D square lattice ($z = 4$ is a number of nearest neighbors on the square lattice). For the threshold $\tilde{E} = 0$. An exact solution of (6.1.5) and (6.1.6), which involves the calculation of elliptic integrals of first and second order (see [2–4, 49]), yields for p-wave and d-wave thresholds:

$$\begin{aligned} \left(\frac{V_C}{4t}\right)_{p-wave} &\approx \frac{1}{1-\frac{2}{\pi}} \approx 2.8, \\ \left(\frac{V_C}{4t}\right)_{d-wave} &\approx \frac{1}{\frac{4}{\pi}-1} \approx 3.7. \end{aligned} \tag{6.1.7}$$

Note that a threshold for a p-wave pairing is lower. Now let us proceed to an s-wave channel. Here an ordinary s-wave pairing is suppressed by large hard-core repulsion U, however an extended s-wave pairing with a symmetry of the order parameter $\Delta_S^{ex} = \Delta_0(\cos p_x d + \cos p_y d)$ is allowed (for ordinary s-wave pairing Δ_S is just Δ_0 and does not depend upon momentum $\vec{p}$). In real space this pairing corresponds to the particles on the neighboring sites. Moreover the pair Ψ-function is zero in the region of a hard core ($r < r_0$), and is centered (has a maximum) in the region of a van der Waals attraction for $r_0 < r < r_1$ (see Fig. 6.1). On the lattice $r_0 \sim d/2$ and $r_1 \sim d$ [2–4].

One can see that the Ψ-function has a region of zero values (for $r < r_0$). But it has no nodes because it does not change its sign for all values of r ($\Psi \geq 0$). The rigorous calculation of the threshold for an extended s-wave pairing yields [2–4, 48, 49]:

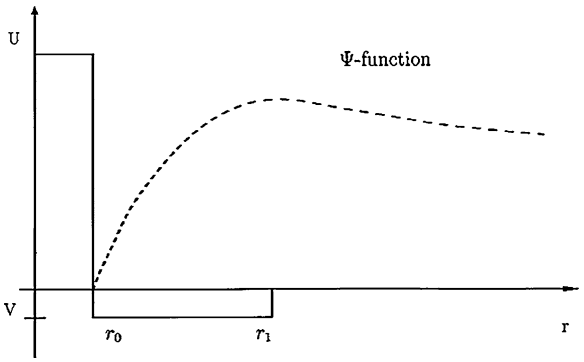

Fig. 6.1 The Ψ-function of an extended s-wave pairing. r_0 is the radius of the hard core repulsion, and r_1 is the radius of the van der Waals attraction. On the lattice, $r_0 \sim d/2$ and $r_1 \sim d$ [2–4]

$$\left(\frac{V_C}{4t}\right)_{s-wave} = 1. \tag{6.1.8}$$

Thus the threshold for s-wave pairing is the lowest (compare with (6.1.7)). Moreover for $V > V_{CS} = W/2 = 4t$ an energy of the bound state has the form:

$$\left|\tilde{E}\right| = \left|\tilde{E}_b^S\right| = 8We^{-\frac{\pi V}{(V-V_{CS})}}. \tag{6.1.9}$$

Of course, in a strong coupling case (for $V \gg W$) $\left|\tilde{E}_b^S\right| \approx V$. Correspondingly, the bound states for p-wave and d-wave pairings yield [2–4, 49]:

$$\begin{aligned} \left|\tilde{E}_b^p\right| &= W\frac{(V - V_{Cp})}{V}\frac{1}{\ln\frac{V}{|V-V_{Cp}|}} \quad \text{for } V > V_{Cp} \approx 1.4W; \\ \left|\tilde{E}_b^d\right| &= W\frac{(V - V_{Cd})}{V} \quad \text{for } V > V_{Cd} \approx 1.85W. \end{aligned} \tag{6.1.10}$$

We can see that for $V \gg W$: $\left|\tilde{E}_b^S\right| \approx V$ while $\left|\tilde{E}_b^p\right| \sim \left|\tilde{E}_b^d\right| \sim W$, and extended s-wave bound state correspond to a global minima in agreement with general theorems of quantum mechanics $\left(\left|\tilde{E}_b^s\right| > \left|\tilde{E}_b^p\right| > \left|\tilde{E}_b^d\right| \text{for fixed } V > V_{Cd} > V_{Cp} > V_{Cs}\right)$.

The T-matrix in an s-wave channel for small and intermediate values of V is given by [2–4, 49]:

$$T_S(|\tilde{E}|) = \frac{W(1 - V/4t)}{\frac{1}{\pi}(1 - V/4t)\ln\frac{8W}{|\tilde{E}|} - \frac{V}{4t}}. \tag{6.1.11}$$

The most important is that a strong Hubbard repulsion U acts only as an excluded volume (for $r < r_0 \sim d/2$), and effectively drops out from (6.1.11) at low energies. It manifests itself only as an additional pole (at very large energies $E \approx U > 0$) in total analogy with antibound state [59–61] in fermionic Hubbard model (it will be considered in Chap. 14). For $V \ll 4t$ the T-matrix:

$$T_S(|\tilde{E}|) \approx \frac{\pi W}{\ln \frac{8W}{|\tilde{E}|}}, \tag{6.1.12}$$

corresponds to repulsion and coincides with the T-matrix for the 2D Bose-Hubbard model at low density. The same T-matrix was obtained by Fukuyama et al., for 2D fermionic Hubbard model at low density [100]. For $V = 4t$: $T_S|\tilde{E}| = 0$ and there is no interaction at all. Finally, for $V > 4t$, $T_S(|\tilde{E}|) <; 0$ corresponds to an attraction and reflects the appearance of the bound state [2–4, 49].

6.1.4 Bethe–Salpeter Integral Equation for S-Wave Pairing of Two Bosons

Let us consider at first the most interesting case of $V > 4t$ and find the critical temperature for an extended s-wave pairing of the two bosons. The solution of the Bethe–Salpeter equation for bosonic systems reads [2–4, 62], (see Ref. [32] in Chap. 4):

$$\Gamma_s = \frac{T_s}{1 + T_s \iint \frac{dp_x dp_y}{(2\pi)^2} \frac{cth\frac{\varepsilon_p - \mu}{2T}}{2(\varepsilon_p - \mu)}}, \tag{6.1.13}$$

where T_s is a T-matrix for s-wave pairing and Γ_s is an s-wave harmonic of the total two-particle vertex Γ in the Cooper channel (for zero total momentum $\vec{P} = \vec{p}_1 + \vec{p}_2 = 0$ and zero total Matsubara frequency $\Omega = \Omega_1 + \Omega_2 = 0$ of the two incoming particles—see Chaps. 5 and 9 also for the case of two fermions). For low density of bosons $n_B d^2 \ll 1$ one has, $\varepsilon_p = -\frac{W}{2} + \frac{p^2}{2m}$, $\mu = -4t + \tilde{\mu}$, and $\xi_p = \varepsilon_p - \mu = \frac{p^2}{2m} - \tilde{\mu}$ for the uncorrelated quasiparticle spectrum counted from the chemical potential level.

The most substantial difference of (6.1.13) from an analogous equation for two fermions is the replacement of $th\frac{\xi_p}{2T}$ by $cth\frac{\xi_p}{2T}$ in its kernel. Moreover, as shown by Miyake in [63] for the 2D attractive Fermi gas $\tilde{\mu} = \varepsilon_F - \frac{|E_b|}{2}$ (where $|E_b|$ is an absolute value of the binding energy of a pair in vacuum). So, in a weak-coupling case, when $\varepsilon_F \gg |E_b|$, the chemical potential $\tilde{\mu} \approx \varepsilon_F > 0$ is positive. In contrast to this, we shall see below that a bosonic chemical potential $\tilde{\mu}$ is always negative even in the weak-coupling case, when a binding energy is much smaller than a degeneracy temperature $|E_b| < T_0 = \frac{2\pi n}{m}$.

Another very important point (see also Chaps. 9 and 13) is that the T-matrix, which enters into the Bethe–Salpeter equation, must be calculated for a total energy $\tilde{E} = 2\tilde{\mu}$ by [2–4, 49] of colliding bosons. The chemical potential $\tilde{\mu}$ can be determined from the requirement of the number of particle conservation. This requirement yields:

$$n_B = \iint \frac{d^2\vec{p}}{(2\pi)^2} \frac{1}{\exp\left\{\frac{p^2/2m-\tilde{\mu}}{T}\right\} - 1}. \tag{6.1.14}$$

From (6.1.14) for the temperatures $|E_b| < T < T_0 < W$ we obtain:

$$\tilde{\mu} = -T \exp\left(\frac{T_0}{T}\right) < 0. \tag{6.1.15}$$

Note that a standard Hartree–Fock shift nU drops out from the expression for bosonic quasiparticle spectrum $\xi_p = \varepsilon_p - \mu$ both in the Bethe–Salpeter equation (6.1.13) and in the equation for the number of particle conservation (6.1.14) in similarity with a fermionic problem. Now we are ready to solve the Bethe–Salpeter equation (6.1.14). The critical temperature T_C corresponds to the pole in (6.1.13),

$$1 + \frac{md^2 T_s(2\tilde{\mu})}{2\pi} I = 0, \tag{6.1.16}$$

where

$$I = \int_0^{\sim W/T_C} \frac{dy\, cth\left(y + \frac{|\tilde{\mu}|}{2T_C}\right)}{y + \frac{|\tilde{\mu}|}{2T_C}} \tag{6.1.17}$$

and $y = \frac{p^2}{4mT_C}$.

An analysis of (6.1.17) shows that the main contribution to the integral comes from the lower limit of integration.

Hence providing $|\tilde{\mu}|/T_C \ll 1$ we have:

$$I \approx \int_0^{W/T_C} \frac{dy}{\left(y + \frac{|\tilde{\mu}|}{2T_C}\right)^2} \approx \frac{2T_C}{|\tilde{\mu}|}. \tag{6.1.18}$$

As a result (6.1.18) can be represented in the following form:

$$\frac{T_C}{|\tilde{\mu}|} = -\frac{\pi}{md^2 T_s(2\tilde{\mu})}. \tag{6.1.19}$$

It is useful now to represent $T_s(2\tilde{\mu})$ in terms of the binding energy E_b. Utilizing (6.1.9) and (6.1.11) we can write:

$$T_S(2\tilde{\mu}) = -\frac{\pi W}{\ln\frac{2|\tilde{\mu}|}{|E_b|}} = -\frac{4\pi}{md^2 \ln\frac{2|\tilde{\mu}|}{|E_b|}}. \tag{6.1.20}$$

It is important to mention here that $\tilde{\mu} < 0$, and hence the T-matrix in (6.1.20) does not contain an imaginary part. In the fermionic case $\tilde{\mu} \approx \varepsilon_F > 0$, and the T-matrix contains an imaginary part corresponding to the resonant scattering. As a result, from (6.1.20) we obtain:

$$4ln\frac{2|\tilde{\mu}|}{|E_b|}=\frac{\tilde{\mu}}{T_C} \tag{6.1.21}$$

Assuming that $|E_b| \ll T_C \ll T_0$, we get (see also Chap. 8): $\tilde{\mu}(T_C) = -T_C \exp\left(\frac{T_0}{T_C}\right)$ and $\frac{|\tilde{\mu}|}{T_C} = \exp\left(-\frac{T_0}{T_C}\right)$.

Later on we will justify this assumption.

As a result from (6.1.21) we will obtain:

$$T_C = \frac{T_0}{\ln\left(\frac{1}{4}\ln\frac{2|\tilde{\mu}|}{|E_b|}\right)}. \tag{6.1.22}$$

Recall that in the case of the fermionic s-wave pairing in two dimensions a critical temperature according to Miyake [63] (see also Chap. 8) reads: $T_C = \sqrt{2\varepsilon_F|E_b|}$.

Let us analyze expression (6.1.22). As we already know $|E_b| = 8We^{-\frac{1}{\lambda}}$, where

$$\lambda = \frac{(V - V_{Cs})}{\pi V}. \tag{6.1.23}$$

Then a condition $|E_b| \ll T_0$ means:

$$\lambda \ll \frac{1}{\ln\frac{W}{T_0}} \ll 1. \tag{6.1.24}$$

Hence $\ln(T_0/|E_b|) = 1/\lambda - \ln(W/T_0) \approx 1/\lambda$, and

$$T_C \approx \frac{T_0}{\ln\left(\frac{1}{4}\ln\frac{T_0}{|E_b|}\right)} \approx \frac{T_0}{\ln\left(\frac{1}{4\lambda}\right)}, \tag{6.1.25}$$

which is in an agreement with [47]. Note that T_C from (6.1.25) satisfies the conditions $|E_b| \ll T_C \ll T_0$, so an assumption used for the derivation of T_C is justified.

For $T < T_C$ the spectrum of the quasiparticles acquires a gap:

$$E_p = \sqrt{\left(\frac{p^2}{2m} + |\tilde{\mu}|\right)^2 - \Delta^2}. \tag{6.1.26}$$

Note that at low densities of bosons a gap Δ becomes isotropic in the principal approximation.

The gap Δ together with the chemical potential $\tilde{\mu}$ must be defined self-consistently from the two coupled equations:

$$1 = \frac{\lambda}{4} \int\limits_{|\tilde{\mu}|/2T}^{\sim W/2T} \frac{dz\, cth\sqrt{z^2 - \Delta^2/4T^2}}{\sqrt{z^2 - \Delta^2/4T^2}}, \tag{6.1.27}$$

and

$$n_B = \frac{\lambda}{4} \int\limits_{|\tilde{\mu}|}^{\sim W} d\xi \frac{1}{\exp\left\{\frac{\sqrt{\xi^2 - \Delta^2}}{T}\right\} - 1}, \tag{6.1.28}$$

where $\xi_p = \frac{p^2}{2m} + |\tilde{\mu}|$ and $z = \xi/2T$.

Of course, the solution of the system of Eqs. (6.1.27) and (6.1.28) exists only if $|\tilde{\mu}| > \Delta$, or, in other words, only if $E_p^2 = |\tilde{\mu}|^2 - \Delta^2 > 0$. The exact solution of these equations yields for zero temperature in an agreement with [47]:

$$|\tilde{\mu}(T = 0)| = \Delta = \frac{|E_b|}{2}. \tag{6.1.29}$$

This result is very important. It justifies our scenario, leading to a linear, soundlike spectrum of the quasiparticles for a small momenta p. Indeed,

$$E_p = \sqrt{\left(\frac{p^2}{2m}\right)^2 + \frac{p^2}{m}|\tilde{\mu}|} = \sqrt{\left(\frac{p^2}{2m}\right)^2 + \frac{p^2}{2m}|E_b|}. \tag{6.1.30}$$

From (6.1.30) for the case $p\xi_0 \ll 1$, where $\xi_0 = \frac{1}{\sqrt{2m|E_b|}}$ is the coherence length of the boson pair, we immediately obtain a linear dispersion law:

$$E_{\mathrm{p}} = cp. \tag{6.1.31}$$

In (6.1.31) $c^2 = \frac{|E_b|}{2m}$ is a sound velocity squared. This means that an inverse compressibility of the system $\kappa^{-1} \sim c^2$ is positive. This fact proves the stability of a superfluid paired state and excludes the possibility of the collapse of the pairs in the system. Note also that close to T_{C} one has:

$$\Delta(T) \approx \Delta(0)\sqrt{\frac{T_C - T}{T_C}}, \tag{6.1.32}$$

which is similar to the BCS theory. We would like to mention that bosonic pairs in the limit $|E_b| \ll T_0$ are extended in full analogy with the BCS theory. That is, the coherence length in this limit,

$$\xi_0 \gg \frac{1}{\sqrt{n}} \gg 1 \tag{6.1.33}$$

is larger than the mean distance between the bosons. The Bose pairs are strongly overlapping in this limit. The pairing takes place in the momentum space in an analogy with the Cooper pairing in the BCS picture of superconductivity.

In the opposite limit $|E_b| \gg T_0$ the pairs are local and the situation closely resembles BEC (or bipolaronic) limit for the fermionic systems [64, 65]. That is, the creation of the bosonic bound pairs is associated with the crossover temperature [2–4]:

$$T_* = \frac{|E_b|}{\ln 1/nd^2}. \tag{6.1.34}$$

The Bose condensation of the pairs occurs at lower temperature [66, 67]:

$$T_C = \frac{T_0}{\ln\ln(1/nd^2)}. \tag{6.1.35}$$

Note that this temperature is obtained in Fisher-Hohenberg theory [66] from the ansatz $\tilde{\mu}(T_C) = -T_C \exp(-T_0/T_C) + f_0 T_0 = 0$, where $f_0 = 1/\ln(1/nd^2)$ is a repulsive interaction between the local pairs and $f_0 T_0$ is a Hartree–Fock contribution to the chemical potential μ_B in 2D repulsive Bose-gas. Thus the superfluid transition takes place only in the case of a residual repulsion between the pairs. Also note that in a dilute Bose-gas in 2D the Berezinskii-Kosterlitz-Thouless (BKT) contribution of vortices [68, 69] is important only very close to T_C, so the mean field expression (6.1.35) gives a very good estimate for the exact BKT critical temperature: $\frac{T_C - T_{BKT}}{T_C} \sim \frac{1}{\ln\ln(1/nd^2)} \ll 1$ [66, 67].

In the case of the local pairs the coherence length is small:

$$\xi_0 \ll \frac{1}{\sqrt{n}}. \tag{6.1.36}$$

The pairs are compact, and the pairing takes place in the real space.

6.1.5 *Possibility of p-Wave and d-Wave Pairing of Two Bosons*

Now let us analyze the solution of the Bethe–Salpeter equation for p- and d-wave two-boson pairings. Here the critical temperatures should be found from the conditions (see [2–4, 49]):

$$1 + T_{p,d}(2\tilde{\mu})\tilde{I}_{p,d} = 0, \tag{6.1.37}$$

where

$$\tilde{I}_{p,d} = \int_0^{2\pi/d} \int_0^{2\pi/d} \frac{dp_x dp_y}{(2\pi)^2} \frac{cth\frac{\varepsilon-\mu}{2T_c}}{2(\varepsilon-\mu)} \left|\varphi_{p,d}\right|^2. \tag{6.1.38}$$

In a low-density limit the φ-functions can be approximated by the following expressions [2–4, 49, 70]:

$$\varphi_p = (p_x + ip_y)d = pde^{i\varphi};$$
$$\varphi_d = \frac{1}{2}(p_x^2 - p_y^2)d^2 = \frac{1}{2}p^2d^2\cos 2\varphi.$$

Hence after an angular integration we obtain:

$$\tilde{I}_p = \frac{m}{2\pi}\int p\,dp \frac{cth\frac{\xi_p}{2T_C}}{2\xi_p} p^2d^2;$$
$$\tilde{I}_d = \frac{m}{16\pi}\int p\,dp \frac{cth\frac{\xi_p}{2T_C}}{2\xi_p} p^4d^4, \tag{6.1.39}$$

where again $\xi_p = \frac{p^2}{2m} + |\tilde{\mu}|$.

Additional factors p^2d^2 and p^4d^4 in the integral expressions for $\tilde{I}_p$ and $\tilde{I}_d$ reflect a well-known fact, that for slow 2D particles in vacuum an s-wave harmonics of the scattering amplitude behaves as $f_0 \sim \ln(1/p^2d^2)$, whereas for a magnetic number $m \neq 0$, the scattering amplitude vanishes for p goes to zero as $f_{\mathrm{m}} \sim (pd)^{2\mathrm{m}}$ (see Quantum mechanics [26] in Chap. 5). The additional factor p^4d^4 leads to the absence of an infra-red singularity for $\varepsilon \to 0$ in $\tilde{I}_d$:

$$\tilde{I}_d \sim \int \frac{d\varepsilon \cdot \varepsilon^2}{\varepsilon^2} \sim \varepsilon \to 0 \quad \left(\varepsilon \sim \frac{p^2}{2m}\right). \tag{6.1.40}$$

For the p-wave channel the infra-red singularity becomes logarithmically weak:

$$\tilde{I}_p \sim \int \frac{d\varepsilon \cdot \varepsilon}{\varepsilon^2} \sim \ln\varepsilon. \tag{6.1.41}$$

This means that the Bethe–Salpeter equation has no solutions in the p- and d-wave channels for $|V|/t < 1$.

Hence the boson pairing with a large coherence length $\xi_0 > \frac{1}{\sqrt{n}}$ is absent in a p-wave channel as well as in a d-wave channel. Here only the limit of the local pairs is possible. For p- and d-wave channels local pairs are created at the crossover (Saha) temperature T_* [2–4] given by (6.1.34), where binding energies $|E_{\mathrm{b}}^{\mathrm{p}}|$ and $|E_{\mathrm{b}}^{\mathrm{d}}|$ are given by (6.1.10) for $V > V_{\mathrm{Cp}}$ and $V > V_{\mathrm{Cd}}$ correspondingly. Remember that for a fixed $V > V_{\mathrm{Cd}} > V_{\mathrm{Cp}}$: $|E_{\mathrm{b}}^{\mathrm{p}}| > |E_{\mathrm{b}}^{\mathrm{d}}|$ and thus $T_*^p > T_*^d$. Providing that the interaction between the local pairs is repulsive in p-wave and d-wave channels, the

mean-field temperature of the Bose condensation of the local pairs should be determined again from the ansatz for the chemical potential $|\tilde{\mu}(T_C)|$ with an account of the repulsive Hartree–Fock shifts in p-wave and d-wave channels (see [66]). In the next section we will show, however, that in the van der Waals model (6.1.2) there is a competing phenomenon of the total phase separation which takes place earlier (at smaller values of V/t) than binding in different (s-wave, p-wave, d-wave channels). Thus it is difficult to get two-boson pairing in the present model.

6.1.6 Total Phase Separation

As we discussed in Sect. 6.1.1, the real collapse is prohibited in our system by large Hubbard repulsion U. However, the phase separation on the two large clusters is allowed. The first cluster corresponds to the Mott–Hubbard [57, 71] Bose solid. In this cluster $n_b d^2 \to 1$, that is, each site on the quadratic lattice is practically occupied by one boson. Such a cluster is localized due to Mott–Hubbard consideration for large $U \gg W$ (where W is a bandwidth). It has no kinetic energy. However, it has a potential energy of the order of $-2V$ for one particle. A second cluster has a very small boson density $n_b d^2 \to 0$. In this cluster for $V < 4t$ the energy per particle is $\varepsilon = -\frac{W}{2} + \frac{4\pi}{m} f_0 n$, where $f_0 = 1/\ln(1/nd^2)$ in the absence of a bound state. Rigorously speaking (see also Chaps. 13 and 15), at a given bosonic density n the phase separation (according to Maxwell construction) results in the formation of the two clusters with the densities $n_1 > n$ and $n_2 < n$ ([48, 49]), where $n_1 d^2$ is close to or identically equal to 1 (one boson per site). The phase separation for $V < 4t$ takes place if the energy per particle in the cluster with the density n_1 becomes smaller than the energy per particle in the cluster with the density n_2 [2–4],

$$-2\eta V \leq -\frac{W}{2}, \tag{6.1.42}$$

where η is an unknown numerical coefficient of the order of 1. Note that in the fermionic t-J model, considered in [48, 49] (see Chap. 13), the Mott–Hubbard cluster with $nd^2 = 1$ has an antiferromagnetic order for electrons with spins $S = ½$ on the square lattice. Hence instead of $2\eta V$ in (6.1.42) one should write $1.18\,J$—the energy per bond on 2D AFM square lattice. As a result (see Chap. 13) in a fermionic case $J_{ps} = 3.8t$. In our system $V_{ps} \approx 2t$, due to the absence of kinetic energy and zero point energy in the case of structureless bosons. In the same time in our case for $nd^2 \to 0$ the phase separation between the Bose solid (see Chap. 2) and the one-particle BEC takes place. According to Dagotto, Riera

et al. [72, 73] for $n_B d^2 \to 1$, the phase separation takes place already for small values of $|V|/t$.

In principle, another scenario of the phase separation connected with the creation of quartets [74] is also possible in our system. It requires an evaluation of the four-particle vertex which is often impossible to do analytically (except for the resonance approximation when the scattering length is much larger than intersite distance d—see the last part of the chapter). However, we think that our scenario of total phase separation takes place earlier, for smaller values of V/t than the quartet formation. This is in agreement with numerical calculations [72, 73] for the 2D fermionic t-J model on the square lattice.

6.1.7 Phase Diagram of the System

In this section we will complete the phase diagram of the system. At first, note that for $V < V_{ps}$ (when the T-matrix for an s-wave channel is repulsive) we have at low density a standard Bogoliubov Bose-gas with a hard-core repulsion. It will be unstable toward a standard one-particle BEC at a critical temperature given again by Fisher-Hohenberg type of formula [see (6.1.35)]. For $V > 2t$ a total phase separation on two large clusters takes place in our system. One of these clusters contains a Mott–Hubbard Bose-solid, another one contains a Bose-gas with one-particle condensation (see Fig. 6.2).

For large densities $n = n_C \leq 1$ ($n_C \equiv 1$ in [54, 55] for structureless bosons) the system will undergo a transition to the Mott–Hubbard Bose solid. As a result, on a qualitative level the phase diagram for our system has the form, presented in Fig. 6.3. Note that our model could be important for the study of the biexcitonic pairing in semiconductors [75, 76] (see also the end of the chapter). In this context we should mention the important results of Lozovik et al. [77]. It could be also important for the understanding of the physics of the gas of kinks and steps on a solid interface of ^{4}He (see Chap. 2). Note that if we change the sign of the nearest neighbors interaction V from attractive in the Hamiltonian (6.1.1) on repulsive, we will get a bosonic model with on-site and intersite repulsions, which gives a disproportionation (a density wave) in some range of parameters U, $|V|$, W and density $n_B d^2$ and can possibly serve as a simple toy model for bosonic

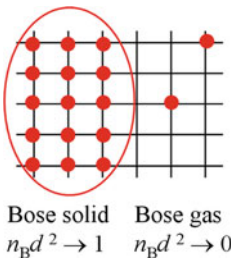

Fig. 6.2 Phase separation on two large clusters. First one corresponds to Bose solid with one boson per site $n_B d^2 \to 1$, the second one to dilute Bose-gas $n_B d^2 \to 0$ with repulsion between bosons [2–4]

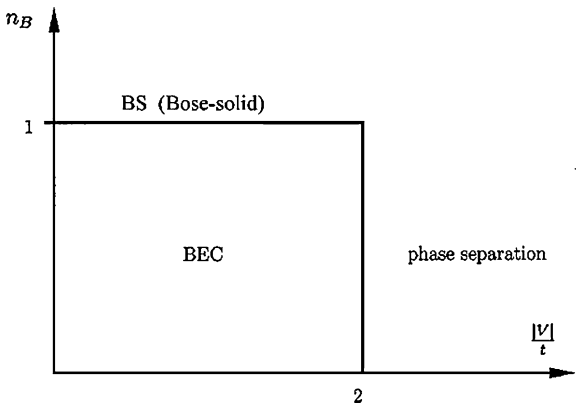

Fig. 6.3 Qualitative phase diagram of the 2D Bose-gas with the van der Waals interaction on the square lattice [2–4]

supersolidity on the lattice (see Chap. 2) in case of moderate values of on-site repulsion U (when double occupation of the site is not totally prohibited) [78–81].

6.1.8 Two-Band Hubbard Model for Two Sorts of Bosons

Let us consider the two-band Hubbard model for two sorts of structureless bosons. The Hamiltonian of the system has the form [2–4]:

$$\hat{H} = -t_1 \sum_{\langle ij \rangle} b_{1i}^{+} b_{1j} - t_2 \sum_{\langle ij \rangle} b_{2i}^{+} b_{2j} + \frac{U_{11}}{2} \sum_i n_{1i}^2 + \frac{U_{22}}{2} \sum_i n_{2i}^2 - \frac{U_{12}}{2} \sum_i n_{1i} n_{2i}, \tag{6.1.43}$$

where t_1 and t_2 and n_1 and n_2 are, respectively, the hopping matrix elements and densities for bosons of sorts 1 and 2. For simplicity, we will consider the case $t_1 = t_2$, which corresponds to the equal masses $m_1 = 1/(2t_1 d^2) = m_2$ of bosons. We also assume that the bottoms of the bands coincide. In the Hamiltonian (6.1.43) U_{11} and U_{22} are Hubbard onsite repulsions for bosons of sorts 1 and 2 respectively. Finally U_{12} is an onsite attraction between bosons of two different sorts (two-band Hubbard model will be also considered in Chaps. 10, 14 and 15 for the case of intraband and interband repulsions).

In the present section we will consider the low-density limit of the model (6.1.43), when both $n_1 d^2 \ll 1$ and $n_2 d^2 \ll 1$ on the square 2D lattice. In this limit we must replace the Hubbard interaction U_{12} by the corresponding T-matrix. The relevant expression for the T-matrix T_{12} is given by:

$$T_{12}(\tilde{E}) = \frac{U_{12}}{1 - U_{12} \int \frac{d^2\vec{p}}{(2\pi)^2} \frac{1}{p^2/2m + |\tilde{E}|}}, \tag{6.1.44}$$

where $\tilde{E}$ is given again by $\tilde{E} = E + W$. The T-matrix has the pole for the energy:

$$\left|\tilde{E}\right| = \left|E_b\right| = W \exp\left(-\frac{4\pi}{md^2 U_{12}}\right) \tag{6.1.45}$$

in the intermediate coupling case ($\left|\tilde{E}_b\right| < W$). In the extremely strong coupling case $U_{12} > W$ the pole corresponds to the energy $|E| = |E_b| \approx U_{12}$. The pole in the T-matrix reflects the appearance of the bound state of the two bosons of different sorts ($b_1 b_2$).

Now we can solve the two-particle problem in the presence of the bosonic background. A simple analysis shows that only local bosonic pairs are possible in our case. They are formed at a high crossover temperature $T_* = \frac{|E_b|}{\ln W/T_0}$, where $T_0 = \min\{T_{01}, T_{02}\}$, and T_{01} and T_{02} are degeneracy temperatures for bosons of the two sorts. Correspondingly the pairs are Bose condensed at lower temperature $T_{C12} = \frac{T_0}{\ln(1/\lambda)}$, where $\lambda = \frac{mU_{12}}{4\pi}$. Our results are valid is the case $|E_b| > \{T_{01}, T_{02}\}$. In the opposite case of higher densities, when at least one of the temperatures T_{01} or T_{02} is larger then $|E_b|$, we have at first a standard one-particle condensation for bosons with higher density. As a result the two-particle pairing between bosons of different sort can take place only as a second superfluid transition inside the superfluid phase with one-particle BEC.

The obtained results for T_* and T_{C12} in low-density case $|E_b| > \{T_{01}, T_{02}\}$ can be applied for anisotropic magnetic traps [2–4] where one of the oscillator frequencies is large: $\{\omega_x; \omega_y\} \ll T_C < (T_0 \sim \omega_z)$. Then the system occupies only the lowest energy level in z-direction and becomes effectively two-dimensional. In this case formulas for T_C are qualitatively correct, because it is possible to make the coherence length of the Bose-gas ξ_0 smaller than an effective size of the trap $R(\varepsilon)$ for $\varepsilon \sim T_C$ [95]. Another limitation on the two-particle pairing is connected with the energy release of the order of $Q \sim |E_b|$ when the pairs are created. Due to this energy release the most energetic particles can overcome the potential barrier and evaporate from the trap (a process which is analogous to an evaporative cooling technique considered in Chap. 5).

Let us now analyze the stability of our system with respect to quartet formation. For simplicity let us consider first an extremely strong-coupling case $\{U_{11}, U_{22}, U_{12}\} > W$ (remind that $m_1 = m_2$ and thus $W_1 = W_2 = W$). In this case the local pairs of two bosons of different sorts have onsite character $\langle b_1 b_2 \rangle \neq 0$ on the lattice. To escape local quartets ($\langle b_1 b_2 b_1 b_2 \rangle$) creation we must satisfy the inequality $U_{11} + U_{22} - 4U_{12} > 0$.

The situation is less trivial in the intermediate coupling case when for the binding energy $|E_b|$ in (6.1.45) we have $T_0 < \left|\tilde{E}_b\right| < W$. In this case the Bose pairs $b_1 b_2$ has the radius $a \gg d$ (though $a < 1/\sqrt{n}$ for equal densities $n_1 = n_2$ and masses $m_1 = m_2$ when degeneracy temperatures $T_{01} = T_{02} = T_0 = 2\pi n/m$). Effectively this situation corresponds to the resonance case for shallow bound states $|E_b| = \frac{1}{ma^2} \ll \frac{1}{mr_0^2}$ (where $r_0 = d$ on the lattice) (see Chap. 5).

In Sect. 6.3 we will define the binding energies $|E_3|$ of the three-particle $b_1 b_2 b_1$ and $|E_4|$ of the four-particle $b_1 b_2 b_1 b_2$ complexes in this case. We will also present

variational calculations for the binding energy and radius of larger bosonic droplets which contain $N > 4$ particles in the intermediate coupling case in 2D. Note that the phase-diagram of the two-component bosons was also investigated on the optical lattices by Kuklov, Prokof'ev and Svistunov [82] and by Demler's group [83].

Note that the results on two-boson pairing are also important for SU(2)—slave-boson theories of high-T_C superconductivity [10, 84, 85] and Schwinger-boson theories of 2D magnets [86–88].

6.1.9 *Slave-Boson Formulation of the t-J Model. Application to High-T_C Systems*

The superconductive pairing in the 2D fermionic t-J model will be considered in details in Chap. 13. Here we will briefly discuss the problem which arises in the approaches to the underdoped t-J model based on the scenarios of spin-charge separation advocated by Anderson et al. and Lee et al. The Hamiltonian of the canonical 2D t-J model reads:

$$\hat{H} = -t \sum_{\langle ij \rangle \sigma} c_{i\sigma}^{+}(1 - n_{i-\sigma}) c_{j\sigma}(1 - n_{j-\sigma}) + J \sum_{\langle ij \rangle} \left(\vec{S}_i \vec{S}_j - \frac{1}{4} n_i n_j \right), \tag{6.1.47}$$

where $c_{i\sigma}^{+}$ and $c_{j\sigma}$ are creation and annihilation operators for electrons on neighboring ($\langle ij \rangle$) sites i and j with spin projection σ, $n_{i\sigma} = c_{i\sigma}^{+} c_{i\sigma}$ is onsite electron density with spin projection σ ($n_i = \sum\limits_{\sigma} n_{i\sigma}$), and $\vec{S}_i = \frac{1}{2} c_{i\mu}^{+} \vec{\sigma}_{\mu\nu} c_{i\nu}$ is electron spin ($\vec{\sigma}_{\mu\nu}$ are Pauli matrices). In slave-boson formulation of the t-J model (based on the scenario of spin-charge separation) close to half-filling ($nd^2 \to 1$ on the 2D square lattice) an electron according to Anderson and Lee [8–10, 84, 85] can be represented as a product of spinon (fermion with charge 0 and spin ½) and holon (boson with charge $|e|$ and spin 0):

$$c_{i\sigma}^{+} = f_{i\sigma}^{+} b_i. \tag{6.1.48}$$

A superconductive d-wave gap (for electrons):

$$\Delta_d = \left\langle c_{i\uparrow} c_{j\downarrow} - c_{i\downarrow} c_{j\uparrow} \right\rangle \tag{6.1.49}$$

is a direct product

$$\Delta_d = \Delta_{sp} \Delta_h \tag{6.1.50}$$

of a spinon d-wave gap

$$\Delta_{sp} = \left\langle f_{i\uparrow} f_{j\downarrow} - f_{i\downarrow} f_{j\uparrow} \right\rangle \tag{6.1.51}$$

and a holon s-wave gap

$$\Delta_h = \langle b_i b_j \rangle. \tag{6.1.52}$$

Then a natural question arises whether $\langle b_i \rangle \neq 0$ and, accordingly, $\Delta_h = \langle b_i \rangle \langle b_j \rangle$, or $\langle b_i \rangle = 0$ but $\langle b_i b_j \rangle \neq 0$. In other words, whether a one particle or two-particle condensation of the holons takes place in our system [10, 89].

This problem is a very difficult one and, surely deserves a very careful analysis. Our preliminary considerations show, however, that the more beneficial conditions for the two-particle condensation may arise in the SU(2) formulation of the t-J model [84], which assumes the appearance of two sorts of holons b_1 and b_2. Note that in the standard U(1) formulation of the model [85] with one sort of holons an effective potential of the two-holon interaction on neighboring sites appearing after the Hubbard-Stratonovich transformation has a form:

$$\left(\frac{8t^2}{J} - \frac{J}{4}\right) \sum_{\langle ij \rangle} b_i^+ b_j b_i b_j. \tag{6.1.53}$$

and thus corresponds to the repulsion for $t > J$ (in 2D cuprates usually $J \sim (1/2 \div 1/3)t < t$). This observation excludes the possibility of the two-holon pairing in the U(1) formulation of the t-J model.

In the SU(2) case it will be desirable to derive conditions when $\langle b_1 \rangle = \langle b_2 \rangle = 0$ but $\langle b_1 b_2 \rangle \neq 0$ for two sorts of holons. For such a nondiagonal pairing, as already discussed above, it is easier to satisfy the stability criteria [2–4]. Note also that the same situation with two sorts of bosons and a possible attraction between them can be realized for 2D magnetic systems. The corresponding bosonic Hamiltonian can be obtained here after a Schwinger transformation of spins [86–88] in extended Heisenberg models.

Concluding this section we would like to emphasize that we analyzed the possibility of the formation of boson pairs with s-wave symmetry and an appearance of total phase separation in a 2D Bose-gas. In addition to that we considered the case of boson pairs with the symmetries of p- and d-wave type. We also considered the qualitative phase diagram for the 2D Bose-gas with the van der Waals interaction between the particles, which, besides a standard one-particle BEC, contains the regions of the Mott–Hubbard Bose solid and a total phase separation. We also considered the situation for two sorts of bosons described by the two-band Hubbard model, and found the conditions for the two-particle pairing between bosons of different sorts. We discussed the applicability of our results for the different physical systems ranging from 2D magnetic traps or optical lattices, submonolayers of ^{4}He and excitons in the semiconductors till Schwinger bosons in magnetic systems and holons in the slave-boson theories of high-T_C superconductors.

Note that for high-T_C systems we considered in this section slave-boson formulation of the t-J model based on the ideas of spin-charge separation. These ideas

were transferred to high-T_C materials from the 1D physics of doped spin chains [98, 99]. We think, however, that for quasi-2D high-T_C systems more suitable are the ideas of spin-charge confinement, which are based on the formation of the AFM-string (of the linear trace of the frustrated spins) which accompany the hole motion on 2D (or 3D) AFM-background of spins ½. In the next section of the present chapter and in Chap. 13 we will consider the scenario of spin-charge confinement (introduced by Laughlin et al. [31, 32]), more detaily with a special emphasis on the formation of composite hole there.

6.2 Composed Fermions in the Fermi-Bose Mixture with Attractive Interaction Between Fermions and Bosons

In Sect. 5.2 we considered composed bosons $f_\uparrow f_\downarrow$ which arise in the Fermi-gas with attraction or in a broad Feshbach resonance in the framework of the one-channel resonance approximation.

In Sect. 6.1 of the present chapter we considered the possibility of two-boson pairing bb or $b_1 b_2$ in the Bose-gas with one ore two sorts of bosons.

For the sake of completeness (to restore the full "supersymmetry" between fermions and bosons, treating them on equal grounds) we will analyze in this section a possibility to form composed fermions $f_\sigma b$ in the Fermi-Bose mixture with attractive interaction between fermions and bosons. Note that in an optical dipole trap it is possible to get an attractive scattering length of the fermion-boson interaction with the help of Feshbach resonance (see Refs. [49, 50] in Chap. 5). Note also that even in the absence of Feshbach resonance it is experimentally possible now to create a Fermi-Bose mixture with attractive interaction between fermions and bosons. For example in [11, 12] such a mixture of ^{87}Rb (bosons) and ^{40}K (fermions) was experimentally studied. Moreover, the authors of [11, 12] experimentally observed the collapse of a Fermi gas with the sudden disappearance of fermionic ^{40}K atoms when the system enters into the degenerate regime. We cannot exclude in principle that it is just a manifestation of the creation of quartets $f_\uparrow b$, $f_\downarrow b$ in the system [6]. Note that in the regime of a strong attraction between fermions and bosons, a phenomenon of phase separation with the creation of larger clusters or droplets is also possible. Note also that for a large mismatch between fermionic and bosonic densities $n_F \ll n_B$, a much slower collapse in the Bose subsystem of ^{87}Rb was experimentally observed. Here, after the formation of composed fermions, a lot of residual (unpaired) bosons are still present. This fact probably can explain a slow collapse in bosonic subsystem [6].

6.2.1 The Theoretical Model

The model of a Fermi-Bose mixture has the following form on a lattice [6]:

$$\begin{aligned}
\hat{H}' &= \hat{H}'_F + \hat{H}'_B + \hat{H}'_{FB}, \\
\hat{H}'_F &= -t_F \sum_{\langle ij\rangle\sigma} f^+_{i\sigma} f_{j\sigma} + U_{FF} \sum_i n^F_{i\uparrow} n^F_{i\downarrow} - \mu_F \sum_{i\sigma} n^F_{i\sigma}, \\
\hat{H}'_B &= -t_B \sum_{\langle ij\rangle} b^+_i b_j + \frac{U_{BB}}{2} \sum_i n^B_i n^B_i - \mu_B \sum_i n^B_i, \\
\hat{H}'_{FB} &= -U_{BF} \sum_{i\sigma} n^B_i n^F_{i\sigma}.
\end{aligned} \tag{6.2.1}$$

This is a lattice analog of the standard Hamiltonian considered for example by Efremov and Viverit [15] for the case of repulsive interaction between fermions and bosons in ^{7}Li-^{6}Li mixture (see Chap. 12). Note that in the Fermi-Bose mixture of ^{3}He and ^{4}He (which will be considered in Chap. 11) the fermion-boson interaction also corresponds to repulsion (see a classical paper [7] by Bardeen, Baym, Pines). In the Hamiltonian (6.2.1) t_F and t_B are fermionic and bosonic hopping amplitudes, $f^+_{\mathrm{i}\sigma}$, $f_{\mathrm{i}\sigma}$ and b^+_i, b_i are fermionic and bosonic creation and annihilation operators. The Hubbard interactions [57] U_FF and U_BB correspond to hard-core repulsions between particles of the same sort. The interaction U_BF corresponds to the attraction between fermions and bosons. $W_\mathrm{F} = 8t_\mathrm{F}$ and $W_\mathrm{B} = 8t_\mathrm{B}$ are the bandwidths in 2D. Finally, μ_F and μ_B are fermionic and bosonic chemical potentials. For the square lattice the uncorrelated spectra of fermions and bosons after Fourier transformation read: $\xi_{p\sigma} = -2t_F(\cos p_x d + \cos p_y d) - \mu_F$ for fermions and $\eta_p = -2t_B(\cos p_x d + \cos p_y d) - \mu_B$ for bosons, where d is a lattice constant.

6.2.2 Intermediate Coupling Case in 2D

In the intermediate coupling case in 2D (see Refs. [31, 32] in Chap. 5 and Chap. 8 for more details) $\frac{W_{BF}}{\ln W_{BF}/T_{0BF}} < U_{BF} < W_{BF}$ the energy of the bound state (for a formation of a composed fermion $f_{\mathrm{i}\sigma} b_\mathrm{i}$) reads [6]:

$$\left|\tilde{E}_b\right| = \frac{1}{2m_{BF}d^2} \frac{1}{\exp\left\{\frac{2\pi}{m_{BF}U_{BF}}\right\} - 1}, \tag{6.2.2}$$

where $\left|\tilde{E}_b\right|$ is counted again from the bottom of the band for composed fermions, $\left|\tilde{E}_b\right| m_{BF} = \frac{m_B m_F}{m_B + m_F}$ is an effective mass, $W_{BF} = \frac{4}{m_{BF}d^2}$ is an effective bandwidth, $m_B = \frac{1}{2t_B d^2}$ and $m_F = \frac{1}{2t_F d^2}$ are the band masses of elementary bosons and fermions. Finally $T_{0BF} = \frac{2\pi n}{m_{BF}}$ is an effective degeneracy temperature. For simplicity we

consider the case of equal densities $n_{\rm B} = n_{\rm F} = n$ which is more relevant for the physics of holons and spinons in underdoped high-$T_{\rm C}$ materials.

Note that in the intermediate coupling case in 2D the binding energy for pairing between fermions and bosons $|\tilde{E_b}|$ is larger than bosonic and fermionic degeneracy temperatures:

$$|\tilde{E_b}| > \left\{ T_{0B} = \frac{2\pi n_B}{m_B}; T_{0F} = \frac{2\pi n_F}{m_F} = \varepsilon_F \right\}, \tag{6.2.3}$$

but smaller than the bandwidths $|\tilde{E_b}| < \{W_B, W_F\}$. In this case the pairing of fermions and bosons $\langle f_\sigma b\rangle$ takes place earlier (at higher temperatures) than both Bose–Einstein condensation of bosons or bibosons ($\langle b\rangle \neq 0$ or $\langle bb\rangle \neq 0$) and superconductive pairing of fermions $\langle f_\sigma f_{-\sigma}\rangle \neq 0$. Note that a matrix element $\langle c_\sigma\rangle = \langle f_\sigma b\rangle$ is nonzero only for the transitions between the states with $|N_{\rm B}; N_{\rm F}\rangle$ and $\langle N_{\rm B} - 1; N_{\rm F} - 1|$, where $N_{\rm B}$ and $N_{\rm F}$ are the numbers of particles of elementary bosons and fermions, respectively [6]. For superconductive state a matrix element for a quartet $\langle c_\sigma c_{-\sigma}\rangle = \langle f_\sigma b, f_{-\sigma} b\rangle \neq 0$ only for the transitions between the states with $|N_{\rm B}; N_{\rm F}\rangle$ and $\langle N_{\rm B} - 2; N_{\rm F} - 2|$. Note also that in the case of a very strong attraction $U_{\rm BF} > W_{\rm BF}$ we have a natural result $|E_b| \approx U_{BF}$, and the effective mass $m^*_{BF} = m_{BF}\frac{U_{BF}}{W_{BF}} \gg m_{BF}$ is additionally enhanced on the lattice (see Nozieres, Schmitt-Rink [14] in Chap. 5). Finally let us emphasize that the diagonal Hubbard interactions $U_{\rm FF}$ and $U_{\rm BB}$ satisfy the inequalities $U_{FF} > \frac{W_F}{\ln(W_F/|E_b|)}$ and $U_{BB} > \frac{W_B}{\ln(W_B/|E_b|)}$ in the intermediate coupling case. Now let us consider the temperature evolution of the system.

6.2.3 Bethe–Salpeter Integral Equation

The temperature evolution is governed again (as in the case of two-fermion or two-boson pairing) by the corresponding Bethe–Salpeter (BS) equation. After analytical continuation $i\omega_n \to \omega + io$ [56] the solution of this equation for the two-particle total vertex Γ acquires a form:

$$\Gamma(\vec{q}, \omega) = \frac{-U_{BF}d^2}{1 - U_{BF}d^2 \int \frac{d^2\vec{p}}{(2\pi)^2} \frac{1 - n_F(\xi_p) + n_B(\eta_{q-p})}{\xi(\vec{p}) + \eta(\vec{q}-\vec{p}) - \omega - io}}, \tag{6.2.4}$$

where $\xi(\vec{p}) = \frac{p^2}{2m_F} - \tilde{\mu}_F$ and $\eta(\vec{q} - \vec{p}) = \frac{p^2}{2m_B} - \tilde{\mu}_B$ are spectra of fermions and bosons at low densities $n_{\rm F}d^2 \ll 1$ and $n_{\rm B}d^2 \ll 1$, the chemical potentials $\tilde{\mu}_F = \frac{W_F}{2} + \mu_F$ and $\tilde{\mu}_B = \frac{W_B}{2} + \mu_B$ are counted from the bottoms of the bands. Note that in the pole of BS equation enters the temperature factor $1 - n_F(\xi(\vec{p})) + n_B(\eta(\vec{q} - \vec{p}))$ in contrast with the factor $1 - n_F(\xi(\vec{p})) - n_F(\xi(\vec{q} - \vec{p}))$ for the standard two-fermion superconductive pairing and $1 + n_B(\eta(\vec{p})) + n_B(\eta(\vec{q} - \vec{p}))$

for the two-boson pairing (considered in Sect. 6.1). The pole of the Bethe–Salpeter equation corresponds to the spectrum of the composed fermions:

$$\omega = \xi^*_{\vec{p}} = \frac{p^2}{2(m_B + m_F)} - \mu_{comp}. \tag{6.2.5}$$

Note that in (6.2.5)

$$\tilde{\mu}_{comp} = \tilde{\mu}_B + \tilde{\mu}_F + \left|\tilde{E}_b\right| \tag{6.2.6}$$

is a chemical potential of composed fermions. Similarly to (6.2.6) in Chap. 8 for two-fermion pairing we will get $\tilde{\mu}_{comp} = 2\tilde{\mu}_F + \left|\tilde{E}_b\right|$ for a chemical potential (see Refs. [31, 32] in Chap. 5) of a composed boson (molecule or dimer) $f_\sigma f_{-\sigma}$, while instead of (6.2.5) we will obtain $\omega = \frac{p^2}{4m_F} - \tilde{\mu}_B$ for a pole of the fermionic BS-equation. Note also that composed fermions are well-defined quasiparticles, since the damping of quasiparticles equals to zero in the case of the bound state ($\tilde{E}_b < 0$), but it becomes nonzero and is proportional to $\tilde{E}_b$ in the case of the virtual state $\left(\tilde{E}_b < 0\right)$. The process of a dynamical equilibrium (boson + fermion $\leftrightarrow$ composed fermion) is again governed by the standard Saha formula (see Sects. 5.2, 6.1 and [30–32] in Chap. 5).

6.2.4 Crossover (Saha) Temperature

In the 2D case Saha temperature reads [6]:

$$\frac{n_B n_F}{n_{comp}} = \frac{m_{BF} T}{2\pi} \exp\left\{-\frac{\left|\tilde{E}_b\right|}{T}\right\}. \tag{6.2.7}$$

The crossover temperature T_* is defined, as usual, from the requirement that the number of composed fermions equals the number of unbound fermions and bosons: $n_{\mathrm{comp}} = n_{\mathrm{B}} = n_{\mathrm{F}} = n_{\mathrm{tot}}/4$, (where $n_{\mathrm{tot}} = n_{\mathrm{B}} + n_{\mathrm{F}} + 2n_{\mathrm{comp}}$ is a total density). This conditions yields:

$$T_* = \frac{\left|\tilde{E}_b\right|}{\ln\left(\left|\tilde{E}_b\right|/T_{0BF}\right)} \gg \{T_{0B}, T_{0F}\}. \tag{6.2.8}$$

Note that in the Boltzmann regime $\left|\tilde{E}_b\right| > \{T_{0B}, T_{0F}\}$. In fact we deal here with the pairing of two Boltzmann particles.

That is why this pairing does not differ drastically from the pairing of two particles of the same type of statistics. Indeed, if we substitute $\tilde{\mu}_B + \tilde{\mu}_F$ in (6.2.6) on $2\tilde{\mu}_B$ or $2\tilde{\mu}_F$ we will get the familiar expressions for the chemical potentials of composed bosons consisting either of two elementary bosons [2–4] or of two elementary fermions (see Refs. [12–14, 31, 32] in Chap. 5).

For lower temperatures $T_0 < T < T_*$ (where $T_0 = \frac{2\pi n}{m_B + m_F}$ is the degeneracy temperature for composed fermions) the numbers of elementary fermions and bosons (for the case of equal densities $n_B = n_F$) are exponentially small. The chemical potential of composed fermions reads $\tilde{\mu}_{comp} = -T\ln(T/T_0)$. Hence $\left|\tilde{\mu}_{comp}\right| \ll \left|\tilde{E}_b\right|$ for $T \ll T_*$.

6.2.5 Three and Four Particles Bound States in the Fermi-Bose Mixture

Note that in a general case to complete the phase-diagram of the Fermi-Bose mixture model with attraction between fermions and bosons we should determine also the binding energies of trios and quartets $|E_3|$ and $|E_4|$ for the complexes $f_\sigma b,b$ and $f_\sigma b,f_{-\sigma}b$ (the complex $f_\sigma b,f_{-\sigma}$ is not formed due to repulsive interaction between a composed fermion $f_\sigma b$ and elementary fermion $f_{-\sigma}$). The knowledge of $|E_3|$ and $|E_4|$ will help us to find the hierarchy of inequalities between the different Saha temperatures,

$$T_*^{(2)} \sim \left|\tilde{E}_b\right|,\ T_*^{(3)} \sim |E_3|,\ T_*^{(4)} \sim |E_4|, \tag{6.2.9}$$

where E_4 and E_3 are counted from the bottoms of the bands for the lattice models $T_*^{(3)}$ and $T_*^{(4)}$ are Saha temperatures for the formation of composed trios and quartets. If, as we will prove in the next section, $T_*^{(4)} > T_*^{(3)} > T_*^{(2)}$ $\left(\text{which requires that } |E_4| > \left\{|E_3|; 2\left|\tilde{E}_b\right|\right\} \text{ to escape decay processes}\right)$ then the phase-diagram of the Fermi-Bose mixture is trivialized. Namely for high temperatures $T > T_*^{(4)}$ the elementary fermions and bosons prevail in the system, while for lower temperatures $T < T_*^{(4)}$ the quartets $f_\uparrow b, f_\downarrow b$ prevail in the system.

The quartets are already composed bosons. They are Bose-condensed below the temperature governed again by the Fisher-Hohenberg type of the formula [66]:

$$T_C \sim \frac{T_0}{16\ln\ln\left(\alpha\frac{|E_4|}{T_0}\right)}, \tag{6.2.10}$$

where for equal masses $m_B = m_F = m$ and equal densities $n_B = n_F = n$ $T_0 = \pi n/m$ and ϕ the coefficient α will be also defined in the next section for scattering of molecule on molecule in 2D.

6.3 Bound States of Three and Four Resonantly Interacting Particles

In this section we will complete the phase-diagram of 2D Fermi-Bose mixture with attraction between fermions and bosons, as well as a phase-diagram of 2D Bose-gas with one or two sorts of bosons by calculating exactly the bound states

energies $|E_3|$ for the three-particle complexes bbb, b_1b_2,b_1, $f_\sigma b,b$ and $|E_4|$ for the four-particle complexes $bbbb$, $b_1b_2b_1b_2$, $f_\sigma bbb$ and $f_\sigma b,f_{-\sigma}b$ in the resonance (one-channel) approximation [24, 25]. We will also present variational calculations of the binding energy of the larger droplet $|E_N|$ with the number of particles in the droplet $N > 4$.

Finally to complete the phase-diagram of the attractive Fermi-gas in the regime of BCS-BEC crossover we will determine the scattering amplitudes a_{2-1} for the scattering of molecules $f_\uparrow f_\downarrow$ on elementary fermions (atoms) f_σ, and a_{2-2} for the scattering of molecules $f_\uparrow f_\downarrow$ on other molecules $f_\uparrow f_\downarrow$ in the resonance approximation for BEC-domain $a \gg r_0$ (see Chap. 5). Note that the scattering length a_{2-1} governs also the inelastic scattering time or a lifetime of the 3D resonance Fermi-gas in BEC-domain, where $|E_b| = 1/ma^2 < 1/mr_0^2$, and $a > 0$ (we do not distinguish between $|E_b|$ and $\left|\tilde{E}_b\right|$ for the gas models in the absence of the lattice).

In the resonance approximation we will get diagrammatically the results for the binding energies $|E_3|$ and $|E_4|$ only in terms of the two-particle binding energy $|E_b|$, while for the scattering amplitudes we will get a_{2-1} and a_{2-2} only in terms of the two-particle s-wave scattering length a [24, 25].

6.3.1 Atom-Molecule Scattering Length for Three Resonantly Interacting Fermions in 3D. Skorniakov-Ter-Martirosian Integral Equation

In this section we will present diagrammatic method [21] to rederive the famous Skorniakov and Ter-Martirosian result (firstly obtained for scattering of neutrons on deutrons in nuclear physics) [18] for dimer-fermion ($f_\uparrow f_\downarrow; f_\uparrow$) scattering length a_{2-1} in the case of three resonantly interacting fermions in 3D.

Following Skorniakov and Ter-Martirosian in the presence of the weakly bound resonance level—$|E_b|$ in a two-particle cross-section, we can limit ourselves to the zero-range interaction potential ($|a| \gg r_0$) between fermions. A two-fermion vertex (two-particle T-matrix in vacuum) can be approximated by a simple one-pole structure, which reflects the presence of the s-wave resonance level in a spin-singlet state:

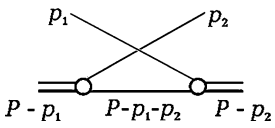

Fig. 6.4 The simplest exchange diagram for the three-particle interaction. The double line corresponds to dimer, the single lines—to elementary fermions [6]. Intermediate single line stands for the vacuum Green's function $G(P\text{-}p_1\text{-}p_2)$, where P is the total 4-momentum of dimer and elementary fermion, $P = \{E, \vec{P}\}$

$$T_{2\alpha\beta,\gamma\delta}(E,\vec{P}) = T_2(E,\vec{P})(\delta_{\alpha\gamma}\delta_{\beta\delta} - \delta_{\alpha\delta}\delta_{\beta\gamma}) = T_2(E,\vec{P})\chi(\alpha,\beta)\chi(\gamma,\delta), \qquad (6.3.1)$$

where in the 3D case

$$T_2(E,\vec{P}) = \frac{4\pi}{m^{3/2}} \frac{\sqrt{|E_b|} + \sqrt{\vec{P}/4m - E}}{E - \vec{P}/4m + |E_b|} \qquad (6.3.2)$$

is given by the ladder sequence of vacuum diagrams (see Sect. 6.2 and Fig. 5.13). E is the total energy and $\vec{P}$ is the total momentum of the incoming particles, m is the fermionic mass, and $|E_b| = 1/ma^2$ is the binding energy ($a = a_F -$ is an s-wave scattering length of two fermions). Indices α, β and γ, δ denote spin state of incoming and outgoing particles. The function $\chi(\alpha, \beta)$ stands for the spin-singlet state $\chi(\alpha,\beta) = \delta_{\alpha\uparrow}\delta_{\beta\downarrow} - \delta_{\alpha\downarrow}\delta_{\beta\uparrow}$. Note that the pole of the vacuum T-matrix (6.3.2) coincides with the pole of two-particle vertex Γ obtained for two-fermion pairing in Sect. 5.2 in the absence of the lattice for $\mu_F = 0$ (and $\mu_B = 2\mu_F + |E_b| = |E_b|$). The simplest process which contributes to the dimer-fermion interaction is the exchange of a fermion (Fig. 6.4).

We will denote it as Δ_3 (see [25]). Its analytical expression is:

$$\Delta_{3\alpha,\beta}(p_1,p_2,P) = -\delta_{\alpha\beta}G(P - p_1 - p_2), \qquad (6.3.3)$$

where we introduce four-momenta $P = (E,\vec{P})$, p_1 and p_2. In (6.3.3) $G(P) = \frac{1}{\omega - \frac{\vec{P}^2}{2m} + i0}$ is a bare fermion Green's function in vacuum. The minus sign on the right-hand side of (6.3.3) comes from the permutation of the two fermions and corresponds to the bare repulsive interaction between dimer and fermion. In order to obtain a full dimer-fermion scattering vertex T_3 we need to build a ladder again from Δ_3 blocks. One can easily verify that the spin projection is conserved in every order of T_3, and thus $T_{3\alpha\beta} = \delta_{\alpha\beta}T_3$. An equation for T_3 will have the diagrammatic representation shown in Fig. 6.5, and in analytical form it is written as:

$$\begin{aligned} T_3(p_1,p_2,P) = &-G(P - p_1 - p_2) \\ &- i\sum_q G(P - p_1 - q)G(q)T_2(P - q)T_3(q,p_2,P), \end{aligned} \qquad (6.3.4)$$

where $\sum_q = \int d^3\vec{q}d\Omega/(2\pi)^4$.

Note that for three resonantly interacting bosons *bb,b* the sign near the first term in right-hand side of (6.3.4) should be changed on "plus". This means that we

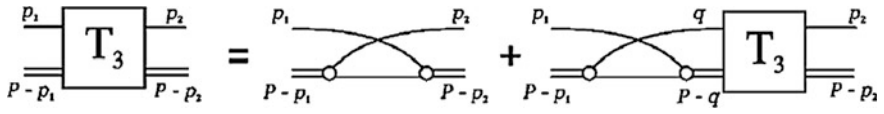

Fig. 6.5 The graphic representation of the equation for the full dimer-fermion scattering vertex T_3. Intermediate double line corresponds to two-particle scattering vertex $T_2(p - q)$ (which describes the bound state of a dimer). Intermediate single lines stand for the vacuum one-particle Green-functions $G(q)$ and $G(P\text{-}p_1\text{-}q)$ [25]

have a bare attraction between a molecule bb and elementary boson b. Correspondingly the bare interaction is also attractive for a molecule $f_\sigma b$ interacting with elementary boson b, but it is repulsive (due to Pauli principle) for the interaction of the molecule $f_\sigma b$ with an elementary fermion $f_{-\sigma}$ having an opposite spin projection.

Returning back to three resonantly interacting fermions ($f_\uparrow f_\downarrow$ and f_σ) we can integrate out the frequency Ω in (6.3.4) by closing the integration contour in the lower half-plane, since both $T_2(P-q)$ and $T_3(q, p_2; P)$ are analytical functions in this region. Moreover, if we are interested in the low-energy s-wave dimer-fermion scattering length $a_3 = a_{2-1}$, we can safely put $P = (E, \vec{P}) = (-|E_b|, 0)$ and $p_2 = 0$. The full vertex T_3 is connected with $a_3 = a_{2-1}$ by the following relation [24, 25]:

$$\left(\frac{8\pi}{m^2 a}\right) T_3(0, 0, -|E_b|) = \frac{3\pi}{m} a_{2-1}. \tag{6.3.5}$$

Introducing a new function $a_{2-1}(k)$ according to the formula:

$$\left(\frac{8\pi}{m^2 a}\right) T_3\left(\left\{\frac{k^2}{2m}, \vec{k}\right\}, 0, -|E_b|\right) = \frac{3\pi}{m} a_{2-1}(k), \tag{6.3.6}$$

and substituting it into Eq. (6.3.4), we obtain the Skorniakov-Ter-Martirosian (STM) equation for the scattering amplitude [18, 24, 25]:

$$\frac{\frac{3}{4} a_{2-1}(k)}{\sqrt{m|E_b|} + \sqrt{\frac{3k^2}{4} + m|E_b|}} = \frac{1}{k^2 + m|E_b|} - 4\pi \int \frac{a_{2-1}(q)}{q^2(k^2 + q^2 + \vec{k}\vec{q} + m|E_b|)} \frac{d^3\vec{q}}{(2\pi)^3} \tag{6.3.7}$$

Solving this equation numerically one obtains the well-known result for the dimer-fermion scattering length [18, 29]:

$$a_{2-1} = a_{2-1}(0) = 1.18|a| > 0. \tag{6.3.8}$$

This result is quite nice since dimer-fermion scattering length in it depends only upon numerical coefficient (see Ref. [64] in Chap. 1) and two-particle s-wave scattering length a.

6.3.2 Three Resonantly Interacting Bosons in 3D. Efimov Effect

As was first shown by Danilov [90] (see also the paper by Minlos and Fadeev [19]) in the 3D case, the problem of three resonantly interacting bosons cannot be solved in the resonance approximation. This statement stems from the fact that in the case of identical bosons (or in the case of the complexes with two bosons and one

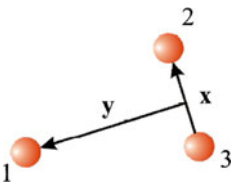

Fig. 6.6 Convenient coordinates $\vec{x} = \vec{r}_2 - \vec{r}_3$ and $\vec{y} = \vec{r}_1 - \frac{\vec{r}_2+\vec{r}_3}{2}$ for the description of fermion (1)-dimer (23) interaction (see Ref. [20]) for the case of equal masses $m_1 = m_2 = m_3$

fermion $f_\sigma b,b$) the homogeneous part of STM-equation (6.3.7) has a nonzero solution at any negative energies. The physical meaning of this mathematical artifact was elucidated by Efimov [16], who showed that a Hamiltonian with only two-particle interaction leads to the appearance of an attractive $1/r^2$ interaction in a three-body system. Since in the attractive $1/r^2$ potential in 3D a particle falls to the center, the short-range physics is important and one cannot replace the exact pair interaction by its resonance approximation. In the excellent review article by Jensen et al. [20] it was nicely illustrated that Efimov effect is present in the dimensions $2.3 < \mathrm{D} < 3.8$. In 3D case it creates the attractive (centripetal) effective potential $V_{eff}(\rho) \approx -\frac{1.26}{\rho^2}$ (see Fig. 6.6) if we introduce convenient relative coordinates ($m_1 = m_2 = m_3$):

$$\begin{aligned} \vec{x} &= \vec{r}_2 - \vec{r}_3, \\ \vec{y} &= \vec{r}_1 - \frac{\vec{r}_2 + \vec{r}_3}{2}, \end{aligned} \tag{6.3.9}$$

which correspond to the relative radius-vector $(\vec{x})$ inside the dimer (2, 3) and the radius-vector $(\vec{y})$ between the elementary particle 1 (falling on dimer) and the dimer's center of mass.

Vectors $\vec{x}$ and $\vec{y}$ define the plane. In this plane we can introduce a hyperradius ρ and angles α_1, α_2 such as:

$$\begin{aligned} x_i &= \rho \sin \alpha_i; \quad i = 1,2, \\ y_i &= \rho \cos \alpha_i; \quad i = 1,2. \end{aligned} \tag{6.3.10}$$

If we rewrite the three-particle Hamiltonian:

$$\hat{H} = \sum_{j=1}^{3} \frac{1}{2m_j} \nabla_j^2 + \sum_{j,k=1}^{3} V\left(\left|\vec{r}_j - \vec{r}_k\right|\right) = \hat{T} + \hat{V} \tag{6.3.11}$$

in terms of $\vec{x}$, $\vec{y}$ and $\vec{R}_{c.m.} = \frac{\vec{r}_1+\vec{r}_2+\vec{r}_3}{3}$ (for equal masses $m_1 = m_2 = m_3$) and then introduce a hyperradius ρ and angles α_i, then in the new coordinates the kinetic part of the Hamiltonian $\hat{T}$ in (6.3.11) will contain the centripetal term according to [20].

Note that in 2D case $V_{eff}(\rho) \approx \frac{1.5}{\rho^2} > 0$—the potential is repulsive and Efimov effect is absent. Thus the STM equation in 2D has a finite number of the solutions for the binding energies E_3 of the three-particle complexes *bbb* and *fbb*.

In 3D case Efimov effect leads to the appearance of the strongly-bound three-particle levels with an energy [19]:

$$|E_{3n}| = \frac{1}{mr_0^2} \exp\left\{-\frac{2\pi n}{\varsigma_0}\right\}, \tag{6.3.12}$$

where $\zeta_0 = 1.006$. The total number of levels is

$$N = \frac{1}{\pi} \ln \frac{a}{r_0}, \tag{6.3.13}$$

where r_0 is the range of the potential.

They lie in the interval:

$$\frac{1}{ma^2} < |E_{3n}| < \frac{1}{mr_0^2}. \tag{6.3.14}$$

Mathematically Efimov's effect is connected with the properties of the kernel of the integral STM equation. If we perform analytically the angular integration in (6.3.7) of the type $\int\limits_{-1}^{1} \frac{d\cos\theta}{a+b\cos\theta} = \frac{1}{b} \ln \frac{a+b}{|a-b|}$ and introduce dimensionless intermediate and incoming momenta $y = qa$ and $x = ka$ (measured in terms of the scattering length a) as well as dimensionless three-particle energy $W_3 = \frac{|E_3|}{|E_b|} = ma^2|E_3|$ (measured in terms of the two-particle binding energies $|E_b|$) and dimensionless 3-particle vertex $\tau_3 = \frac{T_3}{|E_b|} = ma^2 T_3$ then in terms of x, y and W_3 the homogeneous part of STM-equation for τ_3 reads:

$$\tau_3(x, W_3) = \frac{2}{\pi} \int\limits_0^{a/r_0} \frac{y^2 dy}{2xy} \ln\left(\frac{W_3 + x^2 + y^2 + xy}{W_3 + x^2 + y^2 - xy}\right) \frac{1 + \sqrt{3/4y^2 + W_3}}{\sqrt{W_3 + 3/4y^2 - 1}} \cdot \tau_3(y, W_3), \tag{6.3.15}$$

where sign "plus" in front of the integral corresponds for three bosons to the attractive dimer-monomer interactions (Three-particle binding energies E_3 correspond to the poles of τ_3, and consequently for $E = E_3$ homogeneous part of STM-equation should have nonzero solutions). It is possible to show that the kernel in the right-hand side of integral Eq. (6.3.15) is not limited. The integral of the kernel is of the order of 1 on the upper limit so the solutions with large three-particle binding energies $W_3 = \frac{|E_3|}{|E_b|} \gg 1$ are possible. These solutions are "sitting" on the upper limit $y_{\max} = \frac{a}{r_0} \to \infty$ of the integral in (6.3.15). For them we can get $x \sim x_{\max} = \frac{a}{r_0} \gg 1$ and $W_3 \sim W_{3\max} = \frac{a^2}{r_0^2} \gg 1$. Effectively they describe the

situation when the three-particle system goes far away from the resonance (when we add a third particle to resonantly interacting pair of particles). That is why we have deep three-particle levels [see (6.3.14)] in 3D.

6.3.3 Three Resonantly Interacting Bosons in 2D

As we already mentioned, Efimov effect is absent in 2D. Therefore it is possible to describe the binding energies $|E_3|$ of the three-particle complexes *bbb* and $f_\sigma b,b$ in terms of the two-particle binding energies $|E_\mathrm{b}|$ only.

As in the 3D case, the cornerstone in the diagrammatic technique is the two-particle resonance scattering vertex T_2. For two resonantly interacting particles with total mass $2m$ (we assume that all the particles under considerations have the same mass m, which in case of Fermi-Bose mixture means that $m_\mathrm{B} = m_\mathrm{F}$) it can be written in 2D as:

$$\left(\frac{8\pi}{m^2 a}\right) T_2(P) = -\frac{4\pi}{m} \frac{\alpha}{\ln\left(\left(\frac{\vec{P}}{4m} - E\right)|E_b|\right)}, \tag{6.3.16}$$

where $P = (E, \vec{P})$ is 4 momentum and we introduce the factor $\alpha = \{1, 2\}$ in order to take into account whether or not two particles are indistinguishable. It is $\alpha = 2$ for the case of a resonance interaction between identical bosons and $\alpha = 1$ for the case of a resonance interaction between fermion and boson or for the case of two distinguishable bosons. Note that $T_2(P)$ contains a typical for 2D systems logarithm in denominator of (6.3.16). We start with a system of three resonantly interacting identical bosons-*bbb* in 2D. An equation for the dimer-(elementary) boson scattering vertex T_3 which describes interaction between three bosons has the same diagrammatic form as shown in Fig. 6.5; however, the rules for its analytical notation changed. It can be written as:

$$T_3(p_1, p_2, P) = G(P - p_1 - p_2) + i \sum_q G(P - p_1 - q) G(q) T_2(P - q) T_3(q, p_2, P), \tag{6.3.17}$$

where $\sum_q = \int d^3\vec{q} d\Omega/(2\pi)^4$, $P = (E, 0)$ and one should put $\alpha = 2$ for the two-particle vertex T_2 in (6.3.16). As we already mentioned the opposite signs in (6.3.4) for fermions and (6.3.17) for bosons are due to the permutation properties of the particles involved: an exchange of fermions results in a minus sign, while an analogous exchange of bosons brings no extra minus. Finally, we note that the three-particle s-wave (s-wave channel of a boson-dimer scattering) binding energies E_3 correspond to the poles of $T_3(0, 0; -|E_3|)$ and, consequently, at energies $E = E_3$ the homogeneous part of (6.3.17) has a nontrivial solution. Introducing the same dimensionless variables x, y for initial and intermediate momenta, W_3 for

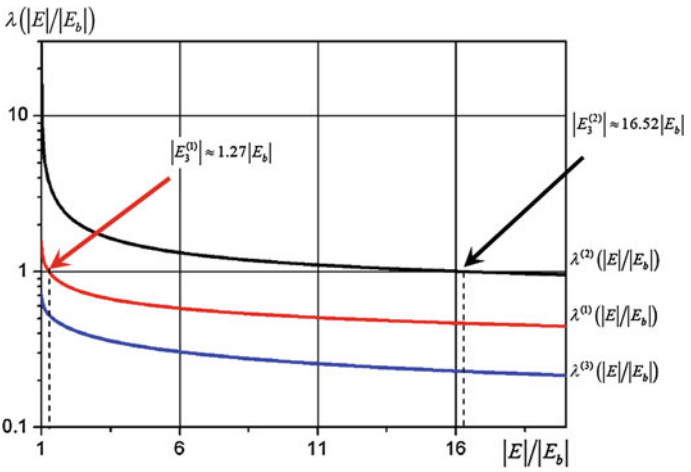

Fig. 6.7 The typical level structure $\lambda(|E|/|E_b|)$ for numerical solution of a homogeneous part of STM-equation. In the case of three identical bosons in 2D two levels $\lambda^{(1)}(|E|/|E_b|)$ and $\lambda^{(2)}(|E|/|E_b|)$ cross the horizontal line $\lambda = 1$ correspondingly for three-particle binding energies $\left|E_3^{(1)}\right| = 1.27|E_b|$ and $\left|E_3^{(2)}\right| = 16.52|E_b|$, while for the third level $\lambda^{(3)}(|E|/|E_b|) < 1$ for all energies $|E|/|E_b|$ and hence it does not represent the three-particle bound state [24, 25]

dimensionless three-particle energy $|E_3|$ and τ_3 for dimensionless three-particle T-matrix T_3 we will get in a 2D case (after the corresponding angular integration $\left(\int_0^{2\pi} \frac{d\varphi}{a+b\cos\varphi} = \frac{\pi}{\sqrt{a^2>b^2}} \text{ for } a^2 > b^2\right)$:

$$\tau_3(x, W_3) = \frac{2}{\pi} \int_0^{a/r_0} \frac{ydy}{\sqrt{(W_3 + x^2 + y^2)^2 - (xy)^2}} \frac{1}{\ln(W_3 + 3/4y^2)} \cdot \tau_3(y, W_3). \tag{6.3.18}$$

It is possible to show that the kernel in 2D STM-equation is limited (in contrast to the 3D case). For large y the integral of the kernel behaves as $\frac{1}{\ln y} \ll 1$.

Hence (in spite of the fact that the integral in (6.3.18) again (as in a 3D case) is governed by large y) there are no solutions for which $x \sim pa$ and W_3 are much larger than 1. Correspondingly deep three-particle levels are absent in the 2D case and the system does not go far away from the resonance when we add the third particle to the two resonantly interacting particles.

Numerical solutions of (6.3.18) are obtained by finding the eigenvalues $\lambda(E)$ of the kernel $\hat{K}$ of the homogeneous part of the integral equation: $T_3 = \hat{K}T_3$. Than $\lambda = 1$ is the condition for the appearance of a three-particle bound state. More precisely: $\lambda(E = E_3) = 1$. The numerical solutions for binding energies of three identical bosons in 2D are presented on Fig. 6.7. We can see that $\lambda(E/|E_b|)$ crosses

the horizontal line $\lambda = 1$ for two three-particle levels at $\left|E_3^{(1)}\right| = 1.27|E_b|$ and $\left|E_3^{(2)}\right| = 16.52|E_b|$. The third level on Fig. 6.7 for all energies corresponds to $\lambda(E/|E_b|) < 1$, and hence does not represent a bound state. Thus we obtained two s-wave three-particle bound states $\left|E_3^{(1)}\right| \approx 1.27|E_b|$ and $\left|E_3^{(2)}\right| \approx 16.52|E_b|$ in agreement with the results of Bruch and Tjon [41] (see also [20]).

6.3.4 The Three-Particle Complex $f_\sigma b,b$ in 2D Case

Let us now consider a complex $f_\sigma b,b$ consisting of one fermion and two bosons. As noted above we consider bosons and fermions with equal masses $m_B = m_F = m$. In agreement with the results of Sect. 6.2 we assume that an attractive fermion-boson interaction U_{FB}, characterized by the radius of the interaction r_{FB} (for the lattice models $r_{FB} = d$), yields a resonant two-body bound state with an energy $E = -|E_b|$, where $|E_b| \ll 1/mr_{FB}^2$ is a shallow bound state (note that for the lattice models the requirement $|E_b| \ll 1/mr_{FB}^2$ is satisfied in the intermediate coupling case for 2D Fermi-Bose mixture with attraction between fermions and bosons considered in Sect. 6.2). At the same time a boson–boson interaction U_{BB}, characterized by the interaction radius r_{BB}, does not yield a resonance. This condition is also fulfilled in our model for Fermi-Bose mixture, since both $U_{FF} > 0$ and $U_{BB} > 0$ correspond to repulsion. Hence, if we are interested in the low-energy physics, the only relevant interaction is U_{FB}, and we can ignore the boson–boson interaction U_{BB} (the latter will give only small corrections of the order $|E_b|mr_{FB}^2 \sim |E_b|md^2 \ll 1$ at low energies). In order to determine three-particle bound states one has to find the poles in the composed fermion $f_\sigma b$—elementary boson b scattering vertex T_3. Since we neglect the boson–boson interaction U_{BB} the vertex T_3 is described by the same diagrammatic equation [see Fig. 6.5 and (6.3.17)] as in the problems of three resonantly interacting bosons. The analytical form of this equation also coincides with (6.3.17) with the minor correction that the resonance scattering vertex T_2 now corresponds to the interaction (U_{FB}) between a boson and a fermion, and therefore we should put $\alpha = 1$ in Eq. (6.3.17) for T_2. Solving the STM-equation for T_3 we find that the $f_\sigma b,b$ complex has only one s-wave bound state with an energy $|E_3| \approx 2.39|E_b|$ [24, 25]. The same result holds for the complex $b_1b_2b_1$ with two bosons of one sort and one boson of different sort. Note that a complex *bff*—consisting of a boson and two spinless identical fermions (or a complex with a boson and spin "up" and spin "down" fermion $bf_\uparrow f_\downarrow$) with resonance interaction U_{FB} does not have any three-particle bound states in the 2D case.

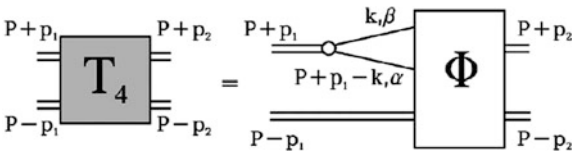

Fig. 6.8 The vertex Φ represents the full dimer–dimer scattering matrix T_4 with one dimer line being cut [24, 25]

6.3.5 *Dimer-Dimer Scattering for Four Resonantly Interacting Fermions in 3D. Exact Integral Equation for Four-Fermion Problem*

Now we can proceed to the problem of dimer–dimer scattering for two molecules $f_\uparrow f_\downarrow$ in 3D case. This problem was firstly solved by Petrov et al. [29] by studying the Schroedinger equation for a 4-fermion wave function.

Inspired by the work of Petrov et al. [29] we are looking for a special vertex, which describes an interaction of two fermions constituting a first dimer with a second dimer (considered as a single object). An obvious candidate for this vertex would be the sum of all the diagrams with two fermionic and one dimer incoming line. It would be natural to suppose that these diagrams should have the same set of outgoing lines—two fermionic and one dimer. However, in this case there will be a whole set of disconnected diagrams contributing to our sum that describes the interaction of a dimer with only one fermion. As was pointed out by Weinberg [22], one can construct a good integral equation of Lippmann–Schwinger type only for connected class of diagrams. Thus we are forced to give attention to the asymmetric vertex $\Phi_{\alpha\beta}(q_1, q_2; p_2, P)$ corresponding to the sum of all diagrams with one incoming dimer, two incoming fermionic lines and two outgoing dimer lines (see Fig. 6.8). This vertex $\Phi_{\alpha\beta}(q_1, q_2; p_2, P)$ is rather straightforwardly related to the standard dimer–dimer scattering vertex $T_4(p_1, p_2; P)$:

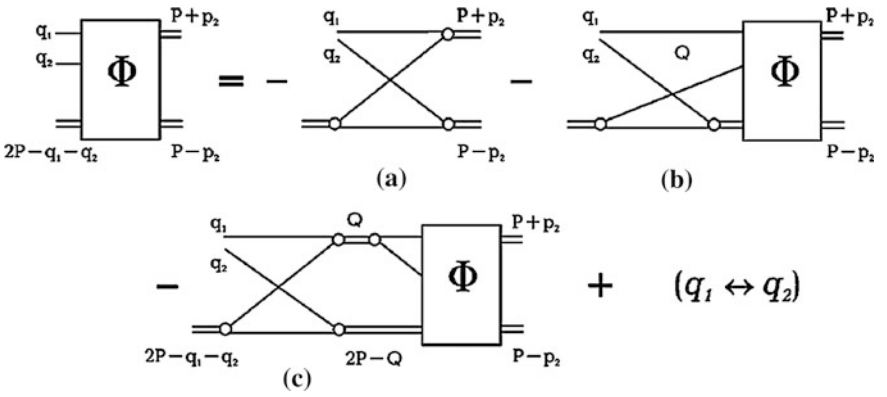

Fig. 6.9 The graphic representation of the equation on function Φ describing dimer–dimer scattering [24, 25]

$$T_4(p_1,p_2,P) = \frac{i}{2}\sum_{k,\alpha,\beta}\chi(\alpha,\beta)G(P+p_1-k)G(k)\Phi_{\alpha\beta}(P+p_1-k,k;p_2,P). \tag{6.3.19}$$

Note that, by definition, in any order of interaction Φ contains only connected diagrams.

The spin part of the vertex $\Phi_{\alpha\beta}$ has the simple form $\Phi_{\alpha\beta}(q_1, q_2; p_2, P) = \chi(\alpha, \beta)\Phi(q_1, q_2; p_2, P)$. A diagrammatic representation of the equation on Φ is given in Fig. 6.9. One can assign some physical meaning to the processes described by these diagrams. The diagram of Fig. 6.9a represents the simplest exchange process in a dimer–dimer interaction. The diagram of Fig. 6.9b accounts for a more complicated nature of a "bare" (irreducible by two dimer lines) dimer–dimer interaction.

Finally the diagram of Fig. 6.9c allows for a multiple dimer–dimer scattering via a bare interaction. The last term in Fig. 6.9 means that we should add another three diagrams analogous to Figs. 6.9a, b and c, but with the two incoming fermions (q_1 and q_2) exchanged. The analytical equation for the vertex Φ can be written as:

$$\begin{aligned}\Phi(q_1,q_2;p_2,P) = &-G(P-q_1+p_2)G(P-q_2-p_2)\\ &-i\sum_k G(k)G(2P-q_1-q_2-k)T_2(2P-q_1-k)\Phi(q_1,k;p_2,P)\\ &+\frac{1}{2}\sum_{Q,k} G(Q-q_1)G(2P-Q-q_2)T_2(2P-Q)T_2(Q)\\ &\quad G(k)G(Q-k)\Phi(k,Q-k;p_2,P)+(q_1\leftrightarrow q_2).\end{aligned} \tag{6.3.20}$$

Since we are looking for an s-wave scattering length we can put $p_2 = 0$ and $P = \{0, -|E_b|\}$. At this point we have a single closed equation for the vertex Φ in momentum representation, which, we believe, is analogous to the equation of Petrov et al. in coordinate representation. To make this analogy more prominent we have to exclude frequencies from the Eq. (6.3.19). This exclusion requires some more mathematical efforts, but we succeeded in doing that in our second (more extended) article on this subject (see Appendix A in Ref. [24]).

The dimer–dimer scattering length is proportional to the full symmetrized vertex $T_4(p_1, p_2; P)$:

$$\left(\frac{8\pi}{m^2 a}\right)^2 T_4(0,0,-2|E_b|,0) = \frac{2\pi(2a_{2-2})}{m}. \tag{6.3.21}$$

In the Born approximation we can consider only the contribution of the first term (Fig. 6.9a) in Φ. Then in this approximation (for the simplest exchange process in dimer–dimer interaction) $\Phi \sim GG$ and $T_4 \sim \Sigma GG\Phi \sim \Sigma GGGG$ (see Fig. 6.10) where the symbol Σ stands for the sum in these estimates.

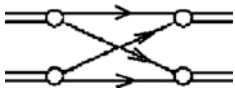

Fig. 6.10 Simplest exchange process which defines the Born approximation for the dimer–dimer T-matrix T_4

In the Born approximation $a_{2-2}(f_\uparrow f_\downarrow f_\uparrow f_\downarrow) = 2|a|$. This result is intuitively transparent since only the interaction between fermions with different spin projections has a resonance character according to Pauli principle. We will get it in the mean-field description of the BCS-BEC crossover and the spectrum of collective excitations in Chap. 7 (see also [93]).

If one skips the second term in (6.3.20), i.e., one omits the diagram in Fig. 6.9b, one arrives at the ladder approximation of Pieri and Strinati [26]. In this approximation we take into account the multiple scattering of two dimmers on each other without the loss of their identity. In the ladder approximation we get $a_{2-2} = 0.78|a|$ in agreement with the results of Pieri and Strinati. The exact Eq. (6.3.20) corresponds to the summation of all diagrams. Moreover the diagrams on the Fig. 6.9b (omitted in [26]) with an account of crossing ($q_1 \leftrightarrow q_2$) describe two types of processes:

(1) there are two incoming dimmers in the beginning, than they are virtually decaying and exchanging one particle with each other;
(2) there are two incoming dimmers in the beginning, than they are virtually decaying forming a virtual 3-particle complex and one elementary fermion. After that 2 dimers are again created.

Note that mathematical structure of the second term in (6.3.20) $\Sigma GGT_2\Phi$ resembles to some extent a mathematical structure of the integral term in STM equation for the trios ΣGGT_2T_3 (Σ stands for the sum again). Thus it takes into account dynamics and moreover allows to write a closed equation on Φ in (6.3.20) only in terms of two-particle T-matrix T_2 and one-particle Green functions G (without explicit utilization of the three-particle T-matrix T_3). Exact solution of (6.3.20) with an account of all these terms (Figs. 6.9a, b and c) together with crossing yields:

$$a_{2-2} = 0.6|a| \tag{6.3.22}$$

in agreement with Petrov et al. [29].

Note also that our approach allows one to find the dimer–dimer scattering amplitude in the 2D case also. Here

$$f_{2-2}(\varepsilon) = \frac{1}{\ln(1.6|E_b|/\varepsilon)} \tag{6.3.23}$$

in agreement with Petrov, Baranov and Shlyapnikov [23]. We will use this result to find coefficient α in formula (6.2.10) for T_C of the Bose condensed quartets $f_\uparrow b, f_\downarrow b$ in the 2D Fermi-Bose mixture with attractive interaction between fermions

and bosons. This formula of Fisher-Hohenberg type $T_C \sim \frac{T_0}{16 \ln \ln \left(\alpha \frac{|E_4|}{T_0} \right)}$ contains in denominator the coefficient α which describes the scattering of quartet on quartet (in the repulsive 2D Bose-gas of quartets $f_\uparrow b, f_\downarrow b$). Thus it is easy to show that for equal masses of fermions and bosons $m_B = m_F$ $\alpha = 4 \cdot 1.6 = 6.4$, where 1.6 is a coefficient under logarithm for scattering of dimer on dimer in 2D in (6.3.23). The binding energy $|E_4|$ for the quartet $f_\uparrow b, f_\downarrow b$ we will define in the next section.

Finally we would like to mention that our results allow one to find the dressed fermionic Green's function, chemical potential, and sound velocity as a function of two-particle scattering length a in the case of the dilute superfluid Bose-gas of weakly interacting dimers $f_\uparrow f_\downarrow$ at low temperatures. The problem of dilute superfluid Bose-gas of di-fermionic molecules was solved by Popov [91] and later deeply investigated by Keldysh and Kozlov in connection with the problem of excitonic (or bi excitonic) superfluidity [92]. These authors managed to reduce the gas problem to a dimer–dimer scattering problem in vacuum, but were unable to express the dimer–dimer scattering amplitude in a single two-fermion parameter. A direct combination of our results with those ones of Popov, Keldysh and Kozlov allows one to get all the thermodynamic values of a dilute superfluid resonance gas of composed bosons. This strategy will be fulfilled in Chap. 7.

6.3.6 Four Particles Bound States

In the 3D case a homogeneous part of the four-particle integral Eq. (6.3.20) has a nontrivial solution for any negative values of the energy for the 4-particle complexes *bbbb*, $f_\uparrow b f_\downarrow b$ and *fbbb*. Thus Efimov effect manifests itself again in a four-particle problem. However, for the same complexes in 2D Efimov effect is absent and the homogeneous part of the four-particles equation has the finite number of the solutions for the negative energy $E < 0$, which can be represented again only in terms of the two-particle binding energy $|E_b|$.

First we will consider four identical resonantly interacting bosons *bbbb*. Any two bosons would form a stable dimer with binding energy $E = -|E_b|$. We are

Table 6.1 Bound states of three and four resonantly interacting particles in 2D [24, 25]

System	Relative[a] interaction	Number of bound states	Energy (in $\|E_B\|$)[b]	α[c]
bbb	U_{bb}	2	1.27, 16.52	2
fbb	U_{fb}	1	2.39	1
fbbb	U_{fb}	1	4.10	1
$bf_\uparrow bf_\downarrow$	U_{fb}	2	2.84, 10.64	1
bbbb	U_{bb}	2	22, 197	2

[a] Interaction that yields resonance scattering. All other interactions are negligible

[b] $m = m_B = m_F$

[c] The indistinguishability parameter in (6.3.16)

going to find a four-particle binding energy of an s-wave bound state of two dimers. Generally speaking (see Sect. 6.1 for example), a bound state could emerge in channels with larger orbital moments (see [94]); however, this question will be considered in the next chapters. To find a binding energy we should examine the analytical structure of the dimer–dimer scattering vertex T_4 and find its poles. The set of equations for T_4 has the same diagrammatic structure as those shown in Figs. 6.8 and 6.9. The analytical expression for the first equation can be written as:

$$T_4(p_1,p_2,P) = \frac{i}{\alpha}\sum_k G(P+p_1-k)G(k)\Phi(P+p_1-k,k;p_2,P), \qquad (6.3.24)$$

and the equation for the vertex Φ:

$$\begin{aligned}\Phi(q_1,q_2;p_2,P) &= G(P-q_1+p_2)G(P-q_2-p_2)\\ &+ i\sum_k G(k)G(2P-q_1-q_2-k)T_2(2P-q_1-k)\Phi(q_1,k;p_2,P)\\ &- \frac{1}{2\alpha}\sum_{Q,k} G(Q-q_1)G(2P-Q-q_2)T_2(2P-Q)T_2(Q)G(k)\\ &G(Q-k)\Phi(k,Q-k;p_2,P) + (q_1 \leftrightarrow q_2),\end{aligned} \qquad (6.3.25)$$

where two-particle T-matrix T_2 in 2D should be taken from (6.3.16) and one should put $\alpha = 2$ for the case of identical resonantly interacting bosons. Solving the above equations for the poles of T_4 as a function of the variable $P = \{0, E\}$, we found two bound states for the *bbbb* complex (see Table 6.1). Certainly, for the validity of our approximation we should have $|E_4| \ll 1/mr_0^2$. For the case of four bosons *bbbb* it means that $197|E_b| \ll 1/mr_0^2$ for the deepest level and hence $a/r_0 \gg \sqrt{197}$. This case can still be realized in the Feshbach resonance scheme.

The case of a four-particles complex $f_\uparrow bf_\downarrow b$, consisting of resonantly interacting fermions and bosons is described by the same Eqs. (6.3.24, 6.3.25), but with the parameter $\alpha = 1$. In this case we found two bound states $|E_4| \approx 2.84|E_b|$ and $|E_4| \approx 10.64|E_b|$. They are also listed in Table 6.1. The same result is valid for two pairs of bosons of different sort $b_1b_2b_1b_2$.

In order to obtain the bound states of the *fbbb* complex one has to find the energies $P = \{0, E\}$ corresponding to nontrivial solutions of the following homogeneous equation:

$$\Phi(q_1,q_2;p_2,P) = i\sum_k G(k)G(2P-q_1-q_2-k)T_2(2P-q_1-k)\Phi(q_1,k;p_2,P) + (q_1 \leftrightarrow q_2). \qquad (6.3.26)$$

This equation corresponds to the diagrams of Fig. 6.9b with an account of crossing (and does not contain the diagrams of Fig. 6.9c). We found a bound state for the *fbbb* complex with an energy $|E_4| \approx 4.10\ |E_b|$.

We summarize the results concerning binding energies of three and four resonantly interacting particles in 2D in the Table 6.1. Note that all our calculations corresponds to the case of particles with equal masses $m = m_B = m_F$, though they can be easily generalized to the case of different masses.

6.3.7 Phase Diagram of the Fermi-Bose Mixture in 2D

In Sect. 6.2.5 we wrote the chain of the Saha crossover temperatures $T_*^{(2)} \sim \left|\tilde{E}_b\right|$, $T_*^{(3)} \sim |E_3|$ and $T_*^{(4)} \sim |E_4|$ for two-particle ($f_\sigma b$), three-particle ($f_\sigma b,b$), and four-particle ($f_\uparrow b,f_\downarrow b$) complexes in the 2D Fermi-Bose mixture on the lattice with attractive (and resonance in the intermediate coupling case) interaction between fermions and bosons. The knowledge of the binding energies of three-particle ($|E_3|$) and four-particle ($|E_4|$) complexes allows us to complete the phase diagram of a Fermi-Bose mixture. Namely the deepest levels for $m = m_B = m_F$ correspond to $|E_3| \approx 2.4\left|\tilde{E}_b\right|$ and $|E_4| \approx 10.6\left|\tilde{E}_b\right|$ for fbb and $f_\uparrow b$, $f_\downarrow b$ complexes, respectively. Thus $|E_4| > \left\{|E_3|, 2|\tilde{E}_b|\right\}$ and we have the following hierarchy of Saha temperatures:

$$T_*^{(4)} > \left\{T_*^{(3)}; T_*^{(2)}\right\}. \tag{6.3.27}$$

Then, as we already assumed in Sect. 6.3.5, the phase diagram becomes rather simple. Namely: for $T > T_*^{(4)}$ elementary fermions and bosons prevail in the system, while for $T < T_*^{(4)}$—the quartets $f_\uparrow b$, $f_\downarrow b$ prevail in the system in case of equal densities $n_B = n_F$. The quartets are Bose-condensed below the temperature: $T_C = T_0/(16 \ln(6.4\ |E_4|/T_0))$, where $|E_4| \approx 10.64\ |\tilde{E}_b|$.

6.3.8 Phase Diagram of 2D Bose-Gas

In the 2D Bose-gas with resonance interaction between bosons or in strongly disbalanced Fermi-Bose mixture for $n_B \gg n_F$ (see [11, 12]) the formation of large droplets containing $N > 4$ particles is possible. The limitation on the number of particles in the droplet is connected with the repulsive hard-core with the radius r_0:

$$R_N > r_0,\ |E_N| < \frac{1}{mr_0^2}, \tag{6.3.28}$$

where R_N and E_N are the radius and the binding energy of the N-particle droplet.

For $N > 4$ the exact solution of the STM-equations is practically impossible (it requires too much of the computer time). Thus we have to restrict ourselves with the variational calculations of R_N and E_N (see Hummer, Son [28]). For 2D case they yield $R_N \sim ae^{-N}$ and $E_N = 1/mR_N^2 \sim |E_b|e^{2N}$ under the condition:

$N < N_{\max} \sim 0.9\ln(a/r_0)$ ([28, 36]). The large droplets were experimentally observed in the disbalanced Fermi-Bose mixture of ^{87}Rb (bosons) and ^{40}K (fermions) for $n_B > n_F$ by Modugno et al. [12].

6.3.9 The Role of the Dimer-Fermion and Dimer–Dimer Scattering Lengths for the Lifetime of the Resonance Fermi-Gas

In case of the resonance Fermi-gas in 3D the dimer-fermion scattering length $a_{2-1} = 1.18\ |a| > 0$ and the dimer–dimer scattering length $a_{2-2} = 0.6\ |a| > 0$ define the relaxation rates of inelastic dimer-fermion and dimer–dimer collisions in the BEC-domain for $a > 0$.

Namely according to Petrov, Salomon and Shlyapnikov [29] the relaxation rates read:

$$\begin{aligned} \alpha_{2-1} &= C_1 \frac{\hbar r_0}{m} \left(\frac{r_0}{a}\right)^{3,33}, \\ \alpha_{2-2} &= C_2 \frac{\hbar r_0}{m} \left(\frac{r_0}{a}\right)^{2,55} \end{aligned} \tag{6.3.29}$$

for dimer-fermion (α_{2-1}) and dimer–dimer (α_{2-2}) inelastic scatterings. In (6.3.29) C_1 and C_2 are numerical coefficients.

Correspondingly the inverse inelastic scattering times $1/\tau_{2-1} \sim n_{atom}\alpha_{2-1}$ and $1/\tau_{2-2} \sim n_{mol}\alpha_{2-2}$ define the molecular transitions from the shallow to deep vibrational levels in the potential well. In course of this process, according to the discussion in Chap. 5 the molecules lose their identity and do not participate in the symmetrization of the dimer wave function. Thus practically $\frac{1}{\tau_{loss}} \sim \frac{1}{\tau_{2-1}} + \frac{1}{\tau_{2-2}}$, where $\frac{dn_{mol}}{dt} \sim \alpha_{2-1} n_{mol} n_{atom} + \alpha_{2-2} n_{mol}^2 \sim \frac{n_{mol}}{\tau_{loss}}$ and the inverse time of the losses of the resonance dimers $1/\tau_{\text{loss}}$ coincides by order of magnitude with the inverse lifetime $1/\tau_{\text{lifetime}}$ of the molecular BEC-condensate.

In the regime of Feshbach resonance for $B \to B_0$: $1/a \to 0$ and the lifetime of Bose-condensate strongly increases. Note that if the numbers of atoms and molecules coincide by the order of magnitude (for $n_{atom} \sim n_{mol}$) the inverse inelastic scattering time $\frac{1}{\tau_{2-1}} \sim \left(\frac{r_0}{a}\right)^{3.33} \frac{T_0}{\hbar} (r_0 p_F)$ (where T_0 is degeneracy temperature) while $\frac{1}{\tau_{2-2}} \sim \left(\frac{r_0}{a}\right)^{2.55} \frac{T_0}{\hbar} (r_0 p_F)$ and hence for $1/a \to 0$ the inverse loss time $\frac{1}{\tau_{loss}} \approx \frac{1}{\tau_{2-2}}$ is defined by dimer–dimer inelastic scatterings mostly (see [29]). Note that usually for the resonance Fermi-gas in BEC-regime $\tau_{\text{lifetime}} \leq 10$ s.

Concluding this section let us emphasize that in the resonance approximation we derive and solve exactly the integral equations for trios and quartets in 3D and 2D.

We evaluate exact scattering amplitudes of molecule on atom (a_{2-1}) and molecule on molecule in the 3D and the 2D resonance Fermi-gas.

We calculate the binding energies of all the possible complexes, consisting of three *bbb*, $b_1 b_2 b_1$, *fbb*, and four *bbbb*, $b_1 b_2 b_1 b_2$, *fbbb*, and $f_\uparrow b f_\downarrow b$ particles as the functions only of the two-particle binding energy $|E_b|$ in the 2D case.

We construct the phase-diagram for the resonance Fermi-Bose mixture in 2D with equal densities of fermions and bosons $n_B = n_F$. We discuss also the possibility of the formation of the large droplets containing 5 and more particles in the 2D Bose-gas and in the disbalanced Fermi-Bose mixture for $n_B > n_F$.

Note that a binding energy of a four-particle complex $b_1 b_2 b_1 b_2$ is important to complete the phase diagram of the two-band Bose-Hubbard model with repulsion between bosons of one sort and attraction between bosons of different sorts, considered in Sect. 6.1. In the intermediate coupling case on the lattice $T_0 < |\tilde{E}_b| < W$ in 2D this model as we already mentioned in Sect. 6.1 corresponds to the resonance interaction between bosons of different sort. Moreover for $|E_4| < W$ the quartets $b_1 b_2 b_1 b_2$ are extended $1/\sqrt{n} > a \gg d$ (not sitting on one site of the lattice) and thus even strong Hubbard repulsions between bosons of the same sort $U_{11} > 0$ and $U_{22} > 0$ cannot prevent the formation of the quartets.

References

1. Nozieres, P., Saint James, D.: J. de Phys. (France), **43**, 1133 (1982)
2. Kagan, M.Yu., Efremov, D.V.: Phys. Rev. B **65**, 195103 (2002)
3. Efremov, D.V., Kagan, M.Yu.: Physica B: Condens. Matt. **329–333**, 30 (2003)
4. Efremov, D.V., Kagan, M.Yu.: Physica B: Acta Physica Polonica **B34**, 591 (2003)
5. Boninsegni, M.: Phys. Rev. Lett. **87**, 087201 (2001)
6. Kagan, M.Yu., Brodsky, I.V., Efremov, D.V., Klaptsov, A.V.: Phys. Rev. A **70**, 023607 (2004)
7. Bardeen, J., Baym, G., Pines, D.: Phys. Rev. **156**, 207 (1967)
8. Anderson, P.W.: Science **235**, 1196 (1987)
9. Anderson, P.W.: Frontiers and Borderlines in Many-Particle Physics. Proceedings of the Varenna Summer School, Varenna (1987)
10. Wen, X.-G., Lee, P.A.: Phys. Rev. Lett. **80**, 2193 (1998)
11. Roati, G., Riboli, F., Modugno, G., Inguscio, M.: Phys. Rev. Lett. **89**, 150403 (2002)
12. Modugno, G., Roati, G., Riboli, F., Ferbaino, F., Brecha, R.J., Inguscio, M.: Science **297**, 2240 (2002)
13. Matera, F.: Phys. Rev. A **68**, 043624 (2003)
14. Mur-Petit, J., Polls, A., Baldo, M., Schulze, H.-J.: Phys. Rev. A **69**, 023606 (2004)
15. Efremov, D.V., Viverit, L.: Phys. Rev. B **65**, 134519 (2002)
16. Efimov, V.N.: Sov. J. Nucl. Phys. **12**, 589 (1971)
17. Stan, C.A., Zwierlein, M.W., Schunck, C.H., Raupach, S.M.F., Ketterle, W.: Phys. Rev. Lett. **93**, 143001 (2004)
18. Skorniakov, G.V., Ter-Martirosian, K.A.: JETP **4**, 648 (1957)
19. Milnos, R., Fadeev, L.D.: JETP **14**, 1351 (1962)
20. Jensen, A.S., Riisager, K., Fedorov, D.V., Garrido, E.: Rev. Mod. Phys. **76**, 215 (2004)
21. Bedaque, P.F., van Kolck, V.: Phys. Lett. B **428**, 221 (1998)
22. Weinberg, S.: Phys. Rev. **133**, B232 (1964)
23. Petrov, D.S., Baranov, M.A., Shlyapnikov, G.V.: Phys. Rev. A **67**, 031601(R) (2003)
24. Brodsky, I.V., Kagan, M.Yu., Klaptsov, A.V., Combescot, R., Leyronas, X.: Phys. Rev. A **73**, 032724 (2006)
25. Brodsky, I.V., Kagan, M.Yu., Klaptsov, A.V., Combescot, R., Leyronas, X.: JETP Lett. **82**, 273 (2005)
26. Pieri, P., Strinati, G.C.: Phys. Rev. B **61**, 15370 (2000)

27. Platter, L., Hammer, H.-W., Meissner, U.-G.: Few-Body Syst. **35**, 169 (2004)
28. Hammer, H.-W., Son, D.T.: Phys. Rev. Lett. **93**, 250408 (2004)
29. Petrov, D.S., Salomon, C., Shlyapnikov, G.V.: Phys. Rev. A **71**, 012708 (2005)
30. Wiegmann, P.B.: Prog. Theor. Phys. Suppl. **107**, 243 (1992)
31. Laughlin, R.B.: Phys. Rev. Lett. **60**, 2677 (1988)
32. Fetter, A.L., Hanna, C.B., Laughlin, R.B.: Phys. Rev. B **39**, 9679 (1989)
33. Laughlin, R.B.: Int. J. Mod. Phys. B **5**, 1507 (1991)
34. Menushenkov, A.P., Kuznetsov, A.V., Klement'ev, K.V., Kagan, M.Yu.: JETP **93**, 615 (2001)
35. Wilchek, F.: Fractional Statistics and Anyon Superconductivity. World Scientific, Singapore (1990)
36. Kagan, M.Yu., Brodsky, I.V., Klaptsov, A.V., Combescot, R., Leyronas, X.: Sov. Phys. Uspekhi **176**, 1105 (2006)
37. Bulaevskii, L.N., Nagaev, E.L., Khomskii, D.I.: JETP **27**, 836 (1968)
38. Brinkman, W.F., Rice, T.M.: Phys. Rev. B **2**, 1324 (1970)
39. Shraiman, B.I., Siggia, E.D.: Phys. Rev. B **42**, 2485–2500 (1990)
40. Belinicher, V.I., Chernyshev, A.L., Shubin, V.A.: Phys. Rev. B **56**, 3381 (1997)
41. Bruch, L.W., Tjon, J.A.: Phys. Rev. A **19**, 425 (1979)
42. Stoof, H.T.C., Houbiers, M., Sackett, C.A., Hulet, R.G.: Phys. Rev. Lett. **76**, 10 (1996)
43. Richard, J.M.: Phys. Rep. **212**, 1 (1992)
44. Casalbuoni, R., Nardulti, G.: Rev. Mod. Phys. **76**, 263 (2004)
45. Valatin, J.G., Butler, D.: Nuovo Cimento **10**, 37 (1958)
46. Iordanskii, S.V.: JETP **20**, 112 (1965)
47. Rice, M.J., Wang, Y.R.: Phys. Rev. B **37**, 5893 (1988)
48. Emery, V.J., Kivelson, S.A., Lin, H.Q.: Phys. Rev. Lett. **64**, 475 (1990)
49. Kagan, M.Yu., Rice, T.M.: J. Phys.: Condens. Matter **6**, 3771 (1994)
50. Fisher, M.P.A., Weichman, P.B., Grinstein, G., Fisher, D.S.: Phys. Rev. B **40**, 546 (1989)
51. Weichman, P.B., Rasolt, M., Fisher, M.E., Stephen, M.J.: Phys. Rev. B **33**, 4632 (1986)
52. Freezicks, J.K., Monien, H.: Europhys. Lett. **26**, 545 (1994)
53. Rokhsar, D.S., Kotliar, B.G.: Phys. Rev. B **44**, 10328 (1991)
54. Kampf, A.P., Zimanyi, G.T.: Phys. Rev. B **47**, 279 (1993)
55. Sheshadri, K., Krishnamurthy, H.R., Pandit, R., Ramakrishnan, T.V.: Europhys. Lett. **22**, 257 (1993)
56. Abrikosov, A.A., Gor'kov, L.P., Dzyaloshinskii, I.E.: Quantum Field Theoretical Methods in Statistical Physics. Prentice-Hall, Englewood Cliffs (1963)
57. Hubbard, J.: Proc. Roy. Soc. London **A276**, 238 (1963)
58. Kanamori, J.: Progr. Theor. Phys. **30**, 275 (1963)
59. Anderson, P.W.: Phys. Rev. Lett. **64**, 1839 (1990)
60. Anderson, P.W.: Phys. Rev. Lett. **65**, 2306 (1990)
61. Anderson, P.W.: Phys. Rev. Lett. **66**, 3226 (1991)
62. Shi, H., Griffin, A.: Phys. Rep. **304**, 1 (1998)
63. Miyake, K.: Progr. Theor. Phys. **69**, 1794 (1983)
64. Alexandrov, A., Ranninger, J.: Phys. Rev. B **23**, 1796 (1981)
65. Ranninger, J., Robaszkiewicz, S.: Physica B **135**, 468 (1985)
66. Fisher, D.S., Hohenberg, P.C.: Phys. Rev. B **37**, 4936 (1988)
67. Popov, V.N.: Theor. Math. Phys. **11**, 565 (1972)
68. Kosterlitz, J.M., Thouless, D.J.: J. Phys. C: Solid State Phys. **6**, 1181 (1973)
69. Berezinskii, V.L.: JETP Lett. **34**, 610 (1972)
70. Baranov, M.A., Kagan, M.Yu.: Z. Phys. B-Cond. Matt. **86**, 237 (1992)
71. Mott, N.F., Davis, E.A.: Electronic Processes in Non-Crystalline Materials. Oxford University Press, Oxford (1979)
72. Dagotto, E., Riera, J.: Phys. Rev. Lett. **70**, 682 (1993)
73. Dagotto, E., Riera, J., Chen, Y.C., Moreo, A., Nazarenko, A., Alcaraz, F., Ortolani F.: Phys. Rev. B **49**, 3548 (1994). Appendix B

74. Ropke, G., Schnell, A., Schunck, P., Nozieres, P.: Phys. Rev. Lett. **80**, 3177 (1998)
75. Keldysh, L.V.: Solid State Comm. **84**, 37 (1992)
76. Babichenko, V.S.: JETP **37**, 311 (1973)
77. Lozovik, Y.E., Berman, O.L., Villander, M.: JETP **88**, 980 (1999)
78. Bartouni, G.G., Hebert, F., Scalettar, R.T.: Phys. Rev. Lett. **97**, 087209 (2006)
79. Sengupta, P., Pryadko, L.P., Alet, F., Troyer, M., Schmid, G.: Phys. Rev. Lett. **94**, 207202 (2005)
80. Bartouni, G.G., Scalettar, R.T.: Phys. Rev. Lett. **84**, 1599 (2000)
81. Batrouni, G.G., Assaad, F.F., Scalettar, R.T., Denteneer, P.J.H.: Phys. Rev. A **72**, 031601R (2005)
82. Kuklov, A.B., Prokof'ev, N.V., Svistunov, B.V.,: Phys. Rev. Lett. **92**, 030403 (2003)
83. Altman, E., Hofstetter, W., Demler, E., Lukin, M.D.: New J. Phys. **5**, 113 (2003)
84. Lee, P.A., Nagaosa, N., Ng, T.-K., Wen, X.-G.: Phys. Rev. B **57**, 6003 (1998)
85. Lee, P.A., Nagaosa, N.: Phys. Rev. B **46**, 5621 (1992)
86. Arovas, D.P., Auerbach, A.: Phys. Rev. B **38**, 316 (1988)
87. Chubukov, A.V.: Phys. Rev. B **44**, 12318 (1991)
88. Irkhin, V.Y., Katanin, A.A., Katsnelson, M.I.: Phys. Rev. B **60**, 1082 (1999)
89. Kotliar, X.G., Liu, J.: Phys. Rev. B **38**, 5142 (1988)
90. Danilov, G.S.: JETP **13**, 349 (1961)
91. Popov, V.N.: JETP **23**, 1034 (1966)
92. Keldysh, L.V., Kozlov, A.N.: JETP **27**, 521 (1968)
93. Combescot, R., Kagan, M.Yu., Stringari, S.: Phys. Rev. A **74**, 042717 (2006)
94. Kagan, M.Yu., Efremov, D.V.: JETP **110**, 426 (2010)
95. Baranov, M.A., Kagan, M.Yu., Kagan, Y.: JETP Lett. **64**, 301 (1996)
96. Bashkin, E.P., Meyerovich, A.E.: Adv. Phys. **30**, 1 (1981)
97. Kagan, M.Yu.: Sov. Phys. Uspekhi **37**, 69 (1994)
98. Fradkin, E.: Field Theories of Condensed Matter Systems. Addison-Wesley, Reading (1991)
99. Haldane, F.D.M.: Phys. Rev. Lett. **66**, 1529 (1991)
100. Fukuyama, H., Hasegawa, Y., Narikiyo, O.: J. Phys. Soc. Jpn. **60**, 2013 (1991)
101. Shuryak, E.: Prog. Part. Nucl. Phys. **53**, 273 (2004)

Chapter 7
BCS-BEC Crossover and the Spectrum of Collective Excitations in s-Wave and p-Wave Resonance Superfluids

In this chapter, using the knowledge of dimer–dimer scattering length $a_{2-2} = 0.6|a| > 0$, we complete the phase-diagram of the resonance Fermi-gas in 3D. We present more detaily the scheme of BCS-BEC crossover developed by Nozieres and Schmitt-Rink (see Ref. [14] in Chap. 5) and construct the phase-diagram of the resonance Fermi-gas in the self-consistent T-matrix approximation (see Refs. [18–21, 68). We define the crossover line $\mu(T) = 0$ which effectively separates BEC-domain (for which $\mu < 0$ and $a > 0$) from the BCS-domain (for which vise versa $\mu > 0$ and $a < 0$). We discuss the critical temperatures of extended Cooper pairing T_C^{BCS} and Bose-condensation for local pairing of two fermions T_C^{BEC} in dilute BCS and BEC limits for $|a|p_F \ll 1$, where p_F is the Fermi-momentum and a is an s-wave two-particle scattering length. We also provide qualitative considerations for the phase-diagram in the unitary limit $1/a \to 0$ and close to unitarity (for large values of the gas parameter $|a|p_F \gg 1$). We observe that in the substance a unitary limit is effectively inside the BCS-domain. We extend our results at finite temperatures on 2D resonance Fermi-gas.

In the second part of this Chapter we provide a brief description of the self-consistent Leggett scheme (see Refs. [12, 13] in Chap. 5) for the BCS-BEC crossover at zero temperature ($T = 0$). We solve the Leggett equations and find the behavior of the superfluid gap Δ and chemical potential μ as the functions of the gas parameter ap_F in the dilute BCS and BEC limits, as well as close to unitarity. The knowledge of the gap Δ and chemical potential allows us to solve Bogoliubov-Anderson equations (see Refs. [1, 2]) and determine the spectrum of collective excitations both in BCS and BEC domains. For small ω and q the spectrum is linear and we can find the behavior of the sound velocity (and Landau critical hydrodynamic velocity (see Ref. [23])) as a function of ap_F. Note that the sound velocity can be defined already from the static Leggett equations (from the knowledge of compressibility or the chemical potential of the system).

In the third part of this Chapter we will extend our results on BCS-BEC crossover in p-wave resonance Fermi-gas (see Refs. [3, 4]). We present experimental results on p-wave Feshbach resonance (see Refs. [5, 6]) in BEC-domain for fully-polarized Fermi-gas where the triplet molecules $^{40}K_2$ and $^6Li_2$ are created

M. Yu. Kagan, *Modern Trends in Superconductivity and Superfluidity*,
Lecture Notes in Physics 874, DOI: 10.1007/978-94-007-6961-8_7,

with $S_{tot} = S^z_{tot} = l = 1$ for total spin of the pair S_{tot}, its z-projection $S_{tot}{}^z$ and relative orbital momentum of the pair l. The p-wave superfluid has a symmetry of triplet A1-phase here.

We will construct the phase-diagram of the BCS-BEC crossover in p-wave resonance superfluid and define again a crossover line $\mu(T) = 0$ which separates BEC-domain of the A1-phase from the BCS-domain [66]. We will also solve the self-consistent Leggett equations at $T = 0$ and find the behavior of the superfluid gap and sound velocity. For low temperatures $T \ll T_C$ we will determine also the temperature behavior of the specific heat $C_v(T)$ and normal density $\rho_n(T)$ both in 3D and 2D triplet superfluid Fermi-gas. We will show that globally phase-diagram of the BCS-BEC crossover for p-wave resonance superfluid resembles that of s-wave resonance superfluid (considered in Sect. 7.1.3). However, in p-wave case there is a special point on the phase-diagram, namely $\mu(T = 0) = 0$ which corresponds to quantum phase-transition (see Refs. [14, 15, 33]). Close to this point the temperature behavior of the normal density $\rho_n(T)$ and specific heat $C_v(T)$ is different in classical and quantum limits $|\mu| \to 0,\ T \to 0$ but either $\frac{|\mu|}{T} \to 0$ or vice versa $\frac{T}{|\mu|} \to 0$ [12, 13]. Note that the point $\mu(T = 0) = 0$ separates in 3D the BCS state with the nodes in the quasiparticle energy (and zeroes in the superconductive gap for triplet A1-phase) form the gapped BEC-domain (where the quasiparticle energy has no zeroes) [14, 15, 33].

7.1 Phase-Diagram of the Resonance Fermi-Gas in 3D and 2D Cases

In Chap. 5 we presented a basic knowledge connected with the Bethe–Salpeter integral equation (see Refs. [22, 25] in Chap. 5), which describes the temperature evolution of the 3D resonance Fermi-gas. We also considered the dilute molecular (BEC) limit at high temperatures $T > T_C{}^{BEC}$. In Chap. 6, from the solution of Skorniakov-Ter-Martirosian equation, we define mean-field ($a_{2-2} = 2|a|$) and exact ($a_{2-2} = 0.6|a|$) dimer–dimer (or molecule–molecule) scattering length which describes a weak repulsion between the composed bosons $f_\uparrow f_\downarrow$ in the dilute BEC limit and for the temperatures $T < T_*$ (where T_* is the crossover Saha temperature which corresponds to the formation of local pairs or molecules $f_\uparrow f_\downarrow$ for positive scattering length $a > 0$). In this Section we will complete the phase-diagram of the resonance Fermi-gas in 3D and in 2D case.

7.1.1 Self-Consistent T-Matrix Approximation

In Chap. 5 we wrote two equations for the T-matrix in attractive 3D Fermi-gas. The first one is for the T-matrix (or scattering length) in vacuum (see Eq. (5.2.6) and Fig. 5.14):

$$T_{vac}(\omega = 0,\ q = 0) = \frac{4\pi a}{m} = -\frac{|U_0|}{1 + |U_0| K_{vac}(0,0)}, \tag{7.1.1}$$

where

$$K_{vac}(0,0) = \int \frac{d^3\vec{p}}{(2\pi)^3}\frac{d\Omega}{(2\pi)} G_{vac}(\Omega,\vec{p}) G_{vac}(-\Omega,\ -\vec{p}) = -\int \frac{d^3\vec{p}}{2\varepsilon_p} \tag{7.1.2}$$

is a Cooper loop in vacuum (a product of two vacuum Green-functions $G_{vac}(\Omega,\ \vec{p}) = \frac{1}{\Omega - \frac{p^2}{2m} + io}$ in the Cooper channel for zero total frequency $\Omega = 0$ and total momentum $\vec{p} = 0$) and $U_0 = -|U_0|$ is Fourier-harmonic of the attractive two-particle potential, $U(q)$ for $q = 0$.

The second one (see Eq. (5.2.12) is for the T-matrix in substance:

$$T(i\omega_n,\ \vec{q}) = -\frac{|U_0|}{1 + |U_0| K(i\omega_n,\ \vec{q})}, \tag{7.1.3}$$

where $K(i\omega_n,\ \vec{q})$ is a Cooper loop in substance for total Matsubara frequency of two (incoming in the Cooper channel) particles ω_{n} and total momentum $\vec{q}$. For fermions $\omega_{\mathrm{n}} = \pi\, T(2n + 1)$. We also emphasized in Chap. 5 that in the T-matrix approximation (when we neglect the difference between irreducible bare vertex $U_{\mathrm{eff}}(q)$ and the Fourier-harmonic of the bare vacuum interaction $U(q)$ the Eq. (7.1.3) for the T-matrix in substance coincides with the solution of the Bethe–Salpeter integral equation for a total two-particle vertex Γ in the Cooper channel.

According to general quantum–mechanical prescriptions (see Refs. [19, 26, 27] in Chap. 5), we should make a renormalization procedure and rewrite (7.1.3) only in terms of observables. Effectively we should replace U_0 in Eq. (7.1.3) by the scattering amplitude a from Eq. (7.1.1). This yields:

$$-\frac{1}{|U_0|} - K_{vac}(0,0) = \frac{m}{4\pi a} \tag{7.1.4}$$

and correspondingly [66]:

$$\begin{aligned} T(i\omega_n,\ \vec{q}) &= \frac{1}{-\frac{1}{|U_0|} - K(i\omega_n,\ \vec{q})} = \frac{1}{\frac{m}{4\pi a} - K(i\omega_n,\ \vec{q}) + K_{vac}(0,0)} \\ &= \frac{4\pi a/m}{1 - \frac{4\pi a}{m}\left(K(i\omega_n,\ \vec{q}) - K_{vac}(0,0)\right)} \end{aligned} \tag{7.1.5}$$

That is precisely a renormalization procedure which comes in condensed matter physics from quantum electrodynamics [17]. Note that a Cooper loop $K(i\omega_n,\ \vec{q})$ in Eq. (7.1.5) reads:

$$K(i\omega_n,\ \vec{q}) = \sum_{\Omega_n} \int \frac{d^3\vec{p}}{(2\pi)^3} G_M(i\Omega_n,\ \vec{p}) G_M(-i\Omega_n + i\omega_n,\ -\vec{p} + \vec{q}) \tag{7.1.6}$$

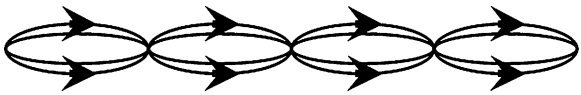

Fig. 7.1 The dressed ladder diagrams in particle–particle channel for the T-matrix given by Eqs. (7.1.5) and (7.1.6) (Refs. [31, 32] in Chap. 6)

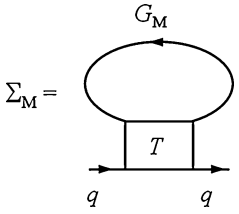

Fig. 7.2 The self-energy $\sum_M (i\omega_n, \vec{q})$ in the self-consistent T-matrix approximation. q is a four momentum $\{\omega_n, \vec{q}\}$ [3, 32]

In graphical form we sum up in the T-matrix approximation the dressed ladder diagrams in particle–particle channel presented on Fig. 7.1 [66], (see Refs. [31, 32] in Chap. 6 and [18–21]).

The Dyson equation for dressed Matsubara Green's function (which enter in the expression (7.1.6) for a Cooper loop) yields:

$$G_M(i\omega_n, \vec{q}) = \frac{1}{i\omega_n - \varepsilon(\vec{q}) + \mu - \Sigma_M(i\omega_n, \vec{q})}. \tag{7.1.7}$$

Finally the Matsubara self-energy Σ_M in the self-consistent T-matrix approximation reads (see Fig. 7.2):

$$\Sigma_M(i\omega_n, \vec{q}) = \sum_{\Omega_n} \int \frac{d^3\vec{p}}{(2\pi)^3} G_M(i\Omega_n - i\omega_n, \vec{p} - \vec{q}) T(i\Omega_n, \vec{p}). \tag{7.1.8}$$

The dressed one-particle Green's function should be normalized on total density for one spin projection $n_{tot}/2$:

$$\sum_{\omega_n} \int \frac{d^3\vec{q}}{(2\pi)^3} G_M(i\omega_n, \vec{q}) = \sum_{\omega_n} \int \frac{d^3\vec{q}}{(2\pi)^3} \frac{1}{G_0^{-1}(i\omega_n, \vec{q}) - \Sigma_M(i\omega_n, \vec{q})} = \frac{n_{tot}}{2} = \frac{p_F^3}{6\pi^2}, \tag{7.1.9}$$

where

$$G_0(i\omega_n, \vec{q}) = \frac{1}{i\omega_n - \varepsilon(\vec{q}) + \mu} \tag{7.1.10}$$

is a bare Matsubara Green's function.

The system of Eqs. (7.1.5)–(7.1.9) constitutes the self-consistent T-matrix approximation. This approximation is energy and momentum conserving ([66] and [18–21, 31, 32] in Chap. 6), and is exact in leading order in the gas parameter ap_{F} for dilute Fermi-systems (see for example Galitskii-Bloom results (see Ref. [28] in Chap. 5), [22] for 3D and 2D repulsive Fermi-gas).

We solve the system of Eqs. (7.1.5)–(7.1.9) perturbatively. As a result in the first iteration we should calculate the T-matrix in Eq. (7.1.5) with the zeroth order Matsubara Green's functions $G_0(i\omega_n,\ \vec{q})$ (see (7.1.10)).

Then the renormalized Cooper loop $K(i\omega_n,\ \vec{q}) - K_{vac}(0,0)$ [which enters in the denominator of Eq. (7.1.5)) reads:

$$K_{ren} = K(i\omega_n, \vec{q}) - K_{vac}(0,0) = \int \frac{d^3\vec{p}}{(2\pi)^3}\left[\frac{1 - n_F\left(\xi_p\right) - n_F\left(\xi_{-p+q}\right)}{i\omega_n - \xi_p - \xi_{-p+q}} + \frac{1}{2\varepsilon_p}\right]. \tag{7.1.11}$$

Correspondingly:

$$T(i\omega_n,\ \vec{q}) = \frac{4\pi a/m}{1 - \frac{4\pi a}{m}K_{ren}(i\omega_n, \vec{q})}. \tag{7.1.12}$$

The pole of the T-matrix in Eq. (7.1.5) for $\omega_n = \vec{q} = 0$ determines the equation for T_{C}:

$$1 - \frac{4\pi a}{m}K_{ren}(0,0) = 0. \tag{7.1.13}$$

The self-energy in the first iteration reads:

$$\Sigma_1(i\omega_n, \vec{q}) = \sum_{\Omega_n}\int \frac{d^3\vec{p}}{(2\pi)^3}T_0(i\Omega_n,\ \vec{p})G_0(i\Omega_n - i\omega_n,\ \vec{p} - \vec{q}). \tag{7.1.14}$$

It enters in the equation of the conservation of the number of particles:

$$\sum_{\omega_n}\int \frac{d^3\vec{q}}{(2\pi)^3}\frac{1}{G_0^{-1}(i\omega_n,\ \vec{q}) - \Sigma_1(i\omega_n,\ \vec{q})} = \frac{n_{tot}}{2} = \frac{p_F^3}{6\pi^2}. \tag{7.1.15}$$

7.1.2 Equation for $\mathbf{T}_C$

The pole of the T-matrix in the 3D case reads:

$$1 + \frac{4\pi a}{m}\int\left[\frac{th\frac{\varepsilon_p - \mu}{2T_C}}{2\left(\varepsilon_p - \mu\right)} - \frac{1}{2\varepsilon_p}\right]\frac{d^3\vec{p}}{(2\pi)^3} = 0. \tag{7.1.16}$$

As we already discussed in Chap. 5, in the BCS-domain for $a < 0$ and $|a|p_F < 1$ (dilute Fermi-gas) the chemical potential $\mu \approx \varepsilon_F > 0$ ($\varepsilon_F = p_F^2/2m$) and the critical temperature: $T_C^{BCS} \sim \varepsilon_F \exp\left\{-\frac{\pi}{2|a|p_F}\right\}$.

In the BEC-domain for $a > 0$ and $ap_F < 1$: the fermionic chemical potential $\mu < 0$ and bosonic chemical potential $\mu_B(T_C) = 2\mu + |E_b| = 0$ (hence, $\mu(T_C) = -|E_b|/2$). A temperature of the Bose–Einstein condensation $T_C^{BEC} \sim 3.31 \frac{(n_{tot}/2)^{2/3}}{2m} \approx 0.2\varepsilon_F$ in an ideal Bose-gas of molecules (composed bosons) with the mass $m_B = 2\,m$ and density $n_B = \frac{n_{tot}}{2} = \frac{p_F^3}{6\pi^2}$.

7.1.3 Self-Energy in the Dilute BEC Limit

In the BEC-domain in the dilute case (for $ap_F < 1$) there is one more characteristic temperature (see Chap. 5) namely: $T_* = \frac{|E_b|}{3/2 \ln \frac{|E_b|}{\varepsilon_F}} \gg T_C^{BEC}$—Saha temperature, which describes smooth crossover ($|E_b| = 1/ma^2$ is a molecular binding energy). For $T = T_*$ the number of molecules ($n_B = n_{F\sigma} = n_{tot}/4$) equals to the number of unpaired fermions with one spin projection σ. For $T_C < T \ll T_*$ we have a slightly non-ideal Bose-gas of composed molecules in a normal (non-superfliud) state. The self-energy $\Sigma_1(i\omega_n, \vec{q})$ in the first iteration to the self-consistent T-matrix approximation (7.1.14) reads (see [66]):

$$\Sigma_1(i\omega_n, \vec{q}) = \frac{8\pi a|\mu| \frac{n_{tot}}{m} \frac{2|\mu|}{|E_b|}}{i\omega_n + q^2/2m - \mu + \mu_B}. \tag{7.1.17}$$

Note that $\Sigma_1(i\omega_n, \vec{q})$ has a "hole like" dispersion $i\omega_n + \xi_q + \mu_B$ ($\xi_q = q^2/2m - \mu$) in contrast to the "particle like" dispersion $\xi(\vec{q})$ in the Matsubara Green's function of the zeroth approximation G_0 (see 7.1.10). For $T_C < T \ll T_*$: $n_{tot} \approx 2n_B$ (number of unpaired fermions is small) and thus:

$$\frac{n_{tot}}{2} = \frac{1}{2\pi^2} \int_0^\infty \frac{k^2 dk}{\exp\left\{\frac{k^2/4m - |E_b| - 2\mu}{T}\right\} - 1}, \tag{7.1.18}$$

where we took into account that $\mu_B = 2\mu + |E_b|$. The same result can be restored from the form of the dressed Green's function $G^{-1}(i\omega_n, \vec{q}) = G_0^{-1}(i\omega_n, \vec{q}) - \Sigma_1(i\omega_n, \vec{q})$ in the first iteration with Σ_1 given by Eq. (7.1.17).

We remind that the T-matrix $T(i\omega_n, \vec{q}) = \frac{4|\mu|\,4\pi a/m}{i\omega_n - q^2/4m + \mu_B}$ for small ω_n and $\vec{q}$. Correspondingly the dressed Green's function can be rewritten as [66]:

$$G(i\omega_n, \vec{q}) \approx \frac{1}{i\omega_n - \xi_q - \frac{8\pi a|\mu| n_{tot}/m}{i\omega_n + \xi_q + \mu_B}} = \frac{1}{i\omega_n - \xi_q - \frac{\Delta_{PG}^2}{i\omega_n + \xi_q + \mu_B}}, \tag{7.1.19}$$

where we put $2|\mu|/|E_b| \approx 1$ ($|\mu| \approx |E_b|/2$ for $T \ll T_*$) and introduced the pseudogap $\Delta_{PG}^2 = 8\pi a|\mu|n_{tot}/m$ according to [38]. Note that $\Delta_{PG}^2 \sim |E_b|\varepsilon_F a p_F$. Intensive discussion of the pseudogap state we can also find in [62–64]. We will return to this interesting problem in the next Section.

The spectral function $A(\omega, \vec{q}) = -\frac{1}{\pi}\mathrm{Im}G(\omega + io, \vec{q})$ reads [66]:

$$A(\omega, \vec{q}) \approx \left(1 - \frac{2\pi a|\mu|n_{tot}/m}{\xi_q^2}\right)\delta(\omega - \xi_q) + \frac{2\pi a|\mu|n_{tot}/m}{\xi_q^2}\delta(\omega + \xi_q + \mu_B). \tag{7.1.20}$$

(Effectively in Eq. (7.1.20) we made analytical continuation $i\omega_n \to \omega + io$). For $T \ll T_*$ the form of $A(\omega, \vec{q})$ in Eq. (7.1.20) reflects the existence of two bands (see Refs. [31, 32] in Chap. 6 and [66]. One is the filled bosonic band. A second one is separated from the first one by large correlation gap $\Delta = |E_b|$ ($\Delta \gg \Delta_{PG}$ for dilute BEC regime). It is almost empty band of unbound fermions. Integrating the spectral weight it is easy to check that in this regime:

$$\frac{4\pi a|\mu|}{m}\frac{1}{2\pi^2}\int_0^\infty \frac{k^2 dk}{\xi_k^2} = \frac{n_{tot}}{2} \approx n_B, \tag{7.1.21}$$

where we used that $|\mu| \approx |E_b|/2 = 1/2ma^2$ in $\xi_k = k^2/2m + |\mu|$. Note that the specific heat of the system

$$C_v = \frac{\partial E}{\partial T} = \frac{\partial}{\partial T}\left[\int \frac{k^2}{4m}\frac{k^2 dk}{2\pi^2}\exp\left(-\frac{k^2}{4mT}\right)\exp\left(\frac{\mu_B}{T}\right)\right] \sim \frac{n_{tot}}{2} = const \tag{7.1.22}$$

is temperature independent in agreement with general thermodynamic requirements [66].

7.1.4 Phase-Diagram of the Resonance Fermi-Gas in 3D

In the first iteration to the self-consistent T-matrix approximation the numerical calculations yield the following qualitative phase-diagram of the BCS-BEC crossover (see Fig. 7.3 and [66]).

On Fig. 7.3 we present a critical temperature T_C versus inverse gas parameter $1/(p_F a)$. The dashed line $\mu(T) = 0$ effectively separates BCS-domain (with $\mu > 0$) from BEC-domain (with $\mu < 0$). Note that according to [66] $\mu(T_C) = 0$ for $T_C \approx 0.29\varepsilon_F$ and $1/(p_F a) \approx 0.37$. Thus in substance the border between BCS and BEC-domain effectively lies in the BEC region of positive scattering length $a > 0$. In the same time a unitary limit in vacuum $1/(p_F a) = 0$ is effectively in the BCS-domain of positive chemical potential $\mu > 0$. Note that on Fig. 7.3 the region of dilute Fermi-gas corresponds to the interval $[-\infty, -1]$ for $1/(p_F a)$, while the

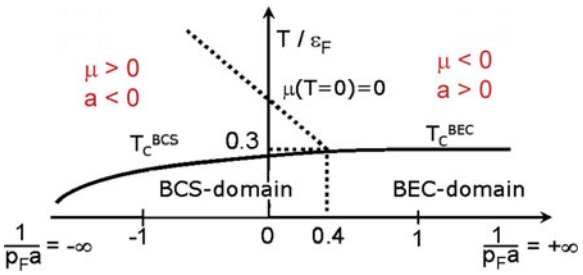

Fig. 7.3 Phase-diagram of the BCS-BEC crossover in the resonance Fermi-gas in 3D (numerical calculations for T_C and μ versus $1/p_F a$ for the first iteration to the self-consistent T-matrix approximation) [66]

region of dilute Bose-gas (of composed bosons or molecules) corresponds to the interval $[1, \infty]$. Close to the unitarity (in the interval $[-1, 1]$) we have strongly interacting gas and cannot apply exact diagrammatic expansions of Galitskii [5.28] and Beliaev [25]. It is interesting to note that while in dilute limit for BEC-domain according to Gor'kov and Melik-Barkhudarov the critical temperature $T_C^{BCS} = 0.28\ \varepsilon_F \exp\left\{-\frac{\pi}{2|a|p_F}\right\}$ has a preexponential factor $0.28\,\varepsilon_F$, in dilute limit for BEC-domain we have very interesting correction to Einstein formula obtained by Kashurnikov, Prokof'ev and Svistunov [26]:

$$T_C^{BEC} = 0.2\,\varepsilon_F\left[1 + 1.3a_{2-2}n_{tot}^{1/3}\right]. \tag{7.1.23}$$

These corrections just take into account the repulsive dimer–dimer scattering length $a_{2\text{-}2} = 0.6|a| > 0$ and correspond to 3D weakly non-ideal Bose-gas with repulsion between composed bosons.

7.1.5 Unitary Limit

In the unitary limit $1/(p_F a) = 0$ there is only one scale, namely, Fermi-energy ε_F both for kinetic and potential energy [30, 68]. Thus in this limit the total energy of the system reads:

$$E = \frac{3}{5}\varepsilon_F N\beta. \tag{7.1.24}$$

It does not depend upon the gas parameter $1/(p_F a)$ and depends only on the universal coefficient β. This coefficient depends only upon the number of components in the Fermi-gas. For the gas with the spin $S = ½$ the number of components is 2 ($S_z = \pm ½$) and $\beta \approx 0.44 > 0$ [27, 28]. Thus it is a gas phase ($E > 0$) according to Monte Carlo simulations by Astrakharchik et al. [27, 28] and Carlson et al. [29]. In a gas phase the chemical potential $\mu = dE/dN = \beta\varepsilon_F = 0.44\varepsilon_F$ at temperature $T = 0$.

For the mixture of protons and neutrons the number of components is 4 and $\beta < 0$. We have a liquid phase here ($E < 0$) according to Heiselberg [30]. To some extent it is an answer on the question formulated some time ago by Zel'dovich in Moscow: whether we can get a dilute liquid in the system of resonantly interacting neutrons? The answer of Heiselberg is negative: without protons we are in the gas-phase for $|a|p_F \gg 1$ (see also [40]).

7.1.6 *Qualitative Interpretation of the Intermediate Region of Large Values of* $|a|p_F \gg 1$ *(*$-1 < 1/(p_F a) < 1$*)*

In the strong coupling limit $|a|p_F > 1$ for BCS-domain ($\mu > 0$ and $a < 0$) nothing dramatic happens. We can qualitatively represent Gor'kov-Melik-Barkhudarov result as:

$$T_C = A\mu \exp\left\{-\frac{\pi}{2|a|\sqrt{2m\mu}}\right\} \text{ for } \mu > 0, \tag{7.1.25}$$

(where we replaced ε_F by μ and p_F by $\sqrt{2m\mu}$).

In the unitary limit $1/a \to -0$, the chemical potential $\mu > 0$ and $T_C = A\mu \approx 0.15\varepsilon_F$ according to numerical calculations of Burovski et al. [31]. In the same time $\mu \approx 0.44\varepsilon_F$ according to [27–29] and thus $A \approx 0.35$ in Eq. (7.1.25), which is close to preexponential factor 0.28 (in front of ε_F) of Gor'kov, Melik-Barkhudarov result.

The situation is more complicated in the strong-coupling BEC limit. Here for $\mu < 0$ and $1 \le ap_F \le 3$ ($a > 0$) the molecules with the small binding energies $|E_b| \le 2\varepsilon_F$ are formed. In the same time $n_{tot}a^3 = \frac{p_F^3 a^3}{3\pi^2} \le 1$ for $ap_F \le 3$ and thus local pairs do not overlap but only touch each other. Hence we have an intermediate situation between the tightly bound molecules and extended Cooper pairs here and can speculate about a formation of Fermi-Bose mixture of molecules and unpaired fermions here (see also Chap. 8). Nevertheless the theory of BCS-BEC crossover near the unitary limit is still far from being completed.

7.2 Self-Consistent Leggett Theory for T = 0

In this Section we will derive and solve the system of Leggett equations (see Refs. [12, 13] in Chap. 5) in 3D resonance Fermi-gas. This system contains the equation for the chemical potential and the equation of the self-consistency for the superfluid gap and describe BCS-BEC crossover in a resonance Fermi-gas at zero temperatures.

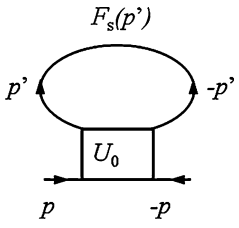

Fig. 7.4 Self-consistent equation for the gap Δ. U_0 is the zeroth Fourier component of the two-particle interaction $U(q)$. $F_S(p')$ is the anomalous Green's function [32]. p and p' are four-momenta $\{\omega, \vec{p}\}$ and $\left\{\omega', \overrightarrow{p'}\right\}$

7.2.1 Leggett Equations for Chemical Potential and Superfluid Gap

The Leggett's equation for the superfluid gap is represented as follows (see Fig. 7.4):

$$\Delta = |U_0| \int F_s(\omega, \vec{q}) \frac{d^3\vec{q}}{(2\pi)^3} \frac{d\omega}{2\pi}, \tag{7.2.1}$$

where

$$F_s(\omega, \vec{q}) = \frac{\Delta}{\omega^2 + E_q^2} \tag{7.2.2}$$

is the anomalous Green's function (see Refs. [3, 4, 32, 67]) allowing the Wick shift $\omega \to i\omega$, U_0 is the zeroth Fourier component of the two-particle interaction $U(q)$.

Note that in a superfluid state at $T = 0$ according to Abrikosov et al. (see Ref. [19] in Chap. 5) we should introduce two Green's functions: normal Green's function G_s of a superfluid state and anomalous Green's function F_s (instead of one Green's function G_N in a normal state for $T > T_C$). In Euclidean form (after the Wick transformation $\omega \to i\omega$) the Green's functions of a superfluid state read [19, 67]:

$$G_s(i\omega, \vec{q}) = -\frac{i\omega + \xi_q}{\omega^2 + E_q^2}, \tag{7.2.3}$$

$$F_s(i\omega, \vec{q}) = -\frac{\Delta}{\omega^2 + E_q^2}, \tag{7.2.4}$$

$$F_s^+(i\omega, \vec{q}) = -\frac{\Delta^+}{\omega^2 + E_q^2}, \tag{7.2.5}$$

where $E_q^2 = \Delta^2 + \xi_q^2$ is uncorrelated spectrum squared of one-particle excitations in superconductor, $\xi_q = q^2/2m - \mu$ and Δ is a superfluid gap. $F_s{}^+$ and Δ^+ in Eq. (7.2.5) are hermitian conjugated from F and Δ. In the graphical form the normal G_s and anomalous Green's functions F_s and hermitian conjugated $F_s{}^+$ are represented on Fig. 7.5.

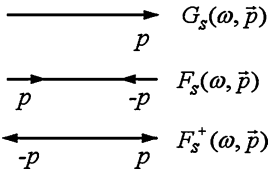

Fig. 7.5 Graphical representation for normal (G_s) and anomalous (F_s and F_s^+) Green's functions in the superconductor at $T = 0$. p is four-momentum $\{\omega, \vec{p}\}$

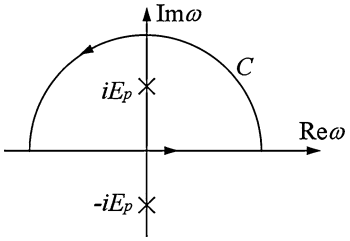

Fig. 7.6 Complex half-plane for frequency integration in the first Leggett's equation (7.2.7) for a superfluid gap Δ. We have one pole $\omega = iE_p$ inside the closed contour C in the upper half-plane

Note that in the absence of an external field, a superfluid gap is real $\Delta = \Delta^+$ and thus $F_s^+(\omega, \vec{p}) = F_s^*(-\omega, -\vec{p}) = F_s(-\omega, -\vec{p})$ for anomalous Green's function F_s^*.

Returning back to the Eq. (7.2.1) for the superfluid gap we can rewrite it as follows:

$$\Delta = |U_0| \int \frac{d^3\bar{p}d\omega}{(2\pi)^4} \frac{\Delta}{(\omega^2 + E_p^2)}, \tag{7.2.6}$$

or for non-zero superfluid gap $\Delta \neq 0$:

$$1 = |U_0| \int \frac{d^3\bar{p}d\omega}{(2\pi)^4} \frac{1}{(\omega^2 + E_p^2)} = |U_0| \int \frac{d^3\bar{p}}{(2\pi)^3} \frac{1}{2E_p}, \tag{7.2.7}$$

where we made frequency integration on the complex half-plane for ω (see Fig. 7.6). This is a standard self-consistency equation familiar for the BCS-theory (see Refs. [12,13, 15, 19, 27] in Chap. 5) with $E_p = \sqrt{\Delta^2 + \xi_p^2}$ for the spectrum. Taking into account renormalization condition (7.1.4): $\frac{m}{4\pi a} = -\frac{1}{|U_0|} + \int \frac{d^3\bar{p}}{(2\pi)^3} \frac{1}{2\varepsilon_p}$ we can represent (7.2.7) as follows:

$$1 + \frac{4\pi a}{m} \int \frac{d^3\bar{p}}{(2\pi)^3} \left(\frac{1}{2E_p} - \frac{1}{2\varepsilon_p} \right) = 0, \tag{7.2.8}$$

where $E_p = \sqrt{(\varepsilon_p - \mu)^2 + \Delta^2}$ and a is an s-wave scattering length in vacuum. Equation (7.2.8) is a first Leggett's equation.

To derive the second Leggett's equation we should use two facts. The first one is connected with the definition of a superfluid density n_s via the integral of a normal Green's function G_s in superconductor:

$$n_s = \int \frac{d\omega}{2\pi} \frac{d^3\bar{p}}{(2\pi)^3} G_S(\omega, \vec{p}). \tag{7.2.9}$$

The second one is connected with the absence of normal excitations in superconductor at $T = 0$. Hence normal density equals to zero and superfluid density $n_S(T = 0) = \frac{n_{tot}}{2} = \frac{p_F^3}{6\pi^2}$. Correspondingly after frequency integration over the contour C (see Fig. 7.6) we will get from Eq. (7.2.9):

$$n_S(T = 0) = \int \frac{d^3\bar{p}}{(2\pi)^3} \frac{E_p - \xi_p}{2E_p} = \int \frac{d^3\bar{p}}{(2\pi)^3} \frac{1}{2} \left(1 - \frac{\xi_p}{E_p}\right) = \frac{n_{tot}}{2} = \frac{p_F^3}{6\pi^2}, \tag{7.2.10}$$

where $\xi_p = p^2/2m - \mu$. It is a second Leggett's equation for chemical potential μ. Note that the Eqs. (7.2.8) and (7.2.10) are valid both in BCS ($\mu > 0$ and $a < 0$) and BEC ($\mu < 0$ and $a > 0$) domains. They can be also applied to describe unitary limit $1/(p_F a) = 0$. Note also that both Nozieres-Schmitt-Rink scheme at $T \neq 0$ and Leggett's scheme at $T = 0$ provide smooth crossover between BCS and BEC regions, at least for singlet s-wave pairing. In the next section we will show that for triplet p-wave pairing (and the symmetry of A1-phase) we can have the point of quantum phase-transition [12, 13] (or even topological phase-transition [14, 15, 33]) for a special point $\mu(T = 0) = 0$ separating BCS and BEC domains at $T = 0$.

In dilute BCS-limit for $|a|p_F \ll 1$ the solution of Leggett's equations yield: $\mu \approx \varepsilon_F > 0$ for the chemical potential and

$$\Delta \approx 1.75 T_C^{BCS} \approx 1.75 \cdot 0.28\, \varepsilon_F \exp\left\{-\frac{\pi}{2|a|p_F}\right\} \approx 0,5\, \varepsilon_F \exp\left\{-\frac{\pi}{2|a|p_F}\right\} \tag{7.2.11}$$

for the superfluid gap.

For dilute BEC-limit $ap_F \ll 1$ the superfluid gap reads:

$$\Delta = \sqrt{2\mu_B |E_b|}, \tag{7.2.12}$$

where $|E_b| = 1/ma^2$ is a binding energy and $\mu_B = \frac{4\pi a_{2-2}}{m_B} n_B > 0$ is a bosonic chemical potential for weakly repulsive Bose-gas of molecules (dimers) with the mass $m_B = 2m$ and density $n_B = n_{tot}/2$. In Eq. (7.2.12) the dimer–dimer scattering length $a_{2-2} > 0$. Note that bosonic chemical potential μ_B is of Hartree–Fock origin and $\mu = -\frac{|E_b|}{2} + \frac{\mu_B}{2} < 0$ for $ap_F \ll 1$. Of course, $\mu_B \ll |E_b|$ in dilute BEC-domain. Thus we have a standard BCS-gap and a standard ratio $\frac{2\Delta}{T_C} \approx 3.5$ in dilute BCS-limit while in dilute BEC-limit the gap is pretty unconventional [see (7.2.12)]. Physically the gap Δ in BEC-domain reflects a creation of bound pairs (molecules). To get the filling of $\Delta^2 = 2\mu_B |E_b|$ in BEC limit let us consider the normal Green's function $G_s(i\omega, \vec{q}) = -\frac{i\omega + \xi_q}{\omega^2 + E_q^2}$. It can be rewritten as:

$$G_s(i\omega,\ \vec{q}) = -\frac{i\omega + \xi_q}{\omega^2 + E_q^2} = \frac{1}{i\omega - \xi_q - \frac{\Delta^2}{i\omega + \xi_q}} = \frac{1}{G_0^{-1} - \Sigma}. \tag{7.2.13}$$

We can see from Eq. (7.2.13) that a normal Green's function of a superfluid state has a two-pole structure, where a resonance self-energy Σ in Eq. (7.2.13) reads:

$$\sum(\omega,\ \vec{q}) = \frac{\Delta^2}{i\omega + \xi_q}. \tag{7.2.14}$$

It is interesting to note that at $T = 0$ a superconductive gap Δ in Eq. (7.2.14) resembles a pseudogap Δ_{PG} for a normal state in BEC-domain for $T \ll T^*$ in Eq. (7.1.19). Moreover if we put $\mu_B = 0$ in the expression for the self-energy of a normal state in Eq. (7.1.19) we will recover the pole structure of $G_s(i\omega,\ \vec{q})$ in Eq. (7.2.13).

In the same time at $T = T_C{}^{BEC}$ a superfluid gap $\Delta\left(T_C{}^{BEC}\right) = \sqrt{2|E_b|\mu_B(T_C{}^{BEC})} = 0$ since $\mu_B\left(T_C{}^{BEC}\right) = 0$, while a pseudogap Δ_{PG} does not drastically changes at T_C and is nonzero. Note that we can rewrite the pseudogap in Eq. (7.1.19) as $\Delta_{PG}^2 \approx 2|E_b|\mu_B(T = 0)$, where $\mu_B(T = 0) = \frac{4\pi a_{2-2}}{m_B} n_B = \frac{\pi a_{2-2} n_{tot}}{m}$ is a Hartree–Fock contribution to the chemical potential in the repulsive Bose-gas of composed bosons. Moreover let us stress that on the level of the T-matrix approximation in the expression for dimer–dimer scattering length a_{2-2} in Eqs. (7.1.19) and (7.2.12–7.2.14) enters mean-field result $a_{2-2} = 2|a|$, while in a more elaborate approach beyond the simple T-matrix scheme it should be $a_{2-2} = 0.6|a| > 0$ (see [43]). Nevertheless the similarity between $\Delta(T = 0)$ and $\Delta_{PG}(T = 0)$ is striking and not accidental. More careful analysis shows, however, that for non-zero temperatures $0 < T < T_C$ inside the superfluid phase, the superfluid gap reads: $\Delta^2(T) = 2|E_b|\mu_B(T)$, where $\mu_B(T) = \frac{2\pi a_{2-2} n_S(T)}{m}$ (see Ref. [19] in Chap. 5). Thus in the superfluid gap squared enters the superfluid density ($2n_s(T)$), while in the pseudogap enters the total density n_{tot}. This fact clarifies the situation. Indeed, for $T = 0$ the superfluid density $n_s(T = 0) = n_{tot}/2$, and hence $\Delta(T = 0) = \Delta_{PG}$. In the same time for $T = T_C{}^{BEC}$ the superfluid density $n_s(T_C{}^{BEC}) = 0$ and thus $\Delta(T_C{}^{BEC}) = 0$ while $\Delta_{PG}(T_C{}^{BEC})$ is still governed by n_{tot} and does not differ much from $\Delta_{PG}(T = 0)$. At finite temperatures $0 < T < T_C{}^{BEC}$ the superfluid density $n_s(T) < n_{tot}/2$, and correspondingly $\Delta(T) < \Delta_{PG}$.

In the unitary limit at $T = 0$ the superfluid gap $\Delta \approx 0.5\varepsilon_F$ and the chemical potential $\mu \approx 0.44\varepsilon_F > 0$ are found by Carlson et al. [29] in the framework of Monte Carlo simulations.

Note that in Leggett's self-consistent scheme $\mu(T = 0) = 0$ for the value of the inverse gas parameter inverse [67]:

$$\frac{1}{p_F a_0} \approx 0.553, \tag{7.2.16}$$

where a_0 is the value of the scattering length at the point $\mu(T = 0) = 0$. Note that in Feshbach resonance p_F is fixed by the requirements of total density conservation, while the scattering length a varies with magnetic field B.

Thus the border between BCS-domain ($\mu > 0$) and BEC-domain ($\mu < 0$) lies in the region of positive values of the scattering length $a_0 > 0$ (for the values of gas parameter $a_0 p_F \approx 1.8$). The superfluid gap at $a_0 p_F$ is rather large and satisfies the relation:

$$\left(\frac{\Delta}{\varepsilon_F}\right)_0^2 = 2\frac{1}{p_F a_0} \approx 1.106, \tag{7.2.17}$$

where the index 0 indicates that the relevant physical quantities are taken for $\mu(T = 0) = 0$. Thus from Eq. (7.2.17) we get $\Delta_0 \approx 1.05\varepsilon_F$ for $a_0 p_F \approx 1.8$. Both the chemical potential μ and the gap Δ vary linearly as function of a–a_0 near the point $\mu = 0$ and $a = a_0$. Namely (see [67]):

$$\frac{\Delta}{\varepsilon_F} = \left(\frac{\Delta}{\varepsilon_F}\right)_0 \left[1 - \frac{\pi}{4}\frac{1}{p_F a_0}\frac{\mu}{\varepsilon_F}\right]; \tag{7.2.18}$$

$$\frac{\mu}{\varepsilon_F} = \left(\frac{1}{p_F a_0} - \frac{1}{p_F a}\right)\frac{p_F a_0}{\left(\frac{\pi}{8}\frac{1}{p_F a_0} + \frac{1}{\pi}p_F^2 a_0^2\right)} \approx \frac{(a - a_0)p_F}{\left(\frac{\pi}{8} + \frac{1}{\pi}p_F^3 a_0^3\right)}. \tag{7.2.19}$$

In would be interesting to compare these results with those of Monte Carlo calculations and with experiments to check how good is the quantitative description of BCS-BEC crossover at $T = 0$ by the self-consistent Leggett's theory. Note that we can represent Δ_0^2 in Eq. (7.2.17) as $\Delta_0^2 = |E_b|_0\, \varepsilon_F p_F a_0$. Hence $\Delta^2{}_0$ resembles the pseudogap $\Delta^2{}_{PG}$ in Eq. (7.2.19).

7.2.2 Sound Velocity in BCS and BEC Limits

Finally note that, as we mentioned in the Introduction, the sound velocity in the resonance Fermi-gas can be obtained not only from the solution of the dynamical problem for the spectrum of collective excitations (see the next Section), but also from the thermodynamic identity for compressibility in a static case at $T = 0$:

$$\kappa^{-1} \sim c_I^2 = \frac{n_{tot}}{m}\frac{\partial\mu}{\partial n_{tot}}, \tag{7.2.20}$$

where n_{tot} is total density and μ is chemical potential. In dilute BCS-limit for $|a|p_F \ll 1$: the chemical potential $\mu \approx \varepsilon_{\mathrm{F}}$ and the superfluid gap $\Delta \sim T_{\mathrm{C}}^{\mathrm{BCS}} \ll \mu$. Here effectively we can calculate sound velocity neglecting the derivative $\partial\Delta/\partial\mu$ and putting $n_{tot} = p_F^3/3\pi^2$, while neglecting the small difference between μ and ε_{F} connected with the superfluid gap squared: $\mu = \varepsilon_F - \alpha\frac{\Delta^2}{\varepsilon_F}\ln\frac{\varepsilon_F}{\Delta} \approx \varepsilon_F$ (see the foundations of the BCS-theory in Ref. [15] of Chap. 5. Thus $\frac{\partial\mu}{\partial n_{tot}} = \frac{2}{3}\frac{\mu}{n_{tot}}$ and $\frac{n_{tot}}{m}\frac{\partial\mu}{\partial n_{tot}} = \frac{2}{3}\frac{\mu}{m} \approx \frac{p_F^2}{3m^2}$. Correspondingly $c_I^2 = \frac{v_F^2}{3}$ and $c_I^{BCS} = \frac{v_F}{\sqrt{3}}$ (where $v_{\mathrm{F}} = p_{\mathrm{F}}/m$ is Fermi velocity). We get the well-known result for Bogoliubov-Anderson sound velocity in neutral (non-charged) superfluid Fermi-gas. Note that in normal Fermi-

gas the sound waves will be overdamped (see Ref. [27] in Chap. 5) and only zero-sound mode will be propagating at $T \to 0$. The superfluid gap causes the final damping of the first sound mode at small frequencies: $\mathrm{Im}\omega \sim \omega^2\tau$, where $\gamma = 1/\tau \sim \Delta^2/\varepsilon_F$ is an inverse scattering time.

To get the sound velocity in the dilute BEC-limit we should recollect that $\mu = -\frac{|E_b|}{2} + \frac{\mu_B}{2}$ and $\mu_B(T) = \frac{4\pi a_{2-2} n_B}{m_B} = \frac{\pi a_{2-2} n_{tot}}{m}$. Thus $\frac{\partial \mu}{\partial n_{tot}} = \frac{1}{2}\frac{\partial \mu_B}{\partial n_{tot}} = \frac{\pi a_{2-2}}{2m}$ and $\frac{n_{tot}}{m}\frac{\partial \mu}{\partial n_{tot}} = \frac{\pi a_{2-2} n_{tot}}{2m^2} = \frac{\mu_B}{m_B}$. Correspondingly $c_I^{BEC} = \sqrt{\frac{\mu_B}{m_B}}$ and we recover the result for Bogoliubov sound velocity in 3D gas of (composed) bosons with weak repulsion (between bosons): $\mu_B = m_B (c_I^{BEC})^2$ [59].

Note that in the dilute limit $|a|p_F \ll 1 \quad c_I^{BEC} \ll c_I^{BCS}$. The sound velocities become equal in the intermediate region for large values of the gas parameter $|a|p_F \gg 1$.

In the unitary limit $c_\mathrm{I} \approx 0.4 v_\mathrm{F}$. Note that for $\mu(T = 0) = 0$ and $a_0 p_\mathrm{F} \approx 1.8$ the sound velocity reads (see [67]):

$$c_I^2 = \frac{p_F^2}{3m^2} \frac{\frac{\pi}{2}\frac{1}{p_F^2 a_0^2}}{\left(1 + \frac{\pi^2}{8}\frac{1}{p_F^3 a_0^3}\right)} \approx 0.132 v_F^2 \tag{7.2.21}$$

and $c_I \simeq 0.36 v_F$.

7.2.3 BCS-BEC Crossover for the 2D Resonance Fermi-Gas

Let us discuss briefly the BCS-BEC crossover and Leggett's equations for the 2D resonance Fermi-gas.

For symmetric attractive potential well in 2D according to Quantum mechanics we have a bound-state of two-particles even for infinitely small attraction between them (see Ref. [26] in Chap. 5). This is in contrast with the 3D case where the bound-state even in symmetric potential well is formed only for deep enough potentials: $|U| \geq \gamma/mr_0^2$, where γ is numerical coefficient, $|U|$ is the depth of the attractive potential and r_0 is the width of the well. Thus there is a threshold for a bound state in 3D. On the level of the two-particle T-matrix in vacuum (see Chap. 5) it corresponds to $|\beta| = 1$ for the value of the Born parameter β. Correspondingly in 3D we have a shallow bound-state $|E_b| \ll 1/mr_0^2$ for $0 < \frac{|\beta|-1}{|\beta|} \ll 1$.

In 2D the threshold for the formation of the bound-state is absent. Thus composed bosons (molecules $f_\uparrow f_\downarrow$) are every time present in 2D attractive Fermi-gas. However the important parameter, namely the ratio of $|E_b|/\varepsilon_F$ is still present in 2D Fermi-gas. Namely, for $\varepsilon_F > |E_b|$ we are still in the BCS-domain according to Miyake (see Ref. [63] in Chap. 6). Here the crossover temperature T_* (which corresponds to the molecule formation) and the critical temperature $T_\mathrm{C}^\mathrm{BCS}$ coincide

and are given by the famous Miyake formula: $T_* = T_C^{BCS} \sim \sqrt{2\varepsilon_F |E_b|}$ (see Chap. 6). Moreover as it was shown by Beasley et al. [45] the difference between T_C^{BCS} (obtained in the mean-field theory) and exact (for 2D) Berezinskii-Kosterlitz-Thouless (BKT) critical temperature (see Refs. [68, 69] in Chap. 6) is small:

$$\frac{\left|T_C^{BCS} - T_C^{BKT}\right|}{T_C^{BCS}} \sim \frac{T_C^{BCS}}{\varepsilon_F} \ll 1 \quad \text{for } |E_b| \ll \varepsilon_F. \tag{7.2.22}$$

Thus the mean-field formula for T_{C} obtained by Miyake is a very good estimate for a critical temperature, which is very close to the exact $T_{\mathrm{C}}^{\mathrm{BKT}}$.

The Cooper pairs are extended for $|E_b| < \varepsilon_F$. Thus in the BCS-domain we have simultaneously collective Cooper pairing in momentum space in substance and the two-particle pairing in real space in vacuum. In the same time for $\varepsilon_F < |E_b|$ we are in BEC-domain. Here we have two characteristic temperatures instead of one: Saha crossover temperature $T_* = |E_b|/\ln\left(|E_b|/\varepsilon_F\right)$ for the formation of molecules and critical temperature $T_{\mathrm{C}}^{\mathrm{BEC}}$ of the Bose-condensation. Note that for $T \ll T_*$ in 2D case we have again a slightly non-ideal Bose-gas of composed molecules with repulsion between them. As we derived in Chap. 6, repulsive interaction between molecules (dimers) in 2D is described by the coupling constant $f_{2-2} = 1/\ln(1.6|E_b|/\varepsilon_F)$. Hence according to Fisher-Hohenberg theory (see Chap. 6 and (see Refs. [67–69] in Chap. 6)) the mean-field critical temperature is given by:

$$T_C^{BEC} = \frac{\varepsilon_F}{4\,\ln(1/f_{2-2})}. \tag{7.2.23}$$

It is again very close to exact BKT critical temperature since

$$\frac{\left|T_C^{BEC} - T_C^{BKT}\right|}{T_C^{BEC}} \sim f_{2-2} \ll 1 \tag{7.2.24}$$

for $|E_b| \gg \varepsilon_F$.

Leggett's Equations in the 2D Case

The mean-field Leggett's scheme for BCS-BEC crossover in 2D resonance Fermi-gas at $T = 0$ works even better then the mean-field approaches at $T = T_{\mathrm{C}}$ since at low temperatures all the vortex-antivortex pairs are well bound in molecules. Thus Leggett's equations well describe the density of superfluid component n_{S}, the velocity of sound c_{I}, the behavior of the superfluid gap Δ, and the chemical potential μ at $T = 0$ [32].

The Leggett's equations in 2D resonance Fermi-gas with s-wave pairing are the evident generalization of the Leggett's equations for the 3D case and yield (see [60, 61]):

$$\frac{n_{tot}}{2} = \frac{p_F^2}{4\pi} = \int_0^{\sim 1/r_0} \frac{pdp}{4\pi}\left(1 - \frac{\xi_p}{E_p}\right); \tag{7.2.25}$$

$$\frac{m}{4\pi}\ln\left(mr_0^2|E_b|\right) = \int_0^{\sim 1/r_0} \frac{pdp}{4\pi}\frac{1}{E_p}, \tag{7.2.26}$$

where r_0 is the range of the attractive potential $U(r) = -|U|e^{-r/r_0}$, $\xi_p = p^2/2m - \mu$, $E_p = \sqrt{\xi_p^2 + \Delta^2}$ is the quasiparticle spectrum in the superfluid state, E_b is the two-particle binding energy and in the l.h.s. of Eq. (7.2.26) we have a typical 2D logarithm ([60, 61]).

For shallow level the binding energy $|E_b| \ll 1/mr_0^2$ and is given by

$$|E_b| = \frac{1}{mr_0^2}\exp\left\{-\frac{4\pi}{m|U_0|}\right\}, \tag{7.2.27}$$

where $|U_0| \sim r_0^2|U|$ is the zeroth Fourier component ($q = 0$) of the vacuum potential *U(r)*. Thus Eq. (7.2.26) for the superfluid gap can be represented in the familiar form

$$1 - |U_0| \int_0^{\sim 1/r_0} \frac{pdp}{4\pi}\frac{1}{E_p} = 0. \tag{7.2.28}$$

We also assume that the Fermi energy $\varepsilon_F \ll 1/mr_0^2$ or $p_F r_0 \ll 1$—we have dilute Fermi-gas in 2D. The solution of Leggett's equations according to Miyake yield:

$$\ln\frac{|\mu| - \mu + \frac{\Delta^2}{2|\mu|}}{|E_b|} = 0, \tag{7.2.29}$$

and

$$2\varepsilon_F = |\mu| + \mu + \frac{\Delta^2}{2|\mu|}. \tag{7.2.30}$$

In the BCS-case $\mu = |\mu| > 0$ we get from Eq. (7.2.29)

$$\frac{\Delta^2}{2|\mu||E_b|} = 1. \tag{7.2.31}$$

Accordingly from Eq. (7.2.30) we obtain

$$2\varepsilon_F = 2|\mu| + \frac{\Delta^2}{2|\mu|}. \tag{7.2.32}$$

If we substitute an expression for Δ^2 in Eq. (7.2.31) into Eq. (7.2.32) we get:

$$2\varepsilon_F = 2|\mu| + |E_b| \text{ or } \mu = |\mu| = \varepsilon_F - \frac{|E_b|}{2} > 0. \tag{7.2.33}$$

Deep in BCS-domain (for $\varepsilon_F \gg |E_b|/2$):

$$\mu \approx \varepsilon_F \text{ and } \Delta^2 = 2\varepsilon_F |E_b|. \tag{7.2.34}$$

We get a famous result of Miyake (see Ref. [63] in Chap. 6) (see also Schmitt-Rink, Varma et al. [60]) and Randeria et al. [61]).

In the BEC-limit $\mu = -|\mu| < 0$. Thus from Eq. (7.2.29) we obtain

$$\frac{\Delta^2}{2|\mu|} + 2|\mu| = |E_b|. \tag{7.2.35}$$

Correspondingly Eq. (7.2.30) reads

$$2\varepsilon_F = \frac{\Delta^2}{2|\mu|} \text{ or } \Delta^2 = 4\varepsilon_F |\mu|. \tag{7.2.36}$$

Substitution of Eq. (7.2.36) into Eq. (7.2.35) yields: $2\varepsilon_F + 2|\mu| = |E_b|$. Accordingly

$$|\mu| = \frac{|E_b|}{2} - \varepsilon_F \text{ or } \mu = -\frac{|E_b|}{2} + \varepsilon_F. \tag{7.2.37}$$

Hence deep in BEC-domain (for $|E_b|/2 \gg \varepsilon_F$): $\mu \approx -\frac{|E_b|}{2} < 0$, and $\Delta^2 \approx 2\varepsilon_F |E_b|$ again in agreement with Miyake et al. Note that the result of Miyake et al. are valid not only in deep BCS and BEC regions, but also in the intermediate case, close to the point $\mu = 0$. Here $\varepsilon_F \approx |E_b|/2$ and for the gap we get: $\Delta \approx 2\varepsilon_F \approx |E_b|$.

7.2.4 Gap Spectroscopy in 3D

The superfluid gap Δ was measured from the threshold of the absorption $\omega = 2\Delta$ of the radiofrequency waves in the experiments of Grimm's group [34, 35] (see also [36, 37, 39]). The gap Δ varies in a magnetic field. Far from Feshbach resonance field (for $|a|p_F < 1$): $\Delta_{BCS} \sim \varepsilon_F \exp\left\{-\frac{1}{|a(B)|p_F}\right\}$, where $a(B) \approx a_{bg}\left(1 + \frac{\Delta}{B - B_0}\right)$ in dilute BCS-domain.

In dilute BEC-domain $\Delta^2_{BEC} = 2\mu_B |E_b| \sim \frac{a_{2-2}}{a^2} \sim \frac{1}{a}$ for $a > 0$ and $ap_F < 1$. Thus with the help of Feshbach resonance we can measure the gap Δ for all the values of the gas parameter ap_F (for all the values of $\Delta B = B - B_0$) in the BCS and BEC domains.

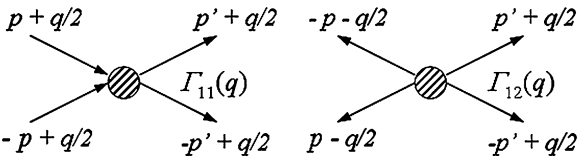

Fig. 7.7 Two vertices $\Gamma_{11}(q)$ and $\Gamma_{12}(q)$ in superconductive state. $p = (\omega, \vec{p})$, $q = (\Omega, \vec{q})$ are four-momenta [67]

7.3 Anderson-Bogoliubov Theory for Collective Excitations

In this section we will present the diagrammatic approach for studying the spectrum of collective excitations in the BCS-BEC crossover at $T = 0$. To do that we will derive a set of the Bethe–Salpeter integral equations for the total vertices $\Gamma(\vec{q}, \omega)$ in the superfluid state of the resonance Fermi-gas at $T = 0$.

7.3.1 Diagrammatic Approach

In order to obtain a system of Bethe–Salpeter equations (see Refs. [22, 25] in Chap. 5), we have to introduce two vertices Γ_{11} and Γ_{12} (see Fig. 7.7) in the Cooper channel for the superfluid state (instead of one vertex Γ in the normal state considered in Chap. 5).

The first one Γ_{11} corresponds to the scattering of two atoms with opposite spins and with two incoming lines and two outgoing ones, while the second one Γ_{12} has four outgoing lines. The second vertex (Γ_{12}) is nonzero only in the superfluid state, while Γ_{11} exists also in the normal state.

The Bethe–Salpeter integral equation for the vertex $\Gamma_{11}(q)$ reads:

$$\begin{aligned}\Gamma_{11}(q) = U(\vec{q}) - U(\vec{q})\Gamma_{11}(q)\int \frac{d^3\bar{p}''}{(2\pi)^3}\frac{d\Omega''}{2\pi} G_S\left(p'' + \frac{q}{2}\right) G_S\left(-p'' + \frac{q}{2}\right) \\ - U(\vec{q})\Gamma_{12}(q)\int \frac{d^3\bar{p}''}{(2\pi)^3}\frac{d\Omega''}{2\pi} F_S\left(p'' + \frac{q}{2}\right) F_S\left(-p'' + \frac{q}{2}\right),\end{aligned} \tag{7.3.1}$$

where we introduced again the normal and anomalous Green's functions $G_s(i\omega, \vec{q}) = -\frac{i\omega + \xi_q}{\omega^2 + \xi_q^2 + \Delta^2}$, $F_s(i\omega, \vec{q}) = -\frac{\Delta}{\omega^2 + \xi_q^2 + \Delta^2}$ in the Euclidean formulation according to Eqs. (7.2.3) and (7.2.4) (see Fig. 7.5). Note that in Eq. (7.3.1) $q = (\Omega, \vec{q})$ is four-momentum and we assume the superfluid gap Δ to be real. Graphically the Bethe–Salpeter equation for $\Gamma_{11}(q)$ is presented on Fig. 7.8.

If we would like to perform the normalization procedure and replace the vacuum interaction $U(\vec{q})$ by the scattering length a (by $4\pi a/m$) (in (7.3.1)), we should simultaneously replace $G_S G_S$ in Eq. (7.3.1) by $(G_S G_S - G_0 G_0)$ where $G_0(\vec{q}, \omega) = (i\omega - \varepsilon_q)^{-1}$ is the vacuum Green's function in Euclidian formulation [see Eqs. (7.1.2) and (7.1.4)]. Analyzing the structure of Eq. (7.3.1), we see that it is

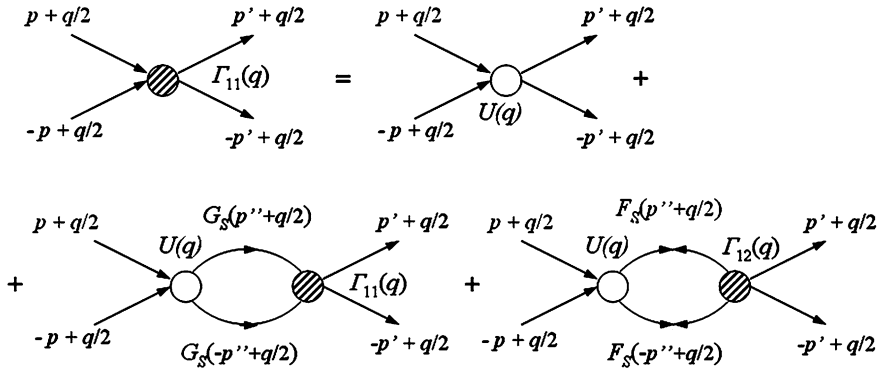

Fig. 7.8 The Bethe–Salpeter equation for the vertex $\Gamma_{11}(q)$ I, p, p', p'', q are 4-momenta [67]

natural to introduce now the elementary response functions χ_{ij} (see Bogoliubov [1] and Anderson [2]) corresponding to the various bubbles appearing in Fig. 7.8. Specifically we define:

$$\begin{aligned} -\chi_{11}(q) &= \frac{1}{g} + \int \frac{d^4p}{(2\pi)^4}\left[G_S\left(p+\frac{q}{2}\right)G_S\left(-p+\frac{q}{2}\right) - G_0(p)G_0(-p)\right], \\ \chi_{12}(q) &= \int \frac{d^4p}{(2\pi)^4} F_S\left(p+\frac{q}{2}\right)F_S\left(-p+\frac{q}{2}\right), \end{aligned} \tag{7.3.2}$$

where $g = 4\pi a/m$ is a coupling constant.

Then Eq. (7.3.1) takes the form:

$$\Gamma_{12}(q)\chi_{12}(q) = 1 + \Gamma_{11}(q)\chi_{11}(q) \tag{7.3.3}$$

Now we have to derive a second Bethe–Salpeter equation for $\Gamma_{12}(q)$. Graphically it has the form shown on Fig. 7.9.

A small difference between Figs. 7.8 and 7.9 is that the anomalous Green's functions $F^+(q)$ appearing in this equation have their arrows outside (instead of inside as in Fig. 7.8 for F). However, for real Δ, they are simply related to the preceding ones by $F^+(p) = F(-p)$. In algebraic form BS-equation for Γ_{12} reads:

$$\begin{aligned} \Gamma_{12}(q) = &- U(\vec{q})\Gamma_{12}(q)\int \frac{d^4p''}{(2\pi)^4} G_S\left(p''-\frac{q}{2}\right)G_S\left(-p''-\frac{q}{2}\right) \\ &- U(\vec{q})\Gamma_{11}(q)\int \frac{d^4p''}{(2\pi)^4} F_S^+\left(p''+\frac{q}{2}\right)F_S^+\left(-p''+\frac{q}{2}\right). \end{aligned} \tag{7.3.4}$$

Note the absence of a free term $U(\vec{q})$ in Eq. (7.3.4). Renormalization requires again the substitution of $G_S G_S$ by $(G_S G_S - G_0 G_0)$ and the replacement of $U(\vec{q})$ by $g = 4\pi a/m$. We see that in Eq. (7.3.4) naturally appear the same response-functions χ_{11} and χ_{12} as in Eq. (7.3.3), but for the four-momentum—q. This leads to the following form of the second BS-equation:

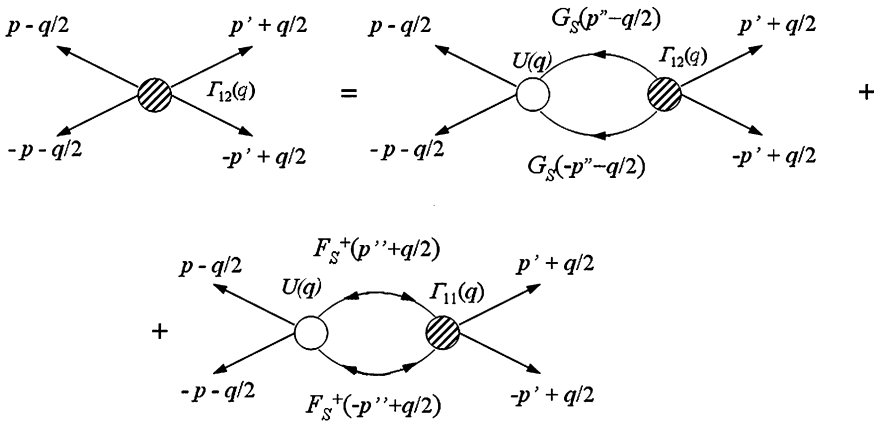

Fig. 7.9 The Bethe–Salpeter equation for $\Gamma_{12}(q)$, p, p', p'', q are 4-momenta [67]

$$\Gamma_{12}(q)\chi_{11}(-q) = \Gamma_{11}(q)\chi_{12}(-q). \tag{7.3.5}$$

From Eqs. (7.3.3) and (7.3.5) the vertices Γ_{11} and Γ_{12} are immediately obtained. However, we are only interested in the pole of these vertices, for which they diverge. This allows us to solve only the homogeneous equations corresponding to Eqs. (7.3.3) and (7.3.5), leading to the following equation for the collective mode:

$$\chi_{11}(q)\chi_{11}(-q) = \chi_{12}^2(q), \tag{7.3.6}$$

where we have used the fact that taking the explicit form of $F_S(p)$ in (7.3.2) into account, one has $\chi_{12}(-q) = \chi_{12}(q)$. This result has already been derived in refs. [41, 42].

In order to obtain a more convenient equation for the collective mode, we can perform the integration over the frequency variable in Eq. (7.3.2). This is easily done by closing the contour in the upper half-plane (see Fig. 7.6) where the quantity to be integrated has two poles, located at $\omega_1 = iE_+$ and $\omega_2 = iE_-$. Here we have introduced the convenient notation $E_\pm = E(\vec{p} \pm \vec{q}/2)$, and we will use similarly $\xi_\pm = \xi(\vec{p} \pm \vec{q}/2)$. The results are:

$$-\chi_{11}(\omega, \vec{q}) = \frac{1}{2}\int \frac{d^3\bar{p}}{(2\pi)^3}\left\{\frac{(E_+ + E_-)(E_+E_- + \xi_+\xi_-) + i\omega(E_+\xi_- + E_-\xi_+)}{E_+E_-[(E_+ + E_-)^2 + \omega^2]} - \frac{1}{E_p}\right\}, \tag{7.3.7}$$

$$\chi_{12}(\omega, \vec{q}) = \frac{1}{2}\int \frac{d^3\bar{p}}{(2\pi)^3}\frac{\Delta^2}{E_+E_-}\frac{E_+ + E_-}{[(E_+ + E_-)^2 + \omega^2]}, \tag{7.3.8}$$

where in Eq. (7.3.7) we have used the Leggett's self-consistency equation for the gap (7.2.8) (which reads: $\frac{1}{g} = \int \frac{d^3\bar{p}}{(2\pi)^3}\left(\frac{1}{2\varepsilon_p} - \frac{1}{2E_p}\right)$) to get rid of the term $1/g$ in Eq. (7.3.2).

Finally to get the spectrum of collective excitations $\omega = \omega(q)$ in the standard form, we should go back to ordinary frequencies in Eqs. (7.3.7) and (7.3.8) by the inverse Wick transformation $i\omega \to \omega$.

From Eqs. (7.3.7) and (7.3.8) we can check that $\chi_{12}(\omega, \vec{q}) = \chi_{12}(-\omega, -\vec{q})$. In the same time $\chi_{11}(\omega, \vec{q}) \neq \chi_{11}(-\omega, -\vec{q})$ due to the presence of a linear in frequency anomalous term in Eq. (7.3.7). It is possible to show that this term is small and can be often neglected in BCS-limit, but it is more substantial in BEC-limit.

7.3.2 The Spectrum of Collective Excitations

The details of the expansions of $E_{\pm} = \sqrt{\xi_{\pm}^2 + \Delta^2}$ and $\xi_{\pm}$ at small $\vec{q}$, as well as the expansions of the expressions under integrals in Eqs. (7.3.7) and (7.3.8) in small ω are presented in (see [67]). Here we will only give the final result for the spectrum. For $a < 0$ and $\mu \approx \varepsilon_F$ (BCS-domain) we get:

$$\omega^2 = c_I^2 q^2 \text{ and } c_I^{BCS} = \frac{v_F}{\sqrt{3}} \tag{7.3.9}$$

for Bogoliubov-Anderson sound mode.

In the same time for $a > 0$ and $\mu < 0$ (BEC-domain) (see Sect. 7.2.2):

$$\omega^2 = c_I^2 q^2 + \left(\frac{q^2}{2m_B}\right)^2 \text{ and } c_I^{BEC} = \sqrt{\frac{\mu_B}{m_B}}. \tag{7.3.10}$$

Thus we get the standard Bogoliubov spectrum for slightly non-ideal Bose-gas with repulsion (see Refs. [19, 27] in Chap. 5 and [25]). The correction to the Bogoliubov spectrum (7.3.10) due to the composed character of the molecules (bosons) are important only for large wave-vectors $qa \gg 1$ [67].

If we introduce a healing length (or a coherence length) $\xi_0 = \frac{1}{\sqrt{n_B a_{2-2}}}$ (see Refs. [19, 27] in Chap. 5, [44]), where $n_B = n_{tot}/2$ and $a_{2-2} = 0.6a$, then there is a small parameter in the theory $\frac{a}{\xi_0} \sim (n_B a^3)^{1/2} \ll 1$. For $q \leq 1/\xi_0$ we get the sound-like linear regime, for $q > 1/\xi_0$ quadratic regime. In the same time the corrections due to the composed character of the bosons start to be important for $q \geq 1/a \ll 1/\xi_0$ (see Fig. 7.10).

Analytically one obtains in dilute BEC limit in the first order in $na^3 \ll 1$ (see [67]):

$$\omega^2 \approx (c_I q)^2 \frac{16 - (qa)^2}{16 + (qa)^2} + \left(\frac{q^2}{4m}\right)^2 \tag{7.3.11}$$

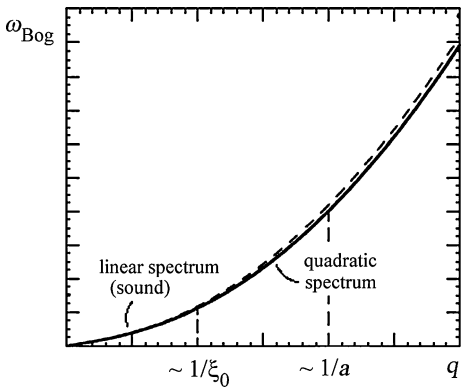

Fig. 7.10 The spectrum of collective excitations in dilute BEC-regime. *The solid line* is Bogoliubov spectrum for pointlike bosons. *The dashed line* indicates the deviations from Bogoliubov spectrum at large wave-vectors $q \geq 1/a \gg 1/\xi_0$ [67], where $\xi_0 = \frac{1}{\sqrt{n_B a_{2-2}}}$ is a healing length [44]

Note that in a simple version of the theory for the collective mode given by Eqs. (7.3.7) and (7.3.8), we will get a mean-field result (see Chap. 6) for the dimer–dimer scattering length $a_{2-2} = 2a$ and correspondingly for bosonic chemical potential $\mu_{\mathrm{B}} = \pi n_{\mathrm{tot}} a_{2-2}/m$. However in a more rigorous theory constructed by Leironais and Combescot [43] the exact result for $a_{2-2} = 0.6a$ in the expression for μ_{B} and sound velocity in BEC-regime can be recovered.

7.3.3 Landau Critical Velocity

We have now basically all the information required to calculate the critical velocity v_{C} (which corresponds to the destruction of the superfluid flow [23, 24]) in the BCS-BEC crossover. Indeed, according to Landau criterion (see Chap. 1), it is given by $v_{\mathrm{C}} = \min[\omega(q)/q]$ where $\omega(q)$ is the energy of the elementary excitation. In our case we have two types of the excitations. First we have bosonic excitations corresponding to the collective mode. If the dispersion relation has an upward curvature (as in our case or in superfluid ^{4}He), then the minimum of $[\omega(q)/q]$ is obtained for $q \to 0$, which gives for v_{C} the sound velocity c_{I}. However, we have to take into account also fermionic single-particle excitations $\omega(q) = \sqrt{\xi_q^2 + \Delta^2}$ and we have to find again the minimum of $[\omega(q)/q]$. Thus we get according to (see Ref. [67]) that:

$$v_C = \min\left\{ c_I; \left(\frac{\sqrt{\Delta^2 + \mu^2} - \mu}{m} \right)^{1/2} \right\}. \tag{7.3.12}$$

Note that deep inside BCS-region for $|a|p_F \ll 1$: $c_I = v_F/\sqrt{3}$, but $v_{\mathrm{C}} = \Delta/p_{\mathrm{F}} \ll c_{\mathrm{I}}$ due to the contribution of the one-particle fermionic excitations (due to the unbinding of the Cooper pairs). The resulting curve for the critical velocity v_{C} and sound velocity c_{I} as the functions of the inverse gas parameter $1/(p_{\mathrm{F}}a)$ are presented on Fig. 7.11. The result displays a kink in the maximum for v_{C},

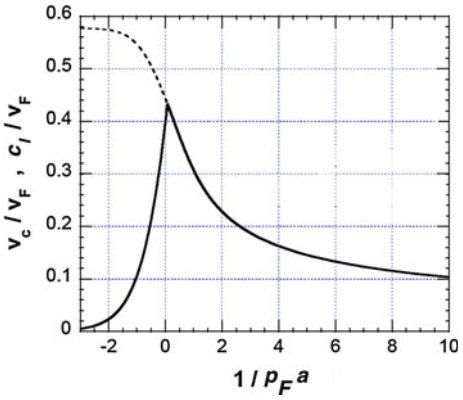

Fig. 7.11 Critical velocity v_C (*full line*) and sound velocity c_l (*dashed line*) as functions of $1/(p_F a)$ (see Ref. [67])

occurring when one switches from bosonic to fermionic excitations. It occurs very near unitarity on the BEC-side. It is worth to note also that in terms of critical velocity, the "strength" of the superfluid is at its highest around unitarity and not on the BEC-side, as one might naively assume.

7.4 Feshbach Resonance and Phase-Diagram for p-Wave Superfluid Fermi-Gas

The first experimental results on p-wave Feshbach resonance [5–11] in ultracold fermionic gases ^{40}K and ^{6}Li make the field of quantum gases closer to the interesting physics of superfluid ^{3}He (see Chap. 11, and Refs. [15, 16]) and the physics of unconventional superconductors [46], such as Sr_2RuO_4, for example. In this context, it is important to bridge the physics of ultracold gases and the low-temperature physics of quantum liquids and anomalous superconductors, and thus to enrich both communities with the experience and knowledge accumulated in each of these fields. In this Section we will describe the transition from the weakly bound Cooper pairs with p-wave symmetry (with a relative orbital momentum of a pair $l = 1$) to strongly bound local p-wave pairs (triplet molecules—see also Chap. 6). We will try to reveal the nontrivial topological effects related to the presence of the nodes in the superfluid gap of the fully-polarized p-wave A1-phase in three dimensions. We note that the symmetry of the A1-phase (where we have a pairing of two fermions with total spin $S = 1$ and its z-projection $S_z = 1$) is relevant both to ultracold Fermi gases in the regime of p-wave Feshbach resonance and to superfluid ^{3}He in the presence of large spin-polarization (see Chaps. 11, 12).

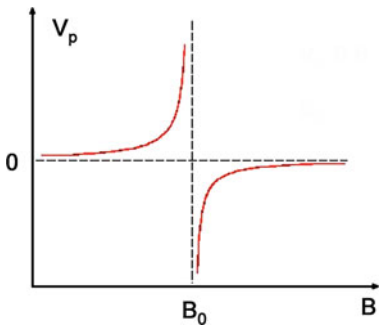

Fig. 7.12 Sketch of the p-wave Feshbach resonance. The scattering volume V_p diverges at $B = B_0$ [3, 4]

7.4.1 *Feshbach Resonance for Fully Polarized p-Wave Resonance Superfluids*

In the first experiments on p-wave Feshbach resonance, experimentalists measured the molecule formation in the ultracold fermionic gas of ^{6}Li atoms close to the resonance magnetic field B_0 [5–9].

In the last years, analogous experiments on p-wave molecules formation in spin-polarized fermionic gas of ^{40}K-atoms were started [10, 11]. The lifetime of p-wave triplet molecules is still rather short [5–11]. Nevertheless the physicists working in ultracold quantum gases began to study intensively the huge bulk of experimental and theoretical wisdom accumulated in the physics of superfluid ^{3}He [16] and anomalous complex superconductors [46].

To understand the essence of p-wave Feshbach resonance, we recall the basic quantum mechanical formula for the p-wave scattering amplitude in vacuum (see Ref. [26] in Chap. 5), [47–49]:

$$f_{l=1}(E) = \frac{p\,p'}{\frac{1}{V_p} + \frac{2mE}{\pi r_0} + i(2mE)^{3/2}}, \tag{7.4.1}$$

where $l = 1$ is the relative orbital momentum for the two-particle problem in the p-wave channel, E is the two-particle energy, $V_p = r_0^2\, a_p$ is the scattering volume, a_p is the p-wave scattering length, r_0 is the interaction range, and p and p' are incoming and outgoing momenta for the scattering amplitude $f_{pp'}(E)$. For Feshbach resonance in the fermionic systems, $p \sim p' \sim p_F$ and usually $p_F r_0 < 1$. The p-wave scattering length a_p, and hence the scattering volume V_p, diverge in the resonance magnetic field B_0 (see Fig. 7.12 and Chap. 5). Thus $1/V_p = 1/a_p = 0$ for $B = B_0$. The imaginary part of the scattering amplitude f_p is small and nonzero only for positive energies $E > 0$. Hence the p-wave Feshbach resonance is intrinsically narrow. We note that for negative energies $E < 0$, there is a triplet molecular bound state:

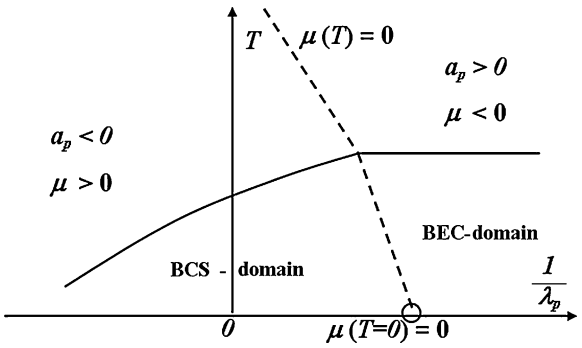

Fig. 7.13 Qualitative picture of the BCS-BEC crossover in the fully-polarized A1-phase for p-wave superfluid. $\lambda_{\mathrm{p}} = V_{\mathrm{p}}\, p_{\mathrm{F}}^3$ is the gas parameter. We indicate the line where $\mu(T) = 0$ and the point of the quantum phase-transition $\mu(T = 0) = 0$ [3, 4]

$$|E_b| = \frac{\pi r_0}{2mV_p} = \frac{\pi}{2m\, r_0\, a_p}. \tag{7.4.2}$$

In the unitary limit, the molecular binding energy $|E_b| \to 0$ for triplet p-wave molecules.

The first theoretical articles on p-wave Feshbach resonance often deal with mean-field two-channel description of the resonance [47–49] (see also Chap. 5). However, in this Chapter we will use again an analog of a resonance approximation and will study the p-wave Feshbach resonance in the framework of one-channel description, which is more close to the physics of superfluid ^{3}He and captures the essential physics of the BCS-BEC crossover in p-wave superfluids rather well.

In magnetic traps (in the absence of the so-called dipolar splitting (see [5–12])) fully-polarized gas or, more precisely, one hyperfine component of the gas is usually studied. In the language of ^{3}He the fermionic pairs with $S_{\mathrm{tot}} = S_{\mathrm{z}}^{\mathrm{tot}} = 1$, or $|\uparrow\uparrow \gg$—pairs are considered for p-wave triplet A1-phase in 3D.

7.4.2 *The Global Phase Diagram of the BCS-BEC Crossover in Fully Polarized A1-Phase*

A qualitative picture of the global phase-diagram of the BCS-BEC crossover in fully-polarized A1-phase is presented in Fig. 7.13. In its gross features, it resembles the phase-diagram of the BCS-BEC crossover for s-wave pairing described in Sect. 7.1 (see Fig. 7.3). However, there is a very interesting question about the origin of the point $\mu(T = 0) = 0$ for 3D A1-phase. We will show in what follows that at the point $\mu(T = 0) = 0$, we probably deal with a quantum phase-transition [12, 13] or even topological phase-transition [14, 15, 33].

On the global phase diagram, the BCS-domain with the chemical potential $\mu > 0$, occupies the region of the negative values of the gas parameter $\lambda_{\mathrm{p}} = V_{\mathrm{p}} p_{\mathrm{F}}^3 < 0$ (or the negative values of the p-wave scattering length a_{p}). It also

stretches to the small positive values of the inverse gas parameter $1/\lambda_p \leq 1$ and is separated from the BEC-domain (where $\mu < 0$ and the inverse gas parameter is large and positive $1/\lambda_p \geq 1$) by the line $\mu(T) = 0$. In the Feshbach resonance regime, the density of "up" spins $n_\uparrow = p_F^3/6\pi^2$ is usually fixed. Deep inside the BCS-domain (for small absolute values of the gas parameter $|\lambda_p| \ll 1$) we have the standard BCS-like formula for the critical temperature of the A1-phase:

$$T_{Cp} \simeq 0.1\, \varepsilon_F\, e^{-\frac{\pi}{2|\lambda_p|}}. \tag{7.4.3}$$

Note that the prefactor in Eq. (7.4.3) for the fully-polarized A1-phase is defined by the second order diagrams of Gor'kov and Melik-Barkhudarov type (see Ref. [17] in Chap. 5) and is approximately equal to $0.1\varepsilon_F$ (see the analysis of Kagan et al. [50–53]).

Deep in BEC-domain (for $\lambda_p \ll 1$) the Einstein formula is again applicable in the leading approximation for Bose-condensation of triplet p-wave molecules with the density $n_\uparrow/2$ and mass $2m$ yielding for a critical temperature

$$T_{Cp} = 3.31\, \frac{(n_\uparrow/2)^{2/3}}{2m}. \tag{7.4.4}$$

Note that the triplet molecules repel each other again. In the unitary limit, $1/\lambda_p = 0$, and from Eq. (7.4.3) we get that $T_{Cp} \approx 0.1\varepsilon_F$ here, and we are still in the BCS-regime (as for the case of s-wave pairing considered in Sect. 7.1). In the rest of this section, we consider low temperatures $T \ll T_C$, i.e., we will work deep in the superfluid parts of the phase diagram for the BCS and BEC-domains of the A1-phase.

7.4.3 Quasiparticle Energy and Nodal Points in the A1-Phase

For $\mu > 0$ (BCS-domain) there are two nodes in the spectrum for $p^2/2m = \mu$ and for angles $\theta = 0$ or π (see the discussion in Chap. 4). For $\mu < 0$ (BEC-domain) $p^2/2m - \mu = p^2/2m + |\mu|$ and there are no nodes. The important point $\mu = 0$ is a boundary between the totally gapped BEC-domain and the BCS-domain with two nodes of the quasiparticle spectrum, which correspond to the south and north poles in Fig. 4.1. The point $\mu = 0$ for $T = 0$ is often called the point of the topological quantum phase transition [14, 15, 33, 54, 55].

7.4.4 Leggett Equations for A1-Phase

The Leggett equations for the fully-polarized A1-phase in three dimensions are the evident generalization of the standard Leggett equations for the s-wave BCS-BEC crossover, derived in Sect. 7.2. The equation for the chemical potential reads:

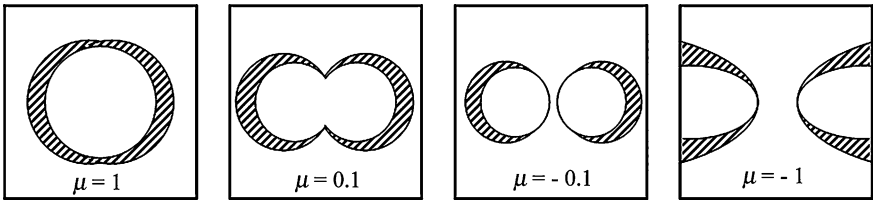

Fig. 7.14 Schematic momentum distribution of the function $\frac{1}{2}\left(1-\frac{\xi_p}{E_p}\right)$ entering Eq. (7.4.5) in the (p_x, p_z) plane for $p_y = 0$, $\Delta_0 = 1$, and $\varepsilon_F = p_F^2/2m$ in the BCS-BEC crossover for the 3D A1 phase. The different values of μ correspond to the situation deep in the BCS domain ($\mu = 1$), deep in the BEC domain ($\mu = -1$), and in the important region close to $\mu = 0$ ($\mu = +0.1$ and $\mu = -0.1$). μ is measured in terms of ε_F [3, 4]

$$n_\uparrow = \frac{p_F^3}{6\pi^2} = \int_0^{1/r_0} \frac{p^2 dp}{2\pi^2} \int_{-1}^{1} \frac{dx}{2}\left(1-\frac{\xi_p}{E_p}\right)\frac{1}{2}, \tag{7.4.5}$$

where $\xi_p = \left(\frac{p^2}{2m}-\mu\right)$, $E_p = \sqrt{\left(\frac{p^2}{2m}-\mu\right)^2 + \frac{\Delta_0^2 p^2}{p_F^2}\sin^2\theta}$—is a quasiparticle spectrum, r_0 is the range of the potential and $x = \cos\theta$. This equation defines the chemical potential μ for a fixed density $n_\uparrow$. The momentum distribution for the function $\frac{1}{2}\left(1-\frac{\xi_p}{E_p}\right)$ in Eq. (7.4.5) is depicted in Fig. 7.14 for the different values of μ corresponding to the BCS and BEC domains.

The second self-consistency equation defines the magnitude of the superfluid gap Δ_0. It is given by:

$$-\pi m \,\mathrm{Re}\frac{1}{f_{l=1}(2\mu)} = \int_{-1}^{1}\frac{dx}{2}\int_0^{1/r_0} p^4 dp\left\{\frac{1}{E_p}-\frac{1}{\xi_p}\right\}, \tag{7.4.6}$$

where

$$\mathrm{Re}\frac{1}{f_{l=1}(2\mu)} = \left(\frac{1}{V_p}+\frac{4m\mu}{\pi\, r_0}\right) \tag{7.4.7}$$

is the real part of the inverse scattering amplitude in p-wave channel for total energy $E = 2\mu$ of colliding particles [3, 4].

Deep in the BCS-domain, the solution of the Leggett equations yields:

$$\Delta_0 \sim \varepsilon_F\, e^{-\frac{\pi}{2|a_p|}} \sim T_{Cp}; \quad \mu \approx \varepsilon_F > 0. \tag{7.4.8}$$

In three dimensions the sound velocity coincides with the result for s-wave pairing and reads: $c_I = \left(\frac{n_\uparrow}{m}\frac{d\mu}{dn_\uparrow}\right)^{1/2} = \frac{v_F}{\sqrt{3}}$.

Deep in the BEC-domain the superfluid gap yields: $\Delta_0 \approx 2\varepsilon_F\sqrt{p_F r_0} \ll \varepsilon_F$ for $p_F r_0 \ll 1$, and the chemical potential $\mu = -\frac{|E_b|}{2} + \frac{\mu_B}{2} < 0$, just as in the s-wave case. Note that the binding energy of a triplet pair (molecule) $|E_b| = \frac{\pi}{2 m r_0 a_p}$. Accordingly:

$$\mu_B \approx \frac{4\varepsilon_F}{3}\sqrt{p_F r_0} \tag{7.4.9}$$

is a bosonic chemical potential which governs the repulsive interaction between two p-wave molecules on a mean-field level [3, 4, 66, 67].

The sound velocity deep in the BEC-domain is given by:

$$c_I = \left(\frac{n_B}{2m}\frac{d\mu_B}{dn_B}\right)^{1/2} \approx \frac{v_F}{\sqrt{3}}\sqrt{p_F r_0} \ll v_F \tag{7.4.10}$$

for $p_F r_0 \ll 1$, where $n_B = n_\uparrow/2$ is the bosonic density.

As $\mu \to 0$ (more rigorously, for $|\mu| < \Delta_0^2/\varepsilon_F$) we have:

$$\Delta_0(\mu = 0) = 2\varepsilon_F\sqrt{p_F r_0} \tag{7.4.11}$$

for the magnitude of the superfluid gap.

For the gas parameter λ_p in the point $\mu = 0$, we obtain:

$$\lambda_p(\mu = 0) = \frac{3\pi}{4} > 0. \tag{7.4.12}$$

Hence, the interesting point $\mu = 0$ is effectively in the BEC-domain (in the domain of the positive p-wave scattering length $a_p > 0$). Accordingly, for $\mu = 0$ the binding energy is:

$$|E_b| = \frac{4}{3}\varepsilon_F p_F r_0. \tag{7.4.13}$$

The sound velocity squared for $\mu = 0$ is given by:

$$c_I^2 = \frac{v_F^2}{3} p_F r_0 \tag{7.4.14}$$

and coincides with Eq. (7.4.10) obtained deep in the BEC-domain. A careful analysis of the Leggett equations close to $\mu = 0$ shows that the derivative $\partial\Delta/\partial\mu$ also has no singularities at this point. The second derivative $\partial^2 n_\uparrow/\partial\mu^2$ is also continuous at $\mu = 0$, and hence the anomaly appears only in higher derivatives in qualitative agreement with the numerical calculations [56, 57] in three dimensions.

The Gap and Compressibility Close to $\mu = 0$ in 2D Axial Phase

Let us briefly consider the situation with the gap and compressibility close to $\mu = 0$ in the 2D axial phase. Note that the quasiparticle energy in the 2D case reads (see Chap. 4 and Refs. [14, 15, 32, 47, 58]): $E_p = \sqrt{\left(\frac{p^2}{2m} - \mu\right)^2 + \frac{\Delta_0^2 p^2}{p_F^2}}$. It has

only one nodal point $E_{\rm p} = 0$ for $\mu = 0$ and $p = 0$. The anomalies in compressibility close to $\mu = 0$ in the 2D case are also stronger then in three dimensions. The careful analysis of the compressibility in two dimensions shows [3, 4, 32] its continuous behavior, but with a kink, which is developed in $\partial n_\uparrow/\partial\mu$ in fully polarized axial phase for $\mu = 0$. This kink can be obtained both on the level of analytic [3, 4] and numerical [56, 57] calculations. To be more specific:

$$\partial n_\uparrow/\partial\mu \sim 1 + \frac{\mu\varepsilon_F}{\Delta_0^2}[1 - \mathrm{sign}\mu], \tag{7.4.15}$$

where sign $\mu = 1$ for $\mu \geq 0$ and -1 for $\mu < 0$.

Hence from Eq. (7.4.15) we get:

$$\partial n_\uparrow/\partial\mu \sim 1 \text{ for } \mu \to +0 \text{ and } \partial n_\uparrow/\partial\mu \to 1 + \frac{2\mu\varepsilon_F}{\Delta_0^2} \text{ for } \mu \to -0. \tag{7.4.16}$$

7.4.5 *Specific Heat at Low Temperatures $T \ll T_C$ in the A1 phase. Classical and Quantum Limits. Quantum Critical Point $\mu(T = 0) = 0$*

In this section we study the thermodynamic functions, namely the specific heat $C_{\rm v}$ in three-dimensional p-wave superfluids with the A1 symmetry at low temperatures $T \ll T_C$. Our goal is to find nontrivial contributions to ρ_n and $C_{\rm v}$ from the nodal points on the mean-field level.

Specific Heat in the Three-Dimensional A1-Phase

The fermionic (quasiparticle) contribution to $C_{\rm v}$ at the mean-field level in three dimensions reads (see Ref. [27, 30] in Chap. 5) for fully-polarized A1-phase:

$$C_v^F = \frac{\partial}{\partial T}\int n_F(E_p/T)E_p\frac{d^3\vec{p}}{(2\pi)^3}^{\sigma}{}_{3D}(0)\int_{-\infty}^{\infty}d\xi_p\int_{-1}^{1}\frac{d\cos\theta}{2}\frac{E_p^2}{T^2}\frac{e^{E_p/T}}{\left(e^{E_p/T}+1\right)^2}, \tag{7.4.17}$$

where $N_{3D}^{\sigma}(0) = \frac{mp_F}{4\pi^2}$ is the density of states at the Fermi surface for one spin-projection σ, $n_F\left(E_p/T\right) = \frac{1}{\left(e^{E_p/T}+1\right)}$ is the quasiparticle (Fermi–Dirac) distribution function, and $E_{\rm p}$ is the quasiparticle energy given after Eq. (7.4.5). For $T \ll \Delta_0$ the fermionic distribution function $n_F \approx e^{-E_p/T}$. In the same time close to the south and north poles $\Delta = \Delta_0|\theta|$ and $d\cos\theta = |\theta|\,d|\theta|$. Correspondingly the results of the calculations deep in the BCS-domain (for $\mu \approx \varepsilon_{\rm F} > 0$) yields (see [16]):

$$C_v^F \sim N_{3D}^{\sigma}(0)\frac{T^3}{\Delta_0^2}. \tag{7.4.18}$$

Thus due to the nodal contribution we have a power-law dependence of the specific heat instead of an exponential one (typical for s-wave pairing) in the BCS A1-phase.

Deep in the BEC-domain (for $\mu \approx -|E_b|/2 < 0$) C_v behaves in the exponential fashion [3, 4]:

$$C_v^F \sim \frac{(2mT)^{3/2}}{4\pi^2}\frac{E_b^2}{4T^2}\, e^{-\frac{|E_b|}{2T}}, \tag{7.4.19}$$

with $|E_b|$ given by Eq. (7.4.2).

Note that bosonic (phonon) contribution from the sound waves yields [23, 24]:

$$C_v^B \sim \frac{\partial}{\partial T}\int \frac{p^2 dp}{2\pi^2} c_I p \frac{1}{\exp\{c_I p/T\} - 1} \sim \frac{T^3}{c_I^3}\frac{1}{2\pi^2} \tag{7.4.20}$$

with a sound velocity $c_I \approx \frac{v_F}{\sqrt{3}}$ deep in BCS-domain and $c_I \approx \frac{v_F}{\sqrt{3}}\sqrt{p_F r_0}$ deep in the BEC-domain. Note that for an important point $\mu = 0$ the expression Eq. (7.4.20) is still valid. Moreover, $c_I \approx \frac{v_F}{\sqrt{3}}\sqrt{p_F r_0}$ again.

Specific Heat of Fermionic Quasiparticles in Classical Limit Close to $\mu \to 0$

Finally in the interesting region of small μ and low temperatures $T \to 0$, $|\mu| \to 0$, but $|\mu|/T \to 0$ in classic limit (according to the terminology of Hertz [12] and Millis [13]) we have nontrivial temperature dependence for C_v^F (see [3, 4]):

$$C_v^F \sim \frac{(2mT)^{3/2}}{2\pi^2}\frac{\varepsilon_F T}{\Delta_0^2}. \tag{7.4.21}$$

This formula is valid both for $\mu \to -0$ (BEC-domain) and for $\mu \to +0$ (BCS-domain). Thus $C_v^F \sim T^{5/2}$ for ($|\mu| \ll T \ll \Delta_0^2/\varepsilon_F$. Note that for small $|\mu|$ but intermediate temperatures $|\mu| \ll \Delta_0^2/\varepsilon_F \ll T \ll \Delta_0$ (when of course we are still in the classical limit) we get more expected result:

$$C_v \sim \frac{(2mT)^{3/2}}{4\pi^2}. \tag{7.4.22}$$

The expressions (7.4.21) and (7.4.22) interpolate at $T \sim \frac{\Delta_0^2}{\varepsilon_F}$. Note that at low temperatures $|\mu| \ll T \ll \Delta_0^2/\varepsilon_F$ the bosonic contribution C_v^B in Eq. (7.4.20) becomes dominant [over C_v^F in Eq. (7.4.21)] for the total specific heat $C_v = C_v^F + C_v^B$. Note also that the condition $T \ll \Delta_0^2/\varepsilon_F$ is equivalent to the condition $T \gg mc_I^2$ when we analyze the bosonic contribution C_v^B to the specific heat.

Specific Heat of Fermionic Quasiparticles in Quantum Limit

We note that in the opposite quantum limit $T \ll |\mu| \ll \Delta_0^2/\varepsilon_F$ (or equivalently $T \to 0$, $|\mu| \to 0$, but $T/|\mu| \to 0$) we get (see [3, 4]):

$$C_v^F \sim \sqrt{\frac{T}{|\mu|}} \frac{\varepsilon_F T}{\Delta_0^2} \frac{(2mT)^{3/2}}{4\pi^2} \text{for } \mu \to +0 \text{ (BCS}-\text{domain)}, \tag{7.4.23}$$

and

$$C_v^F \sim \frac{|\mu|^3}{T^3} e^{-\frac{|\mu|}{T}} \frac{\varepsilon_F T}{\Delta_0^2} \frac{(2mT)^{3/2}}{4\pi^2} \quad \text{for } \mu \to -0 \text{ (BEC}-\text{domain)}. \tag{7.4.24}$$

Hence in the quantum limit fermionic contribution C_v^F behaves very differently for $\mu \to -0$ and $\mu \to +0$ in contrast with the classical limit. It is important to note that for $|\mu|/T \sim 1$ results in Eqs. (7.4.23) and (7.4.24) coincide by order of magnitude and moreover here $C_v^F \sim \frac{(2mT)^{3/2}}{4\pi^2} \frac{\varepsilon_F T}{\Delta_0^2}$ coincides with the classical limit (7.4.21).

Summarizing we see that a power-law fermionic contribution $C_v^F \sim T^{5/2}$ at low temperatures and $C_v^F \sim T^{3/2}$ at intermediate temperatures can be separated from bosonic contribution $C_v^B \sim T^3$ close to the important point $\mu = 0$. We also see very different behavior of C_v^F in BCS and BEC-domains in the quantum limit $T/|\mu| \to 0$.

Note that for $T \neq 0$ we are effectively always in the classical limit $|\mu|/T \to 0$, because the chemical potential μ is continuous close to $\mu = 0$. Hence the real phase transition occurs only at $T = 0$ [in the important point $\mu(T = 0) = 0$ (see [3, 4, 14, 15, 33, 54, 55])]. That is why the point $\mu(T = 0) = 0$ corresponds to the point of quantum phase transition.

Specific Heat for Fully Polarized Axial Phase in 2D

In the two-dimensional fully-polarized axial phase the fermionic contribution to the specific heat deep in the BCS-domain (for $\mu \approx \varepsilon_F > 0$) reads [32]:

$$C_v^F \sim \frac{m}{\pi} \sqrt{\Delta_0 T} \left(\frac{\Delta_0}{T}\right)^2 e^{-\Delta_0/T}, \tag{7.4.24}$$

and we get the standard exponential behavior of the specific heat similar to the case of s-wave superconductors.

In the same time deep in the BEC-domain (for $\mu \approx -|E_b|/2 < 0$) it is given by

$$C_v^F \sim \frac{mT}{\pi} \frac{|\mu|^2}{T^2} e^{-|\mu|/T} \sim \frac{mT}{\pi} \frac{E_b^2}{4T^2} e^{-\frac{|E_b|}{2T}}. \tag{7.4.25}$$

Close to the important point $\mu = 0$ in the classical limit $|\mu| < T < \Delta_0^2/\varepsilon_F$ (or $|\mu|/T \to 0$) the fermionic contribution to the specific heat is given by [32]:

$$C_v^F \sim \int_0^\infty \frac{pdp}{2\pi}\frac{E_p^2}{T^2}\frac{e^{E_p/T}}{\left(e^{E_p/T}+1\right)^2}. \tag{7.4.26}$$

The quasiparticle spectrum for $|\mu| < \Delta_0^2/\varepsilon_F$ can be represented as follows:

$$E_p = \sqrt{\left(\frac{p^2}{2m}-\mu\right)^2 + \frac{\Delta_0^2 p^2}{p_F^2}} \approx \sqrt{\left(\frac{p^2}{2m}\right)^2 + \frac{\Delta_0^2 p^2}{p_F^2}}. \tag{7.4.27}$$

Formally for small $|\mu|$ it is similar to Bogoliubov weakly non-ideal Bose-gas with the sound velocity $(c_I^2)_{\text{Bose-gas}} = \Delta_0^2/p_F^2$. Therefore in the equation of C_v^F in Eq. (7.4.26) we can utilize the well known method introduced for Bogoliubov Bose-gas by Hugenholtz and Pines [59]. Namely we can approximate E_p by the linear spectrum $E_p \approx \Delta_0 p/p_F$ and simultaneously substitute the upper limit of integration in Eq. (7.4.26) by $p_{\max} = \Delta_0 2m/p_F$, where for $p_{\max}$ we get $\left(\frac{p_{\max}^2}{2m}\right)^2 = \frac{\Delta_0^2 p_{\max}^2}{p_F^2}$ in the expression for E_p. Than Eq. (7.4.26) can be rewritten as:

$$C_v^F \sim \int_0^{p_{\max}} \frac{pdp}{2\pi}\frac{\Delta_0^2 p^2}{T^2 p_F^2}\frac{e^{\frac{\Delta_0}{T}\frac{p}{p_F}}}{\left(e^{\frac{\Delta_0}{T}\frac{p}{p_F}}+1\right)^2}. \tag{7.4.28}$$

Introducing now the new dimensionless variable $y = \frac{\Delta_0}{T}\frac{p}{p_F}$ and having in mind that $y_{\max} = \frac{\Delta_0}{T}\frac{p_{\max}}{p_F} = \frac{\Delta_0^2}{T}\frac{2m}{p_F^2} = \frac{\Delta_0^2}{\varepsilon_F T} \gg 1$ for $T < \Delta_0^2/\varepsilon_F$ we finally get:

$$C_v^F \sim \int_0^\infty \frac{ydy}{2\pi} y^2 \frac{e^y}{(e^y+1)^2}\frac{T^2 p_F^2}{\Delta_0^2} \sim \frac{mT}{\pi}\frac{T\varepsilon_F}{\Delta_0^2}. \tag{7.4.29}$$

At the same time C_v^F behaves very differently in quantum limit $T \ll |\mu| \ll \Delta_0^2/\varepsilon_F$(or $T/|\mu| \to 0$). Here in the BEC-domain (for $\mu \to -0$) [3, 4]:

$$C_v^F \sim \frac{mT}{\pi}\frac{\varepsilon_F T}{\Delta_0^2}\frac{|\mu|^3}{T^3}e^{-|\mu|/T}. \tag{7.4.30}$$

In the same time in the BCS-domain (for $(\mu \to +0)$) $C_v^F \sim \frac{mT}{\pi}\frac{\varepsilon_F T}{\Delta_0^2}$ coincides by the order of magnitude with the classical limit (see Eq. (7.4.29)). Thus both in 3D and 2D cases BCS and BEC results ($\mu \to +0$ and $\mu \to -0$) for C_v^F are very different in quantum limit. In 3D both of them are also different from classical limit. In 2D C_v^F is different in quantum and classical limits only for BEC-domain $(\mu \to -0)$.

The fermionic contribution in BEC quantum limit Eq. (7.4.30) interpolates again for $|\mu|/T \sim 1$ with the classical limit $C_v^F \sim \frac{mT}{\pi}\frac{\varepsilon_F T}{\Delta_0^2}$. Finally for higher temperatures $T \sim \Delta_0^2/\varepsilon_F$ we have $C_v^F \sim \frac{mT}{\pi}$. Note that bosonic (phonon) contribution to the specific heat $C_v^B \sim \frac{T^2}{c_l^2}\frac{1}{2\pi}$ for low temperatures $T \ll \Delta_0^2/\varepsilon_F$ has the same order of magnitude as

the fermionic contribution $C_{\rm v}^{\rm F}$ in Eq. (7.4.29) close to the point $\mu = 0$ both in quantum and classical limits, since $c_{\rm I}^2 \sim v_{\rm F}^2 \geq \Delta_0^2/p_{\rm F}^2$ for $\Delta_0 \leq \varepsilon_{\rm F}$ (see [3, 4]).

7.4.6 Normal Density in the Three-Dimensional A1-Phase

The fermionic (quasiparticle) contribution to the normal density in the 3D A1-phase reads (see Ref. [27] in Chap. 5):

$$\rho_n^F = -\frac{1}{3}\int p^2 \frac{\partial n_F(E_p/T)}{\partial E_p}\frac{d^3\vec{p}}{(2\pi)^3}. \tag{7.4.31}$$

Deep in the BCS-domain, the evaluation of $\rho_{\rm n}^{\rm F}$ yields [3, 4, 16]:

$$\rho_n^F \sim \rho\frac{T^2}{\Delta_0^2}, \tag{7.4.32}$$

where $\rho = mn_\uparrow$ is a mass-density for up-spins. We note that rigorously speaking, Eq. (7.4.31) yields longitudinal component of the normal density tensor $\rho_{\rm nl}$. There is a small transverse contribution also $\rho_{\rm ntr} \sim T^4$ firstly obtained by Volovik in [14, 15, 54, 55].

Deep in the BEC-domain the normal density is exponential [3, 4]:

$$\rho_n^F \sim \frac{m}{\pi^2}(2mT)^{3/2}\, e^{-\frac{|E_b|}{2T}}. \tag{7.4.33}$$

Bosonic (phonon) contribution from the sound waves is given by [23, 24]:

$$\rho_n^B \sim \frac{T^4}{c_I^5}. \tag{7.4.34}$$

Equation (7.4.33) is valid for BCS and BEC domains, and also close to the important point $\mu = 0$.

Normal Density of Fermionic Quasiparticles in Classical and Quantum Limits

Close to the important point $\mu = 0$ at low temperatures $|\mu| \ll T \ll \Delta_0^2/\varepsilon_{\rm F}$ (and hence in the classical limit $|\mu|/T \to 0$) we have [3, 4]:

$$\rho_n^F \sim \frac{m}{\pi^2}\frac{\varepsilon_F T}{\Delta_0^2}(2mT)^{3/2}. \tag{7.4.35}$$

Equation (7.4.35) is valid both for $\mu \to +0$ (BCS-domain) and for $\mu \to -0$ (BEC-domain). In the opposite quantum limit $T/|\mu| \to 0$ $\left(T < |\mu| < \Delta_0^2/\varepsilon_{\rm F}\right)$ we obtain in the BCS-domain ($\mu \to +0$) [3, 4]:

$$\rho_n^F \sim \frac{m}{\pi^2}\frac{\varepsilon_F T}{\Delta_0^2} 2mT\sqrt{2m|\mu|}. \tag{7.4.36}$$

In the same time in BEC-domain ($\mu \to -0$) [3, 4]:

$$\rho_n^F \sim \frac{m}{\pi^2}\frac{\varepsilon_F T}{\Delta_0^2} e^{-|\mu|/T} 2m|\mu|\sqrt{2mT}. \tag{7.4.37}$$

Therefore the behavior of $\rho_{\mathrm{n}}^{\mathrm{F}}$ is again very different in the BCS and BEC domains in the quantum limit.

For $|\mu|/T \sim 1$ the results (7.4.36) and (7.4.37) coincide with (7.4.35) by order of magnitude.

At intermediate temperatures $|\mu| \ll \Delta_0^2/\varepsilon_{\mathrm{F}} \ll T \ll \Delta_0$ the quasiparticle contribution to the normal density yields:

$$\rho_n^F \sim \frac{m}{\pi^2}(2mT)^{3/2} \tag{7.4.38}$$

as expected. Note that the bosonic contribution $\rho_{\mathrm{n}}^{\mathrm{B}}$ from Eq. (7.4.34) prevails at these temperatures. Thus close to $\mu = 0$ in the classical limit (for $T \neq 0$) we can again separate the fermionic (quasiparticle) contribution to ρ_{n} ($\rho_{\mathrm{n}}^{\mathrm{F}} \sim T^{5/2}$ at low temperatures and $\rho_{\mathrm{n}}^{\mathrm{F}} \sim T^{3/2}$ at intermediate temperatures) from the bosonic contribution ($\rho_{\mathrm{n}}^{\mathrm{B}} \sim T^4$). We also see very different behavior in the BCS and BEC domains in the quantum limit $T/|\mu| \to 0$.

Normal Density in the Two-Dimensional A1 Phase

In fully-polarized axial phase deep in the BCS regime at $\mu \sim \varepsilon_{\mathrm{F}} > \Delta_0$ the fermionic contribution to the normal density reads [32]:

$$\rho_n^F \sim \frac{m}{\pi} m\Delta_0 e^{-\Delta_0/T}. \tag{7.4.39}$$

Note that here the result for the BCS phase is exponential, since there is no cusps in the superfluid gap where practically gapless fermionic quasiparticles with $\Delta = \Delta_0|\theta\ |$ live in the 3D case.

Deep in the BEC-regime for $\mu \approx -|E_{\mathrm{b}}|/2 < 0$ [32]:

$$\rho_n^F \sim \frac{m}{\pi} mT e^{-\frac{|E_b|}{2T}}. \tag{7.4.40}$$

In the same time bosonic (phonon) contribution from the sound waves:

$$\rho_n^B \sim \frac{T^3}{c_I^4}, \tag{7.4.41}$$

and the Eq. (7.4.41) is valid not only in dilute (deep) BCS and BEC regimes, but also close to the important point $\mu = 0$.

In the classical limit $|\mu| < T < \Delta_0^2/\varepsilon_F$ the fermionic contribution [32]:

$$\rho_n^F \sim \frac{m^2 T}{\pi}\left(\frac{T\varepsilon_F}{\Delta_0^2}\right)^2 \tag{7.4.42}$$

coincides again with the bosonic contribution given by Eq. (7.4.40) by order of magnitude. At higher temperatures $T \geq \Delta_0^2/\varepsilon_F$: $\rho_n^F \sim \frac{m^2 T}{\pi}$ as expected.

In the quantum limit $T \ll |\mu| \ll \Delta_0^2/\varepsilon_F$ the fermionic contribution is exponential [32]:

$$\rho_n^F \sim \left(\frac{|\mu|}{T}\right)^2 \left(\frac{\varepsilon_F T}{\Delta_0^2}\right)^2 \frac{m^2 T}{\pi} e^{-|\mu|/T}. \tag{7.4.43}$$

Equation (7.4.43) is valid both in the BEC-domain (for $\mu \to -0$) and in the BCS-domain (for $\mu \to +0$). It interpolates with a classical limit for $|\mu|/T \sim 1$.

7.4.7 The Spectrum of Orbital Waves in Three-Dimensional p-Wave Superfluids with the Symmetry of the A1-Phase

In Chap. 4 we briefly considered the spectrum of orbital waves in the hydrodynamic (low-frequency regime) of the bosonic (BEC) and fermionic (BCS) A-phase, having in mind first of all superfluid ^{3}He-A and p-wave superfluid Fermi-gases in the regime of Feshbach resonance. Note that in the last case we usually have fully-polarized A1-phase with Cooper pairs having $S_z^{\text{tot}} = 1$ for z-projection of total spin, while in ^{3}He-A $S_z^{\text{tot}} = \pm 1$ for the triplet Cooper pairs. However with respect to orbital hydrodynamics and orbital sector of collective excitations (sound waves and orbital waves), the situation in A-phase and A1-phase is similar.

With this remark we can start our considerations having in mind (see Chap. 4) that for small ω and $\vec{q}$, $\rho_\uparrow \omega \sim \rho_\uparrow q_z^2/m$, where $\rho_\uparrow = m p_{F\uparrow}^3/6\pi^2$ or equivalently

$$\omega \sim q_z^2/m \tag{7.4.44}$$

for orbital waves in BEC-domain. We will show that in the weak-coupling BCS-domain

$$\left(\rho_\uparrow - C_{0\uparrow}\right)\omega \sim \rho \frac{q_z^2}{m} \ln \frac{\Delta_0}{v_F |q_z|}, \tag{7.4.45}$$

where $C_{0\uparrow}$ is the coefficient near anomalous current $\vec{j}_{an} = -\frac{\hbar}{4m} C_{0\uparrow}(\vec{l}\cdot(\vec{\nabla}\times\vec{l}))\vec{l}$ in BCS A1-phase which we carefully discussed in connection with chiral anomaly and mass-current non-conservation in Chap. 4.

As we already mentioned in Chap. 4, the most straightforward way to get the spectrum is to use Vaks, Galitskii, Larkin diagrammatic technique for collective

excitations in p-wave and d-wave superfluids (see Ref. [41] in Chap. 4). The solution of the Bethe–Salpeter integral equation for the Goldstone spectrum ($\omega \to 0$ when $q \to 0$) of orbital waves in Ref. [41] in Chap. 4) involves the Ward identity (see Ref. [28] in Chap. 4) between the total vertex Γ and the self-energy Σ, which is based on the generator of rotations of the $\vec{l}$ vector around perpendicular axis. In the general form, for small ω and $\vec{q} = q_z \vec{e}_z$ it is given by (see Refs. [3, 14, 15]):

$$\int_{-1}^{1} \frac{d\cos\theta}{2} \cos^2\theta \int \frac{p^2 dp}{2\pi^2} \left[\frac{\omega^2}{8E_p^3} + \frac{\omega \xi_p}{4E_p^3} - \frac{p_z^2}{m^2} q_z^2 \frac{1}{4E_p^3} \right] = 0 \tag{7.4.46}$$

Deep in the BCS domain (for $\mu \sim \varepsilon_F > 0$), we can replace $\frac{p^2 dp}{2\pi^2}$ with $N_{3D}^{\sigma}(0) d\xi_p$ for fully-polarized A1 phase (where $N_{3D}^{\sigma}(0) = mp_F^2/4\pi^2$) and p_z^2/m^2 with $v_F^2 \cos^2\theta$. This yields:

$$N_{3D}^{\sigma}(0) \int_{-1}^{1} \frac{d\cos\theta}{2} \cos^2\theta \int d\xi_p \left[\frac{\omega^2}{8E_p^3} + \frac{\omega \xi_p}{4E_p^3} - \frac{v_F^2 \cos^2\theta\, q_z^2}{4E_p^3} \right] = 0. \tag{7.4.47}$$

Using the estimates

$$\int_{-\varepsilon_F}^{\infty} \frac{d\xi_p}{E_p^3} = \frac{1}{\Delta_0^2 \sin^2\theta} \tag{7.4.48}$$

and

$$\int_{-\varepsilon_F}^{\infty} \frac{\xi_p d\xi_p}{E_p^3} \approx \frac{1}{\varepsilon_F}, \tag{7.4.49}$$

we obtain

$$N_{3D}^{\sigma}(0) \left\{ \frac{\omega^2}{\Delta_0^2} \ln \frac{\Delta_0}{\omega} + \frac{\omega}{\varepsilon_F} - \frac{v_F^2 q_z^2}{\Delta_0^2} \ln \frac{\Delta_0}{v_F |q_z|} \right\} = 0. \tag{7.4.50}$$

More rigorously, the equation for the spectrum is biquadratic due to the rotation of the $\vec{l}$ vector, as it should be for bosonic excitations:

$$\left(\frac{\omega^2}{\Delta_0^2} \ln \frac{\Delta_0}{\omega} + \frac{\omega}{\varepsilon_F} \right)^2 \sim \left(\frac{v_F^2 q_z^2}{\Delta_0^2} \ln \frac{\Delta_0}{v_F |q_z|} \right)^2. \tag{7.4.51}$$

For small frequencies $\omega < \Delta_0^2/\varepsilon_F$ the spectrum is quadratic:

$$\frac{\omega}{\varepsilon_F} \sim \frac{v_F^2 q_z^2}{\Delta_0^2} \ln \frac{\Delta_0}{v_F |q_z|}, \tag{7.4.52}$$

or equivalently,

$$\omega \frac{\Delta_0^2}{\varepsilon_F^2} \sim \frac{q_z^2}{m} \ln \frac{\Delta_0}{v_F |q_z|}. \tag{7.4.53}$$

Hence, comparing Eqs. (7.4.53) and (7.4.45), we obtain

$$\frac{\rho_\uparrow - C_{0\uparrow}}{\rho_\uparrow} \sim \frac{\Delta_0^2}{\varepsilon_F^2} \ll 1, \tag{7.4.54}$$

and therefore $C_{0\uparrow} \approx \rho_\uparrow$ deep in BCS domain.

In superfluid ^{3}He-A, for example, $\Delta_0/\varepsilon_F \sim T_C/\varepsilon_F \sim 10^{-3}$ [16], and hence $\frac{\rho - C_0}{\rho} \sim 10^{-6}$ as we mentioned already in Chap. 4. Note that in the strong-coupling case $\Delta_0 \geq \varepsilon_F$: $C_{0\uparrow} \ll \rho_\uparrow$ and disregarding the logarithm in Eq. (7.4.53) we restore the bosonic spectrum (7.4.44). At the same time, for larger frequencies $\Delta_0^2/\varepsilon_F < \omega < \Delta_0$ the spectrum is almost linear:

$$\omega^2 \ln \frac{\Delta_0}{\omega} \sim v_F^2 q_z^2 \ln \frac{\Delta_0}{v_F |q_z|}. \tag{7.4.55}$$

Deep in the BEC-domain for $\mu \approx -|E_b|/2 < 0$, it follows from Eq. (7.4.44) that

$$\omega^2 + |\mu|\omega \sim |\mu| \frac{q_z^2}{m}. \tag{7.4.56}$$

Of course, the exact equation is again biquadratic due to the rotation:

$$\left(\omega^2 + |\mu|\omega\right)^2 \sim \left(|\mu| \frac{q_z^2}{m}\right)^2. \tag{7.4.57}$$

Hence, $\omega \sim q_z^2/m$ for $\omega < |\mu|$ in agreement with (7.4.44). Moreover this means that $\frac{\rho_\uparrow - C_{0\uparrow}}{\rho_\uparrow} = 1$ deep in the BEC-domain, and therefore $C_{0\uparrow} = 0$.

Summarizing Sect. 7.4 we should emphasize, that:

1. Motivated by the recent experiments on p-wave Fechbach resonance in ultracold Fermi-gases, we solve the Leggett equations and construct the phase-diagram of the BCS-BEC crossover in fully-polarized A1-phase.
2. We evaluate compressibility, low temperature specific heat and normal density and find the indications of quantum phase transition close to the important point $\mu(T = 0) = 0$. These indications are connected with a cusp in compressibility as well as with different behavior of C_v and ρ_n in the classical $(|\mu|/T \to 0)$ and the quantum $(T/|\mu| \to 0)$ limits.

Volovik, Green, Read call this point—the point of topological quantum phase transition. It separates gapless from the gapped regions on the phase diagram.

3. Deep in BCS and BEC domains the crossover ideas of Leggett and Nozieres-Schmitt-Rink work pretty well. The phase diagram in these regions resembles in gross features the phase diagram of BCS-BEC crossover for s-wave pairing in resonance superfluids considered in Sects. 7.1 and 7.2.
4. We derived the spectrum of collective excitations (including sound waves and orbital waves) in p-wave superfluids with the symmetry of A1-phase (Fig. 7.14).

References

1. Bogoliubov, N.N.: JETP **34**, 42 (1958)
2. Anderson, P.W.: Phys. Rev. **112**, 1900 (1958)
3. Kagan, M.Yu., Efremov, D.V.: JETP **110**, 426 (2010)
4. Kagan, M.Yu., Efremov, D.V.: Jour. Low Temp. Phys. **158**, 749 (2010)
5. Ticknor, C., Regal, C.A., Jin, D.S., Bohn, J.L.: Phys. Rev. A **69**, 042712 (2004)
6. Regal, C.A., Ticknor, C., Bohn, J.L., Jin, D.S.: Phys. Rev. Lett. **90**, 053201 (2003)
7. Schunck, C.H., Zwierlein, M.W., Stan, C.A., Raupach, S.M.F., Ketterle, W., Simoni, A., Tiesinga, E., Williams, C.J., Julienne, P.S.: Phys. Rev. A **71**, 045601 (2005)
8. Inada, Y., Horikoshi, M., Nakajima, S., Kuwata-Gonokami, M., Ueda, M., Mukaiyama, T.: Phys. Rev. Lett. **101**, 100401 (2008)
9. Fuchs, J., Ticknor, C., Dyke, P., Veeravalli, G., Kuhnle, E., Rowlands, W., Hannaford, P., Vale, C.J.: Phys. Rev. A **77**, 053616 (2008)
10. Gaebler, J.P., Stewart, J.T., Bohn, J.L., Jin, D.S.: Phys. Rev. Lett. **98**, 200403 (2007)
11. Han, Y.-J., Chan, Y.-H., Yi, W., Daley, A.J., Diehl, S., Zoller, P., Duan, L.-M.: Phys. Rev. Lett. **103**, 070404 (2009)
12. Hertz, J.A.: Phys. Rev. B **14**, 1165 (1976)
13. Millis, A.J.: Phys. Rev. B **48**, 7183 (1993)
14. Volovik, G.E.: The Universe in a Helium Droplet. Oxford University Press, Oxford (2002)
15. Volovik, G.E.: Exotic properties of superfluid 3He. World Scientific, Singapore (1992)
16. Vollhardt, D., Wölfle, P.: The superfluid phases of Helium 3. Taylor and Francis, London (1990)
17. Berestetskii, V.B., Lifshitz, E.M., Pitaevskii, L.P.: Quantum electrodynamics, 2nd edn. Pergamon Press, New York (1982)
18. Fresard, R., Glaser, B., Wölfle, P.: J. Phys.: Condens. Matter **4**, 8565 (1992)
19. Haussmann, R.: Zeit. Phys. **B91**, 291 (1993)
20. Drechsler, M., Zwerger, W.: Ann. Phys. (Leipzig) **1**, 15 (1992)
21. Micnas, R., Pedersen, M.H., Schafroth, S., Schneider, T., Rodríguez-Núñez, J.J., Beck, H.: Phys. Rev. B **52**, 16223 (1995)
22. Bloom, P.: Phys. Rev. B **12**, 125 (1975)
23. Landau, L.D., Lifshitz E.M.: Fluid mechanics. Course of Theoretical Physics, Second Edition, vol. 6, Butterworth-Heinemann (1987)
24. Khalatnikov, I.M.: Introduction to the theory of superfluidity. Perseus Books Group, New York (1989)
25. Beliaev, S.T.: JETP **7**, 289 (1958)
26. Kashurnikov, V.A., Prokof'ev, N.V., Svistunov, B.V.: Phys. Rev. Lett. **87**, 120402 (2001)
27. Astrakharchik, G.E., Boronat, J., Casulleras, J., Giorgini, S.: Phys. Rev. Lett. **93**, 200404 (2004)
28. Astrakharchik, G.E., Boronat, J., Casulleras, J., Giorgini, S.: Phys. Rev. Lett. **95**, 230405 (2005)

29. Carlson, J., Chang, S.-Y., Pandharipande, V.R., Schmidt, K.E.: Phys. Rev. Lett. **91**, 050401 (2003)
30. Heiselberg, H.: Phys. Rev. A **63**, 043606 (2001)
31. Burovski, E., Prokof'ev, N., Svistunov, B., Troyer, M.: Phys. Rev. Lett. **96**, 160402 (2006)
32. Kagan, M.Yu., Ogarkov, S.L.: Laser Phys. **18**, 509 (2008)
33. Read, N., Green, D.: Phys. Rev. B **61**, 10267 (2000)
34. Bartenstein, M., Altmeyer, A., Riedl, S., Jochim, S., Chin, C., Denschlag, J.H., Grimm, R.: Phys. Rev. Lett. **92**, 203201 (2004)
35. Chin, C., Bartenstein, M., Altmeyer, A., Riedl, S., Jochim, S., Denschlag, J.H., Grimm, R.: Science **305**(5687), 1128 (2004)
36. Kinast, J., Turlapov, A., Thomas, J.E.: Phys Rev A **70**, 051401(R) (2004)
37. Partridge, G.B., Strecker, K.E., Kamar, R.I., Jack, M.W., Hulet, R.G.: Phys. Rev. Lett. **95**, 020404 (2005)
38. Yang, K.Y., Rice, T.M., Zhang, F.C.: Phys. Rev. B **73**, 174501 (2006)
39. Büchler, H.P., Zoller, P., Zwerger, W.: Phys. Rev. Lett. **93**, 080401 (2004)
40. Bulgac, A., Bertsch, G.F.: Phys. Rev. Lett. **94**, 070401 (2005)
41. Pieri, P., Pisani, L., Strinati, G.C.: Phys. Rev. B **70**, 094508 (2004)
42. Andrenacci, N., Pieri, P., Strinati, G.C.: Phys. Rev. B **68**, 144507 (2003)
43. Leyronas, X., Combescot, R.: Phys. Rev. Lett. **99**, 170402 (2007)
44. Pistolesi, F., Strinati, G.C.: Phys. Rev. B **53**, 15168 (1996)
45. Beasley, M.R., Mooij, J.E., Orlando, T.P.: Phys. Rev. Lett. **42**, 1165 (1979)
46. Proc. of the First Euroconference on Anomalous Complex Superconductors, Crete (Greece) September 1998, ed. by P.B. Littewood and G. Varelogiannes, North-Holland, Amsterdam, 1999
47. Gurarie, V., Radzihovsky, L.: Annals of Physics (Weinheim) **322**, 2 (2007)
48. Klinhammer, F.R., Volovik, G.E.: JETP Lett. **80**, 343 (2004)
49. Cheng, C.H., Yip, S.K.: Phys. Rev. Lett. **95**, 070404 (2005)
50. Kagan, M.Yu., Chubukov, A.V.: JETP Lett., 47, 525 (1988). The calculation of the preexponential factor was done here for the nonpolarized A-phase in the case when the s-wave scattering is totally suppressed. The calculation of the fully-polarized A1-phase yields only a 10% difference from the result of [50] for the prefactor $0.1\varepsilon_F$
51. Baranov, M.A., Chubukov, A.V., Kagan, M.Yu.: Int. Jour. Mod. Phys. B **6**, 2471 (1992)
52. Baranov, M.A., Kagan, M.Yu., Kagan, Yu.: JETP Lett. **64**, 301 (1996)
53. Baranov, M.A., Efremov, D.V., Mar'enko, M.S., Kagan, M.Yu.: JETP **90**, 861 (2000)
54. Volovik, G.E.: Quantum Analogues: From Phase Transitions to Black Holes and Cosmology. In: Unruh, W.G., Schutzhold, R. (eds.) Springer, Berlin (2007)
55. Volovik, G.E.: Lect. Notes Phys. **718**, 31 (2007)
56. Iskin, M., Sa de Melo, C.A.R.: Phys. Rev. Lett. **96**, 040402 (2006)
57. Botelho, S.S., Sa de Melo, C.A.R.: Jour. Low Temp. Phys. **140**, 409 (2005)
58. Volovik, G.E., Solov'ev, A., Yakovenko, V.M.: JETP Lett. **49**, 65 (1989)
59. Hugenholtz, N.M., Pines, D.: Phys. Rev. **116**, 489 (1959)
60. Schmitt-Rink, S., Varma, C.M., Ruckenstein, A.E.: Phys. Rev. Lett. **63**, 445 (1989)
61. Randeria, M., Duan, J.-M., Shieh, L.-Y.: Phys. Rev. Lett. **62**, 981 (1989)
62. Perali, A., Palestini, F., Pieri, P., Strinati, G.C., Stewart, J.T., Gaebler, J.P., Drake, T.E., Jin, D.S.: Phys. Rev. Lett. **106**, 060402 (2011)
63. Schneider, W., Randeria, M.: Phys. Rev. A **81**, 021601 (2010)
64. Nascimbene, S., Navon, N., Jiang, K.J., Chevy, F., Salomon, C.: Nature **463**, 1057 (2010)
65. Wen, H–.H., Mu, G., Luo, H., Yang, H., Shan, L., Ren, C., Cheng, P., Yan, J., Fang, L.: Phys. Rev. Lett. **103**, 067002 (2009)
66. Combescot, R., Leyronas, X., Kagan, M.Yu.: Phys. Rev. A **73**, 023618 (2006)
67. Combescot, R., Kagan, M.Yu., Stringari, S.: Phys. Rev. A **74**, 042717 (2006)
68. Zwerger, W. (ed.): The BCS-BEC crossover and the unitary fermi gas. Lect. Notes Phys., Vol. 836. Springer, Berlin (2012)

Chapter 8
Phase Diagrams and the Physics of the Pseudogap in Superconductors with Attractive Interaction

In this chapter we will analyze basic models with attractive interaction between particles, namely attractive-U fermionic Hubbard model and Fermi-Bose mixture model (see Ref. [6] in Chap. 6 and [63]). We will pay the special emphasis on the physics of pseudogap for its most simple realization, namely for the low density case. In this case there is Saha crossover temperature T_* (see Ref. [30] in Chap. 5) which corresponds to the formation of local pair (consisting of two fermions [see Refs. [12–14] in Chap. 5) in fermionic models or two bosons in bosonic models (See Refs. [1, 2] in Chap. 6) and critical temperature T_C of BEC-transition. However, for intermediate temperatures $T_C < T < T_*$ there is an interesting new phase, appearing in the system, namely a system of normal bosonic metal (see Refs. [31, 32] in Chap. 5). In the framework of 2D attractive-U fermionic Hubbard model we will describe one-particle spectral functions of this phase which correspond to the contribution of two-particle physics in the dressed one-particle Green-function in the framework of self-consistent T-matrix approximation (see Refs. [18–21] in Chap. 7). We will also describe temperature dependence of conductivity and specific heat for the phase of normal bosonic metal. In the last part of the Chapter, we will present the space-separated Fermi-Bose mixture model to describe the normal and superconducting properties of an interesting system, namely of plumbates-bismuthates BaKBiO–BaPbBiO (see Refs. [23, 24, 63]) which in contrast to high-T_C materials are in the regime of Varma's valence skipping [1]. This fact promotes a possibility to form a local pair (with charge 2e) inside of the BiO_6-cluster (which in plumbates-bismuthates plays the role of CuO_6-cluster in cuprates). We will also slow the correspondence between local crystalline and electron structures in plumbates-bismuthates revealed in EXAFS-experiments (see Refs. [23, 24, 63]).

M. Yu. Kagan, *Modern Trends in Superconductivity and Superfluidity*,
Lecture Notes in Physics 874, DOI: 10.1007/978-94-007-6961-8_8,

8.1 Attractive-U Fermionic Hubbard Model

Hamiltonian of the attractive-U fermionic Hubbard model differs from repulsive-U fermionic Hubbard model which will be considered in Chaps. 9, 10, 11 and 12 only in the sign of on-site interaction U: (see 5.2.26)

$$\hat{H} = -t \sum_{\langle ij \rangle \sigma} c^{+}_{i\sigma} c_{j\sigma} - U \sum_{i} n_{i\uparrow} n_{i\downarrow}, \tag{8.1.1}$$

where $n_{i\sigma} = c^{+}_{i\sigma} c_{j\sigma}$ is onsite density,—U is short-range (onsite) attraction between fermions. In 3D case the classical results for this type of models belong to Leggett (see Refs. [12, 13] in Chap. 5) and Nozieres, Schmitt-Rink (see Ref. [14] in Chap. 5). Note that the microscopic origin of attractive hard-core interaction—U a priori is not known. Sometimes theorists have in mind short-range electron–phonon attraction. However, for electron–phonon interaction frequency-dependent retardation effects are often important (see Ref. [64] in Chap. 6 and [2]). Sometimes in similarity with physics of glasses so-called negative-U centers are discussed in connection with attractive-U Hubbard model. We consider here Eq. (8.1.1) just a simple toy-model which catches the most important features of the physics of the pseudogap.

8.1.1 Two Critical Temperatures T_C and T_* in 3D Case

In 3D case the phase-diagram of the attractive-U Hubbard model looks like as follows (see Fig. 8.1).

On Fig. 8.1 T_* is a crossover temperature for creation of fermionic pairs (composed bosons), T_C^{BEC} is a temperature of Bose–Einstein condensation of local pairs, T_C^{BCS} is a temperature of Cooper pairing (for extended electron pairs). At weak coupling ($U < W$, W is a bandwidth) $T_* = T_C^{BCS}$ and thus creation and Bose-condensation of extended pairs take place at the same temperature. However, at strong coupling (for $U > W$) $T_* > T_C^{BCS}$ so at first the local pairs are formed, and then at lower temperature they are Bose-condensed. Correspondingly for intermediate temperatures $T_C^{BEC} < T < T_*$ we have an interesting new phase of a normal bosonic metal (almost all fermions are paired here but not Bose-condensed).

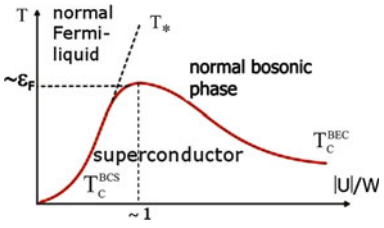

Fig. 8.1 Phase-diagram of the 3D attractive-U Hubbard model on a simple cubic lattice

8.1.2 Weak-Coupling Case

In the weak-coupling case $|U| < |U_C| \sim W = 12t$ (for 3D simple cubic lattice) as we already mentioned in Chap. 5 the critical temperature T_C reads (see Ref. [17] in Chap. 5) for low density $nd^3 \ll 1$:

$$T_c = T_C^{BCS} \approx 0.28\varepsilon_F \exp\left[-\frac{\pi}{2|a|p_F}\right], \tag{8.1.2}$$

where $\lambda = \frac{2|a|p_F}{\pi}$ is 3D gas parameter. Here we have extended Cooper pairs with large coherence length $\xi_0 \sim \hbar v_F / T_C^{BCS} \gg d$, where d is intersite distance. Accordingly the one-particle chemical potential $\mu \approx \varepsilon_F > 0$—and the pairing takes place on the Fermi-surface. Note that the result of Gor'kov, Melik-Barchudarov (8.1.2) is similar to famous BCS-formula (see Refs. [15, 16] in Chap. 5) for superconductive pairing due to electron–phonon attraction, however preexponential factor $0.28\varepsilon_F$ is different. In the weak-coupling (Born) case the s-wave scattering length a reads:

$$|a| = \frac{m|U|d^3}{4\pi} \sim d\frac{|U|}{W} \ll d$$

for the band mass $m = 1/(2td^2)$.

8.1.3 Strong-Coupling Case

In the strong-coupling case $|U| > (|U_C| \sim W)$ in the absence of the lattice we have a famous Einstein formula (see Ref. [30] in Chap. 5) for critical temperature of Bose-condensation (see Chaps. 5 and 6),

$$T_{C,gas}^{BEC} = 3.31\frac{n_B^{2/3}}{m_B} = 3.31\frac{(n/2)^{2/3}}{2m} \approx 0.2\varepsilon_F.$$

On the lattice, as it is shown by Nozieres and Schmitt-Rink (see Ref. [14] in Chap. 5):

$$T_{C,lat}^{BEC} \sim \frac{W}{|U|} T_{C,gas}^{BEC}. \tag{8.1.3}$$

That is due to a large effective mass in the strong-coupling case on the lattice (see Fig. 8.2 and Chap. 5).

$$m^* \sim m\frac{|U|}{W} \tag{8.1.4}$$

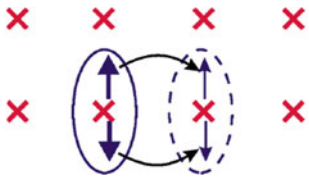

Fig. 8.2 The origin of a heavy effective mass for 3D attractive-U Hubbard model in the strong-coupling case $|U| \gg |U_C| \sim W$ (see Ref. [14] in Chap. 5)

From Fig. 8.2 we note that we should virtually destroy the local pair, and then create it again, thus we have a second order of perturbation theory for m^*.

Crossover temperature T_* (which corresponds to the formation of the local pair) as we discussed in Chap. 5 is given by Saha formula for thermodynamic equilibrium in the process A + B ↔ AB (see Ref. [30] in Chap. 5). It can be determined from the following relation in 3D case:

$$\frac{n_F^2}{n_B} \sim \frac{1}{2}\left(\frac{mT}{\pi}\right)^{3/2} \exp\left\{-\frac{|E_b|}{T}\right\}, \tag{8.1.5}$$

where E_b is a binding energy of a pair (of a composite boson). For $T = T_*$ by definition $n_\mathrm{F} = 2n_\mathrm{B} = n/2$ (see Ref. [30] in Chap. 5). Thus in total analogy with 2D case considered in Chap. 6:

$$T_* \sim \frac{|E_b|}{\frac{3}{2}\ln(|E_b|/T_0)}, \tag{8.1.6}$$

where $T_0 = \varepsilon_\mathrm{F}$ is degeneracy temperature. Note that for $|U| \gg W = 12t$: $|E_\mathrm{b}| \approx 4/(3\pi)\,|U|$. For $T_\mathrm{C}^{\mathrm{BEC}} < T < T_*$ the one-particle chemical potential μ acquires a kink (see Chap. 5):

$$\mu \approx -\frac{|E_b|}{2} - \frac{3}{4}T\ln\left(T_C^{BEC}/T\right) \tag{8.1.7}$$

At $T = T_C^{BEC}$ bosonic chemical potenrial $\mu_B(T_C^{BEC}) = 0$ and thus $\mu = -\frac{|E_b|}{2} + \frac{\mu_B}{2} = -\frac{|E_b|}{2}$. Note that in strong coupling case $|E_b| \sim |U| \gg W$, and it is not necessary to distinguish between E_b and $\tilde{E}_b$, μ and $\tilde{\mu}$ (where $\tilde{E}_b$ and $\tilde{\mu}$ are counted from the bottom of the band).

8.2 Attractive Fermions in 2D

Let us now consider 2D case which is more suitable for high-T_C materials. In this case the phase-diagram of 2D attractive-U Hubbard model looks like as follows (see Fig. 8.3).

On Fig. 8.3 $T_0 = 2\pi n/m$ is degeneracy temperature in 2D, crossover temperature T_* is given by (see Chap. 6):

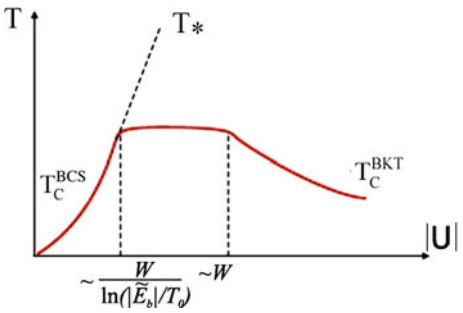

Fig. 8.3 Phase-diagram of the attractive-U Hubbard model in 2D case

$$T_* = \frac{|\tilde{E}_b|}{\ln(T_0/|\tilde{E}_b|)}, \tag{8.2.1}$$

where $E_b = -W + \tilde{E}_b$. Finally T_C^{BKT} is Berezinski-Kosterlitz-Thouless critical temperature (see Refs. [68, 69] in Chap. 6) in the 2D case. We have three regions in Fig. 8.3.

8.2.1 Weak-Coupling Case

First regime corresponds to weak-coupling case:

$$|U| < \frac{W}{\ln\left(T_0/|\tilde{E}_b|\right)}, \tag{8.2.2}$$

where the binding energy is given by:

$$|\tilde{E}_b| \approx W \exp\left\{-\frac{2W}{|U|}\right\} \ll T_0. \tag{8.2.3}$$

In this regime $T_* = T_C$ and the critical temperature on the mean field level yields (see Ref. [63] in Chap. 6):

$$T_C = T_C^{BCS} \sim \sqrt{2T_0|\tilde{E}_b|}$$

This result of Miyake means that in 2D case we have simultaneously a bound state in two-particle problem in vacuum and collective s-wave pairing in substance already for infinitely small attraction (in the symmetric well). Note, that Beasley, Mooji et al. (see Ref. [45] in Chap. 7) on the level of a simple estimate for superfluid density showed that the mean-field result provides a good estimate for T_C in dilute attractive Fermi-gas or Hubbard model. Namely:

$$\frac{T_C^{BKT} - T_C^{BCS}}{T_C^{BCS}} \sim \frac{T_C^{BCS}}{T_0} \ll 1 \tag{8.2.4}$$

and the exact BKT critical temperature is close to a mean-field one.

8.2.2 Intermediate-Coupling Case

Second regime describes intermediate coupling case in 2D. In this regime $\left|\tilde{E}_{\mathrm{b}}\right| > T_0$ (but still $|\tilde{E}_b| < W$) and for Hubbard U:

$$\frac{W}{\ln\left(\left|\tilde{E}_b\right|/T_0\right)} < |U| < W. \tag{8.2.5}$$

The Saha crossover temperature T_* is still given by (8.2.1) with a binding energy (see Refs. [31, 32] in Chap. 5):

$$\left|\tilde{E}_b\right| = \frac{1/md^2}{\exp\left\{\frac{4\pi}{md^2|U|}\right\} - 1} \sim \frac{W}{\exp\left\{\frac{W}{|U|}\right\} - 1} < W. \tag{8.2.6}$$

The mean field critical temperature as we discussed in Chaps. 5, 6 was determined by Fisher-Hohenberg (see also Popov, Refs. [66, 67] in Chap. 6) in the framework of a simple ansatz for 2D dilute Bose-gas of weakly repulsive composed boson (each boson being a local pair of two fermions) (see Chap. 7):

$$T_C = \frac{T_0}{4\ln\ln\left(1.6|\tilde{E}_b|/T_0\right)} < T_0,$$

where $T_0 = \varepsilon_{\mathrm{F}} = n_{\mathrm{el}} W/2$ and n_{el} is dimensionless 2D density ($n_{\mathrm{el}} = 2\varepsilon_{\mathrm{F}}/W$).

8.2.3 Strong-Coupling Case

Finally in the strong-coupling case $|U| \gg W$ the binding energy in 2D: $|E_{\mathrm{b}}| \sim |U|$ and $T_C^{lat} \sim \frac{W}{|U|} T_0$ as in 3D due to Nozieres-Schmitt-Rink considerations in the second order of perturbation theory (see Ref. [14] in Chap. 5). In the next Section, we will mostly concentrate on the most interesting intermediate coupling case with a special emphasis on the phase of a normal bosonic metal. This phase exists at intermediate temperatures $T_{\mathrm{C}} < T < T_*$.

8.3 T-matrix Approximation

To proceed further we need to generalize on the 2D-case the basic equations of the self-consistent T-matrix approximation. At low densities T-matrix approximation is very good (see for example Galitskii-Bloom results [see Ref. [28] in Chap. 5 and [22] in Chap. 7] for 3D and 2D repulsive Fermi-gas). The essence of this approximation is given by the system of Eqs. (8.3.1)–(8.3.4).

$$T(\vec{q}, i\omega_n) = \frac{Ud^2}{1 - Ud^2 K(\vec{q}, i\omega_n)} \tag{8.3.1}$$

for the T-matrix, where in 2D case Ud^2 is the zeroth Fourier component of the potential on the lattice,

$$K(\vec{q}, i\omega_n) = T\sum_{\Omega_n}\int \frac{d^2\vec{p}}{(2\pi)^2} G_M(\vec{p}, i\Omega_n) G_M(-\vec{p}+\vec{q}, -i\Omega_n + i\omega_n) \tag{8.3.2}$$

is a 2D Cooper loop (particle–particle susceptibility) in Matsubara technique for dressed Matsubara Green's functions G_{M}. The Dyson equation for G_{M} yields

$$G_M(\vec{p},\, i\omega_n) = \frac{1}{i\omega_n - \varepsilon(q) \,+\, \mu \,-\, \Sigma_M(\vec{q}, i\omega_n)}. \tag{8.3.3}$$

Finally the Matsubara self-energy Σ_{M} reads:

$$\Sigma_M(\vec{q},\, i\omega_n) = T\sum_{\Omega_n}\int \frac{d^2\vec{p}}{(2\pi)^2} G_M(\vec{p} \,-\, \vec{q}, i\Omega_n \,-\, i\omega_n) T(\vec{p}, i\Omega_n). \tag{8.3.4}$$

The system of Eqs. (8.3.1)–(8.3.4) should be solved together with the equation on the conservation of the total density $n_{tot} = p_F^2/2\pi$ in 2D:

$$\sum_{\omega_n}\int \frac{d^2\vec{q}}{(2\pi)^2} G_M(i\omega_n,\, \vec{q}) = \sum_{\omega_n}\int \frac{d^2\vec{q}}{(2\pi)^2} \frac{1}{G_0^{-1}(i\omega_n,\, \vec{q}) \,-\, \Sigma_M(i\omega_n,\, \vec{q})} = \frac{n_{tot}}{2} = \frac{p_F^2}{4\pi}, \tag{8.3.5}$$

where

$$G_0 = \frac{1}{i\omega_n \,-\, \varepsilon(q) \,+\, \mu} \tag{8.3.6}$$

is a bare Matsubara Green's function. The system of Eqs. (8.3.1)–(8.3.6) is an evident generalization of the system of Eqs. (7.1.5)–(7.1.10) on 2D case.

We should solve this system iteratively.

In the first iteration we calculate the T-matrix in (8.3.1) with zeroth order Green-functions $G_0(i\omega_n, \vec{q})$

Then Cooper loop (particle–particle susceptibility) $K_0(\vec{q}, i\omega)$ in (8.3.1) reads:

$$K(\vec{q},\, i\omega) = \int \frac{d^2\vec{p}}{(2\pi)^2} \frac{1 \,-\, n_F(\varepsilon_p \,-\, \mu) - n_F(\varepsilon_{p-q} \,-\, \mu)}{i\omega \,-\, \varepsilon_p - \varepsilon_{p-q} \,+\, 2\mu}, \tag{8.3.7}$$

where we used that $\varepsilon_{p-q} = \varepsilon_{-p+q}$. Introducing variable $z = i\omega$ we get the following expression for the T-matrix in (8.3.1) for small $z \to 0$ and $q \to 0$:

$$T_0(z, \vec{q} \to 0) \approx \frac{\left|\tilde{E}_b\right| W}{z \,-\, \frac{q^2}{4m} \,+\, \mu_B}, \tag{8.3.8}$$

where $\mu_B = 2\tilde{\mu} + \left|\tilde{E}_b\right| = 2\mu + |E_b|$ is bosonic chemical potential for a gas of composed bosons with $m_{\mathrm{B}} = 2m$ (see Chap. 5), $|\tilde{E}_b|$ given by Eq. (8.2.6) in the intermediate coupling limit $T_0 < \left|\tilde{E}_{\mathrm{b}}\right| < W$ and $\mu = -W/2 + \tilde{\mu}$. In (8.3.8) $q^2/4m$ is

kinetic energy of a local pair with mass $m_B = 2m$. The most important is that T-matrix in (8.3.1) has a structure of a free bosonic propagator (see Refs. [31, 32] in Chap. 5) with a simple pole $z = q^2/4m - \mu_B$.

8.3.1 Conditions for T_C

Note that a superconductive critical temperature T_C is defined for normal Bose-gas phase from the requirement:

$$\mu_B(T_C) = 0. \tag{8.3.9}$$

for bosonic chemical potential. This requirement immediately follows from the structure of the T-matrix:

$$T(z = 0, \vec{q} = 0) = \frac{|E_b|W}{\mu_B} \tag{8.3.10}$$

If $\mu_B \to 0$ than $T(0, 0) \to \infty$ according to Landau-Thouless criterion for the phase-transition (see Refs. [19, 27] in Chap. 5).

8.3.2 Self-Energy in the First Iteration

In the first iteration to the self-energy Σ_1 reads:

$$\Sigma_1(\vec{q}, i\omega_n) = T\sum_{\Omega_n}\int \frac{d^2\vec{p}}{(2\pi)^2} G_0(\vec{p} - \vec{q}, i\Omega_n - i\omega_n)T_0(\vec{p}, i\Omega_n) \tag{8.3.11}$$

with T_0 and G_0 from (8.3.6), (8.3.8).

Note that from (8.3.10), (8.3.11) we just get a condition $\mu_B = 2\mu + |E_b|$.

Dressed Green-function.

Evaluation of $\Sigma_1(z, \vec{q})$ in (8.3.11) for $z = i\omega$ and small $q \to 0$ yields (see Refs. [31, 32] in Chap. 5):

$$\Sigma_1(z, \vec{q}) = \frac{2|E_b|\varepsilon_F}{z + \varepsilon(q) - \mu + \mu_B}. \tag{8.3.12}$$

Accordingly in the first iteration to the self-consistent T-matrix approximation the dressed Green-function G_1 has a two-pole structure (see Refs. [31, 32] in Chap. 5): $G_1(z, \vec{q}) = G_F(z, \vec{q}) + G_B(z, \vec{q})$

$$G_1(z, \vec{q}) = \left(1 - \frac{2|E_b|\varepsilon_F}{(\varepsilon_q - \mu)^2}\right)\frac{1}{(z - \varepsilon(q) + \mu)} + \frac{2|E_b|\varepsilon_F}{(\varepsilon_q - \mu)^2}\frac{1}{(z + \varepsilon(q) - \mu + \mu_B)}, \tag{8.3.13}$$

where $G_B(z, \vec{q}) \approx G_0^2(z, \vec{q})\Sigma_1(z, \vec{q})$ and we can introduce a pseudogap $\Delta_{PG}^2 = 2|E_b|\varepsilon_F$ in similarity with our discussion in Chap. 7.

To get the density of states from G_1 we use the standard formula:

$$N(\omega) = \int \frac{d^2\vec{q}}{(2\pi^2)} \mathrm{Im} G_1(\omega + io, \vec{q}) \tag{8.3.14}$$

where formally in the expression (8.3.13) for $G_1(z, \vec{q})$ we use a standard (Wick) shift $i\omega \to \omega + io$ for "Matsubara" frequency ω.

8.3.3 Density of States Correlation Gap

As a result the density of states for $T_C < T < T_*$ in the normal bosonic metal phase has a form presented on Fig. 8.4.

Summarizing we can say that for intermediate temperatures $T_C \ll T \ll T_*$ we have two strongly asymmetric contributions to the density of states on Fig. 8.4: a contribution from occupied bosonic band and a contribution from an empty fermionic band. The fermionic band has a particle-like dispersion $\xi_q^F = \varepsilon_q - \mu$. A bosonic band has a hole-like dispersion $\xi_q^B = \mu - \varepsilon_q - \mu_B$ (see Fig. 8.5). The intensity of a bosonic band $\sim N_{2D}(0)\frac{\varepsilon_F}{|E_b|}$ is smaller than the intensity of a fermionic band $\sim N_{2D}(0)$ for $|E_b| > \varepsilon_F$. The most important is that a correlation gap $\Delta_{\mathrm{cor}} \approx |E_\mathrm{b}|$ is developed between the bands. This gap is pretty stable at temperatures $T_C \ll T \ll T_*$. Thus in (8.3.13) for a dressed Green's function and for the density of states (see Fig. 8.5) we have a large correlation gap $\Delta_{\mathrm{cor}} \approx |E_\mathrm{b}|$ and a smaller pseudogap (see Chap. 7) $\Delta_{PG}^2 = 2|E_b|\varepsilon_F$, which appears at the edge of the occupied states for $\mu \sim -\frac{|E_b|}{2}$. Moreover for $T = 0$ the pseudogap coincides with a superconductive gap found by Miyake for 2D attractive Fermi gas (see Ref. [63] in Chap. 6). The substantial difference between the pseudogap and superconductive gap is that $\Delta_{SC}^2(T = T_C) = 0$, while Δ_{PG}^2 does not drastically change at T_C. Such a situation with two gaps at $T = 0$ (one large and one small) resembles a qualitative

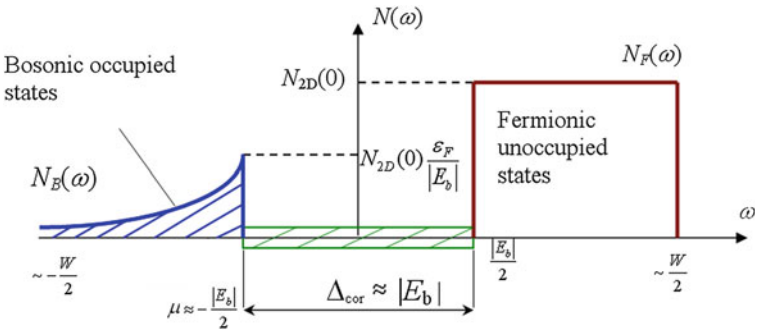

Fig. 8.4 The density of states in the normal bosonic metal phase of the attractive-U 2D Hubbard model in the intermediate coupling case. $\Delta_{\mathrm{cor}} = |E_\mathrm{b}|$ is a correlation gap separating occupied bosonic states from unoccupied fermionic states (see Refs. [31, 32] in Chap. 5)

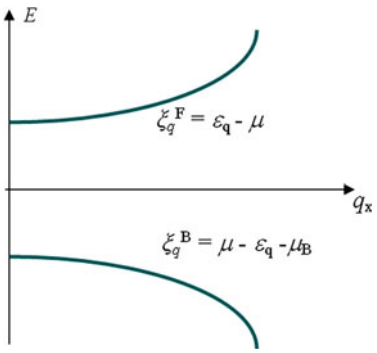

Fig. 8.5 Dispersion of fermionic $\left(\xi_q^F\right)$ and bosonic $\left(\xi_q^B\right)$ bands

picture of P. Nozieres et al. for superconductivity in semiconductors [3]. The role of a correlation gap in semiconductors plays a forbidden gap which separates the valence and conductivity bands.

Let us remind that for $T \ll T_*$ the total number of particles $n = 2n_B + n_F \approx 2n_B$. We can really say that we have a new type of a metal—the normal bosonic metal.

8.3.4 Next Iteration in the T-matrix Scheme

The next iterations will not change the gross-features of the density of states on Fig. 8.4. There will be still a large correlation gap $\Delta_{cor} \sim |E_b|$ and a smaller pseudogap for $|E_b| \gg \varepsilon_F$. The correlation gap will be reduced at higher density of electrons and will finally disappear at $ap_F \geq 1$ (when $|E_b| = 1/ma^2 \leq \varepsilon_F$). In this case the distance between the local pairs $\sim 1/p_F$ becomes of the order of their radius a. So the local pairs will crush each other. We considered this situation more detaily in Chap. 7 when we discussed BCS-BEC crossover in 3D case. For not very large values of the gas-parameter $3 \geq ap_F \geq 1$ in 3D we can expect the coexistence of local pairs and unbound fermions, which is just a Fermi-Bose mixture (see Ref. [66] in Chap. 7) there. Note that the situation with a pseudogap for large values of $|a|p_F > 1$ require the additional investigations both from numerical and analytical sides (see [4, 5] and references therein). From experimental side the pseudogap in underdoped cuprates can be measured from the spectral weight suppression in recent ARPES measurements [6].

8.3.5 η-Resonance

To complete the study of the T-matrix in the first iteration, note that on the 2D square-lattice T-matrix also has a bosonic character but with different sign of dispersion close to the nesting-vector $\vec{Q} = (\pi/d, \pi/d)$ (see Chap. 9 also). Namely for $\vec{q} \to \vec{Q}$ T-matrix reads:

$$T_0(z, \vec{q} \to \vec{Q}) = -\frac{U^2}{z + \frac{(\vec{q}-\vec{Q})^2}{4m^*} + 2\mu + |U|}, \tag{8.3.15}$$

where $m^* = m\frac{|U|}{t}$ in the strong-coupling limit $|U| > W$. This result corresponds to the so-called η-resonances which play an important role in recent attempts to describe high-T_C materials in the framework of SU-5 grand-unification scheme (see Refs. [7–9]) which describes in a unified fashion AFM and SC-instabilities in cuprates. It is also possible starting from (8.3.15) to get Cooper pairs with large total momentum for repulsive-U Hubbard model (see Belyavsky et al. [10, 11]). There is a question, however, how stable these pairs are with respect to the impurities (see Chap. 9).

8.4 Experimental Predictions of the Model

In spite of its simplicity, an attractive-U Hubbard model in the intermediate coupling case in 2D is a very useful toy-model to understand the essential physics of the pseudogap in underdoped cuprates and related materials. It predicts:

1. maximum in spin-susceptibility $\chi(T)$ for $T = T_* \sim |\tilde{E}_b|$, which means that the correlation gap coincides with a spin-gap in this model;
2. a two-band structure of optical conductivity $\sigma(\omega)$ with a bosonic and a fermionic band;
3. large values of $2\Delta/T_C$ in similarity with the STM experiments of Fisher's group [12] on underdoped bismuth family of high-T_C materials (with $2\Delta \sim |\tilde{E}_b|$), as well as asymmetric density of states above T_C;
4. universal features of electron tunneling through the interface between normal fermionic metal and normal bosonic metal. Here the tunneling from fermionic side closely resembles Andreev reflection $e \to h + 2e$ in NS (normal metal—superconductor) structures.

8.4.1 Resistivity in the State of the Normal Bosonic Liquid

For intermediate temperatures $T_C < T < T_*$ the model also predicts interesting (semiconductive type) behavior of resistivity (see Refs. [31, 32] Chap. 5) for normal bosonic metal if we consider a clean case (no impurities) and take into account boson–boson scattering (with Umklapp processes on the lattice—see Chaps. 1, 16). Here in τ-approximation to kinetic equation [13] we get in a 2D case:

$$\begin{aligned} &\rho(T) \sim \sqrt{T/T_0} \text{ for } T_0 < T < T_* \text{ and} \\ &\rho(T) \sim \sqrt{T_0/T} \text{ for } T_C < T < T_0. \end{aligned} \tag{8.4.1}$$

The resistivity characteristics of this type can be obtained in degenerate semiconductors.

8.4.2 The Fermi-Bose Mixture Model

Our toy-model (attractive-U Hubbard model considered in this Chapter) does not capture, of course, all the essential physics of high-T_C materials such as strong short-range (Hubbard) repulsion between conductivity electrons on Cu-sites. The more adequate model is, for instance, a famous t-J model with short-range repulsion and nearest neighbours (nn) van der Waals attractions. The fermionic version of the 2D t-J model will be considered in Chap. 13. For strongly underdoped case of the 2D t-J model we can think about a possible scenario of BCS-BEC crossover (see Ref. [36] in Chap. 6) between local and extended pairs of two composite holes (two spin-polarons or two AFM-strings) in the d-wave channel (see Chap. 13).

However, some additional understanding of several interesting superconductive systems we can get already on the level of a natural extension of attractive-U Hubbard model, namely on the level of a two-band model for the Fermi-Bose mixture (or Fermion-boson model of Ranninger et al. Ref. [65] in Chap. 6 and [14]). As we already mentioned, we can get Fermi-Bose mixture of local pairs and unbound fermions, for example, considering the intermediate coupling case $|E_b| \sim \varepsilon_F$ in the framework of 2D attractive-U Hubbard model (where local pairs start to touch each other). For this case Ranninger et al. (see Ref. [65] in Chap. 6), [14] and later on Larkin, Geshkenbein and Ioffe [15] phenomenologically introduced a model of Fermi-Bose mixture. Moreover the authors of [15] showed that several important experiments in the underdoped high-T_C materials can be naturally explained within the proposed form of the Ginzburg–Landau functional for Fermi-Bose mixture. (The most promising material is bismuth high-T_C family $Bi_2Sr_2Cu_2O_{8+\delta}$ where $p_F\xi_0 \sim 2$, ξ_0 being the coherence length of the Cooper pair). In general the two-band models of the Fermi-Bose mixture can be adequate for the following systems:

1. two-leg and especially three-lag ladders in the isotropic limit $J_\perp = J_\parallel$ [16, 17] (see Chap. 13);
2. PbTe and other degenerate semiconductors. Note that there are 4 families of superconductive semiconductors (see Chernik et al. [18–20]). In PbTe $T_C = 1.4$ K. In other families such as: GeTe, SnTe, and $TlBiTe_2$: $T_C \sim 0.1$ K—the critical temperature is much lower. The experimentalists discuss here the important role of the negative-U centers which is in favor of our model (the fifth family of superconductive semiconductors $SrTiO_3$ is still a subject of a debate with respect to the mechanism of SC (see [64] and the references therein));
3. Fermi-Bose mixture of ^{3}He–^{4}He [21, 22], ^{6}Li–^{7}Li and ^{87}Rb–^{40}K (see Refs. [6, 15] in Chap. 6 and also Chaps. 11 and 12);
4. resonance Fermi-gases in the regime of Feshbach resonance (for the intermediate values of the gas parameter $ap_F \geq 1$ where local pairs touch each other)

(see Chap. 7 on BCS-BEC crossover). Remind that the two-channel Feshbach model (see Refs. [42, 44, 45] in Chap. 5) widely used for ultracold quantum gases is very similar to fermion-boson model of Alexandrov, Ranninger (see Refs. [64, 65] in Chap. 6, and [14]);
5. Fermi-Bose mixture of spinons and holons in underdoped cuprates introduced by Anderson (see Chap. 13).

8.5 Space-Separated Fermi-Bose Mixture and Superconductivity in Bismuthates BaKBiO

Another very interesting systems attracting an attention of both theorists and experimentalists already more than 20 years and probably described by Fermi-Bose mixture model are plumbates-bismuthates [1, 23, 24, 63] BaKBiO–BaPbBiO with $T_C \sim (30 \div 35)$ K for a typical compound $Ba_{1-x}K_xBiO_3$, where $x \geq 0.4$ is K concentration in the superconducting phase.

In these materials an additional resonance peak (an additional band) appears in the one-particle density of states (compare with Fig. 8.5) inside a correlation gap signaling an existence of a second component besides a component associated with normal bosonic metal for $T_C < T < T_*$. The analysis of local crystalline and electronic structures by EXAFS-methods [25] shows that these components (these bands) overlap in energy-space, but are separated in a real space for doping concentrations $x \geq 0.4$ which correspond to a state of superconductive metal. The scenario of space-separated Fermi-Bose mixture can explain the basic transport and SC properties of bismuthates.

Note that $BaBiO_3$, which is a parent compound for the bismuthates $Ba_{1-x}K_xBiO_3$ and plumbates $Ba_{1-x}Pb_xBiO_3$ represents a charge-density wave (CDW) insulator having (in contrast with attractive-U Hubbard model) the two correlation gaps instead of one for the density of states: an optical gap with $E_g = 1.9$ eV and an activation (transport) gap with $E_a = 0.24$ eV [26]. A partial replacement of Ba by K in BaKBiO causes the decrease of the gaps, and as a result, the insulator–metal transition and superconductivity are obtained at the doping level $x \approx 0.37$. The superconductivity remains up to the doping level $x \approx 0.50$ corresponding to the solubility limit of K in BaKBiO, but the maximal critical temperatures $T_C \approx 30$ K are achieved for $x = 0.4$ [27, 28] (see [63]).

8.5.1 Peculiarities of the Local Crystal Structure

A three-dimensional nature of the cubic perovskite-like structure of the bismuthates differs from the two-dimensional one in the high-T_C cuprates (see [63]). The building block in the bismuthates is the BiO_6 octahedral complex (the analogue

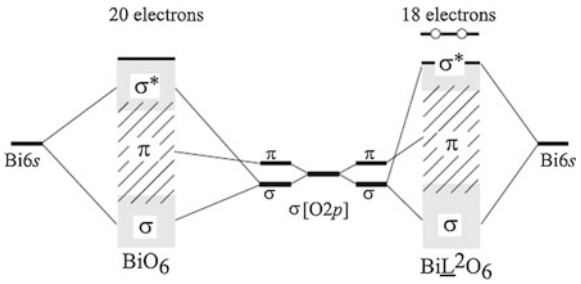

Fig. 8.6 The scheme of the formation of the electron structure for the different octahedral BiO_6 complexes from Menushenkov et al. [63]

of CuO_n ($n = 4, 5, 6$) in high-T_C materials). The octahedral complexes are the most tightly bound items of the structure because of a strong covalence of the Bi6s–O2pσ bonds (see Fig. 8.6). According to the crystallographic data [29], the crystal structure of a parent $BaBiO_3$ compound represents the alternating arrangement of the expanded and contracted BiO_6 octahedra (referred to as the "breathing" distortion) in the barium lattice. This alternation and the static rotation of the octahedra around the axis [110] produce a monoclinic distortion of the cubic lattice. As it is shown in [25, 30, 31] the larger soft octahedron corresponds to the BiO_6 complex with the completely filled Bi6s–O2p orbitals (see Fig. 8.6) and the smaller rigid octahedron correspond to the $Bi\underline{L}^2O_6$ complex. Here L^2 denotes the free level (or the two holes pair) in the antibonding Bi6s–O2pσ orbital of the smaller octahedral complex.

The K doping of $BaBiO_3$ is equivalent to the hole doping and leads to a partial replacement of the larger soft octahedra BiO_6 by the smaller rigid octahedra $Bi\underline{L}^2O_6$ [25]. This causes the decrease and the eventual disappearance of the static breathing and tilting distortions. The lattice must therefore contract despite the practically equal ionic radii of K^+ and Ba^{2+}. As a result, the average structure becomes a simple cubic one at the doping level $x = 0.37$ in accordance with neutron diffraction data [28]. However, the local EXAFS probes [25, 30, 32] showed the significant difference of the local crystal structure from the average one. We found (see [63]) that the oxygen ions belonging to the different BiO_6 and $Bi\underline{L}^2O_6$ octahedra vibrate in a double-well potential, while those having an equivalent of the two equal $Bi\underline{L}^2O_6$ octahedra oscillate in a simple harmonic potential [25, 30]. This very unusual behavior is closely related to the local electronic structure of BaKBiO.

8.5.2 Local Electronic Structure

The coexistence of the two types of octahedra in $BaBiO_3$ with different Bi–O bond lengths and strengths reflects the different electronic structure of BiO_6 complexes. The valence band of $BaBiO_3$ is determined by the overlap of the Bi6s and O2pσ

orbitals [33, 34], and because of a strong Bi6s–O2pσ hybridization, the octahedra can be considered as quasimolecular complexes [35]. Each complex involves ten electron levels consisting of four bonding-antibonding Bi6s–O2pσ orbitals and six nonbonding O2pσ orbitals. A monoclinic unit cell includes two octahedra and contains 38 valence electrons (10 from two bismuth ions, 4 from two barium ions and 24 from six oxygen ions) (see Fig. 8.6). All the Bi–O bond lengths must be equal and local magnetic moments must be present for the equal electron filling of the nearest octahedra ($Bi\underline{L}^1O_6$–$Bi\underline{L}^1O_6$). However, the presence of the two types of octahedra complexes and the absence of any local magnetic moments were observed experimentally [26, 36]. A scheme of valence disproportionation $2\ Bi\underline{L}^1O_6 \rightarrow Bi\underline{L}^2O_6 + BiO_6$ was then proposed in [25] in which the number of occupied states are different in the neighboring octahedral complexes: the octahedra $Bi\underline{L}^2O_6$ contains 18 electrons and has one free level or a hole pair $\underline{L}^2$ in the upper antibonding Bi6s–O2pσ* orbital, while in the octahedron BiO_6 with 20 electrons the antibonding orbital is filled as shown on Fig. 8.6. It is quite natural that the $Bi\underline{L}^2O_6$ octahedra have stiff quasimolecular Bi–O bonds and a smaller radius, while the BiO_6 octahedra represent unstable molecules with the filled antibonding orbital and a larger radius.

Thus in $BaBiO_3$, one has an alternating system of the two types of octahedral complexes filled with local pairs: the hole pairs in $Bi\underline{L}^2O_6$ complexes and the electron pairs in BiO_6 complexes. In other words, the parent compound is a system with the real-space [37] or hard-core [38] bosons (i.e. with at most one boson per site).

The local pairs formation in $BaBiO_3$ was advocated previously, e.g. in [1, 26, 39–44]. The binding mechanism for the pairs is probably of electron nature [1, 40] in accordance with Varma's picture [1] of the pairing due to the skipping of the valence "4+" by the Bi ion. However, one cannot fully exclude the lattice mediated pairing [26, 41], (see Ref. [64] in Chap. 6) in accordance with de Jongh's statement [42] that the preference to retain the close-shell structures overcomes the Coulomb repulsion related to the intrasite bipolaron formation (see Ref. [64] in Chap. 6).

The local electron structure of $BaBiO_3$, combined with the real-space local electron structure is presented in Fig. 8.7a.

The optical gap in similarity with the Varma's suggestion [1] coasts the energy:

$$E_g = E_b + 2E_a = 2E(Bi\underline{L}^1O_6) - E(BiO_6) - E(Bi\underline{L}^2O_6) \qquad (8.5.1)$$

and is observed experimentally as an optical conductivity peak at the photon energy $h\nu = 1.9$ eV [26] (here E_b is the pair binding energy related to the dissociation of pairs).

In accordance with (8.5.1) the optical excitations must provide a local lattice deformation via the transformation of the two different octahedra into equivalent ones: $Bi\underline{L}^2O_6 + BiO_6 \overset{h\nu}{\rightarrow} 2\ Bi\underline{L}^1O_6$. Consequently this dynamical local lattice deformation is manifested in the Raman spectra as an abnormally high amplitude of the breathing-type vibrations of the oxygen octahedra if the resonance

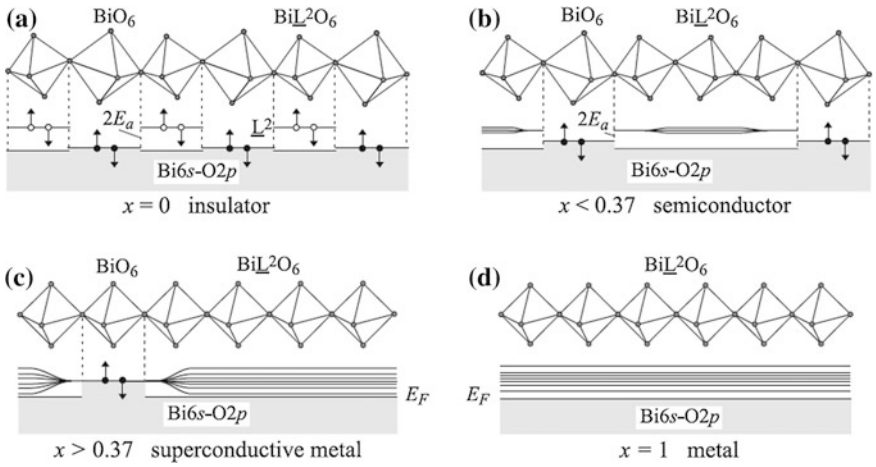

Fig. 8.7 The scheme of the insulator–metal phase transition for the K-doping of $Ba_{1-x}K_xBiO_3$ in the framework of the relationship between the local crystal and the local electronic structures from Menushenkov et al. (see [63]). The local crystal structure of the octahedral complexes (at the *top*) and the local electronic structure (at the *bottom*) are shown on the pictures **a**–**d**. The occupied states of the Bi6s–O2p valence band are marked by *gray*. $2E_a$ is the activation gap. *Black* and *white circles* with *arrows* denote, correspondingly, the electrons and the holes with the opposite spin orientations. **a** The monoclinic phase of an insulator $BaBiO_3$. **b** An orthorhombic phase of a semiconducting BaKBiO at $0 < x < 0.37$. The splitting of free level $\underline{L}^2$ at a spatial overlap of the $Bi\underline{L}^2O6$ octahedra is sketched. **c** An undistorted cubic phase of a superconducting metal at $x > 0.37$. The formation of a Fermi-liquid state is shown arising due to the overlap of an unoccupied fermionic band F with an occupied Bi6s–O2p valence band when the percolation threshold is reached. **d** An undistorted cubic phase of a nonsuperconducting metal at $x = 1$. A Fermi liquid state with Fermi level E_F is shown

excitation with $hv = E_g$ is used [35, 43, 45]. The abrupt decrease of the mode amplitude was observed when the lasers with different wave lengths were used [45].

It is important to emphasize that there are no free fermions in the system. Only the excited fermions can be produced by the unpairing, and they do not give any contribution to the charge transport because of a high value of E_b. The bosonic and the fermionic subsystems are therefore separated energetically (as in Fig. 8.4 for the density of states in the normal bosonic metal phase of the attractive-U Hubbard model) and spatially (this is a specific feature of plumbates-bismuthates). Hence the Fermi-Bose mixture is absent in the parent compound $BaBiO_3$ (in similarity with a low density case $|E_b| > \varepsilon_F$ for attractive-U Hubbard model).

This situation is illustrated on Fig. 8.8a, where we schematically present one-particle density of states. For $x = 0$ the filled bosonic band is separated from the empty fermionic (the excited band F'), by the large optical gap E_g and from the empty bosonic band B by the smaller transport gap $2E_a$. The bosonic band plays the role of a conduction band for bosonic quasiparticles involved in the activation transport. In accordance with (see Refs. [31, 32] in Chap. 5) the filled and empty

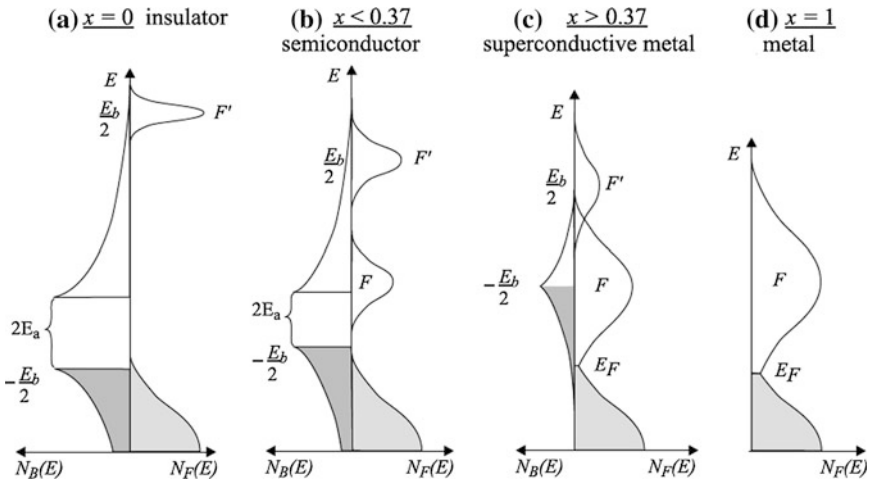

Fig. 8.8 A sketch of the one-particle density of states for $Ba_{1-x}K_xBiO_3$ from Menushenkov et al. (see [63]). The contributions from the bosons $N_B(E)$ and the fermions $N_F(E)$ are depicted separately because the bosonic and fermionic states are spatially separated. The filled (*dark gray*) and the unoccupied (*transparent*) bosonic bands correspond, respectively, to the contributions of the electron and the hole pairs. The bands are separated by the activation gap $2E_a$ which is lowered with a doping level x. An empty fermionic band F', corresponding to the destruction of the pairs, is separated from an occupied bosonic band by the optical gap E_g. An empty fermionic band F is formed due to the splitting of the free level $\underline{L}^2$, which arises from the spatial overlap of the $Bi\underline{L}^2O_6$ octahedra. The filled fermionic band (*gray*) represents the Bi6s–O2p valence band. The band F' and bosonic bands decrease as the doping increases, because of the decrease of the number of the electron pairs, while a band F grows due to the increase in the number of free levels. A Fermi liquid state is formed (**c**, **d**) as a result of the overlap between the band F and the Bi6s-O2p valence band

bosonic bands have, respectively, the hole-like and electron-like dispersions in the representation on the one-particle density of states. Because bosons and fermions are already spatially separated (i.e. belong to different octahedra complexes) we show their densities of states in the different sides of the pictures on Fig. 8.8.

8.5.3 Formation of the Fermi-Bose Mixture

The substitution of the two K^+ ions for the two Ba^{2+} ones modifies the BiO_6 complex to the $Bi\underline{L}^2O_6$ one. As a result, the number of the small stiff $Bi\underline{L}^2O_6$ octahedra increases as $n_0(1+x)/2$ and the number of large soft BiO_6 octahedra decreases as $n_0(1-x)/2$, where $n_0 = 1/d^3$ is the number of the unit cells and d is a lattice parameter. Clusters of the $Bi\underline{L}^2O_6$ complexes are formed with doping, which contract the lattice because of small radii and the rigid bonds of the $Bi\underline{L}^2O_6$ complexes.

The changes in the crystal structure are accompanied by the essential changes in the local electronic structure. A spatial overlap of the $\underline{L}^2$ levels leads to their splitting into an empty fermionic-like band F inside the $Bi\underline{L}^2O_6-\ldots-Bi\underline{L}^2O_6$ Fermi-cluster (see Fig. 8.7b). In the doping range $x < 0.37$ this sufficiently narrow band is still separated from the occupied Bi6s–O2p subband. The number of the empty electron states in the F band increases with x as $\hat{n}_F = n_0(1 + x)$, while the number of the local electron pairs decreases as $n_B = n_0(1 - x)/2$.

The free motion of the pairs is still prevented by the intersite Coulomb repulsion ($E_a \neq 0$), which is screened inside the clusters, however. When the Fermi-clusters are formed, the conductivity becomes finite because of the motion of the pairs through the clusters of the different length. The BaKBiO compounds demonstrate for $x < 0.37$ a semiconducting-type conductivity changing from a simple activation type to Mott's law with variable-range hopping [46]. At the doping level $x \approx 0.37$ (see Figs. 8.7c and 8.8c), the following cardinal changes occur.

1. The breathing and the rotational static lattice distortions transform to the dynamic ones. At the Bose and Fermi cluster borders, where all oxygen ions belong to both the BiO_6 and $Bi\underline{L}^2O_6$ octahedra, the local breathing dynamic distortion is observed as the oxygen ion vibration in a double-well potential [25, 30].
2. The infinite percolating Fermi cluster is formed from the $Bi\underline{L}^2O_6$ octahedra along the [100]-type directions. The empty fermionic band overlaps with a filled one, and F therefore becomes a conduction band. Overcoming of the percolation threshold provides the insulator–metal phase transition and the formation of the Fermi-liquid state for $x \geq 0.37$. The valence electrons previously localized in the $Bi\underline{L}^2O_6$ complexes become itinerant inside the infinite Fermi cluster.
3. The pair localization energy disappears, $E_a = 0$, and therefore local electron pairs originating from the BiO_6 complexes can move freely providing a bosonic contribution to the conductivity. In the metallic phase the two types of carriers are present: the itinerant electrons from the $Bi\underline{L}^2O_6$ complexes (fermions) and the delocalized electron pairs from the BiO_6 complexes (bosons). Although the normal state conductivity is mainly due to a fermionic subsystem, the contribution from a bosonic subsystem was also observed by Hellman and Hartford [47] as the two-particle normal state tunneling.

As a result, at doping levels $x > 0.37$, we have a new type of a spatially separated mixture of the bosonic and the fermionic subsystems describing both metallic and superconducting properties of BaKBiO. We stress that because fermions and bosons belong to the complexes with the different electronic structure, the Fermi and Bose subsystems are spatially separated at any doping level. The densities of these subsystems are related by $2n_B + \hat{n}_F = 2n_0$. (which resembles (8.1.5) for attractive-U Hubbard model). Moreover:

$$\frac{2n_B}{\hat{n}_F} = \frac{1-x}{1+x}. \tag{8.5.2}$$

The pair destruction is prevented by a sufficiently high value of the binding energy, which effectively manifests itself as an optical gap $E_b = E_g \approx 0.5$ eV [48] in superconductive compositions. The unpairing is possible only under the optical excitation to the band F' (see Fig. 8.8c), which does not play any role in the charge transport.

At $x = 1$ all the BiO_6 octahedra are transformed into the $Bi\underline{L}^2O_6$ ones. The Bose system disappears ($n_B = 0$) together with the excited fermionic band F'. Therefore, $KBiO_3$ must be a nonsuperconductive Fermi-liquid metal (see Figs. 8.8d and 8.9d).

We note that a metallic $KBiO_3$ compound exists only hypothetically because the potassium solubility limit $x \approx 0.5$ is exceeded in BaKBiO. However, $BaPbO_3$, which can be viewed as an electronic analogue of $KBiO_3$, demonstrates metallic

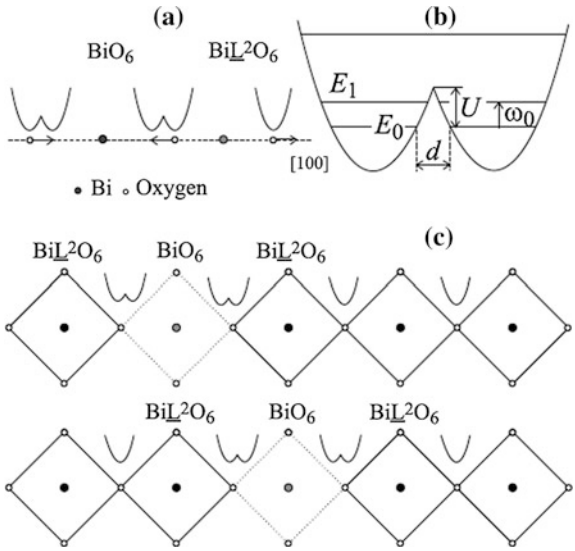

Fig. 8.9 A sketch of the dynamic exchange $BiO_6 \leftrightarrow Bi\underline{L}^2O_6$ from Menushenkov et al. (see [63]) is shown in the BiO_2 plane of the octahedra. **a** A breathing mode of the vibrations along [100]-type direction of the two neighboring octahedra with the different electronic structures. The BiO_6 octahedron transforms to the $Bi\underline{L}^2O_6$ one and vice versa due to the electron pair tunneling between the octahedra. An oxygen ion belonging to such octahedra oscillates in a double-well potential. An oxygen ion belonging to the equivalent neighboring $Bi\underline{L}^2O_6$ octahedra oscillates in a simple parabolic potential. **b** The double-well potential with the energy levels for the vibration of the oxygen ion. The following parameters describe the tunneling barrier between the wells in $Ba_{0.6}K_{0.4}BiO_3$ at low temperatures (see experimental results of Menushenkov et al. [25]): the tunneling frequency $\omega_0 = 200$ K, the barrier height $U = 500$ K, the barrier width $d = 0.07$ Å. **c** The motion of the local electron pair centered on the BiO_6 octahedron through the $Bi\underline{L}^2O_6 \cdots Bi\underline{L}^2O_6$ Fermi cluster. For detailed explanations, see the text

but not superconducting properties. Recent attempts to synthesize $KBiO_3$ at a high pressure have shown that only $K_{1-y}Bi_yBiO_3$ with a partial replacement of the K^+ ions by the Bi^{3+} ones is formed [49]. This replacement must lead to the appearance of the BiO_6 octahedra with the local electron pairs, and the compound $K_{1-y}Bi_yBiO_3$ must therefore be superconducting in accordance with the above discussion. Indeed, superconductivity with $T_C = 10.2$ K was experimentally observed in this compound [49].

Our analysis implies that $BaPbO_3$ must be superconducting at a partial substitution of the Ba^{2+} ions for the trivalent ions because this substitution produces the local electronic pairs as in the case of $K_{1-y}Bi_yBiO_3$. Thus using the La^{3+} doping, it is possible to obtain the spatially separated Fermi-Bose mixture in $BaPbO_3$. The direct experimental proof of this statement was realized by Menushenkov's group [50]. The authors of [50] successfully produced $Ba_{1-x}La_xPbO_3$ using the high-pressure synthesis technique. Superconductivity at $T_C = 11$ K observed in this new compound [50] is a direct evidence in favor of the scenario proposed above.

At the end of this Subsection, we note that our understanding of the insulating state in the parent $KBiO_3$ compound is very similar to the theoretical model by Tarapheder et al. [39, 40]. We agree with the authors of [39, 40] on the following principal positions: (1) the presence of electron-mediated (Varma's type) pairing mechanism [1]; (2) the existence of the charge $\pm 2e$ bosonic bound states that dominate transport properties of $BaBiO_3$; (3) the explanation of the nature of both the transport and optical gap.

However, our description of the K-doped systems strongly differs from their model. Going from insulating $BaBiO_3$ to superconducting BaKBiO ($x \geq 0.37$), Tarapheder et al. were forced to change the nature of the pairing mechanism from the real-space pairing to the k-space one. Thus their description of the superconducting state does not differ from the traditional BCS description that has been discussed for BaKBiO, e.g. in [51–53].

Using the EXAFS results of Menushenkov's group [25, 30], we consistently explain the insulating and superconducting states in BaKBiO within a single approach. In contrast to [39, 40] we showed that the real-space bosons do not disappear in the metallic region of BaKBiO and that they are responsible for superconductivity. At the same time, the Fermi-liquid appears in the BaKBiO system because of the overlapping of the occupied valence band levels and the free ones when we overcome the percolation threshold at $x = 0.37$. An interplay of these Bose and Fermi subsystems explains the main properties of BaKBiO.

8.5.4 Superconductivity in $Ba_{1-x}K_xBiO_3$

Taking the existence of the double-well potential in $Ba_{1-x}K_xBiO_3$ into account, one can consider superconductivity in this compound in the framework of the anharmonic models for high-T_C materials [54, 55, 65]. As it was shown in these

models, if the oxygen ions move in a double-well potential, an order-of-magnitude enhancement of the electron-lattice coupling constant follows automatically from a consistent treatment of this motion [65].

However, as we discussed briefly in present Subsection, the double-well potential arises in the bismuthates from different electron fillings of the nearest octahedra and the tunneling of local pairs between them. The existence of the double-well potential in the metallic phase of BaKBiO ($x \geq 0.37$) therefore indicates that the real-space bosons do not decay with doping. There are at least two additional experimental conformations of this fact: (1) the observation of the optical pseudogap (correlation gap) in superconducting composition [48] and (2) the existence of two types of charge carriers with heavy and light masses [47, 54]. These experimental facts allow us to consider superconductivity in the bismuthates as the motion of local electron pairs. This motion is correlated with the oxygen ion vibrations in the double-well potential and leads to the transformation of the Bose octahedral complexes to the Fermi ones and vise versa in the dynamic exchange process $BiO_6 \leftrightarrow Bi\underline{L}^2O_6$.

Thus taking the existence of the double-well potential in $Ba_{1-x}K_xBiO_3$ into account, one can consider superconductivity in this compound as a long-range order that is established via the local pairs tunneling from one Bose cluster to a nearest one over the Fermi cluster along [100]-type direction.

The pair transfer process correlated with the oxygen vibrations (in other words, the dynamic exchange) is illustrated in Fig. 8.9. The oxygen belonging to the two neighboring octahedra BiO_6 and $Bi\underline{L}^2O_6$ vibrates in the double-well potential, and hence, the electron pair tunneling between the neighboring octahedra occurs when the ion tunnels through the potential barriers between the wells. Because of this interconnection between the pair and the oxygen tunneling process, we can estimate the matrix element of the pair tunneling as $t_B \sim \omega_0 e^{-D}$, where ω_0 is the tunneling frequency,

$$D = \frac{1}{\hbar}\int_{x_0}^{x_1} |p|dx \approx \frac{d}{\hbar}\sqrt{2MU} \tag{8.5.3}$$

is the semiclassical transparency of the barrier in the double-well potential, U and d are the barrier height and width, and M is the oxygen ion mass. We note that relatively small tunneling frequency $\omega_0 = 200$ K (see Fig. 8.9) already incorporates all the electron–phonon polaronic effects.

Note that rigorously speaking a local pair is transferred from one Bose cluster to the nearest one over a Fermi-cluster, which, depending on the doping level, consists of several octahedra. The pairs overcome the Fermi-cluster step by step. A single step, corresponding to the pair transfer into a neighboring octahedron, occurs simultaneously with the oxygen ion tunneling in the double-well potential. The tunneling frequency ω_0 is therefore the same for each step. Assuming that the steps are independent events, the probability of overcoming the Fermi-cluster can be obtained as the product of the probability of each step. The matrix element of

the pair tunneling through the Fermi-cluster can be estimated as $\hat{t}_B \approx \omega_0 e^{-\langle N\rangle D}$, where an average number of steps $\langle N\rangle$ (which is proportional to a Fermi-cluster linear size) can be obtained from the ratio of the concentrations of $Bi\underline{L}^2O_6$ and BiO_6 octahedra. This gives the average number of steps:

$$\langle N\rangle = \left(\frac{1+x}{1-x}\right)^{1/3}. \tag{8.5.4}$$

A natural assumption (see [63]) is that the critical temperature of the onset of superconductivity is of the order of the Bose–Einstein condensation temperature $T_C \sim \hat{t}_B d^2 n_B^{2/3}$ in the bosonic system with a large effective mass $m_B \sim 1/\hat{t}_B d^2$. We recall that $n_B d^3 = (1-x)/2$ in our case. For the parameters of the double-well potential obtained in the [25] (see also Fig. 8.9), we estimated $T_C \sim 50$ K in $Ba_{0.6}K_{0.4}BiO_3$, which is larger than the measured $T_C \approx 30$ K.

However, this estimate does not account for the phase coherence arising due to the relation between the vibrations of oxygen ions and the transfer of pairs. When the pair is transferred from one octahedron to another one, the lattice has a sufficient time to relax due to the longitudinal stretching phonons, each time forming a new configuration before the next tunneling event occurs. Taking the breathing like character of the oxygen ion vibrations in the double-well potential into account (see Fig. 8.9), it is natural to suppose that the breathing mode of each octahedron is coordinated with its neighbors to guarantee a resonant tunneling along [100]-type axes in the system.

From the dispersion of the longitudinal phonon modes studied by the inelastic neutron scattering [55], it follows that the breathing-type vibrations with the wave vector $q_b = (\pi/d, 0)$ are energetically favorable in the superconductive compositions of BaKBiO. Hence a long-range correlation of the vibrations must occur at low temperatures when only the low-energy states are occupied. The bandwidth of the longitudinal stretching mode is of the order of 100 K, and the temperature $T \sim T_C$ is sufficiently high to excite the non-breathing-type longitudinal stretching phonons with the wave vectors shorter than q_b. The thermal excitation of these phonons leads to the destruction of the long-range correlation between the breathing-type vibrations, and hence destructively affects the long-range phase coherence of the local pair transfer.

We note that the anomalous dispersion of the longitudinal stretching phonons observed in [55] reflects the lattice softening with the decrease in the temperature due to the existence of the double-well potential in the superconducting compositions of BaKBiO. A similar dispersion was also observed in the optimally doped high-T_C cuprates $La_{1.85}Sr_{0.15}CuO_4$ and $YBa_2Cu_3O_7$ [56]. The problem of the T_C limitation due to the destruction of the phase coherence is now extensively discussed (see [57] for a review). It is important to mention here also the experimental evidence by Müller et al. [58] for the coexistence of the small bosonic and fermionic charge carriers in $La_{2-x}Sr_xCuO_4$, so the possibility to apply our scenario to high-T_C materials is an interesting open question.

8.5.5 Discussion and Possible Experimental Test of the Proposed Model

We briefly summarize the key points of our concept:

1. The parent compound $BaBiO_3$ represents a system with the initially preformed local electron and hole pairs. Each pair is spatially and energetically localized inside the octahedron volume. The localization energy of a pair determines the transport activation gap E_a. The binding energy of a pair is given by $E_b = E_g - 2E_a$, where E_g is the optical gap.
2. The spatially separated Fermi-Bose mixture of a new type is possibly realized in the superconducting compositions of $Ba_{1-x}K_xBiO_3$ for $x \geq 0.37$. The bosonic bands are responsible for the two-particle normal state conductivity. The overlap of the empty fermionic band F with an occupied valence band Bi6s–O2p provides the insulator–metal phase transition and produces the Fermi-liquid state. This state strongly shunts the normal state conductivity arising from the two-particle Bose transport.
3. The fermionic band F' connected with the destruction of the pair does not play any role in the transport. The excitation energy is sufficiently high to guarantee against the destruction of bosons (a pair binding energy for the superconductive compositions is $E_b \approx 0.5$ eV).
4. The localization energy of the pair is absent for $x \geq 0.37$ ($E_a = 0$), and therefore the bosonic and the fermionic subsystems are separated only spatially. The interplay between them is due to the dynamic exchange $Bi\underline{L}^2O_6 \leftrightarrow BiO_6$, which causes the free motion of the local pairs in the real space.
5. The pairing mechanism in the bismuthates is more likely of the Varma type [1] (due to the skipping of the valence "4+" by the Bi ion) rather than of phonon-mediated origin. The existence of the local pairs and their tunneling between the neighboring octahedra is closely related to the presence of the double-well potential that describes the vibration of the oxygen ions. The lattice is more likely involved in the superconductivity by providing the phase coherence for the motion of local pairs in the real space.

We finally emphasize that the scenario of the Fermi-Bose mixture allows us to qualitatively describe the insulator–metal phase transition and the superconductive state in BaKBiO in the framework of the single approach. To some extent, this scenario explains the contradictions between the results of the local sensitive and integral experimental methods [25, 26, 30, 32, 45, 55, 59–61]. In addition, as we already mentioned Menushenkov's group [50] successfully synthesized a new superconducting oxide $Ba_{1-x}La_xPbO_3$ that can be considered as the direct evidence in favor of our model.

Nevertheless, the additional experiments are required to make a definite conclusion about the nature of superconductivity in these systems.

We propose two direct experiments (see [63] to test our model. (1) To provide the Raman scattering experiment of the superconducting $Ba_{0.6}K_{0.4}BiO_3$ compound

using a resonance optical excitation in the range of the optical gap $E_g \approx 0.5$ eV. In this case a sharp increase in the amplitude of some Raman modes due to local dynamic distortions must be observed at the pair destruction in accordance with our model. (2) To provide measurements of the inelastic neutron scattering in the $Ba_{0.5}K_{0.5}BiO_3$ and $BaPbO_3$ samples. We expect that the dispersion of the longitudinal stretching mode should decrease with a change of the K-doping from $x = 0.4$ to $x = 0.5$ and should be absent in the metallic $BaPbO_3$ compound.

Moreover, it is important to carry out the more precise measurements of the specific heat in the bismuthates for $T \sim T_C$. Note that in the 3D Bose-gas the specific heat behaves as $C_B \sim (T/T_C)^{3/2}$ for the temperatures $T < T_C$, and $C_B = \text{const}$ for $T \gg T_C$. As a result, there is a λ-point behavior of the specific heat for $T \sim T_C$ (see Refs. [27, 30] in Chap. 5). However, the Fermi-Bose mixture gives an additional linear in T contribution from a Fermi-gas $C_F \sim \gamma T$. This contribution could in principle destroy the λ-point behavior of the specific heat in the Fermi-Bose mixture. We note that the currently available experimental results in the bismuthates [62] signal a smooth behavior of the specific heat near T_C, possibly because in all the experiments the contributions of the Fermi and Bose gases are masked by a larger lattice contribution.

References

1. Varma, C.M.: Phys. Rev. Lett. **61**, 2713 (1988)
2. Eliashberg G.M.: JETP **16**, 780 (1963)
3. Nozieres, P., Pistolesi F.: Eur. Phys. Jour. B **10**, 649 (1999)
4. Perali, A.,Palestini, F., Pieri, P., Strinati, G.C.,Stewart, J.T., Gaebler, J.P., Drake, T.E., Jin, D.S.: Phys. Rev. Lett. **106**, 060402 (2011)
5. Gaebler, J.P., Stewart, J.T., Drake, T.E., Jin, D.S., Perali, A., Pieri, P, Strinati, G.C.: Nat. Phys. **6**, 569 (2010)
6. Kondo, T.,Hamaya, Y., Palczewski, A.D.,Takeuchi, T., Wen, J.S., Xu, Z.J., Gu, G., Schmalian, J., Kaminski, A.: Nat. Phys. **7**, 21 (2011)
7. Zhang, S.-C., Science **275**, 1089 (1997)
8. Dorneich, A., Hanke, W., Arrigoni, E., Troyer, M., Zhang, S.-C.: Phys. Rev. Lett **88**, 057003 (2002)
9. Demler, E., Hanke, W., Zhang, S.-C.: Rev. Mod. Phys. **76**, 909 (2004)
10. Belyavsky, V.I., Kapaev, V.V., Kopaev, Y.V.: Phys. Rev. B **80**, 214524 (2009)
11. Belyavsky, V.I., Kopaev, Y.V.:Phys. Rev. B **76**, 214506 (2007)
12. Renner, Ch., Revaz, B., Genoud, J.-Y., Kadowaki, K., Fischer, Ø.: Phys. Rev. Lett. **80**, 149 (1998)
13. Lifshitz, E.M., Pitaevskii, L.P.: Physical Kinetics. Butterworth-Heinemann, Oxford (1981)
14. Chakraverty, B.K., Ranninger, J., Feinberg, D.: Phys. Rev. Lett. **81**, 433 (1998)
15. Geshkenbein, V.B., Ioffe, L.B., Larkin, A.I.: Phys. Rev. B **55**, 3173 (1997)
16. Tsunetsugu, H., Troyer, M., Rice, T.M.: Phys. Rev. B **51**, 16456 (1995)
17. Kagan, M.Yu., Haas, S, Rice, T.M.: Physica C **317/318**, 185 (1999)
18. Chernik, I.A., Berezin, A.V., Lykov, S.N., Sabo, E.P., Titarenko, Y.D.: JETP Lett. **48**, 596 (1988)
19. Chernik, I.A., Berezin, A.V., Zhitinskaya, M.K., Lykov, S.N.: Phys. Solid State **34**, 1316 (1992)

20. Chernik, I.A., Berezin, A.V.: Phys.Solid State **37**, 948 (1995)
21. Kagan, M.Yu.: Sov. Phys. Uspekhi **37**, 69 (1994)
22. Bardeen, J., Baym, G.,Pines, D.: Phys. Rev. **156**, 207 (1967)
23. Menushenkov, A.P., Klementev, K.V., Kuznetsov, A.V., Kagan, M.Yu.: Physica B **31**, 312 (2002)
24. Menushenkov, A.P., Klementev, K.V., Kuznetsov, A.V., Kagan, M.Yu.: In Physics in Local Lattice Distortions. In: Oyanagi, H., Bianconi, A. (eds.) AIP Conference Proceedings, vol. **554**, 269 (2001)
25. Menushenkov, A.P., Klementev, K.V.: Jour. Phys.: Condens. Matter **12**, 3767 (2000)
26. Uchida, S., Kitazawa, K., Tanaka, S.: Phase Transitions **8**, 95 (1987)
27. Cava, R.J., Batlogg, B., Krajewski, J.J., Farrow, R., Rupp Jr, L.W., White, A.E., Short, K., Peck, W.F., Kometani, T.: Nature **332**, 814 (1988)
28. Pei, S., Jorgensen, J.D., Dabrowski, B., Hinks, D.G., Richards, D.R., Mitchell, A.W., Newsam, J.M., Sinha, S.K., Vaknin, D., Jacobson, A.J.: Phys. Rev. B **41**, 4126 (1990)
29. Cox, D.E., Sleight, A.W.: Acta Cryst. B **35**, 1 (1979)
30. Menushenkov, A.P., Klementev, K.V., Konarev, P.V., Meshkov, A.A.: JETP Lett., **67**, 1034 (1998)
31. Menushenkov, A.P.: Nucl. Instr. Meth. Phys. Res. A **405**, 365 (1998)
32. Yacoby, Y., Heald, S.M., Stern, E.A.: Solid State Comm. **101**, 801 (1997)
33. Mattheiss, L.F., Hamann, D.R.: Phys. Rev. B **28**, 4227 (1983)
34. Sleight, A.W., Gillson, J.L., Bierstedt, P.E.: Solid State Comm. **17**, 27 (1975)
35. Sugai, S.: Jpn. Jour. Appl. Phys. Suppl. **26**, 1123 (1987)
36. Uemura, Y.J., Sternlieb, B.J., Cox, D.E., Brewer, J.H., Kadono, R., Kempton, J.R., Kiefl, R.F., Kreitzman, S.R., Luke, G.M., Mulhern, P., Riseman, T., Williams, D.L., Kossler, W.J., Yu, X.H., Stronach, C.E., Subramanian, M.A., Gopalakrishnan, J., Sleight, A.W.: Nature **335**, 151 (1988)
37. Mott, N.F.: Supercond. Sci. Tech. **4**, 559 (1991)
38. Meregalli, V., Savrasov, S.Y.: Phys. Rev. B **57**, 14453–14469 (1998)
39. Taraphder, A., Krishnamurthy, H.R., Pandit, R., Ramakrishnan, T.V.: Europhys. Lett. **21**, 79 (1993)
40. Taraphder, A., Krishnamurthy, H.R., Pandit, R., Ramakrishnan, T.V.: Phys. Rev. B **52**, 1368 (1995)
41. Rice, T.M., Sneddon, L.: Phys. Rev. Lett. **47**, 689 (1981)
42. de Jongh, L.J.: Physica C (Amsterdam) **152**, 171 (1998)
43. Sugai, S.: Solid State Comm., **72**, 1187 (1989)
44. Yu, J., Chen, X.Y., Su, W.P.: Phys. Rev. B **41**, 344 (1990)
45. Tajima, S., Yoshida, M., Koshizuka, N., Sato, H., Uchida, S.: Phys. Rev. B **46**, 1232–1235 (1992)
46. Hellman, E.S., Miller, B., Rosamilia, J.M., Hartford, E.H., Baldwin, K.W.: Phys. Rev. B **44**, 9719 (1991)
47. Hellman, E.S., Hartford Jr. E.H.: Phys. Rev. B **52**, 6822 (1995)
48. Blanton, S.H., Collins, R.T., Kelleher, K.H., Rotter, L.D., Schlesinger, Z., Hinks, D.G., Zheng, Y.: Phys. Rev. B **47**, 996 (1993)
49. Khasanova, N.R., Yamamoto, A., Tajima, S., Wu, X.-J., Tanabe, K.: Physica C (Amsterdam) **305**, 275 (1998)
50. Menushenkov, A.P., Tsvyashchenko, A.V., Eremenko, D.V., Klementev, K.V., Kuznetsov, A.V., Trofimov, V.N., Fomichev, L.N.: Sov. Phys. Solid State **43**, 613 (2001)
51. Shirai, M., Suzuki, N., Motizuki, K.: Jour. Phys.: Condens. Matter **2**, 3553 (1990)
52. Vielsack, G., Weber, W.: Phys. Rev. B **54**, 6614 (1996)
53. Marcos, W.J., Degani, M.H., Kalia, R.K., Vashishta, P.: Phys. Rev. B **45**, 5535 (1992)
54. Lee, J.H., Char, K., Park, Y.W., Zhao, L.Z., Zhu, D.B., McIntosh, G.C., Kaiser, A.B.: Phys. Rev. B **61**, 14815 (2000)
55. Braden, M., Reichardt, W., Schmidbauer, W., Ivanov, A.S., Rumiantsev, A.Y.: Jour. Supercond. **8**, 595 (1995)

56. Pintschovius, L., Reichardt, W.: Physical properties of high temperature superconductors. In: Ginsberg, D.M. (eds.) vol. 4. World Scientific, Singapore (1994)
57. Orenstein, J., Millis, A.J.: Science **288**, 468 (2000)
58. Müller, K.A., Zhao, G., Conder, K., Keller, H.: Jour. Phys.: Condens. Matter **10**, L291 (1998)
59. Qvarford, M., Nazin, V.G., Zakharov, A.A., Mikheeva, M.N., Andersen, J.N., Johansson, M.K.-J., Chiaia, G., Rogelet, T., Soderholm, S., Tjernberg, O., Nylen, H., Lindau, I., Nyholm, R., Karlsson, U.O., Barilo, S.N., Shiryaev, S.V.: Phys. Rev. B **54**, 6700 (1996)
60. Anshukova, N.V., Golovashkin, A.I., Gorelik, V.S., Ivanova, L.I., Mitsen, K.V., Rusakov, A.P., Khashimov, R.N.: Jour. Molec. Struct. **219**, 147 (1990)
61. Salem-Sugui Jr., S., Alp, E.E., Mini, S.M., Ramanathan, M., Campuzano, J.C., Jennings, G., Faiz, M., Pei, S., Dabrowski, B., Zheng, Y., Richards, D.R., Hinks, D.G.: Phys. Rev. B **43**, 5511 (1991)
62. Stupp, S.E., Reeves, M.E., Ginsberg, D.M., Hinks, D.G., Dabrowski, B., Vandervoort, K.G.: Phys. Rev. B **40**, 10878 (1989)
63. Menushenkov, A.P., Kuznetsov, A.V., Klementev, K.V., Kagan, M.Yu.: JETP Lett. **93**, 615 (2001)
64. van der Marel, D., van Mechelen, J. L. M., Mazin, I. I.: Phys. Rev. B **84**, 205111 (2011)
65. Plakida, N.M., Aksenov, V.L., Drechsler, S.L.: Europhys. Lett. **4**, 1309 (1987)

Part III

Chapter 9
Superconductivity in the Low-Density Electron Systems with Repulsion

9.1 Kohn-Luttinger Mechanism of Superconductivity in Purely Repulsive Fermi-Systems

The modern physics of superconductivity (SC) is a very rapidly progressing field of condensed-matter physics where the colossal intellectual efforts of the researchers are concentrated and the new knowledge is accumulated very intensively giving rise to the development of neighboring areas of physics, chemistry, material science and engineering.

The latest progress in this area during last 25 years of experimental and theoretical research in connected with the physics of high-T_C superconductivity in cuprates and other related materials such as plumbates-bismithates, magnesium diborides, superconductors based on FeAs and so on.

One of the most essential and unresolved question in this area connected with the mechanism of superconducting pairing is: whether it is of electron–phonon origin as in standard BCS-like [5–7] superconductors such as Hg, Pb, Nb, Al, or is due to electron–electron interaction as in new unconventional superconductive systems such as ruthenates, organic superconductors, heavy-fermion compounds and so on.

In this chapter we will advocate non-phonon mechanism of superconductivity based on electron–electron interaction. Here according to Prof. Anderson [8] there are two basic questions:

1. to convert the sign of the Coulomb interaction
2. to understand the properties of the normal state in high-T_C materials and other unconventional SC-systems.

We agree with these statements. We will address them in Galitskii-Bloom [9, 33] Fermi-gas approach for low density electron systems. We will prove the existence of SC at low-density limit, in purely repulsive Fermi-systems where we are far from antiferromagnetic (AFM) and structural instabilities. Moreover in this limit we can develop a regular perturbation theory.

M. Yu. Kagan, *Modern Trends in Superconductivity and Superfluidity*,
Lecture Notes in Physics 874, DOI: 10.1007/978-94-007-6961-8_9,

The small parameter of the problem is the gas-parameter:

$$|a|p_F \ll 1;\ \hbar = 1, \tag{9.1.1}$$

where a—is the s-wave scattering length, p_F—is Fermi-momentum. Critical temperatures (T_C-s) which we obtain are not very low. Our theory often "works" even for rather high densities because of intrinsic nature of SC-instability. Our philosophy throughout this chapter is to solve exactly low-density limit and then go to higher densities. The basic mechanism which we address here is enhanced Kohn-Luttinger mechanism of SC [10]. We will also check the normal state of low-density electron systems with respect to marginality [13].

9.2 Unconventional Superconducting Systems

During last 30 years there is a huge progress in experimental and theoretical investigation of unconventional (anomalous) superconductive systems. Among the new materials with anomalous superconductive pairing there are examples of triplet p-wave ($S_{tot} = l = 1$) and singlet d-wave ($S_{tot} = 0$; $l = 2$) superconductors as well as multiband s-wave SC-systems ($S = l = 0$).

The p-wave SC with orbital momenta of the Cooper pair $l = 1$ and total spin of the pair $S_{tot} = 1$ is realized in:

- fermionic isotopes of alkali elements ^{6}Li and ^{40}K in magnetic traps in the regime of Feshbach resonance at ultralow temperatures $T_C \sim (10^{-6} \div 10^{-7})$ K [12, 15]
- superfluid A and B phases of ^{3}He at very low critical temperatures $T_C \sim 1$ mK [11, 14]
- heavy-fermion superconductors $U_{1-x}Th_xBe_{13}$, UNi_2Al_3, $T_C \sim (0.5 \div 1)$ K, heavy electron mass $m^* \sim (100 \div 200)m_e$ due to strong correlations [18, 19]
- ruthenates Sr_2RuO_4, $T_C \sim 1$ K (part of the community assumes d-wave pairing in these materials) [20, 21]
- multiband degenerate semiconductor $SrTiO_3$ $T_C \sim$ (0.7-1.2) K (see Ref. [64] in Chap. 8 (note that other mechanisms of SC connected for example with small polaron formation are also possible here)
- organic superconductor α-(BEDT-TTF)$_2I_3$, $T_C \sim 5$ K [16, 17].

Singlet d-wave pairing is realized in:

- heavy-fermion SC UPt_3, $T_C \sim 0.5$ K, large effective mass $m^* \sim 200\, m_e$ [18, 19]
- high-T_C superconductors [22, 25] $La_{2-x}Sr_xCuO_4$, $YBa_2Cu_3O_{7-\delta}$, $Bi_2Sr_2Ca_2Cu_3O_{10}$, $Tl_2Ba_2Ca_2Cu_3O_{10}$, $HgBa_2Ca_2Cu_3O_8$.

In all the families of high-T_C materials the elementary block CuO is present. They are called cuprates. T_C-s are in the range from 36 K for lanthanum-based family to 160 K for Hg-based family under pressure (the record established T_C in cuprates for today). Note that part of the community still assumes standard s-wave pairing in cuprates.

The highest T_C in unconventional SC corresponds to neutron stars which consist of 98 % of bineutrons and 2 % of biprotons. For bineutrons $S_{tot} = l = 1$, but there is a strong spin–orbit coupling. So the total rotating moment $J = \left|\vec{S}_{tot} + \vec{l}\right| = 2$. According to theoretical predictions $T_C \sim (10^8 \div 10^{10})$ K for neutron stars.

Finally in the end of this section we would like to mention several unconventional SC systems of the multiband character with s-wave pairing [97], namely MgB_2 [26] (very promising for technical applications in electronics and energetics), and recently discovered family on the basis of FeAs such as $BaFe_2(As_{1-x}P_x)_2$ (with the coexistence of ferromagnetic fluctuations and SC) [95], [96]. Note that part of the experimental community still hopes to demonstrate p-wave or d-wave SC in FeAs-based compounds [95, 96].

9.3 3D and 2D Fermi-Gas with Repulsion. Triplet p-Wave Pairing

The basic model to study non-phonon mechanism of SC in low density electron systems is a Fermi-gas model. In Fermi-gas with attraction s-wave scattering length $a < 0$ and we have unconventional s-wave pairing ($S = l = 0$) with a critical temperature:

$$T_{CO} \approx 0.28\, \varepsilon_F\, e^{-\frac{\pi}{2|a|p_F}}. \tag{9.3.1}$$

This result was obtained by Gor'kov and Melik-Barkhudarov [27] soon after the appearance of a famous BCS-theory [6, 7] and differs from the BCS-result in preexponential factor $0.28\varepsilon_F$ (instead of Debye-frequency ω_D in the phonon models typical for conventional SC systems).

9.3.1 3D Fermi-Gas with Repulsion

In Fermi-gas with repulsion $a > 0$—repulsive interaction of two particles in vacuum. We will show that for the effective interaction of two particles in substance (via polarization of a fermionic background) we can convert the sign of the interaction in the triplet p-wave channel (for $S_{tot} = l = 1$) and get:

$$T_{C1} \sim \varepsilon_F e^{-\frac{1}{(ap_F)^2}}, \tag{9.3.2}$$

where $\varepsilon_F = p_F{}^2/2m$ is Fermi-energy. This highly nontrivial result was obtained by Fay and Laser [28] and Kagan and Chubukov [29]. The most important is to understand what is effective interaction U_{eff}? We will show that in momentum space in first two orders of the gas-parameter (9.1.1):

$$U_{eff}(\vec{p},\vec{k}) = \frac{4\pi a}{m} + \left(\frac{4}{m}\right)^2 \Pi(\vec{p}+\vec{k}), \tag{9.3.3}$$

where $\Pi(\vec{p}+\vec{k})$ is a static polarization operator. It is given by a standard formula [31, 35]:

$$\Pi(q) = \int \frac{d^3\vec{p}}{(2\pi)^3} \frac{n_F(\varepsilon_{p+q-}\mu) - n_F(\varepsilon_p - \mu)}{(\varepsilon_p - \varepsilon_{p+q})}, \tag{9.3.4}$$

where $\varepsilon_p = \frac{p^2}{2m}$; $\varepsilon_{p+q} = \frac{(\vec{p}+\vec{q})^2}{2m}$ are the energy spectra and $n_F(\varepsilon_p - \mu) = \frac{1}{e^{\frac{\varepsilon_p - \mu}{T}}+1}$, $n_F(\varepsilon_{p+q} - \mu)$ are Fermi–Dirac distribution functions. At low temperatures $T \ll \varepsilon_F$ polarization operator besides a regular part contains a Kohn's anomaly [32] of the form:

$$\Pi_{\text{sing}}(q) \sim (q - 2p_F)\ln|q - 2p_F| \text{ in 3D}. \tag{9.3.5}$$

In real space Kohn's anomaly leads to Friedel oscillations (RKKY interaction [34]). For dimensionless product of U_{eff} and 3D density of states:

$$N_{3D}(0) = \frac{mp_F}{2\pi^2} \tag{9.3.6}$$

we have in real space (see Fig. 9.1):

$$N_{3D}(0)\, U_{eff}(r) \sim (ap_F)^2 \frac{\cos(2p_F r)}{(2p_F r)^3}. \tag{9.3.7}$$

Thus we start from pure hard-core repulsion in vacuum and get the competition between repulsion and attraction in substance.

It is possible to show [28, 29] that a singular part of U_{eff} "plays" in favor of attraction for large orbital momenta $l \gg 1$, while a regular part of U_{eff}—in favor of repulsion. Standard s-wave pairing is suppressed by hard-core repulsion. However, as it was shown in [28, 29] the Kohn-Luttinger effect can be extended from the large momenta $l \gg 1$ to $l = 1$ and the attractive contribution is dominant even for p-wave channel. The exact solution [28, 29] yields for the critical temperature:

$$T_{C1} \sim \varepsilon_F e^{-\frac{5\pi^2}{4(2\ln 2 - 1)(ap_F)^2}} \tag{9.3.8}$$

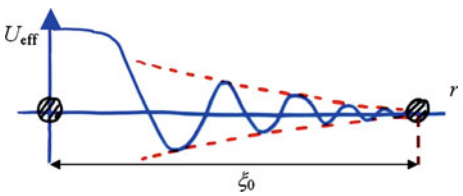

Fig. 9.1 Friedel oscillations in the effective interaction of two particles via polarization of a fermionic background. ξ_0 is a coherence length of a Cooper pair

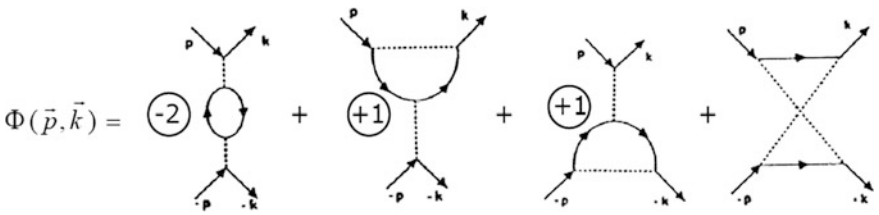

Fig. 9.2 Four diagrams of Kohn-Luttinger [10] which give the contribution to the irreducible bare vertex for the Cooper channel

9.3.2 Triplet p-Wave Pairing

Note that diagrammatically effective interaction U_{eff} corresponds to the irreducible bare vertex and is given by the set of diagrams which cannot be separated by two lines running in the same direction [30, 31] (thus U_{eff} does not contain the Cooper loop). Correspondingly the formula (9.3.3) can be represented as:

$$U_{eff}(\vec{p},\vec{k}) = \frac{4\pi a}{m} + \left(\frac{4\pi a}{m}\right)^2 \Phi(\vec{p},\vec{k}), \tag{9.3.9}$$

where $\Phi(\vec{p},\vec{k})$ is given by 4 diagrams of Kohn-Luttinger [10] (see Fig. 9.2).

First three diagrams cancel each other exactly for contact interaction after spin summation and as a result in accordance with (9.3.3):

$$\Phi(\vec{p},\vec{k}) = \Pi(\vec{p}+\vec{k}) \tag{9.3.10}$$

is given by the fourth diagram on Fig. 9.2. Algebraically $\Pi(\vec{p}+\vec{k})$ is a static polarization operator (9.3.4) in a "crossed" channel (for $\tilde{q} = |\vec{p}+\vec{k}|$ instead of $q = |\vec{p}-\vec{k}|$). For incoming and outgoing momenta $\vec{p}$ and are $\vec{k}$ lying on the Fermi-surface $|\vec{p}| = |\vec{k}| = p_F$ the "crossed" momentum:

$$\tilde{q}^2 = 2p_F^2(1+\cos\theta), \tag{9.3.11}$$

where an angle $\theta = \angle\vec{p}\vec{k}$.

The polarization operator $\Pi(\tilde{q})$ is given by static Lindhard function [35]:

$$\Pi(\tilde{q}) = \frac{N_{3D}(0)}{2}\left[1 + \frac{4p_F^2 - \tilde{q}^2}{4p_F\tilde{q}}\ \ln\frac{2p_F+\tilde{q}}{|2p_F-\tilde{q}|}\right]. \tag{9.3.12}$$

Integration of $\Pi(\tilde{q})$with first Legendre polynomial $P_1(\cos\theta) = \cos\theta$ yields the desired result for p-wave harmonic [28, 29]:

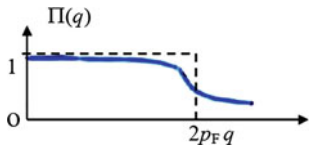

Fig. 9.3 Behavior of static polarization operator $\Pi(q)$ as a function of q with the decrease for $0 < q \leq 2\,p_F$ [38, 45]

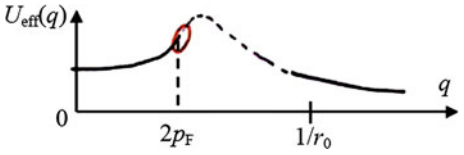

Fig. 9.4 Behavior of effective interaction U_{eff} as a function of q

$$\Pi_1 = \int_{-1}^{1} P_1(\cos\theta)\frac{d\cos\theta}{2}\Pi(\tilde{q}(\cos\theta)) = \frac{N_{3D}(0)}{5}(1 - 2\ln 2) < 0. \qquad (9.3.13)$$

The p-wave critical temperature reads:

$$T_{C1} \sim \frac{2e^C\varepsilon_F}{\pi}e^{-\frac{13}{\lambda^2}}, \qquad (9.3.14)$$

where $\lambda = 2ap_F/\pi$ is effective gas-parameter of Galitskii in 3D [9], C is Euler constant.

9.3.3 Model-Independent Considerations by P. Nozieres

The model-independent proof of the possibility of the p-wave pairing in Fermi-systems with repulsion belongs to Professor P. Nozieres [37]. His way of reasoning is the following: usually for static effective interaction in fermionic substance we have [36, 38]:

$$U_{eff}(q) = \frac{U_0(q)}{\varepsilon(q)}, \qquad (9.3.15)$$

where $\varepsilon(q) = 1 + U(q)\Pi(q)$ is static dielectric function and $\Pi(q)$ is polarization operator given by (9.3.4). It is known from solid-state physics [31, 36] that $\Pi(q)$ is decreasing function of q which behaves as follows (see Fig. 9.3).

That is why effective interaction U_{eff} in (9.3.15) decreases in the interval $0 \leq q \leq 2\,p_F$ which is important for superconductivity (see Fig. 9.4).

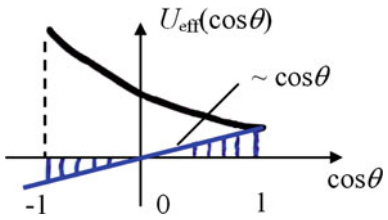

Fig. 9.5 Behavior of $U_{\text{eff}}(\cos\theta)$ and $\cos\theta$ as functions of $\cos\theta$ on the relevant interval $[-1, 1]$

Note that $U_{\text{eff}}(q)$ should strongly decrease for $q > 1/r_0$, where r_0 is the range of the potential. But in the Fermi-gas $1/r_0 \gg 2p_{\text{F}}$ according to (9.3.1) and hence an interval $[0, 2p_{\text{F}}]$ where $U_{\text{eff}}(q)$ increases is an intermediate asymptotics (see Fig. 9.4).

Finally for first Legendre polynomial (which corresponds to p-wave pairing) we have:

$$q^2 = 2p_F^2(1 - \cos\theta), \tag{9.3.16}$$

and accordingly

$$P_1(\cos\theta) = \cos\theta = 1 - \frac{q^2}{2p_F^2}. \tag{9.3.17}$$

Moreover, $\cos\theta = 1$ for $q = 0$ and -1 for $q = 2\,p_{\text{F}}$. Thus, $U_{\text{eff}}(\cos\theta)$ and $\cos\theta$ behave as follows (see Fig. 9.5) as functions of $\cos\theta$.

As a result the p-wave harmonic of U_{eff}:

$$U_{eff}^{l=1} = \int_{-1}^{1} U_{eff}(\cos\theta)\cos\theta\frac{d\cos\theta}{2} < 0, \tag{9.3.18}$$

if $U_{\text{eff}}(\cos\theta)$ for $\cos\theta \in [-1, 0]$ is larger than $U_{\text{eff}}(\cos\theta)$ for $\cos\theta \in [0, 1]$ as in Fig. 9.5. Hence for all effective potentials increasing for q changing from 0 to $2p_{\text{F}}$ we have p-wave SC in the isotropic case and the Kohn's anomaly does not play a decisive role here (in contrast with the case of SC pairing with large orbital momenta $l \gg 1$). Note that in 3D Fermi-gas model $U_{\text{eff}}(\cos\theta)$ is given by (9.3.3) and decreases on the interval $[-1, 1]$ due to crossing $q \to \tilde{q}$ [see (9.3.9)].

9.3.4 Two-Dimensional Case

In 2D Fermi-gas with repulsion dimensionless effective interaction in momentum space reads:

$$N_{2D}(0)U_{eff}(\tilde{q}) = f_0 + f_0^2\Pi(\tilde{q})\frac{4\pi}{m}, \tag{9.3.19}$$

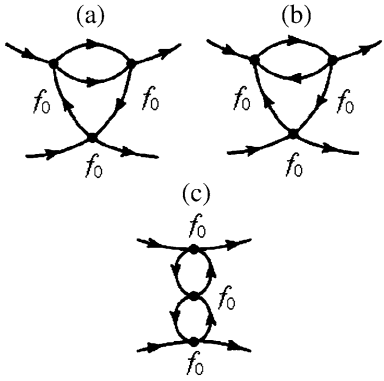

Fig. 9.6 Third order diagrams which contribute to effective interaction and SC in 2D Fermi-gas according to [39–41, 91]. First diagram (a) on this figure was originally evaluated in [39] by Chubukov

where $N_{2D}(0) = \frac{m}{2\pi}$ is 2D density of states,

$$f_0 = \frac{1}{2\ln(1/p_F r_0)} \tag{9.3.20}$$

is 2D gas-parameter of Bloom [33]. Correspondingly in real space effective interaction

$$N_{2D}(0)\, U_{eff}(r) \sim f_0^2 \frac{\cos(2p_F r)}{(2p_F r)^2} \tag{9.3.21}$$

contains much more stronger 2D Friedel oscillations [34].

However, the 2D Kohn's anomaly [32] in polarization operator $\Pi(q)$ has one-sided character

$$N_{2D}(0)\, U_{\text{eff}}(\tilde{q}) \sim f_0^2 \text{Re}\sqrt{\tilde{q} - 2p_F} = 0 \tag{9.3.22}$$

for the important interval for SC $0 \le \tilde{q} \le 2p_F$. Hence strong 2D Kohn's anomaly is ineffective for SC in second order of perturbation theory with respect to gas-parameter f_0 (9.3.20). As it was shown by Chubukov [39] SC appears only in the third order of perturbation theory where the Kohn's anomaly changes its character (see first diagram on Fig. 9.6) and reads:

$$N_{2D}(0)\, U_{\text{eff}}(\tilde{q}) \sim f_0^3 \text{Re}\sqrt{2p_F - \tilde{q}} \neq 0. \tag{9.3.23}$$

Accordingly critical temperature of the p-wave pairing reads in [39]:

$$T_{C1} \sim \varepsilon_F \exp\left\{-\frac{1}{4.1 f_0^3}\right\} \tag{9.3.24}$$

Note that the first third order diagram on Fig. 9.6 considered in [39] is still irreducible with respect to Cooper channel.

Later on the authors of [40] and [41] considered all irreducible skeleton diagrams of the third order in f_0 on Fig. 9.6 on equal grounds and obtained—6.1 f_0^3 (instead of—4.1 f_0^3) in the exponent of (9.3.24) for p-wave pairing critical temperature in 2D Fermi-gas.

9.4 Superconductivity in 3D and 2D Hubbard Model with Repulsion at Low Electron Density

One of the basic models to describe unconventional normal and superconductive states of strongly correlated electron systems is a famous Hubbard model originally introduced by Hubbard [1–4] for the explanation of metal–insulator transition in half-filled narrow band metals. In real space the Hamiltonian of the Hubbard model reads:

$$\hat{H}' = \hat{H} - \mu\hat{N} = -t \sum_{<ij>\sigma} c_{i\sigma}^{+} c_{j\sigma} + U \sum_{i} n_{i\uparrow} n_{i\downarrow} - \mu \sum_{i} n_{i\sigma}, \tag{9.4.1}$$

where $n_{i\sigma} = c_{i\sigma}^{+} c_{i\sigma}$ is electron density with spin-projection $\sigma = |\uparrow\downarrow>$ on site i, t—is hopping integral, U is on site Hubbard repulsion between two electrons with opposite spin-projections, μ is chemical potential.

9.4.1 3D Hubbard Model at Low Density

After Fourier transformation the Hamiltonian (9.4.1) reads:

$$\hat{H}' = \sum_{\vec{p}\sigma} [\varepsilon(p) - \mu] c_{p\sigma}^{+} c_{p\sigma} + U \sum_{\vec{p}\vec{p}'\vec{q}} c_{\vec{p}\uparrow}^{+} c_{\vec{p}'+\vec{q}\downarrow}^{+} c_{\vec{p}+\vec{q}\downarrow} c_{\vec{p}'\uparrow}, \tag{9.4.2}$$

where $\varepsilon(p) = -2t\left(\cos p_x d + \cos p_y d + \cos p_z d\right)$ is uncorrelated electron spectrum on 3D simple cubic lattice, d is intersite distance [1–4, 41–45, 47]. For small electron densities $nd^3 < 1$ (where $n = {p_F}^3/3\pi^2$ is electron density in 3D) the spectrum reads:

$$\varepsilon(p) \approx -\frac{W}{2} + tp^2 d^2, \tag{9.4.3}$$

where $W = 12t$ is a bandwidth in 3D for the simple cubic lattice. If we introduce the uncorrelated band mass according to [44, 45, 47]:

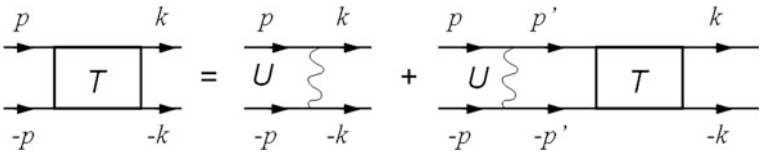

Fig. 9.7 Lippmann-Schwinger equation (Bethe–Salpeter equation in vacuum) for the T-matrix [29, 47] in Kanamori renormalization scheme for Hubbard interaction [1–4]

$$m = \frac{1}{2td^2}, \tag{9.4.4}$$

then for the spectrum we have:

$$\varepsilon(p) = -\frac{W}{2} + \frac{p^2}{2m}. \tag{9.4.5}$$

Correspondingly for the chemical potential at low densities:

$$\mu = -\frac{W}{2} + \varepsilon_F. \tag{9.4.6}$$

Thus according to [1–4, 43, 44] the 3D Hubbard model at low electron densities becomes equivalent to 3D Fermi-gas with δ-functional (hard-core) repulsive interaction between particles. The s-wave scattering length a in the renormalization scheme of Kanamori for Hubbard interaction [45, 46] reads:

$$\frac{4\pi a}{m} = T = \frac{Ud^3}{1 - Ud^3 K_{vac}(0,\,0)}, \tag{9.4.7}$$

where T—is a T-matrix, $K_{vac}(0,0) = -\int \frac{d^3\vec{p}}{(2\pi)^3}\frac{m}{p^2}$—is a Cooper loop for two particles in vacuum for total frequency $\Omega = 0$ and total momentum of two particles $\vec{P} = \vec{p}_1 + \vec{p}_2 = 0$.

Diagrammatically K_{vac} is a product of two vacuum Green-functions, while Lippmann-Schwinger equation [47, 48] for the T-matrix is illustrated on Fig. 9.7.

In the strong-coupling limit $U \gg W$ of the Hubbard model and at low density we have according to [45] (see also [49]):

$$a \sim d, \tag{9.4.8}$$

and thus an effective gas-parameter for the Hubbard model reads[43–45]:

$$\lambda = \frac{2ap_F}{\pi} \approx \frac{2dp_F}{\pi}. \tag{9.4.9}$$

Correspondingly, in analogy with 3D Fermi-gas model, the Hubbard model at low electron density is unstable towards triplet p-wave pairing below the critical temperature [43, 44]

$$T_{C1} \sim \varepsilon_F \exp\left\{-\frac{13}{\lambda^2}\right\}, \tag{9.4.10}$$

where λ is given by (9.4.9). Note that in the absence of the lattice for strong short-range interaction $a \sim r_0$, where r_0 is the range of the potential.

9.4.2 2D Hubbard Model

The uncorrelated electron spectrum for 2D square lattice reads:

$$\varepsilon(p) = -2t\left(\cos p_x d + \cos p_y d\right). \tag{9.4.11}$$

Correspondingly, for low electron density $nd^2 \ll 1$ (where $n = {p_F}^2/2\pi$ is 2D electron density) the spectrum yields again [see (9.4.4) and (9.4.5)]:

$$\varepsilon(p) \approx -\frac{W}{2} + \frac{p^2}{2m}, \tag{9.4.12}$$

where the band mass is still $m = \frac{1}{2td^2}$, but now $W = 8t$ is a bandwidth for 2D square lattice. Correspondingly, the chemical potential $\mu \approx -\frac{W}{2} + \varepsilon_F$ is given again by (9.4.6).

It is convenient to introduce dimensionless 2D density of electrons:

$$n_{el} = \frac{2\varepsilon_F}{W} \tag{9.4.13}$$

which measures the filling of the band in terms of the half-filled band ($n_{\mathrm{el}} = 1$ for $\varepsilon_F = \frac{W}{2}$ in the half-filled case actual for high-T_C superconductors).

The gas-parameter of 2D Hubbard model at the strong-coupling limit $U \gg W$ and low density was derived in [50] and reads:

$$f_0 = \frac{1}{\ln(4W/\varepsilon_F)} = \frac{1}{\ln(8/n_{el})}. \tag{9.4.14}$$

Correspondingly, in similarity with 2D Fermi-gas model the normal state of 2D Hubbard model at low density is unstable towards triplet p-wave pairing below the critical temperature [39–41, 44].

$$T_{C1} \sim \varepsilon_F \exp\left\{-\frac{1}{6.1 f_0^3}\right\} \tag{9.4.15}$$

with gas-parameter f_0 given by Eq. (9.4.14).

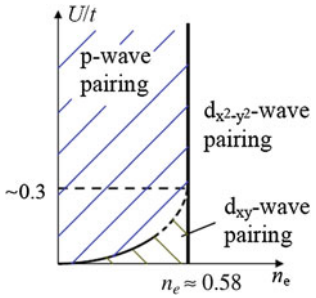

Fig. 9.8 Qualitative phase-diagram for SC- pairing in the 2D Hubbard model at low and moderate electron densities [45]

9.4.3 Qualitative Phase-Diagram at Low Density in 2D

It is interesting to construct qualitative phase-diagram for different SC-instabilities in the 2D Hubbard model at low electron densities. This project was realized in [43–45, 51, 54–57, 101, 102]. To do that it is important to note (see [44, 47, 101, 102]) that p-wave pairing with critical temperature given by (9.4.15) is the most energetically beneficial (it corresponds to the highest T_C) for $U \gg t$ and dimensionless electron density $0 < n_{el} = \frac{2\varepsilon_F}{W} \lesssim 0.58$. In the same time in the weak-coupling case $U \leq 0.3\ t$ and $0 < n_{el} \lesssim 0.52$ the highest T_C corresponds to d_{xy}-pairing according to [51, 57, 101, 102]. For d_{xy}-pairing it is important to take into account the higher order quadratic corrections to parabolic spectrum:

$$\varepsilon(p) - \mu = -2t\big(\cos p_x d + \cos p_y d\big) - \mu = \frac{p^2 - p_F^2}{2m} - \frac{(p_x^4 + p_y^4)d^2}{24m} + \frac{(p_x^6 + p_y^6)d^4}{720m} \tag{9.4.16}$$

The critical temperature of d_{xy}-pairing is given by (see [51]):

$$T_C^{d_{xy}} \sim \varepsilon_F \exp\left\{-\frac{16}{f_0^2 n_{el}^2}\right\} \tag{9.4.17}$$

We should also remember that the superconductive gap for d_{xy}-pairing is given by [51]:

$$\Delta_{d_{xy}} \sim \Delta_0^d \sin(p_x d)\sin(p_y d) \sim \Delta_0^d p_x p_y d^2 \sim \Delta_0^d \sin 2\varphi \tag{9.4.18}$$

for low electron density, where φ is the angle between momentum $\vec{p}$ and x-axis of the square lattice. In the same time more traditional $d_{x^2-y^2}$-pairing actual for optimally doped high-T_C materials [52] correspond to the gap [52, 53]:

$$\Delta_{d_{x^2-y^2}} \sim \Delta_0^d(\cos p_x d - \cos p_y d) \sim \Delta_0^d(p_x^2 - p_y^2)d^2 \sim \Delta_0^d \cos 2\varphi.]] > \tag{9.4.19}$$

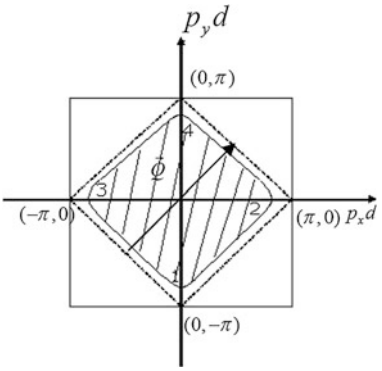

Fig. 9.9 Almost half-filled situation ($n_{el} \to 1$) for the 2D Hubbard model on the *square lattice*. At the corner points (0, π); (0, $-\pi$) and (π, 0); ($-\pi$, 0) the Fermi-surface almost touches the Brillouin zone. We also show the nesting-vector $\vec{Q} = \left(\frac{\pi}{d}, \frac{\pi}{d}\right)$on the figure

In contrast to p-wave pairing it is described by the second-order (in the gas-parameter f_0) contribution to the effective interaction U_{eff}. This result [51] for d_{xy}-pairing was confirmed later on by Zanchi and Schulz [57] in the framework of renormalization group (RG) approach. We can also mention in this respect the papers of Hlubina et al. in which the authors get d_{xy}-pairing in weak-coupling case for $n_{el} \leq 0.62$ [54–56]. Finally for larger electron densities $n_{el} \gtrsim 0.6$ both in weak-coupling ($U \ll W$) and strong-coupling case $d_{x^2-y^2}$-pairing (which is more conventional for optimally doped high-T_C materials) is realized [58–64]. As a result the qualitative phase-diagram of the repulsive-U Hubbard model at low and moderate electron densities in 2D case looks like as follows (see Fig. 9.8).

9.4.4 Superconductivity in 2D Hubbard Model at Larger Electron Densities $n_{el} \leq 1$

At larger densities $n_{el} \leq 1$ close to half-filling $\left(\varepsilon_F \approx \frac{W}{2}\right)$ the spectrum of electrons becomes almost hyperbolic [60, 61]:

$$\varepsilon(p) = \pm \frac{(p_x^2 - p_y^2)}{2m} \tag{9.4.20}$$

close to the corner points where the Fermi-surface almost touches the Brillouin zone (0, π); (0, $-\pi$) and (π, 0); ($-\pi$, 0) (see Fig. 9.9).

There are here the extended almost flat parts of the Fermi-surface which satisfy the perfect nesting criteria for exactly half-filled case ($n_{el} = 1$).

$$\varepsilon(\vec{P} + \vec{Q}) = -\varepsilon(\vec{P}), \tag{9.4.21}$$

where $\vec{Q} = (\pi/d, \pi/d)$ is a nesting-vector for the 2D square lattice.

As a result the Kohn's anomaly becomes logarithmically strong here as in 1D-case (see [32, 60, 61,]). Additional increase for T_C is due to Van-Howe singularity

in the density of states $N_{2D}(0)$ which is also logarithmically strong [36, 61]. As a result both polarization operator $\Pi(q)$ in (9.3.4) and the Cooper loop (in substance) $K(0,0) = -\int \frac{1-2n_F(\varepsilon_p)}{2(\varepsilon_p-\mu)} \frac{d^2\vec{p}}{(2\pi)^2}$ contains $\ln^2$-contribution. Thus, in the weak-coupling case for the coupling constant

$$f_0 = \frac{U}{8\pi\, t} \ll 1 \tag{9.4.22}$$

and in the second order of perturbation theory (in f_0) for the effective interaction we have:

$$U_{\text{eff}} \sim f_0 + f_0^2 \ln^2 \frac{\mu}{t}, \tag{9.4.23}$$

where $\mu \ll t$ is a chemical potential close to half-filling and we still assume that $\mu > T_C{}^{d}$. Note that in the expansion (9.4.23) an effective parameter of the perturbation theory is [60, 61]:

$$f_0 \ln^2 \frac{\mu}{t}. \tag{9.4.24}$$

Correspondingly as it was shown by Kozlov [60] the equation for the $d_{x^2-y^2}$-wave critical temperature $T_C{}^{d}$ reads for almost half-filled case:

$$f_0^2 \ln^3 \frac{t}{\mu} \ln^2 \frac{\mu}{T_C^d} \sim 1, \tag{9.4.25}$$

or equivalently

$$T_C^d \sim \mu \exp\left\{ -\frac{1}{f_0^2 \ln^3 (\frac{t}{\mu})} \right\}. \tag{9.4.26}$$

Thus we see that small coupling constant $f_0 \ll 1$ (9.4.22) is enhanced by large value of $\ln^3(\frac{t}{\mu}) \gg 1$ in (9.4.26)—nice result of Kozlov. For the sake of completeness let us mention here other important articles where $d_{x^2-y^2}$-wave pairing with rather high T_C was obtained by a variety of computational approaches for 2D Hubbard model at optimal doping $n_{el} \sim (0.8 \div 0.9)$ [65–73].

9.4.5 *Parquet Solution at Weak-Coupling and Close to Half-Filling*

Very close to half-filling when $\mu \sim T_C$ we have so-called doubly logarithmic parquet solution of Dzyaloshinskii, Yakovenko [61] with the competition between SC and SDW-instability in particle–particle (SC) and particle-hole (SDW—spin density wave) channels. Here for $\mu \sim T_C$ from (9.4.26) we get:

$$f_0^2 \ln^4 \frac{t}{\mu} \sim f_0^2 \ln^4 \frac{t}{T_C^d} \sim 1. \tag{9.4.27}$$

Hence for the $d_{x^2-y^2}$-wave critical temperature:

$$T_C^d \sim t \exp\left\{-\frac{const}{\sqrt{f_0}}\right\} \tag{9.4.28}$$

an elegant result of [61]. We should mention here also the results of [72–76]. The maximal critical temperature in the 2D Hubbard model according to qualitative considerations of Kivelson et al. [77–79] corresponds to intermediate coupling case $U/W \sim 1$ and optimal concentrations $n_{el} \sim (0.8 \div 0.9)$. T_C here can reach the desired values of 10^2 K realistic for optimally doped cuprates [79, 80, 101, 102].

The border between AFM (or SDW) phase and superconductive phase of the high-T_C superconductor (described by 2D Hubbard model) in weak-coupling case $U \ll W$ and very close to half-filling (for doping concentrations $x = (1 - n_{el}) \ll 1$) according to Kivelson [78] at the temperature $T \to 0$ is given by:

$$x_C = (1 - n_{el}) \sim \exp\left\{-2\pi\sqrt{\frac{t}{U}}\right\}, \tag{9.4.29}$$

and we have the same expression for $\frac{1}{\sqrt{f_0}} \sim \sqrt{\frac{t}{U}}$ in the exponent of (9.4.29) for x_C.

Another interesting observation belongs to Kopaev and Belyavsky [82, 83] namely that the spectrum (9.4.11) on the square lattice at half-filling satisfies also "mirror nesting" property:

$$\varepsilon(P) = -\varepsilon(-P + Q) \tag{9.4.30}$$

This property is in favor of Cooper pairing with large total moment of a pair $\vec{Q}$ in a clean case (no impurities).

9.5 Superconductive Transitions in the Jelly Model for Coulomb Electron Plasma

Very recently in connection with the high-T_C physics Alexandrov and Kabanov [81] raised the very important question of the role of full Coulomb interaction (which is not reduced to onsite Hubbard repulsion but is extended over several coordinate spheres) for non-phonon mechanisms of superconductivity. They claimed that in the 3D jelly model for reasonable electron densities $r_S \leq 20$, where

$$r_S = \frac{1.92}{p_F a_B} \tag{9.5.1}$$

is correlative radius and $a_B = \frac{1}{me^2}$ ($\hbar = 1$) is Bohr radius for electron, the superconductive critical temperatures correspond to the pairing with large orbital momenta ($l \gg 1$) and are very low.

Indeed both the perturbative analysis of Chubukov and Kagan [84] (see also [44]) as well as numerical calculations of Alexandrov and Kabanov [81] provide small critical temperatures in 3D dense electron plasma.

9.5.1 Cascade of Superconductive-Transitions in the Dense Electron Plasma

To be more specific the authors of [44, 84] predicted a cascade of SC-transitions with orbital moment of the Cooper pair l being dependent upon electron density r_S:

$$l > l_C = \frac{|\ln r_S|}{\sqrt{r_S}} \left(1 + \frac{7}{2} \frac{\ln |\ln r_S|}{|\ln r_S|} + \cdots\right). \tag{9.5.2}$$

The critical temperature of the superconductive transition:

$$T_{C_1} \sim \varepsilon_F \exp\left\{-\frac{1}{\lambda_e}\right\}, \tag{9.5.3}$$

where the coupling constant $\lambda_e \sim \left(\frac{4\pi e^2}{\kappa^2} N_{3D}(0)\right)^2 \frac{1}{l^4}$ and $\kappa^2 = \frac{6\pi n e^2}{\varepsilon_F}$ is Thomas-Fermi wave-vector squared [44, 84]. (Thus $\frac{4\pi e^2}{\kappa^2} N_{3D}(0) \sim \frac{1}{2}$ and $\lambda_e \sim \frac{1}{4l^4}$). Note that T_{C_1} corresponds for given density r_S to $l = l_C(r_S)$ from (9.5.2) and is very low. The authors of [81] get qualitatively the same result numerically with maximal but still very low T_C corresponding to f-wave pairing ($l = 3$) for $0 < r_S \leq 18$. We can honestly say that the 3D jelly model is not very promising for superconductivity with reasonable high-T_C in case of dense Coulomb plasma.

9.5.2 The Dilute Electron Plasma

The possibility of the p-wave SC with critical temperatures T_{C1} in the range $\sim(10^{-3} \div 10^{-2})$ K for 3D electron plasma of intermediate and small electron densities ($r_S \gg 1$) (which are relevant for simple and noble metals like Na, K, Ag, Au or for semimetals) was predicted in the papers [84–86]. Here $T_{C1} \sim \varepsilon_F \exp\{-1/|\lambda_1|\}$, where $|\lambda_1| = 0.07$ in [84] and $|\lambda_1| = 0.06$ in [86].

The most realistic region of densities for p-wave pairing in 3D dilute plasma is possibly $20 \leq r_S \leq 35$ according to [84, 86]. In the same time some groups [87, 88] believe more in Khodel-Shaginyan [88] type of Fermi-surface reconstruction (and not in a SC-transition) at these densities or more close to Wigner crystallization instability [36]. It is a very difficult question in particular in 2D where

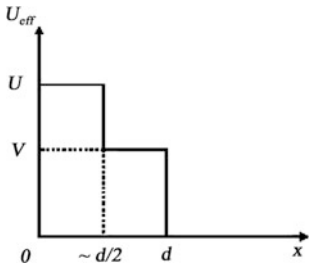

Fig. 9.10 Effective vacuum interaction in Shubin-Vonsovsky model in the strong-coupling case (9.6.3) (see [91])

rigorously speaking we should sum up an infinite parquet class of diagrams for the effective interaction (irreducible bare vertex) U_{eff} in the Cooper channel.

9.6 Superconductivity and Phase Separation in Shubin-Vonsovsky Model

The situation for superconductivity with reasonable T_C becomes much more favorable on the lattice if we consider so-called Shubin-Vonsovsky model [89, 90] with onsite Hubbard repulsion U and additional Coulomb repulsion V on the neighboring sites [90]. In real space the Hamiltonian of the Shubin-Vonsovsky model reads:

$$\hat{H}' = \hat{H} - \mu\hat{N} = -t \sum_{<ij>\sigma} c_{i\sigma}^{+} c_{j\sigma} + U \sum_{i} n_{i\uparrow} n_{i\downarrow} + \frac{V}{2} \sum_{<ij>} n_i n_j - \mu \sum_{i\sigma} n_{i\sigma}, \tag{9.6.1}$$

where $n_i = \sum_{\sigma} n_{i\sigma}$—total density on site i (for both $\uparrow$ and $\downarrow$ projection of electron spin. It is reasonable to assume (see [91]) that in (9.6.1) we have the following estimates for the parameters of the model:

$$U \sim \frac{e^2}{\varepsilon a_B}; \quad V \sim \frac{e^2}{\varepsilon d}; \quad W \sim \frac{1}{md^2}, \tag{9.6.2}$$

where W is a bandwidth, ε is the effective dielectric permittivity and $a_B \sim \frac{\varepsilon}{me^2}$ ($\hbar = 1$) is Bohr radius in ionic media. Thus, for $\varepsilon \sim 1$, $a_B \sim 0.5$ Å and $d \sim (3 \div 4)$ Å and in the limit $a_B/d \ll 1$ we come to the following hierarchy of parameters [91]:

$$U \gg V \gg W. \tag{9.6.3}$$

The effective vacuum interaction in Shubin-Vonsovsky model in real space behaves as follows (see Fig. 9.10) in the strong-coupling case (9.6.3).

9.6.1 p-Wave Superconductivity in Shubin-Vonsovsky Model at Low Density

Note that Shubin-Vonsovsky model [89, 90] is the most repulsive and the most unbeneficial model for SC. In the same time it is useful toy-model to study the effects of intersite Coulomb repulsion on SC and Mott–Hubbard metal-dielectric transition [89–92] as well as the physics of the nanoscale phase separation [93, 94].

After Fourier transformation the Hamiltonian of the Shubin-Vonsovsky model reads:

$$\hat{H}' = \sum_{\vec{p}\sigma} \left[\varepsilon(\vec{p}) - \mu\right] c^{+}_{\vec{p}\sigma} c_{\vec{p}\sigma} + U \sum_{\vec{p}\vec{p}'\vec{q}} c^{+}_{\vec{p}\uparrow} c^{+}_{\vec{p}'+\vec{q}\downarrow} c_{\vec{p}+\vec{q}\downarrow} c_{\vec{p}'\uparrow} + \sum_{\substack{\vec{p}\vec{p}'\vec{q} \\ \sigma\sigma'}} V(\vec{p},\vec{p}') c^{+}_{\vec{p}\sigma} c^{+}_{\vec{p}'+\vec{q}\sigma'} c_{\vec{p}+\vec{q}\sigma'} c_{\vec{p}'\sigma}, \tag{9.6.4}$$

where in 3D case:

$$V(\vec{p},\vec{p}') = V\Big(\cos(p_x - p'_x)d + \cos(p_y - p'_y)d + \cos(p_z - p'_z)d\Big). \tag{9.6.5}$$

At the low density $pd \ll 1$ the expansion up to quadratic terms gives effective vacuum interaction in 3D for s-wave and p-wave harmonics respectively:

$$U^{S}_{eff\ vac} = U + 6V + o(p^2 d^2), \tag{9.6.6}$$

and

$$U^{P}_{eff\ vac} = 2V\vec{p}\vec{p}'d^2 \tag{9.6.7}$$

The renormalization of the effective vacuum interaction in the framework of Kanamori T-matrix approximation [46] yields for s-wave and p-wave scattering lengths [91] in the strong-coupling $U \gg V \gg W$ and low density $nd^3 < 1$ case:

$$a_S \sim d, \tag{9.6.8}$$

and

$$a_P \sim d, \tag{9.6.9}$$

where $T_S = \frac{4\pi a_S}{m}$ and $T_P = \frac{4\pi}{m} 2a_P(\vec{p}\vec{p}')d^2$ are T-matrices in s-wave and p-wave channels.

Thus the dimensionless s-wave gas-parameter $\lambda_S = \lambda = 2dp_F/\pi$ as in the repulsive-U Hubbard model [see (9.9.4)], while the dimensionless p-wave gas-parameter:

$$\lambda_p \sim (p_F d)^3 \tag{9.6.10}$$

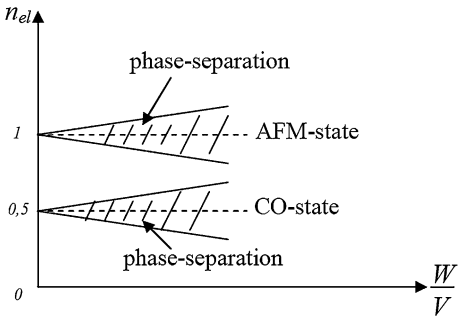

Fig. 9.11 Qualitative phase-diagram of the Shubin-Vonsovsky model in the strong-coupling case. At $n_{el} = 1$ AFM-state appears in the model, while at $n_{el} = 1/2$ we have the checkerboard CO-state [91]

in agreement with general quantum–mechanical consideration for slow particles ($p_F d < 1$) in vacuum (see [48]).

Thus in 3D a normal state of the Shubin-Vonsovsky model at strong-coupling and low densities is again unstable towards triplet p-wave pairing. The irreducible bare vertex in substance reads:

$$N_{3D}(0)\, U_{eff}^{l=1} = \lambda_S^2 \Pi_{l=1} + \lambda_P. \tag{9.6.11}$$

As a result the critical temperature in the main order of the s-wave gas-parameter is given by (9.4.10) again in similarity with 3D Hubbard model.

The presence of the additional Coulomb repulsion V on the neighboring sites in the model changes only the preexponential factor in (9.4.10). Thus situation in the 3D Shubin-Vonsovsky model and low electron density is much more favorable for SC with reasonable T_C even in the most repulsive strong-coupling case (in contrast with the situation in 3D jelly model for dense electron plasma).

Analogously in strong-coupling and low density in 2D case the s-wave dimensionless gas-parameter is again $f_S = f_0 = \frac{1}{\ln(4W/\varepsilon_F)} = \frac{1}{\ln(8/n_{el})}$ [see (9.4.14)] as in the 2D Hubbard model, while the dimensionless p-wave gas-parameter:

$$f_P \sim p_F^2 d^2 \tag{9.6.13}$$

in 2D again in agreement with general quantum–mechanical considerations [48] for slow particles in vacuum. The irreducible bare vertex in substance reads in 2D:

$$U_{eff}^{l=1} N_{2D}(0) = -6.1 f_S^3 + \alpha p_F^2 d^2, \tag{9.6.14}$$

where α is numerical coefficient.

Hence in the main order of 2D s-wave gas-parameter the p-wave critical temperature is given again by (9.4.15) in exact similarity with 2D Hubbard model. The presence of the additional Coulomb repulsion V again changes only the preexponential factor.

Fig. 9.12 Phase-separated state at the densities $1/2 - x_C < n_{el} < 1/2$ with nanoscale metallic clusters inside CO checkerboard insulating matrix. At critical concentration $n_{el} = 1/2 - x_C$ the metallic clusters start to touch each other and all the volume of the sample becomes metallic [91]

9.6.2 Localization and Phase Separation in Shubin-Vonsovsky Model at Larger Densities

At larger dimensionless densities $n_{el} \geq 0.5$ ($n_{el} = 0.5$ corresponds to quarter-filling of the band) there are, however, extended regions of phase-separation in Shubin-Vonsovsky model in the strong-coupling limit $U \gg V \gg W$.

To be more specific in the model [89, 90] there are two types of localization: Mott–Hubbard localization with an appearance of AFM-state at half-filling ($n_{el} \to 1$) [1–4, 89, 90, 92] and Verwey localization with an appearance of checkerboard charge-ordered (CO) state at quarter-filling ($n_{el} \to ½$) [99, 100].

Close to $n_{el} = ½$ and $n_{el} = 1$ we have extended regions of nanoscale phase-separation [92–94, 98]. The qualitative phase-diagram of the Shubin-Vonsovsky model in the strong-coupling case is presented on Fig. 9.11.

If we increase the density from $n_{el} \to 0$ to $n_{el} = ½ - x$, then at the critical concentrations [93, 94]:

$$n_C = 1/2 - x_C \sim \left(\frac{W}{V}\right)^{3/5} \text{ in 3D}, \tag{9.6.16}$$

and

$$n_C = 1/2 - x_C \sim \left(\frac{W}{V}\right)^{1/2} \text{ in 2D} \tag{9.6.17}$$

the system undergoes the first-order phase-transition into a phase-separated state with nanoscale metallic clusters inside charge-ordered checkerboard insulating matrix (see Fig. 9.12). At critical concentration $n_{el} = ½ - x_C$ the metallic clusters start to touch each other. As a result all the sample volume becomes metallic for $n_{el} < ½ - x_C$. The more detailed analysis of Verwey localization at $n_{el} = ½$ and nanoscale phase-separated state for $½ - x_C < n_{el} < ½$ will be a subject of Chap. 15

Thus we can not extend our calculations for T_C in homogeneous case to densities larger than $n_{el} = ½ - x_C$ in the strong-coupling limit of Shubin-Vonsovsky model. However it is interesting to construct SC phase-diagram of the model for $n_{el} < 1/2 - x_C$ and to find the regions of p-wave, d_{xy} and $d_{x^2-y^2}$-pairing. The work along these lines is in progress.

Another interesting problem is to consider the opposite weak-coupling Born case $W > U > V$ which can be realized for large Bohr radius $a_B > d$ or correspondingly for large dielectric permittivity $\varepsilon \gg 1$ (note that real high-T_C materials

are in the difficult intermediate coupling regime $\varepsilon \geq 1$ and $a_B \sim d$). In the weak-coupling case Verwey localization [99] is absent for $n_{el} = ½$ and we can construct superconductive phase-diagram of the Shubin-Vonsovsky model for p-wave, d_{xy} and $d_{x^2-y^2}$-pairing for all densities including almost half-filled case [101, 102].

The first numerical results in this respect were obtained in [79], where the authors found (besides p-wave, d_{xy} and $d_{x^2-y^2}$-pairing) also the regions of extended s-wave pairing and g-wave pairing for $0 < n_{el} < 0.95$. These results were improved in a more elaborate numerical analysis in [101, 102], where the authors took into account all the second order contributions ($\sim U^2$, $\sim UV$, and $\sim V^2$) to effective interaction U_{eff} in the second order of the weak-coupling Born approximation.

References

1. Hubbard, J.: Proc. R. Soc. Lond. A **276**, 238 (1963)
2. Hubbard, J.: Proc. R. Soc. Lond. A **277**, 237 (1964)
3. Hubbard, J.: Proc. R. Soc. Lond. A **281**, 401 (1964)
4. Hubbard, J.: Proc. R. Soc. Lond. A **285**, 542 (1965)
5. Bardeen, J., Cooper, L.N., Schrieffer, J.R.: Phys. Rev. **108**, 1175 (1957)
6. Cooper, L.N.: Phys. Rev. **104**, 1189 (1956)
7. Schrieffer, J.R.: Theory of Superconductivity. Benjamin, New York (1964)
8. Anderson, P.W.: Science **235**, 1196 (1987)
9. Galitskii, V.M.: JETP **34**, 151 (1958)
10. Kohn, W., Luttinger, J.M.: Phys. Rev. Lett. **15**, 524 (1965)
11. Volovik, G.E.: Exotic Properties of Superfluid 3He. World Scientific, Singapore (1992)
12. Regal, C.A., Ticknor, C., Bohn, J.L., Jin, D.S.: Phys. Rev. Lett. **90**, 053201 (2003)
13. Varma, C.M., Littlewood, P.B., Schmitt-Rink, S., Abrahams, E., Ruckenstein, A.E.: Phys. Rev. Lett. **63**, 1996 (1989)
14. Vollhardt, D., Wöelfle, P.: The Superfluid Phases of Helium 3. Taylor and Francis, London (1990)
15. Schunck, C.H., Zwierlein, M.W., Stan, C.A., Raupach, S.M.F., Ketterle, W., Simoni, A., Tiesinga, E., Williams, C.J., Julienne, P.S.: Phys. Rev. A **71**, 045601 (2005)
16. Kee, H.-Y., Raghavan, A., Maki, K.: arXiv:0711.0929 (2007)
17. Kee, H.-Y., Raghavan, A., Maki, K.: Proceedings of the First Euro conference on Anomalous Complex Superconductors, Crete, Greece (1998)
18. Ott, H.R., Rudigier, H., Rice, T.M., Ueda, K., Fisk, Z., Smith, J.L.: Phys. Rev. Lett. **52**, 1915 (1984)
19. Kromer, S., Helfrich, R., Lang, M., Steglich, F., Langhammer, C., Bach, A., Michels, T., Kim, J.S., Stewart, G.R.: Phys. Rev. Lett. **81**, 4476 (1998)
20. Maeno, Y., Rice, T.M., Sigrist, M.: Phys. Today **54**, 42 (2001)
21. Rice, T.M., Sigrist, M.: J. Phys.: Condens. Matter **7**, L643 (1995)
22. Bednorz, J.G., Müller, K.A.: Z. Phys. B: Condens. Matter **64**, 189 (1986)
23. Ginsberg, D. M. (ed.): Physical Properties of High Temperature Superconductors. World Scientific, Singapore (1994)
24. Phillips, J.C.: Physics of High-Tc Superconductors. Academic Press, Boston (1989)
25. Wolf, S.A., Kresin, V.Z.: Novel superconductivity. Plenum Press, New York (1987)
26. Nagamatsu, J., Nakagawa, N., Muranaka, T., Zenitani, Y., Akimitsu, J.: Nature **410**, 63 (2001)

27. Gor'kov, L.P., Melik-Barkhudarov, T.K.: JETP **40**, 1452 (1961)
28. Fay, D., Layzer, A.: Phys. Rev. Lett. **20**, 187 (1968)
29. Kagan, M.Yu., Chubukov, A.V.: JETP Lett. **47**, 525 (1988)
30. Lifshitz, E.M., Pitaevskii, L.P.: Statistical Physics, Part 2. Pergamon Press, Oxford (1988)
31. Abrikosov, A.A., Gor'kov, L.P., Dzyaloshinskii, I.E.: Methods of Quantum Field Theory in Statistical Physics. Prentice Hall, Englewood Cliffs, New Jersey (1963)
32. Kohn, W.: Phys. Rev. Lett. **2**, 393 (1959)
33. Bloom, P.: Phys. Rev. B **12**, 125 (1975)
34. Friedel, J.: Adv. Phys. **3**, 446 (1954)
35. Lindhard, J., Danske Videnskab, Kgl.: Selskab, Mat.-Fys. Medd. **28**(8) (1954)
36. Ashkroft, N.W., Mermin, N.D.: Solid State Physics, vol. 1. Holt, Rinehart and Winston (1976)
37. Nozieres, P.: Private communication to the author
38. Kagan, M.Yu., Ozharovskii, A.V.: Basic mechanisms of superconductivity in strongly correlated electron systems. Lecture course, Part II, Moscow (1999)
39. Chubukov, A.V.: Phys. Rev. B **48**, 1097 (1993)
40. Baranov, M.A., Efremov, D.V., Mar'enko, M.S., Kagan, M.Yu.: JETP **90**, 861 (2000)
41. Efremov, D.V., Mar'enko, M.S., Baranov, M.A., Kagan, M.Yu.: Physica B **284–288**, 216 (2000)
42. Mar'enko, M.S.: PhD Thesis, Kapitza Institute, Moscow (2000)
43. Baranov, M.A., Kagan, M.Yu.: JETP **99**, 1236 (1991)
44. Baranov, M.A., Chubukov, A.V., Kagan, M.Yu.: Int. J. Mod. Phys. B **6**, 2471 (1992)
45. Kagan, M.Yu.: Superconductivity and superfluidity in Fermi-systems with repulsion. Habilitation Thesis, Kapitza Institute, Moscow (1994)
46. Kanamori, J.: Progress Theoret. Phys. **30**, 275 (1963)
47. Kagan, M.Yu., Val'kov, V.V.: JETP **113**, 156–171 (2011)
48. Landau, L.D., Lifshitz, E.M.: Quantum Mechanics: Non-Relativistic Theory. Pergamon Press, New York (1977)
49. Fulde, P.: Electron Correlations in Molecules and Solids. Springer, Berlin (1993)
50. Fukuyama, H., Hasegawa, Y., Narikiyo, O.: J. Phys. Soc. Jpn. **60**, 2013 (1991)
51. Baranov, M.A., Kagan, M.Yu.: Z. Phys. B: Condens. Matter **86**, 237 (1992)
52. Wollman, D.A., van Harlingen, D.J., Lee, W.C., Ginsberg, D.M., Leggett, A.J.: Phys. Rev. Lett. **71**, 2134 (1993)
53. Kagan, M.Yu., Rice, T.M.: J. Phys.: Condens. Matter **6**, 3771 (1994)
54. Hlubina, R.: Phys. Rev. B **59**, 9600 (1999)
55. Mraz, J., Hlubina, R.: Phys. Rev. B **67**, 174518 (2003)
56. Mraz, J., Hlubina, R.: *ibid* **69**, 104501 (2004)
57. Zanuchi, D., Schulz, H.J.: Phys. Rev. B **54**, 9509 (1996)
58. Miyake, K., Schmitt-Rink, S., Varma, C.M.: Phys. Rev. B **34**, 6554 (1986)
59. Scalapino, D.J., Loh Jr, E., Hirsch, J.E.: Phys. Rev. B **34**, 8190 (1986)
60. Kozlov, A.I.: Supercond.: Phys. Chem. Eng. **2**, 64 (1989) (in Russian)
61. Dzyaloshinskii, I.E., Yakovenko, V.M.: JETP **94**, 344 (1988)
62. Schrieffer, J.R., Wen, X.G., Zhang, S.C.: Phys. Rev. B **39**, 11663 (1989)
63. Kampf, A., Schrieffer, J.R.: Physica. B **163**, 267 (1990)
64. Kampf, A., Schrieffer, J.R.: Phys. Rev. B **41**, 6399 (1990)
65. Kyung, B., Landry, J.-S., Tremblay, A.-M.S.: Phys. Rev. B **68**, 174502 (2003)
66. White, S.R.: Phys. Rev. Lett. **69**, 2863 (1992)
67. Monthoux, P., Scalapino, D.J.: Phys. Rev. Lett. **72**, 1874 (1994)
68. Manske, D., Eremin, I., Bennemann, K.H.: Phys. Rev. B **67**, 134520 (2003)
69. Maier, T., Jarrell, M., Schulthess, T.C., Kent, P.R.C., White, J.B.: Phys. Rev. Lett. **95**, 237001 (2005)
70. Haule, K., Kotliar, G.: Phys. Rev. B **76**, 104509 (2007)
71. Pathak, S., Shenoy, V.B., Randeria, M., Trivedi, N.: Phys. Rev. Lett **102**, 027002 (2009)
72. Lee, P.A., Nagaosa, N., Wen, X.-G.: Rev. Mod. Phys. **78**, 17 (2006)

73. Hur, K.L., Rice, T.M.: Ann. Phys. **325**, 1452 (2009)
74. Podolsky, D., Kee, H.-Y., Kim, Y.B.: Europhys. Lett. **88**, 17004 (2009)
75. Zheleznyak, A.T., Yakovenko, V.M., Dzyaloshinskii, I.E.: Phys. Rev. B **55**, 3200 (1997)
76. Shulz, H.J.: Europhys. Lett. **4**, 609 (1987)
77. Raghu, S., Kivelson, S.A., Scalapino, D.J.: Phys. Rev. B **81**, 224505 (2010)
78. Kivelson, S.A.: Plenary talk on Strongly Correlated Electron Systems (SCES) Conference, Cambridge, UK, August–September 2011
79. Raghu, S., Berg, E., Chubukov, A.V., Kivelson, S.A.: Phys. Rev. B **85**, 024516 (2012)
80. Kanigel, A., Chatterjee, U., Randeria, M., Norman, M.R., Souma, S., Shi, M., Li, Z.Z., Raffy, H., Campuzano, J.C.: Phys. Rev. Lett. **99**, 157001 (2007)
81. Alexandrov, A.S., Kabanov, V.V.: Phys. Rev. Lett. **106**, 136403 (2011)
82. Belyavsky, V.I., Kapaev, V.V., Kopaev, Y.V.: Phys. Rev. B **80**, 214524 (2009)
83. Belyavsky, V.I., Kopaev, Yu.V.: Phys. Rev. B **76**, 214506 (2007)
84. Chubukov, A.V., Kagan, M.Yu.: J. Phys.: Condens. Matter **1**, 3135 (1989)
85. Appel, J., Hetszenau, H.: Phys. Rev. **188**, 755 (1969)
86. Küchenhoff, S., Wöelfle, P.: Phys. Rev. B **38**, 935 (1988)
87. Efetov, K., Aleiner, I.: J. Phys.: Condens. Matter **19**, 255215 (2007)
88. Khodel, V.A., Shaginyan, V.R.: JETP Lett. **51**, 488 (1990)
89. Vonsovsky, S.V., Izumov, Y.A., Kurmaev, E.Z.: Superconductivity of Transition Metals, Their Alloys, and Compounds. Springer (1982)
90. Shubin, S., Vonsovsky, S.: Proc. R. Soc. Lond. A **145**, 159 (1934)
91. Kagan, M.Yu., Efremov, D.V., Mar'enko, M.S., Val'kov, V.V.: JETP Lett. **93**, 819 (2011)
92. Mott, N.F., Davis, E.A.: Electronic Processes in Non-Crystalline Materials. Oxford University Press, Oxford (1979)
93. Kagan, M.Yu., Kugel, K.I., Khomskii, D.I.: JETP **93**, 415 (2001)
94. Kagan, M.Yu., Kugel, K.I.: Sov. Phys. Usp. **171**, 577 (2001)
95. Izumov, A.Y.: High T_C superconductors on the basis of FeAs compounds. Publ. Home R&C Dynamic, Moscow (2009). (in Russian)
96. Chubukov, A.V.: Plenary talk in the Proceedings of the Conference Stripes XI, Rome, Italy (2011)
97. Bending, S.J., et al.: Plenary talk on 7th International Conference on Vortex Matter in Nanostructured Superconductors, Rhodes, Greece (2011)
98. Nagaev, E.L.: JETP Lett. **6**, 484 (1967)
99. Verwey, E.J.W.: Nature **144**, 327 (1939)
100. Verwey, E.J.W., Haayman, P.W.: Physica **8**, 979 (1941)
101. Kagan, M.Yu., Val'kov, V.V., Mitskan, V.A., Korovushkin, M.M.: JETP Lett. **97**, 226 (2013)
102. Kagan, M.Yu., Val'kov, V.V., Mitskan, V.A., Korovushkin, M.M.: JETP **117**, 728 (2013)

Chapter 10
Strong T_C Enhancement in Spin-Polarized Fermi-Gas and in Two-Band Superconductors

In previous (Chap. 9) we discuss the possible unconventional SC of p-wave and d-wave character in strongly correlated fermion systems with repulsive interaction between particles. The basic mechanism of SC which we discussed at low electron densities was Kohn-Luttinger mechanism (see Ref. [10] in Chap. 9) and its extension on triplet p-wave pairing by Fay, Laser (see Ref. [28] in Chap. 9) and Kagan, Chubukov (see Ref. [29] in Chap. 9). However, the critical temperatures of 3D and 2D p-wave pairing given by (9.4.10) and (9.4.15) are usually rather low, especially in 3D.

The legitimate question then appears whether it is possible to increase T_C already at low density and to get experimentally feasible critical temperatures?

The answer to this question is positive and is connected with 2 possibilities:

1. To apply external magnetic field (or strong spin-polarization) to triplet p-wave SC [1–4];
2. To consider the two-band situation especially for multiband SC with one narrow band [3–6].

In both cases the most important is to separate the channels for the formation of Cooper pair and for the preparation of the effective interaction [1, 5, 3, 4].

10.1 T_C Enhancement in Spin-Polarized Neutral Fermi-Gas

In magnetic field (or in the presence of the strong spin-polarization) the Cooper pair according to [1] is formed by two fermions with spins "up", while an effective interaction is prepared by two fermions with spins "down" (see Fig. 10.1).

M. Yu. Kagan, *Modern Trends in Superconductivity and Superfluidity*,
Lecture Notes in Physics 874, DOI: 10.1007/978-94-007-6961-8_10,

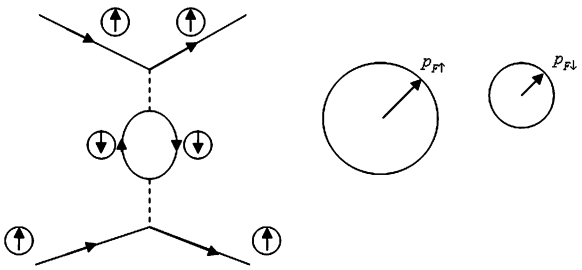

Fig. 10.1 Separation of the channels for Cooper pairing and effective interaction in triplet neutral SC. An effective interaction is proportional to polarization operator $\Pi_{\downarrow\downarrow}(q)$ for *down* (with $p_{F\downarrow}$) spins in the second order of perturbation theory. The Cooper pair is formed by two spins *up* (with $p_{F\uparrow}$) [1, 2, 6]

10.1.1 3D Spin-Polarized Fermi-Gas

As a result the Kohn's anomaly is strongly increased. In the absence of magnetic field (for $H = 0$) the Kohn's anomaly in 3D reads: $(q - 2p_F)\ln|q - 2p_F|$ [see (9.3.5)] where $q^2 = 2p_F^2(1 - \cos\theta)$. Physically Kohn's anomaly is important for $q \to 2p_F$ (diameter of Fermi-sphere) or for angles $\theta \to \pi$—backward scattering between incoming and outgoing momenta $\vec{p}$ and $\vec{k}$ for the Cooper channel $\left(q = \left|\vec{p} - \vec{k}\right|;\ |\vec{p}| = \left|\vec{k}\right| = p_F\right)$. In terms of the angle θ between $\vec{p}$ and $\vec{k}$ $\left(\theta = \angle\vec{p}\vec{k}\right)$ the Kohn's anomaly for $H = 0$ reads:

$$\Pi_{\sin g}(q) \sim (q - 2p_F)\ln|q - 2p_F| \sim (\pi - \theta)^2 \ln(\pi - \theta) \tag{10.1.1}$$

and only second derivative of $\Pi_{\sin g}(\theta)$ with respect to $(\pi - \theta)$ diverges. In the same time for $H \neq 0$ the Fermi-momenta for the particles with spins "up" and "down" are different ($p_{F\uparrow} \neq p_{F\downarrow}$) and thus:

$$\Pi_{\sin g}(\theta) \sim \left(q_\uparrow - 2p_{F\downarrow}\right)\ln\left|q_\uparrow - 2p_{F\downarrow}\right| \sim (\theta - \theta_C)\ln|\theta - \theta_C|, \tag{10.1.2}$$

where θ_C differs from π proportional to $(p_{F\uparrow}/p_{F\downarrow} - 1)$. Correspondingly already first derivative of $\Pi_{\sin g}(\theta)$ with respect to $(\theta - \theta_C)$ diverges. Unfortunately for $H \neq 0$ there is a competing process namely the decrease of the density of states of the fermions with "down" spins in $\Pi_{\downarrow\downarrow}(\theta)$ on Fig. 10.1:

$$N_\downarrow^{3D}(0) = \frac{mp_{F\downarrow}}{4\pi^2}. \tag{10.1.3}$$

As a result of this competition the critical temperature $T_C^{\uparrow\uparrow}$ (for Cooper pair formed by two "up" spins) has strongly non-monotonous (reentrant) behavior with large maximum (see Fig. 10.2).

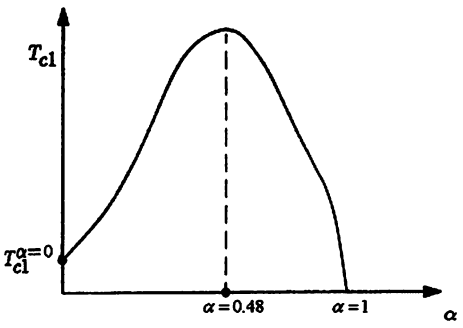

Fig. 10.2 Dependence of the p-wave critical temperature $T_C^{\uparrow\uparrow}$ (for pairing of two *up* spins) from the degree of spin-polarization in 3D polarized Fermi-gas with repulsion [1, 3, 4]

In terms of the polarization degree:

$$\alpha = \frac{n_\uparrow - n_\downarrow}{n_\uparrow + n_\downarrow}, \tag{10.1.4}$$

where $n_\uparrow = p_{F\uparrow}^3/6\pi^2$ and $n_\downarrow = p_{F\downarrow}^3/6\pi^2$ are the densities of "up" and "down" fermions in 3D, the critical temperature has a pronounced maximum for $\alpha = 0.48$ (48 % of the polarization). Correspondingly $\delta = p_{F\uparrow}/p_{F\downarrow} = 1.43$ at maximum (see Ref. [44] in Chap. 9) [1, 3, 4], where in 3D:

$$\alpha = \frac{\delta^3 - 1}{\delta^3 + 1}. \tag{10.1.5}$$

.

Note that polarization operator $\Pi_{\downarrow\downarrow}(q)$ in Fig. 10.1 reads in 3D:

$$\Pi_{\downarrow\downarrow}(q_\uparrow) = N_\downarrow^{3D}(0)\left[1 + \frac{4p_{F\downarrow}^2 - q_\uparrow^2}{4p_{F\downarrow}q_\uparrow}\ln\frac{2p_{F\downarrow} + q_\uparrow}{|2p_{F\downarrow} - q_\uparrow|}\right]. \tag{10.1.6}$$

Correspondingly in terms of $\delta = p_{F\uparrow}/p_{F\downarrow}$ from (10.1.5) and angle θ the transferred momentum squared $q_\uparrow^2 = 2p_{F\uparrow}^2(1 - \cos\theta)$ the polarization operator is given by:

$$\Pi_{\downarrow\downarrow}(\theta) = N_\downarrow^{3D}(0)\left[1 + \frac{1 - \delta^2\sin^2\frac{\theta}{2}}{2\delta\sin\frac{\theta}{2}}\ln\frac{1 + \delta\sin\frac{\theta}{2}}{|1 - \delta\sin\frac{\theta}{2}|}\right]. \tag{10.1.7}$$

The evaluation of p-wave harmonics $\Pi_{\downarrow\downarrow}^{l=1}$ is again elementary and can be done analytically as in unpolarized case (for $\delta = 1$) (see [1]). For us it is important to represent

$$T_{C1}^{\uparrow\uparrow} = T_{C1}(\alpha = 0)\, e^{\frac{f(\alpha)}{\lambda^2}}, \tag{10.1.8}$$

(where $\lambda = 2ap_F/\pi$ is 3D gas-parameter) and show that for small $\alpha \ll 1$ [1]

$$f(\alpha) = \frac{10}{9}\alpha\frac{(7 - 4\ln 2)}{(2\ln 2 - 1)^2} > 0 \tag{10.1.9}$$

is positive and linear in α. Note that for not very strong external magnetic field $\mu_B H < \varepsilon_{F0}$ ($\varepsilon_{F0} = {p_{F0}}^2/2m$ − Fermi-energy for $H = 0$) we have the linear relation between α and H:

$$\alpha \approx \frac{3}{2}\frac{\mu_B H}{\varepsilon_{F0}} \ll 1 \tag{10.1.10}$$

in 3D case. Thus $T_{C1}^{\uparrow\uparrow}$ increases for $\alpha \ll 1$. In the opposite case of practically full polarization ($\alpha \to 1$ or $1-\alpha \to 0$) we have [1, 3, 4]:

$$f(\alpha) = -\frac{9}{2^{2/3}}\frac{1}{(1-\alpha)ln\frac{2}{(1-\alpha)}} \to \infty. \tag{10.1.11}$$

Hence $T_{C1}^{\uparrow\uparrow} \to 0$ for $\alpha \to 1$. The asymptotic behavior of $f(\alpha)$ for $\alpha \ll 1$ and (1-α) $\ll 1$ justifies the appearance of the maximum of $T_{C1}^{\uparrow\uparrow}$ in between. In maximum:

$$\max T_{C1}^{\uparrow\uparrow} = T_{C1}^{\uparrow\uparrow}(\alpha = 0.48) \sim \varepsilon_F e^{-\frac{7}{\lambda^2}}, \tag{10.1.12}$$

and we see that in the second order of perturbation theory the expression in the main exponent for T_C increases practically in 2 times (from $\lambda^2/13$ to $\lambda^2/7$) giving a large T_C-enhancement in 3D spin-polarized Fermi-gas [1, 3, 4]. Note that the behavior of the critical temperature at $\alpha \to 1$ is not accidental in this approximation, namely $T_{C1}^{\uparrow\uparrow}(\alpha = 1) = 0$ because of the absence of "down" spins in fully polarized gas. $T_{C1}^{\uparrow\uparrow}(\alpha = 1)$ is non-zero only in the third order of the gas-parameter $\lambda = 2ap_F/\pi$ which is in accordance with Pauli principle for slow particles in vacuum (see Ref. [48] in Chap. 9) [p-wave harmonic of the scattering amplitude $f_1 \sim (a\ p_F)^3$].

Note also that while deriving Eqs. (10.1.8), (10.1.9) and (10.1.11) we will focused on the main exponents for T_{C1} and ${T_{C1}}^{\uparrow\uparrow}$ neglecting the difference between ε_F and $\varepsilon_{F\uparrow}$ in the perexponential factors.

10.1.2 2D Spin-Polarized Fermi-Gas

This effect is even more pronounced in 2D spin-polarized Fermi-gas. Here, as we discussed in Chap. 9 in unpolarized case the strong Kohn's anomaly $\mathrm{Re}\sqrt{q - 2p_F}$ is ineffective for SC in the second order of perturbation theory for effective interaction $U_{\mathrm{eff}}(q)$. However, the situation is dramatically changed in spin-polarized case.

For $\alpha \neq 0$ in 2D:

$$\Pi_{sing}(q) \sim \mathrm{Re}\sqrt{q_\uparrow - 2p_{F\downarrow}} \neq 0, \tag{10.1.13}$$

and thus 2D Kohn's anomaly is now "switched on" for SC already in the second order of the gas-parameter.

The exact calculation of $\Pi_{\downarrow\downarrow}(q)$ in 2D yields in p-wave channel (for magnetic number $m = 1$):

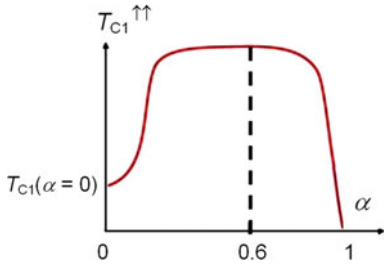

Fig. 10.3 Dependence of the critical temperature $T_{C1}^{\uparrow\uparrow}$ for two *up* spins from the polarization degree α in 2D spin-polarized Fermi-gas [1, 3, 4]

$$N_{\downarrow}^{2D}|U_{eff}^{m-1}| = 8f_0^2\frac{(\delta-1)}{\delta^2}, \tag{10.1.14}$$

where in 2D

$$\alpha = \frac{\delta^2-1}{\delta^2+1}. \tag{10.1.15}$$

Correspondingly the critical temperature for p-wave pairing of two "up" spins reads in second order of 2D gas-parameter f_0:

$$T_{C1}^{\uparrow\uparrow} \sim \varepsilon_F \exp\left\{-\frac{\delta^2}{8f_0^2(\delta-1)}\right\}, \tag{10.1.16}$$

From (10.1.16) we see that for $\delta = 1$ (unpolarized case) $T_{C1}^{\uparrow\uparrow} \to 0$ and superconductive transition arises only in third order of the gas-parameter for the effective interaction.

For $\alpha \to 1$ ($\delta \to \infty$) we again have $T_{C1}^{\uparrow\uparrow} \to 0$ in second order in f_0. Thus, we have a very large maximum in between again. It corresponds to $\delta = p_{F\uparrow}/p_{F\downarrow} = 2$ or, $\alpha = 0.6$. Hence for $T_{C1}^{\uparrow\uparrow}$ in maximum we get:

$$\max T_{C1}^{\uparrow\uparrow} = T_{C1}^{\uparrow\uparrow}(\alpha = 0.6) \sim \varepsilon_F \exp\left\{-\frac{1}{2f_0^2}\right\}. \tag{10.1.17}$$

The dependence of $T_{C1}^{\uparrow\uparrow}$ from α in 2D spin-polarization Fermi-gas is shown on Fig. 10.3.

The maximum is very broad in 2D—it stretches form $\alpha \sim 0.1$ till $\alpha \sim 0.9$.

Note that in this approximation (in second order in gas parameter evaluation of $T_{C1}^{\uparrow\uparrow}$) $T_{C1}^{\uparrow\uparrow}(\alpha = 1) = 0$ again due to the absence of "down" spins in 100 % polarized case.

10.1.3 Spin-Polarized Superfluid ^{3}He

The application of the theory for dilute spin-polarized mixture will be a subject of the next Chapter (Chap. 11). Here we would like to emphasize that even for dense

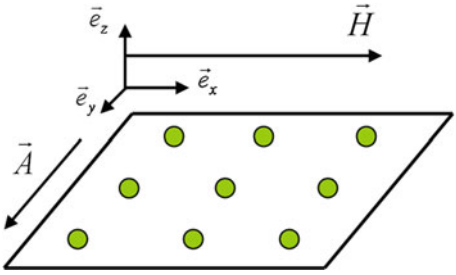

Fig. 10.4 2D electron gas in parallel magnetic field $\overrightarrow{H} = H\overrightarrow{e}_x$. Vector-potential $\overrightarrow{A} = Hz\overrightarrow{e}_y$ does not change the motion of electrons and Cooper pairs in (xy) plane [2–4]

superfluid ^{3}He (where $\lambda \sim 1.3$) we get reasonable estimates for $T_{C1}^{\uparrow\uparrow}$—increase. These estimates are confirmed by the experiments of Frossati et al. [7–9] in Kamerlingh-Onnes Laboratory in Leiden. Namely in unpolarized ^{3}He-A:

$$T_{C1}(\alpha = 0) = 2.7 \text{ mK}. \tag{10.1.18}$$

In the same time for $\alpha = 6$ % of the polarization (in magnetic fields ~ 15 T) $T_{C1}^{\uparrow\uparrow}(\alpha = 6\ \%) \approx 3.2$ m K and we have 20 % increase of T_C.

In maximum for A1-phase of superfluid ^{3}He we predict

$$\max T_{C1}^{\uparrow\uparrow} = T_{C1}^{\uparrow\uparrow}(\alpha = 0.6) = 6.4 T_{C1}. \tag{10.1.19}$$

The similar estimate for reentrant behavior of $T_{C1}^{\uparrow\uparrow}(\alpha)$ and for $T_{C1}^{\uparrow\uparrow}$ in maximum was proposed in [10] on the basis of more phenomenological approach based on Landau Fermi-liquid theory for superfluid ^{3}He.

10.2 T_C Enhancement in Quasi-2D Charged SC in Parallel Magnetic Field

In 2D electron gas in parallel magnetic field: $\vec{H} = H\vec{e}_x$ (see Fig. 10.4) the vector-potential

$$\vec{A} = Hz\vec{e}_y \tag{10.2.1}$$

does not change the motion of electrons and Cooper pairs in (xy) plane [the Ψ-function for this problem $\Psi(\vec{r}) = e^{ip_x x + ip_y y}\phi(z)$].

Hence in this geometry diamagnetic Meissner effect [11] (which changes the motion of the Cooper pair in plane if magnetic field is perpendicular to the plane) is totally suppressed [12–16]. Hence 2D SC in parallel magnetic field becomes equivalent to neutral (uncharged) ^{3}He-monolayer and only Pauli paramagnetic effect is present [2, 14]. According to this effect even if the singlet s-wave pairing organized by two electrons with spins "up" and "down" was present in SC at $H = 0$ it will be totally suppressed in magnetic fields exceeding Pauli paramagnetic limit [14, 15]

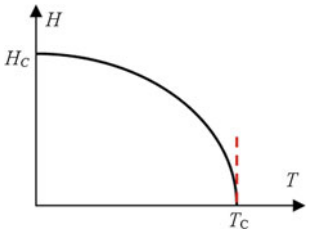

Fig. 10.5 Standard behavior of a critical magnetic field as a function of temperature in 3D superconductors, which are subject of Meissner effect

$$H > H_P = \frac{T_{CO}}{g\mu_B}, \tag{10.2.2}$$

where μ_B is Bohr magneton and g is gyromagnetic ratio (or Lande factor) (note that for $T_{CO} \sim 1$ K and $g \sim 1$: $H_P \sim 1$ T). As a result only p-wave pairing with the symmetry of A1-phase (pairing of two electrons with spins "up") that is with $S_{tot} = S_z^{tot} = 1$ survives in large magnetic fields (the two electrons should lie on the same Fermi-surface with the radius $p_{F\uparrow}$).

Hence instead of a standard behavior of a critical magnetic field H_C versus temperature [11] presented on Fig. 10.5 we have very unusual (reentrant behavior) of p-wave critical temperatures in 2D superconductor in parallel magnetic field (see Fig. 10.6).

The critical temperature of p-wave pairing depends upon polarization degree according to (10.1.16). At small polarization degrees:

$$\alpha = \frac{g\mu_B H}{\varepsilon_{F0}} \ll 1 \tag{10.2.3}$$

in 2D case. For low density electron systems with $\varepsilon_F \sim 30$ K in high magnetic fields $H \sim 15$ T and $g \sim 1$ polarization degree $\alpha \sim 0.5$ and we can get $T_{C1}^{\uparrow\uparrow} \sim 0.5$ K in accordance with (10.1.16) and (10.1.17) which is quite nice.

It is important to note that the results (10.1.16) and (10.1.17) are valid for 2D Fermi-gas with short-range repulsion or for 2D Hubbard model. The question is how these results will change in 2D Coulomb plasma (or 2D electron gas with screened Coulomb interaction). Here the coupling constant f_0 in (10.1.16) and (10.1.17) can be calculated only within accuracy of Random Phase Approximation (RPA) for metallic electron densities with correlation radius $r_S \sim \frac{1}{p_F a_B} \gg 1$ ($a_B = \frac{\varepsilon}{m^* e^2}$ is Bohr radius, m^* is effective mass and ε is effective dielectric permittivity) [15, 17]. It is shown in [17] that in 2D electron gas (2DEG):

$$U_{\text{eff}}(q_\parallel = 0) = \frac{2\pi e^2}{\kappa_{2D}} \tag{10.2.4}$$

is 2D-projection of 3D screened Coulomb interaction. $\kappa_{2D} = 4\pi N_{2D}(0)e^2$ is effective 2D Thomas–Fermi wave vector or screening vector [14, 16], $q_\parallel$ is

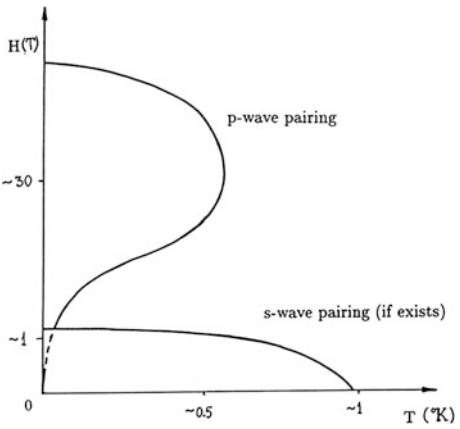

Fig. 10.6 Suppression of s-wave pairing and reentrant behavior of p-wave critical temperatures in 2D SC in parallel magnetic field $H(T)$. p-wave pairing is formed by two electrons living on larger Fermi-surface (with $p_{F\uparrow}$), while effective interaction is formed by two electrons with down spins (with $p_{F\downarrow}$) [2, 3, 4]

projection of vector $\vec{q}$ on (xy) plane and $N_{2D}(0) = m/2\pi$ is a density of states in 2D. (Note that $\kappa_{2D} = 2me^2$ and thus $U_{\text{eff}}(q_\parallel) = \frac{\pi}{m}$.)

Correspondingly the dimensionless coupling constant for screened Coulomb interaction reads:

$$f_0 = N_{2D}(0)U_{\text{eff}}(q_\parallel = 0) = \frac{1}{2} \tag{10.2.5}$$

—remarkable result which is valid also for 3D plasma where $N_{3D}(0) = m\, p_F/2\pi^2$ and $U_{\text{eff}}(q = 0) = \frac{4\pi e^2}{\kappa^2}$. Thus effective gas-parameter for screened Coulomb plasma $f_0 = ½$ does not depend upon density both in 3D and 2D case.

Note that the RPA is exact in 3D and 2D for large densities and small correlation radius $r_S \ll 1$ (dense electron plasma considered in paragraph Sect. 9.5.1), but also it is not bad (at least in 3D) for standard metallic densities ($2 \le r_S \le 6$) because the effective parameter of expansion in the energy-functional of 3D electron plasma is actually $\sim r_S/6$ [15] and (see Refs. [81, 84] in Chap. 9). We can hope that (10.1.16) and (10.1.17) with $f_0 \sim ½$ provides qualitative estimates for 2D dense electron plasma.

Note that the most important experimental limitation to this scenario is connected with the demands on the purity of the sample. In accordance with Abrikosov-Gor'kov results for paramagnetic impurities [18] (more exactly with Larkin results [19] for non-magnetic impurities in p-wave SC) it means that for inverse scattering time:

$$\gamma = 1/\tau < T_{C1} \quad (\hbar = k_B = 1). \tag{10.2.6}$$

For $T_{C1} \sim 0.5$ K we get then $\tau \ge 2{\cdot}10^{-11}$ sec for scattering time of electrons on impurities. Accordingly in 2D case the sheet conductivity for $\varepsilon_F \sim 30$ K and $T_{C1} \sim 0.5$ K:

$$\sigma_{\square} > \frac{e^2}{2\pi\hbar}\frac{2\varepsilon_F}{T_{C1}} \sim 120\frac{e^2}{2\pi\hbar}. \tag{10.2.7}$$

Hence plaquette resistance:

$$R_{\square} < \frac{1}{120}\frac{2\pi\hbar}{e^2} \sim 0.2\ \mathrm{k}\Omega, \tag{10.2.8}$$

and mobility:

$$\mu_{el} = \frac{e\tau}{m^*} = 3 \cdot 10^4 \left(\frac{m_e}{m_e^*}\right)\ \mathrm{cm}^2\,\mathrm{V}^{-1}\,\mathrm{s}^{-1}. \tag{10.2.9}$$

Thus for semimetals or degenerate 2D semiconductive layers with light effective mass $m^* \sim 0.1\ m_e$ (heterostructures, inverse layers):

$$\mu_{el} = 10^5\ \mathrm{cm}^2\,\mathrm{V}^{-1}\,\mathrm{s}^{-1}, \tag{10.2.10}$$

which requires very clean samples.

Note that the highest mobility for GaAs-AlAs heterostructures utilized for the measurements of Fractional Quantum Hall effect $\mu_{el} \sim 10^7\ \mathrm{cm}^2\ \mathrm{V}^{-1}\ \mathrm{s}^{-1}$. In these systems $\varepsilon_F \sim 30$ K for densities $n_{2D} \sim 10^{12}\ \mathrm{cm}^{-2}$, Bohr radius $a_B = \varepsilon/(m^* e^2)$ with effective dielectric permittivity $\varepsilon \sim 4$. Thus, the correlation radius $r_S \sim 4$, so we are far from Wigner crystal case ($r_S \sim 20$ in 2D) [15, 17] and can hope that RPA theory works quite well also in 2D for these densities. Thus, we can justify the estimates for $T_{C1}^{\uparrow\uparrow}$ with $f_0 = ½$ (10.1.16) and (10.1.17) for heterostructures.

Note that if we consider 2D organic superconductors like α-(BEDT-TTF)$_2$I$_3$ or intercalated systems (dichalcogenides) TaS_2, $TaSe_2$ then their mobilities are also very high, but they have Fermi-energies $\varepsilon_F \sim (10^3 \div 10^4)$ K which are very difficult to polarize even with very high magnetic fields (maximal possible stationary magnetic fields are equal to 30 T, maximal fields in pulsed regime are 100 T today, hence polarization degree $\alpha = \frac{g\mu_B H}{\varepsilon_{F0}}$ will be very low and T_C-s will be low).

If we start to think about 2D layer of p-wave heavy-fermion SC like UBe_{13} with $m^* \sim 200\ m_e$ and $\varepsilon_F \sim (30 \div 50)$ K, than we should realize that it is very difficult now to grow very thin films of high quality and it is necessary also to take into account strong spin-orbital coupling and the influence of the crystalline fields in these substances.

It is a very nice challenge for experimentalists to grow very good quality 2D-samples and to apply very parallel magnetic fields or to change gradually tilting angle for a field from $\pi/2$ to 0 and measure an appearance of p-wave SC at very small angles (note that already very small perpendicular component of the magnetic field will destroy SC via diamagnetic Meissner effect).

In the end of this Section let us mention that in principle a reentrant behavior of T_C from magnetic field (similar to the one shown on Fig. 10.6) can be realized even in 3D superconductors in the so-called superquantum limit [20, 21]. This limit corresponds to very high magnetic fields and very small Fermi-energies when Larmor frequency $\omega_L \sim \mu_B H > \varepsilon_F$ (note that $\varepsilon_F \gg T_C$). In this situation we

should take into account Landau quantization of electron levels in magnetic field (diamagnetic one-particle effect). Moreover for $\omega_L > \varepsilon_F$ only one Landau level is filled, so the spectrum of electrons becomes quasi one-dimensional $\varepsilon(p) = \frac{\hbar\omega_L}{2} + \frac{p_z^2}{2m}$ and we again have parquet situation with the necessity to sum up an infinite number of diagrams for effective interaction U_{eff} in particle–particle and particle-hole channels. Halperin and Tesanovic [21] showed that as a result a reentrant behavior takes place (the SC appears again in very high fields).

10.3 Strong T_C Enhancement in the Two-Band Superconductors

Another possibility to enhance the critical temperature of p-wave pairing is to consider the two-band model with two sorts of fermions. To increase T_C we should again separate the channels: the two particles of sort 1 form the Cooper channel (for $p_{F1} > p_{F2}$), and the effective interaction is formed by two particles of sort 2 (see Fig. 10.7).

In this case all the results of (Sect. 10.1) are valid with the change of $\delta = p_{F\uparrow}/p_{F\downarrow}$ on $\delta = p_{F1}/p_{F2}$. The gas-parameters λ and f_0 now depend upon the interaction between the particles of sort 1 and sort 2. In the simplest case it reads $\frac{U_{12}}{2}\sum_i n_{1i}n_{2i}$, where U_{12} is interband interaction, n_{1i} and n_{2i} are the densities of the particles with sort 1 and 2 on site i.

Let us consider the physics which appears in the two-band model for the most interesting case of very different masses of the two sorts of fermions.

10.3.1 The Two-Band Hubbard Model with One Narrow Band

On the lattice the most general and simple model which describes this situation is the two-band Hubbard model with one narrow band. This model is very rich. It describes adequately mixed valence systems [22, 23] such as uranium based

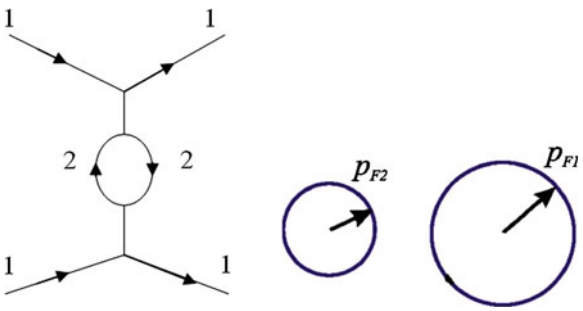

Fig. 10.7 Effective interaction for two sorts of particles with $p_{F1} > p_{F2}$ (see also Fig. 10.1)

heavy-fermions and also some other novel SC and transition metal systems with orbital degeneracy such as complex magnetic oxides (CMR systems) in optimally doped case. Moreover it contains such highly nontrivial effect as electron-polaron effect [24–26] in the homogeneous case. It also shows the tendency towards phase separation [27] for a large mismatch between the densities of heavy and light bands as well as anomalous resistivity characteristics (we will study them in the next chapters). In addition to that it describes anomalous p-wave SC of enhanced Kohn-Luttinger type which we will study detaily in this Section. The Hamiltonian of the two-band Hubbard model in real space reads (see Ref. [47] in Chap. 9 and [6]):

$$\begin{aligned}\hat{H}' = &- t_h \sum_{\langle ij\rangle\sigma} a^+_{i\sigma} a_{j\sigma} - t_L \sum_{\langle ij\rangle\sigma} b^+_{i\sigma} b_{j\sigma} - \varepsilon_0 \sum_{i\sigma} n^\sigma_{ih} - \mu \sum_{i\sigma} \left(n^\sigma_{iL} + n^\sigma_{ih}\right) \\ &+ U_{hh} \sum_i n^\uparrow_{ih} n^\downarrow_{ih} + U_{LL} \sum_i n^\uparrow_{iL} n^\downarrow_{iL} + \frac{U_{hL}}{2} \sum_i n_{iL} n_{ih},\end{aligned} \tag{10.3.1}$$

where t_h and t_L are hopping integrals in heavy and light bands, ε_0 is the center of gravity of the heavy band, and the difference Δ between the bottoms of the bands is given by:

$$\Delta = -\varepsilon_0 + \frac{W_L - W_h}{2} = E^h_{\min} - E^L_{\min}, \tag{10.3.2}$$

U_{hh} and U_{LL} are intraband Hubbard interactions for heavy and light electrons, U_{hL} is interband Hubbard interaction for heavy and light electrons, $n^\sigma_{ih} = a^+_{i\sigma} a_{i\sigma}$, $n^\sigma_{iL} = b^+_{i\sigma} b_{i\sigma}$ are the densities of heavy and light electrons on site i with spin-projection σ, μ is chemical potential.

After Fourier transformation we obtain:

$$\begin{aligned}\hat{H}' = &\sum_{\vec{p}\sigma} \left[\varepsilon_h(p) - \mu\right] a^+_{p\sigma} a_{p\sigma} + \sum_{\vec{p}\sigma} \left[\varepsilon_L(p) - \mu\right] b^+_{p\sigma} b_{p\sigma} + U_{hh} \sum_{\vec{p}\vec{p}'\vec{q}} a^+_{\vec{p}\uparrow} a^+_{\vec{p}'\downarrow} a_{\vec{p}-\vec{q}\downarrow} a_{\vec{p}'+\vec{q}\uparrow} \\ &+ U_{LL} \sum_{\vec{p}\vec{p}'\vec{q}} b^+_{\vec{p}\uparrow} b^+_{\vec{p}'\downarrow} b_{\vec{p}-\vec{q}\downarrow} b_{\vec{p}'+\vec{q}\uparrow} + \frac{U_{hL}}{2} \sum_{\substack{\vec{p}\vec{p}'\vec{q} \\ \sigma\sigma'}} a^+_{\vec{p}\sigma} \left(b^+_{\vec{p}'\sigma'} b_{\vec{p}-\vec{q}\sigma'}\right) a_{\vec{p}'+\vec{q}\sigma},\end{aligned} \tag{10.3.3}$$

where in D dimensions ($D = 2, 3$) for the hypercubic lattice:

$$\begin{aligned}\varepsilon_h(p) - \mu &= -2t_h \sum_{a=1}^{D} \cos(p_a d) - \varepsilon_0 - \mu, \\ \varepsilon_L(p) - \mu &= -2t_L \sum_{a=1}^{D} \cos(p_a d) - \mu,\end{aligned} \tag{10.3.4}$$

are the uncorrelated quasiparticle energies for heavy and light bands (see Fig. 10.8) and $p_\mathrm{a} = \{p_\mathrm{x}, p_\mathrm{y}, \ldots\}$ are Cartesian projections of the momentum.

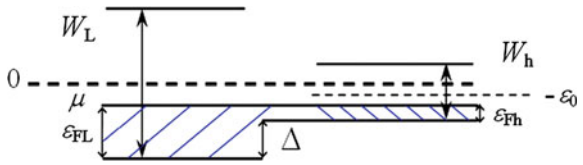

Fig. 10.8 Band structure in the two-band model with one narrow band. W_h and W_L are the bandwidths of heavy and light electrons, e_{Fh} and e_{FL} are the Fermi-energies, $\Delta = -\varepsilon_0 + \frac{W_L - W_h}{2} = E^h_{min} - E^L_{min}$ is the energy difference between the bottoms of the heavy and light bands, with $(-\varepsilon_0)$ being the center of gravity of the heavy band. The center of gravity of the light band is zero, μ is chemical potential (see Ref. [47] in Chap. 9 and [4])

For low densities of heavy and light components $n_{tot}d^D = (n_h + n_L)\, d^D \ll 1$, the quasiparticle spectra are:

$$\begin{aligned} \varepsilon_h(p) - \mu &= -\frac{W_h}{2} + t_h\left(p^2 d^2\right) - \varepsilon_0 - \mu, \\ \varepsilon_L(p) - \mu &= -\frac{W_L}{2} + t_L\left(p^2 d^2\right) - \mu, \end{aligned} \tag{10.3.5}$$

where $W_h = 4Dt_h$ and $W_L = 4Dt_L$ are the bandwidths of heavy and light electrons for D—dimensional hypercubic lattice (for $D = 3$ we have $W_h = 12t_h$ and $W_L = 12t_L$, for $D = 2$ the bandwidths read $W_h = 8t_h$ and $W_L = 8t_L$).

Introducing again (as in one-band Hubbard model in Sect. 9.4) the bare masses of heavy and light components:

$$m_h = \frac{1}{2t_h d^2}; \quad m_L = \frac{1}{2t_L d^2} \tag{10.3.6}$$

and Fermi-energies:

$$\varepsilon_{Fh} = \frac{p^2_{Fh}}{2m_h} = \frac{W_h}{2} + \mu + \varepsilon_0, \quad \varepsilon_{FL} = \frac{p^2_{FL}}{2m_L} = \frac{W_L}{2} + \mu \tag{10.3.7}$$

we finally obtain uncorrelated quasiparticle spectra (for temperatures $T \to 0$) as:

$$\varepsilon_h(p) - \mu = \frac{p^2}{2m_h} - \varepsilon_{Fh}, \quad \varepsilon_L(p) - \mu = \frac{p^2}{2m_L} - \varepsilon_{FL}. \tag{10.3.8}$$

In deriving (10.3.5)–(10.3.8) we implicitly assumed that the difference between the bottoms of the heavy and light bands Δ on Fig. 10.8 is not too large, and hence the parabolic approximation for the spectra of both bands is still valid. We note that there is no one-particle hybridization in Hamiltonians (10.3.1), (10.3.3) but there is a strong two particle hybridization $\frac{U_{hL}}{2}\sum_i n_{ih} n_{iL}$ connected with interband Hubbard interaction $U_{12} = U_{hL}$.

We assume that $m_h \gg m_L$ and therefore:

$$W_h/W_L = m_L/m_h \ll 1 \tag{10.3.9}$$

We also assume that the strong-coupling situation $U_{hh} \sim U_{LL} \sim U_{hL} \gg W_L \gg W_h$ takes place (note that U_{hL} is large because in reality light particles experience strong scattering on the heavy ones as if on a quasiresonance level).

Finally throughout this chapter we will consider the simplest case where the densities of the bands are of the same order: $n_h \sim n_L \sim n$ (where in 3D $n = \frac{p_F^3}{3\pi^2}$, and in 2D $n = \frac{p_F^2}{2\pi}$). In the end of this Section note that the two-band Hubbard model with one narrow band is natural generalization of the well-known Falikov-Kimball model with one finite mass and one infinitely large mass [28] but contains much more rich physics due to a finite width of a heavy band (instead of a localized level in [28]) which allows an interesting dynamics of the heavy component.

10.3.2 The Kanamori T-Matrix Approximation

In (Sect. 9.4) when we discussed SC in 3D and 2D one-band Hubbard model at low density we already acquainted ourselves with Kanamori T-matrix approximation (see Ref. [46] in Chap. 9). Let us apply the same scheme for a two-band Hubbard model. In the 3D case the solution of the corresponding Lippmann-Schwinger equations (see Ref. [47–49] in Chap. 9) yield (see Fig. 10.9):

$$\begin{aligned} T_{hh} &= \frac{U_{hh}d^3}{\left(1 - U_{hh}d^3 K_{hh}^{vac}(0,0)\right)} \approx \frac{U_{hh}d^3}{\left(1 + \frac{U_{hh}}{8\pi t_h}\right)}; \\ T_{hL} &\approx \frac{U_{hL}d^3}{\left(1 + \frac{U_{hL}}{8\pi t_{hL}^*}\right)}; T_{LL} = \frac{U_{LL}d^3}{\left(1 + \frac{U_{LL}}{8\pi t_L}\right)}, \end{aligned} \tag{10.3.10}$$

where $K_{hh}^{vac}(0,0) = -\int_0^{\sim 1/d} \frac{d^3\vec{p}}{(2\pi)^3}\frac{m_h}{p^2}$ is a Cooper loop for heavy particles in vacuum, the effective hopping integrals

$$t_{hL}^* = \frac{1}{2d^2 m_{hL}^*} \text{ and } m_{hL}^* = \frac{1}{2t_{hL}^* d^2} = \frac{m_h m_L}{(m_h + m_L)} \approx m_L \tag{10.3.11}$$

is an effective mass for T-matrix T_{hL} for $m_h \gg m_L$ (note that T-matrix T_{hL} describes the scattering of heavy electrons on the light ones).

Accordingly $t_{hL}{}^* \sim t_L$ is an effective hopping integral for this T-matrix. The quantities $U_{hh}d^3$, $U_{hL}d^3$ and $U_{LL}d^3$ play the role of the zeroth Fourier components for the intraband and interband Hubbard interactions U_{hh}, U_{LL} and U_{hL} in 3D. As a result in the strong-coupling case for $U_{hh} \sim U_{LL} \sim U_{hL} \gg W_L \gg W_h$ we have:

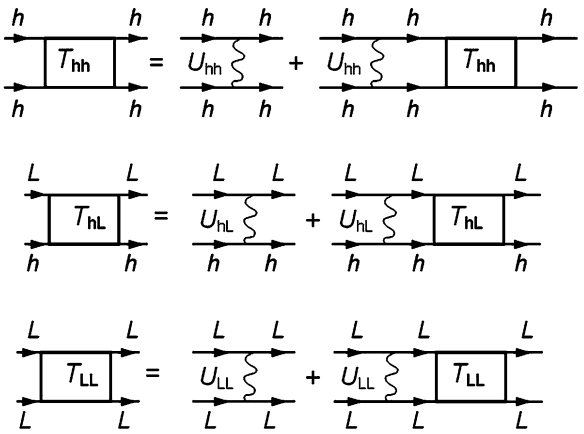

Fig. 10.9 Lippmann-Schwinger equations for T-matrices $T_{\rm hh}$, $T_{\rm LL}$ and $T_{\rm hL}$ for the two-band model with heavy (h) and light (l) electrons, $U_{\rm hh}$ and U_{LL} are the intraband Hubbard interactions, $U_{\rm hL}$ is the interband Hubbard interaction between heavy and light particles (see Ref. [47] in Chap. 9 and [6])

$$T_{hh} \approx 8\pi\, t_h d^3; \quad T_{hL} \approx T_{LL} \approx 8\pi\, t_L d^3. \tag{10.3.12}$$

The s-wave scattering lengths for the two-band Hubbard model $a = \frac{mT}{4\pi} = \frac{T}{8\pi\, td^2}$ then read in the strong-coupling case:

$$a_{\rm hh} = a_{\rm hL} = a_{\rm LL} \approx d. \tag{10.3.13}$$

Correspondingly, the gas-parameter of Galitskii $\lambda = 2ap_{\rm F}/\pi$ in the case of equal densities of heavy and light bands $n_{\rm h} = n_{\rm L}$ is given by:

$$\lambda = \left(\lambda_L \approx \frac{2dp_{FL}}{\pi}\right) = \left(\lambda_h \approx \frac{2dp_{Fh}}{\pi}\right) = \frac{2dp_F}{\pi}. \tag{10.3.14}$$

In the 2D case for strong Hubbard interactions and low densities the vacuum T-matrices for $n_{\rm h} = n_{\rm L}$ with logarithmic accuracy are given by (see Ref. [47] in Chap. 9 and [6]):

$$\begin{aligned} T_{hh} &\approx \frac{U_{hh}d^2}{\left(1 + \frac{U_{hh}d^2}{8\pi t_h}\int\limits_{\sim p_F^2}^{\sim 1/d^2} \frac{dp^2}{p^2}\right)} \approx \frac{U_{hh}d^2}{1 + \frac{U_{hh}}{8\pi\, t_h}\ln\frac{1}{p_F^2 d^2}}; \\ T_{LL} &\approx \frac{U_{LL}d^2}{1 + \frac{U_{LL}}{8\pi\, t_L}\ln\frac{1}{p_F^2 d^2}}; \quad T_{hL} \approx \frac{U_{hL}d^2}{1 + \frac{U_{hL}}{8\pi\, t_{hL}^*}\ln\frac{1}{p_F^2 d^2}}, \end{aligned} \tag{10.3.15}$$

where Ud^2 plays the role of zeroth Fourier component of the Hubbard potential in 2D. As a result, in the strong-coupling case, the 2D gas-parameter of Bloom (see Ref. [33] in Chap. 9) for equal densities $n_{\rm h} = n_{\rm L}$ reads:

$$f_0 = f_{0L} = f_{0h} \approx \frac{1}{2\ln\frac{1}{p_F d}}. \tag{10.3.16}$$

10.3.3 Evaluation of the Self-Energies of Heavy and Light Bands

Let us now evaluate the self-energies of heavy and light bands. In the two-band model the self-energies of heavy and light particles read (see Fig. 10.10):

$$\Sigma_{\mathrm{h}} = \Sigma_{\mathrm{hh}} + \Sigma_{\mathrm{hL}} \quad \text{and} \quad \Sigma_{\mathrm{L}} = \Sigma_{\mathrm{LL}} + \Sigma_{\mathrm{Lh}}. \tag{10.3.17}$$

In 3D case the full T-matrices T_{hh} in substance which enter in the first diagram for Σ_h in Fig. 10.10 has the form:

$$T_{hh}(\Omega, \vec{p}) = \frac{U_{hh} d^3}{(1 - U_{hh} d^3 K_{hh}(\Omega, \vec{p}))}, \tag{10.3.18}$$

where according to [6] and Ref. [47] in Chap. 9:

$$K_{hh}(\Omega, \vec{p}) = \int \frac{d^3\vec{p}'}{(2\pi)^3} \frac{(1 - n_h^F(\varepsilon_{p'+p} - \mu) - n_h^F(\varepsilon_{-p'} - \mu))}{(\Omega - \varepsilon_h(p' + p) - \varepsilon_h(-p') + 2\mu + i0)} \tag{10.3.19}$$

is a Cooper loop in substance (the product of the two Green's functions in the Cooper (particle–particle) channel), $n_{\mathrm{h}}^{\mathrm{F}}(\varepsilon\text{-}\mu)$ is the Fermi–Dirac distribution function for heavy particles, and similarly for the full T-matrices T_{hL}, T_{Lh} and T_{LL} and Cooper loops K_{hL}, K_{Lh} and K_{LL}.

If we expand the T-matrix for heavy particles in first two orders in the gas-parameter, than according to Galitskii (see Ref. [9] in Chap. 9) we obtain:

$$T_{hh}(\Omega, \vec{p}) = \frac{4\pi a_h}{m_h} + \left(\frac{4\pi a_h}{m_h}\right)^2 \left(K_{hh} - K_{hh}^{vac}\right) + o\left[\left(\frac{4\pi a_h}{m_h}\right)^3 \left(K_{hh} - K_{hh}^{vac}\right)^2\right], \tag{10.3.20}$$

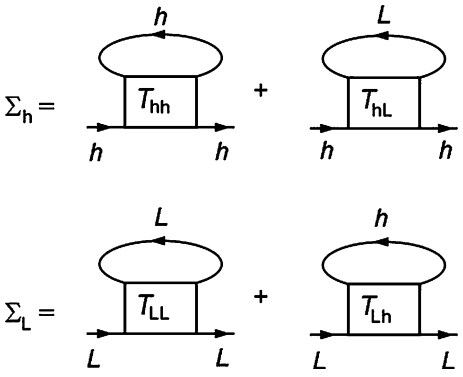

Fig. 10.10 The self-energies of heavy and light particles in the T-matrix approximation. T_{hh}, T_{LL}, T_{Lh}, and T_{hL} are full T-matrices of heavy and light particles in substance (see Ref. [47] in Chap. 9 and [6])

where

$$\frac{4\pi a_h}{m_h} \approx \frac{U_{hh} d^3}{\left(1 - U_{hh} d^3 K_{hh}^{vac}\right)} \tag{10.3.21}$$

coincides with the Kanamori approximation for the vacuum T-matrix and

$$K_{hh}^{vac}(\Omega, \vec{p}) = \int \frac{d^3\vec{p}'/(2\pi)^3}{\left(\Omega - \frac{(\vec{p}'+\vec{p})^2}{2m_h} - \frac{p'^2}{2m_h}\right)} \tag{10.3.22}$$

is the Cooper loop in vacuum (rigorously speaking the scattering length is defined by $K_{hh}^{vac}(0,0)$, but the difference between $K_{hh}^{vac}(\Omega, \vec{p})$ and $K_{hh}^{vac}(0,0)$ is proportional to the gas-parameter $a_h p_{Fh}$ and is small). K_{hh} in (10.3.20) is the full Cooper loop (cooperon) in substance for heavy particles given by (10.3.19). If we consider the low densities and the energies close to ε_F we can show that the terms neglected in T_{hh} are small with respect to the gas-parameter

$$\frac{4\pi a_h}{m_h}\left(K_{hh} - K_{hh}^{vac}\right) \sim a_h p_{Fh}. \tag{10.3.23}$$

The self-energy of heavy particles Σ_{hh} in the first two orders of the gas-parameter is given by:

$$\begin{aligned}\Sigma_{hh}(p) = &\sum_k T_{hh}(k+p) G_h(k) \approx \frac{4\pi a_h}{m_h} \sum_k G_h(k) \\ &- \left(\frac{4\pi a_h}{m_h}\right)^2 \sum_k \left(K_{hh} - K_{hh}^{vac}\right) G_h(k) + o(a_h p_{Fh})^3.\end{aligned} \tag{10.3.24}$$

The first term becomes $\frac{4\pi a_h}{m_h} n_h$ which is just the Hartree-Fock contribution (see Refs. [9, 30] in Chap. 9). In the second term we can make an analytic continuation $i\omega \to \omega + io$ for bosonic propagator K_{hh} and fermionic propagator G_h [29–31]. As a result (bearing in mind that $\mathrm{Im} K_{hh}^{vac} = 0$) we obtain the imaginary part of $\Sigma_{hh}^{(2)}$ as:

$$\begin{aligned}\mathrm{Im}\Sigma_{hh}^{(2)}(\varepsilon, \vec{p}) &= \left(\frac{4\pi a_h}{m_h}\right)^2 \sum_k \mathrm{Im} K_{hh}\left(\varepsilon_k + \varepsilon - \mu, \vec{k} + \vec{p}\right)\left[n_B(\varepsilon_k + \varepsilon - \mu) + n_F(\varepsilon_k - \mu)\right] \\ &= -\left(\frac{4\pi a_h}{m_h}\right)^2 \pi \int \frac{d^3\vec{k}}{(2\pi)^3} \int \frac{d^3\vec{p}'}{(2\pi)^3}\left[1 - n_h^F\left(\vec{p} + \vec{p}' + \vec{k}\right) - n_h^F(-\vec{p}')\right] \\ &\times \left[n_B(\varepsilon_k + \varepsilon - \mu) + n_F(\varepsilon_k - \mu)\right] \cdot \delta\left[\varepsilon + \varepsilon_h\left(\vec{k}\right) - \varepsilon_h\left(\vec{p} + \vec{p}' + \vec{k}\right) - \varepsilon_h(-\vec{p}') + \mu\right],\end{aligned} \tag{10.3.25}$$

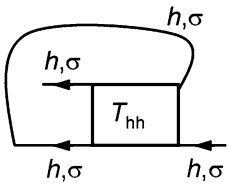

Fig. 10.11 An exchange—type diagram for the self-energy Σ_{hh}^{σ} which contains the matrix element $a_{\sigma}^{+}a_{\sigma}^{+}a_{\sigma}a_{\sigma}$ and thus is absent in the Hubbard model (see Ref. [47] in Chap. 9)

and similarly for the real part of $\Sigma_{hh}^{(2)}$:

$$\mathrm{Re}\Sigma_{hh}^{(2)}(\varepsilon,\vec{p})=\left(\frac{4\pi a_h}{m_h}\right)^2\sum_k\left[\mathrm{Re}K_{hh}\left(\varepsilon_k+\varepsilon-\mu,\vec{k}+\vec{p}\right)-\mathrm{Re}K_{hh}^{vac}\left(\varepsilon_k+\varepsilon_p-2\mu,\vec{k}+\vec{p}\right)\right]$$
$$*\left[n_B(\varepsilon_k+\varepsilon-\mu)+n_F(\varepsilon_k-\mu)\right], \tag{10.3.26}$$

where for the real part of a Cooper loop in vacuum we have:

$$\mathrm{Re}K_{hh}^{vac}\left(\varepsilon_k+\varepsilon_p,\vec{k}+\vec{p}\right)=\int\frac{d^3\vec{p'}}{(2\pi)^3}P\frac{2m_h}{\vec{k}^2+\vec{p}^2-\left(\vec{p'}+\vec{k}+\vec{p}\right)^2-\vec{p'}^2}. \tag{10.3.27}$$

Thus $\mathrm{Re}K_{hh}^{vac}$ is calculated in resonance for $\Omega=\varepsilon_k+\varepsilon_p$ (or for $\varepsilon=\varepsilon_p$ - μ), where P is the principal value. In (10.3.25) and (10.3.26) $n_B(\Omega)=\frac{1}{(e^{\Omega/T}-1)}$ and $n_F(\Omega)=\frac{1}{(e^{\Omega/T}+1)}$ are the bosonic and fermionic distribution functions and hence:

$$n_B(\varepsilon_k+\varepsilon-\mu)+n_F(\varepsilon_k-\mu)=\frac{1}{2}\left[cth\frac{(\varepsilon_k+\varepsilon)-\mu}{2T}+th\frac{\varepsilon_k-\mu}{2T}\right]. \tag{10.3.28}$$

The real part of a Cooper loop in substance for heavy particles is given by:

$$\mathrm{Re}K_{hh}\left(\varepsilon_k+\varepsilon-\mu,\vec{k}+\vec{p}\right)=\int\frac{d^3\vec{p'}}{(2\pi)^3}\frac{\left[1-n_h^F\left(\vec{p}+\vec{p'}+\vec{k}\right)-n_h^F\left(-\vec{p'}\right)\right]}{\left[\varepsilon+\varepsilon_h\left(\vec{k}\right)-\varepsilon_h\left(\vec{p}+\vec{p'}+\vec{k}\right)-\varepsilon_h\left(-\vec{p'}\right)+\mu\right]}. \tag{10.3.29}$$

The analytic continuation for $\Sigma_{hh}^{(2)}$ in a 2D case is similar to the one in the 3D case.

We note that for $T\to 0$, the bosonic distribution function $n_B(\Omega)\to 0$ and the fermionic distribution function $n_F(\Omega)\to\theta(\Omega)$—to the step-function. Hence at low temperatures $\mathrm{Im}\Sigma_{hh}$ and $\mathrm{Re}\Sigma_{hh}$ acquire the standard form (see Refs. [9, 30, 31] in Chap. 9). We will analyze their behavior at finite temperatures more detaily in Chap. 14.

Note that for higher temperatures we should keep in mind that $n_B(\Omega) \to T/\Omega$ for $T \gg \Omega$. The fermionic distribution function is "washed out" by temperature. Accordingly, $n_F(\Omega) = \frac{1}{2}\left(1 - \frac{\Omega}{2T}\right)$. These approximations are important when we evaluate $\mathrm{Im}\Sigma$ for higher temperatures $T > W_h$ in Chap. 14 (see Ref. [47] in Chap. 9 and [6]).

We note that in contrast with the model of slightly non-ideal Fermi-gas (see Refs. [9, 30, 31] in Chap. 9) the Hubbard model does not contain an exchange-type diagram for Σ_{hh} (see Fig. 10.11) because the T-matrix in this diagram corresponds to incoming and outgoing heavy particles with the same spin-projection $a_\sigma^+ a_\sigma^+ a_\sigma a_\sigma$, while the Hubbard model contains only the matrix elements $a_\uparrow^+ a_\downarrow^+ a_\downarrow a_\uparrow$ with different spin-projections.

We also note that when we expand the T-matrix up to the second order in the gas-parameter, we implicitly assume that the T-matrix itself does not have a simple pole structure of the type of a bosonic propagator. This is a case for a partially filled heavy band $n_h d^D \ll 1$ and the low energy sector where $0 < \varepsilon < W_h \ll U_{hh}$. Effectively we neglect the lattice in this expansion.

However if we take the lattice into account, then in case of repulsive Hubbard interaction U_{hh} we will get two poles for the full (unexpanded) T-matrix of heavy particles in (10.3.18). The first one is connected with the so-called antibound state predicted by Hubbard (see Refs. [1–4] in Chap. 9) and Anderson [32–34] and corresponds to large positive energy:

$$\varepsilon \sim U_{hh} > 0. \tag{10.3.30}$$

Physically it describes an antibound pair of two heavy particles with the energy of U_{hh} on the same lattice site. It therefore reflects the presence of the upper Hubbard band already at low densities $n_h d^D \ll 1$ [35]. But we will show that the intensity of the upper Hubbard band (UHB) is small at low densities and for low energy sector. The more detailed discussion of the antibound state will be a subject of Chap. 14.

A second pole in the full T-matrix found by [36–38] corresponds to negative energy and in the 2D case yields:

$$\varepsilon \approx -2\varepsilon_{Fh} - \frac{2\varepsilon_{Fh}^2}{W_h} < 0. \tag{10.3.31}$$

It describes the bound state of the two holes below the bottom of the heavy band ($\varepsilon < -2\varepsilon_{Fh}$). Therefore, it has zero imaginary part and does not contribute to $\mathrm{Im}T$. (This mode produces nonanalytic corrections to $\mathrm{Re}\Sigma_{hh} \sim |\varepsilon|^{5/2}$ in 2D). We will also consider this mode more detaily in Chap. 14. In the forthcoming Sections we can neglect both these two contributions to the T-matrices and self-energies.

10.3.4 Electron Polaron Effect

For temperatures $T \to 0$ the one-particle Green's functions for heavy and light electrons are given by (see Refs. [30, 31] in Chap. 9):

$$G_h(\omega, \vec{q}) = \frac{1}{(\omega - \varepsilon_h(q) + \mu - \Sigma_h(\omega, \vec{q}))} \approx \frac{Z_h}{(\omega - \varepsilon_h^*(q) + \mu + io)}, \quad (10.3.32)$$

and respectively

$$G_L(\omega, \vec{q}) \approx \frac{Z_L}{(\omega - \varepsilon_L^*(q) + \mu + io)}, \quad (10.3.33)$$

where according to Galitskii (see Ref. [9] in Chap. 9):

$$\varepsilon_h^*(q) - \mu = \frac{(q^2 - p_{Fh}^2)}{2m_h^*} \text{ and } \varepsilon_L^*(q) - \mu = \frac{(q^2 - p_{FL}^2)}{2m_L^*} \quad (10.3.34)$$

are renormalized quasiparticle spectra, and

$$Z_h^{-1} = \left(1 - \frac{\partial \mathrm{Re}\Sigma_h^{(2)}(\omega, \vec{q})}{\partial \omega}\bigg|_{\substack{\omega \to 0 \\ q \to p_{Fh}}}\right); \; Z_L^{-1} = \left(1 - \frac{\partial \mathrm{Re}\Sigma_L^{(2)}(\omega, \vec{q})}{\partial \omega}\bigg|_{\substack{\omega \to 0 \\ q \to p_{FL}}}\right) \quad (10.3.35)$$

are inverse Z-factors (see Ref. [30, 31] in Chap. 9), [39, 40] of heavy and light electrons. The leading contribution to $\mathrm{Im}\Sigma_h^{(2)}$ in (10.3.35) comes from the substitution of $\mathrm{Re}\Sigma_{hL}^{(2)}(\omega, \vec{q})$ to Z_h^{-1}, which is described by a formula similar to (10.3.26), and yields:

$$1 - Z_h^{-1} = \lim_{\substack{\omega \to 0 \\ q \to p_{Fh}}} \frac{\partial \mathrm{Re}\Sigma_{hL}^{(2)}(\omega, \vec{q})}{\partial \omega} \sim -\left(\frac{4\pi a_{hL}}{m_{hL}^*}\right)^2 \iint \frac{d^D\vec{p}}{(2\pi)^D} \frac{d^D\vec{p}'}{(2\pi)^D} \cdot \frac{\left[1 - n_L^F(\vec{p}' + \vec{p}) - n_h^F(-\vec{p}')\right] n_L^F(\vec{p} - \vec{q})}{\left[\varepsilon_L(\vec{p} - \vec{q}) - \varepsilon_L(\vec{p}' + \vec{p}) - \varepsilon_h(-\vec{p}') + \mu\right]^2}, \quad (10.3.36)$$

where $n_B(\Omega) \to 0$, $n_F(\Omega)$ is a step function for $\Omega/T \gg 1$; $a_{hL} \approx d$ in 3D is connected with the vacuum T-matrix T_{hL}, and $m_{hL}^* \approx m_L$. Replacing in (10.3.36) $\frac{d^D\vec{p}}{(2\pi)^D}\frac{d^D\vec{p}'}{(2\pi)^D}$ by $N_L^2(0)d\xi_L(\vec{p})d\xi_L(\vec{p}\prime)$ (where $\xi_L(p) = \varepsilon_L(p) - \mu$, $N_L(0)$ is a density of states of light particles, $D = 2, 3$), and taking into account that in (10.3.36) $\varepsilon_L(\vec{p} - \vec{q}) - \mu < 0$ while $\varepsilon_L(\vec{p}' + \vec{p}) - \mu > 0$ we can easily verify that for $m_h \gg m_L$ or equivalently for $\varepsilon_{FL} \gg \varepsilon_{Fh}$ this expression contains a large logarithm both in 3D and 2D cases (see [24, 25]). Hence, the Z-factor of the heavy particles in 3D in the leading approximation in the gas-parameter $\lambda = 2dp_{FL}/\pi$ is given by:

$$Z_h^{-1} \approx 1 + 2\lambda^2 \ln \frac{m_h}{m_L}. \tag{10.3.37}$$

Correspondingly, in 2D:

$$Z_h^{-1} = 1 + 2f_0^2 \ln \frac{m_h}{m_L}, \tag{10.3.38}$$

where $f_0 = \frac{1}{2\ln(1/p_{FL}d)}$ is 2D gas-parameter of Bloom.

We note that the contribution to Z_h^{-1} from $\mathrm{Re}\Sigma_{hh}{}^{(2)}$ does not contain a large logarithm and thus is smaller than the contribution from $\mathrm{Re}\Sigma_{hL}{}^{(2)}$ at low electron density. The analogous calculation for Z_L with $\mathrm{Re}\Sigma_{LL}{}^{(2)}$ and $\mathrm{Re}\Sigma_{Lh}{}^{(2)}$ yields only $Z_L^{-1} \sim 1 + \lambda^2$ in 3D and $Z_L^{-1} \sim 1 + f_0^2$ in 2D (does not contain a large logarithm).

Correspondingly for the effective mass of a heavy particle according to (see Ref. [31] in Chap. 9), [39, 40] we have:

$$\frac{m_h}{m_h^*} = Z_h \left(1 + \frac{\partial \mathrm{Re}\Sigma_{hL}^{(2)}(\varepsilon_h(\vec{q}) - \mu, \vec{q})}{\partial \xi_h(\vec{q})}\bigg|_{\varepsilon_h(q) \to \mu} \right), \tag{10.3.39}$$

where the second term in brackets corresponds to the momentum dependence of the self-energy Σ_{hL}, and $\xi_h(\vec{p}) = \varepsilon_h(\vec{p}) - \mu$.

Note that as usual the Z-factor contributes to the enhancement of a heavy mass:

$$\frac{m_h^*}{m_h} \sim Z_h^{-1} \sim \left(1 + 2\lambda^2 \ln \frac{m_h}{m_L} \right) \text{in 3D}. \tag{10.3.40}$$

Analogous calculations for Z-factor contribution to the light mass yields only (as we discussed already)

$$\frac{m_L^*}{m_L} \sim Z_L^{-1} \sim 1 + \lambda^2 \text{ in 3D} \tag{10.3.41}$$

If the effective parameter $2\lambda^2 \ln(m_h/m_L) > 1$ we are in the situation of strong electron polaron effect (strong EPE). To obtain the correct polaron exponent in this region of parameters diagrammatically, we should sum up at least the so-called maximally crossed diagrams for $\mathrm{Re}\Sigma_{hL}$ [41]. But this exponent can be also evaluated in a different manner, based on the non-adiabatic part of the many particle wave-function [24, 25] which describes the heavy particle dressed in a cloud of virtual electron—hole pairs of light particles. This yields:

$$\frac{m_h^*}{m_h} \sim Z_h^{-1} = \left(\frac{m_h}{m_L} \right)^{\frac{b}{(1-b)}}, \tag{10.3.42}$$

where $b = 2\lambda^2$ in 3D and $b = 2f_0^2$ in 2D.

For $b = ½$ or equivalently for $\lambda = ½$ in 3D or $f_0 = ½$ in 2D (as for the coupling constant for screened Coulomb interaction in 3D and 2D electron plasma in the RPA-theory—see preceding Sect. 10.2 of this chapter), we are in the so-called unitary limit. In this limit according to [24, 25] the polaron exponent:

$$\frac{b}{(1-b)} = 1, \tag{10.3.43}$$

and hence:

$$\frac{m_h^*}{m_h} = \frac{m_h}{m_L}, \tag{10.3.44}$$

or equivalently:

$$\frac{m_h^*}{m_L} = \left(\frac{m_h}{m_L}\right)^2. \tag{10.3.45}$$

Thus starting from the ratio between the bare masses $m_h/m_L \sim 10$ (obtained, for instance, in LDA-approximation [42]) we finish in the unitary limit with $m_h^*/m_{Lh} \sim 100$ (due to many-body electron-polaron effect), which is a typical ratio for uranium-based heavy-fermion systems [43–47].

10.3.5 Other Mechanisms of Heavy Mass Enhancement

We note that rigorously speaking [see (10.3.39)] the momentum dependence of $\mathrm{Re}\Sigma_{hL}^{(2)}(\varepsilon_h(\vec{q}) - \mu, \vec{q})$ is also very important for the evaluation of the effective mass. Preliminary estimates of Prokof'ev, Kagan (see [6, 48] and Ref. [47] in Chap. 9) show that in the zeroth approximation in m_L/m_h in 3D case close to the Fermi-surface (for $\varepsilon_h(\vec{q}) - \mu = \left(q^2 - p_{Fh}^2\right)/2m_h \to 0$ and $q \to p_{Fh}$):

$$\mathrm{Re}\Sigma_{hL}^{(2)}(\varepsilon_h(\vec{q}) - \mu, \vec{q}) \approx 2\left(\frac{4\pi a_{hL}}{m_L}\right)^2 \int \frac{d^3\vec{p}}{(2\pi)^3} \Pi_{LL}(0,\vec{p}) n_h^F(\vec{p} - \vec{q}), \tag{10.3.46}$$

where [see also (9.3.4)]

$$\Pi_{LL}(0,\vec{p}) = \int \frac{d^3\vec{p}'}{(2\pi)^3} \frac{\left[n_L^F(\varepsilon_{p'+p} - \mu) - n_L^F(\varepsilon_{p'} - \mu)\right]}{\varepsilon_L(\vec{p}') - \varepsilon_L(\vec{p}' + \vec{p})} \tag{10.3.47}$$

is a static polarization operator for light particles. Having in mind that $|\vec{p} - \vec{q}| < p_{Fh}$ and $q \approx p_{Fh}$ we can see that $\vec{p} \to 0$ and use the asymptotic form for $\Pi_{LL}(0,\vec{p})$ at small $p \ll p_{FL}$ (if the densities of heavy and light bands are not very different and $p_{FL} \sim p_{Fh}$):

$$\lim_{p\to 0}\Pi_{LL}(0,\vec{p}) = N_L^{3D}(0)\left[1-\frac{p^2}{12p_{FL}^2}\right], \tag{10.3.48}$$

where $N_{\rm L}^{3D}(0) = m_{\rm L}p_{\rm FL}/2\pi^2$ is the density of states for light electrons in 3D. The substitution of $\lim_{p\to 0}\Pi_{LL}(0,\vec{p})$ from (10.3.48) to (10.3.46) yields:

$$\mathrm{Re}\Sigma_{hL}^{(2)}(\varepsilon_h(\vec{q})-\mu,\vec{q}) \approx \mathrm{Re}\Sigma_{hL}^{(2)}(0,p_{Fh}) - \frac{\left(q^2-p_{Fh}^2\right)}{2m_h}\frac{\lambda^2}{9}\frac{m_h n_h}{m_L n_L}, \tag{10.3.49}$$

where $\lambda = 2dp_{FL}/\pi$ is a 3D gas parameter, $n_{\rm h} = p_{\rm Fh}^3/3\pi^2, n_{\rm L} = p_{\rm FL}^3/3\pi^2$ are the densities of heavy and light bands.

The first term in (10.3.49) describes $\mathrm{Re}\Sigma_{hL}^{(2)}(\varepsilon_h(\vec{q})-\mu,\vec{q})$ on the Fermi-surface (for $\varepsilon_{\rm h}(q)-\mu = 0$ and $q = p_{\rm Fh}$). It reads:

$$\mathrm{Re}\Sigma_{hL}^{(2)}(0,p_F) \approx \frac{4\lambda^2}{3}\frac{n_h}{n_L}\varepsilon_{FL}\left(1-\frac{2p_{Fh}^2}{15p_{FL}^2}\right) > 0 \text{ for } p_{\rm FL}\sim p_{\rm Fh}. \tag{10.3.50}$$

It is renormalization of the effective chemical potential of the heavy band in the second order of the gas parameter due to the interaction of light and heavy particles.

We note that according to Refs. [30, 31] in Chap. 9 the renormalized heavy-particle spectrum is given by:

$$\varepsilon_h^*(q)-\mu = \left(\frac{q^2}{2m_h}-\mu_h^{eff}\right)+\frac{2\pi}{m_L}n_L(\mu)a_{hL}+\mathrm{Re}\Sigma_{hL}^{(2)}(\varepsilon_h(\vec{q})-\mu,\vec{q}) = \frac{\left(q^2-p_{Fh}^2\right)}{2m_h^*}, \tag{10.3.51}$$

where the scattering length $a_{\rm hL} \approx d$, an effective chemical potential $\mu_h^{eff} = \mu_h + W_h/2 + \varepsilon_0$ is counted from the bottom of a heavy band, and the Hartree-Fock term $\frac{2\pi}{m_L}n_L(\mu)a_{hL}$ represents the contribution to the self-energy $\mathrm{Re}\Sigma_{\rm hL}^{(1)}$ in the first-order in the gas parameter. From (10.3.51) collecting the terms proportional to $\varepsilon_h(\vec{q})-\mu = \left(q^2-p_{Fh}^2\right)/2m_h$ we obtain:

$$\frac{\left(q^2-p_{Fh}^2\right)}{2m_h^*} = \left[\varepsilon_h(q)-\mu\right]\left(1-\frac{\lambda^2}{9}\frac{m_h n_h}{m_L n_L}\right). \tag{10.3.52}$$

Correspondingly, the effective mass of a heavy particle is given by:

$$\frac{m_h}{m_{h*}} = 1+\left.\frac{\partial\mathrm{Re}\Sigma_{hL}^{(2)}(\varepsilon_h(q)-\mu,q)}{\partial(\varepsilon_h(q)-\mu)}\right|_{\varepsilon_h(q)\to\mu} = 1-\frac{\lambda^2}{9}\frac{m_h n_h}{m_L n_L}. \tag{10.3.53}$$

As a result we obtain much more dramatic (linear in $m_{\rm h}/m_{\rm L}$) enhancement of $m_{\rm h}^*$ than in EPE (which yields only logarithmic in $m_{\rm h}/m_{\rm L}$ enhancement $m_{\rm h}/m_{\rm h}* \sim 1 - 2\lambda^2\ln(m_{\rm h}/m_{\rm L})$ due to the Z-factor of a heavy particle). For $m_{\rm h}/m_{\rm L} \sim 10$ the contribution to $m_{\rm h}^*$ in (10.3.53) becomes larger than the contribution to Z-factor in

(10.3.40) for a large density mismatch $n_h \geq 5n_L$ between the heavy and light bands. In general in the second order of the gas parameter in 3D:

$$\frac{m_h*}{m_h} = 1 + \frac{\lambda^2}{9}\frac{m_h n_h}{m_L n_L} + 2\lambda^2 \ln\frac{m_h}{m_L}. \tag{10.3.54}$$

We note that the contribution to m_h^*/m_h from $\mathrm{Re}\Sigma_{hh}^{(2)}(\varepsilon_h(q) - \mu, \vec{q})$ associated with the "heavy–heavy" interaction is small in comparison with the contribution to m_h^* from $\mathrm{Re}\Sigma_{hL}^{(2)}$ (which is associated with "heavy-light" interaction) due to the smallness of the ratio between the bare masses: $m_L/m_h \ll 1$. We can now collect the terms which do not depend upon $\varepsilon_h(q) - \mu$ in (10.3.51). This gives the effective chemical potential of heavy electrons:

$$\mu_h^{eff} = \frac{p_{Fh}^2}{2m_h} + \frac{2\pi}{m_L} n_L(\mu) a_{hL} + \mathrm{Re}\Sigma_{hL}^{(2)}(0, p_{Fh}). \tag{10.3.55}$$

We note that the contributions to μ_h^{eff} from the Hartree-Fock term $\frac{2\pi}{m_L} n_L(\mu) a_{hL}$ of heavy electrons and from $\mathrm{Re}\Sigma_{hh}^{(2)}(0, p_{Fh})$ (which is connected with "heavy–heavy" interaction) are small in comparison with "heavy-light" contributions due to the smallness of the ratio between the bare masses: $m_L/m_h \ll 1$.

2D situation.

In 2D the static polarization operator for light particles is [6, 49], and (see Ref. [47] in Chap. 9):

$$\Pi_{LL}(0, \vec{p}) = \frac{m_L}{2\pi}\left[1 - \mathrm{Re}\sqrt{1 - \frac{4p_{FL}^2}{p^2}}\right], \tag{10.3.56}$$

and hence for $p < 2p_{\mathrm{FL}}$: $\Pi_{LL}(0, \vec{p}) = \frac{m_L}{2\pi}$—does not contain any dependence on p^2 in contrast to the 3D case. Thus, EPE in 2D is a dominant mechanism of the heavy mass enhancement and in general in the second order of the gas parameter $\frac{m_h*}{m_h} = 1 + 2f_0^2 \ln\frac{m_h}{m_L}$; $\frac{m_L*}{m_L} \sim 1 + f_0^2$ in 2D.

In the end of this Subsection we would like to note that the important role of the interband ("heavy"-"light") Hubbard repulsion U_{hL} for the formation of a heavy mass $m^* \sim 100\, m_e$ in a two-band Hubbard model was also emphasized in [50] for the LiV_2O_4 HF compound.

The tendency towards phase-separation.

We also note that for large density mismatch $n_h \gg n_L$ we could have a tendency towards phase-separation in a two-band model [6] in 3D. Namely if we evaluate the partial compressibility of the heavy component (the sound velocity of heavy particles squared):

$$\kappa_{hh}^{-1} \sim c_h^2 = \frac{n_h}{m_h}\left(\frac{\partial \mu_h^{eff}}{\partial n_h}\right) \tag{10.3.57}$$

we already see the tendency towards phase-separation $\kappa_{hh}^{-1} < 0$ (towards negative compressibility) in the strong coupling limit and low densities $\lambda^2 \frac{m_h p_{Fh}}{m_L p_{FL}} \geq 1$ in qualitative agreement with a more phenomenological (mean-field type) variational approach [27].

The tendency towards phase-separation at low electron fillings also manifests itself for the asymmetric Hubbard model (where only interband Hubbard repulsion U_{hL} between heavy and light electrons is present and intraband Hubbard repulsions U_{hh} and U_{LL} are absent) in the limit of strong asymmetry $t_h \ll t_L$ [51] between heavy and light bandwidths.

In the end of this Section we emphasize that the physics of EPE and evaluation of Z_h in [24, 25] are to some extent connected with the well-known results of Nozieres et al. [26, 52] on infrared divergences in the description of the Brownian motion of a heavy particle in a Fermi-liquid [53, 54] and on the infrared divergences for the problem of X-ray photoemission from the deep electron levels, as well as with the famous results of Anderson [55, 56] on the orthogonality catastrophe for the 1D chain of N electrons under the addition of one impurity to the system.

Finally we mention a competing mechanism [57–60] proposed by Fulde for the explanation of the effective mass in praseodymium (Pr) and in some uranium-based molecules like $U(C_8H_8)_2$. Later on Fulde et al. [58–60] generalized this mechanism on some other uranium-based heavy-fermion (HF) compounds with localized and delocalized orbitals. This mechanism has a quantum-chemical nature and is based on the scattering of conductive electrons on localized orbitals as if on the two-level systems. The mass-enhancement is here governed by non-diagonal matrix elements of the Coulomb interaction which are not contained in the simple version of a two-band model (10.3.1). In this context we also mention [61] where the authors considered the mass-enhancement of conductivity electrons due to their scattering on local f-levels splitted by the crystalline field.

We note that de Haas van Alphen (dHvA) experiments [62–65] together with ARPES (angle-resolved photoemission spectroscopy) experiments [66, 67] and thermodynamic measurements [44, 45, 68] are the main instruments to reconstruct the Fermi-surface for HF-compounds and to determine the effective mass (thus verifying the predictions of different theories regarding the mass enhancement in uranium-based HF-compounds).

10.3.6 Anomalous Superconductivity in the Two-Band Model with One Narrow Band

For the sake of completeness let us consider briefly superconductivity problem in the same type of models [5] and namely in the two-band model with narrow band [6]. Let us concentrate on a 2D case where critical temperatures are higher already at low densities and consider the most typical case (see Fig. 10.8) $m_h > m_L$ and

$p_{Fh} > p_{FL}$. We assume however, that still the mismatch between the densities is not large enough to produce phase-separation. Note that in 2D case where only EPE is present the restrictions on a homogeneous state could be more mild than in a 3D case. At low densities $n_L d^2 < n_h d^2 \ll 1$ the maximal T_C corresponds to p-wave pairing and is governed by the enhanced Kohn-Luttinger mechanism of SC (see Ref. [10] in Chap. 9), [1, 5]. The general expression for the effective interaction U_{eff} of the heavy particles (for the irreducible bare vertex for the Cooper channel) in the first two orders in the gas-parameter reads:

$$U_{eff}\left(\vec{p}_h, \vec{p}'_h\right) = T_{hh} + T_{hh}^2 \Pi_{hh}\left(0, \tilde{\vec{q}}_h = \vec{p}_h + \vec{p}'_h\right) - 2T_{hL}^2 \Pi_{LL}\left(0, \vec{q}_h = \vec{p}_h - \vec{p}'_h\right), \tag{10.3.58}$$

where $\vec{p}_h$ and $\vec{p}'_h$ are incoming and outgoing momenta for the heavy particles in the Cooper channel, $|\vec{p}_h| = |\vec{p}'_h| = p_{Fh}$ and:

$$q_h^2 = 2p_{Fh}^2(1 - \cos\varphi);\ \tilde{q}_h^2 = 2p_{Fh}^2(1 + \cos\varphi) \tag{10.3.59}$$

are transferred momentum squared (for q_h^2) and transferred momentum with an account of crossing squared (for $\tilde{q}_h^2$). These formulas are exactly analogous to (9.3.11), (9.3.16) but correspond to 2D case, φ is an angle between $\vec{p}_h$ and $\vec{p}'_h$. Note that, as we discussed in Chap. 9, both transferred momenta $q_h \le 2p_{Fh}$ and $\tilde{q}_h \le 2p_{Fh}$ for superconductivity problem. The second term in (10.3.58) is connected with an exchange diagram [see Fig. 9.2 and (9.3.10)] for heavy electrons while the third term with is a static polarization operator (10.3.47) for light electrons.

In (10.3.58) for Π_{hh} and Π_{LL} we get:

$$\begin{aligned}
\Pi_{hh}\left(0, \tilde{\vec{q}}_h\right) &= Z_h^2 \frac{m_h^*}{2\pi}\left[1 - \mathrm{Re}\sqrt{1 - \frac{4p_{Fh}^2}{\tilde{q}_h^2}}\right], \\
\Pi_{LL}(0, \vec{q}_h) &= Z_L^2 \frac{m_L^*}{2\pi}\left[1 - \mathrm{Re}\sqrt{1 - \frac{4p_{FL}^2}{q_h^2}}\right],
\end{aligned} \tag{10.3.60}$$

where Z_h and m_h^* are the Z-factor and the effective mass of heavy particles, Z_L and m_L^* are the Z-factor and the effective mass of light particles, p_{Fh} and p_{FL}—are Fermi-momenta for heavy and light particles. Having in mind that $Z_L \sim m_L/m_L^* \sim (1 - f_0{}^2)$, we can put $Z_L \sim 1$ and $m_L^* \sim m_L$ in all the forthcoming estimates. Finally in (10.3.58) for $p_{Fh} > p_{FL}$ the Kanamori T-matrices read in the strong coupling case in 2D:

$$T_{hh} = \frac{4\pi}{m_h^*} \frac{1}{\ln\left(\frac{1}{p_{Fh}^2 d^2}\right)} > 0,\ T_{hL} = \frac{4\pi}{m_L^*} \frac{1}{\ln\left(\frac{1}{p_{Fh}^2 d^2}\right)} > 0. \tag{10.3.61}$$

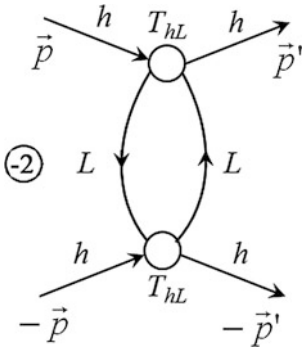

Fig. 10.12 The leading contribution to the effective interaction U_{eff} for the p-wave pairing of heavy particles via polarization of light particles. The open circles stand for the vacuum T-matrix T_{hL} [5, 6]

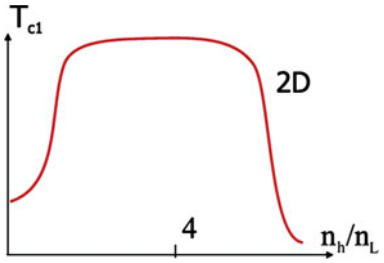

Fig. 10.13 Dependence of the critical temperature T_{C1} from the relative filling of heavy and light bands $n_{\text{h}}/n_{\text{L}}$ in the two-band model with one narrow band. The maximum for T_{C1} corresponds to $n_{\text{h}}/n_{\text{L}} = 4$ in 2D [3–6]

Having in mind that $\tilde{q}_h \leq 2p_{Fh}$ we get that: $\Pi_{hh}\left(0, \tilde{\vec{q}}_h\right) = Z_h^2\, m_h^*/2\pi$ and does not contain any dependence upon transferred momentum with crossing $\tilde{q}_h$.

In the same time $\Pi_{LL}(0, \vec{q}_h)$ contains nontrivial dependence upon q_{h} for $p_{\text{Fh}} > p_{\text{FL}}$. We can say [1, 5, 6] that large 2D Kohn's anomaly becomes effective for SC—problem already in the second order of the gas-parameter and we have the pairing of heavy electrons via polarization of light electrons (see Fig. 10.12).

Note that a standard s-wave pairing is suppressed in a two-band Hubbard model by short-range Hubbard repulsion which yields $T_{\text{hh}} > 0$ in the first-order contribution to U_{eff} in (10.3.58).

According to Landau-Thouless criterion (see Ref. [30] in Chap. 9) the maximal critical temperature in our model corresponds to triplet p-wave pairing (to pairing with magnetic quantum number $m = 1$ in 2D) and reads:

$$-U_{eff}^{m=1} N_{2D}^{h*}(0) Z_h^2 \ln \frac{\varepsilon_{Fh}^*}{T_{C1}} = 1, \tag{10.3.62}$$

where $N_{2D}^{h^*}(0) = m_{\text{h}}^*/2\pi$ is an effective 2D density of states for heavy electrons with effective heavy mass m_{h}^*; $\varepsilon_{\text{Fh}}^* = p_{\text{Fh}}^2/2m_{\text{h}}^*$—is renormalized Fermi-energy for heavy electrons; $U_{\text{eff}}^{m=1}$ is a p-wave harmonic of the effective interaction. It is given by:

$$U_{eff}^{m=1} = \int_0^{2\pi} U_{eff}[q(\cos\varphi)]\cos\varphi\frac{d\varphi}{2\pi} \tag{10.3.63}$$

It is shown in [1, 5, 6] that $U_{eff}{}^{m=1}$ depends upon relative occupation of the two bands $p_{\mathrm{Fh}}/p_{\mathrm{FL}}$ and yields:

$$U_{eff}^{m=1} = N_{2D}^{L^*}(0)\frac{(p_{Fh}/p_{FL}-1)}{\left(p_{Fh}^2/p_{FL}^2\right)}T_{hL}^2(-2)<0, \tag{10.3.64}$$

where $m = 1$ is magnetic quantum number in 2D.

Moreover it corresponds to attraction. In (10.3.64) $N_{2D}^{L^*}(0) = m_L^*/2\pi$ is effective 2D density of states for light electrons. We can see that $U_{eff}{}^{m=1} \to 0$ for $p_{\mathrm{Fh}}/p_{\mathrm{FL}} \to 1$ and $p_{\mathrm{Fh}}/p_{\mathrm{FL}} \to \infty$. It is easy to show that $U_{eff}{}^{m=1}$ has rather large and broad maximum [1, 5, 6] for $p_{\mathrm{Fh}} = 2p_{\mathrm{FL}}$ or equivalently for $n_{\mathrm{h}} = 4n_{\mathrm{L}}$ (see Fig. 10.13). In maximum an effective interaction reads:

$$U_{eff}^{m=1} = -\frac{1}{2}N_{2D}^{L^*}(0)\left(\frac{4\pi}{m_L^*\ln\left(1/p_{Fh}^2d^2\right)}\right)^2. \tag{10.3.65}$$

Correspondingly Landau-Thouless criterion for superconducting temperature T_{C1} yields:

$$\frac{m_h^*}{m_L^*}Z_h^2 2f_0^2\ln\frac{\varepsilon_{Fh}^*}{T_{C1}} = 1, \tag{10.3.66}$$

where $f_0 = \frac{1}{\ln\left(1/p_{Fh}^2d^2\right)}$ is a 2D gas parameter. For $f_0^2\ln\frac{m_h}{m_L} \le 1$ EPE is weak and $m_h^* \approx m_h$. Thus, $Z_h \approx 1$, $\varepsilon_{Fh}^* \approx \varepsilon_{Fh}$ and Landau-Thouless criterion reads: $\left(\frac{m_h}{m_L}\right)2f_0^2\ln\frac{\varepsilon_{Fh}}{T_{c1}} = 1$. An effective gas-parameter which enters the formula for T_{C1} for weak EPE is thus $f_0\left(\frac{m_h}{m_L}\right)^{1/2}$. In the weak-coupling Born approximation for $U_{hh} \sim U_{hL} \sim U_{LL} < W_h < W_L$ the critical temperature $T_{C1} \sim \varepsilon_{Fh}\exp\left\{-\frac{1}{2\tilde{f}_0^2}\right\}$, where $\tilde{f}_0 = \frac{\sqrt{m_Lm_h}U_{hL}}{4\pi}$ is connected with interband Hubbard interaction U_{hL} and proportional to geometric average of heavy and light masses $\sqrt{m_Lm_h}$ (see Ref. [45] in Chap. 9, [5]). In the opposite strong-coupling case $U_{hL} > W_h > W_L$ and weak EPE the critical temperature $T_{C1} \sim \varepsilon_{Fh}\exp\left\{-\frac{1}{2\tilde{f}_0^2}\right\}$ with an effective gas-parameter:

$$\tilde{f}_0 = \sqrt{\frac{m_h}{m_L}}\frac{1}{\ln\left(\frac{1}{p_{Fh}^2d^2}\right)}. \tag{10.3.67}$$

It is interesting to emphasize that in the unitary limit $f_0 \to ½$ the strong EPE yields for the heavy-mass enhancement $m_h^*/m_L \sim (m_h/m_L)^2$ and for Z-factor of heavy particle $Z_h \sim m_h/m_h^* \sim m_L/m_h$.

If we assume that still $m_L^* \approx m_L$ even in the unitary limit (for $f_0^2 = 1/4$) then we get for the combination $\frac{m_h*}{m_L*} Z_h^2$ in (10.3.66):

$$\frac{m_h*}{m_L*} Z_h^2 \sim \frac{m_h*}{m_L} \left(\frac{m_h}{m_h*}\right)^2 \sim \frac{m_h^2}{m_L^2} \frac{m_L^2}{m_h^2} \sim 1. \tag{10.3.68}$$

Thus for the critical temperature T_{C1} in the unitary limit $f_0 \to 1/2$ we can get:

$$T_{C1} \sim \varepsilon_{Fh}^* \exp\left\{-\frac{1}{2f_0^2}\right\} \sim \varepsilon_{Fh}^* e^{-2}. \tag{10.3.69}$$

It means that for typical (for uranium-based HF compounds) values of $\varepsilon_{\mathrm{Fh}}^* \sim (30 \div 50)$ K the critical temperatures are in the range of 5 K already at low density which is quite reasonable.

Note that in a phase-separated state we have the droplets (clusters) with the density-ratio n_h/n_L larger or smaller than the density ratio in a homogeneous state [6]. For example in a fully phase-separated state we have two large clusters (1, 2) with $n_{h1} > n_h > n_{h2}$ (that is so-called Maxwell construction [69] typical for phase-separated systems and first-order phase transitions). Thus, the expression (10.3.64) for the critical temperature T_{C1} as a function of relative occupation is valid for both clusters, but with local values of $(p_{Fh}/p_{FL})_1$ and $(p_{Fh}/p_{FL})_2$. Correspondingly the critical temperatures will be different for these two clusters at least in zeroth approximation when we neglect the Josephson coupling or proximity effect [11, 29–31] between the neighboring clusters or droplets.

To finish the consideration of SC in the two-band model let us discuss briefly an effective interaction (irreducible bare vertex) for light electrons in the Cooper channel. It reads:

$$U_{eff}(\vec{p}_L, \vec{p}'_L) = T_{LL} + T_{LL}^2 \Pi_{LL}\left(0, \tilde{\vec{q}}_L = \vec{p}_L + \vec{p}'_L\right) - 2T_{hL}^2 \Pi_{hh}((0, \vec{q}_L = \vec{p}_L - \vec{p}'_L), \tag{10.3.70}$$

where incoming and outgoing momenta $|\vec{p}_L| = |\vec{p}'_L| = p_{FL}$ and both transferred momenta $\tilde{q}_L \le 2p_{FL}$; $q_L \le 2p_{FL}$ for SC-problem. The Kanamori T-matrix for light electrons T_{LL} in the strong coupling case reads $T_{LL} = \frac{4\pi}{m_L^*} \frac{1}{\ln\left(1/p_{FL}^2 d^2\right)} > 0$. Using the expressions for Π_{LL} and Π_{hh}:

$$\begin{aligned} \Pi_{LL}\left(0, \tilde{\vec{q}}_L\right) &= Z_L^2 \frac{m_L^*}{2\pi} \left[1 - \mathrm{Re}\sqrt{1 - \frac{4p_{FL}^2}{\tilde{q}_L^2}}\right], \\ \Pi_{hh}(0, \vec{q}_L) &= Z_h^2 \frac{m_h^*}{2\pi} \left[1 - \mathrm{Re}\sqrt{1 - \frac{4p_{Fh}^2}{q_L^2}}\right], \end{aligned} \tag{10.3.70}$$

and having in mind that $p_{Fh} > p_{FL}$ we get:

$$U_{eff}\left(\vec{p}_L, \vec{p}'_L\right) \approx T_{LL} + T_{LL}^2 \frac{m_L^* Z_L^2}{2\pi} - 2\frac{m_h^*}{2\pi} Z_h^2, \tag{10.3.71}$$

where we can put $Z_L \sim m_L/m_L^* \sim 1$.

Thus an effective interaction for light electrons does not contain any nontrivial dependence from $\vec{q}_L$ and $\tilde{\vec{q}}_L$, and hence anomalous superconductivity with magnetic quantum number $m \neq 0$ is absent for light electrons in this approximation. Note that the standard s-wave pairing for light electrons is also suppressed by first order repulsive term $T_{LL} > 0$ in U_{eff} (10.3.71). However, an inclusion of Moskalenko-Suhl-Geilikman term [70–73], which describes rescattering of a Cooper pair between two bands and is given by:

$$K \sum_{pp'} \left(a_p^+ a_{-p}^+ b_{p'} b_{-p'} + h.c.\right) \tag{10.3.72}$$

in the Hamiltonian of the two-band model (10.3.3) already in the case of infinitely small K makes the light band superconductive at the same temperature as the heavy one. This interesting fact was illustrated for standard s-wave pairing in [70] and for p-wave pairing in [74]. Thus, T_{C1} in (10.3.62) is a mutual SC temperature in the two-band model with one narrow band [74]. Of course superconductive gaps for heavy and light bands open simultaneously at $T = T_{C1}$, but then "live their separate lives" for $T < T_{C1}$ (see [70]).

To conclude this Section let us note that we discuss briefly the SC-instability which arises in the two-band model at low electron density. The leading instability of the enhanced Kohn-Luttinger type (see Ref. [10] in Chap. 9, [1, 3, 4, 5]) corresponds to triplet p-wave pairing of heavy electrons via polarization of light electrons. In 2D or quasi-2D case T_C can reach experimentally realistic values already at low densities for layered dichalcogenides CuS_2, $CuSe_2$ and semimetallic superlattices InAs-GaSb, PbTe-SnTe with geometrically separated bands belonging to neighboring layers (see [5], and Ref. [44] in Chap. 9). Note that p-wave SC is widely discussed in 3D heavy-fermion systems like $U_{1-x}Th_xBe_{13}$ (see Refs. [18, 19] in Chap. 9) and in layered ruthenates Sr_2RuO_4 (see Refs. [20, 21] in Chap. 9, [75]) with several pockets (bands) for conducting electrons [76]. Note also that when we increase the density of a heavy-band and go closer to half-filling ($n_h \to 1$) the d-wave superconductive pairing (as in UPt_3) becomes more beneficial in the framework of the spin-fluctuation theory in the heavy band (see Refs. [58, 59] in Chap. 9). Different mechanisms of SC in HF-compounds including odd-frequency pairing introduced by Coleman, Miranda, Tsvelik are discussed in [77–79].

Note also that the multiband physics is important for some superconductive systems with conventional s-wave pairing including Nb [11]. MgB_2 (see Ref. [26] in Chap. 9) and new superconductors based on FeAs-compounds like $BaFe_2(As_{1-x}P_x)_2$ (see Refs. [95–97] in Chap. 9). For these compounds

superconductive gaps in different bands are also open simultaneously at the same critical temperature due to Suhl-Moskalenko-Geilikman theory. All of them are very important for technical applications in electronics and energetics.

Note that the two-band Hubbard model discussed in this Section is applicable also for degenerate case when there are two orbitals belonging to the same atom (in this case one atom is a source of electrons of two sorts). We have then the two-band degenerate Hubbard model. In this model $U = U_{hh} = U_{LL} = U_{hL} + 2J_H$ (where J_H is Hund's coupling) [80]. Close to half-filling this model becomes equivalent to the *t-J* orbital model [81] and contains for $J < t$ and at optimal doping the SC d-wave pairing [82] governed by superexchange interaction between the different orbitals of AFM-type ($J > 0$) with $J \sim t^2/U \sim 300$ K for not very different values of t_h and t_L [80, 81]. The physics of the *t-J* model will be described in detail in Chap. 13.

References

1. Kagan, M.Yu., Chubukov, A.V.: JETP Lett. **50**, 483 (1989)
2. Baranov, M.A., Efremov, D.V., Kagan, M.Yu.: Physica C: Supercond. **218**, 75 (1993)
3. Kagan, M.Yu., Efremov, D.V., Mar'enko, M.S., Val'kov, V.V.: Sov. Low Temp. Phys. **38**, 1102 (2012)
4. Kagan, M.Yu., Efremov, D.V., Mar'enko, M.S., Val'kov, V.V.: Jour. of Supercond. and Novel Magn. **26**, 2809 (2013)
5. Kagan, M.Yu.: Phys. Lett. A **152**, 303 (1991)
6. Kagan, M.Yu., Val'kov, V.V.: Sov. Phys. Low Temp. Special issue dedicated to 100th anniversary of Prof. Schoenberg, D., 37, 84 (2011) and also in "A lifetime in magnetism and superconductivity: a tribute to professor David Schoenberg", Cambridge Scientific Publishers (2011)
7. Frossati, G., Wiegers, S.A.J., Hata, T., Jochemsen, R., van de Haar, P.G., Roobol, L.P.: Czech. J. Phys. **440**, 909 (1990)
8. Wiegers, S.A.J., Hata, T., van de Haar, P.G., Roobol, L.P., van Woerkens, C.M.C.M., Jochemsen, R., Frossati, G.: Physica B: Cond. Matt **165–166**, 733 (1990)
9. Roobol, L.P., Jochemsen, R., van Woerkens, C.M.C.M., Hata, T., Wiegers, S.A.J., Frossati, G.: Physica B: Cond. Matt. **165–166**, 639 (1990)
10. Frossati, G., Bedell, K.S., Wiegers, S.A.J., Vermeulen, G.A.: Phys. Rev. Lett. **57**, 1032 (1986)
11. Tinkham, M.: Introduction to Superconductivity. McGraw-Hill, New York (1975). Gennes de, P.G.: Superconductivity in metals and alloys. W.A. Benjamin Inc., New York (1966)
12. Scharnberg, K., Klemm, R.A.: Phys. Rev. B **22**, 5233 (1980)
13. Klemm, R.A., Scharnberg, K.: Phys. Rev. B **24**, 6361 (1981)
14. Clogston, A.M.: Phys. Rev. Lett. **9**, 266 (1962)
15. Abrikosov, A.A.: Foundations of the theory of metals. Nauka, Moscow (in Russian) (1987). Kittel, C.: Introduction to solid state physics 6th edn. New York (1986)
16. Zavaritskii, N.V.: Bull. Russ. Acad. Sci. **78**, 665 (1951) (in Russian)
17. Ando, T., Fowler, A.B., Stern, F.: Rev. Mod. Phys. **54**, 437 (1982)
18. Abrikosov, A.A., Gor'kov, L.P.: JETP **124**, 1243 (1961)
19. Larkin, A.I.: JETP **31**, 784 (1970)
20. Rieck, C.T., Scharnberg, K., Klemm, R.A.: Physica C: Supercond. **170**, 195 (1990)
21. Tesanović, Z., Halperin, B.I.: Phys. Rev. B **36**, 4888 (1987)

22. Keitler, H., Grewe, N.: In: Falicov, L.M. (ed.) Valence fluctuations in solids. North Holland Publishing Co., New York, (1981)
23. Newns, D.M., Read, N.: Adv. Phys. **36**, 799 (1987)
24. Kagan, Y., Prokof'ev, N.V.: JETP **66**, 211 (1987)
25. Kagan, Y., Prokof'ev, N.V.: JETP **63**, 1276 (1986)
26. Iche, G., Nozieres, P.: Physica A **91**, 485 (1978)
27. Sboychakov, A.O., Kugel, K.I., Rakhmanov, A.L.: Physica. Rev. B **76**, 195113 (2007)
28. Falicov, L.M., Kimball, J.C.: Phys. Rev. Lett. **22**, 997–999 (1969)
29. Mahan, G.D.: Many Particle Physics. Plenum, New York (1981)
30. Negele, J.W., Orland, H.: Quantum Many Particle Systems. Addison-Wesley, Redwood City (1988)
31. Fetter, A.L., Walecka, J.D.: Quantum Theory of Many-Particle Systems. McGrow-Hill, New York (1971)
32. Anderson, P.W.: Phys. Rev. Lett. **64**, 1839 (1990)
33. Anderson, P.W.: Phys. Rev. Lett. **65**, 2306 (1990)
34. Anderson, P.W.: Phys. Rev. Lett. **66**, 3226 (1991)
35. Kagan, M.Yu., Val'kov, V.V., Wölfle, P.: Sov. Phys. Low. Temp. **37**, 1046 (2011)
36. Engelbrecht, J.R., Randeria, M.: Phys. Rev. Lett. **65**, 1032 (1990)
37. Engelbrecht, J.R., Randeria, M.: Phys. Rev. Lett. **66**, 3225 (1991)
38. Engelbrecht, J.R., Randeria, M.: Phys. Rev. B **45**, 12419 (1992)
39. Galitskii, V.M., Migdal, A.B.: JETP **7**, 86 (1958)
40. Pines, D., Nozieres, P.: Theory of Quantum Liquids, vol. 1. W.A Benjamin Inc., New York (1966)
41. P. Nozieres, Lectures in College de France (unpublished)
42. Kohn, W., Sham, L.J.: Phys. Rev. A **140**, 1133 (1965)
43. Lee, P.A., Rice, T.M., Serene, J.W., Sham, L.J., Wilkins, J.W.: Comments Condens. Matter Phys. **12**, 99 (1986)
44. Stewart, G.R.: Rev. Mod. Phys. **56**, 755 (1984)
45. Ott, H.R.: Prog. Low Temp. Phys. **11**, 215 (1987)
46. Grewe, N., Steglich, F.: In: Gachneider Jr, K.A., Eyring, L. (eds.) Handbook on the Physics and Chemistry of Rare Earths, vol. 14. North-Holland, Amsterdam (1991)
47. Fulde, P., Keller, J., Zwicknagl, G.: In: Ehrenreich, H., Turnbull, D. (eds.) Solid State Physics, vol. 41. Academic, San Diego (1988)
48. Prokof'ev, N.V., Kagan, M.Yu. (unpublished)
49. Afans'ev, A.M., Kagan, M.Yu.: JETP **43**, 1456 (1962)
50. Kusunose, H., Yotsuhashi, S., Miyake, K.: Phys. Rev. B **62**, 4403 (2000)
51. Farkašovský, P.: Phys. Rev. B **77**, 085110 (2008)
52. Nozieres, P., de Dominicis, C.T.: Phys. Rev. **178**, 1097 (1969)
53. Landau, L.D.: JETP **3**, 920 (1957)
54. Landau, L.D.: JETP **5**, 101 (1957)
55. Anderson, P.W.: Phys. Rev. Lett. **18**, 1049 (1958)
56. Anderson, P.W.: Phys. Rev. **164**, 352 (1967)
57. White, R.M., Fulde, P.: Phys. Rev. Lett. **47**, 1540 (1981)
58. Zwicknagl, G., Yaresko, A., Fulde, P.: Phys. Rev. B **65**, 081103 (2002)
59. Zwicknagl, G., Yaresko, A., Fulde, P.: Phys. Rev. B **68**, 052508 (2003)
60. Koga, M., Liu, W., Dolg, M., Fulde, P.: Phys. Rev. B **57**, 10648 (1998)
61. Kagan, Y., Kikoin, K.A., Prokof'ev, N.V.: JETP Lett., **56**, 219 (1992)
62. Lifshitz, I.M., Kosevich, A.M.: JETP **2**, 636 (1955)
63. Shoenberg, D.: Magnetic Oscillations in Metals. Cambridge University Press, Cambridge (1984)
64. Taillefer, L., Lonzarich, G.G.: Phys. Rev. Lett. **60**, 1570 (1988)
65. Wasserman, A., Springford, M., Hewson, A.C.: J. Phys.: Condens. Matter **1**, 2669 (1989)
66. Ito, T., Kumigishira, H., Kim, H.-D., Takahashi, T., Kimura, N., Haga, Y., Yamamoto, E., Onuki, Y., Harima, H.: Phys. Rev. B **59**, 8923 (1999)

67. Arko, A.J., Joyce, J.J., Andrews, A.B., Thompson, J.D., Smith, J.L., Moshopoulou, E., Fisk, Z., Menovsky, A.A., Canfield, P.C., Olson, C.G.: Physica B: Condens. Matter **230–232**, 16 (1997)
68. Berton, A., Chaussy, J., Cornut, B., Flouquet, J., Odin, J., Peyrard, J., Holtzberg, F.: Phys. Rev. B **23**, 3504 (1981)
69. Landau, L.D., Lifshitz, E.M.: Statistical Physics, Part I. Butterworth-Heinemann, Oxford (1999)
70. Suhl, H., Matthias, T.B., Walker, L.R.: Phys. Rev. Lett. **3**, 552 (1959)
71. Geilikman, B.T.: JETP **21**, 796 (1965)
72. Geilikman, B.T.: Sov. Phys. Uspekhi, **88**, 327 (1966)
73. Geilikman, B.T.: Sov. Phys. Uspekhi, **109**, 65 (1973)
74. Baranov, M.A., Kagan, M.Yu.: JETP **75**, 165 (1992)
75. Steglich, F., Aarts, J., Bredl, C.D., Cordier, G., Boer de, F.R., Lieke, W., Rauchschwalbe, U.: Superconductivity in d- and f-band Metals. Kernforschungszentrum, Karlsruhe (1982)
76. Sigrist, M., Ueda, K.: Rev. Mod. Phys. **63**, 239 (1991)
77. Coleman, P., Miranda, E., Tsvelik, A.: Phys. Rev. Lett. **70**, 2960 (1993)
78. Flint, R., Dzero, M., Coleman, P.: Nature Phys. **4**, 643 (2008) and references therein
79. Coleman, P.: Handbook of Magnetism and Advanced Magnetic Materials. Fundamentals and Theory, vol. 1. Wiley, Hoboken (2007)
80. Kugel, K.I., Khomskii, D.I.: Sov. Phys. Uspekhi. **136**, 621 (1982)
81. Ishihara, S., Inoue, J., Maekawa, S.: Phys. Rev. B **55**, 8280 (1997)
82. Kagan, M.Yu., Rice, T.M.: J. Phys.: Condens. Matt. **6**, 3771 (1994)

Chapter 11
Fermionic Superfluidity in Three- and Two-Dimensional Solutions of ^{3}He in ^{4}He

In this chapter, we will discuss fermionic superfluidity in the Fermi-Bose mixture (in the solution) of ^{3}He in ^{4}He both in three- and in two-dimensional case. We will present the foundations of the classical Bardeen-Baym-Pines theory [1], as well as Bashkin and Meyerovich [2] results for fermionic s-wave pairing in unpolarized ^{3}He–^{4}He mixtures in 3D case, as well as in 2D case for ^{3}He submonolayers on Andreev levels [3] (which are formed on the free surface of superfluid ^{4}He with vacuum) and on grafoil substrates [4, 5]. We also present the Fermi-gas approach to the p-wave fermionic superfluidity in ^{3}He-subsystem based on Kohn and Luttinger [6–11] mechanism for the pairing of two ^{3}He quasiparticles via polarization of the fermionic background.

We will illustrate that the critical temperatures of the p-wave pairing can be strongly increased in a spin-polarized case both for 3D and especially for 2D situation [7] and discuss the possible experimental test of the proposed theory.

11.1 Bardeen-Baym-Pines Theory for the Solutions of ^{3}He in ^{4}He. Direct and Exchange Interactions

One of the most interesting and still experimentally unresolved problems in low-temperature physics is the search for fermionic superfluidity in three-dimensional and particularly in two-dimensional (thin films, submonolayers) [7] solutions of ^{3}He in ^{4}He. In this subsection, we will concentrate on new experimental approaches and theoretical results that have been published on this topic. We will stress particularly the role of thin ^{3}He films and submonolayers as ideal two-dimensional systems for experimental verification of various theories actual in connection with the problem of high-T_C superconductivity.

Note that a solution of ^{3}He in ^{4}He is the simplest low-density Fermi-system of ^{3}He atoms in an inert superfluid ^{4}He condensate, which makes a solution of this kind an ideal object for the development and testing of methods belonging to the realm of Fermi-liquid theory. These methods have been used successfully in

M. Yu. Kagan, *Modern Trends in Superconductivity and Superfluidity*,
Lecture Notes in Physics 874, DOI: 10.1007/978-94-007-6961-8_11,

describing the normal properties of the solutions (thermodynamic characteristics, transport coefficients) [2] and in the prediction of possible superfluidity of the ^{3}He subsystem in such solutions [1, 12, 13]. The first classical theory of superfluidity of three-dimensional solutions was proposed by Bardeen, Baym and Pines (BBP) in 1967 [1]. They established an elegant analogy between pairing of two ^{3}He atoms in a solution via the polarization of the ^{4}He background (exchange of virtual phonons) and the electron–phonon interaction in the Bardeen, Cooper and Schrieffer (BCS) theory of superconductivity (Fig. 11.1). In accordance with the ideas of Bardeen, Baym and Pines, the total interaction between two ^{3}He particles in a solution consists of two components, direct and exchange:

$$V(r) = V_{dir}(r) + V_{exch}(r). \tag{11.1.1}$$

The direct interaction includes the contribution of hard-core repulsion at short distances (V_1) and of the van der Waals attraction (V_2) at large distances:

$$V_{dir}(r) = V_1(r) + V_2(r). \tag{11.1.2}$$

The exchange interaction $V_{\text{exch}}(r)$ represents the interaction of two ^{3}He atoms via a local change in the density of ^{4}He. This is an analogue of the deformation potential in the BCS theory.

The corresponding expression in the momentum space is:

$$V(q) = V_{dir}(q) + V_{exch}(q), \tag{11.1.3}$$

where $V_{\text{exch}}(q)$ is due to the exchange of a virtual phonon in the three-dimensional case and the exchange of a quantum of third sound in the two-dimensional situation [14, 15].

At low temperatures and concentrations the subsystem of ^{3}He atoms is a low-density Fermi-liquid, i.e. it is effectively a Fermi-gas. Therefore, the superfluid transition in this liquid is described by the BCS theory and it depends decisively on the amplitude and the sign of the total interaction $V(q)$ on the Fermi surface. More rigorously, we have $\vec{q} = \vec{p} - \vec{p'}$, where $\vec{p}$ and $\vec{p'}$ are the momenta of the incoming and outgoing particles in the Cooper channel, $|\vec{p}| = |\vec{p'}| = p_F$, and $q^2 = 2p_F^2(1 - \cos\theta)$, $\theta = \sphericalangle(\vec{p}\vec{p}\,')$. Thus the only quantity which must be determined

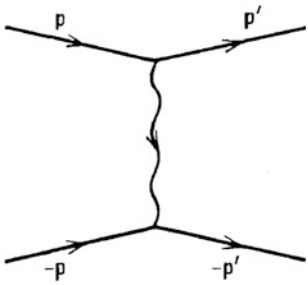

Fig. 11.1 Interaction of two ^{3}He atoms via the polarization of the superfluid ^{4}He background [7]

when we deal with the Cooper problem is the value of the s-wave harmonic of the potential $V(q)$ on the Fermi surface:

$$V_{l=0} = \int_{-1}^{1} V(q(\cos\theta))\frac{d\cos\theta}{2}. \tag{11.1.4}$$

11.1.1 Three-Dimensional Case. Spin Diffusion Measurements

The deformation potential has the following form in the momentum space:

$$V_{exch}(q) = g_q^2 \frac{2\omega_q}{(\varepsilon_p - \varepsilon_{p-q})^2 - \omega_q^2}, \tag{11.1.5}$$

where g_q is the coupling constant and ω_q is the frequency of the phonon spectrum of ^{4}He. If $|\varepsilon_{p+q} - \varepsilon_p| < \omega_q < \omega_D$ (where ω_D is Debye frequency), we find that $V_{exch}(q) = -\frac{2g_q^2}{\omega_q} < 0$.

In complete analogy with the BCS theory we have $g_q^2 \sim q$, $\omega_\mathrm{q} = c_I\mathrm{q}$, where c_I is the first sound velocity in ^{4}He, so that the final result is $V_{exch}(q \to 0) = const$. In the case of the solutions, this constant is $-(1+\alpha)^2 \frac{m_4 {c_I}^2}{n_4} < 0$, where $\alpha \approx 0.28$ is the relative increase in the volume of the solution owing to the replacement of a ^{4}He atom with a ^{3}He atom; n_4 and m_4 are the density and mass, respectively, of ^{4}He. We should note that in the low-density case (for small concentration of ^{3}He in the solution) we have $\omega_\mathrm{D} > \varepsilon_\mathrm{F}$ and the whole volume of the Fermi sphere (and not only the Debye shell) participates in the superconductive pairing in contrast with the standard BCS theory.

The direct interaction of ^{3}He atoms in the momentum space is found from the thermodynamic identity describing the derivative of the chemical potential with respect to the density and has the following form:

$$V_{dir}(q=0) = \frac{\partial\mu_{3\uparrow}}{\partial n_{3\downarrow}} = (1 + 2\alpha)\frac{m_4 {c_I}^2}{n_4} > 0, \tag{11.1.6}$$

where $\mu_{3\uparrow}$ and $n_{3\downarrow}$ represent, respectively, the chemical potential of ^{3}He atoms with "up" spin and the density of ^{3}He atoms with "down" spin. The result is:

$$V(q=0) \equiv V_{l=0} = V_{exch}(q=0) + V_{dir}(q=0) = -\alpha^2 \frac{m_4 {c_I}^2}{n_4} < 0. \tag{11.1.7}$$

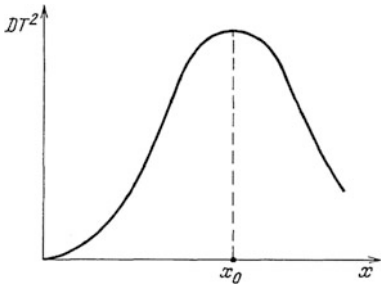

Fig. 11.2 Approximate experimental dependence of the product DT^2, representing the spin diffusion in a solution, on the concentration x of ^{3}He [7, 12]

We can therefore conclude that at very low ^{3}He concentrations (when $p_F \to 0$ and, consequently, $q \to 0$) the total interaction is attractive and we can expect the spherically symmetric singlet s-wave pairing which is standard in the BCS theory.

However, spin diffusion experiments show that the situation is far from trivial (see [12] and the references therein). In these experiments the dependence of DT^2 (D is the spin diffusion coefficient and T is the temperature) of the ^{3}He concentration was determined. The experimental curves in [12] are strongly non-monotonic and exhibit a maximum at a certain concentration x_0 approximately equal to 4 % (see Fig. 11.2). They are approximately described by the expression:

$$DT^2 \propto \frac{x^{2/3}}{V_{l=0}^2 - \frac{2}{3}V_{l=0}V_{l=1} + \frac{11}{35}V_{l=1}^2}. \tag{11.1.8}$$

A theoretical analysis of these experimental curves shows that the absolute value of the s-wave harmonic of the total potential $V_{l=0}$ decreases with an increase in the concentration x, than vanishes at $x = x_0$, and at higher concentrations becomes repulsive. On the other hand, for $x \geq x_0$ the p-wave harmonic of the total potential $V_{l=1}$ is significant and attractive (although smaller than $V_{l=0}$ at $x = 0$). These circumstances lead to the two possible approaches to the fermionic superfluidity in the solution.

11.1.2 Two Possible Approaches to the Fermionic Superfluidity in the Solutions

In the first approach it is assumed that the total interaction of two ^{3}He atoms described by $V(q)$ exhibits significant momentum dependence and, moreover, its sign is reversed at the values of the vector q of the order of the Fermi momentum when the concentration is x_0, i.e. when it is $p_F(x_0)$. This hypothesis leads to the model potential of the BBP theory [1]:

$$V(q) = V(q=0)\cos\frac{q}{k_s},\ k_s \sim p_F(x_0). \tag{11.1.9}$$

The BBP model potential was improved in 1989 by van de Haar et al. [12]. They introduced the concentration dependence of the amplitude of the potential $V(q = 0)$:

$$V(q=0) = -\frac{m_4 {c_I}^2}{n_4}\alpha^2(1 + \gamma\frac{x}{x_{\max}}), \tag{11.1.10}$$

where $x_{\max}$ is the solubility limit of ^{4}He at a given pressure P and $\gamma(P)$ is a fitting parameter. In both theories [1] and [12] the s-wave harmonic of the total interaction is maximal and attractive at low concentrations and then it begins to decrease in absolute value, changing sign to become a repulsive one at concentrations corresponding to $p_F \sim k_s$. At higher concentrations the p-wave harmonic of $V(q)$ becomes attractive. Therefore, van de Haar, Frossati and Bedell predict singlet s-wave pairing in a solution at low concentrations of ^{3}He and triplet p-wave pairing at high concentrations. It should be pointed out that the two fitting parameters $k_s = k_s(p)$ and $\gamma(P)$, extracted from the experiments on spin diffusion and magnetostriction, are used in the improved model potential of van de Haar, Frossati and Bedell [12].

The second approach, adopted by us and by others [2, 7, 13], does not rely on any model potential. In this approach the only microscopic parameter of the system is the s-wave scattering length $a = \frac{m}{4\pi}V_{l=0}$, which is dependent on the pressure and concentration. It is assumed that its sign is reversed at a concentration corresponding to the maximum of the DT^2 curve (see Fig. 11.3).

It should be pointed out that the higher harmonics $(V_{l=1}, V_{l=2}, \ldots)$ appear in the second order of the perturbation theory but not because of the momentum dependence of the total interaction $V(q)$: they originate from the scattering length a because of the effective interaction of two ^{3}He particles via the fermionic background of their own ^{3}He subsystem.

The relationship between these two approaches is approximately the following. Let us assume, for the sake of simplicity, that the direct interaction of two ^{3}He particles in a solution is described by:

$$V_{dir}(r) = \begin{cases} V_1;\ r < r_1, \\ -V_2;\ r_1 < r < r_2, \end{cases} \tag{11.1.11}$$

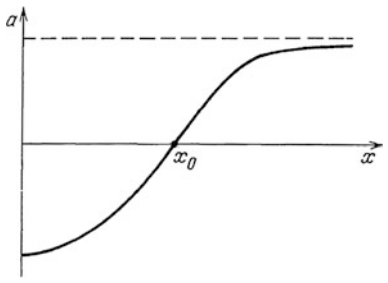

Fig. 11.3 Qualitative dependence of the scattering length in a solution from the concentration of ^{3}He. At $x = 100$ % the value of $a(x)$ tends to the scattering length of pure ^{3}He and is approximately equal to $2/p_{F0}$ at zero pressure [7] (here p_{F0} is the Fermi momentum of pure ^{3}He)

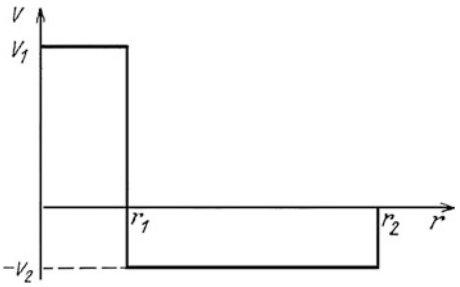

Fig. 11.4 Model representation of the direct interaction of two particles in a solution as a function of the distance r between them [7] (see also Fig. 6.1 in Chap. 6)

where the first term is responsible for the hard-core repulsion at short distances and the second term is due to the van der Waals attraction at long distances (see Fig. 11.4 and Fig. 6.1).

At low ^{3}He concentrations in a solution, i.e. in the case when $p_F r_1 \ll p_F r_2 \ll 1$, the s-wave harmonic of the direct interaction is $V_{dir}^{l=0} = V_1^{l=0} - V_2^{l=0}$. Then, if

$$V_1^{l=0} - V_2^{l=0} - V_{exch}^{l=0} < 0, \tag{11.1.12}$$

but

$$V_1^{l=0} - V_{exch}^{l=0} > 0, \tag{11.1.13}$$

we have the low-density Fermi-gas with the gas parameter $p_F r_1 \ll 1$ and with a scattering length which changes its sign at $p_F \sim 1/r_2$. Naturally, this approach ignores the p-wave harmonic of the van der Waals interaction, which need not be small in the transition region $p_F r_2 \sim 1$. It should be pointed out that at high concentrations when $p_F r_2 \gg 1$ we find that $V_2^{l=1}$ is small and of the same order as $V_2^{l=0}$. In this chapter the second (Fermi-gas) approach to the problem of superfluidity in the solutions will be mainly used.

11.1.3 Three-Dimensional Fermi-Gas with Attraction

The expression for the temperature of the superfluid transition in a Fermi-gas with attraction was first obtained by Gor'kov and Melik-Barkhudarov in 1961 [16], soon after the creation of the BCS-theory. Bashkin and Meyerovich [2] used this expression to describe the superfluidity of the solutions at very low concentrations of ^{3}He. For the concentrations in the range $x < x_0$ and an attractive s-wave scattering length $a < 0$ the expression for the s-wave critical temperature reads:

$$T_{C0} = 0.28\varepsilon_{F0} x^{2/3} \exp\left(-\frac{\pi}{2|a|p_{F0} x^{1/3}}\right), \tag{11.1.14}$$

where ε_{F0} and p_{F0} are the Fermi energy and momentum of pure ^{3}He. It is worth noting that the preexponential factor in this expression is proportional to ε_F and not ω_D, as in the case of the phonon model.

According to the estimates of Østgaard and Bashkin [17], the maximum value of T_{C0} is $T_{C0}(1\ \%) \sim 10^{-4}$ K. Frossati and his colleagues [12] proposed a lower critical temperature with maximal $T_{C0} = T_{C0}(2\ \%) \sim (4{\cdot}10^{-6} \div 10^{-5})$ K. In their estimates they obtained the larger value of T_{C0} of the order of 10^{-5} K by extracting the fitting parameters from the magnetostriction experiments, and $4{\cdot}10^{-6}$ K from the spin diffusion experiments. At a given concentration x the gas parameter of the theory is $ap_{F0}x^{1/3}$, and it depends weakly on the pressure.

11.1.4 Three-Dimensional Fermi-Gas with Repulsion

At higher concentrations ($x > x_0$) the scattering length changes its sign $a > 0$, and s-wave pairing becomes impossible. Nevertheless, even in this case the subsystem of ^{3}He atoms in a solution may become a superfluid, but this is now due to an instability with respect to triplet p-wave pairing. As we already discussed in Chap. 9, the mechanism for the realization of p-wave pairing was first considered by Fay and Layzer [10] and Kagan, Chubukov [7] following pioneering ideas of Kohn and Luttinger [6]. It is related to the presence of Kohn's anomaly (of the Friedel oscillations [18]) in the effective interaction of Fermi particles via the polarization of the Fermionic background. As a result the purely repulsive short-range potential between two particles in vacuum gives rise to an effective interaction in substance with the competition between attraction and repulsion in it. A rigorous calculation [7, 10] shows that for all the harmonics of the effective potential (except the s-wave harmonic) the attraction wins in this competition and the p-wave harmonic is the most attractive. Consequently, a three-dimensional Fermi-gas with repulsion is unstable with respect to the superfluid transition with the triplet p-wave pairing below the critical temperature:

$$T_{C1} \sim \varepsilon_{F0}x^{2/3} \exp\left\{-\frac{5\pi^2}{4(2\ln 2 - 1)a^2 p_{F0}^2 x^{2/3}}\right\}, \tag{11.1.15}$$

where maximal T_{C1} corresponds to the pressures $P = 10$ bar, when we have the maximal solubility of ^{3}He $x_{max} = 9.5$ %. In this case it equals to $(10^{-10}$–$10^{-9})$ K. The triplet pairing temperature of this order of magnitude was predicted also by Bardeen et al. [1]. Frossati and others [12] give a more optimistic estimate for the triplet pairing case. At the maximal concentration $x_{max} = 9.5$ % the value of T_{C1} lies between 10^{-6} and 10^{-4} K. The lower temperature of the p-wave pairing (10^{-6} K) is obtained in [12] when the fitting parameters are extracted from transport experiments and the higher temperature (10^{-4} K) follows from magnetostriction experiments. Note that at zero pressure the maximal solubility of ^{3}He in the solution is only 6.4 % [1, 2].

11.2 Two-Dimensional Case. ^{3}He-Submonolayers

A solution of ^{3}He in ^{4}He is also very interesting because it can be made purely two-dimensional. In superconducting electron systems a film is regarded as a two-dimensional if its thickness L is much less than the coherence length $\zeta_0 \sim 1000$ Å. In ^{3}He films on grafoil (exfoliated graphite) and in monolayers and submonolayers the radius of the localization of ^{3}He atoms in the third dimension (which is the film thickness) is indeed of the order of the distance between the atoms d. Therefore, by analogy with inversed layers in heterostructures, we are also dealing here with a purely two-dimensional system, and, moreover, our system is free of impurities. In this sense a two-dimensional solution of ^{3}He in ^{4}He can be regarded as a bridge between superfluidity and superconductivity, particularly high-temperature superconductivity. In fact, the majority of modern theories of high-T_C superconductivity rely on the two-dimensional or quasi-two-dimensional behavior (see this chapter, Chaps. 12, 13 and 14) for the unusual normal properties (resistivity, susceptibility, small Z-factor) of these materials, as well as to account for the high temperature of their superconducting transition. Two-dimensional helium films and particularly monolayers and submonolayers with a low two-dimensional ^{3}He density are ideal objects for experimental verification of the different fashionable theories of high-T_C superconductivity, such as the theory of a marginal Fermi-liquid (see Chap. 14) proposed by Varma et al. [19] or a somewhat similar theory of the Luttinger liquid proposed by Anderson [20]. These topics will be discussed again at the end of this subsection. At this stage we will provide a brief review of the history of the experimental discovery and theoretical prediction of the existence of a two-dimensional solution.

11.2.1 Surface Andreev Levels

The first experiments were carried out by Esel'son and Bereznyak [21] and by Atkins and Narahara [22]. These experiments revealed a nontrivial temperature dependence of the surface tension (in fact, the surface free energy) of a weak solution of ^{3}He in ^{4}He. The experiments were interpreted by Andreev [3] who postulated the existence of surface ^{3}He-impurity levels on the free surface of superfluid ^{4}He with vacuum (which are similar to some extent to Tamm's surface levels in metals). This idea was subsequently confirmed by detailed experiments of Zinov'eva and Boldarev [23] and of Edwards et al. [24] as well as by the variational calculations (cf. the review of Edwards and Saam [25] and the literature cited there). The correct interpretation of the experimental results yields the following parameters representing the surface state: $\varepsilon = -\Delta - \varepsilon_0 + \frac{p_{||}^2}{2m^*}$, where $\Delta = 2.8$ K is the binding energy of a ^{3}He quasiparticle in the bulk (Andreev [3], Bashkin and Meyerovich [2]), $\varepsilon_0 = 2.2$ K is the difference between the binding energies of a ^{3}He quasiparticle in the bulk and on the surface; $m^* = 1.5\ m_3$ is the

hydrodynamic effective mass governing the motion of ^{3}He quasiparticles along the surface. It should be pointed out that, according to the variational calculations of Lekner [26] and Saam [27], the appearance of the Andreev levels is due to a combination of the effects associated with the van der Waals interaction between ^{3}He and the ^{4}He density profile (which varies when we approach the free surface) and with the difference between the energies of the zero-point motion of ^{3}He and ^{4}He. Such effects lead to the localization of ^{3}He atoms near the free surface. In the same time ^{3}He atoms can move freely along the surface of ^{4}He, which is almost equipotential because the hydrodynamic condition $\mu_4 = const$ (see Chap. 1) is satisfied on this surface. The wave function of the Andreev state is $\Psi = \Psi(z)\exp(i\vec{p}_{||}\vec{r}_{||})$ with $\Psi(z) \sim \exp(-z/d)$, where d is the radius of localization along the normal to the surface.

11.2.2 Superfluid Thin ^{4}He-Films

The first experiments on thin ^{4}He films (film thickness is less than 25 Å) of the same kind as the experiments of Zinov'eva and Boldarev [23] and of Edwards et al. [24], were carried out by Gasparini et al. [28]. Gasparini and others determined the contribution of the surface states of ^{3}He to the specific heat of the thin films. They also proposed the first theoretical interpretation of the results [29]. Subsequently several experimental papers were published by Hallock et al. [4, 30–32], who measured the magnetization and the spin–lattice relaxation time of ^{3}He submonolayers formed on the surface of thin ^{4}He films.

The theoretical interpretation of the experiments of Hallock et al. proposed by Dalfovo and Stringari [33], Pavloff and Treiner [34], Krotscheck et al. [35] require the assumption that not one but two Andreev levels exist on the surface of a thin ^{4}He film. The energy of the first Andreev layer, $E_1 = -\Delta - \varepsilon_1 + \frac{p_{||}^2}{2m_1}$, is practically identical with the energy of the Andreev level ($\varepsilon_1 \cong \varepsilon_0$) on a bulk surface, differing only in respect of the effective mass $m_1 \approx 1.35\, m_3$. The energy of the second Andreev level is still lower than the energy of ^{3}He in the bulk and is given by the expression $E_2 = -\Delta - \varepsilon_2 + \frac{p_{||}^2}{2m_2}$, where in the limit of zero concentration of ^{3}He and not too thin films we have $m_2 \approx 1.6\, m_3$ and $\varepsilon_2 \approx 0.4$ K; consequently, $\varepsilon_2 - \varepsilon_1 = 1.8$ K.

The wavefunction of the first Andreev level is localized mainly near the free surface and has a significant tail ($\sim$3 Å) above the surface. At the same time the wavefunction of the second Andreev level penetrates partly into the film. Two Andreev levels (instead of one) appear according to [33–35] because of the competition between the size effect (vanishing of the Ψ-function of ^{3}He near the substrate and consequent increase of the kinetic energy $E_{kin} \sim (\nabla_z \Psi)^2 \sim 1/L^2$ of ^{3}He) and the van der Waals attraction by the substrate (which is proportional to $1/L^3$ and tends to reduce the energy). In the case of thin and moderately thick

films the van der Waals attraction is stronger than the size-effect repulsion and, therefore, the energy of the second Andreev level is still lower than the energy of ^{3}He in the bulk.

In the case of very thick films the van der Waals attraction of the substrate (proportional to $1/L^3$) may become unimportant compared with the kinetic energy, and the energy of the second Andreev level may prove to be higher than the energy of ^{3}He in the bulk. In this case the second level evidently vanishes by merging with the bulk levels. At a fixed film thickness, the van der Waals attraction of the substrate depends on whether the substrate is "strong" or "weak". On a weak substrate (Cs, Rb, K, Na, Li, Mg, H_2) it is found that ^{4}He is in the liquid phase. On a strong substrate (Ag, Au, Cu, Al) one or two solid ^{4}He layers are formed on it, and ^{4}He is in a liquid phase only starting from the third and following layers. The presence of one or two solid layers reduces the van der Waals attraction of the substrate and increases the kinetic energy, leading to a possible disappearance of the second Andreev level at lower thicknesses of the film.

We would like to emphasize that the topic of surface levels in the films is not fully understood yet. There is an alternative point of view according to which the second Andreev level can exist not only in thin films, but also in the bulk.

It is thus clear that in the case of not very thin and not very thick films there are definitely two Andreev levels whose energies differ by $\varepsilon_2 - \varepsilon_1 = 1.8$ K. Their existence is manifested in Hallock experiments by the presence of a step in the dependence of the magnetization on the surface density of ^{3}He. This step appears when the density of ^{3}He is equal to 0.85 of a monolayer. At lower densities the second Andreev level is not important, and we are dealing with a purely two-dimensional one-level system whose spectrum is $E = -\Delta - \varepsilon_1 + \frac{p_{||}^2}{2m_1}$ and the wave-function is $\Psi = \Psi(z)\exp(i\vec{p}_{||}\vec{r}_{||})$.

11.2.3 Spin Susceptibility of ^{3}He-Submonolayers

Another important result reported by Hallock et al. is an analysis of the temperature dependence of the susceptibility. At low temperatures ($T \ll T_F$) the susceptibility depends weakly on temperature, and for surface densities from 0.03 to 0.3 of a monolayer it is well described by an expression for a two-dimensional Fermi-gas with weak repulsive interaction (with coupling constant f_0) between the particles [36, 37]:

$$\chi = \chi_0 \frac{1 + \frac{1}{2}F_1^s}{1 + F_0^a} \sim \chi_0(1 + f_0), \tag{11.2.1}$$

where χ_0 is susceptibility of the non-interacting 2D Fermi-gas, $F_1^s \sim f_0^2$ and $F_0^a \sim f_0$ are two-dimensional harmonics of the Landau quasiparticle interaction function, $f_0 \sim \frac{1}{2\ln 1/(p_F r_0)}$ is a two-dimensional coupling constant (introduced in this chapter) and r_0 is the range of the potential.

At the surface densities from 0.005 to 0.03 we have $\chi < \chi_0$, which supports the attractive sign of the coupling constant (this is also true for the gas-parameter $a(x)p_{F0}x^{1/3}$ in the case of three-dimensional solutions). Note that the exact surface densities at which the 2D coupling constant changes its sign can be determined from the measurements at lower temperatures $T < T_F$, since $T_F \sim T_{F0}x$ is small and the transition from the Fermi-gas behavior of the susceptibility to the Curie law occurs very early.

Concluding this subsection we must mention that there is also another purely two-dimensional system, namely ^{3}He on the surface of grafoil which has very similar properties at a low surface density of ^{3}He (cf. experiments carried out by Saunders group [5, 38]). The rest of our discussion of fermionic superfluidity in purely two-dimensional low-density systems can be also applied to 3He on grafoil, subject only to small modifications.

11.2.4 Possibility of the Superfluid Transition in the Two-Dimensional Solutions

We shall now consider the possibility of the superfluid transition in a two-dimensional ^{3}He submonolayers on the surface of ^{4}He.

By analogy with the tree-dimensional case, the total interaction between two ^{3}He particles on the surface is given by the expression:

$$V(\vec{r}, z) = V_{dir}(\vec{r}, z) + V_{exch}(\vec{r}, z), \tag{11.2.2}$$

where the exchange interaction $V_{exch}(\vec{r}, z)$ is governed by the sum of the residual parts (which are not used to form Andreev level) of the deformation potential of the interaction between two ^{3}He particles via the polarization of ^{4}He, and of the van der Waals attraction of the substrate. These residual parts of the exchange interaction are related primarily with the interaction of ^{3}He particles with the curved surface of superfluid ^{4}He in the field of surface waves of a third sound. The spectrum of third sound waves is of the form $\omega^2 = \frac{\alpha}{\rho}(\kappa^2 + q^2)q \cdot \mathrm{th}(qL)$ [39, 40], where the first term in the parentheses describes the contribution of the van der Waals potential of the substrate and the second one represents the local surface change in the density of ^{4}He. In the case of thin films the contribution of the first term predominates, i.e. the dynamic part of the van der Waals potential of the substrate is more important than "surface phonons" (which are called riplons). Consequently, a reduction in the film thickness changes the spectrum from the purely riplon type $\omega^2 = \frac{\alpha}{\rho}q^3$, where α is the surface tension [41] to an acoustic spectrum with a linear dispersion law [39] $\omega^2 = \frac{\alpha\kappa^2}{\rho}q^2L$, where κ is the capillary constant of the van der Waals potential and L is the film thickness $qL \ll 1$.

In the two-dimensional problem it is important, as always, to determine the two-dimensional projection of the three-dimensional potential $V(\vec{r}, z)$. In close analogy with the two-dimensional projection of the Coulomb interaction (briefly

considered in Chap. 10 in the momentum space), in the real space it is given by the expression:

$$V(\vec{r}_1 - \vec{r}_2) = \iint V(\vec{r}_1 - \vec{r}_2, z_1 - z_2)|\Psi(z_1)|^2|\Psi(z_2)|^2 dz_1 dz_2, \tag{11.2.3}$$

where $\Psi(z)$ is the wave function of Andreev level. The two-dimensional projection of the total interaction can be represented in the form:

$$V(r) = V_{dir}(r) + V_{exch}(r), \tag{11.2.4}$$

and correspondingly in the momentum space

$$V(q_{||}) = V_{dir}(q_{||}) + V_{exch}(q_{||}). \tag{11.2.5}$$

In (11.2.5) $V_{exch}(q_{||})$ is due to the exchange of a virtual quantum of the third sound. Note that in the case of thin films $qL \ll 1$: $V_{exch}(q_{||} = 0)$ is given by $V_{exch}(q_{||} = 0) = -m_4 c_{III}^2$ [14, 15], where c_{III} is the velocity of the third sound. It is given by:

$$c_{III}^2 = \frac{3V_{sub}h_4}{m_4 n_4 (d + h_4)^4} \tag{11.2.6}$$

In (11.2.6) V_{sub} is the amplitude of the van der Waals potential of the substrate, d and h_4 are the thicknesses of the solid (d) and the superfluid (h_4) layers, so $L = d + h_4$ is a total film thickness (We recall that in the case of well-wetted substrate, such as Au, Ag, Cu, etc., the first ^{4}He layer on the substrate solidifies).

It should be pointed out that, as in the three-dimensional problem, the limiting frequency of surface waves $\omega_D \sim m_4 c_{III}^2$ is much higher than the Fermi energy ε_{F}. Therefore, we are again dealing with an antiadiabatic situation, when the whole volume of the two-dimensional Fermi sphere (and not only its Debye shell) is important in the problem of the possibility of a superfluid transition.

We shall now consider the direct part of the total interaction. By analogy with the three-dimensional case, we have:

$$V_{dir}(q_{||} = 0) = V_1(q_{||} = 0) + V_2(q_{||} = 0), \tag{11.2.7}$$

where V_1 is determined by the hard-core repulsion between two ^{3}He particles at short distances, whereas V_2 is due to the attractive interaction of two ^{3}He particles at large distances (see Fig. 11.4).

As pointed out at the end of the preceding subsection, the experiments of Hallock et al. [4, 30–32] on the dependence of the magnetization of a submonolayer on the surface density of ^{3}He demonstrate that the total interaction of two ^{3}He particles on the surface of a thin film is attractive when the ^{3}He concentration is small ($x < 3$ %), and repulsive when the concentration is higher. Therefore, the direct part of the total interaction can be represented again in a model form shown in Fig. 11.4, i.e.:

$$V_{dir}(r) = \begin{cases} V_1, r < r_1 \\ -V_2, r_1 < r < r_2 \end{cases}, \tag{11.2.8}$$

where $1/r_2 \sim p_F(x = 3\%)$. If the submonolayer density is such that $p_F^2 < \frac{1}{r_1^2}$ ($p_F r_1 < 1$), we can try to use the Fermi-gas approach again. It should be pointed out, that the experiments of Hallock et al. demonstrate, that at ^{3}He densities less than 0.3 of a monolayer (x <30 %) we are indeed dealing with a weakly interacting low-density two-dimensional Fermi-gas.

11.2.5 Two-Dimensional Fermi-Gas with Attraction

A special feature of the two-dimensional case is that for purely attractive potential (without hard-core repulsion part) even if the attraction is infinitely weak, we are dealing with the coexistence of two phenomena [42–44]: the pairing of two particles in vacuum in the coordinate space and the Cooper pairing of two particles in substance in the momentum space in the presence of a filled Fermi sphere. In the case of a purely attractive potential the energy of a bound state in vacuum in weak-coupling case reads:

$$E_b = -\frac{1}{mr_0^2}\exp\left(-\frac{4\pi}{m|U_0|}\right), \tag{11.2.9}$$

where U_0 is the s-wave harmonic of the potential and r_0 is the range of the potential. In the weak-coupling case $|f_0| = \frac{m|U_0|}{4\pi} \ll 1$ for the 2D gas-parameter f_0. The s-wave critical temperature according to Miyake is $T_{C0} = \sqrt{2\varepsilon_F|E_b|}$ for $\varepsilon_F \gg |E_b|$ (see Chaps. 7 and 8).

The situation is more complicated in the case of the potential with a repulsive core and an attractive tail (see Fig. 11.4). Here as it was shown in [45] in the case of strong hard-core repulsion $V_1 \gg \left\{|V_2|; \frac{1}{mr_1^2}\right\}$ we have a threshold for s-wave two-particle pairing. The first solution for the bound state for $k = \sqrt{m|E_b|} \to 0$ appears when $\kappa r_1 \geq 0.4$ and $\kappa r_2 \geq 1.6$, where $\kappa = \sqrt{m(|V_2| - |E_b|)}$. It means that an attractive tail must be at least four times more extended than a hard-core region ($r_2 \geq 4r_1$). The coordinate part of the Ψ-function in this case monotonously increases in the interval between r_1 and r_2 (in close analogy with a solution for the bound-state of the extended s-wave pairing in the low-density 2D t-J model with released constraint which will be considered in Chap. 13 or with a lattice gas with van der Waals potential considered in Chap. 6). Thus we can say, that r_2 is the mean distance between the two particles. The threshold condition can be represented as $m|V_{2C}|r_2^2 \approx 2.6$. Note that mr_2^2 corresponds to $1/2t = md^2$ in a lattice model (where the role of r_1 plays $d/2$ and the role of r_2 plays d-the intersite distance). It means that a threshold in a continuous model is larger than in a lattice

model (see Chap. 6). Note that the coordinate part of the two-particle Ψ-function does not depend upon the statistics of two particles—it is the same for two fermions with spins "up" and "down" in singlet ($S_{\text{tot}} = 0$) state which will be considered in Chap. 13 and for two spinless and structureless bosons considered in Chap. 6. Hence the situation in continuous van der Waals model remains qualitatively the same as in the lattice model (see Figs. 6.1, 11.4 and [45]).

The equation for the energy spectrum reads (see [45]):

$$\frac{\kappa(Y_0(\kappa r_1)J_1(\kappa r_2) - J_0(\kappa r_1)Y_1(\kappa r_2))}{Y_0(\kappa r_1)J_0(\kappa r_2) - J_0(\kappa r_1)Y_0(\kappa r_2)} = \frac{kK_1(kr_2)}{K_0(kr_2)}, \tag{11.2.10}$$

where $k = \sqrt{m|E_b|}$ and $\kappa = \sqrt{m(|V_2| - |E_b|)}$, J_0, Y_0 and J_1, Y_1 are the Bessel functions of zeroth and first orders, K_0 and K_1 are the Macdonald functions of zeroth and first order.

For shallow bound state $|E_b| \ll \frac{1}{mr_2^2}$ close to the threshold $\frac{|V_2|-|V_{2C}|}{|V_2|} \ll 1$ we have (see [46]):

$$|E_b| \sim \frac{1}{mr_2^2}\exp\left\{-\frac{1}{\lambda}\right\}, \tag{11.2.11}$$

where $\lambda = \frac{|V_2|-|V_{2C}|}{\pi|V_2|}$. When the amplitude of the van der Waals attraction strongly exceeds $|V_{2C}| \approx \frac{2.6}{mr_2^2}$, the binding energy $|E_b| \leq \frac{1}{mr_2^2}$. Note that the famous Miyake formula is still valid for the potential with the hard-core repulsion and the van der Waals attractive tail in the weak coupling case $|E_b| \ll \varepsilon_F$. In this case $|E_b| \ll T_{C0} \ll \varepsilon_F$. In the opposite strong-coupling (or very diluted) case when $|E_b| \gg \varepsilon_F$, as we discussed in Chaps. 7 and 8, we have two characteristic temperatures: the bound pairs are formed at the crossover Saha temperature [47] $T_* \sim \frac{|E_b|}{\ln\frac{|E_b|}{\varepsilon_F}}$, while the pairs are Bose-condensed at Fisher-Holenberg s-wave critical temperature [48] $T_{C0} = \frac{\varepsilon_F}{2\ln\ln\frac{|E_b|}{\varepsilon_F}}$.

We note that even in the strong-coupling case $T_{C0} \leq \varepsilon_F$, where $\varepsilon_F = \varepsilon_{F0}x$ and x is the 2D ^{3}He concentration. We shall conclude this subsection with a rough estimate for the s-wave temperature of the superfluid transition in 2D. According to Bashkin, Kurihara and Miyake we can expect T_{C0} of the order of 1 mK or less when the surface density of ^{3}He is of the order of 0.01 of a monolayer.

11.2.6 Two-Dimensional Fermi-Gas with Repulsion

When the ^{3}He surface density exceeds 0.03 of a monolayer, the total interaction between ^{3}He particles changes sign and the s-wave pairing becomes impossible. However, even in this case ^{3}He subsystem will become unstable towards triplet p-wave pairing [36, 37] below the critical temperature $T_{C1} \sim \varepsilon_F \exp\left\{-\frac{1}{6.1f_0^3}\right\}$ in

the third order in f_0 for the effective interaction $U_{\text{eff}}(q)$ (see Chap. 9), where $\varepsilon_F = \varepsilon_{F0}x$ and $f_0 = \frac{1}{\ln \frac{1}{p_{F0}^2 x r_1^2}}$ is 2D coupling constant, r_1 is the range of the hard-core part of the potential [36, 37]. An estimate of the superfluid transition temperature obtained by Chubukov [36] is $T_{C1} \sim 10^{-4}$ K for densities ~ 0.3 of a monolayer corresponding to the limit of the validity of the Fermi-gas description.

It should be pointed out that the allowance for quatric corrections to the spectrum of ^{3}He quasiparticles $\varepsilon(p) = \frac{p^2}{2m}(1 - \gamma \frac{p^2}{p_C^2})$, results in the appearance of the p-wave pairing already in a second order of the perturbation theory for effective interaction. This yields $T_{C1} \sim \varepsilon_F \exp\left\{-\frac{1}{\gamma f_0^2}\right\}$ as demonstrated by Baranov and Kagan [49]. However, the superfluid transition temperature now depends exponentially on the small constant γ representing the quartic corrections to the quadratic spectrum of quasiparticles and, therefore, T_{C1} is very small.

11.3 Superfluidity in Polarized Solutions

We shall now consider briefly the situation in strongly (spin) polarized solutions.

It is well known that the singlet s-wave pairing in a strongly polarized solution is suppressed by a paramagnetic effect. This means that in magnetic fields larger than the paramagnetic limit $H > \frac{T_{C0}}{\mu_B}$ (see Chap. 10), where μ_B is the nuclear Bohr magneton for ^{3}He, the singlet s-wave superfluid state is destroyed. The influence of an external magnetic field (or of the spin polarization) on the triplet p-wave pairing temperature is less trivial.

11.3.1 Three-Dimensional Polarized Solutions

Chubukov and Kagan [9] showed that the p-wave pairing temperature of a three-dimensional polarized gas with repulsion depends strongly and nomonotonically on the degree of polarization α (see Chap. 10 and Fig. 10.2): it rises strongly at low and intermediate polarization (for $S_{tot} = S_{tot}^z = 1$), passes through a maximum when the polarization is 48 %, and falls on further increase of polarization. At a pressure of 10 bar the maximal possible concentration of ^{3}He is $x = 9.5$ % and the temperature in the maximum corresponds to $10^{-6} - 10^{-5}$ K [7], which is much higher than $T_{C1} \sim 10^{-10} \div 10^{-9}$ K corresponding in [7] to the case when $\alpha = 0$. An account of preexponential factors for T_{C1} further increases the critical temperature especially in magnetic field [50]. A qualitatively similar dependence of T_{C1} on α with a maximum at $\alpha = 32$ % was also predicted by van de Haar, Frossati and Bedell [12]. The temperature at the maximum predicted by these authors for the same values of pressure and concentration is somewhat higher and amounts to $10^{-5} - 10^{-4}$ K.

The hope for experimental creation of strongly polarized solutions is based primarily on the elegant idea of Castraing and Nozieres [51]. In their classical paper they proposed to create a strong polarization in a liquid solution by fast melting of a solid solution. The idea is that a solid solution (and pure crystalline ^{3}He) does not have a kinetic energy of the degeneracy of ^{3}He atoms associated with the Pauli principle. Therefore, the application of a magnetic field of the order of the Curie temperature:

$$\mu_B H \sim T_C \sim T \sim 1 \text{ mK and } H \sim 1 \text{ T} \tag{11.2.12}$$

leads to an almost full polarization of the solid solution. It should be pointed out that a significant brute force polarization in a liquid solution can be achieved only by applying very high external magnetic fields $\mu_B H \sim \varepsilon_F \sim 0.1$ K and $H \sim 100$ T. These fields is difficult to reach experimentally.

In the same time fast melting of a strongly polarized ($\alpha \sim 90$ %) solid solution should, according to the estimates of Castraing and Nozieres [51], produce a liquid solution with $\alpha \sim 30$ % which is close to the maximum of T_C in the theory of van de Haar, Frossati and Bedell. Naturally, this polarization is of a nonequilibrium nature, but its lifetime is very long ($\sim$30 min) because of the long relaxation time in the liquid phase.

Another very important idea for the increase of the critical temperature is the suggestion of Meyerovich et al. [52, 53] according to which the maximal solubility of a strongly polarized solution may be 3–4 times higher than the maximal solubility in the absence of polarization ($x_{\max}(\alpha) \sim 30$ % instead of $x_{\max}(\alpha = 0) \sim 9.5$ %). A combination of the ideas of Castraing, Nozieres and Meyerovich may produce an even greater increase (to $10^{-4} - 10^{-3}$ K) in the superfluid transition temperature of a strongly polarized solution.

11.3.2 Two-Dimensional Polarized Solutions

The situation in two-dimensional polarized submonolayers at ^{3}He densities from 0.03 to 0.3 of a monolayer is even more favorable from the point of view of the superfluid transition temperature. As it was shown in Chap. 10, the competition between a strong 2D Kohn's anomaly and a reduction of the density of states of the "down" spins (antiparallel to the field) again gives rise to a nonmonotonic dependence of triplet p-wave temperature T_{C1} on the degree of polarization α, with a very strong maximum at $\alpha = 60$ % (see Fig. 10.3 and [7, 9, 54]). It should be pointed out that the maximum is very broad and extends from 10 to 90 % of the polarization.

Estimates in [7] indicate that the critical temperature is fairly high now in experimentally achievable fields $H \sim 15$ T. In fact, for the two-dimensional solution with surface density $n_3 \sim 0.05$ of a monolayer and the Fermi-energy $\varepsilon_F \sim 0.13$ K, the application of such a magnetic field produces a polarization degree $\alpha = \frac{\mu_B H}{\varepsilon_F} \sim 10\%$. In this case the triplet p-wave pairing temperature (for $S_{tot} = S^z_{tot} = 1$) can reach a value $T_{C1}^{\uparrow\uparrow} \sim 1$ mK, which is quite nice and promising.

11.4 Experimental Situation and Limitations on the Existing Theories

In the introduction to the Sect. 11.1 we pointed out that the search for fermionic superfluidity of ^{3}He in three-dimensional and two-dimensional solutions has not resulted in experimental success yet. The published experimental results demonstrating the absence of superfluidity at certain pressures and concentrations impose some limits on the various theoretical estimates of the superfluid transition temperature. They are forcing both theorists and experimentalists to concentrate on those ranges of the parameters where the experiments have not been carried out yet. The review of Østgaard and Bashkin [17] contains the experimental results obtained by the groups of Pobell [55] and Ogawa [56] (we must also mention here more recent experimental results of Saunders group for the 2D case [57–59]). They demonstrate the absence of the superfluid transition in the three-dimensional solutions right down to 0.2 mK for ^{3}He concentrations of 1, 5 and 6.4 %. They show that the temperature both of the singlet s-wave pairing and the temperature of the triplet p-wave pairing (we recall that the s-wave pairing is suppressed for the ^{3}He concentrations exceeding 4 % in 3D) most probably lie below 0.2 mK.

The estimates of Østgaard and Bashkin concerning s-wave pairing in 3D case show that the most promising way is to seek the singlet superfluidity at ^{3}He concentrations amounting to $\sim$0.5–1 %. van de Haar, Frossati and Bedell [12] assume that the optimal concentration lies in the interval 1.5–2.5 %. The corresponding temperature T_{C0} is of the order of 0.1 mK for the results of the both groups. According to the estimates of Frossati, Bedell, Meyerovich and Kagan, the triplet superfluidity is most likely to occur at the maximal possible concentration of ^{3}He $x_{max} \approx 9.5$ % which corresponds to the pressure 10 bar, under strong polarization conditions (in strong effective magnetic fields). As pointed out above, when the polarization is very strong, it may be possible to reach ^{3}He concentrations even exceeding 9.5 %. The most realistic estimates once again (similar to the estimates for an s-wave temperature T_{C0}) predict a triplet pairing temperature T_{C1} only of the order of 0.1 mK or lower. Therefore, we obviously can expect that both the singlet and the polarization-enhanced triplet pairing temperatures cannot exceed the value of the order of 0.1 mK.

It seems that the situation in the two-dimensional solutions is more favorable with respect to T_C from the experimental point of view. The most important experimental results, imposing limits on the theoretical estimates were obtained for 2D ^{3}He submonolayers on the surface of thin ^{4}He films by Pobell [55, 60] and on the surface of grafoil by Saunders et al. [58, 59]. The authors of [55] performed the measurements of the viscous penetration length with the aid of torsional oscillations. The scheme of their experiment is shown on Fig. 11.5.

Pobell reached temperatures of 0.85 mK and did not observe the superfluid transition in the range of surface concentrations from 0.1 to 1 monolayer. Even more severe restrictions on T_C impose the experiments of Saunders group [58, 59]

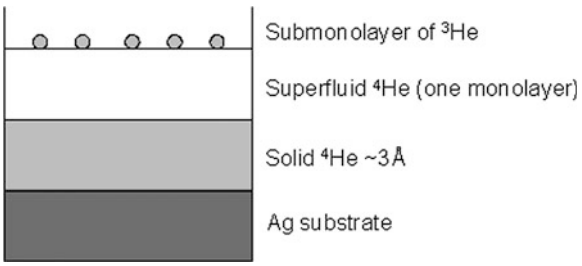

Fig. 11.5 The principal scheme of Pobell experiments [7, 55, 60] on the search of fermionic superfluidity in the submonolayers of ^{3}He on the surface of very thin film of superfluid ^{4}He

who did not find the fermionic superfluid transition up to the temperatures 0.1 mK for ^{3}He surface coverages from 0.05 till 1 monolayer on the grafoil substrate.

These experimental data suggest that the fermionic superfluidity in two-dimensional solution should be searched either at lower ^{3}He densities ($n_3 < 0.03$ of a monolayer, when the total interaction corresponds to the attraction) or at a little bit higher densities $n_3 \sim 0.05 \div 1$ of a monolayer (for repulsive total interaction) when we apply a strong magnetic field $H \sim 15 \div 30$ T. In both cases we can probably expect the singlet superfluidity in the absence of a magnetic field (for concentrations $n_3 < 0.03$ of a monolayer) and the field-enhanced triplet superfluidity (for $n_3 \sim 0.05 \div 1$ of a monolayer) at temperatures of the order of 1 mK or less. These temperatures are ten times higher than in 3D case and in principle can be achieved experimentally.

11.5 Two-Dimensional Monolayers as a Bridge Between Superfluidity and High-T_C Superconductivity

In conclusion of this chapter let us stress again that the two-dimensional ^{3}He submonolayers on the surface of thin ^{4}He films and on grafoil are ideal two-dimensional systems for experimental verification of many currently popular theories of the normal and superconducting state of quasi-two-dimensional high-T_C superconductors, including marginal Fermi-liquid theory of Varma et al. [19] and Luttinger liquid theory of Anderson [20]. The most valuable experimental information which can impose limitations on different theories of high-T_C SC is connected with the measurements of a magnetic susceptibility $\chi = \chi_0 \frac{1+\frac{1}{2}F_1^s}{1+F_0^a}$ at low temperatures $T < T_F$ and small densities. The knowledge of Landau harmonics F_0^a, F_1^s, which enter in the expression for χ [61, 62], will help us to answer the question whether Landau Fermi-liquid theory exists in a 2D case even at low densities, and, if it exists, what are the non-trivial corrections to Landau expansion for measurable quantities such as effective mass or zero-sound velocity, which are missing in a standard 3D situation. We will address this topic more detaily in Chap. 14, when we will study the singularity in Landau quasiparticle interaction function $f(\vec{p}, \vec{p'})$ for almost parallel momenta $\vec{p} || \vec{p'}$ and small transfered momentum $\vec{q} = \vec{p} - \vec{p'} \to 0$ [63, 64] in 2D and

consider detaily the doubts of Anderson [20] on the validity of Landau Fermi-liquid description due to the existence of this singularity. We will show in Chap. 14 that in the framework of perturbation theory [63, 64] the singularity is much weaker $f(\vec{p},\vec{p'}) \sim \frac{1}{\sqrt{q}}$ then Anderson's prediction $f(\vec{p},\vec{p'}) \sim \frac{1}{q}$. Moreover, it exists only for a narrow angle region $\varphi \sim q^{3/2}$ close to the angle $\varphi = 0$, thus not destroying Landau Fermi-liquid completely but leading only to nontrivial temperature corrections to the effective mass $(m^*/m - 1) \sim (1/2)F_1^s \sim f_0^2 T/\varepsilon_F$ and other observables. It will be very interesting to check experimentally the predictions of the perturbation theory of Prokof'ev, Stamp [63], Baranov et al. [64] on the ^{3}He submonolayers at low temperatures and surface densities. To do that it is important to expand the susceptibility measurements of Hallock and Godfrin [65] groups for ^{3}He submonolayers on the surface of thin film of superfluid ^{4}He and Saunders group for ^{3}He submonolayers on grafoil on lower temperatures and surface densities where we are in degenerate (Pauli) situation. Note that earlier experiments [4, 5, 30–32, 38] have been carried out primarily at intermediate and high temperatures (at which there is a transition to Curie law).

References

1. Bardeen, J., Baym, G., Pines, D.: Phys. Rev. **156**, 207 (1967)
2. Bashkin, E.P., Meyerovich, A.E.: Adv. Phys. **30**, 1 (1981)
3. Andreev, A.F.: JETP **23**, 939 (1966)
4. Valles Jr, J.M., Highley, R.H., Johnson, B.R., Hallock, R.B.: Phys. Rev. Lett. **60**, 428 (1988)
5. Saunders, J., Lusher, C.P., Cowan, B.P.: Phys. Rev. Lett. **64**, 2523 (1990)
6. Kohn, W., Luttinger, J.M.: Phys. Rev. Lett. **15**, 524 (1965)
7. Kagan, M.Yu.: Sov. Phys. Uspekhi **37**, 69 (1994)
8. Kagan, M.Yu., Chubukov, A.V.: JETP Lett. **47**, 614 (1988)
9. Kagan, M.Yu., Chubukov, A.V.: JETP Lett. **50**, 517 (1989)
10. Fay, D., Layzer, A.: Phys. Rev. Lett. **20**, 187 (1968)
11. Chubukov, A.V., Kagan, M.Yu.: Invited paper in Proceedings of the Conference on Physical Phenomena at High Magnetic Fields, Tallahassee, Florida, p. 239 (1991)
12. van de Haar, P.G., Frossati, G., Bedel, K.S.: J. Low Temp. Phys. **77**, 35 (1989)
13. Fay, D.: Phys. Rev. B **16**, 537 (1977)
14. Kurihara, S.J.: Jour. Phys. Soc. Jpn **52**, 1311 (1983)
15. Monarkha, Yu.P., Sokolov, S.S.: Sov. Jour. Low. Temp. Phys **16**, 90 (1990)
16. Gor'kov, L.P., Melik-Barkhudarov, T.K.: JETP **40**, 1452 (1961)
17. Østgaard, E., Bashkin, E.P.: Physica B **178**, 134 (1992)
18. Friedel, J.: Adv. Phys. **3**, 446 (1954)
19. Varma, C.M., Littlewood, P.B., Schmitt-Rink, S., Abrahams, E., Ruckenstein, A.E.: Phys. Rev. Lett. **63**, 1996 (1989)
20. Anderson, P.W.: Phys. Rev. Lett. **65**, 2306 (1990)
21. Esel'son, B.N., Bereznyak, N.G.: Dokl. Akad. Nauk USSR **99**, 569 (1954)
22. Atkins, K.R., Narahara, Y.: Phys. Rev. A **138**, 437 (1965)
23. Zinov'eva, K.N., Boldarev, S.T.: JETP **29**, 585 (1969)
24. Edwards, D.O., Shen, S.Y., Eckardt, J.R., Fatouros, P.P., Gasparini, F.M.: Phys. Rev. B **12**, 892 (1975)
25. Edwards, D.O., Saam, W.F.: Progr. Low Temp. Phys A **7**, 283 (1978)

26. Lekner, J.: Philos. Mag **22**, 669 (1970)
27. Saam, W.F.: Phys. Rev. A **4**, 1278 (1971)
28. Gasparini, F.M., Bhattacharyya, B.K., Di Pirro, M.J.: Phys. Rev. B **29**, 4921 (1984)
29. Bhattacharyya, B.K., Di Pirro, M.J., Gasparini, F.M.: Phys. Rev. B **30**, 5029 (1984)
30. Highley, R.H., Sprague, D.T., Hallock, R.B.: Phys. Rev. Lett. **63**, 2570 (1989)
31. Alikacem, N., Sprague, D.T., Hallock, R.B.: Phys. Rev. Lett. **67**, 2501 (1991)
32. Hallock, R.: Physics Today **51**, 30 (1998) and references therein
33. Dalfovo, F., Stringari, S.: Phys. Scr. **38**, 204 (1988)
34. Pavloff, N., Treiner, J.: JLTP **83**, 331 (1991)
35. Krotscheck, E., Saarela, M., Epstein, J.L.: Phys. Rev. B **38**, 111 (1988)
36. Chubukov, A.V.: Phys. Rev. B **48**, 1097 (1993)
37. Efremov, D.V., Mar'enko, M.S., Baranov, M.A., Kagan, M.Yu.: Physica B 284–288, 216 (2000)
38. Lusher, C.P., Cowan, B.P., Saunders, J.: Phys. Rev. Lett. **67**, 2497 (1991)
39. Khalatnikov, I.M.: An Introduction to the Theory of Superfluidity. Perseus Publishing, Cambridge (2000)
40. Putterman, S.J.: Superfluid Hydrodynamics. North-Holland Publishing Company, New York (1974)
41. Landau, L.D., Lifshitz, E.M.: Fluid Mechanics: vol. 6 (Course of Theoretical Physics), Butterworth-Heinemann, Oxford (1987)
42. Miyake, K.: Prog. Theor. Phys **69**, 1794 (1983)
43. Randeria, M., Duan, J.M., Shich, L.Y.: Phys. Rev. Lett. **62**, 981 (1989)
44. Schmitt-Rink, S., Varma, C.M., Ruckenstein, A.E.: Phys. Rev. Lett. **63**, 445 (1989)
45. Efremov, D.V., Kagan, M.Yu.: Physica B, 329–333, 30 (2003)
46. Kagan, M.Yu., Efremov, D.V.: Phys. Rev. B **65**, 195103 (2002)
47. Landau, L.D., Lifshitz, E.M.: Statistical Physics. Part I, Butterworth-Heinemann, Oxford (1999)
48. Fisher, D.S., Hohenberg, P.C.: Phys. Rev. B **37**, 4936 (1988)
49. Baranov, M.A., Kagan, M.Yu.: JETP **72**, 689 (1991)
50. Efremov, D.V., Mar'enko, M.S., Baranov, M.A., Kagan, M.Yu.: JETP **90**, 861 (2000)
51. Castraing, B., Nozieres, P.: Jour. Phys. (Paris) **40**, 257 (1979)
52. Meyerovich, A.E.: JETP Lett. **37**, 32 (1983)
53. Roobol, L.P., Steel, S.C., Jochemsen, R., Frossati, G., Bedell, K.S., Meyerovich, A.E.: Europhys. Lett. **17**, 219 (1992)
54. Baranov, M.A., Chubukov, A.V., Kagan, M.Yu.: Int. Jour. Mod. Phys. B **6**, 2471 (1992)
55. Pobell, F.:Private communication to the author
56. Ishimoto, H., Fukuyama, H., Nishida, N., Miura, Y., Takano, Y., Fukuda, T., Tazaki, T., Ogawa, S.: Jour. Low Temp. Phys **77**, 133 (1989)
57. Casey, A., Patel, H., Nyeki, J., Cowan, B.P., Saunders, J.: Jour. Low Temp. Phys **113**, 293 (1998)
58. Saunders, J., Casey, A., Patel, H., Nieki, J., Cowan, B.: Physica B **280**, 100 (2000)
59. Morley, G.W., Casey, A., Lusher, C.P., Cowan, B., Saunders, J., Parpia, J.M.: Jour. Low Temp. Phys **126**, 557 (2002)
60. Mueller, R.M., Chocholacs, H., Buchal, Ch., Kubota, M., Owers-Bradley, J.R., Pobell, F.: Proceedings of Symposium on Quantum Fluids and Solids, Sanibel Island, FL. In: Adams, E.D., Ihas, G.G. (eds.) AIP Conference Proceeding No 103, p. 192 American Institute of Physics, New York, (1983)
61. Lifshitz, E.M., Pitaevskii, L.P.: Statistical Physics, Part II. Pergamon Press, Oxford (1988)
62. Pines, D., Nozieres, P.: The Theory of Quantum Liquids. Benjamin, New York (1966)
63. Prokof'ev, N.V.: In review of P.C.E. Stamp, Jour. Phys. (Paris) **3**, 625 (1993)
64. Baranov, M.A., Kagan, M.Yu., Mar'enko, M.S.: JETP Lett. **58**, 734 (1993)
65. Morhard, R.-D., Bauerle, C., Bossy, J., Bunkov, Yu.M., Fisher, S.N., Godfrin, H.: Phys. Rev. B **53**, 2658 (1996)

Chapter 12
Triplet Pairing and Superfluid Phase-Diagram in Fermi Gas of Neutral Particles and in Superfluid ^{3}He

In this chapter we will discuss s-wave and p-wave superfluidity in a Fermi-gas of neutral particles at ultracold temperatures in the restricted geometry of the magnetic traps.

We will show that in the case of exactly equal densities of the trapped components with different projections of the nuclear spin J_z the Fermi-gas will be unstable towards singlet s-wave pairing predicted by Stoof et al. [1].

We also show that in the case of the density disbalance between the trapped components with different J_z the s-wave pairing is suppressed due to Landau criterion of superfluidity [2]. However, in this case the system will be also unstable towards p-wave superfluid pairing at ultralow temperatures [3, 4]. We discuss the possibility to increase T_C of the p-wave pairing for optimal relative densities (n_i/n_j) of the trapped hyperfine components. We discuss the metastability of the system and possible phase-separation at higher densities. We present the estimates for T_C in disbalanced fermionic ^{6}Li with an account of preexponential factors [3, 4]. We also present a simple estimate for the pair size in the trap which helps to extend the estimate for T_C in the infinite free space to a trap of a finite dimension.

We briefly discuss the dilute Fermi-Bose mixture of ^{6}Li-^{7}Li in the trap and the possibility to enhance p-wave fermionic T_{C1} via the polarization of a bosonic component [5] which is described by the density–density correlation function.

In the end of the chapter we construct Ginzburg–Landau (GL) [6, 7] functional for p-wave superfluid Fermi-gas and calculate the coefficients $\beta_1 \ldots \beta_5$ (near quartic terms) in Ginzburg–Landau expansion with an account of the Rainer and Serene [8, 9] strong-coupling corrections.

On the level of the exact knowledge of T_{C1} (with an account for preexponential factors) [4] and of the GL-functional we construct the phase-diagram (find all the global minima of GL-functional) for the superfluid state of the p-wave Fermi-gas both in 3D and 2D case. We indicate the regions of B- and A-phases [10–15] of the triplet p-wave Fermi-gas [9, 16] in the absence of magnetic field, as well as A1 and A2-phases [17–19] in strong magnetic field. We do not find the trace of exotic

M. Yu. Kagan, *Modern Trends in Superconductivity and Superfluidity*,
Lecture Notes in Physics 874, DOI: 10.1007/978-94-007-6961-8_12,

(third) phase of p-wave superfluid (different from A and B phases in 3D or axial phase in 2D) on the level of our calculations in the absence of a magnetic field. We note that a hope to get a third exotic phase in 3D can be possibly connected with weak magnetic fields $H < H_p = \frac{T_{C1}}{\mu_B}$ and intermediate values of coupling constant $\lambda = 2ap_F/\pi \sim 1$ [20].

12.1 Fermionic Superfluidity of ^{6}Li in the Magnetic Traps at Ultracold Temperatures

As we already mentioned in the introduction to Chap. 5, one of the most important events of the past years in condensed-matter physics was the discovery of Bose–Einstein condensation in gases of alkali elements ^{87}Rb [21], ^{7}Li [22] and ^{23}Na [23] in the confined geometry of magneto-optical traps.

In this section we consider the fundamental possibility of achieving a superfluid instability of a different type—with respect to Cooper pair formation in a nonideal atomic Fermi gas with a scattering length of large absolute value. For ^{6}Li we shall consider the case of an attractive scattering length $a < 0$, though formally our results for p-wave pairing will be proportional to a^2 and thus will not depend upon the sign of a.

Note that as we discussed in Chaps. 5 and 6, the quasiresonance scattering length could be further dramatically increased by absolute value in adiabatically switched magnetic field if we work close to Feshbach resonance [24–26, 27, 28] (we remind that this field is additional to the inhomogeneous field which forms the trap itself). Namely, $a = a_{bg}\left(1 + \frac{\Delta}{B - B_{res}}\right)$, where $B_{\text{res}} \sim 830$ Gs is a resonance field for ^{6}Li. For virtual level (as we have for ^{6}Li) $a_{\text{bg}} < 0$ [29] and $|a_{\text{bg}}| \sim (15 \div 20)$ Å. Thus, as we discussed in Chap. 5, for $B \geq B_{\text{res}}$: $a < 0$ while for $B < B_{\text{res}}$: $a > 0$. Moreover, close to the resonance field B_{res} the absolute values of the scattering length $|a|$ could reach (2–3) 10^3 Å in ^{6}Li. Throughout this section we will work in the BCS-limit of Feshbach resonance $a < 0$ ($B \geq B_{\text{res}}$), where we have virtual level and assume very large absolute value of the scattering length. Note that in the opposite situation ($B < B_{\text{res}}$)$a > 0$—there is a real level in the potential well and we are in the BEC-limit of strongly bound ^{6}Li$_2$—molecules (or dimers) [24–26, 27, 28] which are formed at some higher (Saha) temperatures $T_* \sim |E_{\text{b}}|$ [30]—the binding energy of the molecule, and Bose-condensed at a critical temperature $T_C \sim 3.31\frac{(n/2)^{2/3}}{2m} \sim 0.2\varepsilon_F$ governed by Einstein formula.

This situation is realized in the experiments of Grimm, Ketterle and Jin groups and is discussed in detail in Chap. 5.

12.1.1 s-Wave Pairing in Trapped Fermi-Gas with Exactly Equal Densities of Different Components

The case of an attractive scattering length $a < 0$ for trapped Fermi-gas was first considered by Stoof et al. [1]. As it was shown by Gor'kov and Melik-Barkhudarov [31], in this case s-wave pairing is possible in the system with a critical temperature $T_{C0} \approx 0.28\varepsilon_F \exp\{-\frac{1}{\lambda}\}$, where $\lambda = \frac{2|a|p_F}{\pi}$ is the gas parameter. For ^{6}Li with $n \sim 10^{14}$ cm^{-3} and $|a| \sim (2 \div 3)\ 10^3$ Å we have $T_{C0} \sim 10^{-6}$ K according to the estimates of Stoof et al. [1].

We note that s-wave pairing in the presence of a nuclear spin I must be understood as a pairing in which the orbital angular momentum of the pair $l = 0$, and the total spin of the pair is even. The total spin of the pair is formed from the total spins $\vec{J} = \vec{I} + \vec{S}$ of the two atoms. The structure of the levels is determined by the hyperfine interaction $U_{hf}\vec{S}\,\vec{I}$, where $\vec{S}$ is electron spin and $\vec{I}$ is nuclear spin. In practice, however, experimental realization of the s-wave pairing in Fermi-gasses of alkali elements requires several important conditions to be satisfied. First of all, in the case of an attractive scattering length a substantial limitation on the density of the system, namely $\lambda < 1$, arises in Fermi gasses due to the fact that the compressibility of the gas must be positive. Even for $\lambda < 1$, however, s-wave pairing is suppressed on an account of the presence of a very weak magnetic field $\vec{B}$ in the system, which often is a case in a magnetic trap. Indeed, effective decoupling of the nuclear and electron spins occurs in the fields $B > H_{hf} = U_{hf}/|\mu_B^{el}| \sim 10^{-2}$ T (μ_B^{el}—electron Bohr magneton). As a result, s-wave pairing becomes possible only for atoms with different z-projections of the nuclear spin I_z. However, in magnetic fields $B \sim H_{\mathrm{hf}}$ the Zeeman splitting $\Delta E \sim \mu_B^{nucl} H_{hf} I_z \sim 10^{-5}$ K of the components with different z-projections of a nuclear spin I_z (μ_B^{nucl}—nuclear Bohr magneton) is much greater than the realistic values of $T_{C0} \sim 10^{-6}$ K (and even of ε_F), and thus s-wave pairing is completely suppressed. It is important to note that even in the absence of a magnetic field the s-wave pairing of the atoms with different hyperfine components is possible only if the densities of the components are very close to each other: $\frac{|\varepsilon_{F1} - \varepsilon_{F2}|}{\varepsilon_{F1}} \ll \frac{T_{C0}}{\varepsilon_{F1}} \ll 1$. In the disbalanced Fermi-gas with $|\varepsilon_{F1} - \varepsilon_{F2}| \geq T_{CO}$ an s-wave pairing is suppressed due to Landau criterion of superfluidity (the Cooper pairs will have large total linear momentum $|\vec{P}|$ exceeding T_{C0}/v_F). We note also that in the case of a repulsive scattering length, s-wave pairing is impossible even if the components have identical densities and magnetic field is strictly zero.

12.1.2 Triplet p-Wave Pairing in the Disbalanced Case

The realistic hope to achieve superfluidity in disbalanced Fermi-gas of alkali elements lies in the unconventional triplet p-wave pairing, which is an analog of

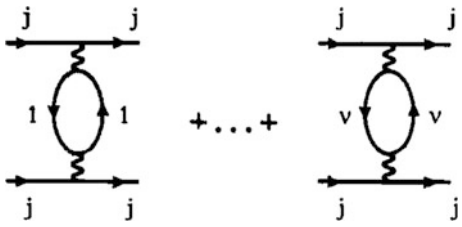

Fig. 12.1 Loop diagrams determining in the second order of the gas parameter the effective interaction of the two atoms of the same component via the excitation of virtual particle-hole pairs of the other components [3]. The term with $i = j$ is omitted in the sum

the A1-phase [6] of superfluid ^{3}He with $S_{tot} = S_z^{tot} = 1$. This type of pairing takes place between the atoms of the same component and is not destroyed by a magnetic field. As we already discussed in Chaps. 10 and 11, the hope to obtain triplet p-wave pairing with reasonable T_C is connected with the presence of Kohn anomaly (Friedel oscillations) in the effective interaction of two Fermi-particles via polarization of a fermionic background [32–34, 35]. The critical temperature of the p-wave pairing $T_{C1} \sim \varepsilon_F \exp\left\{-\frac{13}{\lambda^2}\right\}$ describes the pairing of the atoms of the same component (with $S_z = ½$ in case of ^{3}He) via the excitation of the particle-hole pairs of the other component (with $S_z = -½$ for ^{3}He) and does not depend on the sign of the scattering length. Curiously, this simple formula for T_{C1} works rather well as an extrapolation for intermediate values $\lambda \sim 1$, giving the reasonable estimate $T_{C1} \sim 10^{-3}\ \varepsilon_F \sim 10^{-3}$ K for the dense ^{3}He (with $\lambda = 1.3 \div 1.4$). Another important point (see Ref. [7] in Chap. 11 and Refs. [3, 4] in Chap. 10) is that we can substantially increase the critical temperature T_{C1} already at low density considering a partially spin-polarized or multi component situation.

In our case the number of components equals $\nu = 2I + 1$. It is obvious that a magnetic field interacts mainly with the electron spin. Therefore, in the fields $B > H_{hf} \gg \varepsilon_F/|\mu_B^{el}|$ our problem actually becomes practically equivalent to the problem of a multicomponent fully polarized (with respect to electron spin) Fermi system with identical masses of the components. As we discussed in Chap. 10 the effective interaction determining the critical temperature of the superfluid transition is given in the second order of the gas parameter by the loop diagrams presented on Fig. 12.1 [3]. The effective interaction $U_{\text{eff}}(q_j)$ is represented in algebraic form as:

$$U_{eff}(q_j) = \left(\frac{4\pi a}{m}\right)^2 \sum_{i \neq j} \Pi_{ii}(\vec{q_j}), \tag{12.1.1}$$

where

$$\Pi_{ii}(\vec{q_j}) = \int \frac{d^3\vec{p}}{(2\pi)^3} \frac{n_{Fi}\vec{p} - n_{Fi}(\vec{p} - \vec{q_j})}{\varepsilon_i(\vec{p} - \vec{q_j}) - \varepsilon_i\vec{p}} \tag{12.1.2}$$

is polarization operator for the i-th component and $\vec{q_j} = \vec{p_j} - \vec{p_j}'$ is the difference between the momenta of the particles of the type j entering and leaving the Cooper channel.

After integration of $U_{\text{eff}}(q_j)$ with the first Legendre polynomial $\cos\theta = 1 - \frac{q_j^2}{2p_{Fj}^2}$ we get the following critical temperature in the case when the densities of the v components are all the same $n_1 = n_2 = \ldots = n_v$ [3]:

$$T_{C1} \sim \varepsilon_F \ \exp\left\{-\frac{13}{(v-1)\lambda^2}\right\}. \tag{12.1.3}$$

We note that the critical temperature is the same for each component and in (12.1.3) ε_F and λ depend upon the density of the individual component. We note also that for $v = 2$ we restore the result [32, 33] for ^{3}He. Finally we understand that T_{C1} in (12.1.3) does not depend upon the sign of the scattering length. To increase T_{C1} further we use the result of Ref. [3] and Ref. [7] Chap. 11 where it is shown that the dependence of T_{C1} from the relative density ratio of the different components is strongly nonmonotonic and has a pronounced and extended maximum for $n_j/n_i \sim 3$ ($p_{Fj}/p_{Fi} \sim 1.4$). In the optimal situation $n_j \sim 3n_i$ (for all $i \neq j$) the critical temperature for the j-th component reads:

$$T_{C1} \sim \varepsilon_{Fj} \exp\left\{-\frac{7}{(v-1)\lambda_{eff}^2}\right\}, \tag{12.1.4}$$

where $\lambda_{eff}^2 = \left(\frac{2a}{\pi}\right)^2 p_{Fi} p_{Fj}$.

Note that while deriving (12.1.4) we in fact considered the Hamiltonian:

$$\hat{H} = \hat{H}_0 + \hat{H}_{\text{int}} = \sum_{i=1}^{v} \sum_{\vec{p}} \varepsilon_i(\vec{p}) a_{\vec{p}i}^+ a_{\vec{p}i} + \frac{2\pi a}{mV_s} \sum_{i \neq j} \sum_{\vec{p}\vec{p}'\vec{q}} a_{\vec{p}i}^+ a_{\vec{p}'j}^+ a_{\vec{p}'-\vec{q}j} a_{\vec{p}+\vec{q}i}, \tag{12.1.5}$$

where i designates the projections of the nuclear spin, i.e., the number of the components, and we have dropped the electron spin index, since we are working with a completely polarized spin system of electrons.

On the basis of the Hamiltonian (12.1.5) only (without an allowance of the term considered in Chap. 10 which rescatters the Cooper pairs between different bands or different components) we can say that the components with the density less than n_j become superfluid at lower temperature than (12.1.4).

We should note also the following circumstance. In the case of large and repulsive scattering length the formulas (12.1.3) and (12.1.4) must hold, at least as an extrapolation, right up to the values of the gas parameter $\lambda \sim 1$, resulting in experimentally achievable values for T_C. In the case of an attractive scattering length, for the optimal situation $n_j \sim 3n_i$, the limits imposed on the system density by the stability conditions are also not too stringent and once again give $\lambda_{\text{eff}} \leq 1$. As a result for disbalanced ^{6}Li with $v = 3$ components and densities $n \sim 10^{14}$ cm^{-3} we have $T_{C1} \sim 10^{-8}$ K on the basis of (12.1.3) and (12.1.4).

12.1.3 Stability of the System Towards Phase Separation

Stability of the system towards phase separation is governed, as usual, by the condition of positive compressibility $\chi^{-1} \sim c^2 > 0$, where $c^2 = \frac{N}{m}\frac{\partial \mu}{\partial N} = \frac{N}{m}\frac{\partial^2 E}{\partial N^2}$ is sound velocity squared. In our case $N = \sum_i N_i$ is the total number of particles in all the components, and

$$E = \frac{3}{5}\sum_{i=1}^{v} \varepsilon_{Fi} N_i - \frac{4\pi a}{m}\sum_{i\neq j} N_i N_j \tag{12.1.6}$$

is the total energy of the system. Remind that a is s-wave ($l = 0$) scattering length for two fully polarized in electron spin ^{6}Li particles with different z-projections of the nuclear spin I_z (see Fig. 12.2). Note that according to Pauli principle only particles from different components scatter on each other in the case of short-range interaction. The stability criterion for compressibility of the system $c^2 > 0$ together with $c_i^2 = \frac{N_i}{m}\frac{\partial \mu_i}{\partial N_i} > 0$ (for partial compressibility of i-th component) yields

$$\lambda_{eff} = \frac{2|a|}{\pi}(p_{Fi} p_{Fj})^{1/2} \lesssim 1 \tag{12.1.7}$$

12.1.4 Metastability of the System

We also note that, as we already discussed in Chap. 5, both bosonic (BEC) and fermionic (BCS-condensates) are inherently metastable due to three-particle recombination [37–40] and spin-relaxation [41, 29] processes. We emphasized in Chap. 5 that while typical lifetime of Bose-condensates is of the order of 10s, the BCS-condensates are much more fragile and their lifetime is much shorter.

12.1.5 The Cooper Problem for s-Wave and p-Wave Pairing in Confined Geometry of the Traps

We note that in this section we evaluate T_{C0} and T_{C1} in free and infinite space. In principle we should recalculate the critical temperatures for the confined geometry of magnetic traps. However, we can write the simple estimates which allow us to expand our results on a confined geometry. Namely, we should guarantee, as we already mentioned in Chap. 5, that

1. $\varepsilon_F \gg \hbar\omega$—a lot of particles in the trap. This inequality is satisfied because the usual number of particles in the trap is 10^9–10^{10}.
2. $\varsigma_0 \ll R_{\varepsilon \simeq \varepsilon_F}$—a size of a Cooper pair (a correlation length) is smaller than the size of the confining potential at the Fermi-level. We know that $\varsigma_0 = \hbar v_F / T_C$.

From the other hand for the confining potential $U(r) = \frac{m\omega^2 R^2(\varepsilon \simeq \varepsilon_F)}{2} = \varepsilon_F$, and correspondingly $R_{\varepsilon \simeq \varepsilon_F} = \frac{p_F}{m\omega}$. Thus, from $\varsigma_0 \ll R_{\varepsilon \simeq \varepsilon_F}$ we get $T_C > \frac{\varepsilon_F}{p_F R}$. Note that $p_F R \sim N^{1/3}$, where N is a total number of particles, and hence $T_C > \varepsilon_F/N^{1/3}$. Note also that in spherically-symmetric (3D) parabolic trap the level spectrum reads [42] $E = \hbar\omega(n_x + n_y + n_z + 3/2)$ and the density of states $\rho(\varepsilon) = \frac{\varepsilon^2}{(\hbar\omega)^3}$. It means that $N = \left(\frac{\varepsilon_F}{\hbar\omega}\right)^3$ and $N^{1/3} = \frac{\varepsilon_F}{\hbar\omega}$ is a number of levels in the trap. As a result $T_C > \hbar\omega$, and quasiclassical criterion for T_C reads:

$$\varepsilon_F \gg T_C \gg (\varepsilon_F/N^{1/3} = \hbar\omega) \tag{12.1.8}$$

Note that in arbitrary potential well criterion (12.1.8) coincides with Migdal criterion [43] well known in nuclear physics for the validity of quasiclassical approximation in spherically-symmetric nuclei.

12.2 p-Wave Pairing in the Fermi-Bose Mixture of ^{6}Li-^{7}Li with Repulsive Interaction Between the Different Isotopes

The further increase of p-wave critical temperature can be obtained in the dilute Fermi-Bose mixture of alkali isotopes ^{6}Li and ^{7}Li [5] (or ^{6}Li and bosonic ^{87}Rb). For this system, as it was shown by Efremov and Viverit [5], T_{C1} is governed not only by Kohn-Luttinger mechanism [3, 32, 33] considered in previous section, but also by the interaction of two fermions via polarization of bosonic media. The bosonic media is described by the density–density correlation function, and effective interaction $U_{eff}(q) = U_{eff}^{FFF}(q) + U_{eff}^{FBF}(q)$, where $U_{eff}^{FFF}(q)$ corresponds to the interaction of two fermions via polarization of fermionic background [see Fig. 12.1 and (12.1.1)], while $U_{eff}^{FBF}(q)$ describes the interaction of two fermions via polarization of bosonic background. Note that the Hamiltonian of the Fermi-Bose mixture in [5] reads:

$$\hat{H}' = \hat{H}_F + \hat{H}_B + \hat{H}_{FB}, \tag{12.2.1}$$

where fermionic part of (12.2.1)

$$\hat{H}_F = \sum_{\vec{p}\alpha} \xi_{\vec{p}\alpha} a^+_{\vec{p}\alpha} a_{\vec{p}\alpha} + \frac{U_{FF}}{2} \sum_{\substack{\vec{p}\vec{p}'\vec{q} \\ \alpha\beta}} a^+_{\vec{p}-\vec{q}\alpha} a^+_{\vec{p}'+\vec{q}\beta} a_{\vec{p}'\beta} a_{\vec{p}\alpha}; \tag{12.2.2}$$

bosonic part for $T < T_C^{BEC}$ (in ^{7}Li-subsystem):

$$\hat{H}_B = \sum_{\vec{p}} \varepsilon_{\vec{p}} b^+_{\vec{p}} b_{\vec{p}} + \frac{U_{BB}}{2} \sum_{\vec{p}\vec{p}'\vec{q}} b^+_{\vec{p}-\vec{q}} b^+_{\vec{p}'+\vec{q}} b_{\vec{p}'} b_{\vec{p}}, \tag{12.2.3}$$

and finally Fermi-Bose interaction

$$\hat{H}_{FB} = U_{BF} \sum_{\vec{p}\vec{p}'\vec{q}} a^{+}_{\vec{p}-\vec{q}\alpha} b^{+}_{\vec{p}'+\vec{q}} b_{\vec{p}'} a_{\vec{p}\alpha}. \tag{12.2.4}$$

In (12.2.1) $\xi_{p\alpha} = \frac{p^2}{2m_\alpha} - \varepsilon_{F\alpha}$ is the fermionic spectum, $U_{FF} = \frac{4\pi a_{FF}}{m_F}$ is the fermion–fermion interaction, α corresponds to the components with different I_z (fully polarized in electron spin) and $m_1 = \ldots\ m_\alpha = \ldots\ m_F$ the masses of different fermionic components coincide. We work at $T < \{T_C^{BEC};\ \varepsilon_{F\alpha}\}$ and assume that $T_{C1} < \{T_C^{BEC};\ \varepsilon_{F\alpha}\}$. Than in zeroth approximation bosonic chemical potential $\mu_{bos} \to 0$ (it is non-zero only in the next order of the gas-parameter due to boson–boson interaction $\mu_{bos} = \frac{4\pi a_{BB}}{m_B} n_B$), and $\varepsilon_p \approx \frac{p^2}{2m_B}$ is the bosonic spectrum. The boson–boson interaction $U_{BB} = \frac{4\pi a_{BB}}{m_B} > 0$ corresponds to repulsion and stabilizes Bose-condensation in ^{7}Li-subsystem. Finally, in this chapter, in contrast to Chap. 6 we consider following Efremov, Viverit repulsive fermion-boson interaction $U_{BF} = \frac{4\pi a_{BF}}{m_{BF}}$ and $m_{BF} = \frac{m_B m_F}{m_B + m_F}$ [5].

The effective interaction of Fermi atoms via polarization of bosonic media reads in the second order of perturbation theory in U_{BF}:

$$U_{FBF}(\vec{q}) = U_{BF}^2 \chi(\vec{q}, 0), \tag{12.2.5}$$

where boson–boson correlation function $\chi(\vec{q}\omega)$ reads:

$$\chi(\vec{q}, \omega) = \frac{n_B q^2}{m_B} \frac{1}{\omega^2 - \varepsilon_q(\varepsilon_q + 2n_B U_{BB})}. \tag{12.2.6}$$

In (12.2.6) $\varepsilon_q = \frac{q^2}{2m_B}$, and thus $E_q^2 = \varepsilon_q(\varepsilon_q + 2n_B U_{BB})$ is Bogoliubov quasiparticle spectrum for slightly non-ideal Bose-gas [2]. Hence

$$\chi(\vec{q}, 0) = -\frac{n_B q^2}{m_B} \frac{1}{\varepsilon_q(\varepsilon_q + 2n_B U_{BB})} = -\frac{4n_B m_B}{(q^2 + 4m_B n_B U_{BB})}. \tag{12.2.7}$$

Introducing the sound velocity $c_B = \left(\frac{n_B U_{BB}}{m_B}\right)^{1/2}$, Efremov and Viverit finally get:

$$U_{FBF}(\vec{q}, 0) = -\frac{U_{BF}^2}{U_{BB}} \frac{1}{\left(1 + \left(\frac{q}{2m_B c_B}\right)^2\right)}. \tag{12.2.8}$$

The attractive p-wave harmonic of U_{FBF} further increases T_{C1} for the pairing of two ^{7}Li atoms in the Fermi-Bose mixture. Note that Efremov-Viverit mechanism connected with static boson–boson correlation function is effective for dilute bosonic subsystem. If the superfluid bosonic subsystem is dense (as in the case of superfluid ^{4}He in ^{3}He-^{4}He solutions) and $v_F \ll c_B$ then the Bardeen, Baym, Pines mechanism of frequency-dependent phonon exchange becomes dominant [44, 45].

12.3 Ginzburg–Landau Functional for Triplet Superfluid Fermi Gas and for Superfluid ^{3}He

In the last section of this chapter we will construct Ginzburg–Landau functional for p-wave superfluid Fermi gas [6, 7] with an account of strong-coupling corrections for the coefficients $\beta_1 \ldots \beta_5$ near quartic terms [8]. On the basis of the knowledge of Ginzburg–Landau functional we will find all the global minima of the GL-Free energy and thus complete the superfluid phase diagram of p-wave Fermi gas. We will consider 3D and 2D case both in the absence of magnetic field and in the presence of strong magnetic field (or strong polarization). We will find that in the absence of magnetic field the global minima of the GL-functional correspond to triplet B- and A-phases well known in the physics of superfluid ^{3}He [10, 11]. In strong magnetic fields $H > H_{\rm p} = T_{\rm C1}/\mu_B^{nucl}$ isotropic B-phase is totally suppressed, and the global minima of the phase diagram correspond to triplet A_1 and A_2 phases. In 2D case the global minima of the GL-functional corresponds to planar or axial phases [19]. In this section we will mostly consider two-component repulsive Fermi gas with $\lambda = \frac{2ap_F}{\pi} > 0$ having in mind dilute and dense ^{3}He in 3D (or ^{3}He submonolayers in 2D with the gas-parameter $f_0 = \frac{1}{2\ln(1/p_F r_0)} > 0$). Note that for dense ^{3}He repulsive gas-parameter $\lambda \sim (1.3 \div 1.4) > 1$ in 3D, and rigorously speaking, the perturbation theory does not work both for effective interaction (for $T_{\rm C1}$) and for $\beta_1 \ldots \beta_5$ with an account of strong-coupling corrections. However, even in dense ^{3}He $T_{\rm C1}/\varepsilon_{\rm F} \sim 10^{-3} \ll 1$, and thus our naive estimates for $T_{\rm C1}$ and β-s (especially for their combinations which enter in observables) could be useful as a starting point for a more rigorous analysis in the case of a dense system.

12.3.1 Global Phase Diagram of a Superfluid Fermi Gas with Repulsion and of a Superfluid ^{3}He

The search for the microscopic nature of the mechanisms which stabilize the superfluid phases of ^{3}He other than isotropic B-phase (or more generally, of a triplet superfluid Fermi system) has continued to hold interest for many years now. A classic result in this field was obtained by Anderson, Brinkman and Morel [11, 12], who proposed a spin-fluctuation mechanism for stabilizing the anisotropic A-phase of ^{3}He back in early 1970s. A more rigorous mathematical framework was constructed for that mechanism by Brinkman et al. [13]. Later papers by Bartoon and Moore [14], Jones [15], Volovik and Mineev [46], Mermin and Stare [7], Bruder and Vollhardt [47], and Marchenko [48] constituted a comprehensive group-theory analysis of all possible phases of a superfluid triplet Fermi system. Conditions on the coefficients $\beta_1 \ldots \beta_5$ in front of quartic (in order parameter $\Delta_{\alpha\beta}$ or in three by three matrix $A_{\rm ik}$) terms in the Ginzburg–Landau free energy [6] which would be required for the stabilization of a local minimum of each of the 18 possible phases were also described in these papers.

Superfluid ^{3}He is of course the topic of primary interest in research on triplet superfluidity. Until now, numerous pieces of experimental evidence give rise to the belief that only two superfluid phases—the isotropic B-phase and the anisotropic A-phase could exist in the 3D case. However, some experimental studies, in particular by Pecola et al. [49] (on the zero sound experiments in the distorted B-phase and in the transition region (phase boundary) between B and A phases at low pressure); Frossati et al. [50] (on reentrant superfluidity of liquid ^{3}He in high magnetic fields), and Gould et al. [51, 52] (on the magnetic suppression of the B-phase), as well as some theoretical papers (for example by Capel et al. [53–55]) on the phase diagram of a superfluid ^{3}He in the presence of Hubbard interaction) hint at a possible realization of some exotic superfluid phases (different from A and B) in ^{3}He. We are talking about bulk (3D) ^{3}He. In thin films the possibility of the realization of planar and axial phases is generally acknowledged. The torsional oscillation experiments to measure triplet superfluidity in these films were performed by Saunders group [56], but did not reveal the presence of the exotic phase to our best knowledge. Note that currently one of the most popular candidates for the role of a third phase in the bulk is the so-called axiplanar noninert phase of Mermin and Stare [7], whose parameters are close to those of the A-phase.

In the present section we concentrate our efforts to analyze from the first principle calculations the possible existence of various superfluid phases in a triplet Fermi system. For this purpose we select a very simple and exactly solvable model of a triplet Fermi gas with a short-range repulsion. It can be shown in this model that both the temperature of the triplet superfluid transition [see [4] and (12.1.3), (12.1.4)] and the values of the coefficients $\beta_1 \ldots \beta_5$ in the Ginzburg–Landau free energy depend only on a single microscopic parameter $\lambda = \frac{2ap_F}{\pi}$ [9, 16–18].

12.3.2 GL-Functional in the Weak-Coupling Case

For p-wave superfluids the tensor structure of an order parameter (of a superfluid gap) reads (see Vollhardt, Wölfle [6]):

$$\Delta_{\alpha\beta} = \Delta(T) i(\sigma_2\sigma_i)_{\alpha\beta} A_{ik} n_k, \tag{12.3.1}$$

where $\Delta_{\alpha\beta}$ is (2×2) matrix in spin space, $\{\sigma_2; \sigma_i\}$ are the Pauli matrices, $\vec{n} = \vec{p}/p_F$ is a unit vector in momentum space, $\Delta(T)$ is a magnitude of the superfluid gap. Finally A_{ik} is (3×3) matrix of an order parameter in triplet p-wave fermionic superfluid (or triplet superconductor) with $S_{tot} = l = 1$. Accordingly in terms of A_{ik} the GL-functional reads:

$$\begin{aligned}\Delta F_{GL} = {} & \alpha Sp(AA^+) + \beta_1 \left|Sp(AA^T)\right|^2 + \beta_2 (Sp\, AA^+)^2 + \beta_3 Sp\left((AA^T)(AA^T)^*\right) \\ & + \beta_4 Sp\left((AA^+)^2\right) + \beta_5 Sp((AA^+)(AA^+)^*),\end{aligned} \tag{12.3.2}$$

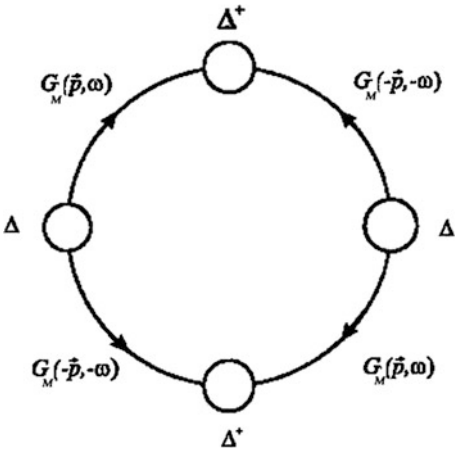

Fig. 12.2 The skeleton diagram for $\beta_i^{W.C.}$ in the weak-coupling case (see [36]). $G_M(\vec{p},\omega)$ stands for the Matsubara Green-function of the normal state, while Δ and Δ^+ stand for the superfluid gap

where symbols (+) and (*) stand for hermitian and complex conjugation, respectively. Of course, $A^+ = (A^T)^*$ and correspondingly $Sp(AA^T) = \sum_{ij} A_{ij}A_{ji}$.

Hence GL-functional contains five different quartic invariants proportional to A^4 and five different β-s. In the weak-coupling case $\beta_i^{W.C.}$ are connected with each other by the following relation (both in dense superfluid ^{3}He [6] and in dilute superfluid Fermi gas with repulsion [36, 57]):

$$-\beta_5^{W.C.} = \beta_4^{W.C.} = \beta_3^{W.C.} = \beta_2^{W.C.} = -2\beta_1^{W.C.}. \tag{12.3.3}$$

The skeleton diagram for $\beta_i^{W.C.}$ in the weak-coupling case is presented on Fig. 12.2.

Analytically:

$$\begin{aligned}\beta_1^{W.C.} &= -\frac{2}{15}\sum_{\omega_n}\int\frac{d^3\vec{p}}{(2\pi)^3}G_M^2(\vec{p},\omega_n)G_M^2(-\vec{p},-\omega_n)\cdot\Delta^4(T)\\ &= \frac{N_{3D}(0)}{2T_{C1}^2}\frac{7\xi(3)}{120\pi^2}\Delta^4(T),\end{aligned} \tag{12.3.4}$$

where $\omega_n = \pi T(2n+1)$ is Matsubara fermionic frequency, $\xi(x)$ is Riemann dzeta function, and $\xi(3) \approx 1.204$, $N_{3D}(0) = \frac{mp_F}{2\pi^2}$ is 3D density of states. The coefficient α in front of quadratic in A_{ik} term in (12.3.1) is given by the ladder series of diagrams [36] (see Fig. 12.3) and reads:

$$\alpha \sim \frac{1 + U_{eff}^{l=1}K(T)}{\left(U_{eff}^{l=1}\right)^2 K(T)}\Delta^2(T), \tag{12.3.5}$$

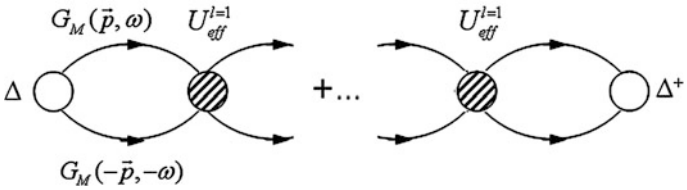

Fig. 12.3 Ladder approximation for the coefficient $1/\alpha$ in GL-functional for $T \to T_C$ (see [36]). $U_{eff}^{l=1}$ stands for attractive p-wave harmonic of the effective interaction

where $K(T) \sim N_{3D}(0)\ln(\varepsilon_F/T)$ is a Cooper loop, $1 = -U_{eff}^{l=1}K(T_{C1})$ is Landau-Thouless condition for T_{C1}, and $U_{eff}^{l=1}$ is attractive p-wave harmonic of the effective interaction.

Algebraically (see [6]):

$$\alpha = \frac{2}{3}N_{3D}(0)\ln\frac{T}{T_C}\cdot\Delta^2(T). \tag{12.3.6}$$

The absolute minimum of the GL-functional in the weak-coupling approximation (with the values of α and β-s given by (12.3.3), (12.3.4) and (12.3.6)) corresponds to isotropic B-phase for $T \to T_{C1}$ both for superfluid Fermi gas with repulsion and superfluid ^{3}He [6, 9, 16–18, 36, 57]. It is important to note that for $T \to 0$ the triplet superfluid B-phase also corresponds to the minimum of the thermodynamic potential Ω. Namely, as it was shown in [36] at $T = 0$ for superfluid Fermi gas with repulsion:

$$\Omega_S - \Omega_N = -\frac{N_{3D}(0)\Delta^2}{12}. \tag{12.3.7}$$

12.3.3 Exact Evaluation of T_{C1} in Repulsive Fermi Gas Allowing for Higher Orders of Perturbation Theory

Before proceeding to strong-coupling corrections, it is important to get the exact expression for T_{C1} with the preexponential factor, which arises due to an account of the higher orders ($\sim\lambda^3$ and $\sim\lambda^4$) of the perturbation theory for effective interaction [4], as well as due to an account of the retardation effects [4, 58]. The diagrams of third and fourth order in λ for effective interaction are presented on Fig. 12.4 (see [4]).

The accurate calculation yields in repulsive case for effective interaction [4]:

$$N_{3D}(0)U_{eff}^{l=1} = -0.077\lambda^2 - 0.33\lambda^3 - 0.26\lambda^4, \tag{12.3.8}$$

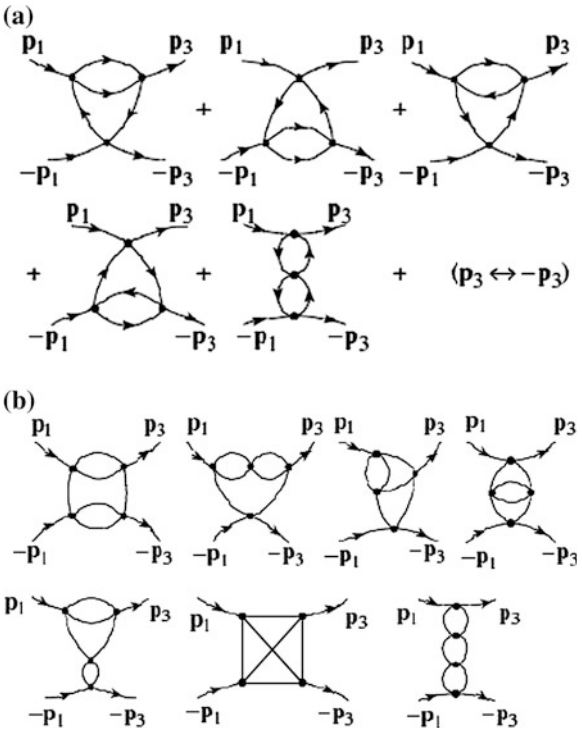

Fig. 12.4 Third (**a**) and fourth (**b**) order diagrams (in gas parameter λ) for effective interaction U_{eff} [4] (see also Fig. 9.8)

and thus the critical temperature reads:

$$T_{C1} = \frac{2}{\pi} e^{C} \varepsilon_F \exp\left\{ -\frac{1}{\left(0.077\lambda^2 + 0.33\lambda^3 + 0.26\lambda^4\right)} \right\}, \tag{12.3.9}$$

where C is Euler constant.

Note that the evaluation of the preexponential factor in (12.3.8) and (12.3.9) was performed for two-component repulsive Fermi gas (such as ^{3}He) with $\lambda = \frac{2ap_F}{\pi}$ [4].

It is interesting that the third and fourth order in λ contributions to T_{C1} also correspond to attraction (as the second order contribution). For $\lambda \to 0$ we can get the following asymptotic formula from (12.3.8):

$$T_{C1} \approx \frac{2}{\pi} e^{C} \varepsilon_F \exp\left\{ -\frac{13.0}{\lambda^2} + \frac{42.0}{\lambda} - 190 \right\}. \tag{12.3.10}$$

In practice this formula works till $\lambda \lesssim 1/4$. For higher values of λ we should use (12.3.9) or some other extrapolation formula (see [4]). Hence superfluid critical temperature is enhanced by higher order diagrams but it is difficult to evaluate T_C exactly for $\lambda \geq 1$ (a remark of Rainer [59]).

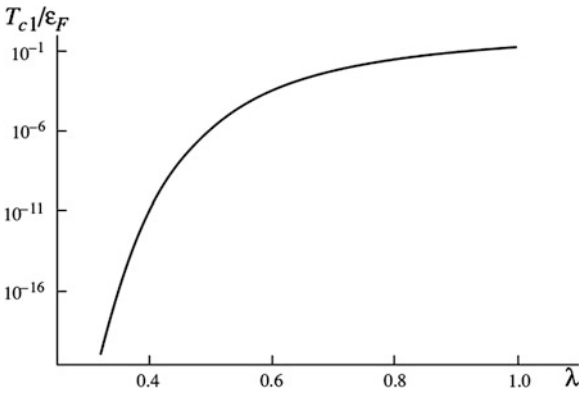

Fig. 12.5 The dependence of T_{C1}/ε_F on the gas parameter λ in the two-component Fermi gas ($S_z = \pm 1/2$) with repulsion [4]

Nevertheless the estimates for disbalanced ^{6}Li, which combine the increase of T_C due to optimal density ratio of different components with an evaluation of the preexponential factors, increase T_{C1} up to $(10^{-7} \div 10^{-6})$ K [4]. The effect is even more prominent in two-component repulsive Fermi gas and in ^{3}He (where $\lambda \geq 1$) [4]. Here according to (12.3.9) the dependence of T_{C1}/ε_F on the gas parameter λ is presented on Fig. 12.5. We see the strong increase in T_{C1}/ε_F ratio when λ increases from 0.4 to 1.0.

12.3.4 Strong-Coupling Corrections in a Superfluid Fermi Gas with Repulsion

Strong-coupling corrections make the situation with global phase diagram of a triplet superfluid Fermi gas with repulsion less trivial. We will show that incorporating strong-coupling (in T_{C1}/ε_F) corrections, analogous to those discussed by Rainer and Serene [8], we can also stabilize the anisotropic A-phase. Note that in this approximation other likely candidates for the role of a third phase (axiplanar, planar and polar phases) either lie above the B and A phases on the energy scale or are not even local minima of the GL-functional in repulsive Fermi gas.

The strong-coupling corrections to the coefficients β_i which we found in [9] reads:

$$\Delta\beta_i = \left|\beta_i^{W.C.}\right| \frac{T_{C1}}{\varepsilon_F}\left[\gamma_i\lambda^2 + \delta_i\lambda^3\right], \tag{12.3.11}$$

where $T_{C1} = \frac{2}{\pi}e^C\varepsilon_F \exp\left\{-\frac{1}{\left(0.077\lambda^2+0.33\lambda^3+0.26\lambda^4\right)}\right\}$, according to (12.3.9), and γ_i, δ_i are numerical coefficients.

On Fig. 12.6 we show the diagrams of the next order in T_{C1}/ε_F for the free-energy (GL functional), which violate the weak-coupling relations (12.3.3) between β-s in (12.3.11), according to Rainer and Serene [8] and yield the contribution of the order of $(T_{C1}/\varepsilon_F)\left|\beta_i^{W.C.}\right|$ to coefficients β_i (see (12.3.11)).

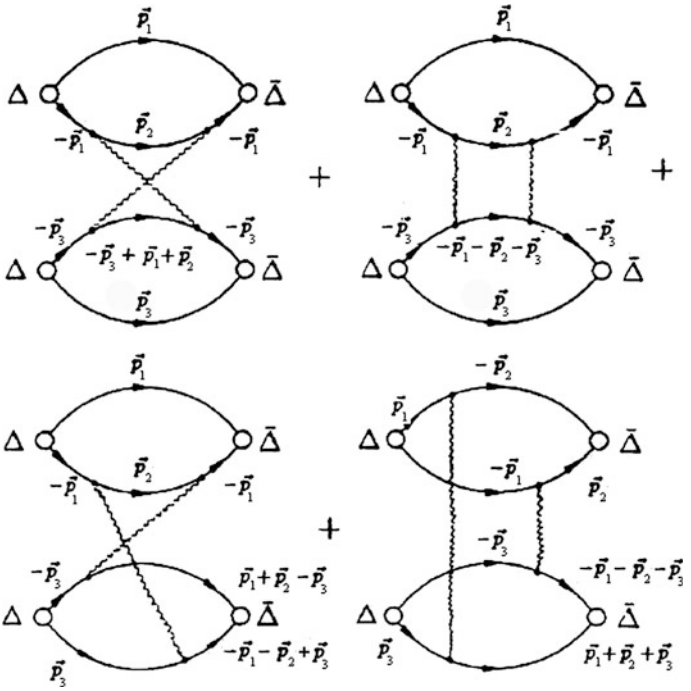

Fig. 12.6 Feynman diagrams making the contribution of the order of $(T_{C1}/\varepsilon_F)\left|\beta_i^{W.C.}\right|$ to the coefficients β_i which violate weak-coupling relations (12.3.3) between these coefficients [9]

It is not difficult to show that at the order of T_{C1}/ε_F the contribution of all four diagrams to the coefficients β_i are given by the expression:

$$
\begin{aligned}
&-\frac{T^3}{2}\sum_{n_1n_2n_3}\int\frac{d^3\vec{p}_1d^3\vec{p}_2d^3\vec{p}_3}{(2\pi)^9}|\Gamma(\vec{p}_i,\omega_i)|^2Q(\vec{p}_1,\omega_1)Q(\vec{p}_3,\omega_3)\\
&\qquad G_M(\vec{p}_2,\omega_2)G_M(\vec{p}_1+\vec{p}_2-\vec{p}_3,\omega_1+\omega_2-\omega_3)\cdot\\
&-\frac{T^3}{4}\sum_{n_1n_2n_3}\int\frac{d^3\vec{p}_1d^3\vec{p}_2d^3\vec{p}_3}{(2\pi)^9}|\Gamma(\vec{p}_i,\omega_i)|^2Q(\vec{p}_1,\omega_1)Q(\vec{p}_3,\omega_3)\\
&\qquad G_M(\vec{p}_2,\omega_2)G_M(-\vec{p}_1-\vec{p}_2-\vec{p}_3,-\omega_1-\omega_2-\omega_3)\cdot\\
&+T^3\sum_{n_1n_2n_3}\int\frac{d^3\vec{p}_1d^3\vec{p}_2d^3\vec{p}_3}{(2\pi)^9}|\Gamma(\vec{p}_i,\omega_i)|^2F(\vec{p}_3,\omega_3)Q(\vec{p}_1,\omega_1)\\
&\qquad G_M(\vec{p}_2,\omega_2)F^+(\vec{p}_1+\vec{p}_2-\vec{p}_3,\omega_1+\omega_2-\omega_3)\cdot\\
&-\frac{T^3}{8}\sum_{n_1n_2n_3}\int\frac{d^3\vec{p}_1d^3\vec{p}_2d^3\vec{p}_3}{(2\pi)^9}|\Gamma(\vec{p}_i,\omega_i)|^2F(\vec{p}_1,\omega_1)F^+(\vec{p}_2,\omega_2)\\
&\qquad F(\vec{p}_3,\omega_3)F^+(\vec{p}_1+\vec{p}_2+\vec{p}_3,\omega_1+\omega_2+\omega_3).
\end{aligned}
\tag{12.3.12}
$$

where $G_M(\vec{p},\omega) = (i\omega - \xi_p)^{-1}$ is the Matsubara Green's function, $\omega_n = \pi T(2n+1)$ is the Matsubara fermionic frequency, $\xi_p = \frac{p^2 - p_F^2}{2m}$ is the quasi-particle spectrum, $Q(\vec{p},\omega) = G_M^2(-\vec{p},-\omega)G_M(\vec{p},\omega)\left|\hat{\Delta}\right|^2$,

$$F(\vec{p},\omega) = G_M(\vec{p},\omega)\hat{\Delta}G_M(-\vec{p},-\omega),$$

and correspondingly for $F^+(\vec{p},\omega)$,

$\hat{\Delta}_{\alpha\beta} = \Delta(T)i(\sigma_2\sigma_i)_{\alpha\beta}A_{ik}n_k$, is a triplet superfluid gap, σ_i are the Pauli matrices. Finally, $\sum_{\omega_n} \to T\sum_n$ for the summation over Matsubara frequencies.

The wavy lines in Fig. 12.6 correspond to the total two-particle vertex Γ (the total antisymmetrized vertex). In first two orders of the gas-parameter it can be calculated at vanishing frequencies on the Fermi-surface $\Gamma(\vec{p}_i,\omega_i) \to \Gamma(p_F\vec{n}_i,0)$.

In the case of a Fermi gas it is given by

$$\Gamma_{\alpha\beta;\gamma\delta}(\vec{p}_1,\vec{p}_2;\vec{p}_3,\vec{p}_1+\vec{p}_2-\vec{p}_3) = \Gamma_s\delta_{\alpha\gamma}\delta_{\beta\delta} + \Gamma_a\vec{\sigma}_{\alpha\gamma}\vec{\sigma}_{\beta\delta}, \tag{12.3.13}$$

where $\vec{\alpha}_{\alpha\gamma}$, $\vec{\alpha}_{\beta\delta}$ are the Pauli matrices.

In (12.3.13) symmetric part of the two-particle vertex

$$\Gamma_S = \frac{g}{2} + 2g^2\Pi(\vec{p}_2-\vec{p}_3) + g^2\mathrm{K}(\vec{p}_1+\vec{p}_2) - g^2\Pi(\vec{p}_1-\vec{p}_3), \tag{12.3.14}$$

where Π and K stand for 3D polarization operator: $\Pi(q) = \frac{mp_F}{4\pi^2}\left[1 + \frac{4p_F^2-q^2}{4p_Fq}\ln\frac{2p_F+q}{|2p_F-q|}\right]$, and the Cooper loop (see [9]):

$$K(p) = \frac{mp_F}{2\pi^2}\left[1 + \frac{\sqrt{1-p^2/4p_F^2}}{2}\ln\frac{\sqrt{1-p^2/4p_F^2}-1}{\sqrt{1-p^2/4p_F^2}+1}\right] \tag{12.3.15}$$

respectively. Note that K(p) in (12.3.15) is regularized at large momenta and $g = 4\pi a/m > 0$.

The asymmetric part of Γ reads:

$$\Gamma_a = -\left[\frac{g}{2} + g^2\mathrm{K}(\vec{p}_1+\vec{p}_2) + g^2\Pi(\vec{p}_1-\vec{p}_3)\right]. \tag{12.3.16}$$

Note that in Eq. (12.3.12) $\vec{p_1} = \vec{p_3}$ and thus we are dealing with $\Gamma_s(\vec{p_1},\vec{p_2};\vec{p_1}\vec{p_2})$ and $\Gamma_a(\vec{p_1},\vec{p_2};\vec{p_1}\vec{p_2})$.

Hence effectively in (12.3.12)–(12.3.14), (12.3.16) $\Gamma_s = \frac{g}{2} + 2g^2\Pi(\vec{p_2}-\vec{p_1}) + g^2K(\vec{p_1}+\vec{p_2}) - g^2\Pi(0)$; $\Gamma_a = -\left[\frac{g}{2} + g^2K(\vec{p_1}+\vec{p_2}) + g^2\Pi(0)\right]$.

Some rather involved transformations of the integrals in (12.3.1) show that, as in [8], the strong-coupling corrections for the coefficients β_i are determined by bilinear combinations of spherical harmonics of the total vertex, evaluated for $\vec{p}_1 = \vec{p}_3$. In other words we have (see [9, 60, 61]):

$$\Delta\beta_i = \left|\beta_i^{W.C.}\right| \frac{T_{C1}}{2\varepsilon_F}\left[r_{1i}(\Gamma_{os})^2 + r_{2i}(\Gamma_{oa})^2 + r_{3i}(\Gamma_{os}\Gamma_{oa}) + \ldots\right], \tag{12.3.17}$$

where r_{1i}, r_{2i}, r_{3i},… are numerical factors, and

$$\Gamma_{os} = \int \Gamma_s(\vec{p}_1\vec{p}_2;\vec{p}_1\vec{p}_2)\frac{d\cos\theta}{2} = \frac{g}{2} + g\lambda\left(\frac{2\ln 2+1}{6}\right); \quad \theta = \angle\vec{p}_1\vec{p}_2,$$
$$\Gamma_{oa} = -\frac{g}{2} - g\lambda\left(\frac{5-2\ln 2}{6}\right);\ \Gamma_{1s} = g\lambda\left(\frac{7\ln 2-1}{5}\right);\ \Gamma_{1a} = -g\lambda\left(\frac{2+\ln 2}{5}\right), \tag{12.3.18}$$

where $\lambda = \frac{2ap_F}{\pi}$ is an effective gas parameter in 3D.

All the other harmonics (Γ_2, Γ_3, etc.) are much smaller that $|\Gamma_1|$. A direct calculation of the numerical factors r_i leads to the following final result for the coefficients β_i [9, 60, 61]:

$$\begin{aligned}
\beta_1 &= \left|\beta_1^{W.c.}\right|\left\{-1 + \frac{T_{C1}}{2\varepsilon_F}(-75.4\lambda^2 + 0.2\lambda^3)\right\},\\
\beta_2 &= \left|\beta_1^{W.c.}\right|\left\{2 + \frac{T_{C1}}{2\varepsilon_F}(-7.0\lambda^2 + 29.4\lambda^3)\right\},\\
\beta_3 &= \left|\beta_1^{W.c.}\right|\left\{2 + \frac{T_{C1}}{2\varepsilon_F}(-6.4\lambda^2 - 13.3\lambda^3)\right\},\\
\beta_4 &= \left|\beta_1^{W.c.}\right|\left\{2 + \frac{T_{C1}}{2\varepsilon_F}(-48.3\lambda^2 - 108.8\lambda^3)\right\},\\
\beta_5 &= \left|\beta_1^{W.c.}\right|\left\{-2 + \frac{T_{C1}}{2\varepsilon_F}(-108.9\lambda^2 - 183.2\lambda^3)\right\}.
\end{aligned} \tag{12.3.19}$$

Note that for $\lambda \to 0$ $T_{C1}/\varepsilon_F = \frac{2}{\pi}e^C \exp\left\{\frac{42.0}{\lambda}\right\}\exp\{-190\}\exp\left\{-\frac{13.0}{\lambda^2}\right\}$ (see [4]). Thus, the preexponential factor is $\frac{2e^C}{\pi}\exp\{-190\}\exp\left\{\frac{42.0}{\lambda}\right\}$, while the main exponent is $\exp\left\{-\frac{13.0}{\lambda^2}\right\}$ (see [4]). Note also that in principle, expression (12.3.19) can be used to calculate and compare the free energies of all 18 possible phases of superfluid Fermi gas with repulsion. In this subsection we will restrict ourselves with a look at the phases which are cited most commonly in the literature: the B-phase, the A-phase, the polar phase, the planar phase, and the axiplanar phase. In our approximation it is rather simple to show that the polar, planar and the axiplanar phases either lie above the B-phase on the energy scale or completely fail to qualify as even local minima of the free energy. The situation regarding the A-phase is less trivial. According to [6], the conditions for the stabilization of the A-phase are:

$$\beta_4 + \beta_5 - 2\beta_1 - \beta_3 < -\frac{1}{2}(\beta_1 + \beta_3) < 0. \tag{12.3.20}$$

At the order of λ^2 we find $\beta_4 + \beta_5 - 2\beta_1 - \beta_3 = 0$ from (12.3.19), and the A-phase is not yet stabilized. It s possible to show that this result corresponds to a certain sum-rule [60]. In the next order, λ^3, we find:

$$\beta_4 + \beta_5 - 2\beta_1 - \beta_3 = -\frac{T_{C1}}{2\varepsilon_F} \cdot 558.3\ \lambda^3 < 0, \tag{12.3.21}$$

and inequalities (12.3.20) can be written as:

$$\begin{aligned} \frac{T_{C1}}{2\varepsilon_F}\left[81.8\ \lambda^2 + 13.1\ \lambda^3\right] &< 1, \\ \frac{T_{C1}}{2\varepsilon_F}\left[81.8\ \lambda^2 + 571.3\ \lambda^3\right] &> 1. \end{aligned} \tag{12.3.22}$$

In real ^{3}He $T_{C1}/\varepsilon_F \sim 10^{-3}$. Nevertheless, because of the very large numerical coefficients ($\sim$600) in front of $(T_{C1}/2\varepsilon_F)\cdot\lambda^3$ in the second inequality in (12.3.22), the conditions for the realization of the A-phase can in principle be satisfied for $\lambda > 1$. At zero pressure in real ^{3}He we will have $\lambda \sim 1.3$. With increasing pressure, λ increases, making it easier to satisfy inequalities (12.3.22). Note that the increase of λ is limited by melting line on the phase diagram of ^{3}He for pressure $P = 35$ bar. Let us compare our results with the results of some previous studies. The total vertex of the Anderson-Brinkman-Morel spin-fluctuation theory is given by the expression $\Gamma_(q) = \frac{g/2}{(1-\Pi(q)g/2)}$, where the polarization operator $\Pi(q) \approx \frac{mp_F}{2\pi^2}\left[1 - \frac{q^2}{12p_F^2}\right]$ is expanded in series (in q/p_F) near the ferromagnetic instability corresponding to small values $q \to 0$. Expressions (12.3.14), (12.3.16) which we have derived for Γ_s and Γ_a, contain, in addition to the polarization operator, also a Cooper loop. The calculations of Γ_s and Γ_a are not based on the assumption of the proximity to the ferromagnetic instability in (12.3.18) and (12.3.16) $\frac{g}{2}\Pi(0) \nrightarrow 1$. Thus, the strong-coupling corrections to the coefficients β_i which we have found differ considerably both in sign and in absolute value from the Anderson-Brinkman-Morel [11, 12] corrections.

It can be shown that our strong-coupling corrections are analogous to the strong-coupling corrections discussed by Rainer and Serene in [8]. The Fermi gas approach has the advantages that (first) we know the microscopic mechanism for stabilization of triplet pairing in a Fermi gas with repulsion, and second we can derive an explicit expression for the total two-particle vertex in the gas approximation, and thereby pursue the expressions for the coefficients β_i to the point of numbers.

12.3.5 *The Global Minima of the GL-Functional in Spin-Polarized Superfluid Fermi Gas*

As we already discussed in Chap. 10 at small magnetic fields $H < H_p = \frac{T_{C1}}{\mu_B^{nucl}} \sim (2 \div 3)$ T (μ_B^{nucl}—nuclear Bohr magneton) there are three superfluid

transitions in triplet superfluid Fermi gas (and real superfluid ^{3}He). They are governed by critical temperatures $T_{C1}^{\uparrow\uparrow}$, $T_{C1}^{\uparrow\downarrow}$ and $T_{C1}^{\downarrow\downarrow}$ (see Fig 12.7). These temperatures correspond respectively to the pairing with $S_z^{\rm tot} = 1$ (A1-phase), $S_z^{\rm tot} = 0$ (B-phase), and $S_z^{\rm tot} = -1$ (A2-phase). In magnetic fields larger than the paramagnetic limit $H > H_{\rm p}$ the $S_z^{\rm tot} = 0$ projection of a triplet Cooper pair is totally suppressed. As a result for $H > H_{\rm p}$ the phase diagram contains only A1 and A2 phases even in the weak-coupling approximation. The strong-coupling corrections do not change the situation qualitatively.

Accordingly, our hope for finding new phases in triplet superfluid Fermi gas with repulsion can be connected only with weak magnetic fields ($H < H_{\rm p}$). The possible existence of a third phase in weak magnetic fields was pointed out in theoretical papers by Capel et al. [53–55].

12.3.6 Critical Temperatures for the Superfluid Transitions to A1, A2 and B Phases in Spin-Polarized Fermi Gas

Note that in weak magnetic fields according to [18, 63] we get for the triplet superfluid Fermi gas the following critical temperatures (see Fig. 12.7):

$$
\begin{aligned}
T_{C1}^{\uparrow\uparrow} &= T_C^{A1} \approx T_{C1}\left(1 + \frac{A\alpha}{\lambda^2} + \frac{\tilde{B}\alpha^2}{\lambda^2}\right), \\
T_{C1}^{\downarrow\downarrow} &= T_C^{A2}(\text{bare}) \approx T_{C1}\left(1 - \frac{A\alpha}{\lambda^2} + \frac{\tilde{B}\alpha^2}{\lambda^2}\right), \\
T_{C1}^{\uparrow\downarrow} &= T_C^{B}(\text{bare}) = T_{C1}\left(1 - \eta\frac{\mu_B^2 H^2}{T_{C1}^2}\right),
\end{aligned}
\tag{12.3.23}
$$

where (see Chap. 10 and [18, 63])

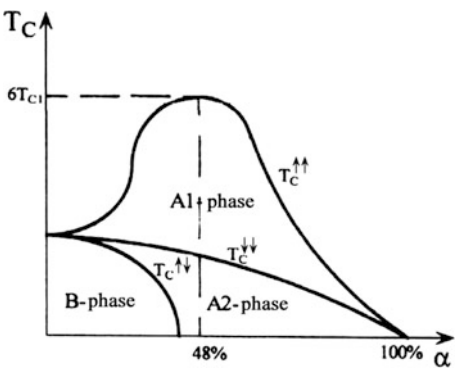

Fig. 12.7 The dependence of the critical temperatures $T_{C1}^{\uparrow\uparrow}$, $T_{C1}^{\uparrow\downarrow}$ and $T_{C1}^{\downarrow\downarrow}$ on the degree of polarization α in triplet superfluid Fermi gas [62]

$$A = \frac{10(7-4\ln 2)}{9(2\ln 2-1)^2} \approx 31.5, \quad \tilde{B} = B + \frac{1}{2}\frac{A^2}{\lambda^2},$$
$$B \approx 37.2\left(\ln\frac{1}{\alpha} - 2.9\right), \tag{12.3.24}$$

η is numerical coefficient (of the order of 1), $\alpha = \frac{3}{2}\frac{\mu_B^{nucl}H}{\varepsilon_F}$ is polarization degree. We will show in the next subsection that $T_{C1}^{\uparrow\uparrow}$ and $T_{C1}^{\downarrow\downarrow}$ really correspond to A1 and A2 phases. Note also that the general formula for $T_{C1}^{\uparrow\uparrow}$ in repulsive Fermi gas (derived for the main exponent of T_{C1} in Chap. 10) reads: $T_{C1}^{\uparrow\uparrow} = T_{C1}\exp\left\{\frac{\Phi(\alpha)}{\lambda^2}\right\}$, where $\Phi(\alpha) = A\alpha + B\alpha^2 + \bar{o}(\alpha^3)$ for small $\alpha \ll 1$. It is important to emphasize that in triplet superfluid Fermi gas the coefficient B in front of α^2 in $T_{C1}^{\uparrow\uparrow}$ contains a logarithmic contribution $\sim\ln(1/\alpha)$ (see (12.3.24) and [63]). This nonanalyticity $\alpha^2\ln(1/\alpha)$ is present in dilute Fermi gas but is absent in Fermi-liquid theories for dense superfluids [64, 65].

If we include higher order corrections for $T_{C1}^{\uparrow\uparrow}$ into account, than the full dependence of $T_{C1}^{\uparrow\uparrow}$ from polarization degree α (which includes polarization dependence of the corrections to the main exponent) for different values of the gas-parameter λ is given by Fig. 12.8.

Analytically we can represent $T_{C1}^{\uparrow\uparrow}$ as follows: $T_{C1}^{\uparrow\uparrow}/\varepsilon_{F\uparrow} = A\exp\left\{-\frac{1}{\lambda^2 f_1(\alpha)+\lambda^3 f_2(\alpha)+\lambda^4 f_3(\alpha)}\right\}$, where at zero polarization the functions $f_1(\alpha)$, $f_2(\alpha)$, and $f_3(\alpha)$ reads: $f_1(\alpha=0) \approx 0.077$, $f_2(\alpha=0) \approx 0.33$, and $f_3(\alpha=0) \approx 0.26$. Moreover, $f_1(\alpha)$ and $\Phi(\alpha)$ are connected by the relation $\Phi(\alpha) = 13 - 1/f_1(\alpha)$ and thus $\Phi(\alpha=0) = 0$. Correspondingly for fully polarized gas: $f_1(\alpha=1) = 0$. Thus, with an account of the main exponent only $T_{C1}^{\uparrow\uparrow}/\varepsilon_{F\uparrow} = A\exp\left\{-\frac{1}{\lambda^2 f_1(\alpha)}\right\}$ we get

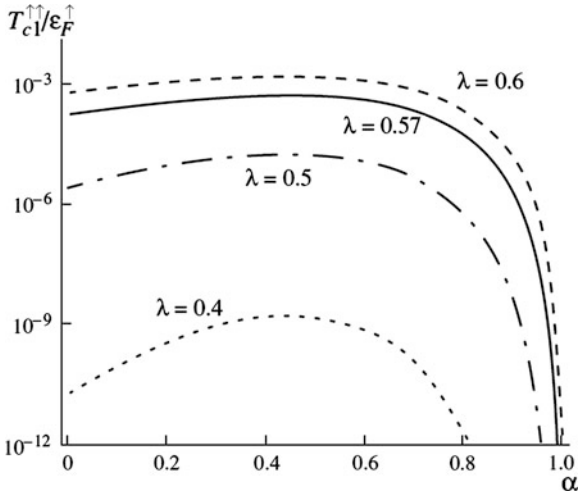

Fig. 12.8 Dependence of $T_{C1}^{\uparrow\uparrow}/\varepsilon_F^{\uparrow}$ on the degree of polarization α for various λ in spin-polarized Fermi gas [4]

$T_{C1}^{\uparrow\uparrow} = 0$ for $\alpha = 1$. However, an account of the corrections to this result connected with $\lambda^3 f_2(\alpha)$ and $\lambda^4 f_3(\alpha)$ terms in the effective interaction $U_{eff}^{(l=1)}$ makes $T_{C1}^{\uparrow\uparrow}$ almost zero already for α smaller than 1 at small values of $\lambda \leq 0.5$ (see Fig. 12.8). At larger values of λ the critical temperature $T_{C1}^{\uparrow\uparrow}$ is almost zero only for $\alpha = 1$. The maximum for $T_{C1}^{\uparrow\uparrow}$ corresponds to $\alpha \approx 0.48$ for small $\lambda \leq 0.4$ and shifts to smaller $\alpha \approx 0.4$ (in qualitative agreement with the predictions of the Fermi-liquid theory [64, 65]) for larger $\lambda \geq 0.6$. The maximum in $T_{C1}^{\uparrow\uparrow}$ also becomes a little bit more shallow with the increase of λ (see Fig. 12.8 and [4]). Finally, at small spin-polarizations the width of A1-phase is almost linear in α [18, 29, 66]:

$$\frac{T_{C1}^{\uparrow\uparrow} - T_{C1}^{\downarrow\downarrow}(\text{bare})}{T_{C1}} \approx \frac{2A\alpha}{\lambda^2}, \tag{12.3.25}$$

where $A \approx 31.5$ according to (12.3.24) and correspondingly $T_{C1}^{\uparrow\uparrow} \approx T_{C1}\left(1 + \frac{A\alpha}{\lambda^2}\right)$, while bare $T_{C1}^{\downarrow\downarrow} \approx T_{C1}\left(1 - \frac{A\alpha}{\lambda^2}\right)$.

We should stress that in (12.3.25), (12.3.23) T_C^{A2} is a bare critical temperature for the transition to A2-phase (where not only two spins "up", but also two spins "down" form the triplet Cooper pairs). We will show in the next subsection that T_C^{A2} will be renormalized by strong-coupling corrections to GL-functional.

If we extrapolate our results on dense superfluid ^{3}He and choose $\lambda \approx 1.4$ (which is the case for pressures $P = 35$ bar close to the melting line on ^{3}He phase-diagram), than we get from (12.3.23) (with an account of $A \approx 31.5$ from (12.3.24) and $\alpha = \frac{3}{2}\frac{\mu_B^{nucl} H}{\varepsilon_F}$):

$$\frac{T_{C1}^{\uparrow\uparrow} - T_{C1}^{\downarrow\downarrow}}{T_{C1}} = \gamma H, \tag{12.3.26}$$

where $\gamma \approx 3.6 \times 10^{-3}$ (1/kGs) [18, 60, 63, 66].

This result not only qualitatively but also quantitatively is very close to experimentally measured width of the A1-phase by Frossati group [50, 67, 68] in Kamerling Onnes Laboratory in Leiden. Note that the authors of [50, 67, 68] measured viscosity of superfluid ^{3}He in large magnetic fields up to 15 T (till polarization degrees of $\alpha = 0.07$). Note also that in moderate magnetic fields (up to 6 T) very similar results for the width of the A1-phase were experimentally obtained in classical papers [69, 70]. For highest (available in the lab) stationary magnetic fields $H = 15$ T Frossati et al., got $T_C^{\uparrow\uparrow} = T_C^{A1} = 3.14$ mK, which is 20 % larger than $T_{C1} = 2.5$ mK in the absence of field. The authors call their result—"high-temperature superfluidity". Note that the Fermi-gas theory predicts very similar results here, namely $T_C^{A1} \approx 3.2$ mK for $\lambda \sim 1.4$ and $\alpha = 0.06$ [18, 63, 66]. Finally, both Fermi-gas theory and metamagnetic model of the Fermi-liquid type [64, 65] (which is based on the so-called *s-p* approximation [65]) predict reentrant superfluid behavior for $T_{C1}^{\uparrow\uparrow}$ (see Fig. 12.8) with a pronounced maximum,

correspondingly, at $\alpha = 0.48$ or smaller in [18, 63, 66] and $\alpha = 0.35$ in [64, 65]. $T_{C1}^{\uparrow\uparrow}$ in maximum is 6.4 T_{C1} in Fermi-gas theory (for $\lambda \sim 1.4$) and 5.6 T_{C1} in Fermi-liquid theory. Note that the possibility to get so high polarization degrees is connected with the elegant idea of Castraing, Nozieres [71]. According to it (as we already discussed in Chap. 11) to get very strong (non-equilibrium but long-living) polarization in liquid ^{3}He we should rapidly melt spin-polarized paramagnetic ^{3}He crystal. If we apply magnetic field $H \sim 15$ T, we could practically fully polarize the crystal and, after rapid melting, get more than 30 %-polarized liquid ^{3}He with a lifetime (a magnetic relaxation time) of the order of 30 min [72]. Note again that brute force (thermodynamically equilibrium) polarization by an external magnetic field ($H \leq 20$ T) can produce only polarization degree $\alpha \leq 0.08$. This polarization is still much higher than polarization degree $\alpha \sim 0.011$ (corresponding to paramagnetic limit $H_p \sim 2 \div 3$ T) at which the temperature $T_C^{\uparrow\downarrow} = T_C^B$ (governing the transition to B-phase in (12.3.23)) tends to zero. Note that for $H > H_p$ the results for $T_{C1}^{\uparrow\uparrow}$ and $T_{C1}^{\downarrow\downarrow}$ in Fermi-gas approach do not depend upon the sign of the scattering length a.

12.3.7 Strong-Coupling Corrections in Superfluid Spin-Polarized Fermi Gas

In this subsection we generalize the evaluation of the strong-coupling corrections on the case of strong magnetic fields $H > H_p$, where B-phase (the $S_z^{tot} = 0$ projection of the total spin $S_{tot} = 1$ of the triplet Cooper pair) is totally suppressed. In other words, $\Delta_{\uparrow\downarrow}$ component of 2×2 order parameter matrix $\Delta_{\alpha\beta}$ in (12.3.1) is zero, and there are only two critical temperatures $T_{C1}^{\uparrow\uparrow}$ and $T_{C1}^{\downarrow\downarrow}$ corresponding to $S_z = 1$ ($\Delta_{\uparrow\uparrow}$) and $S_z = -1$ ($\Delta_{\downarrow\downarrow}$). Exact analytical expressions for $T_{C1}^{\uparrow\uparrow}$ and $T_{C1}^{\downarrow\downarrow}$ as a function of the gas parameter λ and magnetic field (or spin-polarization $\alpha = \frac{N_\uparrow - N_\downarrow}{N_\uparrow + N_\downarrow}$) were obtained in [63] and [4]. The results (see also Figs. 12.7, 12.8) show strongly nonmonotonic behavior of $T_{C1}^{\uparrow\uparrow}$ with a large and broad maximum at $\alpha = 0.48$. In the same time $T_{C1}^{\downarrow\downarrow}$ is monotonically decreasing function of α. We will show that $T_{C1}^{\uparrow\uparrow}$ and $T_{C1}^{\downarrow\downarrow}$ really correspond to A1 and A2 phases. The Ginzburg–Landau free energy functional in strong magnetic field can be rewritten in the following convenient form [17, 61, 73]:

$$\Delta F_{GL} = F_S - F_N = a_\uparrow \Delta_{0\uparrow\uparrow}^2 M_+ + b_\uparrow \Delta_{0\uparrow\uparrow}^4 \left(2M_+^2 + |N_+|^2\right) + a_\downarrow \Delta_{0\downarrow\downarrow}^2 M_- + b_\downarrow \Delta_{0\downarrow\downarrow}^4 \left(2M_-^2 + |N_-|^2\right) + \Delta_{0\uparrow\uparrow}^2 \Delta_{0\downarrow\downarrow}^2 \cdot (\delta M_+ M_- + \beta |R|^2 + \gamma |P|^2), \tag{12.3.27}$$

where $M_+ = A_{+k}^* A_{+k}, M_- = A_{-k}^* A_{-k}, N_+ = A_{+k} A_{+k}, N_- = A_{-k} A_{-k}, R = A_{+k} A_{-k}$, $P = A_{+k} A_{-k}^*$ and symbol (*) corresponds to complex conjugation.

In (12.3.27):

$$A_{+k} = iA_{2k} - A_{1k}; \quad A_{-k} = iA_{2k} + A_{1k}; \tag{12.3.28}$$

$$a_\uparrow = \frac{1}{3}N_{3D}(0)\ln\frac{T}{T_{C_1}^{\uparrow\uparrow}},\ a_\downarrow = \frac{1}{3}N_{3D}(0)\ln\frac{T}{T_{C_1}^{\downarrow\downarrow}}; \tag{12.3.29}$$

$$b_\uparrow = b_\downarrow = \eta\frac{N_{3D}(0)}{15T^2}\left[1 + \bar{\bar{o}}\left(\lambda^2\frac{T}{\varepsilon_F}\right)\right], \tag{12.3.30}$$

where η is numerical coefficient.

In (12.3.27):

$$\delta = 2\beta_2 + 2\beta_5; \quad \beta = 4\beta_1 + 2\beta_3; \quad \gamma = 2\beta_4 + 2\beta_5 \tag{12.3.31}$$

are the coefficients in front of the strong-coupling invariants with the structure $\Delta_{0\uparrow\uparrow}^2\Delta_{0\downarrow\downarrow}^2$. Note that $\Delta_{\alpha\beta} = \Delta_{0\alpha\beta}(T)i(\sigma_2\sigma_i)_{\alpha\beta}A_{ik}n_k$ and $A_{3k} = 0$ for $H > H_p$.

Let us consider first the case of weak-coupling. In this case $\delta = \beta = \gamma = 0$ and GL-functional is reduced to the two independent superfluids with $S_z^{tot} = 1$ ($\Delta_{\uparrow\uparrow}$) and $S_z^{tot} = -1$ ($\Delta_{\downarrow\downarrow}$). The direct minimization of the free energy $\frac{\partial\Delta F_{GL}}{\partial A_{\pm k}} = \frac{\partial\Delta F_{GL}}{\partial A_{\pm k}^*} = 0$ yields four minima of ΔF_{GL} [61].

For $T < T_{C1}^{\downarrow\downarrow} < T_{C1}^{\uparrow\uparrow}$ the first one corresponds to:

$$\Delta_{0\uparrow\uparrow}^2 M_+ = -\frac{a_\uparrow}{4b_\uparrow}; \quad \Delta_{0\downarrow\downarrow}^2 M_- = -\frac{a_\downarrow}{4b_\downarrow}; \quad N_+ = N_- = 0, \tag{12.3.32}$$

the second one corresponds to:

$$\Delta_{0\uparrow\uparrow}^2 M_+ = -\frac{a_\uparrow}{6b_\uparrow}; \quad \Delta_{0\downarrow\downarrow}^2 M_- = -\frac{a_\downarrow}{6b_\downarrow}; \quad |N_+| = M_+ \text{ and } |N_-| = M_-. \tag{12.3.33}$$

For the third one and the fourth one correspondingly $\Delta_{0\uparrow\uparrow}^2 M_+ = -\frac{a_\uparrow}{6b_\uparrow}$, $\Delta_{0\downarrow\downarrow}^2 M_- = -\frac{a_\downarrow}{4b_\downarrow}(|N_+| = M_+, |N_-| = 0)$, and $\Delta_{0\uparrow\uparrow}^2 M_+ = -\frac{a_\uparrow}{4b_\uparrow}$, $\Delta_{0\downarrow\downarrow}^2 M_- = -\frac{a_\downarrow}{6b_\downarrow}(|N_-| = M_-, |N_+| = 0)$.

The GL free energy on the first extremum is given by:

$$\Delta F_{GL} = -\frac{a_\uparrow^2}{8b_\uparrow} - \frac{a_\downarrow^2}{8b_\downarrow}, \tag{12.3.34}$$

on the second one we have:

$$\Delta F_{GL} = -\frac{a_\uparrow^2}{12b_\uparrow} - \frac{a_\downarrow^2}{12b_\downarrow}, \tag{12.3.35}$$

Correspondingly on the third and on the fourth one $\Delta F_{GL} = -\frac{a_\uparrow^2}{12b_\uparrow} - \frac{a_\downarrow^2}{8b_\downarrow}$, and $\Delta F_{GL} = -\frac{a_\uparrow^2}{8b_\uparrow} - \frac{a_\downarrow^2}{12b_\downarrow}$.

Expressions (12.3.34) and (12.3.35) show that the global minima corresponds to the first case with $N_+ = N_- = 0$. For $T_{C1}^{\downarrow\downarrow} < T < T_{C1}^{\uparrow\uparrow}$ the global extremum conditions are satisfied for three degenerate phases:

$$A1 = \frac{1}{2}\begin{pmatrix} 1 & i & 0 \\ i & -1 & 0 \\ 0 & 0 & 0 \end{pmatrix}; \quad E = \frac{1}{\sqrt{2}}\begin{pmatrix} 1 & 0 & 0 \\ 0 & 1 & 0 \\ 0 & 0 & 0 \end{pmatrix}; \quad \sigma_3 = \frac{1}{\sqrt{2}}\begin{pmatrix} 1 & 0 & 0 \\ 0 & -1 & 0 \\ 0 & 0 & 0 \end{pmatrix}. \tag{12.3.36}$$

(Note that E phase coincides with the well-known planar phase [6]).

For $T < T_{C1}^{\downarrow\downarrow}$ the global extremum corresponds again to E and σ_3 phases together with the A2 phase. The last one has the form:

$$A2 = \frac{1}{\sqrt{2(1-\varepsilon^2)}}\begin{pmatrix} 1 & i & 0 \\ i\varepsilon & -\varepsilon & 0 \\ 0 & 0 & 0 \end{pmatrix}; \quad \varepsilon = \frac{\Delta_{0\uparrow\uparrow} - \Delta_{0\downarrow\downarrow}}{\Delta_{0\uparrow\uparrow} + \Delta_{0\downarrow\downarrow}}. \tag{12.3.37}$$

Of course for $\Delta_{0\uparrow\uparrow} = \Delta_{0\downarrow\downarrow}$ (in the absence of magnetic field) $\varepsilon = 0$. The appearance of the strong-coupling term proportional to $\Delta_{0\uparrow\uparrow}^2\Delta_{0\downarrow\downarrow}^2$ mixes $S_z = 1$ and $S_z = -1$ superfluids below the critical temperature $T_{C1}^{\downarrow\downarrow}$. There are two consequences of this fact; the first one is an increase of $T_{C1}^{\downarrow\downarrow}$ (in comparison with a bare value) due to the interaction between up–up and down–down Bose-condensates. Of course $\Delta_{0\uparrow\uparrow}$ is also renormalized below $T_{C1}^{\downarrow\downarrow}$. The second one is lifting of the degeneracy between the phases which correspond to the global minima. Indeed, for A2 phase we have [17]:

$$N_+ = N_- = 0; \quad R = 0; \quad |P|^2 = M_+M_-, \tag{12.3.38}$$

and the Ginzburg–Landau free energy on this extremum is given by:

$$\Delta F_{GL}(A2 \text{ phase}) = -\frac{a_\uparrow^2}{8b_\uparrow} - \frac{a_\downarrow^2}{8b_\downarrow} + (\delta + \gamma)\frac{a_\uparrow a_\downarrow}{16 b_\uparrow b_\downarrow}. \tag{12.3.39}$$

At the same time for the planar (E) and σ_3 phases:

$$N_+ = N_- = 0; \quad P = 0; \quad |R|^2 = M_+M_-, \tag{12.3.40}$$

and, accordingly, the Ginzburg–Landau free energy reads:

$$\Delta F_{GL}(E, \sigma_3 \text{ phases}) = -\frac{a_\uparrow^2}{8b_\uparrow} - \frac{a_\downarrow^2}{8b_\downarrow} + (\delta + \beta)\frac{a_\uparrow a_\downarrow}{16 b_\uparrow b_\downarrow}. \tag{12.3.41}$$

Formulae (12.3.39) and (12.3.40) show that to answer the question which phase has a lower energy we need to calculate the combinations $(\delta + \beta)$ and $(\delta + \gamma)$ of the strong-coupling coefficients. These calculations can be performed in the same way as in the absence of magnetic field (see [8, 9] and previous subsection). The

analytical results in nonzero magnetic fields can be restored here only in the leading order in the parameter $\lambda^2 \frac{T_{C1}}{2\varepsilon_F} \left|\beta_1^{W.C.}\right|$ (see [17] for more details):

$$\begin{cases} \delta^{(2)} \approx 126.2 \dfrac{T_{C1}}{2\varepsilon_F} \lambda^2 \left|\beta_1^{W.C.}\right| \left(\dfrac{2v^3}{1+v^3}\right)^{1/3} \left[-0.18 - 1.68v^2\right], \\ \beta^{(2)} \approx 126.2 \dfrac{T_{C1}}{2\varepsilon_F} \lambda^2 \left|\beta_1^{W.C.}\right| \left(\dfrac{2v^3}{1+v^3}\right)^{1/3} \left[-1.0 - 1.51v^2\right], \\ \gamma^{(2)} \approx 126.2 \dfrac{T_{C1}}{2\varepsilon_F} \lambda^2 \left|\beta_1^{W.C.}\right| \left(\dfrac{2v^3}{1+v^3}\right)^{1/3} \left[-1.0 - 1.51v^2\right] \end{cases} \tag{12.3.42}$$

For the maximal stationary magnetic field $H \sim 20$ T ($\alpha = 0.08$ and $v = \frac{p_{F\downarrow}}{p_{F\uparrow}} = \left(\frac{1-\alpha}{1+\alpha}\right)^{1/3} = 0.95$) which we can create by brute force δ, β and γ differ only on 10 % from their zero-field values. Coefficients β and γ identically coincide in this order even in nonzero magnetic field. That is why the A2 phase, planar phase and σ_3 phase are still degenerate. To lift the degeneracy we need to calculate δ, β and γ in the next order. In zero magnetic field we have from β values in (12.3.19):

$$\begin{cases} \delta^{(3)} \approx -302.9 \frac{T_{C1}}{2\varepsilon_F} \lambda^3 \left|\beta_1^{W.C.}\right|, \\ \beta^{(3)} \approx 1114 \frac{T_{C1}}{2\varepsilon_F} \lambda^3 \left|\beta_1^{W.C.}\right|, \\ \gamma^{(3)} \approx -1021 \frac{T_{C1}}{2\varepsilon_F} \lambda^3 \left|\beta_1^{W.C.}\right| < \beta^{(3)} \end{cases} \tag{12.3.43}$$

These values show that A2 phase is energetically more favorable. The numerical results for complete magnetic field dependence of δ, β and γ in third order in $\lambda = \frac{2ap_F}{\pi}$ is presented on Fig. 12.9.

At small spin-polarizations $\alpha \approx 3/2\,(1-v)$ all the coefficients δ, β and γ behave linearly in α. For $H = 20$ T they again differ only on 10 % from their zero-field values.

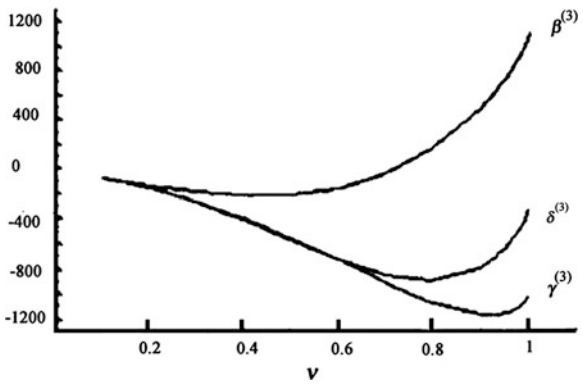

Fig. 12.9 Magnetic field dependence of strong-coupling coefficients δ, β and γ in third order in gas parameter $\lambda = \frac{2ap_F}{\pi}$ (in units $\lambda^3 \frac{T_{C1}}{2\varepsilon_F} \left|\beta_1^{W.C.}\right|$ obtained numerically in [17])

However, for spin-polarization $\alpha = 0.3$ ($v = 0.8$), which can be created by a rapid melting of ^{3}He crystal by Castaing, Nozieres method [71], this difference becomes rather significant. Moreover, δ and β have nonmonotonic dependence from v with pronounced minimum, while γ is monotonically decreasing function. For $v \to 0$ ($\alpha \to 1$) there are no down spins in the system and that is why δ, β and γ saturate to the same zero value. The most important thing is that γ is smaller than β for all magnetic fields. Hence A2 phase is global extremum of the free energy.

Concluding this subsection, we would like to stress that we have calculated the strong-coupling corrections to the free energy of a triplet superfluid Fermi gas in high magnetic fields and found that the phase diagram of the system contains only A1 and A2 phases. Note again that in pure (dense) ^{3}He $\lambda \sim 1$ and our results can be used only as a qualitative estimate. Nevertheless, due to the *intrinsic* character of a superfluid transition in spin-polarized Fermi gas, our philosophy is the following: if there are no exotic phases at low densities, there is a small chance to obtain them at higher densities. Hence we consider the present calculations as a strong argument against the possibility of a new phase of ^{3}He [49–52, 68] in a high magnetic field. Having in mind the results of the previous subsection in zero magnetic field (no new phase either), we consider any novelty in a phase diagram of superfluid ^{3}He to be very unlikely (at least in three dimensions). The only hope here can be connected with the region of finite magnetic fields smaller than paramagnetic limit $H_p \sim (2 \div 3)$ T of the destruction of the B phase [20].

12.4 GL-Functional and Global Phase-Diagram of the 2D Superfluid Fermi Gas with Repulsion

The situation in the two-dimensional case differs from the three-dimensional situation with respect to the matrix of the order parameter A_{ik}. Namely, the orbital space now has one degree of freedom less. In the same time a spin space is still three-dimensional. That is why now the matrix of the order parameter has a row of zeroes in contrast with the bulk ^{3}He. It is interesting to note that if we change spin variables on orbital ones, than this situation will be similar to the 3D situation in strong magnetic fields $H > H_p$ considered in the end of the previous section [17, 19, 74]. In the last 3D case $A_{3k} = 0$. Thus, in 2D superfluid Fermi gas with repulsion $A_{k3} = 0$. It is convenient here again to introduce the new variables $A_{k+} = iA_{k2} - A_{k1}$ and $A_{k-} = iA_{k2} + A_{k1}$ similarly to [17].

Than the GL-functional will have a form [19, 74]:

$$\Delta F_{GL} = F_S - F_N = a\Delta_0^2(M_+ + M_-) + b\Delta_0^4\left(M_+^2 + M_-^2\right) + c\Delta_0^4\left(\left|N_+\right|^2 + \left|N_-\right|^2\right) + \Delta_0^4(\delta M_+ M_- + \beta|R|^2 + \gamma|P|^2), \tag{12.3.44}$$

where $M_+ = A^*_{k+}A_{k+}, M_- = A^*_{k-}A_{k-}, N_+ = A_{k+}A_{k+}, N_- = A_{k-}A_{k-}, R = A_{k+}A_{k-}$, $P = A_{k+}A^*_{k-}$ similarly to (12.3.27, 12.3.28) with a substitution of $A_{\pm k}$ by $A_{k\pm}$. The coefficients in (12.3.44) read: $b = \frac{\beta_2+\beta_4}{2}$, $c = \frac{\beta_3}{2}$, $\delta = \beta_2 + \beta_5$, $\beta = 2\beta_1 + \beta_3$, $\gamma = \beta_4 + \beta_5$, $\Delta_0(T)$ is still an amplitude of the gap. The extrema of GL free energy are again governed by the conditions $\frac{\partial \Delta F_{GL}}{\partial A_{k\pm}} = \frac{\partial \Delta F_{GL}}{\partial A^*_{k\pm}} = 0$, which are reduced to the system of eight equations for the variables M_+, M_-, N_+, N_-, R, P, and the gap $\Delta_0(T)$.

The solution of these equations define eight different phases of 2D superfluid Fermi gas with repulsion. In the weak-coupling approximation the GL-functional has the local minima corresponding to the two 2D phases, namely to the axial phase (A) and planar phase (E):

$$A = \sqrt{\frac{1}{2}}\begin{pmatrix} 1 & 0 & 0 \\ i & 0 & 0 \\ 0 & 0 & 0 \end{pmatrix}; \; E = \frac{1}{\sqrt{2}}\begin{pmatrix} 1 & 0 & 0 \\ 0 & 1 & 0 \\ 0 & 0 & 0 \end{pmatrix} \tag{12.3.45}$$

The matrices E and A are similar to E and A_2 in (12.3.36), (12.3.37) for $\varepsilon = 0$ ($\Delta_{0\uparrow\uparrow} = \Delta_{0\downarrow\downarrow}$) in case of zero magnetic field. The five other phases: polar and bipolar, axiplanar, λ and η correspond to the saddle point while β-phase correspond to the local maximum of the GL-functional.

The strong-coupling corrections lift the degeneracy between planar and axial phases in favor of an axial phase [19]:

$$F_{axial} - F_{planar} \sim -\frac{N_{2D}(0)}{T_{C1}^2}\frac{T_{C1}}{\varepsilon_F}\int \frac{d\varphi}{2\pi}|\sin\varphi||\Gamma_a(\vec{p}_1, \vec{p}_2; \vec{p}_1, \vec{p}_2)|^2 < 0, \tag{12.3.46}$$

where spin-asymmetric part of quasiparticle scattering amplitude Γ_a should be calculated on the Fermi-surface ($\vec{p}_1 = p_F\vec{n}_1$, $\vec{p}_2 = p_F\vec{n}_2$), and φ is an angle between $\vec{p}_1$ and $\vec{p}_2$. Expression (12.3.46) is negative independently of the character of the interaction in the system. Thus, the axial phase corresponds to global minima of the GL-functional in 2D superfluid Fermi gas with repulsion at least for temperatures T close to T_{C1} (where GL-expansion is valid).

Concluding this section, we can say, that again (as in 3D case) we did not find any local minima of the GL-functional corresponding to exotic phases in 2D triplet superfluid Fermi gas.

Thus B-phase at low pressures and A-phase at high pressures in the bulk as well as an axial phase in 2D case are the only global minima of the GL-functional for triplet superfluid Fermi gas in the absence of magnetic field, while A1 and A2-phases are the global minima of the GL-functional in strong magnetic fields exceeding the paramagnetic limit ($H > H_p$) in the bulk. The hopes to find a new exotic phase, as we mentioned already, can be connected only with the region of small and moderate magnetic fields $H < H_p \sim (2 \div 3)$ T. Note also that in real ^{3}He the crossover from 3D to purely 2D case via reduction of the ^{3}He film thickness or cell thickness in slab geometry is rather smooth. Namely, in a confined (slab) geometry the effect of the boundaries is in favor of the formation of the

3D A-phase. The typical cell thickness in these systems is of the order of 2000 ÷ 3000 Å, which is much larger than the zero-temperatures coherence length ξ_0 (according to [75] the coherence length in ^{3}He varies from 90 Å to 404 Å as the pressure drops from 34.2 bar to 0 bar). It follows from [76] that in a slab geometry at temperatures close to T_C the A-phase can exist at pressures lower than in the purely 3D situation.

Therefore the superfluid phase diagram in zero magnetic field contains in real ^{3}He an additional narrow stripe of A-phase between the region corresponding to the B-phase and the normal state (see [6]). The region of the phase diagram occupied by the A-phase grows as one decreases the cell thickness.

On the other hand in a purely 2D case an axial phase (analog of the A-phase) exists in a wide range of densities, at least in the regime where the Ginzburg-Landau approach is legitimate. From this point of view the crossover from the 3D case to the 2D case is consistent both in ^{3}He and in triplet superfluid Fermi gas with repulsion.

References

1. Stoof, H.T.C., Houbiers, M., Sackett, C.A., Hulet, R.G.: Phys. Rev. Lett. **76**, 10 (1996)
2. Lifshitz, E.M., Pitaevskii, L.P.: Statistical Physics, Part 2. Pergamon Press, New York (1988)
3. Baranov, M.A., Kagan, M.Yu., Kagan, Y.: JETP Lett. **64**, 301 (1996)
4. Efremov, D.V., Mar'enko, M.S., Baranov, M.A., Kagan, M.Yu.: JETP **90**, 861 (2000)
5. Efremov, D.V., Viverit, L.: Phys. Rev. B **65**, 134519 (2002)
6. Vollhardt, D., Wölfle, P.: The superfluid phases of Helium 3. Taylor and Francis, London (1990)
7. Mermin, N. D., Stare, C.: Phys. Rev. Lett. **30**, 1135 (1973)
8. Rainer, D., Serene, J.W.: Phys. Rev. B **13**, 4745 (1976)
9. Baranov, M.A., Efremov, D.V., Kagan, M.Yu., Capel, H.W., Mar'enko, M.S.: JETP Lett. **59**, 268 (1994)
10. Balian, R., Werthamer, N.R.: Phys. Rev. **131**, 1553 (1963)
11. Anderson, P.W., Morel, P.: Phys. Rev. **123**, 1911 (1961)
12. Brinkman, W.F., Anderson, P.W.: Phys. Rev. A **8**, 2732 (1973)
13. Brinkman, W.F., Serene, J.W., Anderson, P.W.: Phys. Rev. A **10**, 2386 (1974)
14. Barton, G., Moore, M.A.: J. Phys. C **7**, 4220 (1974)
15. Jones, R.B.: J. Phys. C **10**, 657 (1977)
16. Brussaard, P., Baranov, M.A., Kagan, M.Yu., van Weert, C.G., Capel, H.W.: Physica A **234**, 643 (1997)
17. Baranov, M.A., Efremov, D.V., Kagan, M.Yu., Capel, H.W., Mar'enko, M.S., Brussaard, P., van Weert, C.G.: JETP Lett. **62**, 610 (1995)
18. Kagan, M.Yu,. Brussaard, P., Capel, H.W.: Phys. Lett. A **221**, 407 (1996)
19. Mar'enko, M.S., Efremov, D.V., Ozharovskii, A.V., Baranov, M.A., Kagan, M.Yu:. J. Low Temp. Phys. **126**, 551 (2002)
20. Capel, H.W., Brussaard, P., Kagan, M.Yu.: unpublished
21. Anderson, M.H., Ensher, J.R., Matthews, M.R., Wieman, C.E., Cornell, E.A.: Science **269**, 198 (1995)
22. Bradley, C.C., Sackett, C.A., Tollett, J.J., Hulet, R.G.: Phys. Rev. Lett. **75**, 1687 (1995)
23. Davis, K.B., Mewes, M.O., Andrews, M.R., van Druten, N.J., Durfee, D.S., Kurn, D.M., Ketterle, W.: Phys. Rev. Lett. **75**, 3969 (1995)

24. Regal, C.A., Ticknor, C., Bohn, J.L., Jin, D.S.: Nature **424**, 47 (2003)
25. Greiner, M., Regal, C.A., Jin, D.S.: Nature **426**, 537 (2003)
26. Zwierlein, M.W., Stan, C.A., Schunck, C.H., Raupach, S.M.F., Gupta, S., Hadzibabic, Z., Ketterle, W.: Phys. Rev. Lett. **91**, 250401 (2003)
27. Jochim, S., Bartenstein, M., Altmeyer, A., Hendl, G., Riedl, S., Chin, C., Denschlag, J.H., Grimm, R.: Science **302**, 2101 (2003)
28. Herbig, J., Kraemer, T., Mark, M., Weber, T., Chin, C., Nägerl, H.-C., Grimm, R.: Science **301**, 1510 (2003)
29. Abraham, E.R.I., McAlexander, W.I., Gerton, J.M., Hulet, R.G., Côté, R., Dalgarno, A.: Phys. Rev. A **55**, R3299 (1997)
30. Landau, L.D., Lifshitz, E.M.: Statistical Physics, Part I. Butterworth-Heinemann, Oxford (1999)
31. Gor'kov, L.P., Melik-Barkhudarov, T.K.: JETP **13**, 1018 (1961)
32. Kagan, M.Yu., Chubukov, A.V.: JETP Lett. **47**, 614 (1988)
33. Baranov, M.A., Chubukov, A.V., Kagan, M.Yu.: Int. J. Mod. Phys. B **6**, 2471 (1992)
34. Baranov, M.A., Kagan, M.Yu.: JETP **75**, 165 (1992)
35. Fay, D., Layzer, A.: Phys. Rev. Lett. **20**, 187 (1968)
36. Baranov, M.A., Kagan, M.Yu.: Physica B **191**, 341 (1993)
37. Kagzan, Y., Shlyapnikov, G.V., Glukhov, N.A.: JETP Lett. **41**, 238 (1985)
38. Kagan, Y., Shlyapnikov, G.V., Glukhov, N.A.: ibid **35**, 320 (1982)
39. Kagan, Y., Shlyapnikov, G.V., Glukhov, N.A., ibid **40**, 287 (1984)
40. Kagan, Y., Shlyapnikov, G.V., Glukhov, N.A.: Phys. Lett. A **101**, 27 (1984)
41. Kagan, Y., Shlyapnikov, G.V., Walraven, J.T.M.: Phys. Rev. Lett. **76**, 2670 (1996)
42. Landau, L.D., Lifshitz, E.M.: Quantum Mechanics: Non-relativistic theory. Pergamon Press, New York (1977)
43. Migdal, A.B.: Qualitative methods in quantum theory. Westview Press, Boulder (2000)
44. Bardeen, J., Baym, G., Pines, D.: Phys. Rev. **156**, 207 (1967)
45. Bardeen, J., Baym, G., Pines, D.: Phys. Rev. Lett. **17**, 372 (1966)
46. Volovik G.E., Mineev, V.P.: Sov. Sci. Rev. Sect. A2, **173** (1980) (unpublished study)
47. Bruder, C., Vollhardt, D.: Phys. Rev. B **34**, 131 (1986)
48. Marchenko, V.I.: JETP **66**, 79 (1987)
49. Pekola, J.P., Kyynäräinen, J.M., Manninen, A.J., Torizuka, K.: Physica B **165–166**, 613 (1990)
50. Frossati, G., Wiegers, S.A.J., Hata, T., Jochemsen, R., van de Haar, P.G., Roobol, L.P.: Czech. J. Phys. **40**, 909 (1990)
51. Gould, C.M.: Physica B **178**, 266 (1992)
52. Tang, Y.H., Hahn, I., Bozler, H.M., Gould, C.M.: Phys. Rev. Lett. **67**, 1775 (1991)
53. Nijhoff, F.W., Capel, H.W., Den Breems, A.: Physica A **130**, 375 (1985)
54. Nijhoff, F.W., Capel, H.W., Den Breems, A.: Physica A **135**, 295 (1986)
55. Capel, H.W., Nijhoff, F.W., Den Breems, A.: Physica A **139**, 256 (1986)
56. Morley, G.W., Casey, A., Lusher, C.P., Cowan, B., Saunders, J., Parpia, J.M.: J. Low Temp. Phys. **126**, 557 (2002)
57. Brussaard, P., van Weert, C.G.: Physica A **228**, 102 (1996)
58. Alexandrov, A.S., Golubov, A.A.: Phys. Rev. B **45**, 4769 (1992)
59. Rainer, D.: Private communication to the author
60. Kagan, M.Yu.: Habilitation Thesis, Kapitza Institute, (1994)
61. Efremov, D.V.: PhD Thesis, Kapitza Institute (1999)
62. Kagan, M.Yu., Ozharovskii, A.V., Lecture course, Part II, Moscow (1999)
63. Kagan, M.Yu., Chubukov, A.V.: JETP Lett. **50**, 483 (1989)
64. Frossati, G., Bedell, K.S., Wiegers, S.A.J., Vermeulen, G.A., Phys. Rev. Lett. **57**, 1032 (1986)
65. Dy, K.S., Pethick, C.J.: Phys. Rev. **185**, 373 (1969)
66. Roobol, L.P., Jochemsen, R., van Woerkens, C.M.C.M., Hata, T., Wiegers, S.A.J., Frossati, G.: Physica B **165–166**, 639 (1990)

67. Wiegers, S.A.J., Hata, T., van de Haar, P.G., Roobol, L.P., van Woerkens, C.M.C.M., Jochemsen, R., Frossati, G.: Physica B **165–166**, 733 (1990)
68. Bedell, K.S., Sanchez-Castro, C.: Phys. Rev. Lett. **57**, 854 (1986)
69. Sagan, D.C., de Vegvar, P.G.N., Polturak, E., Friedman, L., Yan, S.-S., Ziercher, E.L., Lee, D.M.: Phys. Rev. Lett. **53**, 1939–1942 (1984)
70. Israelsson, U.E., Crooker, B.C., Bozler, H.M., Gould, C.M.: Phys. Rev. Lett. **53**, 1943 (1984)
71. Castaing, B., Nozieres, P.: J. de Physique (France) **40**, 257 (1979)
72. Wiegers, S.A.J., Kranenburg, C.C., Hata, T., Jochemsen, R., Frossati, G., Europhys. Lett. **10**, 477 (1989)
73. Brussard, P., PhD Thesis, Amsterdam University (1997)
74. Mar'enko, M.S.: PhD Thesis, Kapitza Institute, (2000)
75. Ichikawa, K., Yamasaki, S., Akimoto, H., Kodama, T., Shigi, T., Kojima, H.: Phys. Rev. Lett. **58**, 1949 (1987)
76. Li, Y.-H., Ho, T.-L.: Phys. Rev. B **38**, 2362 (1988)

Chapter 13
Spin-Charge Separation and Confinement in Ladder Systems and in High-T_C Superconductors

13.1 Introduction

In the present Chapter on the level of 2D isotropic t-J model [1–3] and strongly anisotropic (quasi-1D) t-J model [4–6] we will describe the superconductive phase diagram of layered cuprates and quasi-1D ladder materials [5, 7, 8, 113]. We present the basic ideas of the physics of spin-charge separation [2, 9–14] and spin-charge confinement [15, 16]. Note that spin-charge separation is actual for 1D AFM spin-chains [9–12, 17–19] and for extended regions of the phase diagrams of ladder systems with odd number of "legs" (odd number of coupled spin-chains such as three-leg ladders [20, 21], five-leg ladders and so on). Note also that in terminology used for ladder systems (see [5] for a review) each spin-chain, is called the "leg", while interchain AFM-coupling and hopping (in doped case) are described in terms of "rungs" (see Fig. 13.1).

The system with spin-charge separation are usually described in terms of Luttinger Fermi-liquid (LL) [9–12]. For LL the group velocities of spinons v_S (spin excitations) and holons v_C (charge excitations) are different [14], so the charge transfer (charge-density waves CDW) and spin transfer (spin-density waves SDW) are also described by different group velocities $v_S \neq v_C$. This phenomena can be better understood if we use electroneutrality considerations. They are important for charge transfer, and so the crystalline lattice (the ions) also participate in the process. However, we can neglect the ions for spin transfer. Thus we can understand the difference between the group velocities of CDW and SDW in 1D systems. Correspondingly in LL spin excitations (spin waves) are gapless Goldstone modes while charge excitations can be gapped or gapless depending upon the model (the finite mass can be generated for charge excitations in analogy with plasmons in metals). This leads to slow (power-law) decay of spin–spin correlations, while charge–charge correlations can be even rapidly exponentially decaying in 1D. If we, vice a versa, consider the ladders with even number of legs (characteristic example of two-leg ladder [22, 23] is presented on Fig. 13.1), then we will fall in another universality class as people call it. Namely the two-leg ladder will be described by quite different Luther-Emery (LE) liquid [11, 24, 25].

M. Yu. Kagan, *Modern Trends in Superconductivity and Superfluidity*,
Lecture Notes in Physics 874, DOI: 10.1007/978-94-007-6961-8_13,

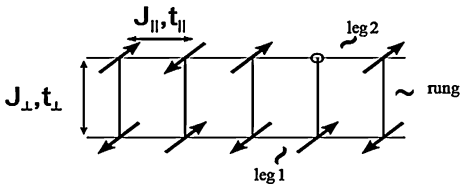

Fig. 13.1 A typical example of the two-leg ladder (a coupled system of two spin-chains). The interchain AFM-coupling and hopping (if at least one leg is doped) $J_\perp, t_\perp$ are described in terms of rungs. $J_\parallel, t_\parallel$ are AFM-coupling and hopping along the legs

In LE liquid we have opposite situation: the spin–spin correlations are exponentially decaying while density–density (and SC gaps) correlations are slowly decaying. In LL the dominant instability is towards SDW-formation, while in LE liquid it is towards CDW-formation and strong SC-fluctuations which favor SC if we include small interaction between ladders (see [22, 23, 26]). In the limit of strong-coupling along the rungs $J_\perp \gg \{J_\parallel, t_\parallel, t_\perp\}$ we will show (see Fig. 13.2) that for two holes it is energetically beneficial to occupy the same rung, thus forming a rung-boson (or biholon or local Cooper pair) with charge $2e$.

In the same time in this limit the spins on the rung also form local Kondo-singlets with the Ψ-function $|\Psi_S\rangle = \frac{1}{\sqrt{2}}|\uparrow\downarrow - \downarrow\uparrow\rangle$ and with an energy $E_s = -\frac{3}{4}J_\perp$. We can say that the rung-boson (or biholon or a local Cooper pair) moves in this limit in the surrounding of local (rung) Kondo-singlets [22, 23]. Kondo-singlets play the pole of holes in effective 1D-model for the rungs. The effective 1D-model for this case is equivalent to 1D Bose-Hubbard model for rung-bosons [27]. In general we can say that LE-liquid is equivalent to 1D repulsive Bose-gas of composite (rung) bosons, while LL is equivalent (for the three-leg ladder for example) to 1D repulsive Fermi-gas or repulsive 1D Hubbard model of composite (rung) fermions [26, 28]. When we increase the number of legs (starting with three-leg ladders) the phase diagrams become more sophisticated. They contain both regions of LL and LE-liquid depending upon the relation between the parameters $\{J_\perp, t_\perp\}$ and $\{J_\parallel, t_\parallel\}$ describing AFM-coupling and hopping along the rungs and legs, respectively [20, 21]. The difference between even- and odd-numbers of legs becomes less pronounced when we increase the number of legs,

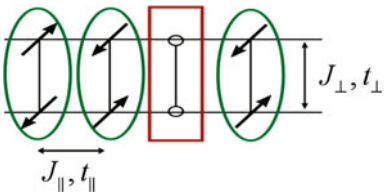

Fig. 13.2 The bound state of two holes on one rung in the strong-coupling limit of the anisotropic t-J model for the two-leg ladder $J_\perp \gg \{J_\parallel, t_\parallel, t_\perp\}$. In this limit the spins on the rung form local Kondo-singlets (see Fig. 13.11)

but still there is no smooth transition to the limit when N (number of legs) $\rightarrow \infty$. However, in the isotropic limit of the model $J = J_{\perp} = J_{\parallel}$, $t = t_{\perp} = t_{\parallel}$ and $J/t \sim 1/2 \div 1/3$ (typical for 2D high-T_C materials) there is a tendency towards the coexistence of LL and LE-liquids. Thus there is a motive of the Fermi-Bose mixture of effective (rung) fermions and bosons in the isotropic limit [29]. Correspondingly we can consider underdoped limit of 2D high-T_C materials in the framework of a strongly interacting Fermi-Bose mixture of spinons and holons [30]. Note that the strong interaction between spinons and holons in the underdoped cuprates can be connected with linear (confinement) potential describing Bulaevskii-Nagaev-Khomskii [1] Brinkman-Rice [31] AFM-string [32]. It is easier however, to proceed at first to more simple overdoped limit of 2D isotropic t-J model (see the beginning of Sect. 13.4).

In the second part of the Chapter we consider isotropic 2D t-J model [1–3]. At first we analyze superconductive phase diagram of this model in strongly overdoped case (for small and intermediate electron densities where Landau Fermi-liquid picture is valid). We find the regions of extended s-wave, p-wave and $d_{x^2-y^2}$-wave pairings as well as the tendency towards phase separation at large values of J/t and low density [33–35]. We present then the simple estimates for d-wave critical temperature in the optimally doped case [34] and get reasonable $T_C \sim 100$ K typical for cuprates here [36–39]. Then we return back to the difficult corner of the phase diagram of the t-J model for which $n_{el} = 1 - x \rightarrow 1$ ($x \ll 1$—underdoped case) and $J/t \sim (1/2 \div 1/3)$. Here in agreement with Fermi-Bose mixture ideas [29] introduced in the first part of the Chapter, we propose a scenario of the BCS-BEC crossover for pairing of two composite holes [15, 16] (two strings [32], or two spin-polarons [40, 41]) in the d-wave channel [30]. Note that each composite hole (each string or spin polaron) contains spinon and holon interacting via confinement potential. Here we are inspired by the ideas of Laughlin on spin-charge confinement [15, 16] and the analogies between composite holes in underdoped state of the 2D t-J model and quark-gluon physics (physics of quark bags) in quantum chromodynamics (QCD) [42–48]. [Note that alternative slave-boson [49–53] spin-charge separation scenario was considered briefly (see also [54]) in connection with 2D underdoped t-J model in Chap. 6].

In the end of the Chapter, we briefly discuss the possible BCS-BEC crossover scenario for high-T_C materials.

13.2 Spin-Charge Separation and Luttinger Liquid in Doped Spin-Chains

We start the present Section with a brief enumeration of the powerful analytical methods developed in 1D physics (usually they are not so effective for higher dimensionalities).

They include Bethe-ansatz (Bethe [17]) for a 1D chain of spins $S = ½$, exact solutions in 1D Hubbard model for arbitrary density n and coupling strength U/t (Lieb, Wu [18], see also Mattias, Lieb [116]), nonlinear sigma model with the topological term for halfinteger and integer spins, and methods of conformal field theory in 1 space + 1 time dimensions (Haldane [9, 10], Belavin et al. [55], Itzykson et al. [56], Pruisken [57], Frahm, Korepin [58, 59], Hawakami, Yang [60]) as well as bosonization methods (Tonomaga [14], Luttinger [61]). While the exact solutions (see also Kawakami et al. [60, 62]) are very useful to describe the ground state of 1D Hubbard model or 1D interacting Fermi-gas at different coupling strengths, the bosonization methods help to represent the energy of the low-lying excited states of the 1D interacting Fermi-systems as a sum of the energies of the independent bosonic oscillators.

We can say that to some extent bosonization method is ideologically similar to the hydrodynamical method presented in the first part of the manuscript. Effectively it is based on the introduction of the collective bosonic variables describing charge and spin-density fluctuations. However, bosonization methods could give slightly more than hydrodynamics since in some models (such as Tomonaga-Luttinger model for example) they describe not only oscillations with small frequencies and k-vectors, but also help to restore density–density and spin–spin correlations at large k-vectors of the order of $2p_F$ related to giant 1D Kohn's anomaly (see also Chap. 9 for more details).

For the introduction to the bosonization method we can recommend an excellent review-article of Brazovskii and Kirova [63], pioneering articles [64–68] on abelian and nonabelian bosonization and textbooks [46–48, 69] of Fradkin, Tsvelik et al., and Gimarchi.

We are much more modest in the present Section and will study mostly a 1D doped spin-chain with AFM-interaction between nearest neighbor spins $S = ½$ in the framework of the 1D t-J model.

13.2.1 1D t-J Model for Doped Spin-Chains

Let us consider 1D t-J model for doped spin-chains with AFM interaction ($J > 0$) between spins $S = ½$. In the absence of doping the Hamiltonian is of the Heisenberg type and reads:

$$\hat{H} = J \sum_{\langle ij \rangle} \vec{S}_i \vec{S}_j. \tag{13.1.1}$$

It is well known that in 1D spin-fluctuations destroy long-range AFM ordering. Spin excitations are gapless. Spin correlations decay in a power fashion in this model:

$$\left\langle \vec{S}(x)\vec{S}(0)\right\rangle \sim \frac{\cos(2p_F x)}{x^{1+\beta}}, \tag{13.1.2}$$

where β is model-dependent parameter. For small J the parameter $\beta = ½$ and $1 + \beta = 3/2$. Note also that exact solution for 1D spin-chain is available for $S = ½$: $E = -JN\ln 2$, where N is the number of sites (see Bethe [17]). At low doping $n = 1 - x$ ($x \ll 1$) the system is described by the 1D t-J model [18, 19]:

$$\hat{H} = -t\sum_{\langle ij\rangle} c_{i\sigma}^{+} c_{j\sigma} + J\sum_{\langle ij\rangle} \vec{S}_i\vec{S}_j. \tag{13.1.3}$$

It is shown in [70] that for $J < 2t$ the 1D t-J model [18, 71] belongs to the universality class of Luttinger liquid (LL). The same universality class as we mentioned already describes 1D repulsive Hubbard model and 1D Fermi-gas with repulsion. The basic instability in 1D t-J model for $J < 2t$ is with respect to spin-density wave (SDW).

13.2.2 Spin-Charge Separation in Doped 1D Spin-Chains

As we already mentioned, one of the most important features of LL is a phenomenon of spin-charge separation. Let us illustrate this phenomenon for a doped spin-chain, described by 1D t-J model, following Fulde (see Fig. 13.3 and [13]).

Qualitatively we can describe Fig. 13.3 in the following manner: in the initial moment t_0 spinon and holon are nearby. The holon starts to move on the left hand side. As a result the domain wall of two frustrated spins (in Ising limit) is created at $t = t_1$ [46–48]. Finally in the moment $t = t_3$ the holon is separated from the domain wall by a regular structure of non-frustrated spins (in Ising limit). The distance between spinon and holon is $R = (v_S - v_C)\Delta t$ ($\Delta t = t_3 - t_0$). Note that, as we discussed in the Introduction to this Chapter, spinon and holon possess the

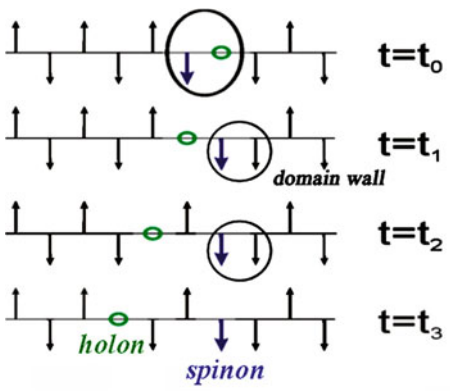

Fig. 13.3 Illustration of spin-charge separation in 1D according to Fulde (in "Strong correlations in molecules and Solids" [13]). If in the initial moment $t = t_0$ spinon and holon are nearby, than in the final moment $t = t_3$ there is a final distance $R = (v_S - v_C)\Delta t$ between them ($\Delta t = t_3 - t_0$)

different group velocities $v_S \neq v_C$ due to the fact that in the charge transfer (charge-density wave or CDW) participate both electrons and ions because of electroneutrality. In the same time in the spin transfer (SDW) participate only electrons. Of course, a presented picture of spin-charge separation is oversimplified. When we are speaking about domain wall, for example, we should understand what approximation is better: slave-boson [53, 73] (according to which a spinon is fermion $f_{i\sigma}$ with charge 0 and spin ½ while a holon is boson b_i with charge e and spin 0), or slave-fermion [73–75] where vice a versa holon is a spinless fermion h_i, while spinon is an $S = 1$ boson S_i^+ (S_i^-) (a bit similar to magnon). It seems that slave-fermion approximation is more reliable here [76] since a domain-wall corresponds with some degree of precaution to a localized magnon.

13.2.3 The Dressed Green-Function in 1D Luttinger Liquid

The dressed Green-function in standard Landau Fermi-liquid has a simple one-pole structure close to the Fermi-surface (for $p \to p_F$). Correspondingly we get in 3D or 2D Fermi-gas [72]: $G(\omega, \vec{p}) = \frac{Z}{\omega - \xi_p + i\delta}$, where $\xi_p = \frac{p^2 - p_F^2}{2m^*}$ is uncorrelated quasiparticle spectrum, and Z is quasiparticle residue or Z-factor. However, in 1D systems, which are described by Luttinger liquid and are subject of spin-charge separation, the situation is drastically changed. The dressed Green-function does not have a simple one-pole structure close to the Fermi-surface. Instead of that it often has a brunch-cut in momentum space for p ϵ $[-p_F, p_F]$. In the most simple Tomonaga model for 1D spinless fermions, for example, according to Dzyaloshinskii, Larkin [77, 78]:

$$G(\omega, p) \sim \frac{Z(\omega)}{\sqrt{[\omega - v_F(|p| - p_F)][\omega - u(|p| - p_F)]}}, \tag{13.1.4}$$

where Z-factor is vanishing on the Fermi-surface:

$$Z(\omega) \sim \omega^\alpha \to 0 \text{ for } \omega \to 0 \text{ (or for } |p| \to p_F), \tag{13.1.5}$$

and the power $\alpha > 0$ depends upon the model.

Let us emphasize that the Green-function has a typical square-root in denominator of (13.1.4) and moreover the velocity $u \neq v_F$. If we include spin degrees of freedom, the expression for the dressed one-particle Green-function $G(\omega, p)$ becomes rather cumbersome in momentum space (see Ren, Anderson [79] and Medden, Schonhammer [39]) containing a hypergeometric function [114].

However is real space it has a typical for spin-charge separation square-root again (see [46, 47, 80–82]). If we make the Wick transformation $t \to i\tau$ and introduce conformal variables $z = \tau + \frac{ix}{v}$ and $\bar{z} = \tau - \frac{ix}{v}$, then the Green-function $G(x, \tau)$ in Tonomaga-Luttinger model reads in the weak-coupling case [46]:

$$G(x,\tau)=\left(\frac{a^2}{v_s^2\tau^2+x^2}\right)^{\frac{\alpha}{2}}\left[\frac{\exp(ik_Fx)}{\sqrt{(v_s\tau-ix)(v_c\tau-ix)}}+\frac{\exp(-ik_Fx)}{\sqrt{(v_s\tau+ix)(v_c\tau+ix)}}\right],$$

where $0<\alpha<1/8$ is model-dependent parameter and $\alpha=1/8$ in strong-coupling limit (of the Hubbard model). Of course the velocities v_C and v_s are different. In weak-coupling limit of Tonomaga-Luttinger or 1D Hubbard model $v_C=v-g/2\pi$ and $v_s==v+g/2\pi$, where $g=U/4t<1$ is a coupling constant. In strong-coupling limit of 1D Hubbard model $v_C/v_s\sim 1/g\ll 1$ [46]. Thus for short-range repulsive interactions in 1D both spinons and holons are gapless. The charge excitations could be gapped in LL in case of long-range repulsive interactions. Finally let us repeat that if we have for example a two-leg ladder (a coupled system of the two spin chains), then the system falls in another universality class of Luther-Emery (LE) liquid. As we already mentioned LE liquid is equivalent to 1D Fermi-gas with *strong* attraction or to 1D Bose-gas with repulsion. In LE liquid we always have a gapless (Bogoliubov) spectrum for charge excitations. In fact in this case we have a sound wave in 1D Bogoliubov Bose-gas. The spectrum for spin excitations is gapped. We can say that while in LL the basic instability is towards spin-density wave (SDW) formation, in LE liquid the basic instability is towards charge-density wave (CDW) formation and strong superconductive (SC) fluctuations. LL describes spin-chains with half-integer spins and extended regions of phase-diagrams of odd-leg ladders (see the discussion of three-leg ladders in the next Sections). LE liquid describes spin-chains with integer spins (see Haldane [9, 10]) and extended regions of phase-diagrams of even-leg ladders. It is seductive to describe 2D high-T_C materials as a Fermi-Bose mixture of strongly interacting LL and LE liquids (see the next Section).

13.2.4 The Distribution Function for Interacting Particles in Luttinger Liquid

The interacting particles (not quasiparticles) distribution function $N_{\text{int}}(p)=\int\frac{d\omega}{2\pi}G(\omega,p)$ with $G(\omega,\ p)$ being a dressed one-particle Green-function from (13.1.4) does not have a finite jump on the Fermi-surface [7, 9–12, 83, 84]: $Z\to 0$ for $\omega\to 0$ [see (13.1.5) for Luttinger liquid (LL)]. Instead of the jump $N_{\text{int}}(p)$ possesses the power-law singularity close to p_F which reads (see Lieb, Mattias [84], Fulde [13] and Fig. 13.4):

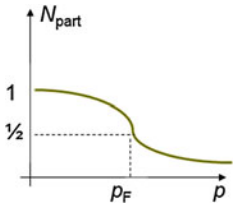

Fig. 13.4 Interacting particles distribution function in LL. There is no jump at $p=p_F$. Instead of it there is power-law singularity (see [13])

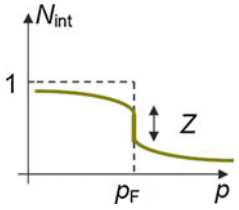

Fig. 13.5 Interacting particles distribution function in Landau Fermi-liquid with a finite jump ($Z \neq 0$) at $p = p_F$ (see [72, 117])

$$N_{\text{int}}(p) = \frac{1}{2} - const|p - p_F|^{\alpha} sign(p - p_F). \tag{13.1.6}$$

The exponent α depends upon the model. In strong-coupling limit of 1D Hubbard model $U \gg t$ (which close to half-filling is practically equivalent to t-J model with $J = \frac{4t^2}{U} > 0$ yielding the same energy $E = -JN\ln 2$ as for a 1D spin-chain exactly at half-filling) this constant $\alpha = 1/8$.

For comparison on Fig. 13.5 we present the interacting particles distribution function for Landau Fermi-liquid (LFL) with a finite jump ($Z \neq 0$) for $p = p_F$ [72, 117].

Note also that the imaginary part of the dressed (by interactions) one-particle Green-function in Landau Fermi-liquid has a sharp quasiparticle δ-functional peak for $\omega = \xi_p = \varepsilon(p) - \mu$ and a broad incoherent background (see Fig. 13.6).

In contrast to the situation on Fig. 13.6 in Luttinger liquid a quasiparticle δ-functional peak is absent ($Z = 0$) and we have only noncoherent background in imaginary part of the dressed one-particle Green-function. Note that in spite of these substantial differences both LFL and LL conserve the volume of the Fermi-sphere due to the Luttinger theorem [61, 72], which means that the number of

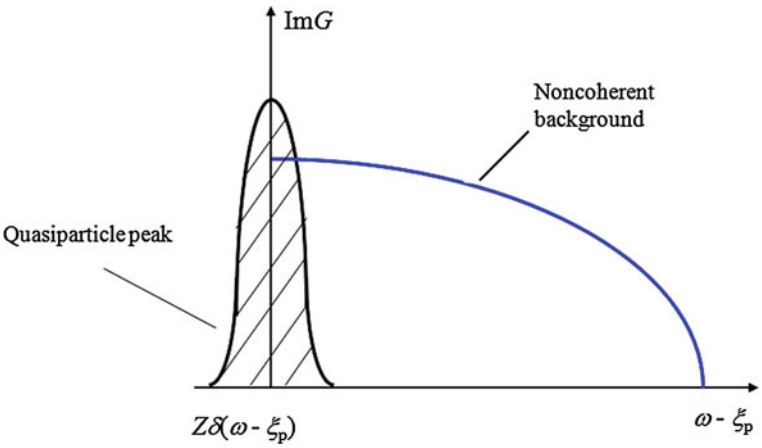

Fig. 13.6 Imaginary part of the dressed one-particle Green-function in Landau Fermi-liquid theory. There is a sharp δ-functional quasiparticle peak and a broad incoherent background on top of it

interacting particles (N_{int}) equals to the number of free fermions in them ($n = p_F^3/6\pi^2$ in 3D case, $n = p_F^2/4\pi$ in 2D, and $n = p_F/\pi$ in 1D for spinless particles).

It is interesting to stress that (as we will see later on) in the case of spin-charge confinement (typical for 2D high-T_C compounds) the dressed one-particle Green-function (see Lee et al. [49–52]) reads:

$$G(\omega, \vec{p}) \sim \frac{Z(\omega)}{\omega - \xi(p) + io} + G_{incoh}(\omega, \vec{p}), \tag{13.1.7}$$

where $\xi(p) = E(p) - \mu$ is a spectrum of a 2D AFM-string, $E(p) = E_0 + Jp^2$ is a string energy (see Sect. 13.4.8) [32]. Thus, the dressed one-particle Green-function for a composite hole (for a string) has a simple (one-pole) structure close to the Fermi-energy [for small $\xi(p)$] in the case of spin-charge confinement and corresponds to Landau Fermi-liquid.

13.3 Two-Leg Ladder Systems. Spin-Charge Confinement. Luther-Emery Liquid

In the introduction to this Chapter we already illustrated the structure of the two-leg ladders on Figs. 13.1 and 13.2. Let us present several experimentally available examples of the two-leg ladder materials $(VO)_2P_2O_7$, $LaCuO_{2.5}$, $SrCu_2O_3$, and NaV_2O_5 [5]. There is also one example of the ladder material $Sr_xCa_{14-x}Cu_{24}O_{41}$ [7, 8] where superconductivity was observed with critical temperatures $T_C \sim (9 - 12)$ K for pressures $P \sim (3 \div 4)$ GPa. Note that in NaV_2O_5 a strongly anisotropic case $J_\perp \sim 4\, J_\parallel$ is realized. On Fig. 13.7 we present a typical in-plane situation for the two-leg ladder materials. It is instructive also to present a crystalline structure of a typical two-leg ladder material $SrCu_2O_3$ (see Fig. 13.8).

Note that in contrast to stripes in high-T_C materials [33, 85] the ladders are stable (strong) defects of the crystalline lattice which are not fluctuating and exist even in the absence of doping. According to the Goodenough rules [86, 87] for the chemical bond we have strong coupling (AFM superexchange) inside the ladder corresponding to the Cu–O-Cu bond angle π (see Fig. 13.9), and weak coupling FM-type of the bond (with Cu–O-Cu angle $\pi/2$) between the ladders.

It is important that for two-leg ladder a spin susceptibility acquires a gap (see [5] and Fig. 13.10):

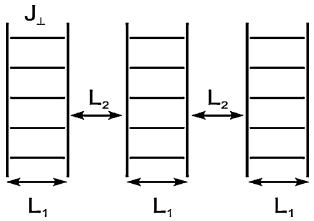

Fig. 13.7 In-plane situation for two-leg ladder materials

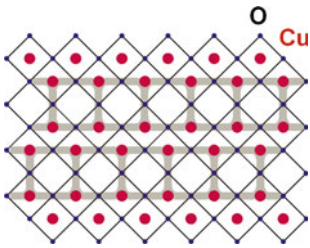

Fig. 13.8 Crystalline structure of a typical two-leg ladder material $SrCu_2O_3$. In the center of each elementary CuO_4 plaquette there is Cu atom (*red circle*), while in the corners of the plaquette there are four O-atoms (see [5])

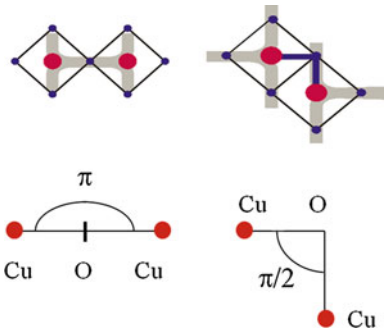

Fig. 13.9 Strong coupling AFM superexchange with an angle π for Cu–O-Cu bond and weak coupling FM Cu–O-Cu bond (with an angle $\pi/2$) between the ladders

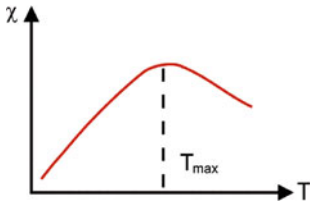

Fig. 13.10 Spin susceptibility for two-leg ladder materials

$$\chi(T) \sim \frac{1}{\sqrt{T}} e^{-\Delta/T} \tag{13.2.1}$$

From Fig. 13.10. We see that $\Delta \sim T_{\max}$, and moreover for $T \ll T_{\max}$: $\chi(T) \to 0$.

13.3.1 Anisotropic t-J Model

In the absence of doping the two-leg ladders are described by anisotropic Heisenberg Hamiltonian:

$$\hat{H} = J_{\parallel} \sum_{i\,a} \vec{S}_{ia} \vec{S}_{i+1a} + J_{\perp} \sum_{i\,a} \vec{S}_{ia} \vec{S}_{ia+1}, \tag{13.2.2}$$

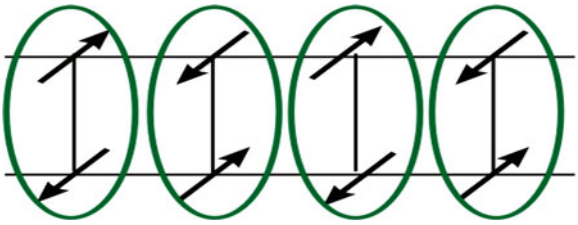

Fig. 13.11 Local Kondo-singlets in the strong coupling limit $J_\perp \gg J_\parallel$ of the anisotropic Heisenberg model for two-leg ladders in the absence of doping

where $J_\parallel$ is AFM-exchange along the legs and $J_\perp$—along the rungs (see Fig. 13.2), the index i is a rung index and index $a = 1, 2$ corresponds to the leg 1 and leg 2. For $J_\perp \gg J_\parallel$ the spin-singlets are formed on the each rung (see Fig. 13.11). The ground state for $J_\parallel = 0$ corresponds to dimerized spin-liquid with $S_{\rm tot} = 0$. The total energy in this case $E_s = -\frac{3}{4}J_\perp N_{rung}$ and the Ψ-function $\Psi_s = \prod_i |\Psi_{si}\rangle$, where $|\Psi_{si}\rangle = \frac{1}{\sqrt{2}}|\uparrow\downarrow - \downarrow\uparrow\rangle$ (see Introduction to this Chapter).

Spin-gap Δ in the magnetic susceptibility is in fact the difference between singlet and triplet energies: $\Delta = E_{\rm t} - E_{\rm S}$. For $J_\perp \ll J_\parallel$: $\Delta \sim \exp\{-1/J_\perp\}$ (see [22, 23]). For $J_\perp = J_\parallel$ (isotopic point): $\Delta = 0.5J_\perp$. Finally for $J_\perp \gg J_\parallel$: $\Delta \to J_\perp$. The last result is evident since for $J_\perp \gg J_\parallel$: $E_{\rm t} = (1/4)J_\perp$, while $E_{\rm S} = -(3/4)J_\perp$. Note that the spin-gap opens already at $J_\perp \to 0$ (see Fig. 13.12 and [22, 23]). Thus $J_\perp = 0$ is a singular point.

Spin correlator acquires an exponential form:

$$\left\langle \vec{S}(r)\vec{S}(0)\right\rangle > \sim \exp\left(-\frac{r}{\xi}\right), \tag{13.2.3}$$

where the correlation length $\xi = \frac{v_s}{\Delta}$. In the limit of low-doping two-leg ladder is described by the anisotropic t-J model (see Fig. 13.2):

$$\hat{H} = -t_\parallel \sum_{i a \sigma} c^+_{ia\sigma} c_{i+1a\sigma} - t_\perp \sum_{i a \sigma} c^+_{ia\sigma} c_{ia+1\sigma} + J_\parallel \sum_{i a} \vec{S}_{ia}\vec{S}_{i+1a} + J_\perp \sum_{i a} \vec{S}_{ia}\vec{S}_{ia+1} \tag{13.2.4}$$

where $t_\parallel$ and $t_\perp$ are the hoppings along the legs and along the rungs, respectively, $c^+_{ia\sigma}$ corresponds to the creation of electron on rung i and leg a with spin-projection σ.

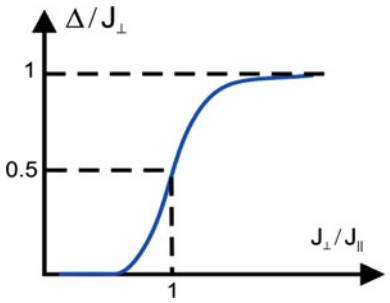

Fig. 13.12 Spin-gap in anisotropic Heisenberg model (see [6])

In the strong coupling limit $J_\perp \gg \{J_\parallel, t_\parallel, t_\perp\}$ it is more energetically beneficial for two holes to create a bound state on the rung [biholon or local Cooper pair (see Fig. 13.2)]. Biholon moves in the surrounding of spin-singlets. Its effective mass reads:

$$m_{eff} \sim \left(\frac{1}{t_\parallel d^2}\right)\frac{J_\perp}{t_\parallel} \gg \frac{1}{t_\parallel d^2}. \tag{13.2.5}$$

We have 1D Bose-gas with repulsion for bosons (biholons) on the rungs. It belongs to the universality—class of Luther-Emery (LE) liquid. In this type of model there are strong SC fluctuations:

$$\langle \Delta(r)\Delta(0)\rangle \sim \frac{1}{r^{1+\gamma}}. \tag{13.2.6}$$

Note that according to Efetov, Larkin [27] already a small interaction between the ladders (see Figs. 13.7 and 13.8) stabilizes a finite T_C in the system.

13.3.2 Resistivity in Two-Leg Ladders Materials

For the material $La_{1-x}Sr_xCuO_{2.5}$ with two-led ladders resistivity behaves as follows (see Fig. 13.13).

From Fig. 13.13 we can see that for $x \geq 0.15$ resistivity $R(T)$ behaves in a metallic fashion in analogy with high-T_C materials. At small doping $x \leq 0.10$ the resistivity behaves in a semiconductor fashion.

13.3.3 Superconductivity in Ladder Materials

Superconductivity was experimentally observed in $Sr_xCa_{14-x}Cu_{24}O_{41}$ (see [7, 8]). In this compound in analogy with high-T_C material YBaCuO there are chains and planes. We have two-leg ladders in planes (see Fig. 13.14).

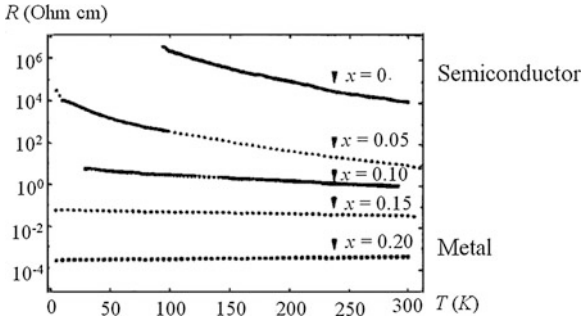

Fig. 13.13 Resistivity characteristic $R(T)$ in the two-leg ladders material $La_{1-x}Sr_xCuO_{2.5}$ for different doping levels (see [5])

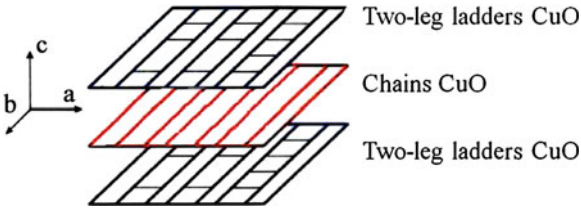

Fig. 13.14 The crystalline "sandwich" structure of superconductive material $Sr_xCa_{14-x}Cu_{24}O_{41}$. There are two-leg ladders in two adjacent CuO planes and CuO chains in between (see [7, 8])

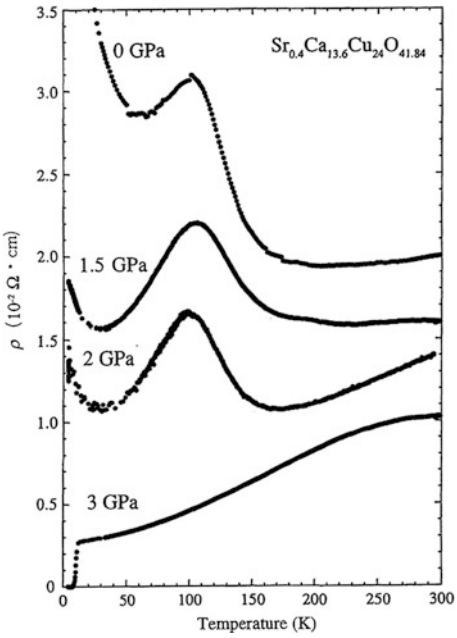

Fig. 13.15 Resistivity characteristics $R(T)$ in the material $Sr_xCa_{14-x}Cu_{24}O_{41}$. For $P = 3$ GPa we observe the SC-transition at $T_C = 12$ K see [7, 8])

For $x = 0.4$ and pressures $P < 3$ GPa the holes mostly occupy the chains. Resistivity has a semiconductive character (see Fig. 13.15). For $x = 0.4$ and pressures 3 GPa $< P <$ 4.5 GPa the holes mostly occupy the ladders. Resistivity behaves in a metallic fashion $\rho \sim \rho_0 + AT^{\alpha}$ with $1 < \alpha < 2$. Here at $T < T_C$ ($T_C = 12$ K for $P = 3$ GPa and $T_C = 9$ K for $P = 4.5$ GPa) SC arises in the system [5].

Intermediate conclusions for SC in $Sr_xCa_{14-x}Cu_{24}O_{41}$.

Let us emphasize once more that:

1. for $x = 0.4$ and $P > 3$ GPa the lattice is compressed and hence the holes mostly occupy the planes which contain two-leg ladders. This fact leads to metallic behavior of resistivity. As a result SC arises in the system.
2. For further increase of hole-concentration x we will have an additional transfer of hole states from chains to planes.

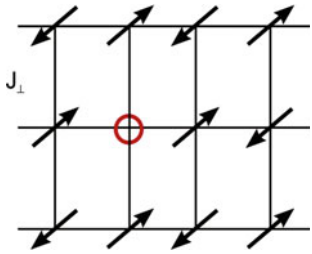

Fig. 13.16 Doped three-leg ladder

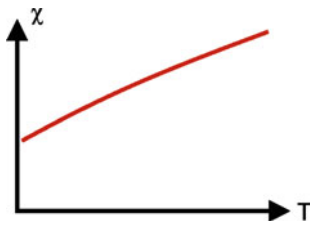

Fig. 13.17 Spin-susceptibility $\chi(T)$ for three-leg ladders. $\chi(T) \to const$ for $T \to 0$ and the spin-gap is absent

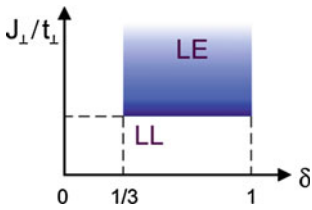

Fig. 13.18 Phase-diagram of three-leg ladders at strong coupling along the rungs $\{J_\perp, t_\perp\} \gg \{J_\parallel, t_\parallel\}$. There are extended regions of LL and LE-liquid on the phase-diagram [21]

3. For the first time SC was observed in $Sr_xCa_{14-x}Cu_{24}O_{41}$ for $x = 0.2$. In these materials SC arises for $P > 2.6$ GPa. The critical temperature is $T_C = 5$ K. In this case the hole concentration corresponds to hole density of 0.2 holes per Cu-atom of the ladder.

13.4 Three-Leg Ladders. Anisotropic t-J Model for Strong-Coupling Along the Rungs

The typical examples of three-leg ladder materials are $Sr_2Cu_3O_5$ and $CsCuCl_3$ (see Fig. 13.16 and [20, 26]).

In the limit of not very strong exchange $J_\perp$ along the rungs the spin-gap in susceptibility $\chi(T)$ is absent (see Fig. 13.17).

For low temperatures $T \to 0$ we can see from Fig. 13.17 that $\chi(T) \to const$ and the spin-gap is absent. In the limit $\{J_\perp, t_\perp\} \gg \{J_\parallel, t_\parallel\}$—we have strong coupling along the rungs [21]. In this limit the phase-diagram of three-leg ladders at low temperatures $T \to 0$ has extended regions of LL and for large $J_\perp/t_\perp$-ratio also the region of LE-liquid (see [21] and Fig. 13.18).

Fig. 13.19 Spinon $f_{i\sigma}$ for three spins on the rung described by Ψ-function (13.3.1). It corresponds to the rung spin $S_{tot} =$ ½ and $S^z_{tot} = \pm$½ [21]

13.4.1 Exact Diagonalization of One Rung Problem

To construct more precisely the phase-diagram of three-leg ladder at strong coupling along the rungs $\{J_\perp, t_\perp\} \gg \{J_\parallel, t_\parallel\}$, we first should diagonalize (solve exactly) the one rung problem. Here in the limit $J_\parallel = t_\parallel = 0$ the Ψ-function of 3 spins (and zero holes) on the rung (see Fig. 13.19) reads:

$$\Psi_0 = \frac{1}{\sqrt{6}}[|\uparrow\uparrow\downarrow\rangle - 2|\uparrow\downarrow\uparrow\rangle + |\downarrow\uparrow\uparrow\rangle]. \tag{13.3.1}$$

The Ψ-function Ψ_0 describes a spinon $f^+_{i\sigma}$ [2] with an energy $E_0 = -\frac{3}{2}J_\perp$, a rung spin $S_{tot} =$ ½ and projection of the rung spin $S^z_{tot} = \pm$ ½.

The Ψ-function of 2 spins and 1 hole on the rung (see Fig. 13.20) corresponds to a holon b^+_i and reads (see [21]):

$$\Psi_1 = \frac{1}{\sqrt{4+2\alpha^2}}[|\uparrow\downarrow 0\rangle - |\downarrow\uparrow 0\rangle + \alpha|\uparrow 0\downarrow\rangle - \alpha|\downarrow 0\uparrow\rangle + |0\uparrow\downarrow\rangle - |0\downarrow\uparrow\rangle]. \tag{13.3.2}$$

The energy of this configuration is given by:

$$E_1 = -\frac{4t_\perp^2}{\sqrt{J_\perp^2 + 8t_\perp^2} - J_\perp} = -\frac{2t_\perp}{\alpha}. \tag{13.3.3}$$

The total spin for this configuration $S_{tot} = 0$.

For 1 spin and 2 holes on the rung the Ψ-function reads:

$$\Psi_2 = \frac{1}{2}\left[|\uparrow 00\rangle + \sqrt{2}|0\uparrow 0\rangle + |00\uparrow\rangle\right] = \frac{1}{2}\left[c^+_{i1\uparrow} + \sqrt{2}c^+_{i2\uparrow} + c^+_{i3\uparrow}\right]|000\rangle. \tag{13.3.4}$$

The energy of this configuration $E_2 = -\sqrt{2}t_\perp$. It corresponds to a spinon $h^+_{i\sigma}$ (Fig. 13.21) with $S_{tot} =$ ½ and $S^z_{tot} = \pm$½.

Finally for three holes on the rung the Ψ-function is trivial $\Psi_3 = |000\rangle$ and total energy $E_3 = 0$. It corresponds to a holon a^+_i with $S_{tot} = 0$ (Fig. 13.22).

Fig. 13.20 Holon b_i^+ for the rung with 2 spins and 1 hole. The total spin for this configuration $S_{tot} = 0$ [21]

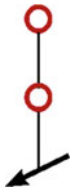

Fig. 13.21 Spinon $h_{i\sigma}^+$ for 1 spin and 2 holes on the rung. The total spin for this configuration $S_{tot} = {}^1/_2$ and $S_{tot}^Z = \pm{}^1/_2$ [21]

Fig. 13.22 Holon a_i^+ for three holes on the rung. The total spin of this trivial configuration $S_{tot} = 0$ [21]

13.4.2 Qualitative Phase-Diagram

Now if we switch on small (but non-zero) $J_{\|}$ and $t_{\|}$ we get the following phase-diagram of three-leg ladder systems (see Fig. 13.23). On Fig. 13.23 LL I corresponds to the admixture of the rungs with 2 spins and 3 spins, LL II—to the admixture of the rungs with 2 spins and 1 spin, LL III—to the admixture of the empty rungs and the rungs with 1 spin. In the same time LE-liquid corresponds to an admixture of the empty rungs and the rungs with 2 spins [21]. It is realized for doping $x > 1/3$ (see [21]) and:

$$\frac{J_\perp}{t_\perp} > \left(\frac{J_\perp}{t_\perp}\right)_{crit} = \frac{3}{\sqrt{2}}. \tag{13.3.5}$$

Let us consider the phase-diagram on Fig. 13.23 more detaily. In the case of LL I when we include $t_{\|} \neq 0$ the hopping takes place due to an exchange between a rung with 3 spins and a rung with 2 spins (with a hole) (see Fig. 13.24).

In this situation a composite fermion

$$g_{i\sigma}^+ = f_{i\sigma} b_i^+ \tag{13.3.6}$$

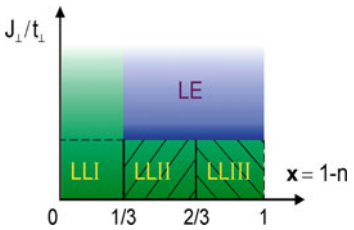

Fig. 13.23 Phase-diagram of three-leg ladder systems at strong coupling along the rungs. There are three different regions of LL: LL I, LL II, and LL III (depending upon doping $x = 1 - n_{el}$) and a region of LE-liquid for larger values of $J_\perp/t_\perp$ and $x > 1/3$

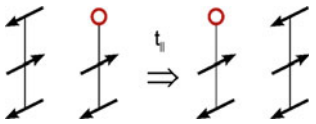

Fig. 13.24 The hopping between a rung with 3 spins and a rung with 2 spins (with a hole) in case when $t_\parallel \neq 0$ [21]

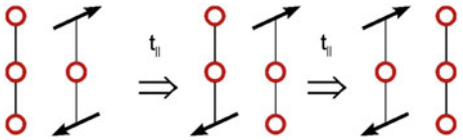

Fig. 13.25 The hopping (for $t_\parallel \neq 0$) between an empty rung and the rung with 2 spins [21]

arises in the problem. In the limit $\{J_\perp, t_\perp\} \gg \{J_\parallel, t_\parallel\}$ a composite fermion satisfies the standard fermionic anticommutational relations:

$$\left\{ g^+_{i\sigma},\ g_{i\sigma} \right\} = g^+_{i\sigma} g_{i\sigma} + g_{i\sigma}\, g^+_{i\sigma} = 1. \tag{13.3.7}$$

Hence LL I corresponds to repulsive 1D Hubbard model for composite fermions $g_{i\sigma}$ described by the Hamiltonian:

$$\hat{H} = -t_{eff} \sum_{\langle ij \rangle \sigma} g^+_{i\sigma} g_{j\sigma} + U_\infty \sum_i n_{i,\sigma} n_{i,-\sigma}, \tag{13.3.8}$$

where U_∞ is infinitely strong Hubbard repulsion on site i between composite fermions. In the similar way we can understand LL II and LL III. The situation changes, however, for LE-liquid. Here the hopping (for $t_\parallel \neq 0$) takes place due to an exchange between an empty rung and the rung with 2 spins (see Fig. 13.25).

It is easy to see that a composite boson

$$d^+_i = a_i b^+_i \tag{13.3.9}$$

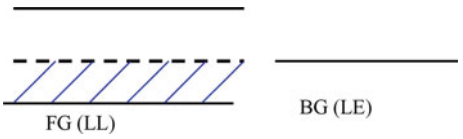

Fig. 13.26 The coexistence of Fermi-gas (LL) and Bose-gas (LE) in the isotropic limit in the energy space

arises in the problem. Thus LE liquid corresponds to 1D Bose-gas with repulsion between composite bosons described by the Hamiltonian:

$$\hat{H} = -t_{eff} \sum_{\langle ij \rangle} d_i^+ d_j + \frac{1}{2} U_\infty \sum_i n_i^2. \tag{13.3.10}$$

It is interesting to note that in contrast with (13.3.8) (where $t_{\text{eff}} \sim t$) in (13.3.10) $t_{eff} \sim t_{\|}^2 \Big/ J_\perp$ —appears only in the second order of perturbation theory.

13.4.3 N-leg Ladders

When we increase the number of legs the difference between the ladders with even and odd numbers of legs becomes less pronounced. For $N \to \infty$ the spin-gap in the ladders with even number of legs decreases exponentially. In strong coupling limit:

$$\Delta_{2N} \sim \frac{\Delta_2}{2^N} \sim \frac{J_\perp}{2^N} \to 0. \tag{13.3.11}$$

Hence for $N \to \infty$ the spin excitations in the ladders with even number of legs are practically gapless (as in LL). Note that for $N \to \infty$ we proceed to two-dimensional anisotropic t-J model, and for $\{J_\perp, t_\perp\} \gg \{J_\|, t_\|\}$ - to 1D $t_\perp$-$J_\perp$ model [21]. The universality class of this model corresponds to LL with spin-charge separation. This limit, however, is not realistic for 2D high-T_C compounds.

13.4.4 The Gap in the Energy Spectrum for Three-Leg Ladders in Anisotropic Limit

Returning back to three-leg ladders and their phase-diagram, we see that for doping $x > 1/3$ and $J_\perp > \frac{3t_\perp}{\sqrt{2}}$ there is an energy gap for $t_\perp > t_\|$. By the order of magnitude it reads:

$$\Delta = \frac{E_{LE} - E_{LL}}{N_{rung}} \sim t_\perp - t_\|. \tag{13.3.12}$$

This gap separates LE and LL in energetic space.

13.4.5 Coexistence of Bosonic Luther-Emery Liquid and Fermionic Luttinger Liquid in Isotopic Limit

The real high-T_C materials correspond, however, to the difficult isotropic limit

$$J_\perp = J_{||} = J; \quad t_\perp = t_{||} = t; \quad J \sim 0.3t \tag{13.3.13}$$

In this case the numerical calculations [20] show the tendency to a coexistence of Bose-gas (LE) and Fermi-gas (LL) in the energy space (see Fig. 13.26). In this case the energy gap

$$\Delta = \frac{E_{LE} - E_{LL}}{N_{rung}} \to 0 \tag{13.3.14}$$

vanishes due to isotropic condition ($t_\perp = t_{||}$) for hopping integrals. Hence in the isotropic limit we have Fermi-Bose mixture of LL and LE-liquids (see Geshkenbein, Ioffe, Larkin [29]).

13.4.6 Strongly Interacting Mixture of Spinons and Holons in High-T_C Superconductors

We already mentioned briefly a Fermi-Bose mixture of spinons and holons in Chap. 6. Our project for underdoped high-T_C superconductors reads: starting with a strongly interacting Fermi-Bose mixture of spinons $f^+_{i\sigma}$ and holons b_i to derive an effective one-band model for the weakly interacting composite holes (or spin-polarons)

$$h_{i\sigma} = f_{i\sigma}\, b_i. \tag{13.3.15}$$

We will qualitatively consider this scenario in the last part of this Chapter on the basis of Bulaevskii-Nagaev-Khomskii [1], Brinkman-Rice [31] ideas on the formation of AFM-string [1]. But at first we will understand the more simple overdoped limit of the isotropic t-J model in 2D case [33, 34], where Landau Fermi-liquid picture is valid and where we will have different SC instabilities, including d-wave pairing actual for real cuprates.

13.5 Superconductivity in Isotropic 2D t-J Model

In this Section we will consider different superconductive pairings (s-wave, d-wave, p-wave) which arise in isotropic 2D t-J model in overdoped case, as well as a possible scenario of BCS-BEC crossover (or of a bosonic motive) which arises in an underdoped case of the t-J model.

13.5.1 Superconductive Pairing in Overdoped 2D t-J Model

In connection with high-T_C superconductivity in the overdoped case we consider isotropic t-J model [1, 2] with released constraint [34]. The Hamiltonian of the model reads:

$$\hat{H} = -t\sum_{\langle ij\rangle\sigma} c^{+}_{i\sigma}c_{j\sigma} + U\sum_{i} n_{i\uparrow}n_{i\downarrow} + J\sum_{\langle ij\rangle}\left(\vec{S}_i\vec{S}_j - \frac{1}{4}n_in_j\right), \tag{13.4.1}$$

where $n_{i\sigma} = c^{+}_{i\sigma}c_{i\sigma}$ is onsite electron density for spin projection σ, $\vec{S}_i = \frac{1}{2}c^{+}_{i\mu}\vec{\sigma}_{\mu\nu}c_{i\nu}$ is an operator of electron spin on site i, $\vec{\sigma} = \{\sigma_1, \sigma_2, \sigma_3\}$—are Pauli matrices. We assume that $U \gg \{J; t\}$. Note that by setting $U \to \infty$ we recover the standard canonical t-J model for $n \to 1$ (which we briefly considered in Chap. 6 with respect to the possibility of biholon pairing in the slave-boson formulation of the model in the underdoped case):

$$\hat{H} = -t\sum_{\langle ij\rangle\sigma} \tilde{c}^{+}_{i\sigma}\tilde{c}_{j\sigma} + \tilde{J}\sum_{\langle ij\rangle}\left(\vec{S}_i\vec{S}_j - \frac{1}{4}n_in_j\right), \tag{13.4.2}$$

with $\tilde{c}_{i\sigma} = c_{i\sigma}(1 - n_{i-\sigma})$ and $\tilde{J} = J + \frac{4t^2}{U}(= J \text{ for } U \to \infty)$. Note also that the t-J model was derived many years ago by Bulaevskii and coworkers [1] to describe the strong-coupling limit of the single-band Hubbard model. The study of this model has become very active in 1990-ties due to Anderson's proposal [2] that is was the appropriate model to describe the doped CuO_2 planes that are the key ingredients of the high-T_C cuprates. Later on Zhang and Rice [3] elucidated the relationship of the t-J model to a multiband Hubbard description with Cu $3d_{x^2-y^2}$ and O $2p_\sigma$ orbitals. The careful numerical investigation of Hybersten and coworkers [88] established the parameter values in the mapping of the multiband Hubbard model for the CuO_2 planes into a one-band t-J model, namely $J \sim 0.3t$. In the single-band Hubbard model the mapping to a t-J model is valid only in the strong-coupling limit which leads to the values $J \ll t$. In a more general model other values of J/t can occur. A lot of work has been done to clarify analytically the relationship between the t-J and multiband Hubbard models, see e.g. [89] and reference therein. In this Section we will treat the ratio J/t simply as a parameter to be varied arbitrarily.

Finally let us emphasize that in the canonical form of the t-J model it is convenient to add $-\frac{1}{4}n_in_j$ to the Heisenberg term $\vec{S}_i\vec{S}_j$ in (13.4.1) and (13.4.2).

In fact the Hamiltonian (13.4.1) of the t-J model with released constraint corresponds to a model with strong onsite repulsion U and small AFM attraction $\sim J$ on the neighboring sites. Effectively we have the van der Waals interaction potential in this model (see Fig. 13.27 and [34]). The bosonic version of the model with van der Waals interaction was considered in Chap. 6 with respect to the possibility of the two-boson pairing.

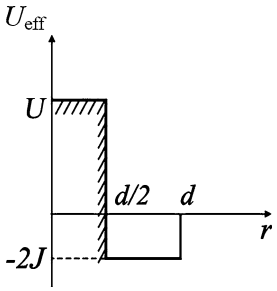

Fig. 13.27 Effective vacuum interaction of the van der Waals type in the 2D isotropic t-J model with released constraint (see also Fig. 6.1)

13.5.2 Superconductive phase-diagram of the 2D overdoped t-J model

For small and intermediate electron densities $0 < n_{\text{el}} \leq 0.75$ (overdoped case $x \leq 0.25$ for a hole doping) the SC phase-diagram of the 2D t-J model with released constraint has the regions of extended s-wave pairing for $J > 2t$ and phase-separation for $J > 3.8t$ and $n_{\text{el}} \to 0$. For small values of $J/t < 1$ it has the regions of p-wave and $d_{x^2-y^2}$ SC pairing (see [33, 34] and Fig. 13.28).

13.5.3 Extended s-Wave Pairing for J > t and Low Electron Densities

At low electron densities and $J > J_{\text{CO}} = 2t$ an extended s-wave pairing arises in the 2D t-J model at low electron density (see [33]). The superconductive gap for extended s-wave pairing on the 2D square lattice reads (see also Chap. 6):

$$\Delta_S = \Delta_0^S(\cos p_x d + \cos p_y d). \tag{13.4.3}$$

The pair Ψ-function is zero for $r \leq d/2$—in the region of strong Hubbard interaction $U \gg \{J, t\}$ and thus $U\Psi = 0$ in the effective Schrödinger equation. It has a maximum for $r \sim d$ (see Figs. 6.1 and 13.29) which is centered on the neighboring sites. Thus the pair Ψ-function has a region of zero values but does not change its sign. For $J > J_{\text{CO}} = 2t$ there is a bound state of two electrons with the binding energy $E_b = -W + \tilde{E}_b$, where:

$$\left|\tilde{E}_b\right| = 8We^{-\frac{\pi J}{(J-J_{CO})}}. \tag{13.4.4}$$

for moderately large $J \geq J_{\text{CO}}$ [34]. For large $J >> W$ [33]

$$E_b = -J - \frac{20t^2}{J}. \tag{13.4.5}$$

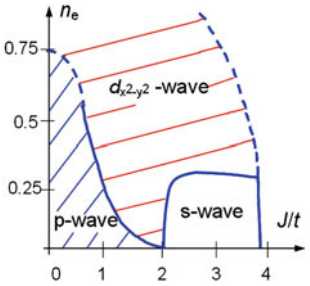

Fig. 13.28 Superconductive phase-diagram of the 2D t-J model in the overdoped case (for small and intermediate electron densities) [34]

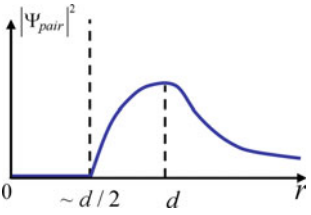

Fig. 13.29 Pair Ψ-function squared for the extended s-wave pairing in the 2D t-J model (see also Fig. 6.1)

In the BCS-case for $|\tilde{E}_b| < \varepsilon_F$ and extended Cooper pairing the mean-field superconductive critical temperature is given by famous Miyake formula [90] (see Chaps. 6 and 8):

$$T_{CS} \sim \sqrt{2\varepsilon_F |\tilde{E}_b|}, \tag{13.4.6}$$

where $|\tilde{E}_b|$ is determined by (13.4.4).

In the BEC-case for $|\tilde{E}_b| > \varepsilon_F$ and local pairing we have two characteristic temperatures:

$$T_* \sim \frac{|\tilde{E}_b|}{\ln(|\tilde{E}_b|/\varepsilon_F)} - \tag{13.4.7}$$

Saha crossover temperature [91] which describes creation of local pairs (dimers) and superconductive critical temperature:

$$T_{CS} = \frac{\varepsilon_F}{4 \ln \ln(|\tilde{E}_b|/\varepsilon_F)} \tag{13.4.8}$$

given by Fisher, Hohenberg formula [92] for slightly non-ideal 2D Bose-gas with repulsion between local pairs (dimers) (see also Popov [93]). The more detailed discussion of the BCS-BEC crossover [94–97] in 2D attractive Fermi-gas is presented in Chaps. 6 and 8.

13.5.4 Phase-Separation at Large J/t and Low Electron Density

The energy of BEC-phase becomes negative at larger J/t (where $|\tilde{E}_b| > > \varepsilon_F$)we have here a liquid of local pairs (dimers) with an energy:

$$E_{BEC} - E_N \approx -N\frac{|\tilde{E}_b|}{2} < 0, \tag{13.4.9}$$

where N is a number of particles.

If we further increase the J/t-ratio at low electron densities, than the formation of quartets [30, 34, 98] or larger complexes will become energetically beneficial on the 2D square lattice. But as it was shown by Emery, Kivelson and Lin [33], the liquid phase (which is formed earlier then the threshold for quartet formation) becomes unstable towards total phase-separation (see also Chaps. 9 and 15) on two large clusters for $J > J_{\mathrm{P.S}} = 3.8t$: PM-cluster with electron density $n_{\mathrm{el}} \to 0$ and AFM-cluster with $n_{\mathrm{el}} \to 1$. The threshold value for the total phase-separation $J_{\mathrm{P.S}} = 3.8t$ can be defined from a simple estimate (see also numerical calculations of Dagotto et al. [99]):

$$\frac{E_{AFM} - E_N}{N} = -\frac{1.18J}{2} \leq \frac{E_{BEC} - E_N}{N} = -\frac{|\tilde{E}_b|}{2}, \tag{13.4.10}$$

where $1.18J$ is an AFM-energy per bond for the 2D square lattice.

13.5.5 p-Wave Pairing for J < t and Low Electron Densities

For small values of J/t and low electron densities the triplet p-wave pairing, governed by Kohn-Luttinger mechanism [35, 100, 101] corresponds to a leading SC-instability in the system below the critical temperature:

$$T_{Cp} \sim \varepsilon_F e^{-\frac{1}{6.1f_0^3}} \tag{13.4.11}$$

(see Chap. 9 for more details). The p-wave SC gap for the 2D square lattice reads:

$$\Delta_p = \Delta_{0p}(\sin p_x d + i \sin p_y d). \tag{13.4.12}$$

In the case of 2D t-J model with released constraint the coupling constant f_0 for $J < J_{\mathrm{CO}} = 2t$ and low density in (13.4.11) is given by [34]:

$$f_0 = \frac{mT_s(\tilde{E} = 2\varepsilon_F)}{4\pi} = \frac{1}{\ln\frac{4W}{\varepsilon_F} + \frac{\pi J}{J - J_{CO}} + i\pi}. \tag{13.4.13}$$

Note that $T_s(\tilde{E} = 2\varepsilon_F)$ in (13.4.13) is the T-matrix in the s-wave channel relevant for the Cooper problem (where $\tilde{E} = 2\varepsilon_F > 0$). Thus for $J/t \to 0$ and $\varepsilon_F << W$ the coupling constant $f_0 \approx \left(\ln \frac{4W}{\varepsilon_F}\right)^{-1}$ as in the 2D Hubbard model [102]. It is possible to demonstrate by direct comparison of the critical temperatures in different channels (see Fig. 13.28) that p-wave pairing is dominant for $J < t$ and low electron densities $n_{el} = 2\varepsilon_F/W \ll 1$.

13.5.6 d-Wave Pairing in the Overdoped 2D t-J Model

For $n_{el} \geq (0.6 - 0.7)$ and not very small ratio of $J/t \sim (1/2 \div 1/3)$, which are just the typical values for high-T_C materials, d-wave pairing becomes dominant over p-wave pairing in the 2D t-J model with released constraint. The equation for the critical temperature in the $d_{x^2-y^2}$-channel reads (see [34]) in the weak-coupling case $J/t < 1$:

$$1 = Jd^2 \int\int \frac{dp_x}{2\pi}\frac{dp_y}{2\pi}\phi_d^2 \frac{\text{th}\left(\frac{\varepsilon_p - \mu}{2T_{Cd}}\right)}{2(\varepsilon_p - \mu)}, \tag{13.4.14}$$

where J is just AFM attractive interaction, $\phi_d = (\cos p_x d - \cos p_y d)$ is an eigenfunction for $d_{x^2-y^2}$-pairing on the 2D square lattice, $\varepsilon_p - \mu = -2t(\cos p_x d + \cos p_y d) - \mu$ is the uncorrelated quasiparticle spectrum in 2D.

As a result we get for d-wave pairing [34, 38]:

$$T_{Cd} \sim \varepsilon_F e^{-\frac{\pi t}{2Jn_{el}^2}}. \tag{13.4.15}$$

Extrapolation of these results on $J/t \sim (1/2 \div 1/3)$ and $n_{el} \sim 0.85$ ($x \sim 0.15$—optimal doping) yields the rough estimate $T_{Cd} \sim \varepsilon_F e^{-5} \sim 10^2$ K for $\varepsilon_F \sim 10^4$ which is quite reasonable for cuprates [34, 38].

13.5.7 d-Wave Pairing at Small Hole Densities $x = (1 - n_{el}) \ll 1$

In the opposite case of small hole densities $x = (1 - n_{el}) \ll 1$ the similar to (13.4.14) equation for T_C with the spin-polaronic spectrum $\varepsilon(p)$ was derived by Plakida's group [36, 37] using diagrammatic technique for the Hubbard operators [103, 104]. In the weak-coupling BCS-case for $T_C < E_F(x)$ the critical temperature in the paramagnetic region reads [36, 37]:

$$T_C^d \sim \sqrt{WE_F(x)}e^{-\frac{1}{\lambda}}, \tag{13.4.16}$$

where $\lambda \sim JN_0(x) \sim 0.3$ is a coupling constant, $E_F(x)$ is Fermi-energy, $N_0(x)$ is an averaged density of states. T_C is maximal at optimal doping $x \sim x_{opt} \sim 0.15$, where $E_F(x_{opt}) \sim W/2$ and where we effectively have a crossover from a small hole-like Fermi-surface to a large electronic one.

In maximum again $T_C^d \sim 10^2$ K. Note that Plakida et al., also considered generalized one-band 2D t-J model derived from multiband Hubbard model [105, 106] (or two-band Emery model [115]) when we neglect the interband Hubbard repulsion between d- and p-orbitals ($U_{dp} = 0$). In this case the local constraint [see (13.4.2)] is also not very important (as in the Kagan and Rice approach [34]) and we can neglect also the kinematical interaction of Zaitsev et al. [107–109].

13.5.8 Possible Bosonic Region of the Phase-Diagram of the 2D t-J Model in the Underdoped Case

In the extreme underdoped case very close to half-filling for $x \ll x_{opt}$ we have the physics of pseudogap at $T_C \leq T \leq T_*$ (see also Chap. 8) and a bosonic-type Uemura plot for T_C ($T_C(x) \sim x$) [111]. If we assume the bosonic character of the pseudogap (connected with SC-fluctuations of preformed pairs, and not with AFM-fluctuations), then we could expect the formation of local pairs consisting of two spin-polarons at some higher temperatures $T_* \sim \left|\tilde{E}_b\right|$ (their binding energy) and BEC of local pairs at lower temperatures $T_C \leq E_F(x) \leq T_*$. Note that in this region of the phase-diagram we have small hole Fermi-surface with $E_F(x) \sim Jx$ according to Lee et al. [52]. In this limiting case our philosophy, however, is more close to the ideas of Laughlin et al. [15, 16] on spin-charge confinement than to the philosophy of Anderson [2] and Lee [49–51] on spin-charge separation in the 2D t-J model (see also Chen et al. [110] on spin-charge binding in the t-J model). Note that there is a crucial difference between spin-charge binding and spin-charge confinement. While in the first case we have spin-charge binding at low temperatures and spin-charge separation at high temperatures, in the second case we have spin-charge confinement everytime (at arbitrary high temperatures). Let us stress that Laughlin [15, 16] assumed the spin-charge confinement in the strongly interacting Fermi-Bose mixture of spinons and holons at small hole density in analogy with the confinement in quark-gluon plasma in QCD [42–48]. As we already mentioned in the introduction to this Chapter, the spin-charge confinement leads to the creation of composite holes [15, 16] (or spin-polarons [40, 41] or strings [1, 31, 32]). The basic results here are connected with the ideas of Bulaevskii, Nagaev, Khomskii [1] and Brinkman-Rice [31] on the formation of AFM-string for a hole motion in 2D AFM-background of spins $S = ½$.

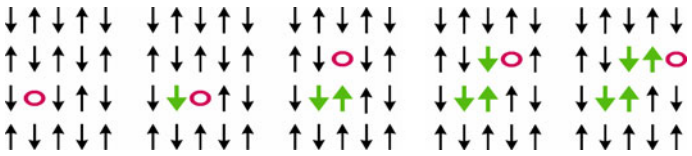

Fig. 13.30 Formation of the string for a motion of a hole in 2D AFM-background of spins $S = ½$ on the square lattice (see [13])

13.5.9 String-Like Solution for a Composite Hole

The illustration of the formation of the confinement potential (of the linear trace of frustrated spins which accompany a hole motion in 2D AFM-background of spins $S = ½$) is presented on Fig. 13.30.

In a simple picture the Ψ-function of a string is a solution of a Schrödinger equation with linear potential $V(r) = \frac{zJS^2}{2} r$ for a spinon-holon interaction (z is the number of nearest neighbors ($z = 4$) on the square lattice):

$$-\frac{\hbar^2}{2m}\Delta\Psi + \frac{zJS^2}{2} r\Psi = E\,\Psi, \tag{13.4.17}$$

where Δ corresponds to Laplace operator. The solution of this expression is given by [1, 13, 31, 113] $\Psi \sim Ai(r)$ for Airy function. The effective radius of a string-oscillator [1] does not depend upon dimensionality for $D = 2$ and 3 and yields:

$$r_0 \sim \left(\frac{t}{zJS^2}\right)^{1/3}. \tag{13.4.18}$$

As a result the energy of a string:

$$E_0 \sim -\frac{z}{\sqrt{z-1}} + \left(zJS^2\right)^{2/3} t^{1/3}, \tag{13.4.19}$$

where the bottom of the band also changes for a string motion [13].

An account of the quantum fluctuations connected with the term $J(S_i^+ S_j^- + S_i^- S_j^+)$ in the 2D t-J model leads to the dispersion of composite hole with a spectrum (see [13])

$$E_h(q) = E_0 + J(\cos q_x d + \cos q_y d)^2 \tag{13.4.20}$$

(here we neglect the difficulties connected with the so-called Trugman paths [83] which could destroy a string after several traversing of elementary plaquette assuming as usual that their statistical weight is small [13, 83]).

The Green-function of a composite hole has a simple one-pole structure of the type (see Eq. (13.1.7) and also Lee et al. [49–52]):

$$G(\omega, \vec{q}) \sim \frac{J/t}{\omega - E_0 - Jq^2 + \mu + io} + G_{incoh}(\omega, \vec{q}).$$

13.5.10 The Two-Particle Problem for Composite Holes. Possibility of BCS-BEC Crossover in the d-Wave Channel

Residual interaction of the two composite holes for a small hole concentration $x \ll 1$ has a dipole–dipole character according to hydrodynamic approach of Shraiman, Siggia [32]:

$$V(r) \sim \frac{\lambda}{r^2}. \tag{13.4.21}$$

It was shown by Belinicher group [40, 41] that this interaction can lead to a shallow bound state of the two composite holes (two spin-polarons) in the $d_{x^2-y^2}$-wave channel. It is quite appealing to consider T_C versus x dependence for strongly underdoped high-T_C superconductors as the BCS-BEC crossover for the pairing of two composite holes (two spin-polarons) in the d-wave channel [30].

Note that if we solve the two-particle problem for composite holes (two string-oscillators) interacting via dipole–dipole potential we will find according to Belinicher et al. [40, 41] the binding energy for $d_{x^2-y^2}$-pairing (counted from the bottom of the band):

$$\left|\tilde{E}_b\right| \sim 0.02\, t \sim T_*. \tag{13.4.22}$$

In the same time the BEC critical temperature for small hole concentration reads:

$$T_C^{BEC} \sim J\, x < T_*, \tag{13.4.23}$$

where $J \sim (0.3 \div 0.5)\ t$ and effective mass of a pair $m^* \sim 1/(Jd^2)$.

In the opposite limit of larger hole concentration, as we already mentioned, we have BCS-type $d_{x^2-y^2}$-pairing described by Kagan, Rice [34] and Plakida [36, 37].

Concluding this Chapter, note once more that while spin-chains and three-leg ladders are grossly described by the physics of spin-charge separation, the two-leg ladders and possibly underdoped high-T_C materials are more close to the ideas of the physics of spin-charge confinement. In the same time strongly overdoped 2D cuprates are well described by more standard Landau Fermi-liquid picture and show the tendency towards superconductive instabilities for p-wave and $d_{x^2-y^2}$-

wave pairing at small J/t-values as well as towards extended s-wave pairing and total phase-separation at larger J/t-values and low electron densities.

The rough extrapolation of the low electron density results on optimal doping yields for parameter values typical for cuprates $J/t \sim (1/2 \div 1/3)$ and $n_{el} \sim 0.85$ the reasonable temperatures for d-wave pairing ($T_{Cd} \sim 10^2$ K).

The physics of the strongly underdoped t-J model could be possibly described by the scenario of the BCS-BEC crossover for the pairing of two composite holes (two spin-polarons or two AFM strings) in the $d_{x^2-y^2}$-wave channel.

References

1. Bulaevskii, L.N., Nagaev, E.L., Khomskii, D.I.: Sov. Phys. JETP **27**, 836 (1968)
2. Anderson, P.W.: Frontiers and Borderlines in Many-Particle Physics, Proceedings, Varenna Summer School, Varenna (1987)
3. Zhang, F.C., Rice, T.M.: Phys. Rev. B **37**, 3759 (1988)
4. Hayward, C.A., Poilblanc, D.: Phys. Rev. B **53**, 11721 (1996)
5. Dagotto, E., Rice, T.M.: Science **271**, 618 (1996)
6. Dagotto, E., Riera, J., Scalapino, D.: Phys. Rev. B **45**, 5744 (1992)
7. Uehara, M., Nagata, T., Akimitsu, J., Takahashi, H., Môri, N., Kinoshita, K.: J. Phys. Soc. Jpn. **65**, 2764 (1996)
8. Mayaffre, H., Auban-Senzier, P., Nardone, M., Jérome, D., Poilblanc, D., Bourbonnais, C., Ammerahl, U., Dhalenne, G., Revcolevschi, A.: Science **279**, 345 (1998)
9. Haldane, F.D.M.: J. Phys. C **14**, 2585 (1981)
10. Haldane, F.D.M.: Phys. Rev. Lett. **47**, 1840 (1981)
11. Emery V.J.: In: Devreese, J.T. (eds.) Highly Correlated One-dimensional Solids, Plenum, New York (1979)
12. Sólyom, J.: Adv. Phys. **28**, 201 (1979)
13. Fulde, P.: Electron Correlations in Molecules and Solids. Springer-Verlag, Berlin (1991)
14. Tomonaga, S.: Progr. Theor. Phys. **5**, 349 (1950)
15. Laughlin, R.B.: Phys. Rev. Lett. **60**, 2677 (1988)
16. Fetter, A.L., Hanna, C.B., Laughlin, R.B.: Phys. Rev. B **39**, 9679 (1989)
17. Bethe, H.: Z. Phys. **71**, 205 (1931)
18. Lieb, E.H., Wu, F.Y.: Phys. Rev. Lett. **20**, 1445 (1968)
19. Shiba, H., Ogata M.: Strongly correlated electron systems. In: Baskaran, G., Tosatti, E., Ruckenstein, A.E., Lu Y. (eds.) Progress in High Temperature Superconductivity, vol. 29, World Scientific, Singapore (1991)
20. White, S.R., Scalapino, D.J.: Phys. Rev. B **57**, 3031 (1998)
21. Kagan, M.Yu., Haas, S., Rice, T.M.: Physica C 317/318, 185 (1999)
22. Tsunetsugu, H., Troyer, M., Rice, T.M.: Phys. Rev. B **51**, 16456 (1995)
23. Troyer, M., Tsunetsugu, H., Rice, T.M.: Phys. Rev. B. **53**, 251 (1996)
24. Luther, A.: Phys. Rev. B **14**, 2153 (1976)
25. Luther, A., Peschel, I.: Phys. Rev. B **12**, 3908 (1975)
26. Rice, T.M., Haas, S., Sigrist, M., Zhang, F.-C.: Phys. Rev. B **56**, 14655 (1997)
27. Efetov, K.B., Larkin, A.I.: Sov. Phys. JETP **42**, 390 (1976)
28. Frischmuth, B., Haas, S., Sierra, G., Rice, T.M.: Phys. Rev. B **55**, R3340 (1997)
29. Geshkenbein, V.B., Ioffe, L.B., Larkin, A.I.: Phys. Rev. B **55**, 3173 (1997)
30. Kagan, M.Yu., Brodsky, I.V., Klaptsov, A.V., Combescot, R., Leyronas, X.: Sov. Phys. Uspekhi **176**, 1105 (2006)
31. Brinkman, W.F., Rice, T.M.: Phys. Rev. B **2**, 1324–1338 (1970)

32. Shraiman, B.I., Siggia, E.D.: Phys. Rev. B **42**, 2485–2500 (1990)
33. Emery, V.J., Kivelson, S.A., Lin, H.Q.: Phys. Rev. Lett. **64**, 475–478 (1990)
34. Kagan, M.Yu., Rice, T.M.: J. Phys.: Condens. Matter **6**, 3771–3780 (1994)
35. Baranov, M.A., Chubukov, A.V., Kagan, M.Yu.: Int. J. Mod. Phys. B **6**, 2471 (1992)
36. Plakida, N.M., Anton, L., Adam, S., Adam, G.H.: JETP **124**, 367 (2003)
37. Plakida, N.M., Anton, L., Adam, S., Adam, G.H.: JETP Lett. **74**, 36 (2001)
38. Kagan, M.Yu., Efremov, D.V., Mar'enko, M.S., Val'kov, V.V.: J. Supercond. Novel Magn. **26**, 2809 (2013)
39. Meden, V., Schönhammer, K.: Phys. Rev. B **46**, 15753 (1992)
40. Belinicher, V.I., Chernyshev, A.L., Shubin, V.A.: Phys. Rev. B **56**, 3381 (1997)
41. Belinicher, V.I., Chernyshev, A.L., Dotsenko, A.V., Sushkov, O.P.: Phys. Rev. B **51**, 6076 (1995)
42. Itzykson, C., Zuber, Z.-B.: Quantum Field Theory, vol. 2. Dover Publications, New York (2006)
43. Itzikson, C., Drouffe, J.M.: Statistical Field Theory. Cambridge University Press, Cambridge (1989)
44. Zinn-Justin, J.: Quantum Field Theory and Critical Phenomena, 2nd edn. Oxford University Press, Oxford (1993)
45. Brezin, E., Zinn-Justin, J. (eds.): Fields, Strings and Critical Phenomena. Proceedings of Les Houches X (1988). North-Holland (1990)
46. Tsvelik, A.M.: Quantum Field Theory in Condensed Matter Physics. Cambridge University Press, Cambridge (1998)
47. Gogolin, A.O., Nersesyan, A.A., Tsvelik, A.M.: Bosonization and Strongly Correlated Systems. Cambridge University Press, Cambridge (1999)
48. Fradkin, E.: Field Theories of Condensed Matter Systems. Addison-Wesley, Reading (1991)
49. Wen, X.G., Lee, P.A.: Phys. Rev. Lett. **80**, 2193 (1998)
50. Lee, P.A., Nagaosa, N., Ng, T.K., Wen, X.G.: Phys. Rev. B **57**, 6003 (1998)
51. Lee, P.A., Nagaosa, N., Wen, X.G.: Rev. Mod. Phys. **78**, 17 (2006)
52. Lee, P.A., Nagaosa, N.: Phys. Rev. B **46**, 5621 (1992)
53. Kotliar, G., Liu, J.: Phys. Rev. B **38**, 5142 (1988)
54. Kagan, M.Yu., Efremov, D.V.: Phys. Rev. B **65**, 195103 (2002)
55. Belavin, A.A., Polyakov, A.M., Zamolodchikov, A.B.: Nucl. Phys. B **241**, 333 (1984)
56. Itzykson, C., Saleur,H., Zuber, J.-B. (eds.): Conformal Invariance and Applications to Statistical Mechanics. World Scientific, Singapore (1988)
57. Pruisken, A.M.M.: Nucl. Phys. B **235**, 277 (1984)
58. Frahm, H., Korepin, V.E.: Phys. Rev. B **42**, 10553 (1990)
59. Frahm, H., Korepin, V.E.: Phys. Rev. B **43**, 5653 (1991)
60. Kawakami, N., Yang, S.-K.: Phys. Rev. Lett. **65**, 2309 (1990)
61. Luttinger, J.M.: J. Math. Phys. **4**, 1154 (1963)
62. Kawakami, N., Okiji, A. In: Fukuyama, H., Maekawa, S., Emu, N.A.B., Kaisha, K., Malozemoff, A.P. (eds.) Strong correlations and superconductivity: proceedings of the IBM Japan international symposium, Mt. Fuji, Japan, 21–25 May 1989. Springer, Berlin 1989
63. Brazovskii, S.A., Kirova, N.N.: Sov. Sci. Rev. Sect. A **5**, 100 (1984). Harwood Academic, New York
64. Coleman, S.: Phys. Rev. D **11**, 2088 (1975)
65. Mandelstam, S.: Phys. Rev. D **11**, 3026 (1975)
66. Polyakov, A., Wiegmann, P.B.: Phys. Lett. B **131**, 121 (1983)
67. Polyakov, A., Wiegmann, P.B.: Phys. Lett. B **141**, 223 (1984)
68. Witten, E.: Comm. Math. Phys. **92**, 455–472 (1984)
69. Giamarchi, T.: Quantum Physics in One Dimension. Oxford University Press, Oxford (2004)
70. Ogata, M., Luchini, M.U., Sorella, S., Assaad, F.F.: Phys. Rev. Lett. **66**, 2388 (1991)
71. Schulz, H.J.: Phys. Rev. Lett. **64**, 2831 (1990)

72. Abrikosov, A.A., Gor'kov, L.P., Dzyaloshinskii, I.E.: Quantum Field Theoretical Methods in Statistical Physics. Prentice-Hall, Englewood Cliffs (1963)
73. Arovas, D.P., Auerbach, A.: Phys. Rev. B **38**, 316 (1988)
74. Chubukov, A.V.: Phys. Rev. B **44**, 12318 (1991)
75. Irkhin, V.Y., Katanin, A.A., Katsnelson, M.I.: Phys. Rev. B **60**, 1082 (1999)
76. Kagan, M.Yu.: Lecture Course in Moscow Engineering Physical Institute. Moscow (1999)
77. Dzyaloshinskii, I.E., Larkin, A.I.: JETP **61**, 791 (1971)
78. Dzyaloshinskii, I.E., Larkin, A.I.: ibid **65**, 411 (1973)
79. Ren, Y., Anderson, P.W.: Phys. Rev. B **48**, 16662 (1993)
80. Voit, J.: Phys. Rev. B **47**, 6740 (1993)
81. Voit, J.: J. Phys.: Condens. Matter **5**, 8305 (1993)
82. Voit, J.: Rep. Prog. Phys. **58**, 977 (1995)
83. Trugman, S.A.: Phys. Rev. B **37**, 1597 (1988)
84. Lieb, E.H., Mattis, D.C.: Mathematical Physics in One Dimension. Academic, London (1966)
85. Zaanen, J., Gunnarsson, O.: Phys. Rev. B **40**, 7391 (1989)
86. Goodenough, J.B.: Phys. Rev. **100**, 564 (1955)
87. Emery, V.J., Kivelson, S.A.: Physica C **209**, 597 (1993)
88. Hybertsen, M.S., Schlüter, M., Christensen, N.E.: Phys. Rev. B **39**, 9028 (1989)
89. Unger, P., Fulde, P.: Phys. Rev. B **47**, 8947 (1993)
90. Miyake, K.: Progr. Theor. Phys. **69**, 1794 (1983)
91. Landau, L.D., Lifshitz, E.M.: Statistical Physics, Part I. Butterworth-Heinemann, Oxford (1999)
92. Fisher, D.S., Hohenberg, P.C.: Phys. Rev. B **37**, 4936 (1988)
93. Popov, V.N.: Theor. Math. Phys. **11**, 565 (1972)
94. Leggett, A.J.: Modern Trends in the Theory of Condensed Matter. In: Pekalski, A., Przystawa, J. (eds.) Proceedings of the XVI Karpacz Winter School of Theoretical Physics, p. 14. Springer, New York (1980)
95. Nozieres, P., Schmitt-Rink, S.: J. Low Temp. Phys. **59**, 195 (1985)
96. Kagan, M.Yu., Fresard, R., Capezzali, M., Beck, H.: Phys. Rev. B **57**, 5995 (1998)
97. Kagan, M.Yu., Fresard, R., Capezzali, M., Beck, H.: Physica B **284–288**, 447 (2000)
98. Kagan, M.Yu., Brodsky, I.V., Efremov, D.V., Klaptsov, A.V.: Phys. Rev. A **70**, 023607 (2004)
99. Dagotto, E., Riera, J.: Phys. Rev. Lett. **70**, 682 (1993)
100. Chubukov, A.V.: Phys. Rev. B **48**, 1097 (1993)
101. Efremov, D.V., Mar'enko, M.S., Baranov, M.A., Kagan, M.Yu.: Physica B **284–288**, 216 (2000)
102. Fukuyama, H., Hasegawa, Y., Narikiyo, O.: J. Phys. Soc. Jpn. **60**, 2013 (1991)
103. Izumov, Y.A.: Sov. Phys. Uspekhi **169**, 225 (1999)
104. Izumov, Y.A., Khassan-Ogly, F.A., Skryabin, Y.N.: Field Theoretical Methods in the Theory of Ferromagnetism. Science Publishing House, Moscow (1974)
105. Val'kov, V.V., Ovchinnikov, S.G.: Quasiparticles in Strongly-Correlated Systems. Publishing House of Siberian branch of RAS, Novosibirsk (2001)
106. Ovchinnikov, S.G., Val'kov, V.V.: Hubbard Operators in the Theory of Strongly Correlated Electrons. Imperial College Press, London (2004)
107. Zaitsev, R.O.: JETP **41**, 100 (1975)
108. Zaitsev, R.O.: JETP **70**, 1100 (1976)
109. Zaitsev, R.O., Ivanov, V.A.: Sov. Phys. Solid State **29**, 1475 (1987)
110. Chen, Y., Förster, D., Larkin, A.I.: Phys. Rev. B **46**, 5370 (1992)
111. Uemura, Y.J. et al.: Phys. Rev. Lett. **66**, 2665 (1991)
112. Landau, L.D., Lifshitz, E.M.: Quantum Mechanics: Non-Relativistic Theory. Pergamon Press, Oxford (1977)
113. Balents, L., Fisher, M.P.A.: Phys. Rev. B **53**, 12133 (1996)

114. Gradshteyn, I.S., Ryzhik, I.M.: Table of integrals, series, and products. In: Jeffrey, A., Zwillinger, D. (eds.) Academic, New York (1994)
115. Emery, V.J.: Phys. Rev. Lett. **58**, 2794 (1987)
116. Mattis, D.C., Lieb, E.H.: J. Math. Phys. **5**, 349 (1950)
117. Lifshitz, E.M., Pitaevskii, L.P.: Statistical Physics, Part 2. Pergamon, New York (1980)

Part IV

Chapter 14
The Search for Non-Fermi Liquid Behavior in the Normal State of Low Density Fermion Systems

In this chapter we consider the normal state of the basic one-band and two-band models (in particular Fermi-gas [1, 5–7] and Hubbard models [13]) in 3D and 2D case at low electron densities. We will check these models with respect to Luttinger [2, 3] or marginal Fermi-liquid behavior [4]. Note that both in marginal Fermi-liquid (MFL) and Luttinger liquid (LL) there is no jump in the interacting particles distribution function on the Fermi-surface ($Z = 0$). Moreover the quasiparticles are strongly damped. In marginal Fermi-liquid, for example, $\gamma \sim \mathrm{Im}\varepsilon \sim T$ for the imaginary part of the quasiparticle energy which defines their lifetime $\gamma \sim 1/\tau$. This behavior according to [4] can explain linear resistivity $R \sim T$ typical for optimally doped or slightly overdoped high-T_C systems. We will show that at low electron densities both in 3D and 2D cases there are non-trivial corrections to the Galitskii-Bloom Fermi-gas expansions [5, 6], but globally Landau Fermi-liquid picture [1, 7] is not destroyed at low temperatures both in one-band and two-band models.

Note that some authors propose more drastic violations of the Fermi-liquid picture (for instance Khodel, Shaginyan theory of the fermionic condensate [8] with two jumps in the particle distribution function instead of one for the finite-range or long-range potentials). We will not discuss these proposals in the present chapter, concentrating only on short-range repulsive potentials in 3D and 2D systems.

14.1 The Search for Non-fermi Liquid Behavior in 2D Systems at Low Density

It is well known that Fermi-liquid description [1, 7] is valid for 3D systems at low densities of excitations. In the same time 1D systems are described by Luttinger liquid [2, 3, 9] with vanishing Z-factor ($Z = 0$), and thus with the absence of a quasiparticle peak in the spectral functions. In the 2D case common wisdom also assumes the applicability of Landau Fermi-liquid description for low-density systems. It is based on Galitskii-Bloom [5, 6] Fermi-gas expansion in terms of the

M. Yu. Kagan, *Modern Trends in Superconductivity and Superfluidity*,
Lecture Notes in Physics 874, DOI: 10.1007/978-94-007-6961-8_14,

gas parameter which in the 2D case for the lattice models reads $f_0 = \frac{1}{\ln\frac{1}{nd^2}}$, where n is the density and d is the intersite distance (in the absence of the lattice $d \to r_0$—the range of the potential). Anderson in his papers [10–12] doubts the validity of the Fermi-liquid description in 2D systems already at low electron densities and assumes that, in analogy with 1D case, they are described by Luttinger liquid with vanishing Z-factor ($Z = 0$). His doubts about the applicability of the Galitskii-Bloom approach are connected with three main points:

1) The presence of the upper Hubbard band in 2D (and 3D) lattice models already at low electron density [13–15], which according to Anderson should strongly violate the Fermi-gas expansion in the 2D case [10–12, 15].

2) The singularity which according to Anderson arises in the Landau f-function in a 2D repulsive Fermi-gas even in the absence of the lattice [16, 17], and which violates Landau Fermi-liquid description of the observables (effective mass, compressibility, spin susceptibility) in terms of Landau harmonics $f_0^{(s,a)}$, $f_1^{(s,a)}$ and so on [17].

3) The related problem of a finite phase-shift δ_0, which according to Anderson, enters in the singular ("forward-scattering") term in the quasiparticle-interaction function. In similarity with the physics of the orthogonality catastrophe [18], the finite phase-shift should lead to the Luttinger liquid behavior with $Z = 0$ in 2D low-density systems.

In the forthcoming debate [10–12, 15–17, 19–24] it has become clear that both the authors who agree with Anderson and those who disagree (who adhere to Fermi-gas ideas) have some fairly strong arguments. The debate actually centers on the choice of the correct state to serve as the basis for constructing the regular procedure of successive approximations in the interactions (more precisely, in only that part of the interactions which is ignored in the choice of the ground state).

We are among the supporters of the Fermi-liquid ideas. Using these ideas as a framework, we attempt in this section to analyze the first two points of the debate and show that there are non-trivial corrections to Galitskii-Bloom Fermi-gas expansion due to the singularity in the 2D Landau f-function [17] or due to the presence of the upper Hubbard band already at low densities [15, 22, 23], but overall Fermi-liquid picture is not destroyed in the 2D case for the lattice models and in the absence of a lattice.

Note that the third point of the debate, connected with the finite phase-shift, was resolved by Prokof'ev and Stamp in favor of the Fermi-liquid picture in 2D in [16]. In a detailed and transparently written review-article [16] it was shown that the relevant phase-shift (which enters in the expression for the observables) should be averaged in 2D low-density systems over an angle φ, which is equivalent to the evaluation of δ_0 with Pauli-restricted density of states. Than globally $\delta_0 = 0$, restoring the Fermi-liquid picture with non vanishing Z-factor $Z \neq 0$. We recommend to our readers the review-article of Stamp [16] as a good basis for further thoughts on this interesting topic. In the present chapter we will not detaily discuss it. We only mention that effectively it is rather difficult to separate the evaluation of the averaged phase-shift from the evaluation of Landau harmonics presented in the next subsection.

14.1.1 Singularity in Landau f-function in 2D Low-Density Fermion Systems

In this subsection we analyze in more details the second point of the debate, concerning the existence of a singularity in the Landau quasiparticle interaction function $f(\vec{p},\vec{p}')$. This point has not previously received much attention and was detaily considered first in [17]. We show that singularities which arise in the f-function even in the second order of the perturbation theory lead to non-trivial corrections to the Fermi liquid parameters, but they do not disrupt the overall Fermi liquid picture.

According to the classical results of Landau's Fermi liquid theory [1, 7], the f-function is given by the following expression in the second order of the perturbation theory:

$$f_{+-}(\vec{p},\vec{p}') = f_s - f_a = \frac{\partial^2 E}{\partial n_+(\vec{p})\partial n_-(\vec{p}')} = f_0 - \frac{4mf_0^2}{(2\pi)^2}\int d^2\vec{p}_1 d^2\vec{p}_2\,\theta(p_F^2 - p_1^2)\left\{\frac{\delta(\vec{p}+\vec{p}'-\vec{p}_1-\vec{p}_2)}{p^2+p'^2-p_1^2-p_2^2} + \frac{1}{4}\frac{\delta(\vec{p}+\vec{p}_1-\vec{p}'-\vec{p}_2)}{p^2+p_1^2-p'^2-p_2^2} + \frac{1}{4}\frac{\delta(\vec{p}'+\vec{p}_1-\vec{p}-\vec{p}_2)}{p'^2+p_1^2-p^2-p_2^2}\right\}, \tag{14.1.1}$$

$$f_{++}(\vec{p},\vec{p}') = f_s + f_a = \frac{\partial^2 E}{\partial n_+(\vec{p})\partial n_+(\vec{p}')} = -\frac{2mf_0^2}{(2\pi)^2}\frac{1}{4}\int d^2\vec{p}_1 d^2\vec{p}_2\,\theta(p_F^2 - p_1^2)\left[\frac{\delta(\vec{p}+\vec{p}_1-\vec{p}'-\vec{p}_2)}{p^2+p_1^2-p'^2-p_2^2} + \frac{\delta(\vec{p}'+\vec{p}_1-\vec{p}-\vec{p}_2)}{p'^2+p_1^2-p^2-p_2^2}\right], \tag{14.1.2}$$

where $\theta(x)$ is a step function and the 2D coupling constant f_0 is given by [6]:

$$f_0 = \frac{mU_0/4\pi}{\left(1 + mU_0/4\pi \ln\frac{1}{p_F^2 r_0^2}\right)}, \tag{14.1.3}$$

which is a standard formula for the 2D case. Here p_F is the Fermi momentum, and U_0 and r_0 are the zeroth Fourier component and the range of the potential. For a non-Born (strong) repulsive potential and low density $f_0 = \frac{1}{2\ln(1/p_F r_0)}$.

The notation f_{++} and f_{+-} refers to the spin. Usually $f(\vec{p},\vec{p}')$ is calculated on the Fermi surface ($p = p' = p_F$). In 3D case it takes the familiar form found by Abrikosov and Khalatnikov [1, 7, 52]. Taking a careful look at the expression for f_{+-} we see that it is of the following form:

$$f_{+-}(\vec{p},\vec{p}') = f_0 + f_0^2 K + f_0^2 \Pi, \tag{14.1.4}$$

where

$$K = \int \frac{1 - \theta(p_F^2 - p_1^2) - \theta(p_F^2 - (\vec{p} + \vec{p}' - \vec{p}_1)^2)}{p^2 + p'^2 - p_1^2 - (\vec{p} + \vec{p}_1 - \vec{p}_1)^2} \frac{d^2\vec{p}_1}{(2\pi)^2}, \tag{14.1.5}$$

is the expression for the Cooper loop for $T \to 0$ in 2D. In complete analogy with the 3D case, this expression yields (for $p = p' = p_F$):

$$K = \frac{m}{4\pi} \ln \frac{4p_F^2 - k^2}{k^2}, \tag{14.1.6}$$

where $\vec{k} = \vec{p} + \vec{p}'$ is the momentum of the center of mass.

Expression (14.1.5) contains a standard logarithmic singularity when the angle between $\vec{p}$ and $\vec{p}'$ is equal to π (and thus $\vec{k} = 0$). This situation leads to a Cooper pairing in the case of an attractive potential. That case is of no further interest for our purposes here. In the present section we consider repulsive Fermi-gas at high temperatures $T > T_C$ (but $T \ll \varepsilon_F$, so we can effectively take a limit $T \to 0$ in (14.1.1)–(14.1.5).

The third and fourth terms in f_{+-} [see (14.1.1)] correspond to a diagram of an exchange nature. For a short-range potential, this diagram is equivalent to a polarization operator at a nonzero frequency:

$$\Pi(\pm\Omega, \vec{q}) = \int \frac{\theta(\varepsilon_F - \varepsilon_p) - \theta(\varepsilon_F - \varepsilon_{\vec{p}+\vec{q}})}{\varepsilon_p - \varepsilon_{p+q} \pm \Omega} \frac{d^2\vec{p}}{(2\pi)^2}, \tag{14.1.7}$$

where the role of the frequency Ω is played by the energy difference between the scattering particles. $(p^2 - p'^2)/2m$ and $\vec{q} = \vec{p} - \vec{p}'$ is exactly equal to the momentum transfer. If, as usual, we restrict the discussion to an evaluation of the f-function on the Fermi surface, then we have $p = p' = p_F$ and $\Omega = 0$. According to Yu. Kagan and Afanas'ev [25], the polarization operator in this case is:

$$\Pi(0, \vec{q}) = \frac{m}{2\pi} \left[1 - \mathrm{Re} \sqrt{1 - \frac{4p_F^2}{q^2}} \right]. \tag{14.1.8}$$

For $p = p' = p_F$ the transferred momentum $\vec{q} = |\vec{p} - \vec{p}'| \leq 2p_F$ and $\Pi(0, \vec{q}) = \frac{m}{2\pi}$ does not contain any singularities.

The situation changes radically if we allow a deviation from the Fermi surface in terms of the momenta $\vec{p}$ and $\vec{p}'$. In this case, according to Stern et al. [36] and a later discussion by Fukuyama et al. [22, 23], we have:

$$\Pi(\Omega, \vec{q}) = \frac{m}{2\pi} \left[1 + sign\left(\frac{m\Omega + q^2}{2p_F q}\right) \frac{p_F}{q} \mathrm{Re} \sqrt{\left(\frac{m\Omega + q^2}{2p_F q}\right)^2 - 1} - sign\left(\frac{m\Omega - q^2}{2p_F q}\right) \frac{p_F}{q} \mathrm{Re} \sqrt{\left(\frac{m\Omega - q^2}{2p_F q}\right)^2 - 1} \right], \tag{14.1.9}$$

where $\Omega = \frac{\vec{p}^2 - (\vec{p}')^2}{2m}$ and $\vec{q} = \vec{p} - \vec{p}'$. For $\vec{p}$ and $\vec{p}'$ quasiparallel and close to each other in absolute value $\Omega \approx v_F q$. But in 2D $\Pi(\Omega, \vec{q})$ has a narrow antiscreening region with a minimum corresponding just to $\Omega = v_F q$ (see Fig. 14.1). The magnitude in minimum is proportional to $1/\sqrt{q}$. The antiscreening region where $\Pi(\Omega, \vec{q}) < 0$ leads to the gapless charge-density excitations or plasmons in 2D. Note that in 3D case $\Pi(v_F q, q) \sim \ln q$—singularity is weaker than in 2D.

We introduce now small deviations from the Fermi surface, $\varepsilon = \frac{p - p_F}{p_F}$ and $\varepsilon' = \frac{p' - p_F}{p_F}$ for the amplitudes of the vectors $\vec{p}$ and $\vec{p}'$. If we also introduce the angle between these vectors $\varphi = \angle \vec{p}\vec{p}'$ (see Fig. 14.2), we can reduce the polarization operator for nearly parallel vectors near the Fermi surface (ε, ε', $\varphi \to 0$) to the following form through a simple straightforward calculation:

$$\frac{2\pi}{m}\Pi(\Omega, \vec{q}) - 1 \sim \frac{sign(\varepsilon - \varepsilon')}{(\varepsilon - \varepsilon')^2 + \varphi^2} \mathrm{Re}\varphi \left[\sqrt{2\varepsilon(\varepsilon - \varepsilon')^2 - \varphi^2} - \sqrt{2\varepsilon'(\varepsilon - \varepsilon')^2 - \varphi^2} \right]. \tag{14.1.10}$$

It can be seen from this expression that, as we move upward from the Fermi surface in terms of the magnitude of the momenta (e.g. $\varepsilon > 0$, $\varepsilon' = 0$), there exists a small angular interval $\varphi \sim \varepsilon^{3/2}$ near an almost parallel orientation of $\vec{p}$ and $\vec{p}'$ in which polarization operator and thus the Landau f-function acquire a square-root singularity:

$$f(\varepsilon > 0, \varepsilon' = 0) \sim \frac{f_0^2}{\sqrt{\varepsilon}} \quad \text{for } \varphi < \varepsilon^{3/2}. \tag{14.1.11}$$

If we remove away from the Fermi surface upward in terms of the magnitude of both momenta ($\varepsilon > 0$, $\varepsilon' > 0$) the singularity in the f-function is of the form $f_0^2/(\sqrt{\varepsilon} + \sqrt{\varepsilon'})$.

The singular part of the f-function in a 2D Fermi-gas was originally calculated by Prokof'ev (see the review by Stamp [16]). It was later found independently by Baranov, Kagan, Mar'enko [17]. In Anderson's papers [10–12] it is assumed, by

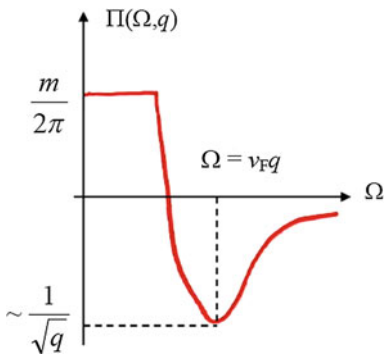

Fig. 14.1 The frequency dependence of polarization operator $\Pi(\Omega, \vec{q})$ with an antiscreening region in 2D

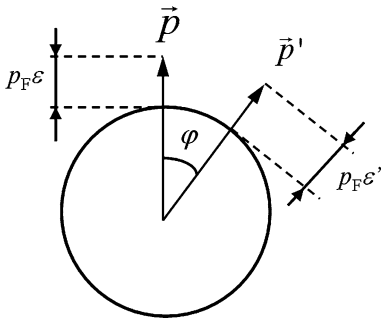

Fig. 14.2 The angle φ between quasiparallel and close in absolute value momenta $\vec{p}$ and $\vec{p}'$. The deviations of $\vec{p}$ and $\vec{p}'$ from p_F are measured in terms of $\varepsilon = \frac{p-p_F}{p_F}$ and $\varepsilon' = \frac{p'-p_F}{p_F}$ [16, 17]

analogy with the situation in 1D Fermi systems [2, 3, 9], that the *f*-function has a more singular form:

$$f_{+-} \sim 1/q \sim 1/\sqrt{(\varepsilon - \varepsilon')^2 + \varphi^2} \quad \text{for } q = |\vec{p} - \vec{p}'| \to 0 \tag{14.1.12}$$

in our notations.

If the perturbation theory results would indeed confirm Anderson's hypothesis, this would mean a complete failure of Landau's Fermi liquid theory in the 2D case, since the Landau harmonics $f_0, f_1, \ldots$ would become logarithmically divergent. For $\varepsilon = \varepsilon' = 0$, we see that according to (14.1.12) $f_{+-} \sim 1/\varphi$ for the *f*-function and, for example,

$$f_0 = \int f(\varphi) d\varphi \sim \int \frac{d\varphi}{\varphi} \sim \ln \varphi \text{ as } \varphi \to 0. \tag{14.1.13}$$

Actually the singularity found in the second order perturbation theory (14.1.9), (14.1.10) is far weaker $f_{+-} \sim 1/\sqrt{\varepsilon}$, not $1/\varepsilon$. In addition, it exists in a very narrow angular interval $\varphi \sim \varepsilon^{3/2}$.

Here we also see a distinction between the 2D and 1D cases, since the presence of one more integration variable, φ renders the divergences weaker. Note that a more rigorous and sophisticated theory for the *f*-function and weak anomalies in it was constructed later on by Chubukov, Maslov [26–28].

14.1.2 Temperature Corrections to the Thermodynamic Variables in 2D Fermi-Gas

To find the temperature corrections to some thermodynamic properties—the compressibility, susceptibility, and the effective mass—we use equations which generalize the standard Fermi liquid expressions for these properties to the case in which quasiparticles deviate from the Fermi surface. In this case we find for effective mass m^*, magnetic susceptibility $\chi(T)$, and sound velocity squared ${c_1}^2(T)$:

$$\begin{cases} \dfrac{m*}{m} = 1 + \dfrac{m}{2\pi}\displaystyle\int f_s(\varepsilon,\varepsilon',\varphi)\cos\phi\,\frac{\partial n}{\partial\varepsilon}\frac{n'}{\partial\varepsilon'}\,d\varepsilon\,d\varepsilon'\frac{d\varphi}{2\pi} + o\left(\frac{T^2}{\varepsilon_F^2}\right), \\ \chi(T) = \chi_0\dfrac{m*}{m}\left(1 + \dfrac{m}{2\pi}\displaystyle\int f_a(\varepsilon,\varepsilon',\varphi)\frac{\partial n}{\partial\varepsilon}\frac{\partial n'}{\partial\varepsilon'}\,d\varepsilon\,d\varepsilon'\frac{d\varphi}{2\pi}\right)^{-1} + o\left(\frac{T^2}{\varepsilon_F^2}\right), \\ c_1^2(T) = \dfrac{N}{m}\left(\dfrac{\partial\mu}{\partial N}\right)_T = \dfrac{v_F^2}{2}\left(1 + \dfrac{m}{2\pi}\displaystyle\int f_s(\varepsilon,\varepsilon',\varphi)\frac{\partial n}{\partial\varepsilon}\frac{\partial n'}{\partial\varepsilon'}\,d\varepsilon\,d\varepsilon'\frac{d\varphi}{2\pi}\right) + o\left(\frac{T^2}{\varepsilon_F^2}\right), \end{cases} \tag{14.1.14–14.1.16}$$

After substitution of the singular part of the f-function into (14.1.14–14.1.16), we find the following expression (the singular part contributes to only $f_s = \frac{f_{+-}+f_{++}}{2}$ and not to $f_a = \frac{f_{++}-f_{+-}}{2}$) according to (14.1.1) and (14.1.2) for m^*, $\chi(T)$, and ${c_1}^2(T)$:

$$\frac{m^*(T) - m^*(0)}{m^*(0)} \sim \frac{\chi(T) - \chi(0)}{\chi(0)} \sim \frac{c_1^2(T) - c_1^2(0)}{c_1^2(0)} \sim f_0^2\frac{T}{\varepsilon_F}. \tag{14.1.17}$$

Correspondingly, the corrections to the specific heat and the entropy are proportional to $f_0^2T^2/\varepsilon_F$. The correction terms in the thermodynamic potential are evidently of the order of $\Delta\Omega \sim f_0^2T^3/\varepsilon_F^2$ in the 2D case. Note that the summation of ladder diagrams does not strengthen the singularity. Corrections of the same type to the specific heat were found in [29] through the analysis of the corrections to the self-energy. The temperature dependence of these corrections are the same as the standard paramagnon corrections $\sim -T^2\ln T$ in the 2D case.

On the other hand, the corrections to the susceptibility in (14.1.15), (14.1.17) are much larger than the paramagnon corrections at low temperatures (we should stress, however that there are no paramagnons at all in our case of a low density 2D Fermi gas). Calculations of the susceptibility are notified by the experiments of Hallock's group and Saunders group [30–32] and also by the experiments of Godfrin's group [33]. These experiments are based on utilization of NMR-technique to measure the temperature dependence of χ in submonolayers of ^{3}He on graphite and on the free surface (on the surface Andreev's levels) of a thin film of superfluid ^{4}He. At low temperatures, the corrections, which we have found, will determine the temperature dependence of the susceptibility. So far, reliable experimental data correspond mainly to intermediate and high temperatures (at which there is a transition from the primarily Pauli susceptibility of degenerate Fermi gas to the Curie law).

As we have already mentioned, $f(\vec{p},\vec{p}')$ acquire a singular part because of a singularity in the 2D polarization operator $\Pi(\Omega,\vec{q})$ for $\vec{q} = |\vec{p} - \vec{p}'| \to 0$, $\Omega = \frac{p^2-p'^2}{2m} \to 0$ and $\Omega/v_{\mathrm{F}}q \to 1$. In a sense, this singularity is an exchange analog of a zero-sound mode (a collective mode in normal Fermi liquid) in a pole of the vertex function. The solution of the Bethe–Salpeter equation in the zero-sound channel (which is equivalent to the solution of a collisionless kinetic equation [34]) leads to the following corrections to the velocity of the 2D zero-sound:

$$\frac{c_0(T)-c_0(0)}{c_0(0)} \sim f_0^2 \frac{T}{\varepsilon_F} \quad \text{at} \quad \frac{T}{\varepsilon_F} < f_0^2. \tag{14.1.18}$$

Note that at $T = 0$, the 2D zero-sound velocity is $c_0(0) \approx v_F(1 + f_0^2)$. Attempts of the parquet enhancement of the zero-sound singularity (involving mutual insertions of polarization loops singular in terms of the variables $\vec{q} = |\vec{p} - \vec{p}'| \to 0$ and $t = |\vec{p} + \vec{p}'| - 2p_F \to 0$) do not result in an amplification of the anomaly.

In summary of this subsection, it can be concluded that the singularity we have found does not lead to a total collapse of the Fermi liquid picture in the 2D Fermi gas in contrast with the assumption of Anderson [10–12]. It leads only to nontrivial temperature corrections to Landau harmonics and thus to the thermodynamic properties of the low-density 2D systems.

14.2 Antibound State on the Lattice: Manifestation of the Upper Hubbard Band at Low Density

In this section we will consider the first point of Anderson's doubts [10–12] connected with an existence of the antibound state in 2D and 3D models (such as Hubbard model) on the lattice. We will show that an antibound state leads to a two-pole structure of the dressed one-particle Green-function $G(\omega, \vec{k})$ in the self-consistent T-matrix approximation [15]. Moreover the second pole in the Green-function will correspond to the manifestation of the upper Hubbard band already at low density. However again we will get only non-trivial corrections to the Galitskii-Bloom Fermi-gas expansions [5, 6] in 3D and 2D case, but globally Landau Fermi-liquid picture will not be completely destroyed in 3D and 2D low density models on the lattice. Note that at low electron density ($nd^{\mathrm{D}} \ll 1$—practically empty band) and in the strong-coupling case $U \gg W$ the effective vacuum interaction in the 3D and 2D Hubbard model [13, 14] can be described by the Kanamori T-matrix approximation. We will now mostly concentrate on a 2D case. In the low energy sector $\varepsilon \leq \varepsilon_{\mathrm{F}}$ and in the framework of this description the 2D Hubbard model (as we discussed in Chap. 9) becomes equivalent to a 2D Fermi-gas model with quadratic spectrum and short-range repulsion [15, 22, 23]. Thus it can be characterized by the 2D gas-parameter of Bloom [6]:

$$\varepsilon_p - \mu = \frac{p^2}{2m} - \varepsilon_F \tag{14.2.1}$$

where $n = p_{\mathrm{F}}^2/2\pi$ is the electron density in 2D (for both spin projections, taking into account that $n_\sigma = n_{-\sigma} = n/2$ in the unpolarized case), p_{F} is the Fermi-momentum, d is the intersite distance. Accordingly many properties of the 2D

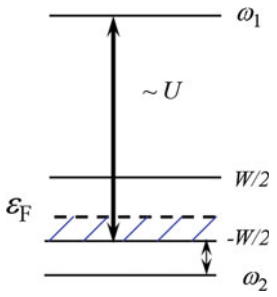

Fig. 14.3 The pole structure of the T-matrix in the 2D repulsive Hubbard model at low density. There are two poles of the T-matrix for the lattice problem—the antibound state of Hubbard-Anderson (ω_1) which lies above the upper edge of the band and Engelbrecht-Randeria mode (ω_2) which lies below the bottom of the band [10–15, 19–21]

Hubbard model at low electron density, and in particular the quasiparticle damping near the Fermi-surface:

$$\gamma \sim \mathrm{Im}\Sigma(\varepsilon_p, \vec{p}) \sim f_0^2 \frac{(\varepsilon_p - \mu)^2}{\varepsilon_F^2} \ln\left|\frac{\varepsilon_F}{\varepsilon_p - \mu}\right|, \tag{14.2.2}$$

(where $\mathrm{Im}\Sigma$ is an imaginary part of the self-energy) have Landau Fermi-liquid character (amended with the specific 2D logarithm [22, 23, 53]). In (14.2.2) $\varepsilon_p - \mu \approx \frac{p^2}{2m} - \varepsilon_F$ is a quasiparticle spectrum in the low energy sector $\varepsilon \leq \varepsilon_\mathrm{F}$ and f_0 is given by (14.2.1). Correspondingly, the averaging of $\mathrm{Im}\Sigma(\varepsilon_p, \vec{p})$ with fermionic distribution function $n_F(\varepsilon_p/T)$ produces the familiar result $\gamma(T) \sim \mathrm{Im}\Sigma(T) \sim T^2 \ln T$ in 2D. Accordingly the Z-factor (the quasiparticle residue) $Z \sim \left(1 - \frac{\partial \mathrm{Re}\Sigma}{\partial \omega}\right)^{-1}$ is non vanishing for $\omega \to 0$. However, as it first mentioned by Hubbard [13, 14] and Anderson [10–12], for $U \gg W$ the presence of a band of a finite width in the lattice problem produces at high energies an additional pole in the two-particle T-matrix, well separated from all other poles with the energy (see Fig. 14.3):

$$\varepsilon \sim U > 0. \tag{14.2.3}$$

This pole is usually called the antibound state (the T-matrix on Fig. 14.3 has one more non-trivial pole first found by Engelbrecht and Randeria [19–21], which we will briefly analyze in the end of this section). Already in the first iteration of the self-consistent T-matrix approximation the pole connected with an antibound state yields a non-trivial contribution to the self-energy $\Sigma(\varepsilon, \vec{p})$. As a result the dressed one-particle Green-function acquires a two pole structure, very similar to the Hubbard-I approximation [13, 14].

14.2.1 The Theoretical Model

We again (as in the Chap. 9) consider the simplest 2D Hubbard model on the square lattice [15]:

$$\hat{H}' = \hat{H} - \mu\hat{N} = -t \sum_{<ij>\sigma} c^{+}_{i\sigma}c_{j\sigma} + U\sum_{i} n_{i\uparrow}n_{i\downarrow} - \mu\sum_{i\sigma} n_{i\sigma}, \tag{14.2.4}$$

where $n_{i\sigma} = c^{+}_{i\sigma}c_{i\sigma}$ is the density operator of electrons on site i with spin-projection σ, U is Hubbard repulsion, t—is hopping integral, μ is chemical potential. The bandwidth $W = 8t$ on the square lattice. After Fourier transformation we get:

$$\hat{H}' = \sum_{\vec{p}\sigma} \left[\varepsilon_p - \mu\right] c^{+}_{p\sigma}c_{p\sigma} + U\sum_{\vec{p}\vec{p}'\vec{q}} c^{+}_{\vec{p}\uparrow}c^{+}_{\vec{p}'\downarrow}c_{\vec{p}-\vec{q}\downarrow}c_{\vec{p}'+\vec{q}\uparrow}, \tag{14.2.5}$$

where $\varepsilon_p - \mu = -2t\left(\cos p_x d + \cos p_y d\right) - \mu$ is the quasiparticle spectrum of the uncorrelated problem. For low electron density $p_F d \ll 1$ we can often use the quadratic approximation for the spectrum:

$$\varepsilon_p - \mu \approx \frac{p^2 - p_F^2}{2m}, \tag{14.2.6}$$

where $m = \frac{1}{2td^2}$ is the band mass, $\mu \approx -\frac{W}{2} + \varepsilon_F$ is the chemical potential and $\varepsilon_p = -2t\left(\cos p_x d + \cos p_y d\right) \approx -\frac{W}{2} + tp^2d^2 = -\frac{W}{2} + \frac{p^2}{2m}$. We will mostly consider the physically more transparent strong-coupling case $U \gg W$ at low electron density $nd^2 \ll 1$.

14.2.2 T-Matrix Approximation

We start with the standard definition of the T-matrix in 2D [5, 6] in the singlet channel:

$$T(\omega, \vec{q}) = \frac{Ud^2}{1 - Ud^2\int \frac{d^2\vec{p}}{(2\pi)^2}\frac{1-n_{F\sigma}(\varepsilon_p-\mu)-n_{F-\sigma}(\varepsilon_{q-p}-\mu)}{(\omega-\varepsilon_p-\varepsilon_{q-p}+2\mu+io)}}. \tag{14.2.7}$$

The poles of the T-matrix are governed by the condition:

$$1 = Ud^2\int \frac{d^2\vec{p}}{(2\pi)^2}\frac{1 - n_{F\sigma}(\varepsilon_p - \mu) - n_{F-\sigma}(\varepsilon_{q-p} - \mu)}{(\omega - \varepsilon_p - \varepsilon_{q-p} + 2\mu + io)}. \tag{14.2.8}$$

For the antibound state for which $\omega \sim U$ we can expand (14.2.8) and get (see also [15, 35]):

$$1 \approx Ud^2 \int \frac{d^2\vec{p}}{(2\pi)^2} \frac{1 - n_{F\sigma}(\varepsilon_p - \mu) - n_{F-\sigma}(\varepsilon_{q-p} - \mu)}{\omega + 2\mu} \left[1 + \frac{\varepsilon_p + \varepsilon_{p-q} - 2\mu}{\omega + 2\mu}\right], \tag{14.2.9}$$

where $\varepsilon_{p-q} = \varepsilon_{q-p}$ and it is convenient to leave $\omega + 2\mu$ in denominator.

Equivalently we can write (introducing $\tilde{\omega} = \omega + 2\mu$):

$$\begin{aligned} 1 \approx & \frac{Ud^2}{\tilde{\omega}} \int \frac{d^2\vec{p}}{(2\pi)^2} \left[1 - n_{F\sigma}(\varepsilon_p - \mu) - n_{F-\sigma}(\varepsilon_{p-q} - \mu)\right] \\ & + \frac{Ud^2}{\tilde{\omega}^2} \int \frac{d^2\vec{p}}{(2\pi)^2} \left[1 - n_{F\sigma}(\varepsilon_p - \mu) - n_{F-\sigma}(\varepsilon_{p-q} - \mu)\right](\varepsilon_p + \varepsilon_{p-q}) \end{aligned} \tag{14.2.10}$$

and we use that $\int \frac{d^2\vec{p}}{(2\pi)^2}(\varepsilon_p + \varepsilon_{p-q}) = 0$ when we integrate over the Brillouin zone. Thus:

$$1 \approx \frac{U}{\tilde{\omega}}(1 - nd^2) - \frac{Ud^2}{\tilde{\omega}^2} \int \frac{d^2\vec{p}}{(2\pi)^2} \left[n_{F\sigma}(\varepsilon_p - \mu) + n_{F-\sigma}(\varepsilon_{p-q} - \mu)\right](\varepsilon_p + \varepsilon_{p-q}), \tag{14.2.11}$$

where we used that in unpolarized case $n_\sigma = n_{-\sigma} = n/2$ $= \int \frac{d^2\vec{p}}{(2\pi)^2} n_{F\sigma}(\varepsilon_p - \mu) = \int \frac{d^2\vec{p}}{(2\pi)^2} n_{F-\sigma}(\varepsilon_{p-q} - \mu)$.

Note that

$$1 = d^2 \int\limits_{BZ} \frac{d^2\vec{p}}{(2\pi)^2} = d^2 \int\limits_{-\pi/d}^{\pi/d} \frac{dp_x}{2\pi} \int\limits_{-\pi/d}^{\pi/d} \frac{dp_y}{2\pi} \tag{14.2.12}$$

for the integration over the Brillouin zone. Hence:

$$1 = \frac{U}{\tilde{\omega}}(1 - nd^2) - \frac{Ud^2}{\tilde{\omega}^2} \int \frac{d^2\vec{p}}{(2\pi)^2} \left[n_{F\sigma}(\varepsilon_p - \mu) + n_{F-\sigma}(\varepsilon_{p-q} - \mu)\right](\varepsilon_p + \varepsilon_{p-q}). \tag{14.2.13}$$

In the second term of the r.h.s of (14.2.13) the integration is restricted by Fermi-factors, and hence we can use quadratic approximation for the spectrum $\varepsilon_p \approx -\frac{W}{2} + \frac{p^2}{2m}$ and correspondingly for $\xi_p = \varepsilon_p - \mu = \frac{p^2}{2m} - \varepsilon_F$. Then for the second term we get:

$$-\frac{Ud^2}{\tilde{\omega}^2}N_{2D}(0)\left[2\int\limits_{-\varepsilon_F}^{0}\xi_p d\xi_p+\int\limits_{-\varepsilon_F}^{0}d\xi_p\int\limits_{0}^{\pi}\frac{d\varphi}{\pi}\left(\frac{p^2+q^2-2pq\cos\varphi}{2m}-\varepsilon_F\right)\right.$$
$$\left.+\int\limits_{-\varepsilon_F}^{0}d\xi_p\int\limits_{0}^{\pi}\frac{d\varphi}{\pi}\left(\frac{p^2+q^2+2pq\cos\varphi}{\varphi}\varphi-\varepsilon_F\right)\right]-\frac{Ud^2}{\tilde{\omega}^2}2\mu n, \tag{14.2.14}$$

where $N_{2D}(0)=m/2\pi$ is the 2D density of states for the quadratic spectrum. After simple calculations (14.2.14) can be represented by:

$$-\frac{Ud^2}{\tilde{\omega}^2}N_{2D}(0)\left[4\int\limits_{-\varepsilon_F}^{0}\xi_p d\xi_p+2\int\limits_{-\varepsilon_F}^{0}\frac{q^2}{2m}d\xi_p\right]-\frac{Ud^2}{\tilde{\omega}^2}2\mu n. \tag{14.2.15}$$

Thus the second term in r.h.s of (14.2.13) finally reads:

$$\frac{Ud^2}{\tilde{\omega}^2}N_{2D}(0)2\varepsilon_F\left(\varepsilon_F-\frac{q^2}{2m}\right)-\frac{Ud^2}{\tilde{\omega}^2}2\mu n, \tag{14.2.16}$$

where we used that $\int n_{F-\sigma}(\varepsilon_{p-q}-\mu)(\varepsilon_p-\mu)\frac{d^2\vec{p}}{(2\pi)^2}=\int n_{F-\sigma}(\varepsilon_p-\mu)(\varepsilon_{p+q}-\mu)\frac{d^2\vec{p}}{(2\pi)^2}$. Hence the Eq. (14.2.13) for the antibound state yields:

$$1\approx\frac{U}{\tilde{\omega}}(1-nd^2)-\frac{Ud^2}{\tilde{\omega}^2}\frac{m\varepsilon_F}{\pi}\left[\frac{q^2}{2m}-\varepsilon_F\right]-\frac{Ud^2}{\tilde{\omega}^2}2\mu n. \tag{14.2.17}$$

Accordingly for the antibound state (using that $\frac{m\varepsilon_F}{\pi}=\frac{p_F^2}{2\pi}=n$):

$$\begin{aligned}\tilde{\omega}_{ab}&\approx U(1-nd^2)-\frac{2\mu nd^2}{(1-nd^2)}+\frac{nd^2}{(1-nd^2)}\left(\varepsilon_F-\frac{q^2}{2m}\right)\\&=U(1-nd^2)+\frac{nd^2}{(1-nd^2)}(\varepsilon_F-2\mu)-\frac{nd^2}{1-nd^2}\frac{q^2}{2m}.\end{aligned} \tag{14.2.18}$$

Hence $\omega_{ab}=-2\mu+U(1-nd^2)+\frac{nd^2}{1-nd^2}(\varepsilon_F-2\mu)-\frac{nd^2}{(1-nd^2)}\frac{q^2}{2m}$.

In analogy with attractive-U Hubbard model (see [37–39] and Chap. 9) we can introduce "bosonic" chemical potential:

$$\mu_B=2\mu-|E_b|\approx 2\varepsilon_F-\left|\tilde{E}_b\right|, \tag{14.2.19}$$

where $|\tilde{E}_b|=W+|E_b|$ is counted again from the bottom of the band. In (14.2.19):

$$|E_b|=U(1-nd^2)+\frac{nd^2}{(1-nd^2)}(\varepsilon_F-2\mu)\approx U(1-nd^2)+nd^2W \tag{14.2.20}$$

is a "binding" energy of an antibound pair. In the same time—($q^2/4m^*$) in (14.2.18) stands for the spectrum of the antibound pair. The effective mass of the antibound pair reads:

$$m^* = m\frac{1-nd^2}{2nd^2} \gg m \quad \text{for } nd^2 \ll 1. \tag{14.2.21}$$

Then we can represent ω_{ab} for the antibound state as:

$$\omega_{ab} = |E_b| - 2\mu - \frac{q^2}{4m^*} = -\frac{q^2}{4m^*} - \mu_B, \tag{14.2.22}$$

which is quite nice. The spectrum (14.2.22) closely resembles the pole of the attractive-U Hubbard model for $\left|\tilde{E}_b\right| > \varepsilon_F$ in [37–39]. The important difference is, however, in the relative sign between 2μ and $|E_{\text{b}}|$. In the attractive-U Hubbard model $\mu_{\text{B}} = 2\mu + |E_{\text{b}}|$ and the real pairs are created below the bottom of the band. Thus $\mu \approx -|E_{\text{b}}|/2$ and $\mu_{\text{B}} \to 0$ at low temperatures. In the repulsive-U Hubbard model for low electron density $nd^2 \ll 1$: $\mu \approx -W/2 + \varepsilon_{\text{F}}$ for low temperatures—lies inside the band, and $\mu_B \approx -\left|\tilde{E}_b\right| \sim -U$ for $U \gg W$. Only in the case of half-filled band $nd^2 = 1$ (one electron per site) the chemical potential $\mu \approx U/2$ "jumps" in the middle of the Mott–Hubbard gap $\Delta_{\text{MH}} = U$. This situation resembles that for the semiconductors: the chemical potential for $nd^2 = 1$ lies in the middle of the forbidden band. Another important difference is connected with the hole-like dispersion in (14.2.21) that is with the sigh minus in front of $q^2/4m^*$. The T-matrix close to the pole reads [15]:

$$T(\omega, \vec{q}) = \frac{U\omega}{\left(\omega + \frac{q^2}{4m^*} + \mu_B + io\right)}. \tag{14.2.23}$$

14.2.3 Imaginary Part of the Self-Energy

In the first iteration to the self-consistent T-matrix approximation [15, 40–42] the imaginary part of the self-energy $\text{Im}\Sigma(\omega, \vec{k})$ reads:

$$\begin{aligned}\text{Im}\Sigma(\omega,\vec{k}) &= \int \frac{d^2\vec{p}}{(2\pi)^2}\text{Im}T(\omega+\varepsilon_p-\mu,\vec{p}+\vec{k})\left[n_F(\varepsilon_p-\mu)+n_B(\varepsilon_p-\mu+\omega)\right] \\ &= \pi\int \frac{d^2\vec{p}}{(2\pi)^2}U(\omega+\varepsilon_p-\mu)\delta(\omega+\varepsilon_p-\mu+\mu_B+\frac{(\vec{p}+\vec{k})^2}{4m^*})\left[n_F(\varepsilon_p-\mu)+n_B\left(-\frac{(\vec{p}+\vec{k})^2}{4m^*}-\mu_B\right)\right],\end{aligned} \tag{14.2.24}$$

where $n_F(\varepsilon_p - \mu)$is a fermionic distribution function (for one spin projection), $n_B\left(-\frac{(\vec{p}+\vec{k})^2}{4m^*} - \mu_B\right)$is a bosonic distribution function. Having in mind that $\mu_{\text{B}} = 2\mu - |E_{\text{b}}| \sim -U$ we get for $U \gg T$ [15]:

$$n_B\left(-\frac{(\vec{p}+\vec{k})^2}{4m^*}-\mu_B\right)=\frac{1}{\exp\left(-\frac{(\vec{p}+\vec{k})^2}{4m^*T}\right)\exp\left(-\frac{\mu_B}{T}\right)-1}\to 0. \tag{14.2.25}$$

Thus:

$$\mathrm{Im}\Sigma(\omega,\vec{k})=\pi U\int\frac{d^2\vec{p}}{(2\pi)^2}\left[-\frac{(\vec{p}+\vec{k})^2}{4m^*}-\mu_B\right]\delta\left(\omega+\varepsilon_p-\mu+\mu_B+\frac{(\vec{p}+\vec{k})^2}{4m^*}\right)\cdot n_F(\varepsilon_p-\mu)\,. \tag{14.2.26}$$

Here again we have the important difference with attractive-U Hubbard model where at low temperatures $T\to 0$: $2n_\mathrm{B}=n$, while $n_\mathrm{F}=0$. In repulsive-U Hubbard model we have vice versa situation: $n_\mathrm{B}=0$ and $n_{\mathrm{F}\text{-}\sigma}=n_{\mathrm{F}\sigma}=n/2$ for $T\to 0$. Having in mind that $m^*/m\gg 1$ for $nd^2\ll 1$ we can neglect $(\vec{p}+\vec{k})^2/4m^*$ in (14.2.26). Thus we get [15]:

$$\begin{aligned}\mathrm{Im}\Sigma(\omega,\vec{k})&=-\pi N_{2D}(0)U\mu_B\int\limits_{-\varepsilon_F}^{0}d\xi_p\delta(\omega+\xi_p+\mu_B)\\&=-\pi N_{2D}(0)U\mu_B[\theta(\omega+\mu_B)-\theta(\omega+\mu_B-\varepsilon_F)],\end{aligned} \tag{14.2.27}$$

where we again used notation $\xi_p=\varepsilon_p-\mu$.

14.2.4 Real Part of the Self-Energy

Correspondingly the real part of the self-energy $\mathrm{Re}\Sigma(\omega,\vec{k})$ yields (see [15, 40–42]):

$$\mathrm{Re}\Sigma(\omega,\vec{k})=\int\frac{d^2\vec{p}}{(2\pi)^2}\mathrm{Re}T(\omega+\varepsilon_p-\mu,\vec{p}+\vec{k})\left[n_F(\varepsilon_p-\mu)+n_B(\omega+\varepsilon_p-\mu)\right], \tag{14.2.28}$$

and again neglecting $n_\mathrm{B}(\omega+\varepsilon_\mathrm{p}\text{-}\mu)$ for low temperatures $U\gg T$ we get:

$$\mathrm{Re}\Sigma(\omega,\vec{k})=UN_{2D}(0)\int n_F(\xi_p)d\xi_p\frac{\omega+\xi_p}{\omega+\xi_p+\mu_B+\frac{(\vec{p}+\vec{k})^2}{4m^*}}. \tag{14.2.29}$$

For $m^*/m\gg 1$: $(\vec{p}+\vec{k})^2/4m^*$ is small again and thus:

$$\begin{aligned}\mathrm{Re}\Sigma(\omega,\vec{k})&=UN_{2D}(0)\int\limits_{-\varepsilon_F}^{0}d\xi_p\frac{\omega+\xi_p}{\omega+\xi_p+\mu_B}\\&=UN_{2D}(0)\left[\varepsilon_F-\mu_B\ln\frac{|\omega+\mu_B|}{|\omega+\mu_B-\varepsilon_F|}\right].\end{aligned} \tag{14.2.30}$$

Assuming that $|\omega + \mu_B| > \varepsilon_F$ and expanding the logarithm in the second term of (14.2.30) we get:

$$\mathrm{Re}\Sigma(\omega, \vec{k}) = UN_{2D}(0)\frac{\varepsilon_F \omega}{\omega + \mu_B} = U\frac{nd^2}{2}\frac{\omega}{\omega + \mu_B}. \tag{14.2.31}$$

Thus the pole of the dressed one-particle Green-function [7, 15] $G^{-1}(\omega, \vec{k}) = G_0^{-1}(\omega, \vec{k}) - \Sigma(\omega, \vec{k})$ reads:

$$\omega - \varepsilon_k + \mu - U\frac{nd^2}{2}\frac{\omega}{\omega + \mu_B} = 0. \tag{14.2.32}$$

Correspondingly:

$$\omega^2 + \left(\mu_B - \varepsilon_k + \mu - U\frac{nd^2}{2}\right)\omega - (\varepsilon_k - \mu)\mu_B = 0, \tag{14.2.33}$$

and again introducing $\xi_k = \varepsilon_k - \mu$ we get:

$$\left(\omega + \frac{\mu_B - \xi_k - U\frac{nd^2}{2}}{2}\right)^2 - \left(\frac{\mu_B - \xi_k - U\frac{nd^2}{2}}{2}\right)^2 - \xi_k\mu_B = 0. \tag{14.2.34}$$

As a result:

$$\omega_{1,2} = -\frac{\mu_B - \xi_k - U\frac{nd^2}{2}}{2} \pm \sqrt{\left(\frac{\mu_B - \xi_k - U\frac{nd^2}{2}}{2}\right)^2 + \xi_k\mu_B}. \tag{14.2.35}$$

Having in mind that $\mu_B \sim -U$ we can expand the square root in (14.2.35). Then:

$$\omega_{1,2} = -\frac{\mu_B - \xi_k - U\frac{nd^2}{2}}{2} \pm \left(\left|\frac{\mu_B - \xi_k - U\frac{nd^2}{2}}{2}\right| + \frac{\xi_k\mu_B}{\left|\mu_B - \xi_k - U\frac{nd^2}{2}\right|}\right). \tag{14.2.36}$$

We know that $\mu_B < 0$ and $|\mu_B| \gg \{\xi_k, Und^2/2\}$. That is why:

$$\left|\frac{\mu_B - \xi_k - U\frac{nd^2}{2}}{2}\right| = -\frac{\mu_B - \xi_k - U\frac{nd^2}{2}}{2}, \tag{14.2.37}$$

and hence:

$$\omega_{1,2} = -\frac{\mu_B - \xi_k - U\frac{nd^2}{2}}{2} \mp \left(\frac{\mu_B - \xi_k - U\frac{nd^2}{2}}{2} + \frac{\xi_k\mu_B}{\mu_B - \xi_k - U\frac{nd^2}{2}}\right). \tag{14.2.38}$$

Finally:

$$\begin{cases} \omega_1 = -\left(\mu_B - \xi_k - U\frac{nd^2}{2}\right) - \frac{\xi_k \mu_B}{\mu_B - \xi_k - U\frac{nd^2}{2}}, \\ \omega_2 = \frac{\xi_k \mu_B}{\mu_B - \xi_k - U\frac{nd^2}{2}}. \end{cases} \tag{14.2.39}$$

14.2.5 The Dressed Green-Function. Comparison with Hubbard-I Approximation

Now we are ready to calculate the dressed Green-function $G(\omega, \vec{k})$. It reads:

$$\begin{aligned} G(\omega, \vec{k}) &= \frac{\omega + \mu_B}{(\omega - \omega_1)(\omega - \omega_2)} = \frac{\omega + \mu_B}{(\omega_1 - \omega_2)}\left[\frac{1}{(\omega - \omega_1)} - \frac{1}{(\omega - \omega_2)}\right] \\ &= \frac{\omega_1 + \mu_B}{(\omega_1 - \omega_2)}\frac{1}{(\omega - \omega_1)} - \frac{\omega_2 + \mu_B}{(\omega_1 - \omega_2)}\frac{1}{(\omega - \omega_2)}. \end{aligned} \tag{14.2.40}$$

Let us check the poles structure:

$$\begin{cases} \omega - \omega_1 = \omega + \left(\mu_B - \xi_k - U\frac{nd^2}{2}\right) + \frac{\xi_k \mu_B}{\mu_B - \xi_k - U\frac{nd^2}{2}}, \\ \omega - \omega_2 = \omega - \frac{\xi_k \mu_B}{\mu_B - \xi_k - U\frac{nd^2}{2}}. \end{cases} \tag{14.2.41}$$

But $\mu_B = 2\mu - |E_b| \approx -|E_b| \approx -U\,(1 - nd^2)$, and

$$\mu_B - \frac{Und^2}{2} \approx -U\left(1 - \frac{nd^2}{2}\right) \tag{14.2.42}$$

Of course $\left|\mu_B - \frac{Und^2}{2}\right| \gg \xi_k$. Hence:

$$\begin{cases} \omega - \omega_1 = \omega - \xi_k - U\left(1 - \frac{nd^2}{2}\right) + \frac{\xi_k(1-nd^2)}{1-\frac{nd^2}{2}} \approx \omega - U\left(1 - \frac{nd^2}{2}\right) - \frac{nd^2}{2}\xi_k, \\ \omega - \omega_2 = \omega - \frac{\xi_k(1-nd^2)}{1-\frac{nd^2}{2}} \approx \omega - \xi_k\left(1 - \frac{nd^2}{2}\right). \end{cases} \tag{14.2.43}$$

Correspondingly, the first term in (14.2.40) yields:

$$\frac{\omega_1 + \mu_B}{(\omega_1 - \omega_2)}\frac{1}{(\omega - \omega_1)} = \frac{1}{(\omega - \omega_1)}\frac{(1 - nd^2/2) - (1 - nd^2)}{(1 - nd^2/2)} \approx \frac{nd^2}{2(\omega - \omega_1)}. \tag{14.2.44}$$

The second term in (14.2.40) reads:

$$\frac{\omega_2+\mu_B}{(\omega_1-\omega_2)}\frac{1}{(\omega-\omega_2)}=-\frac{1}{(\omega-\omega_2)}\frac{(1-nd^2)}{(1-nd^2/2)}\approx-\frac{1}{(\omega-\omega_2)}\left(1-\frac{nd^2}{2}\right). \tag{14.2.45}$$

Thus for the dressed Green-function we have:

$$G(\omega,\vec{k})=\frac{nd^2/2}{\omega-U\left(1-\frac{nd^2}{2}\right)-\frac{nd^2}{2}(\varepsilon_k-\mu)}+\frac{1-nd^2/2}{\omega-(\varepsilon_k-\mu)\left(1-\frac{nd^2}{2}\right)}. \tag{14.2.46}$$

This result is very elegant one since via a simple calculation we completely recover the Hubbard-I approximation [13, 43]. The first pole in (14.2.46) corresponds to the upper Hubbard band (UHB). Thus $Z_{\mathrm{UHB}}=nd^2/2$. The second pole corresponds to the lower Hubbard band (LHB) with the Z-factor $Z_{\mathrm{LHB}}=1-nd^2/2$. Of course, $Z_{\mathrm{UHB}}+Z_{\mathrm{LHB}}=1$. We can rewrite $G(\omega,\vec{k})$ as:

$$G(\omega,\vec{k})=\frac{Z_{LHB}}{\omega-(\varepsilon_k-\mu)Z_{LHB}+io}+\frac{Z_{UHB}}{\omega-U\left(1-\frac{nd^2}{2}\right)-Z_{UHB}(\varepsilon_k-\mu)+io}. \tag{14.2.47}$$

14.2.6 Hartree–Fock Contribution to the Thermodynamic Potential

Note that the second iteration to the self-consistent T-matrix approximation does not change the gross features of (14.2.47). Thus the antibound state yields nontrivial corrections to Landau Fermi-liquid picture already at low electron density, but does not destroy it in 2D. The simplest Hartree–Fock contribution to the thermodynamic potential Ω from the upper Hubbard band (see Fig. 14.4) yields:

$$\Delta\Omega=\int\!\!\int\Sigma(\omega,\vec{p})G_0(\omega,\vec{p})\frac{d^2\vec{p}}{(2\pi)^2}\frac{d\omega}{2\pi} \tag{14.2.48}$$

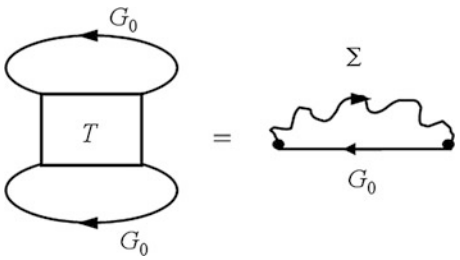

Fig. 14.4 The simplest Hartree–Fock contribution to the thermodynamic potential Ω from the upper Hubbard band

with $G_0(\omega,\vec{k}) = \frac{1}{\omega-\varepsilon_k+\mu+i\sigma}$, and $\Sigma(\omega,\vec{k})$ given by (14.2.31). Thus $\Delta\Omega \sim Z_{\mathrm{UHB}} n\, \varepsilon_{\mathrm{F}} \sim n^3 > 0$ [15].

14.2.7 Engelbrecht–Randeria Mode

For the sake of completeness let us discuss as well the Engelbrecht–Randeria mode [19–21] which we briefly mentioned in the beginning of this section (see Fig. 14.4). It also corresponds to the pole of the T-matrix for $U \gg W$ and $nd^2 \ll 1$. According to [19–21] it has a spectrum for $q < 2p_{\mathrm{F}}$:

$$\omega_{ER} \approx \omega_q - \exp\left\{-\frac{1}{f_0}\right\}\frac{\omega_q^2}{2\varepsilon_F}, \tag{14.2.49}$$

where $\omega_q = \frac{q^2}{4m} - 2\varepsilon_F$ and $\exp\left\{-\frac{1}{f_0}\right\} = nd^2$ in agreement with (14.2.1). Note that for $q = 0$:

$$\omega_{ER} = -2\varepsilon_F - 2\varepsilon_F nd^2 < 0. \tag{14.2.50}$$

Note also that while antibound state exists both in 2D and 3D physics, the Engelbrecht-Randeria mode is specific for the 2D Hubbard model and it has a collective character. The collective character of Engelbrecht-Randeria mode is connected with the fact that in the absence of the fermionic background (for $\varepsilon_{\mathrm{F}} = 0$) $\omega_{\mathrm{ER}} = 0$ in (14.2.50). Moreover $\omega_{\mathrm{ER}} < -2\varepsilon_{\mathrm{F}}$. Hence this mode lies below the bottom of the band (see Fig. 14.4). Recall that the antibound state lies above the upper edge of the band on Fig. 14.4. In terms of "bosonic" chemical potential μ_{B}:

$$\omega_{ER} \approx \frac{q^2}{4m} - \mu_B, \tag{14.2.51}$$

where $\mu_{\mathrm{B}} = 2\mu + |E_{\mathrm{b}}|$, fermionic chemical potential $\mu \approx -W/2 + \varepsilon_{\mathrm{F}}$ and the binding energy for Engelbrecht-Randeria mode $|E_{\mathrm{b}}| \approx W + 2\varepsilon_{\mathrm{F}}\, nd^2$.

14.2.8 Discussion: The Possible Bridge Between Fermi-Gas and Gutzwiler Type of Expansions for Partially Filled Bands

In this section we considered the excitation spectrum of the repulsive-U Hubbard model at low electron density, where a small parameter (gas parameter) allows a controlled diagrammatic expansion. On the level of the first iteration to the self-consistent T-matrix approximation we found the contribution of the T-matrix pole corresponding to the antibound state to the self-energy Σ. As a result we got a two

pole structure of the dressed one-particle Green-function which closely resembles the Hubbard-I approximation.

It would be interesting to find the possible contribution of the upper Hubbard band to the ground-state energy and compressibility and to build the bridge between the Galitskii-Bloom [5, 6] Fermi-gas expansions for the ground-state energy (or compressibility) and the Gutzwiler type of expansion [44–46] for partially filled band when the electron density is increased.

For the sake of completeness we also analyzed the Engelbrecht-Randeria mode which corresponds to the pairing of two holes below the bottom of the band. According to [19–21] this mode, when keeping the full q-dependence for $0 \leq q \leq 2p_{\mathrm{F}}$, gives nonanalytic corrections $\sim |\omega|^{5/2}$ to the imaginary part of the self-energy $\mathrm{Im}\Sigma(\omega)$ in 2D. It also contributes to the thermodynamics at $T = 0$ in the same order in density as the contribution of the antibound state $\Delta\Omega \sim \varepsilon_{\mathrm{F}} nnd^2 \sim n^3 > 0$ amounting to an increase of the thermodynamic potential Ω [19–21]. Thus the Engelbrecht-Randeria mode as well as the Hubbard-Anderson mode corresponding to the antibound state yield interesting corrections to the Landau Fermi-liquid picture in 2D already at low electron density, but do not destroy it in contrast to the 1D case, where we have the Luttinger liquid state [2, 3, 9] and a vanishing Z-factor (quasiparticle residue) $Z \to 0$ for $\omega \to 0$.

14.3 The Search for Marginal Fermi Liquid Behavior in the Two-Band Models

In this section we will search for marginal Fermi liquid behavior in the two-band mixed valence systems. We will analyze inverse scattering times $\gamma = 1/\tau$ in different temperature regimes, as well as anomalous resistivity characteristics and weak-localization effects [40–42, 47, 48] in the homogeneous state of the two-band Hubbard model with one narrow band. This model can adequately describe uranium-based heavy-fermion compounds and possibly CMR-systems (manganites for example) in optimally doped regime (phase-separated low-doped manganites will be considered detaily in Chaps. 15 and 16). We will show that resistivity characteristics in 3D case of this model are typical for many uranium-based heavy-fermion compounds (such as e.g. UNi_2Al_3).

Resistivity characteristics in the 2D case are typical for many optimally doped layered manganites in the homogeneous state.

At low temperatures $T < W_{\mathrm{h}}^*$ (W_{h}^* is an effective width of the heavy band) Landau Fermi-liquid description is valid both for $\gamma(T)$ and resistivity $R(T)$, however there are interesting temperature dependences of $R(T)$ for higher temperatures $T > W_{\mathrm{h}}^*$ in 3D and 2D systems, when the heavy component is marginal.

14.3.1 Resistivity in the Two-Band Model with One Narrow Band

In Chap. 10 we discussed electron-polaron effect and enhanced Kohn-Luttinger mechanism of SC in the two-band model with one narrow band. In this section on the basis of the same formalism (namely self-consistent T-matrix approximation for the self-energies of heavy and light bands) we will discuss anomalous resistivity characteristics which appear in the homogeneous state of the two-band systems especially in high-temperature regime $T > W_h^*$ of a destroyed heavy band and in the 2D case [40–42, 49]. We remind that we consider a clean case (no real impurities in the system) and only the processes of electron–electron scattering. Nevertheless we will show that in the regime of a destroyed heavy band the heavy particles are moving diffusively in the surrounding of light particles, and thus the heavy component becomes marginal. In the same time light electrons scatter on the heavy ones in this regime as if on almost immobile static impurities. The resistivity in 3D systems goes on saturation at high temperatures as in the case of uranium-based HF compounds like UNi_2Al_3. In the 2D case we should take into account weak localization corrections of Altshuler-Aronov type [40–42, 48, 49] to classical (Drude) results for conductivity of a light band at high temperatures already in the clean case (when real impurities are absent). We will show that these corrections lead to the additional localization of the light band [40–42, 49, 54]. Moreover at high temperatures $T \geq W_h^*$ the additional localization of the light band and the additional narrowing of the heavy band (due to Electron-polaron effect) are governed by the same parameter $f_0^2 \ln \frac{m_h}{m_L} > 1$ (considered in Chap. 10 for the Z-factor of heavy particles). As a result the resistivity in 2D will have a maximum and then the localization tail at higher temperatures. Such resistivity characteristics are typical for layered CMR materials in the regime of optimal doping as well as for some layered intermetallic alloys (like Gd_5Ge_4 [51]).

14.3.2 Evaluation of the Self-Energies at Low Temperatures in the Two-Band Model

We start with the evaluation of the inverse scattering times $\gamma = 1/\tau$ via imaginary parts of the self-energies of heavy and light particles calculated in (10.3.25) of Chap. 10. In the homogeneous case we should average the second order contributions to the self-energies $\Sigma^{(2)}(\varepsilon(q) - \mu, \vec{q})$ in (10.3.25, 10.3.26) with the fermionic distribution function $n_F\left(\frac{\varepsilon(q)-\mu}{T}\right)$. We obtain than the following expressions for the imaginary parts $\mathrm{Im}\Sigma^{(2)}(T)$ of heavy and light electrons at low temperatures $T < W_h$ and for equal densities $n_h = n_L$ in the heavy and light bands in 3D:

$$\begin{aligned} \mathrm{Im}\Sigma_{LL}^{(2)}(T) &= \lambda^2 \frac{T^2}{\varepsilon_{FL}}, \\ \mathrm{Im}\Sigma_{Lh}^{(2)}(T) &= \lambda^2 \frac{T^2}{\varepsilon_{Fh}} \frac{m_h}{m_L}, \end{aligned} \tag{14.3.1}$$

and correspondingly

$$\begin{aligned} \mathrm{Im}\Sigma_{hh}^{(2)}(T) &= \lambda^2 \frac{T^2}{\varepsilon_{Fh}}, \\ \mathrm{Im}\Sigma_{hL}^{(2)}(T) &= \lambda^2 \frac{T^2}{\varepsilon_{Fh}}. \end{aligned} \tag{14.3.2}$$

In the 2D case we get exactly the same results with the change of λ^2 on f_0^2, where $\lambda = \frac{2p_F d}{\pi}$ and $f_0 = \frac{1}{2\ln\frac{1}{p_F d}}$ are 3D and 2D gas-parameters of Galitskii and Bloom (in a more rigorous consideration the inverse scattering times contain specific 2D logarithms $\gamma = 1/\tau \sim \mathrm{Im}\Sigma^{(2)}(T) \sim T^2 \ln T$ [22, 23]). We will ignore them for our rough estimates. From (14.3.1) and (14.3.2) we can see that all imaginary parts of the self-energies $\mathrm{Im}\Sigma^{(2)}(T)$ and thus all the inverse scattering times $\gamma = 1/\tau = \mathrm{Im}\sum^{(2)}(T)$ behave in a standard Landau Fermi-liquid fashion $\gamma \sim T^2$ for low temperatures $T < W_\mathrm{h}$. Moreover, $\mathrm{Im}\Sigma_{Lh}^{(2)}(T) \gg \mathrm{Im}\Sigma_{LL}^{(2)}$ and hence

$$\mathrm{Im}\Sigma_{L}^{(2)}(T) = \mathrm{Im}\Sigma_{Lh}^{(2)}(T) + \mathrm{Im}\Sigma_{LL}^{(2)}(T) \approx \mathrm{Im}\Sigma_{Lh}^{(2)}(T). \tag{14.3.3}$$

14.3.3 Classical (Drude) Results for Resistivity at Low Temperatures

We can now estimate the Drude conductivity [34, 40–42] for the light band:

$$\sigma_L = \frac{n_L e^2 \tau_L}{m_L},$$

where a naive estimate for τ_L yields:

$$\gamma_L = 1/\tau_L = \mathrm{Im}\Sigma_{L}^{(2)}(T) \approx \mathrm{Im}\Sigma_{Lh}^{(2)}(T). \tag{14.3.4}$$

Thus $1/\tau_\mathrm{L} \approx 1/\tau_\mathrm{Lh}$. Correspondingly we obtain for the conductivity of light electrons in the 3D case:

$$\sigma_L \approx \sigma_{Lh} = \frac{n_L e^2 \tau_{Lh}}{m_L} = \frac{n_L e^2}{\lambda^2 T^2} \frac{\varepsilon_{Fh} m_L}{m_h m_L} = \frac{n_L e^2}{\lambda^2 p_{Fh}^2} \left(\frac{\varepsilon_{Fh}}{T}\right)^2. \tag{14.3.5}$$

In 2D we should replace again λ^2 by ${f_0}^2$ in (14.3.5). Introducing the minimal Mott-Regel conductivities [34, 40–42, 47, 48, 55, 56]:

$$\sigma_{\min} = \left(\frac{e^2}{\hbar}\right) p_F \text{ in 3D,} \quad \text{and } \sigma_{\min} = \frac{e^2}{\hbar} \text{ in 2D} \tag{14.3.6}$$

and working in the units where $\hbar = 1$, in the case of equal densities of heavy and light bands $n_{\mathrm{h}} = n_{\mathrm{L}}$ we obtain in 3D:

$$\sigma_L \approx \sigma_{Lh} = \frac{\sigma_{\min}}{\lambda^2}\left(\frac{\varepsilon_{Fh}}{T}\right)^2. \tag{14.3.7}$$

In 2D we replace λ^2 on ${f_0}^2$ in (14.3.7).

14.3.4 The Role of Umklapp Processes

We note that, strictly speaking, the nondiagonal conductivity σ_{Lh} (which is defined by the scattering of light electrons on the heavy ones) is finite only due to an account of Umklapp processes [34, 40–42, 50]:

$$\vec{p}_{1L} + \vec{p}_{2h} = \vec{p}_{3L} + \vec{p}_{4h} + \vec{K}, \tag{14.3.8}$$

where $K \sim \pi/d$ is the wave-vector of the reciprocal lattice. We would like to remind that due to Umklapp processes the momentum is transferred from electron subsystem to the lattice thus forming the finite conductivity [34, 40–42, 50]. Returning back to (14.3.8) note that for $p_{\mathrm{Fh}} \sim p_{\mathrm{FL}}$ the Umklapp processes are effective for not very small densities in the heavy and light bands (otherwise the conductivity σ_{Lh} would be exponentially small). Hence, within the accuracy of our estimates:

$$\sigma_{Lh} = \frac{\sigma_{\min}}{\lambda^2}\left(\frac{W_h}{T}\right)^2, \tag{14.3.9}$$

where we replace $\varepsilon_{\mathrm{Fh}}$ in (14.3.7) by W_{h}. The situation with the conductivity of the heavy band is slightly more tricky since $\mathrm{Im}\Sigma^{(2)}_{\mathrm{hh}}(T) \sim \mathrm{Im}\Sigma^{(2)}_{\mathrm{hL}}(T)$ and hence $\sigma_{\mathrm{hh}} \sim \sigma_{\mathrm{hL}}$. However, for a crude estimate, we can again consider only the non-diagonal part of the conductivity σ_{hL} and take Umklapp processes (14.3.8) into account. Then:

$$\sigma_{hL} \sim \sigma_{Lh} = \frac{\sigma_{\min}}{\lambda^2}\left(\frac{W_h}{T}\right)^2 \tag{14.3.10}$$

in the 3D case. We note that the estimates (14.3.9, 14.3.10) can be verified by the exact solution of coupled kinetic equations for heavy and light particles with an account of Umklapp processes [54].

The total resistivity in 3D is given by:

$$R = \frac{1}{\sigma_h + \sigma_L} \sim \frac{\lambda^2}{\sigma_{\min}} \left(\frac{T}{W_h}\right)^2. \tag{14.3.11}$$

(In 2D λ^2 is replaced by ${f_0}^2$ in (14.3.10) and (14.3.11)). It behaves in Landau Fermi-liquid manner $R(T) \sim T^2$ for low temperatures $T < W_{\rm h}$. In case of large heavy-mass enhancement $m_{\rm h}^* \gg m_{\rm h}$ we can replace $W_{\rm h}$ by $W_{\rm h}^*$ in (14.3.10) and (14.3.11).

14.3.5 The Regime of a Destroyed Heavy Band at High Temperatures $T > W_h^*$

For higher temperatures $T > W_{\rm h}^*$ the heavy band is totally destroyed (more precisely it is destroyed for $\lambda^2 T = W_{\rm h}^*$ in 3D and ${f_0}^2 T = W_{\rm h}^*$ in 2D as we will see shortly). To be accurate we first calculate the effective chemical potential $\mu_{\rm h}^{\rm eff} = \mu + W_{\rm h}/2 + \varepsilon_0$ (introduced in Chap. 10) in this situation.

14.3.5.1 The Chemical Potential at Higher Temperatures $T > W_{\rm h}^*$

Generally speaking, $n_{\rm h} + n_{\rm L} = n_{\rm tot} = const$, i.e. only the total density is conserved. In our case, however, for large difference between the bare masses $m_{\rm h} \gg m_{\rm L}$ each density of the band is conserved practically independently $n_{\rm h} \approx const$ and $n_{\rm L} \approx const$. For heavy particles all the states in the band are uniformly occupied at these temperatures. For $T > W_{\rm h}$ (assuming $m_{\rm h}^*/m_{\rm h} \sim 1$) the effective chemical potential of the heavy particles is given by:

$$\mu_h^{eff} = \mu + \frac{W_h}{2} + \varepsilon_0 \sim -T \ln\left(\frac{1}{n_h d^D}\right), \tag{14.3.12}$$

where $W_{\rm h}$ is a heavy bandwidth, $-\varepsilon_0$ is the center of gravity of a heavy band.

Hence we have the Boltzman behavior of $\mu_{\rm h}^{\rm eff}$ [40–42]. The Fermi–Dirac distribution function for heavy particles is:

$$\begin{aligned} n_h(\varepsilon - \mu) &= \frac{1}{e^{\frac{p^2/2m_h - \mu_h^{eff}}{T}} + 1} \approx \frac{1}{(1 + p^2/(2m_h T))e^{-\mu_h^{eff}/T} + 1} \approx \frac{e^{\mu_h^{eff}/T}}{1 + (p^2/2m_h T)} \\ &\approx e^{\mu_h^{eff}/T} = const. \end{aligned} \tag{14.3.13}$$

For light particles for the temperatures $W_h \ll T \ll W_L$ (since $m_h \gg m_{L)}$ the effective chemical potential has approximately the same position as for $T = 0$. Indeed for $\mu_L^{\text{eff}} = \mu + W_L/2$ (introduced in Chap. 10) we have:

$$n_L(\varepsilon - \mu) = \frac{1}{e^{\frac{p^2/2m_L - \mu_L^{eff}}{T}} + 1} \approx \frac{1}{e^{\frac{p^2 - p_{FL}^2}{2m_L T}} + 1} \approx \theta\left(-\frac{p^2}{2m_L} + \varepsilon_{FL}\right). \tag{14.3.14}$$

Thus $n_L(\varepsilon - \mu)$ is given by the step function for $T \ll \varepsilon_{FL}$ and hence the effective chemical potential of light particles:

$$\mu_L^{eff} \approx \varepsilon_{FL}. \tag{14.3.15}$$

14.3.6 Evaluation of the Imaginary Parts of the Self-Energies at Higher Temperatures $W_h^* < T < W_L$

For light particles the imaginary part of the self-energy $\text{Im}\Sigma_{LL}^{(2)}(T) = \lambda^2 T^2/W_L$ in 3D (and $f_0^2 T^2/W_L$ in 2D) does not change.

In the same time:

$$\text{Im}\Sigma_{Lh}^{(2)}(T) = \lambda^2 W_h \frac{m_h}{m_L} \gg \text{Im}\Sigma_{LL}^{(2)}(T) \tag{14.3.16}$$

in the 3D case for $W_h^* < T < W_L$ (for $T < W_L$. we have $T^2/W_L < W_h\, m_h/m_L$). The same inequality holds in 2D. Note that $\text{Im}\Sigma_{Lh}^{(2)}(T)$ in (14.3.16) describes almost elastic scattering of light electrons on the heavy ones as if on immobile (static) impurities in the zeroth order in $W_h/W_L \ll 1$. We note that $W_h\, m_h = W_h^* m_h^*$. For heavy electrons we should take into account the bosonic contribution $n_B(\Omega) \approx T/\Omega$ and the fermionic contribution $n_F(\Omega) \approx \frac{1}{2}\left(1 - \frac{\Omega}{2T}\right)$ for $\Omega/T \ll 1$ to $\text{Im}\Sigma^{(2)}$ and thus to scattering times. This yields:

$$\text{Im}\Sigma_{hh}^{(2)}(T) = \lambda^2 W_h \text{ in 3D and } f_0^2 W_h \text{ in 2D}, \tag{14.3.17}$$

which describes the scattering of heavy electrons on each other in the situation when they uniformly occupy the heavy band and can transfer to each other only an energy $\sim W_h$ [57, 58]. Since $m_h^* \gg m_h$ we can replace W_h by W_h^* in (14.3.17). At the same time, for the scattering of heavy particles on the light ones we have in 3D [40, 42]:

$$\text{Im}\Sigma_{hL}^{(2)}(T) = \lambda^2 T \gg \text{Im}\Sigma_{hh}^{(2)}(T), \tag{14.3.18}$$

and analogous linear in T ($f_0^2 T$) behavior in 2D. Thus (14.3.18) describes the marginal Fermi liquid behavior [4] for diffusive motion of heavy electrons in the surrounding of light electrons.

We note that to derive (14.3.18) for $W_L > T > W_h$ and in the zeroth order in the mass ratio $m_L/m_h \ll 1$, we should rewrite expression for $\mathrm{Im}\Sigma^{(2)}_{hL}(\varepsilon_h(p) - \mu, \vec{p})$ derived in Chap. 10 in the form (using the notation $\xi_h(p) = \varepsilon_h(p) - \mu$, $\xi_L(p) = \varepsilon_L(p) - \mu$):

$$\mathrm{Im}\Sigma^{(2)}_{hL}(\varepsilon_h(p) - \mu, \vec{p}) = -\pi\left(\frac{4\Pi a_{hL}}{m_L}\right)^2 N_{L3D}{}^2(0) \int\int d\xi_{Lp'} d\xi_{Lk} \delta(\xi_{Lp'} - \xi_{Lk}) \\ n_F(\xi_{Lk})\left[1 - n_F(\xi_{Lp'})\right] \tag{14.3.19}$$

After the δ-function integration this yields:

$$\mathrm{Im}\Sigma^{(2)}_{hL}(\varepsilon_h(p) - \mu, \vec{p}) \approx -\pi\lambda^2 \int d\xi_{Lk} n_F(\xi_{Lk})[1 - n_F(\xi_{Lk})] \\ \sim \pi\lambda^2 \int_{-\infty}^{+\infty} d\varepsilon \frac{e^{\varepsilon/T}}{(1+e^{\varepsilon/T})^2} \sim \lambda^2 T \text{ in 3D and } \sim f_0^2 T \text{ in 2D.} \tag{14.3.20}$$

14.3.7 Resistivity for $T > W_h^*$ in the 3D Case

From the previous section we have for the scattering times of heavy and light particles for $T > W_h{}^*$:

$$\frac{1}{\tau_L} \approx \frac{1}{\tau_{Lh}} = \lambda^2 W_h \frac{m_h}{m_L}. \tag{14.3.21}$$

We note that $\lambda^2 W_h\, m_h/m_L = \lambda^2 W_h{}^* m_h{}^*/m_L \sim \lambda^2 W_L$ in (14.3.21). In the same time:

$$\frac{1}{\tau_h} \approx \frac{1}{\tau_{hL}} = \lambda^2 T, \tag{14.3.22}$$

and hence the heavy component is marginal, but the light one is not. The conductivity of the light band is given by:

$$\sigma_L = \frac{n_L e^2 \tau_L}{m_L} \approx \frac{n_L e^2 \tau_{Lh}}{m_L} = \frac{\sigma_{\min}}{\lambda^2}. \tag{14.3.23}$$

For the heavy band the Drude formula must be modified by the Einstein relation [34] $\partial n_h/\partial T \sim W_h{}^*/T$ since $T > W_h{}^*$. We then immediately obtain:

$$\sigma_h = \frac{\sigma_{\min}}{\lambda^2}\left(\frac{W_h*}{T}\right)^2. \tag{14.3.24}$$

As a result, the resistivity is:

$$R = \frac{1}{\sigma_h + \sigma_L} = \frac{\lambda^2}{\sigma_{\min}} \frac{(T/W_h^*)^2}{1 + (T/W_h^*)^2} = \frac{\lambda^2}{\sigma_{\min}} \frac{1}{1 + (W_h^*/T)^2}. \tag{14.3.25}$$

For $T > W_h^*$ the resistivity $R \sim \lambda^2/\sigma_{\min}$ saturates. We thus obtain a residual resistivity at high temperatures due to the conductivity of the light band. This is a very nontrivial result of [40–42, 49, 59].

14.3.8 Discussion

When $W_h^* < 1/\tau_h$ or, equivalently, $\lambda^2 T > W_h^*$, the coherent motion in the heavy band is totally destroyed. The heavy particles begin to move diffusively in the surrounding of light particles. In this regime, rigorously speaking, the diagrammatic technique can be used only for light particles and not for the heavy ones.

But the exact solution of the density matrix equation obtained in [57, 58] shows that Σ_{hL} is qualitatively the same for $\lambda^2 T > W_h^*$ as in our estimates, and the inverse scattering time $1/\tau_{hL}$ is also qualitatively the same due to its physical meaning (scattering of light electrons on heavy ones as if on immobile impurities). That is why σ_h and σ_L and hence $R(T)$ behave smoothly for $\lambda^2 T \geq W_h^*$.

14.3.8.1 The Idea of a Hidden Heavy Band for High-T_C Systems

The resistivity $R(T)$ in 3D acquires the form (see Fig. 14.5) that is frequently obtained in uranium-based HF (for example in UNi_2Al_3).

We note that $R(T)$ on Fig. 14.5 mimics a linear behavior in a crossover region of intermediate temperatures $T \sim W_h^*$ between T^2 at low temperatures $T \ll W_h^*$ and const (for the saturation of the resistivity) at $T \gg W_h^*$. The same holds for magnetoresistance in the well-known experiments of P.L. Kapitza:

$$\frac{R(H) - R(0)}{R(0)} \sim \frac{(\Omega_C \tau)^2}{1 + (\Omega_C \tau)^2} \sim \begin{cases} (\Omega_C \tau)^2 & \text{for } \Omega_C \tau < 1, \\ const & \text{for } \Omega_C \tau > 1, \end{cases} \tag{14.3.26}$$

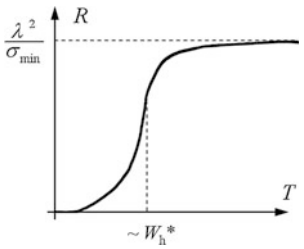

Fig. 14.5 The resistivity $R(T)$ in the two-band model with one narrow band in 3D [40–42, 54, 59]

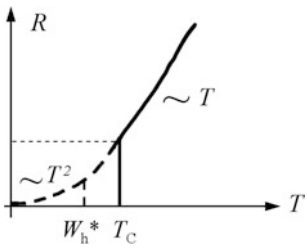

Fig. 14.6 Possible resistivity characteristics $R(T)$ in superconductive materials with a hidden heavy band for $W_h^* < T_C$ (W_h^* is an effective width of a heavy band) [40–42, 54]

where Ω_C is the cyclotron frequency. In the crossover region $\Omega_C\tau \sim 1$ (usually τ is the scattering time of electrons on impurities) the magnetoresistance mimics linear behavior in Ω_C. It then follows that for $T > W_h^*$, heavy electrons are marginal but light electrons are not. The natural question arises whether it is possible to make light electrons also marginal and as a result to obtain the resistivity characteristics for which $R(T) \sim T$ is marginal for $T > W_h^*$, but $R(T) \sim T^2$ for $T < W_h^*$. Such resistivity characteristics could serve as an alternative scenario for the explanation of the normal properties in optimally doped or slightly overdoped high-T_C materials if we assume the existence of a hidden heavy band with a bandwidth smaller than superconducting critical temperature T_C: $W_h^* < T_C$ (see Fig. 14.6).

To obtain the Fermi-liquid behavior $R(T) \sim T^2$ at low temperatures we should then suppress SC by a large magnetic field H to low critical temperatures $T_C(H) < W_h^*$.

14.4 Weak-Localization Corrections in the 2D Case

The tendency towards marginalization of the light component manifests itself in the 2D case. We know that logarithmic corrections [47, 48] to the classical Drude formula for conductivity occur in 2D due to weak localization effects (connected with quantum–mechanical backward scattering of electrons on impurities ensemble). But according to our ideology heavy particles play the role of impurities for scattering of light particles on them. That is why the correct expression for the conductivity of the light band σ_L in the absence of spin-orbital coupling is given by:

$$\sigma_L^{loc} = \frac{\sigma_{\min}}{f_0^2}\left[1 - f_0^2 \ln\frac{\tau_\varphi}{\tau}\right], \tag{14.4.1}$$

where, according to the weak-localization theory in 2D, τ is the elastic time and τ_φ is the inelastic (decoherence) time connected with the Ψ-function phase-memory breaking. In our case:

$$\tau = \tau_{ei} = \tau_{Lh}, \quad \text{while } \tau_\varphi = \tau_{ee} = \tau_{LL}, \text{ and } \tau_{LL}, \gg \tau_{Lh}, \tag{14.4.2}$$

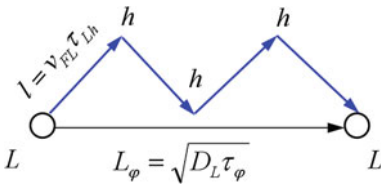

Fig. 14.7 Multiple scatterings of a light particle on heavy ones in the time interval between the scattering of a light particle on another light particle. L_φ is the diffusive length, l is the elastic length, D_L and v_FL are the diffusion coefficient and the Fermi-velocity for light electrons, and τ_Lh and τ_φ are the elastic time for the scattering of light electrons on heavy ones and the inelastic (decoherence) time [40–42, 49, 54, 59]

where τ_ei and τ_ee are the times associated with the scattering of electrons on impurities and other electrons, respectively. Hence, between two scatterings of a light particle on another light one, it many times scatters on heavy particles (see Fig. 14.7).

14.4.1 Altshuler-Aronov Effect

As a result, the motion of light particles becomes much slower (also of the diffusive type) and two characteristic lengths appear in the theory: the elastic length

$$l = v_{FL}\tau_{Lh}, \tag{14.4.3}$$

and the diffusive length:

$$L_\varphi = \sqrt{D_L\tau_\varphi}, \tag{14.4.4}$$

where D_L is the diffusion coefficient and v_FL is the Fermi-velocity for light electrons. That is why in a more rigorous theory according to [48, 49, 54] we should replace the inverse scattering time $1/\tau_{LL}$ in 2D:

$$\frac{1}{\tau_{LL}(\varepsilon)} \sim \frac{f_0^2}{m_L}\int_0^\varepsilon d\omega \int_0^\omega d\varepsilon' \int_0^\infty \frac{q\,dq}{(v_{FL}q)^2} = f_0^2\frac{\varepsilon^2}{W_L}\ln\frac{W_L}{\varepsilon} \tag{14.4.5}$$

by the renormalized quantity $1/\tilde{\tau}_{LL}$:

$$\frac{1}{\tilde{\tau}_{LL}(\varepsilon)} \sim \frac{f_0^2}{m_L}\int_0^\varepsilon d\omega \int_0^\omega d\varepsilon' \int_0^\infty \frac{q\,dq}{(i\varepsilon' + D_L q^2)^2}, \tag{14.4.6}$$

where f_0 is the 2D gas-parameter. In fact we replace $v_\mathrm{FL}q$ with the pole of the diffusive type $i\varepsilon' + D_\mathrm{L}\,q^2$. Hence the characteristic wave-vectors in the evaluation

of $\tilde{\tau}_{LL}$ are $q \sim \sqrt{\varepsilon'/D_L}$in (14.4.6), where ε' is an energy variable. Thus Altshuler-Aronov effect (originally proposed for electron–electron scattering in dirty metal) yields in 2D [48, 49]:

$$\frac{1}{\tilde{\tau}_{LL}(\varepsilon)} = f_0^2 \frac{\varepsilon}{N_L^{2D}(0) D_L}, \tag{14.4.7}$$

where $N_{\mathrm{L}}{}^{2\mathrm{D}}(0) = m_{\mathrm{L}}/2\pi$ is the 2D density of states for light electrons. For the diffusion coefficient we can use the estimate:

$$D_L = v_{FL}^2 \tau_{Lh}. \tag{14.4.8}$$

Hence, having in mind that according to (14.3.21) the inverse scattering time is $\frac{1}{\tau_{Lh}(\varepsilon)} = f_0^2 W_h \frac{m_h}{m_L} \approx f_0^2 W_L$ (where we replaced λ^2 in (14.3.9) by $f_0{}^2$) we obtain:

$$\frac{1}{\tilde{\tau}_{LL}(\varepsilon)} \sim \frac{f_0^2 f_0^2 W_L \varepsilon}{m_L v_{FL}^2/\pi} \sim f_0^4 \varepsilon. \tag{14.4.9}$$

Therefore $1/\tilde{\tau}_{LL}$ also becomes marginal for $\varepsilon \sim T$. For logarithmic corrections to the conductivity of the light band we have:

$$\frac{\tau_\varphi}{\tau} = \frac{\tilde{\tau}_{LL}}{\tau_{Lh}} = \frac{W_L}{f_0^2 T} \gg 1, \tag{14.4.10}$$

and thus

$$\sigma_L^{loc} = \frac{\sigma_{\min}}{f_0^2} \left[1 - f_0^2 \ln \frac{W_L}{f_0^2 T} \right]. \tag{14.4.11}$$

For $f_0{}^2 T \sim W_{\mathrm{h}}$ we get $\ln \frac{W_L}{f_0^2 T} \sim \ln \frac{W_L}{W_h}$ and

$$Z_h \sim \frac{\sigma_L^{loc}}{\sigma_L} = 1 - f_0^2 \ln \frac{W_L}{W_h}. \tag{14.4.12}$$

Therefore, for $f_0{}^2 T \sim W_{\mathrm{h}}$ an enhancement of the Z-factor of the heavy particle due to Electron-polaron effect and the additional localization of light particles due to Altshuler-Aronov effect are governed by unique parameter $f_0{}^2 \ln(m_{\mathrm{h}}/m_{\mathrm{L}})$ in 2D [40–42, 49, 59].

14.4.2 *Justification of the Expression for Localization Corrections in 2D with an Account of the Recoil Energy*

In principle the impurities (heavy particles) are mobile and have some recoil energy. That is why the formula $\frac{\sigma_L^{loc}}{\sigma_L} = 1 - f_0^2 \ln \frac{W_L}{f_0^2 T}$ should be justified (at least

regarding the temperature exponent under logarithm T or T^{α}). For the justification of this expression we need to estimate the loss of energy by one light particle before it collides with another light particle. The number of collisions with heavy particles between the scattering of a light particle on another light one is L_{φ}/l. The maximal loss of energy in one collision is W_h^*. The total loss is $W_h^* \frac{L_{\phi}}{l} = W_h^* \sqrt{\frac{W_L}{f_0^2 T}}$. The energy of light particle itself is T. It means that for $W_h^* \sqrt{\frac{W_L}{T}} < T$ or equivalently for

$$T > W_h^* \left(\frac{W_L}{f_0^2 W_h^*} \right)^{1/3} \tag{14.4.13}$$

the loss of energy is small and heavy particles can be regarded as immobile impurities. Hence the exponent α in T^{α} under logarithm is 1.

14.4.3 Resistivity in the 2D Case: Maximum and Localization Tail

Qualitatively the resistivity behaves in 2D as:

$$R = \frac{f_0^2}{\sigma_{\min}} \frac{1}{1 - f_0^2 \ln \frac{W_L}{f_0^2 T} + \left(\frac{W_h^*}{T} \right)^2}. \tag{14.4.14}$$

It has a maximum at $T_{\max} \sim W_h^*/f_0$ and a localization tail at higher temperatures (see Fig 14.8 and [40–42, 49, 59]).

It would be very interesting to find the magnetoresistance in the 2D or layered case in a two-band model with one narrow band for a strong quantizing magnetic field H oriented perpendicular to the layers [40–42]. Note that such behavior of resistivity (with a maximum and then with a localization tail) could be relevant for some mixed valence systems possibly including optimally doped layered CMR-systems (layered manganites for example). A similar behavior with a metallic low temperature dependence of the resistivity for $T < 130$ K and the

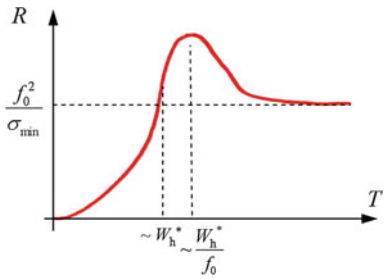

Fig. 14.8 Resistivity $R(T)$ in the 2D case for the two-band model with one narrow band. The resistivity exhibits a maximum and localization tail at higher temperatures $T > W_h^*$[40–42, 49, 59]

insulating high-temperature dependence was also observed in layered intermetallic alloys Gd_5Ge_4, where the authors of [51] assume the existence of a strongly correlated narrow band at low temperatures.

Concluding this chapter, note that we search for non-Fermi liquid behavior in basic one-band and two-band models in 3D and 2D case. We found very interesting corrections to the Galitskii-Bloom [5, 6] Fermi-gas expansions both on the lattice and without it, at $T \to 0$ and at higher temperatures. But globally Landau Fermi-liquid picture is not destroyed at low electron densities and low temperatures in one-band and two-band 3D and 2D models.

References

1. Lifshitz, E.M., Pitaevskii, L.P.: Statistical Physics, Part 2. Pergamon, New York (1980)
2. Haldane, F.D.M.: J. Phys. C: Solid State Phys. **14**, 2585 (1981)
3. Emery, V.J.: Highly Conducting one dimensional solids. In: Devreese, J. (eds.) Plenum, New York (1979)
4. Varma, C.M., Littlewood, P.B., Schmitt-Rink, S., Abrahams, E., Ruchenstein, A.E.: Phys. Rev. Lett. **63**, 1996 (1989)
5. Galitskii, V.M.: Sov. Phys. JETP **7**, 104 (1958)
6. Bloom, P.: Phys. Rev. B **12**, 125 (1975)
7. Abrikosov, A.A., Gor'kov, L.P., Dzyaloshinskii, I.E.: Quantum Field Theoretical Methods in Statistical Physics. Pergamon, New York (1965)
8. Khodel', V.A., Shaginyan, V.R.: JETP Lett. **51**, 488 (1990)
9. Sólyom, J.: Adv. Phys. **28**, 201 (1979)
10. Anderson, P.W.: Phys. Rev. Lett. **64**, 1839 (1990)
11. Anderson, P.W.: Phys. Rev. Lett. **65**, 2306 (1990)
12. Anderson, P.W.: Phys. Rev. Lett. **66**, 3226 (1991)
13. Hubbard, J.: Proc. Roy. Soc. London **A276**, 238 (1963)
14. Kanamori, J.: Progr. Theor. Phys. **30**, 275 (1963)
15. Kagan, M.Yu., Val'kov, V.V., Wölfle, P.: Sov. Low Temp. Phys. **37**, 834–839 (2011)
16. Stamp, P.C.E.: Jour. Phys. (France) 3, 625 (1993) (N.V. Prokof'ev, unpublished)
17. Baranov, M.A., Kagan, M.Yu., Mar'enko, M.S.: JETP Lett. **58**, 710 (1993)
18. Anderson, P.W.: Phys. Rev. Lett. **18**, 1049 (1958)
19. Engelbrecht, J.R., Randeria, M.: Phys. Rev. Lett. **65**, 1032 (1990)
20. Engelbrecht, J.R., Randeria, M.: Phys. Rev. Lett. **66**, 3225 (1991)
21. Engelbrecht, J.R., Randeria, M.: Phys. Rev. B **45**, 12419 (1992)
22. Fukuyama, H., Narikiyo, O., Hasegawa, Y.: J. Phys. Soc. Jpn. **60**, 372 (1991)
23. Fukuyama, H., Narikiyo, O., Hasegawa, Y.: J. Phys. Soc. Jpn. **60**, 2013 (1991)
24. Fabrizio, M., Tossatti, E., Parola, A.: Doctoral Thesis (M. Fabrizio) (1992)
25. Afanas'ev, A.M., Kagan, M.Yu.: Sov. Phys. JETP **16**, 1035 (1962)
26. Chubukov, A.V., Maslov, D.L., Gangadharaiah, S., Glazman, L.I.: Phys. Rev. Lett. **95**, 026402 (2005)
27. Gangadharaiah, S., Maslov, D.L., Chubukov, A.V., Glazman, L.I.: Phys. Rev. Lett. **94**, 156407 (2005)
28. Chubukov, A.V., Maslov, D.L.: Phys. Rev. B **81**, 245102 (2010)
29. Coffey, D., Bedell, K.S.: Phys. Rev. Lett. **71**, 1043 (1993)
30. Higley, R.H., Sprague, D.T., Hallock, R.B.: Phys. Rev. Lett. **63**, 2570 (1989)
31. Alikacem, N., Sprague, D.T., Hallock, R.B.: Phys. Rev. Lett. **67**, 2501 (1991)
32. Lusher, C.P., Cowan, B.P., Saunders, J.: Phys. Rev. Lett. **67**, 2497 (1991)

33. Godfrin, H.: Private communication to the author
34. Lifshitz, E.M., Pitaevskii, L.P.: Physical Kinetics, vol. 10 (Course of Theoretical Physics). Butterworth-Heinemann, Oxford (1981)
35. Val'kov, V.V., Mitskan, V.A.: Sov. Phys. Met. Metallogr. **100**, 510 (2005)
36. Ando, T., Fowler, A.B., Stern, F.: Rev. Mod. Phys. **54**, 437 (1982)
37. Kagan, M.Yu., Fresard, R., Capezzali, M., Beck, H.: Phys. Rev. B **57**, 5995 (1998)
38. Kagan, M.Yu., Fresard, R., Capezzali, M., Beck, H.: Physica B **284–288**, 447 (2000)
39. Combescot, R., Leyronas, X., Kagan, M.Yu.: Phys. Rev. A **73**, 023618 (2006)
40. Kagan, M.Yu., Val'kov, V.V.: Sov. Low Temp. Phys. **37**, 69 (2011)
41. Kagan, M.Yu., Val'kov, V.V.: JETP **140**, 179 (2011)
42. Kagan, M.Yu., Val'kov, V.V.: A Lifetime in Magnetism and Superconductivity: a Tribute to Professor David Shoenberg. Cambridge Scientific Publishers, Cambridge (2011)
43. Fulde, P.: Electron Correlations in Molecules and Solids. Springer-Verlag, Berlin (1991)
44. Gutzwiller, M.C.: Phys. Rev. Lett. **10**, 159 (1963)
45. Vollhardt, D.: Rev. Mod. Phys. **56**, 99 (1984)
46. Vollhardt, D., Wölfle, P., Anderson, P.W.: Phys. Rev. B **35**, 6703 (1987)
47. Imry, Y.: Introduction to Mesoscopic Physics, 2nd edn. Oxford University Press, Oxford (2002)
48. Altshuler, B.L., Aronov A.G.: Electron–electron interactions in disordered systems. In: Efros, A.L., Pollack, M. (eds.) Modern Problems in Condensed Matter Systems, vol. 10, p. 1. North Holland, Amsterdam (1985)
49. Kagan, M.Yu., Aronov, A.G.: Czech. Jour. Phys. **46**, 2061 (1996)
50. Landau, L.D.: Phys. Ztshr. Sow. **10**, 154 (1936)
51. Levin, E.M., Pecharsky, V.K., Gschneidner Jr, K.R., Miller, G.J.: Phys. Rev. B **64**, 235103 (2001)
52. Abrikosov, A.A., Khalatnikov, I.M.: Sov. Phys. ZhETF **33**, 1154 (1957)
53. Hodges, C., Smith, H., Wilkins, J.W.: Phys. Rev. B **4**, 302 (1971)
54. Kagan, M.Yu.: Habilitation Thesis, Kapitza Institute, Moscow (1994)
55. Mott, N.F.: Metal-Insulator Transitions, Taylor and Francis, London (1974)
56. Mott, N.F., Davis, E.A.: Electronic Processes in Non-Crystalline Materials. Oxford University Press, USA (1979)
57. Kagan, Y., Prokof'ev, N.V.: Sov. Phys. ZhETF **93**, 356 (1987)
58. Kagan, Y., Prokof'ev, N.V.: Sov. Phys. ZhETF **90**, 2176 (1986)
59. Kagan, M.Yu., Val'kov, V.V.: Jour. Supercond. Novel Magn. **25**, 1379 (2012)

Chapter 15
Nanoscale Phase Separation in Complex Magnetic Oxides

Nanoscale phase-separation together with the anomalous (marginal) behavior of resistivity are among the most interesting normal properties of many strongly-correlated electron systems.

In this chapter we will consider another very interesting family of strongly-correlated electron systems, which is called manganites [1–3] or the systems with colossal magnetoresistance (CMR-systems) [4]. These systems have a lot of striking similarities with high-T_C superconductors (or cuprates) with respect to their crystalline and electronic structure especially in a layered class of manganites. They also exhibit rich phase-diagrams [5–12] with extended regions of nanoscale phase separation. In these regions we get ferromagnetic metallic droplets of the size of 10–1000 Å embedded into the insulating matrices of antiferromagnetic or paramagnetic type in close similarity with the physics of stripes in high-T_C superconductors [13–17]. The CMR-family is very promising for applications in magnetorecording technologies due to their anomalous transport properties and first of all due to the phenomena of colossal negative magnetoresistance (colossal up to 10^2–10^3 times decrease of resistivity in moderately strong magnetic fields 2–6 T).

15.1 Inhomogeneous States and Nanoscale Phase Separation in Complex Magnetic oxides. Similarities with Cuprates

Manganites, the Mn-based magnetic oxide materials typified by $LaMnO_3$, have been under investigation for more than 50 years [1–3] but attracted particular attention after the discovery in 1994 of the colossal magnetoresistance (CMR) effect first obtained for Ca-doped $LaMnO_3$ film [4]. There is currently considerable review literature on these materials (see e.g., [5–12]) and it is worthwhile noting that in [11] a bibliography of more than 600 references is given. This large body of the original and review literature is due to in part to the potential technological applications of

M. Yu. Kagan, *Modern Trends in Superconductivity and Superfluidity*,
Lecture Notes in Physics 874, DOI: 10.1007/978-94-007-6961-8_15,

colossal magnetoresistance, but also reflects the manganites suitability for studying the physics of strongly-correlated systems. In particular, the interaction of spin, charge and orbital degrees of freedom in these materials as well as their phase diagrams are of interest. On the other hand, the possibility of various types of inhomogeneous charge and spin states in manganites-lattice and magnetic polarons, droplets and stripes structures etc.,—is currently receiving special attention.

Similar phenomena occur in many strongly correlated systems where the potential energy of the interaction of electrons exceeds their kinetic energy. In particular (as we mentioned in the introduction), such phenomena are being widely discussed in connection with high-T_C superconductors [13–17]. Of earlier examples, ferromagnetic (FM) droplets (ferrons) in antiferromagnetic (AFM) state at low doping levels [18–21] and ferromagnetic spin-polarons in a paramagnet (PM) [22, 23] are particularly notable. A string (linear track of frustrated spins) created by a hole passing through an AFM insulator [24, 25] as well as paramagnetic polarons (spin-bags [26]) should also be mentioned in connection with mechanisms of SC in underdoped cuprates [27–29] and Chap. 13. All these phenomena are examples of the so-called electron nanoscale phase separation effect, which results from individual charge carriers changing their local electron environment (it is favorable for such regions to be as far apart as possible to minimize the Coulomb energy). Along with this small-scale (nanoscale) phase separation, manganites, as many other materials showing first-order transitions (between the AFM and FM-phases, for example), display yet another type of phase separation, related to the fact that there is a large region of coexistence for various phases in the material. One example of such large-scale separation is the formation of relatively large FM-droplets (100–1000 Å in size) in an AFM-matrix [30, 31].

A noteworthy feature of manganites is the strong interaction between the electronic and lattice subsystems due to the fact that Mn^{3+} is a Jahn–Teller ion [32] and therefore any phase-separation gives rise to elastic lattice distortions which can be detected experimentally. Another characteristic feature is charge ordering (CO), i.e., a regular (often checkerboard) arrangement of Mn^{3+} and Mn^{4+} ions, when the material in fact obtains an additional lattice period and hence acquires a superstructure. Note that charge ordering usually appears at quarter-filling that is at densities close to ½. Along with a superstructure, nontrivial spin and orbital ordering may result from charge ordering. An example is the well-known zigzag magnetic structure (referred to usually as CE) in compounds of the type $Pr_{0.5}Ca_{0.5}MnO_3$ [33, 34], in which charge ordering is accompanied by the formation of zigzag magnetic chains. The interaction of spin, charge, and orbital degrees of freedom can also lead to stripe [35] (rather than droplet) structures at high concentrations of an alkaline-earth element (Ca, Ba, Sr). Because of the strong interaction with the lattice, it turns out that in manganites (as opposed to HTSC systems) such structures are not dynamic but static and are observable with electron diffraction and X-ray small-angle scattering techniques.

In this chapter, we will focus on the small-scale phase separation, in which the microscopic nature of charge redistribution manifests itself most clearly. We will consider free [36] and bound [37, 38] FM-polarons inside AFM, PM and CO-

matrices [39] (including FM-polarons on frustrated AFM-lattices [40]) as well as so-called orbital ferrons [41] inside orbitally ordered matrix [42]. The basic models which we use for free and bound FM-polarons is ferromagnetic Kondo lattice model or double exchange model of de Gennes [43] (with or without Coulomb interactions). While for orbital ferrons we use the degenerate two-band Hubbard model (considered with respect to KL-superconductivity and anomalous resistivity in Chaps.10 and 14) which is reduced to the orbital t–J model [44].

Note that the effects of phase-separation on the transport properties are considered in Chap. 16.

15.2 Crystal Structure: Electronic and Transport Properties of Manganites

In this section we will study crystal structure, phase diagram and basic electronic and transport properties of manganites including the CMR-effect in this family of materials.

Ideal crystal structure of 3D manganites $Ln_{1-x}A_xMnO_3$ (Ln = La, Pr, Nd, Sm; A = Ca, Sr, Ba) corresponds to cubic cell (perovskite structure) see Fig. 15.1. Real structure is slightly orthorombically distorted due to Jahn–Teller (JT) effect [32].

15.2.1 Overall Phase-Diagram of Manganites

Overall phase-diagram of typical manganites ($La_{1-x}Ca_xMnO_3$) is presented on Fig. 15.2. At low doping levels $0.02 < x < 0.16$ and low temperatures we have phase-separation (PS) on metallic FM droplets inside AFM insulating matrix [8, 18–21, 36]. At optimal doping concentration $x_{opt} = 0.25$ we have FM-metal for $T < T_C$—Curie temperature, which exhibits phenomena of colossal negative magnetoresistance (CMR). For these concentrations we have two-band mixed-valence

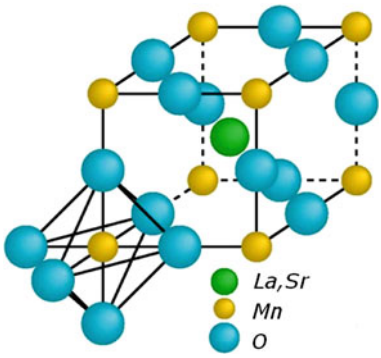

Fig. 15.1 Crystal structure of ideal 3D manganites $Ln_{1-x}A_xMnO_3$ (Ln = La, Pr, Nd, Sm; A = Ca, Sr, Ba)

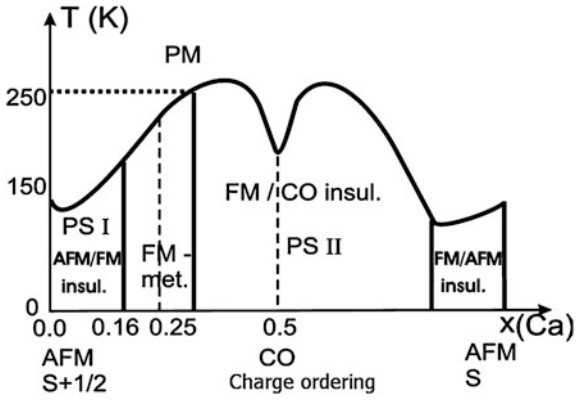

Fig. 15.2 Overall phase-diagram of typical 3D perovskite manganite $La_{1-x}Ca_xMnO_3$, x is a hole concentration

situation (see Chap. 16). At $x = 0.5$ (quarter-filling) and low temperatures we have checkerboard charge ordering (CO). Around $x = 0.5$ we have extended region of PS II on metallic FM droplets inside CO insulating matrix [39]. For $x \leq x_C = 0.16$ we have also the beautiful physics of orbital ordering [42], described by degenerate two-band Hubbard model with metallic orbital polarons inside insulating AFM orbital matrix [41]. Finally at very small doping levels $x \sim$ (1–2) % and low temperatures we have magnetic polarons bound by Coulomb interaction on Ca accepting centers with extended coat of slowly decreasing tails of spin-distortions. These bound magnetic polarons were first predicted by de Gennes [43] and obtained in a simple model in [37]. Effectively they behave as a magnetic impurity.

For $x = 0$ and $x = 1$ we have ideal AFM ordering for spins $S + ½$ and spins S ($S = 3/2$), respectively. Close to $x = 1$ we have again PS on FM droplets inside AFM insulating matrix at low temperatures. At high temperatures and low doping levels ($x \ll 1$ and $T > T_N$—Neel temperature) and at $x \sim x_{opt}$ and $T > T_C$ temperature ferrons (FM-droplets) inside insulating PM matrix [22, 23] are formed.

15.2.2 Resistivity at Optimal Concentrations

At optimal concentration $x_{opt} = 0.25$ and $T_C = 250$ K we have simultaneously FM → PM transition coinciding with metal–insulator transition (see Fig. 15.3.).

For low temperatures $T < T_C$:

$$\rho \sim \rho_0 + AT^{\beta}, \tag{15.2.1}$$

where $\beta \sim 2.5$, and $\frac{d\rho}{dT} > 0$ corresponds to metallic behavior.

For high temperatures $T > T_C$:

$$\rho \sim Be^{A/T}, \tag{15.2.2}$$

and $\frac{d\rho}{dT} < 0$ corresponds to insulating thermoactivative behavior.

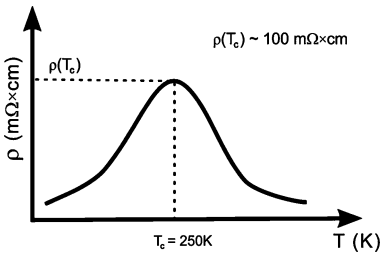

Fig. 15.3 Resistivity at optimal doping concentrations. At maximum (for $T_C = 250$ K) resistivity $\rho(T_C) \sim 100$ mΩ · cm

This curve can be explained in two ways: by electron tunneling from one FM-cluster (droplet) to a neighboring one via insulating barrier (see Chap. 16) or possibly in the framework of the two-band model, especially for layered quasi 2D manganites (see Chap. 14).

15.2.3 Colossal Magnetoresistance

At optimal concentration $x_{opt} = 0.25$ we have phenomena of colossal magneto-resistance [4], namely resistivity strongly decreases in the presence of moderately strong magnetic fields $H \sim$ (2–4) T (see Fig. 15.4).

Magnetoresistance is defined as (see [8] for example):

$$(MR) = \frac{\Delta R}{R(H)} = \frac{R(H) - R(0)}{R(H)} \approx -\frac{R(0)}{R(H)} \sim -(10^2 \div 10^3) \qquad (15.2.3)$$

(colossal negative magnetoresistance).

It is interesting that for optimal concentration $x_{opt} = 0.25$ magnetization behaves as follows (see Fig. 15.5).

15.2.4 Electronic Structure of Manganites

Essential for electronic structure of manganites are 5 *d*-orbitals of Mn-ions splitted by the crystalline field on 3 localized t_{2g}-orbitals d_{xy}, d_{xz}, d_{yz} and 2 conductive e_g-

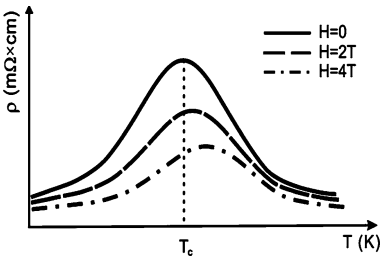

Fig. 15.4 Strong decrease of resistivity in the presence of magnetic field in optimally doped manganites. *Solid line* corresponds to the absence of magnetic field ($H = 0$), *dashed line* for $H = 2$ T and *dashed-dotted line* for $H = 4$ T

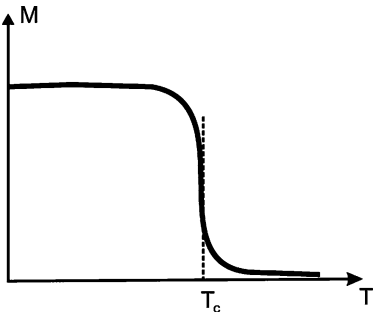

Fig. 15.5 Temperature dependence of magnetization in manganites at optimal concentration $x_{opt} = 0.25$

orbitals $d_{3z^2-r^2}, d_{x^2-y^2}$. On localized t_{2g}-orbitals according to Hund's rule a local spin $S_{loc} = 3/2$ is formed.

Manganites are in a mixed valence situation, so Mn^{3+} and Mn^{4+}-ions are present. For Mn^{4+} ion both conductive orbitals e_g are empty (see Fig. 15.6).

In the same time for Mn^{3+} ion one conductive e_g-orbital is filled and one is empty (see Fig. 15.7). Note that e_g-conductive orbitals are additionally splitted by Jahn–Teller effect in Mn^{3+} ion.

This splitting is due to the different distortion of $d_{x^2-y^2}$-octahedra in xy-plane and $d_{3z^2-r^2}$-octahedra along z-axis (see Fig. 15.8). As a result Jahn–Teller gap

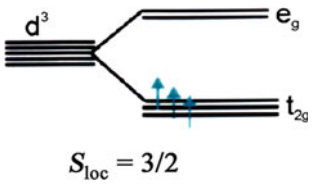

Fig. 15.6 Electronic structure of d-orbitals for Mn^{4+} ion

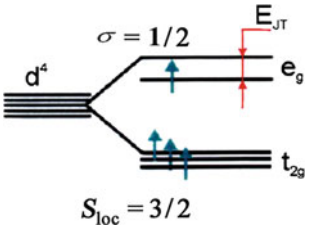

Fig. 15.7 Electronic structure of Jahn–Teller Mn^{3+} ion

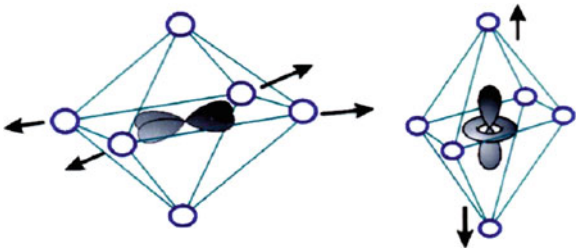

Fig. 15.8 Different distortion of $d_{x^2-y^2}$-octahedra in xy-plane and $d_{3z^2-r^2}$-octahedra along z-axis

(E_{JT}) appears. We assume that E_{JT} is large, so for low doping concentration $x \ll x_C = 0.16$ only one conduction band is occupied. Note that close to $x_C = 0.16$ we have two occupied conductive bands and the beautiful physics of orbital ordering. Note also that for low doping a spin of conductivity electron $\vec{\sigma}$ is coupled ferromagnetically (oriented parallel) to the local spin $S_{loc} = 3/2$.

15.3 The Minimal Theoretical Model for Manganites

The basic theoretical model for manganites is FM Kondo-lattice model or double-exchange model firstly introduced by de Gennes in 1960 [43]. The Hamiltonian of the double-exchange model reads:

$$\hat{H} = -J_H \sum_i \vec{S}_i \vec{\sigma}_i - t \sum_{\langle ij \rangle \sigma} c^+_{i\sigma}\, c_{j\sigma} + J \sum_{\langle ij \rangle} \vec{S}_i \vec{S}_j, \tag{15.3.1}$$

where J_H is large Hund's type (FM) interaction between local spin $\vec{S}$ and spin of conductivity electron $\vec{\sigma}$ on site i, t—is hopping integral for conductivity electron and J is AFM (Heisenberg) exchange between local spins, $c^+_{i\sigma}$, $c_{j\sigma}$—are creation and annihilation operators for conductivity electron with spin-projection σ on sites i and j, respectively. For one conductive band we have the following hierarchy of parameters:

$$J_H S \gg t \gg JS^2. \tag{15.3.2}$$

For real manganites the typical values of the parameters: $J_H S \approx 1$ eV; $t \approx 0.3$ eV (the bandwidth is narrowed by electron–phonon polaron effect); $JS^2 \approx 0.001$ eV. Double occupancy is prohibited in (15.3.1) by large Hund's term, so it is not necessary to add Hubbard repulsion term $U \sum_i n_{i\uparrow} n_{i\downarrow}$ to Hamiltonian (15.3.1). In fact we can insert projection operators in the kinetic term in (15.3.1) and write $-t \sum_{<ij>\sigma} P c^+_{i\sigma} c_{j\sigma} P$.

15.3.1 Homogeneous Canting for Small Densities

In classical physics conductivity electron can hop freely in FM surrounding of local spins, but cannot hop in AFM surrounding. Thus the only possibility for conductivity electron is to cant the local spins (belonging to different sublattices) when it hops from one site to a neighboring one (see Fig. 15.9).

Note that for large Hund's coupling $J_H > W$ (W is a bandwidth for conductivity electrons) the term $-J_H \sum_i \vec{S}_i \vec{\sigma}_i$ corresponds to a minimal energy for $\vec{S}_i \| \vec{\sigma}_i$. Correspondingly the total spin on site i, $\left|\vec{S}_{tot}\right| = S + 1/2$.

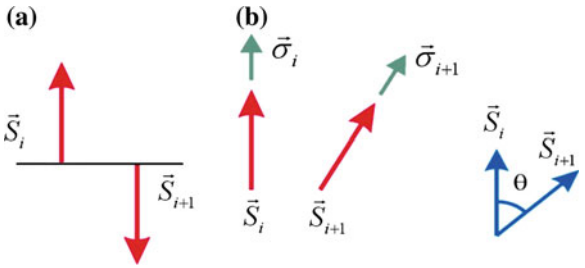

Fig. 15.9 Ideal AFM-lattice of local spins. **a** With local spins $\vec{S}_i$ and $\vec{S}_{i+1}$ on neighboring sites belonging to different sublattices. **b** The canted structure with the angle θ between neighboring local spins $\vec{S}_i$ and $\vec{S}_{i+1}$, which is created by conductivity electron hopping from site i, to a neighboring site $i + 1$

An important point is that Ψ-function of conduction electrons has a spinor character. That is why electron hopping results in an effective rotation of the components of the Ψ-function on the angle $\theta/2$ (where θ is the canting angle between sublattices). Thus an effective hopping integral for the electron in the surrounding of canted local spins reads [43, 45]:

$$t_{eff} = t\cos(\theta/2). \tag{15.3.3}$$

15.3.2 Canted State Instability

An energy of a classical canted state of de Gennes reads:

$$E = -zt\cos(\theta/2)\,n + \frac{zJS^2}{2}\cos\theta \tag{15.3.4}$$

where z is the number of nearest-neighbors, n is a concentration of conductivity electrons (for $La_{1-x}Ca_xMnO_3$: $n = 1 - x$, where x is hole doping). In (15.3.4) first term describes the decrease of kinetic energy and second one the increase in the interaction energy between the local spins. If we minimize this energy with respect to $\cos(\theta/2)$ we get:

$$\frac{dE}{d\cos(\theta/2)} = 0, \quad \text{and} \quad \cos(\theta/2) = \frac{t}{2JS^2}n, \tag{15.3.5}$$

thus an optimal $\cos(\theta/2)$ depends linearly upon electron density. Correspondingly an optimal energy of a homogeneous canted state:

$$E = -\frac{zt^2n^2}{4JS^2} - \frac{zJS^2}{2} \tag{15.3.6}$$

However it is easy to note that a canted state has a negative compressibility [36]:

$$\kappa^{-1} = \frac{d^2E}{dn^2} = -\frac{zt^2}{2JS^2} < 0. \tag{15.3.7}$$

Negative compressibility reflects an instability of a homogeneous canted state towards phase-separation.

15.3.3 Small FM-Polarons Inside AFM-Matrix

The most energetically beneficial type of phase-separation corresponds to the creation of small FM-polarons (ferrons) inside AFM-matrix [18–21]. The energy of this phase-separated state reads for spherical magnetic polaron in 3D:

$$E_{pol} = -tn(z - \frac{\pi^2 d^2}{R^2}) + \frac{zJS^2}{2}\frac{4}{3}\pi\left(\frac{R}{d}\right)^3 n - \frac{zJS^2}{2}\left[1 - \frac{4}{3}\pi\left(\frac{R}{d}\right)^3 n\right], \tag{15.3.8}$$

where $\Omega = \frac{4}{3}\pi\left(\frac{R}{d}\right)^3$ is a volume of a spherical polaron (spherical FM-droplet) in isotropic 3D case,—tzn is a bottom of the band in an infinite FM-cluster (where electron can hop freely), $tn\frac{\pi^2 d^2}{R^2}$ is a delocalization kinetic energy of conductivity electron in a spherical potential well of the radius R (see Fig. 15.10).

It can be obtained from boundary condition $\Psi(r = R) = 0$ for the Ψ-function $\Psi \sim \sin(kr)$ which corresponds to the deepest bound state of a conductivity electron in a spherical potential well of the width R (self-trapping of conductivity electron in FM-droplet with a radius R).

The second term in (15.3.8) corresponds to the loss in AFM exchange interaction energy of local spins inside the ferrons, while the third term describes AFM exchange interaction energy between the local spins in the region which are free from FM-polarons (see Fig. 15.11).

Minimization of a polaron energy (15.3.8) with respect to the polaronic radius R yields in the 3D case:

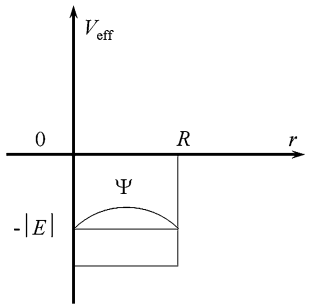

Fig. 15.10 The spatial extension of the conductivity electron Ψ-function corresponding to the deepest bound state in a spherical potential well with a width equal to the radius of the polaron R

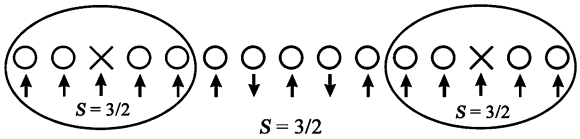

Fig. 15.11 Self-trapping of conductivity electron in a spherical droplet of radius R for small density n of conductivity electrons. The local spins $S = 3/2$ inside the droplets are oriented ferromagnetically. Outside the droplets there are no conductivity electrons (charge carriers) while the local spins $S = 3/2$ are oriented antiferromagnetically [8, 19–21]

$$\frac{dE_{pol}}{dR} = 0 \text{ and } \frac{R_{pol}}{d} = \left(\frac{\pi t}{2zJS^2}\right)^{1/5}. \tag{15.3.9}$$

Correspondingly the optimal polaronic energy reads:

$$E_{pol} = -tzn + \frac{5}{3}\pi\, zn(\pi t)^{3/5}\left(2zJS^2\right)^{2/5} - \frac{zJS^2}{2}. \tag{15.3.10}$$

The canting angle $\theta = 0$ inside the ferron (FM-region) and $\theta = \pi$ (AFM-region) outside the ferron. The boundary of Mott-Nagaev-Kasuya ferrons [18–21] is rigid: an angle θ changes from 0 to π on a distance of the order of d. Note that for typical values of $t \sim 0.3$ eV and $JS^2 \sim 0.001$ eV the polaron radius $R \sim (2 \div 3)d \sim 10$ Å (has nanoscale dimensions), and the number of local spins inside the ferrons is $\frac{4}{3}\pi\left(\frac{R}{d}\right)^3 \sim 4 \cdot (2^3 \div 3^3) \sim (30 \div 100)$. Thus a FM-polaron is a bound state of one conductivity electron and $(30 \div 100)$ local spins. Such an object is very difficult to describe diagrammatically, so the only possible description is a variational one presented in this chapter.

Note also that we described nanoscale phase-separation at small electron density $n \ll 1$. In the opposite case of large electron density $n \to 1$, or correspondingly small hole doping $x = 1 - n \ll 1$, we have again the same nanoscale phase-separation on FM-droplets inside AFM-insulating matrix, but now the role of conductivity electron plays a hole. Thus effectively inside the ferrons we have one local spin $S = 3/2$ surrounding by total spins $S_{tot} = S + 1/2$ oriented ferromagnetically, while outside the ferron we have antiferromagnetically oriented total spins $S_{tot} = S + 1/2$ (see Fig. 15.12). This structure is totally equivalent to that in the t–J model [72] where local Kondo-singlets or Zhang-Rice singlets are formed

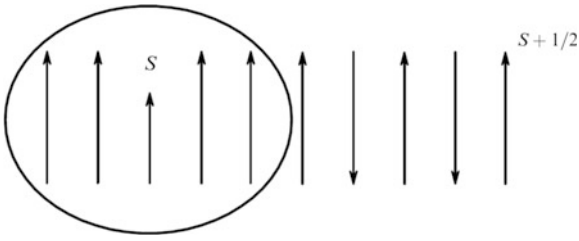

Fig. 15.12 Structure of the phase-separated state at the electron densities $n \to 1$ (at the small doping level $x = 1 - n \ll 1$) [8]

by AFM Kondo-interaction J_K between spin of conductivity electron $\sigma = 1/2$ and local spin $S = 1/2$. Here we have FM interaction J_H between local spin $S = 3/2$ and conduction electron spin $\sigma = 1/2$, which leads to the formation of $S_{tot} = 2$ in the strong-coupling case. Note that on the overall phase-diagram of hole-doped manganites $La_{1-x}Ca_xMnO_3$ on Fig. 15.2 the horizontal axis corresponds to hole doping x, and thus the PS I in the left corner of the phase-diagram (for $x \to 0$) correspond to the situation described by Fig. 15.12, while Fig. 15.11 correspond to the phase separation in the right corner of the phase-diagram for $x \to 1$ (n $\to$ 0).

15.3.4 Quantum Canting

In Sect. 15.3.2 we considered classical canted state of de Gennes and proved its instability with respect to nanoscale phase-separation on small FM-polarons inside AFM-matrix (Sect. 15.3.3).

In a more sophisticated quantum canting approach [18, 19, 36] there are two bands, instead of one, corresponding respectively to $S_{tot} = S + 1/2$, but $S^z_{tot} = S \pm 1/2]] >$.

Their spectra read (see Nagaev [18, 19]):

$$t_{\pm}(\theta) = \frac{t}{2S+1}\left[\sqrt{2S+1+S^2\cos^2\frac{\theta}{2}} \pm S\cos\frac{\theta}{2}\right], \tag{15.3.10}$$

where $t_+(\theta)$ corresponds to $S^z_{tot} = S \pm 1/2$ and $t_-(\theta)$—to $S^z_{tot} = S - 1/2$.

For $\theta \to 0$ (FM-case) $t_+ = t$, $t_- = \frac{t}{2S+1}$. For $\theta \to \pi$ (AFM-case) $t_+ = t_- = \frac{t}{\sqrt{2S+1}}$. That is an interesting result. While in classical picture a conductivity electron cannot hop in AFM-background, in quantum approach its effective hopping integral is proportional to $\frac{t}{\sqrt{S}}$. Moreover for $\theta = \pi$ there is a "string"-type of motion for conductivity electron between the two bands: on site i it forms $S_{tot} = S^z_{tot} = S + 1/2$ with local spin S, while on neighboring site $i + 1$: $S_{tot} = |S + 1/2|$ but $S^z_{tot} = S - 1/2$ and so on with alternating values of S^z_{tot} [47, 48]. Note that the classical one band canting of de Gennes corresponds for $S \gg 1$ to the region of small angles where $S^2\cos^2(\theta/2) \gg 2S + 1$ and $t_+ \approx t\cos(\theta/2)$, while $t_- \to 0$.

15.3.5 Compromise Between Quantum Canting and Formation of FM-Polarons

An energy functional with the normalization condition for the Ψ-function of a polaronic state in the case of quantum canting reads for continuum model [46, 49, 50]:

$$F = -\int dV\left[t(\theta)\ \left(z|\Psi|^2 + \Psi^*\Delta\Psi\right) - zJS^2\cos^2\frac{\theta}{2} - \beta|\Psi|^2\right] \qquad (15.3.11)$$

with $t(\theta)$ given by (15.3.10) and β is Legendre multiplier $\left(\int dV|\Psi|^2 = 1\right)$, Δ is the Laplace operator, z is the number of the nearest neighbors. The minimization of F with respect to Ψ^* yields:

$$\frac{\delta F}{\delta\Psi^*} = 0:\ t(\theta)\,(2z\Psi + \Delta\Psi) + \Delta[t(\theta)\,\Psi] - 2\beta\,\Psi = 0. \qquad (15.3.12)$$

In the same time the minimization of F with respect to canting angle θ reads:

$$\frac{\delta F}{\delta\theta} = 0:\ \left[\left(z|\Psi|^2 + \Psi^*\Delta\Psi\right)\frac{d\,t(\theta)}{d\,\cos\theta/2} - 2zJS^2\cos\frac{\theta}{2}\right]\sin\frac{\theta}{2} = 0. \qquad (15.3.13)$$

15.3.5.1 Electronic Wave Function and the Dependence of the Canting Angle from the Radius

The normalized electronic wave function $\Psi(r)$ and the dependence of the canting angle from the radius r (function $\theta(r)$) were calculated in [49, 50] by the same numerical method which was proposed originally in [46] for 1D ferrons. The numerical results are presented on Fig. 15.13 for parameter $\alpha = t/JS^2 = 100$. Note that as we showed in Sect. 15.3.3 the polaronic radius $R_{\rm pol}$ given by (15.3.9) can be expressed in terms of α as $R_{pol} = d\left(\frac{\pi\alpha}{2z}\right)^{1/5}$ in 3D.

We see from Fig. 15.13 that a canting angle is essentially $\theta = 0$ for $r < 0.5R_{\rm pol}$ and then rather rapidly goes to π on the interval $0.5R_{\rm pol} \div 1.5R_{\rm pol}$.

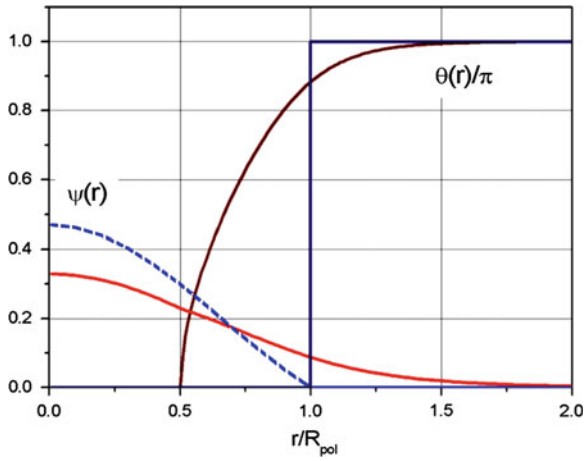

Fig. 15.13 Dependence of the electronic Ψ-function and the canting angle θ from dimensionless variable $r/R_{\rm pol}$ for $\alpha = t/JS^2 = 100$. *Solid line* for $\Psi(r)$ corresponds to quantum two-band canting, while the *dashed line* to classical one band canting [49, 50]

The Ψ-function is zero outside ferrons (for $r > R_{\mathrm{pol}}$) in the case of classical one-band canting. In quantum two-band canting it has rather rapidly decreasing tail for $r > R_{\mathrm{pol}}$.

15.3.5.2 Comparison of Nagaev-Mott and exact solution

According to (15.3.10) the optimal polaronic energy in terms of parameter α reads for Nagaev-Mott FM-polarons:

$$\frac{E_{N-M}}{t} = -z + \frac{5}{3} z\pi^2 \left(\frac{2z}{\pi\alpha}\right)^{2/5} - \frac{z}{2\alpha}. \tag{15.3.14}$$

In the same time the energy of AFM-string:

$$\frac{E_{AFM}}{t} = -\frac{z}{\sqrt{2S+1}}. \tag{15.3.15}$$

On Fig. 15.14 we present the comparison for the energy of Nagaev-Mott and exact numerical solution as functions of the parameter α.

From Fig. 15.14 we see that the self-trapped FM-polaron state is beneficial for $\alpha > \alpha_C \approx 75$ (for $S = 3/2$). A bound state disappears and conductivity electron moves freely (a string type of motion) through AFM-media for $\alpha < \alpha_C$. Here the energy does not depend upon α in agreement with (15.3.15). Note that for most manganite families $\alpha > \alpha_C$, and FM-polarons are essentially beneficial even in a picture of the two-band quantum canting.

Note that in cuprates $t/J \sim 3$ and $S = ½$, so the parameter $\alpha \ll \alpha_C$. Hence the FM-polarons are usually not stabilized in high-T_C compounds. Instead of them we have AFM-string (string-oscillators) of Bulaevskii, Nagaev, Khomskii, Brinkman,

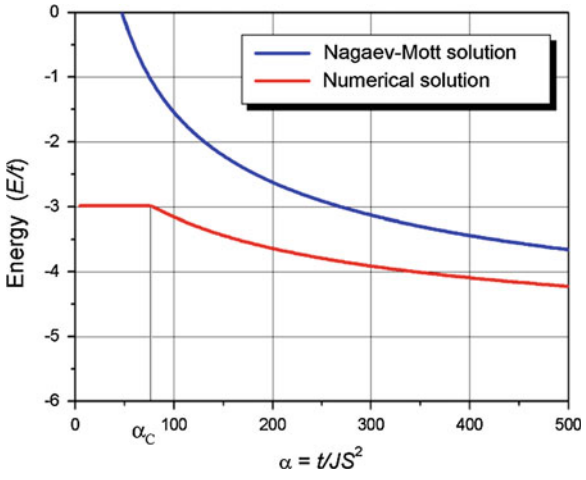

Fig. 15.14 Comparison of Nagaev-Mott solution for the FM-polarons and exact numerical solution for the reduced energy E/t as functions of the parameter $\alpha = t/JS^2$. Thick *solid line* corresponds to Nagaev-Mott solution, while thin *solid line* to exact numerical solution [49, 50]

Rice [24, 25]. They represent the linear trace of frustrated spins which accompany the hole when it moves in AFM-background. Thus in cuprates we have a physics of spin-charge confinement considered in Chap. 13 analogous to the confinement physics in quark-gluon plasma in quantum chromodynamics (QCD) [51–53].

15.4 Temperature Ferrons: FM-Polarons in a Layered Case

In this section we will consider two more types of FM-polarons, namely temperature ferrons and ferrons in a layered case.

15.4.1 Temperature Ferrons

At optimal concentration $x \sim x_{\text{opt}}$ and low temperatures $T < T_C$ (T_C is Curie temperature), as we already mentioned, we have a homogeneous state of FM-metal. However even in this range of concentrations at high temperatures $T > T_C$ there is again a phase-separation on FM-droplets, but now inside paramagnetic (PM) insulating matrix.

The radius of the droplet for the hierarchy of the parameters $zJS^2 \leq T_C < T < t$ can be defined from the minimization of the free-energy [22, 23]:

$$\Delta F = -tn\left(z - \frac{\pi^2 d^2}{R^2}\right) + T\ln(2S+1)\frac{4}{3}\pi\left(\frac{R}{d}\right)^3 n, \tag{15.4.1}$$

where the second term describes the reduction of the spin-entropy inside the ferron.

As a result after minimization of ΔF with respect to polaron radius R we get again in the 3D case [22, 23]:

$$R_{pol}^{T} \sim d\left(\frac{\pi t}{2T\ln(2S+1)}\right)^{1/5}. \tag{15.4.2}$$

Note that effectively polaronic radius of temperature ferrons is given by the same expression as the radius of Nagaev-Mott-Kasuya FM-polaron at $T = 0$ with the substitution of zJS^2 by $T\ln(2S + 1)$.

15.4.2 Polarons in a Layered Case

Besides cubic (perovskite type) of manganites such as $Ln_{1-x}Ca_xMnO_3$ there is another family which is typified as layered manganites with the general chemical

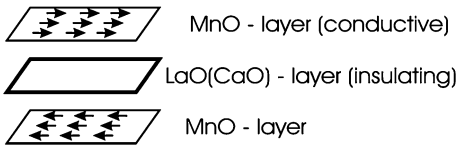

Fig. 15.15 The crystal and magnetic structure of layered manganites. There are conductive MnO-layers separated by insulating LaO(CaO)-layers in this family of manganites. Conductive layers are ferromagnetic but FM-moments of neighboring MnO layers are antiparallel (A1 magnetic structure) [8]

formula $(La, Ca)_{n+1}Mn_nO_{3n+1}$ ($n \geq 1$, for $n = 1$: $La_{2-x}Ca_xMnO_4$). The layered manganites strongly resemble high-T_C compounds. Electronic transport in them takes place in conductive MnO-layers which are separated by insulating LaO(-CaO)-layers (layers of charge reservoir) see Fig. 15.15.

In the layered case we again have the tendency towards nanoscale phase-separation on FM-polarons inside AFM-matrix. The most favorable in a layered case is an ellipsoidal shape of a ferron elongated in the direction parallel to conductive layers (see Fig. 15.16 and [8]).

The volume of the ellipsoidal ferron is given by [8]:

$$\Omega = \frac{4\pi}{3}\left(\frac{R_{\|}}{d}\right)^2 \frac{R_{\perp}}{d}. \tag{15.4.3}$$

Note that in the most general case of 3D anisotropic AFM—lattice the most beneficial shape of the ferrons again corresponds to the ellipsoid of rotation. Moreover its volume reads [40]:

$$\Omega = \frac{4\pi}{3}\left(\frac{\pi\, t_{eff}}{4\bar{J}S^2}\right)^{3/5}, \tag{15.4.4}$$

where effective hopping integral t_{eff} is given by geometrical average of the hopping integrals along the main axis:

$$t_{eff} = (t_x \cdot t_y \cdot t_z)^{1/3}. \tag{15.4.5}$$

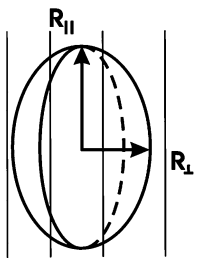

Fig. 15.16 FM-droplet of an ellipsoidal shape which is the most energetically beneficial in layered manganites. The droplet is elongated in the direction parallel to conductive FM layers of MnO ($R\| > R_{\perp}$) [8]

In the same time an effective AFM exchange integral $\overline{J}$ is given by the algebraic average (by the sum) of Heisenberg exchanges along the main axis:

$$\bar{J} = (J_x + J_y + J_z). \tag{15.4.6}$$

15.4.3 FM-Polarons on a Square-Lattice

On a square lattice in 2D the optimal shape of a ferron is a circle $\Omega = \pi\,(R/d)^2$ with a radius [38, 40]:

$$\frac{R_{pol}}{d} \sim \left(\frac{t\,\alpha_o^2}{8\pi JS^2}\right)^{1/4}, \tag{15.4.7}$$

where $\alpha_0 \approx 3\pi/4$ is a first zero of the Bessel function, $J_0(kR) = 0$ for $kR_0 = \alpha_0$. Note that in 2D $R_{\rm pol}/d \sim (t/JS^2)^{1/4}$ instead of $(t/JS^2)^{1/5}$ in the 3D-case [8].

For 2D anisotropic AFM-lattice the optimal shape of a ferron is an ellipse [40] with a volume:

$$\Omega = \pi\left(\frac{t_{eff}\,\alpha_0^2}{4\pi \bar{J}S^2}\right)^{1/2}, \tag{15.4.8}$$

where $t_{eff} = (t_x \cdot t_y)^{1/2}$ and $\bar{J} = (J_x + J_y)$.

Note that this type of nanoscale phase-separation is typical for a variety of quasi-2D (layered) cobaltites with low spin (a hole) in the center of a ferron surrounded (in analogy with the situation presented on Fig. 15.12) by high spin in case of a hole-doping.

15.4.4 FM-Polarons on a Triangular Lattice in 2D

Finally in the end of this Section let us consider frustrated lattices with AFM-interaction between neighboring local spins. On a frustrated triangular lattice for planar (2D) spin configuration the most beneficial shape of a ferron corresponds again to the circle with a volume [38]:

$$\frac{\Omega_{triangle}}{\Omega_{square}} = \left(\frac{4}{3}\right)^{1/2} = \left(\frac{m_{triangle}}{m_{square}}\right)^{1/2}, \tag{15.4.9}$$

measured in terms of the volume of a circular ferron on a square lattice. It is possible to show [38] that the ratio of volumes is connected with the square-root of the effective mass ratio on triangular and square lattices in (15.4.9).

15.5 Free and Bound Magnetic Polarons

For very small doping concentration conductivity electrons are bound to Ca (Sr) impurity centers. Hence ferrons are also localized in this case [37]. An appearance of the conductivity in Mn–O subsystem and delocalization transition in the system of ferrons correspond to generalized Mott criterion [21, 49]. Having in mind that at low temperatures the system becomes metallic for $x_{\text{met}} \sim 16$ % (at this concentration the FM-droplets start to overlap organizing an infinite metallic cluster), we conclude that ferrons are delocalized for $x_{\text{Mott}} < x < x_{\text{met}}$. For $x < x_{\text{Mott}}$ we have bound magnetic polarons [37]. We will show that, in contrast with free magnetic polarons, the bound polarons have a large intermediate region where a canting angle is changed gradually from almost 0 to almost π.

The existence of such ferrons (behaving effectively as magnetic impurities) was first assumed by de Gennes in 1960 in a seminal paper on the double exchange [43]. We can get them explicitly in a following simple model.

15.5.1 The Minimal Model for the Bound Magnetic Polarons

The bound magnetic polarons with extended coat of spin-distortions for $x \ll x_{\text{Mott}}$ are described by the Hamiltonian [37]:

$$\hat{H} = -J_H \sum_i \vec{S}_i \vec{\sigma}_i - t \sum_{\langle n,m\rangle \sigma} c^+_{n\sigma} c_{m\sigma} + J \sum_{\langle n,m\rangle} [\vec{S}_n \vec{S}_m + S^2]$$
$$- V_{imp} \sum_{n\sigma} \frac{c^+_{n\sigma} c_{n\sigma}}{|\vec{n} - \vec{n}_0|} - K \sum_n [(S_{nx}) - S^2] \qquad (15.5.1)$$

where for convenience we added the term $\sim JS^2$ in the Heisenberg exchange interaction. It is a double exchange model with Coulomb interaction between conductivity electrons and nonmagnetic Ca (Sr) donor impurity, as well as with one-site anisotropy. Ca (Sr) impurity is situated in the middle of some elementary lattice cells of the crystal (see Fig 15.17).

In Hamiltonian (15.5.1) we assume the following hierarchy of parameters [37]:

$$(J_{\text{H}} S \sim V_{\text{imp}}) \gg t \gg J S^2 \gg K, \qquad (15.5.2)$$

where V_{imp} is an amplitude of Coulomb attraction between impurity and conductivity electron, K—is a constant of one-site anisotropy, $\vec{S}_n = S\vec{e}_n$ is a classical

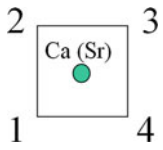

Fig. 15.17 Nonmagnetic Ca (Sr) impurity is situated in the middle of some elementary cells of the crystal

local spin, $\vec{n}$ is a unit vector, $\vec{\sigma} = 1/2\ c^{+}_{n\mu}\vec{\sigma}_{\mu\nu}c_{n\nu}$ is a spin of conductivity electron, $\vec{\sigma} = \{\sigma_x, \sigma_y, \sigma_z\}$ are Pauli matrices, $\vec{n}_0$ is a unit vector in the direction of impurity, x is an easy magnetic axis.

15.5.2 The Variational Procedure

The variational procedure is detaily described in [37, 38]. Here we present a brief sketch of the method. First of all note that:

$$\vec{S}_n = S(\sin\theta_n\cos\varphi_n,\ \sin\varphi_n\sin\theta_n,\ \cos\theta_n) - \tag{15.5.3}$$

is parametrization of a classical spin ($S \gg 1$) in 3D. In 2D case all $\theta_n = \pi/2$.

The Ψ-function of the conductivity electron in 3D reads:

$$|\Psi\rangle = \sum_n \Psi_n \left(\cos\frac{\theta_n}{2}c^{+}_{n\uparrow} + \sin\frac{\theta_n}{2}\exp(-i\varphi_n)c^{+}_{n\downarrow}\right)|0\rangle, \tag{15.5.4}$$

where $\sum|\Psi_n|^2 = 1$ is normalization condition.

The variational parameters of the problem are Ψ_n, θ_n, φ_n. In the beginning we solve an electron problem (we minimize the energy of the system with respect to Ψ_n). The Ψ-function of the system in our approximation coincides with the Ψ-function of conductivity electron. Moreover $H_M|\Psi\rangle = E_M|\Psi\rangle$, where E_M is magnetic energy: $E_M = JS^2\sum_{\langle nm\rangle}(1-\cos\nu_{nm}) - KS^2\sum_n[\sin^2\theta_n\cos^2\varphi_n - 1]$ and ν_{nm} is an angle between local spins $\vec{S}_n$ and $\vec{S}_m$ on the neighboring sites (see Fig 15.18).

Let us average the Hamiltonian (15.5.1) over Ψ-function $|\Psi\rangle$. Then we get:

$$\langle\Psi|H|\Psi\rangle = \langle\Psi|H_{el}|\Psi\rangle + \langle\Psi|H_m|\Psi\rangle = \langle\Psi|H_{el}|\Psi\rangle + E_M, \tag{15.5.5}$$

where

$$\langle\Psi|H_{el}|\Psi\rangle = -t\sum_{<nm>}(T_{nm}\Psi^*_n\Psi_m + c.c.) - \frac{J_H S}{2} - V_{imp}\sum_n\frac{|\Psi_n|^2}{|\vec{n}-\vec{n}_0|}, \tag{15.5.6}$$

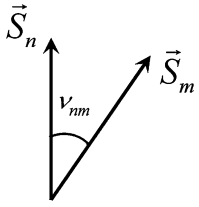

Fig. 15.18 The angle ν_{nm} is an angle between local spins $\vec{S}_n$ and $\vec{S}_m$ on the neighboring sites

and

$$T_{nm} = \cos\frac{v_{nm}}{2}e^{-i\omega_{nm}} \tag{15.5.7}$$

is classical de Gennes type canted state.

Note that in general $T_{\rm nm}$ in (15.5.7) contains a phase-factor $\omega_{\rm nm}$ [54] which is often called in the literature the topological Berry-phase [55]. However in our simple approach we will get the solutions with trivial topology both in the 3D and the 2D case.

Formally

$$\cos v_{nm} = \cos\theta_n\cos\theta_m + \sin\theta_n\sin\theta_m\cos(\varphi_n - \varphi_m), \tag{15.5.8}$$

and

$$\omega_{nm} = \arg\left[\cos\frac{\theta_n}{2}\cos\frac{\theta_m}{2} + \sin\frac{\theta_n}{2}\sin\frac{\theta_m}{2}e^{i(\varphi_n-\varphi_m)}\right]. \tag{15.5.9}$$

In the 2D case $\omega_{\rm nm} = v_{\rm nm}/2$. At low doping the electron is bound by the impurity electrostatic potential. In the limit of strong electron-impurity coupling $V_{\rm imp} \to \infty$, the electron wave-function $\Psi_{\rm n}$ will be nonzero only on sites nearest to the impurity. Let us focus first on the 2D case. (The three-dimensional case can be considered in the similar way). Supposing that $\Psi_{\rm n} \neq 0$ only for $\vec{n}_1 = (1,1)$, $\vec{n}_2 = (1,0)$, $\vec{n}_3 = (0,0)$ and $\vec{n}_4 = (0,1)$ for 2D square lattice (in total analogy it is nonzero only on 8 closest to impurity sites on 3D simple cubic lattice and on 3 closest to impurity sites on 2D frustrated triangular lattice). After minimization of $\langle\Psi|H|\Psi\rangle$ or equivalently of $\langle\Psi|H_{el}|\Psi\rangle$ we will get the system of 8 equations for 3D simple cubic lattice, 4 equations for 2D square lattice and 3 equations for 2D triangular lattice. From these equations it is possible to determine the energy of conductivity electron $E_{\rm el}$. The most simple expression for $E_{\rm el}$ we will have for 2D square lattice which reads:

$$E_{el} = -\frac{J_H S}{2} - V_{imp}\sqrt{2} - t\varepsilon(c_{ij}), \tag{15.5.10}$$

where

$$\varepsilon(c_{ij}) = \frac{1}{\sqrt{2}}\left\{c_{12}^2 + c_{23}^2 + c_{34}^2 + c_{41}^2 + \sqrt{\left((c_{12}-c_{34})^2 + (c_{23}+c_{41})^2\right)\left((c_{12}+c_{34})^2 + (c_{23}-c_{41})^2\right)}\right\}^{1/2} \tag{15.5.11}$$

and we use the notation:

$$c_{ij} = \cos\frac{v_{n_i n_j}}{2} \tag{15.5.12}$$

Note that in (15.5.11) we consider topologically trivial solution with $\Delta\omega = \omega_{12} + \omega_{23} + \omega_{34} + \omega_{41} = 0$ [37] (For the nontrivial Berry-phase $\Delta\omega \neq 0$).

The electron energy $E_{\rm el}$ in (15.5.10) has a minimum when all spins $\vec{S}_n$ are parallel to each other. Thus, we have a bound magnetic polaron state: a ferromagnetic core embedded in the antiferromagnetic matrix.

15.5.3 Magnetic Structure of a Bound Ferron

To find magnetic structure of a bound ferron it is convenient to perform the transformation of the variational angles $\varphi_{\rm n} \to \varphi_{\rm n} + \pi$, $\theta_{\rm n} \to \pi - \theta_{\rm n}$ for one of the sublattices of cubic (quadratic) lattice. As a result, an AFM order becomes FM, and vice versa. Such a transformation allows us to work with continuously changing orientation of spins outside the ferron core. The total energy $E = E_{\rm el} + E_{\rm M}$ then reads (both in 3D cubic and 2D square lattices):

$$E = E_{el} + JS^2 \sum_{<nm>} (1 - \cos v_{nm}) - KS^2 \sum_n (\sin^2 \theta_n \cos^2 \varphi_n - 1). \quad (15.5.13)$$

Here $E_{\rm M} = 0$ for the state without a ferron.

If we minimize the total energy over the angles $\varphi_{\rm n}$ and $\theta_{\rm n}$ we get two types of the solutions. The first one corresponds to "bare" magnetic polaron. It is a bound magnetic polaron with completely polarized spins embedded in purely AFM-background. The total magnetic moment of such polaron is parallel to the easy axis. The ferron energy reads:

$$E_p^0 = -2t + 16JS^2 \quad \text{for 2D square lattice,} \quad (15.5.14)$$

and

$$E_p^0 = -3t + 48JS^2 \quad \text{for 3D simple cubic lattice.} \quad (15.5.15)$$

The bound magnetic polaron (15.5.14), (15.5.15) corresponds to the trivial solution of the problem. However, there is also another solution corresponding to the magnetic polaron state with magnetic moment perpendicular to the easy axis. We call it a "coated" magnetic polaron. It creates long-range spin-distortions of AFM-matrix outside the region of electron localization. When such "coated" polaron is formed, we lose in gradient energy and in the energy of magnetic anisotropy, but we win in surface energy and in the magnetic exchange energy.

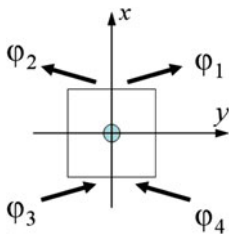

Fig. 15.19 The spin symmetry inside the ferron after the lattice transformation [37]

15.5.4 "Coated" Ferrons on the 2D Square Lattice

The easiest way to understand the structure of a "coated" ferron is to consider 2D square lattice. Here for planar configuration all the local spins lie in *xy*-plane (all $\theta_n = \pi/2$). The spin symmetry inside the ferron (after the lattice transformation) reads (see Fig. 15.19):

$$\varphi_1 = \varphi_3 = \varphi_0;\ \varphi_2 = \varphi_4 = -\varphi_0, \quad 0 < \varphi_0 < \pi/2. \tag{15.5.16}$$

After minimization of the total energy with respect to $\varphi_n (\nu_{nm} = \varphi_n - \varphi_m)$ we get the following set of nonlinear equations:

$$\sum_{\vec{\Delta}} \sin(\varphi_m - \varphi_n) - \frac{\kappa_0}{2}\sin(2\varphi_n) = \frac{t}{2JS^2}\sum_i \delta_{n n_i}(-1)^i \cos^2 \varphi_{n_i}, \tag{15.5.17}$$

where $\kappa_0 = 2\ K/J$ δ_{nm} is the Kronecker symbol, and $|\vec{\Delta}| = |\vec{n} - \vec{m}|$ is the distance between neighboring sites on the square lattice. Thus $\vec{\Delta}$ equals to $(\pm 1, 0)$ and $(0, \pm 1)$.

The system of Eq. (15.5.17) with the boundary conditions (15.5.16) were solved numerically in [37] for the square cluster containing 40 × 40 sites. The further growth of the number of sites in the cluster does not change the obtained results. The initial angle φ_0 is also found. The calculated magnetic structure is presented on Fig. 15.20. The magnetization of the ferron core is smaller than the magnetization of the FM-saturation ($\varphi_0 < \pi/2$) for this solution. The coat of the ferrons has a magnetic moment which is antiparallel to the magnetic moment of the core. In the same time both magnetic moments of the coat and of the core are perpendicular to the easy axis *x*. The angle φ_0 is close (but still smaller) than $\pi/2$. Note that on the left figure the core is almost ferromagnetic (ferrimagnetic) while the matrix corresponds to inhomogeneously distorted AFM-structure. In the same time on the right Fig. 15.20 we have a vice—a versa situation: the core is almost AFM, while the coat is inhomogeneous and ferromagnetic.

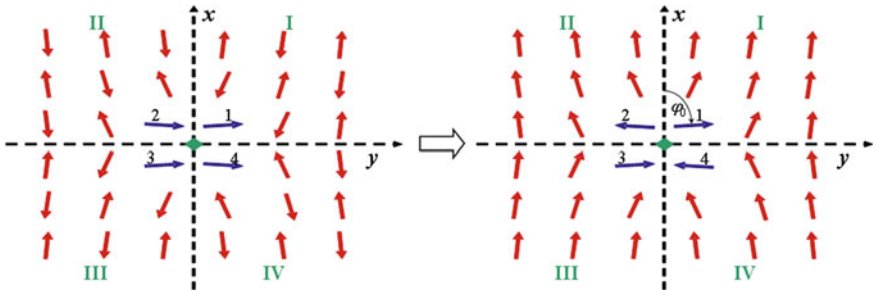

Fig. 15.20 "Coated" magnetic polaron before (left figure) and after (right figure) transformation of angles in one sublattice. The magnetic structure is calculated by solving (15.5.17) at $t/JS^2 = 50$ and $\kappa_0 = 5 \times 10^{-3}$. At these values of parameters, $\varphi_0 \approx 85°$. x is an easy axis [37]

15.5.5 "Coated" Ferrons in the Continuum Limit

In order to get analytical estimations for the spatial distribution of the spin distortions, we find an approximate solution to (15.5.17) in the continuum limit. Namely, angles for 2D square lattice φ_n are treated as values of continuous function $\varphi(\vec{r})$ at points $\vec{r} = \vec{n} - \vec{n}_0$ (further on in our calculations we sometimes put interatomic distance $d = 1$ but restore it in final expressions). Assuming that outside the magnetic polaron the following condition is met $\left|\varphi_{\vec{n}+\vec{\Delta}} - \varphi_{\vec{n}}\right| \ll 1$, we can expand $\varphi(\vec{r} + \vec{\Delta})$ in the Taylor series up to the second order in Δ:

$$\varphi(\vec{r} + \vec{\Delta}) \approx \varphi(\vec{r}) + \Delta^{\alpha}\partial_{\alpha}\varphi(\vec{r}) + \frac{1}{2}\Delta^{\alpha}\Delta^{\beta}\partial_{\alpha}\partial_{\beta}\varphi(\vec{r}) + \cdots \tag{15.5.18}$$

Substituting this expansion into (15.5.17), we find that function $\varphi(\vec{r})$ outside the magnetic polaron should satisfy the 2D sine–Gordon equation [37]:

$$\Delta\varphi - \frac{\kappa_0}{2}\sin 2\varphi = 0, \tag{15.5.19}$$

In the range of parameters under study, $\kappa \ll J$, that is, $\kappa_0 \ll 1$, we can linearize this equation. As a result, we obtain:

$$\Delta\varphi - \kappa_0\varphi = 0. \tag{15.5.20}$$

15.5.6 The Boundary Conditions in the Continuum Limit

This equation should be solved with the boundary conditions, which at infinity reads: $\varphi(\vec{r}) \to 0$ for $r \to \infty$, and with some boundary conditions at the surface of

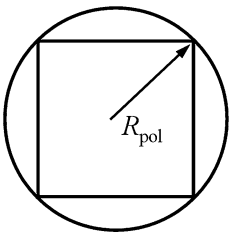

Fig. 15.21 The Dirichlet boundary condition on the surface of the magnetic polaron. We model the magnetic polaron by a circle of radius $R_{pol} = d/\sqrt{2}$

the magnetic polaron. We model the magnetic polaron by a circle of radius $R_{pol} = d/\sqrt{2}$ (see Fig. 15.21) and choose the Dirichlet boundary conditions as:

$$\varphi(\vec{r})|_{r=R_{pol}} = \tilde{\varphi}(\xi), \tag{15.5.21}$$

where we introduce polar coordinates (r, ξ) in the xy-plane. The function $\tilde{\varphi}(\xi)$ can be found in the following way. Note, that $\tilde{\varphi}(\xi)$ should satisfy the symmetry conditions (15.5.16) at points $\xi_i = \pi(2i-1)/4$:

$$\tilde{\varphi}(\xi_i) = \varphi_0, \quad i = 1,\ 2,\ 3,\ 4. \tag{15.5.22}$$

Since the function $\tilde{\varphi}(\xi)$ is a periodic one, it can be expanded in the Fourier series:

$$\tilde{\varphi}(\xi) = \sum_{m=0}^{\infty} (a_m \cos m\xi + b_m \sin m\xi). \tag{15.5.23}$$

In (15.5.23) we neglect the terms with $m > 2$ which allows us to keep the minimum number of terms to satisfy the conditions (15.5.22). It follows from (15.5.22) that $a_0 = a_1 = a_2 = b_1 = 0$. Finally (having in mind that for $m = 0$ sin $m = 0$) we obtain:

$$\tilde{\varphi}(\xi) = \varphi_0 \sin 2\xi.$$

The solution to (15.5.20) with boundary condition (15.5.21) is:

$$\varphi(\vec{r}) = \frac{\varphi_0}{K_2(R_{pol}/r_0)} K_2(r/r_0) \sin 2\xi, \tag{15.5.24}$$

where $r_0 = d/\sqrt{\kappa_0}$ and $K_2(x)$ is the Macdonald function [56]. In fact $r_0 = d/\sqrt{J/2K} \gg d$ plays the role of the "coat" radius (the role of the relaxation length of spin distortions). Indeed, within the range $|\vec{r}| < r_0$ (more exactly for $R_{pol} < |\vec{r}| < r_0$) $\varphi(\vec{r})$ behaves as R_{pol}^2/r^2, whereas at large distances, it decreases exponentially $\varphi(\vec{r}) \sim \exp(-r/r_0)$. The function $\varphi(\vec{r})$ at $\xi = \pi/4$ and the numerical results for $\varphi_{n,n}$ on the 2D square lattice are plotted on Fig. 15.22.

We see that for $t/JS^2 = 50$ and $\kappa_0 = 5 \times 10^{-2}$ an effective "coat" radius which separates slow power-law decrease of $\varphi(\vec{r})$ from a rapid exponential one is given by $r_0 = 4.5\ d$.

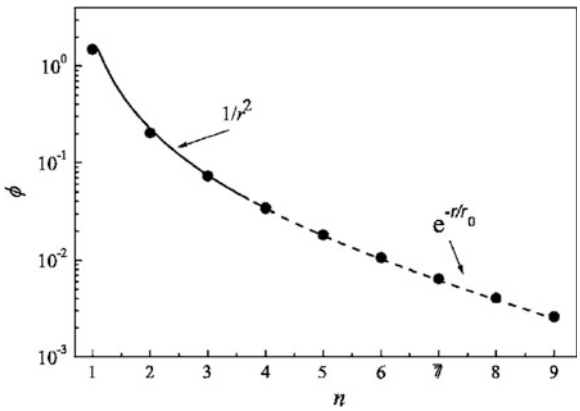

Fig. 15.22 A decrease with distance of an angle $\varphi(\vec{r})$ between distorted spin and easy axis (x-axis) for "coated" magnetic polaron on 2D square lattice. The circles correspond to exact numerical solution of the discrete problem on 40×40 square cluster at $t/JS^2 = 50$, $\kappa_0 = 5 \times 10^{-2}$ ($r_0 = 4.5\ d$). The solid curve corresponds to analytical solution (15.5.24) in the continuum limit. At small distances $\varphi(\vec{r})$ decreases proportionally to $1/r^2$ while at large distances $r \gg r_0$ it decreases exponentially [37]

15.5.7 Energy of a "Coated" Ferron on a Square Lattice

If we substitute the numerical solution of the discrete Eq. (15.5.17) into the total energy given by (15.5.10–15.5.12) and take into account that for planar spins configuration on 2D square lattice $v_{\mathrm{nm}} = \varphi_{\mathrm{n}} - \varphi_{\mathrm{m}}$—than we get an exact numerical estimate for an energy of a "coated" magnetic polaron. However it is more simple to get an analytical estimate for the total energy in the continuum limit. In this limit $E = E_{\mathrm{el}} + E_{\mathrm{M}}$ and correspondingly E_{el} and E_{M} are given by:

$$E_{el} = -\frac{J_H S}{2} - V_{imp}\sqrt{2} - 2t \sin \varphi_0, \tag{15.5.25}$$

and

$$E_M = 8JS^2\left(1 + \frac{\kappa_0}{4}\right)\sin^2 \varphi_0 + \frac{JS^2}{2}\int\limits_{r \geq R_{pol}} d^2\vec{r}\left[(\vec{\nabla}\varphi)^2 + \kappa_0\varphi^2\right]. \tag{15.5.26}$$

Substituting $\varphi(\vec{r})$ from (15.5.24) to (15.5.25) and performing the integration we get:

$$E_M = 8JS^2\left(1 + \frac{\kappa_0}{4}\right)\sin^2 \varphi_0 + \frac{JS^2\varphi_0^2}{2} I\left(\frac{R_{pol}}{r_0}\right), \tag{15.5.27}$$

where

$$I(x) = 2\pi\left(1 + \frac{xK_1(x)}{2K_2(x)}\right). \tag{15.5.28}$$

Since $R_{\rm pol} \ll r_0$, the value of the function $I(x)$ for $x = R_{\rm pol}/r_0 \ll 1$ is close to 2π.

The optimal angle φ_0 is determined by the minimization of the ferron energy (15.5.25) and (15.5.27):

$$\cos\varphi_0 - \frac{4JS^2}{t}\left(1 + \frac{\kappa_0}{4}\right)\sin(2\varphi_0) - \frac{JS^2\varphi_0}{2t} I\left(\frac{R_{pol}}{r_0}\right) = 0. \tag{15.5.29}$$

For $R_{\rm pol} \ll r_0$ from (15.5.29) it follows that:

$$\varphi_0 = \frac{\pi}{2}\left[1 - o\left(\frac{JS^2}{t}\right)\right]. \tag{15.5.30}$$

We can compare now the energies of "bare" and "coated" magnetic polarons (see Fig. 15.23). We see that the energy difference $\Delta E = E_{pol} - E_{pol}^{(o)}$ between "coated" and "bare" magnetic polarons is negative at small values of anisotropy ($\kappa_0 \ll 1$) thus stabilizing the "coated" ferron.

We see that in exact numerical solution the "coated" ferron is more energetically beneficial than a "bare" one till larger anisotropy ($\kappa_0 \sim 0.7$ for $t/JS^2 = 50$) in exact solution than in approximate analytical solution in the continuum limit.

To conclude this Section note that absolutely the same variational procedure for 3D simple cubic lattice yields in continuum approximation for $\varphi(\vec{r})$:

$$\varphi(r) \sim \frac{R_{pol}^4}{r^4} \quad \text{for } R_{\rm pol} < r < r_0, \tag{15.5.31}$$

and

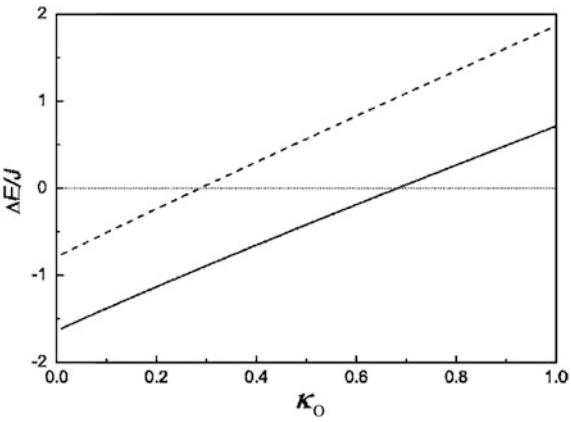

Fig. 15.23 The energy difference ΔE between "coated" and "bare" ferrons versus $\kappa_0 = 2\ K/J$ at $t/JS^2 = 50$. *Solid curve* corresponds to exact numerical solution, whereas *dashed curve* is calculated analytically in the continuum limit [37]

$$\varphi(r) \sim \exp(-r/r_0) \quad \text{for } r > r_0. \tag{15.5.32}$$

Finally for 2D frustrated triangular lattice we have very slowly decaying coat of spin-distortions [38]:

$$\varphi(r) \sim \frac{R_{pol}}{r} \quad \text{for } R_{\text{pol}} < r < r_0, \tag{15.5.33}$$

and

$$\varphi(r) \sim \exp(-r/r_0) \quad \text{for } r > r_0. \tag{15.5.34}$$

15.5.8 Generalized Mott Criterion

We consider that x_{Mott} which governs the transition from bound to free magnetic polarons can be qualitatively defined via the radius r_0 of the coat-extension for bound magnetic polaron [38]. In 3D the coats overlap at:

$$x_{Mott} \sim \frac{3}{4\pi}\left(\frac{d}{r_0}\right)^3. \tag{15.5.35}$$

So $x_{\text{Mott}} \sim (0.1 \div 0.2)$ % for typical $r_0 \sim (5 \div 6)d$.

Note that for free magnetic polarons $R_{\text{pol}} \sim 2d$ in 3D cubic lattice. However, the structures of free and bound magnetic polarons are quite different. A free polaron has a saturated FM core of the size of R_{pol} and very rapidly (exponentially) decaying spin-distortions outside it [18–21]. In the same time "coated" magnetic polaron bound by nonmagnetic donor impurity has a small and an almost saturated FM core of the radius $\sim d$ and extended coat of slowly-decaying spin-distortions at intermediate distances $d < r < r_0$. Their radius $r_0 \gg d$. For $x \ll x_{\text{Mott}}$ the coats of the bound polarons do not overlap and we are effectively in an insulator (Mott limit) for strong Coulomb attraction $V_{\text{imp}} > V_{\text{c}}$. Note that if $V_{\text{imp}} < V_{\text{C}}$ (where $V_{\text{C}} \sim 2t$ see [38]), then according to the preliminary estimates the FM core of the bound magnetic polaron starts to grow and could reach the typical value of the core of the free magnetic polaron. So, the free and bound magnetic polarons are very similar for $V_{\text{imp}} < V_{\text{C}}$. Note that in real manganites $V_{\text{imp}} \sim V_{\text{C}}$.

Finally for 2D square lattice:

$$x_{Mott} \sim \frac{1}{\pi}\left(\frac{d}{r_0}\right)^2 \sim (0.5 \div 1)\ \% \tag{15.5.36}$$

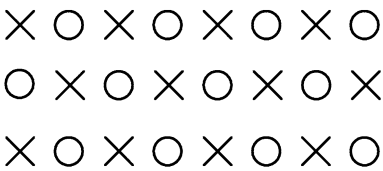

Fig. 15.24 Verwey charge ordering at $x = ½$ with a checkerboard distribution of Mn^{3+} (*crosses*) and Mn^{4+} (*empty circles*) ions, which on the figure play the role of electrons and holes respectively

15.6 Phase Separation in Charge-Ordered Manganites

In this Section we will consider the nanoscale phase separation and formation of small metallic droplets (polarons) in manganites and other systems with charge-ordering. Note that the problem of charge-ordering in magnetic oxides has attracted the attention of theorists since the discovery of the Verwey transition in magnetite Fe_3O_4 in the end of the 1930s [57, 58]. An early theoretical description of this phenomenon was given, e.g., in [59]. This problem was reexamined later in the numbers of papers in connection with the colossal magnetoresistance in manganites [34, 60, 61]. The mechanisms stabilizing the charge ordered state can be different: the Coulomb repulsion of charge carriers (the energy minimization requires keeping the carriers as far away as possible, similarly to Wigner crystallization) or the electron-lattice interaction leading to the effective repulsion of electrons at the nearest-neighbor sites. In all the cases, charge ordering can arise in mixed-valence systems if the electron bandwidth is sufficiently small. In the opposite case, the large electron kinetic energy stabilizes the homogeneous metallic state. In real materials, in contrast to the Wigner crystallization, the underlying lattice periodicity determines the preferential types of charge ordering (CO). Thus, in the simplest bipartite lattice, to which belongs the colossal magnetoresistance manganites of the type of $Ln_{1-x}A_xMnO_3$ (where Ln = La, Pr and A = Ca, Sr) or layered manganites $Ln_{2-x}A_xMnO_4$, $Ln_{2-2x}A_{1+2x}Mn_2O_7$, the optimum conditions for the formation of the charge ordered state exist for the doping $x = ½$ ($n = 1 - x = ½$—quarter filling). At this value of x the concentration of Mn^{3+} and Mn^{4+} are equal and the simple checkerboard arrangement is possible (see Fig. 15.24). The most remarkable fact here is that even at $x \neq ½$ (in the underdoped manganites with $x < ½$), only the simplest version of charge ordering is experimentally observed with the alternated checkerboard structure of the occupied and empty sites in the basal plane [62]. In other words, this structure corresponds to the doubling of the unit cell, whereas more complicated structures with a longer period (or even incommensurate structures) do not actually appear in this case.

A natural question then arises as to how the extra or missing electrons can be redistributed for an arbitrary doping level such that the superstructure remains the same for $x = ½$? To answer this question, the experimentalists introduced the concept of the incipient CO-state corresponding to the distortion of a long-range

charge ordering by microscopic metallic clusters [35, 63]. In fact the existence of this state implies a kind of nanoscale phase separation [39] discussed in this chapter. There is a growing evidence nowadays suggesting that an interplay between the charge ordering and the tendency toward phase separation plays the essential role in the CMR-materials [7, 8, 33, 66, 67].

In this Section we consider a simple model allowing us to clarify the situation at an arbitrary doping. The model includes both the Coulomb repulsion of electrons on the neighboring sites and the magnetic interaction responsible for the magnetic ordering in manganites (in fact it is FM Kondo-lattice model with nn Coulomb repulsion). After demonstrating the instability of the system toward phase separation in certain doping ranges, we consider the simplest form of the phase separation, namely, the formation of nanoscale metallic droplets in the insulating CO-matrix [39]. We estimate parameters of such droplets and complete the phase diagram of manganites illustrating the interplay between charge ordering, magnetic ordering and phase separation. We note that the CO mechanism considered below (Coulomb repulsion) is not the only one. The electron-lattice interaction can also play an important role (see e.g., [64]). In application to manganites, one must also take the orbital interactions into account [61, 64, 65]. Nanoscale phase separation in orbitally ordered matrix [41] will be considered in the next Section. The orbital interactions explain the zigzag structures [61] and may be also important in explaining the fact that the CO in half-doped perovskite manganites is a checkerboard one only in the basal plane, but it is "in-phase" along the c-direction. However the nature of this CO state is not clear yet. We also emphasize that the CO is often observed in manganites at higher temperatures then the magnetic ordering, and thus one must seek a model that does not heavily rely on magnetic interactions. In contrast to magnetic interactions, the Coulomb interaction is one of the important factors that is always present in the systems under consideration. Moreover it has a universal nature and does not critically depend on specific features of the particular system. Consequently, our treatment can be also applied to other CO systems such as magnetite Fe_3O_4 [57, 58], cobaltites [68], nickelates [69] etc.

15.6.1 The Simplest Model for Charge Ordering

As the starting point, we consider a simple lattice model for CO-state:

$$\hat{H} = -t \sum_{<i,j>} c_i^+ c_j + V \sum_{<i,j>} n_i n_j - \mu \sum_i n_i, \qquad (15.6.1)$$

where t is the hopping integral, V is the nearest-neighbor Coulomb interaction (a similar nn repulsion can be also obtained via the interaction with the breathing-type optical phonons), μ is the chemical potential, and c_i^+ and c_j—are one-electron creation and annihilation operators, $n_i = c_i^+ c_i$ is the one site density. The

symbol $\langle i, j \rangle$ denotes the summation over the nearest-neighbor sites. We omit the spin and orbital indices for simplicity in (15.6.1). As mentioned in the introduction to this Section the spin and orbital effects play the important role in the formation of the real structure in specific compounds; in this Section, however, we emphasize the most robust effects related to the nearest-neighbor Coulomb repulsion. The magnetic effects are discussed in the following Subsections of the Sect. 15.6. We also assume that the double occupancy does not occur in this model because of the strong onsite repulsion between electrons and thus we can insert projection operators in the kinetic term in (15.6.1). Effectively we consider extended Hubbard model with additional Coulomb repulsion on the neighboring sites under the condition that onsite Hubbard repulsion $U \gg \{V, W$—the bandwidth$\}$. This model is sometimes called Verwey model [57, 58] or Shubin-Vonsovsky model [70]. Shubin-Vonsovsky model was considered in Chap. 9 with respect to superconductivity. Note that for the models where we conserve the spin of fermions we often write $V/2$ instead of V in the second term in Eq. (15.6.1) - see Chap. 9 for example. Originally it was introduced for better description (in comparison with simple Hubbard model) of Mott's metal-dielectric transition. Note that: while the Mott–Hubbard localization (Mott–Hubbard dielectric state) corresponds to the density $n = 1$ ($x = 0$), Verwey localization (Verwey CO insulating state) corresponds to $n = ½$ ($x = ½$). Hamiltonian (15.6.1) explicitly accounts for the correlation effect that is most important for the formation of CO-state, namely, the electron repulsion on neighboring sites. The long-range part of the Coulomb interaction only leads to the renormalization of the bandwidth W and does not significantly affect the properties of the uniform CO-state. However, it can produce a qualitative effect on the structure of phase-separated state (see the discussion in the beginning of the Sect. 15.6.4).

The models of the type (15.6.1) with the nn repulsion responsible for the charge ordering are the most popular in describing this phenomenon, see e.g., [59, 60, 62, 71] and reference therein. Hamiltonian (15.6.1) captures the main physical effects. We will add some extra terms to it in the Sect. 15.6.4 (where we will consider FM Kondo-lattice model with additional nn Coulomb repulsion).

In the main part of this section, we always speak about electrons. However, in application to real manganites we mostly have in mind less than half-doped (underdoped) systems of the type $Ln_{1-x}A_xMnO_3$ with $x < ½$. For real system one must therefore substitute holes for our electrons. All the theoretical treatment in terms of hole density x or electron density $n = (1 - x)$ remains qualitatively the same. There are some important differences, however, for the nanoscale phase-separated state for electron densities $n > ½$ and $n < ½$ connected e.g., with possible stripe formation. We will discuss these differences in the next subsections where we will study the nanoscale phase-separation in details. Note also that in principle there are hole-doped and electron-doped families of manganites in similarity with high-T_C materials, but the properties of electron-doped manganites are not so well understood yet.

In what follows, we consider the simplest case of square (2D) or cubic (3D) lattices, where the simple two-sublattice ordering occurs for $n = ½$. As mentioned

in the introduction to this Section, this is the case in layered manganites, whereas in 3D perovskite manganites, this ordering occurs only in the basal plane (the ordering is "in-phase" along the *c*-direction). A more complicated model is apparently needed to account for this behavior (see [39] and discussion therein).

For $n = ½$ a model (15.6.1) was analyzed in many papers; we follow the treatment of Khomskii in [59]. As mentioned above, the Coulomb repulsion (the second term in (15.6.1)) stabilizes the CO-state in the form of a checkerboard arrangement of the occupied and empty sites, whereas the first term (band energy) opposes this tendency. At arbitrary values of the electron density n we first consider a homogeneous charge ordered solution and use the same ansatz as in [59], namely

$$n_i = n\left[1 + (-1)^i \tau\right]. \tag{15.6.2}$$

This expression implies the doubling of the lattice periodicity with the local densities:

$$n_1 = n(1 + \tau); \quad n_2 = n(1 - \tau) \tag{15.6.3}$$

at the neighboring sites. We note that at $n = ½$ for a general form of the electron dispersion without nesting, the charge ordered state exists only for a sufficiently strong repulsion $V > V_C = 2t$ [59] (or $zV > 2zt = W$). The order parameter is $\tau < 1$ for finite $V/2t$, and the ordering is not complete in general, i.e., an average electron density n_i differs from zero or one even at $T = 0$. (The ideal CO-state described by Fig. 15.24 with filled and empty sites is realized in the strong-coupling case $V \gg V_C$). Thus for Verwey localization (for insulating checkerboard CO-state) we need a hierarchy of parameters $U \gg V \gg W$ in Verwey (Shubin-Vonsovsky) model.

We use the coupled Green function approach as in [59] and [39], which yields:

$$\begin{cases} (E + \mu)G_1 - t_k G_2 - zVn(1 - \tau)G_1 = \dfrac{1}{2\pi}, \\ (E + \mu)G_2 - t_k G_1 - zVn(1 + \tau)G_2 = 0, \end{cases} \tag{15.6.4}$$

where G_1 and G_2 are the Fourier transforms of the normal lattice Green functions $G_{il} = \ll c_i c_l^+ \gg$ for the sites i and l belonging respectively, to the same sublattice or to the different sublattices, z is the number of nearest neighbors, and t_k is the Fourier transform of the hopping matrix element. In deriving (15.6.4), we performed a mean-field decoupling and replaced the averages $\langle c_i^+ c_i \rangle$ by the onsite densities n_i in (15.6.4). The solution of (15.6.4) leads to the following spectrum:

$$E + \mu = Vnz \pm \sqrt{(Vn\tau z)^2 + t_k^2} = Vnz \pm \omega_k. \tag{15.6.5}$$

The spectrum defined by (15.6.5) resembles the spectrum of superconductor (SC) and, hence, the first term under the square root is analogous to the superconducting gap squared. In other words, we can introduce the CO-gap by the

formula: $\Delta = Vn\tau z$. It depends upon the density not only explicitly, but also via the density dependence of τ. We thus obtain:

$$\omega_k = \sqrt{\Delta^2 + t_k^2}. \tag{15.6.6}$$

We note a substantial difference between the spectrum of CO-state (15.6.6) and SC-state, namely the chemical potential μ does not enter under the square root in (15.6.6) for $n \neq ½$, which is in contrast to the spectrum of SC, where $\omega_k = \sqrt{\Delta^2 + (t_k - \mu)^2}$. We can then find the Green functions G_1 and G_2:

$$\begin{cases} G_1 = \dfrac{A_k}{E + \mu - Vnz - \omega_k + io} + \dfrac{B_k}{E + \mu - Vnz + \omega_k + io} \\ G_2 = \dfrac{t_k}{2\omega_k}\left[\dfrac{1}{E + \mu - Vnz - \omega_k + io} + \dfrac{1}{E + \mu - Vnz + \omega_k + io}\right] \end{cases}, \tag{15.6.7}$$

where

$$A_k = \frac{1}{4\pi}\left(1 - \frac{\Delta}{\omega_k}\right);\ B_k = \frac{1}{4\pi}\left(1 + \frac{\Delta}{\omega_k}\right). \tag{15.6.8}$$

They have the two-pole structure, corresponding to the lower and upper Verwey bands. After the standard Wick transformation $E + io \to iE$ in the expression for G_1 we find the densities in the following form:

$$\begin{aligned} n_1 = n(1+\tau) &= \int \left[\left(1 - \frac{\Delta}{\omega_k}\right) n_F(\omega_k - \mu + Vnz) + \left(1 + \frac{\Delta}{\omega_k}\right) n_F(-\omega_k - \mu + Vnz)\right] \frac{d^D\vec{k}}{2\Omega_{BZ}} \\ n_2 = n(1-\tau) &= \int \left[\left(1 + \frac{\Delta}{\omega_k}\right) n_F(\omega_k - \mu + Vnz) + \left(1 - \frac{\Delta}{\omega_k}\right) n_F(-\omega_k + \mu + Vnz)\right] \frac{d^D\vec{k}}{2\Omega_{BZ}}, \end{aligned} \tag{15.6.9}$$

where $D = 3$ or 2, $n_F(y) = \frac{1}{(e^{y/T}+1)}$ is the Fermi–Dirac distribution function and Ω_{BZ} is the volume of the first Brillouin zone.

Adding and subtracting the two equations for n_1 and n_2 we obtain the resulting systems of equations for n and μ:

$$\begin{aligned} 1 &= Vz \int \frac{1}{\omega_k}\left[n_F(-\omega_k - \mu + Vnz) - n_F(\omega_k - \mu + Vnz)\right] \frac{d^D\vec{k}}{2\Omega_{BZ}}, \\ n &= \int \left[n_F(-\omega_k - \mu + Vnz) + n_F(\omega_k - \mu + Vnz)\right] \frac{d^D\vec{k}}{2\Omega_{BZ}}. \end{aligned} \tag{15.6.10}$$

For low temperatures ($T \to 0$) and $n \leq ½$, it is reasonable to assume that $\mu - Vnz$ is negative. Therefore $n_F(\omega_k - \mu + Vnz) = 0$ and $n_F(-\omega_k - \mu + Vnz) = \theta(-\omega_k - \mu + Vnz)$ is the step function.

It is easy to see that for $n = ½$ the system of Eq. (15.6.10) yields identical results for all

$$-\Delta \leq \mu - Vnz \leq \Delta. \tag{15.6.11}$$

From this point of view $n = ½$ is the indifferent equilibrium point. For infinitely small deviation from $n = ½$, that is, for densities $n = ½ - 0$, the chemical potential must be defined as:

$$\mu = -\Delta + \frac{Vz}{2} = \frac{Vz}{2}(1 - \tau). \tag{15.6.12}$$

If we consider the strong coupling case $V \gg 2t$ ($zV \gg W$) and assume a constant density of states inside the band, we have:

$$\tau = 1 - \frac{2W^2}{3V^2z^2} \tag{15.6.13}$$

for a simple cubic lattice and, therefore:

$$\mu = \frac{W^2}{3Vz}. \tag{15.6.14}$$

We note that for the density $n = ½$ the CO-gap Δ appears for an arbitrary interaction strength V. This is due to the existence of nesting in our simple model.

In the weak coupling case $V \ll 2t$ and with perfect nesting, we have:

$$\Delta \sim W \exp\left\{-\frac{W}{Vz}\right\}, \tag{15.6.15}$$

and τ is exponentially small. For $zV \gg W$ or, accordingly, for $V \gg 2t$, it follows that $\Delta \approx Vz/2$ and $\tau \to 1$. As mentioned above, for a general form of the electron dispersion without nesting, the CO exists only if the interaction strength V exceeds a certain critical value of the order of the bandwidth (see [59]). In what follows, we restrict ourselves to the physically more instructive strong-coupling case $V \gg 2t$.

For the constant density of states (flat band) the integrals in (15.6.10) can be taken explicitly and the system of Eq. (15.6.10) can be easily solved for arbitrary n. We note, however, that in the strong coupling case $V \gg 2t$ and the small density deviations from ½ ($\delta \ll 1$), the results are not very sensitive to the form of the electron dispersion. That is why we do not need to solve the system of equations (15.6.10) exactly.

We now consider the case where electron density $n = ½ - \delta$ with $\delta \ll 1$ being the density deviation from ½. In this case $\mu = \mu(\delta, \tau)$ and we have two coupled equations for μ and τ. As a result:

$$\mu(\delta) \approx Vnz(1 - \tau) - \frac{4W^2}{Vz}\delta^2 \approx \frac{W^2}{3Vz} + \frac{4W^2}{3Vz}\delta + o(\delta^2). \tag{15.6.16}$$

The energy of the CO-state (counted from the energy of a homogeneous metallic state $E_N = 0$) is therefore given by:

$$E_{CO}(\delta) = E_{CO}(0) - \frac{W^2}{3Vz}\delta - \frac{2W^2}{3Vz}\delta^2 + o(\delta^3), \tag{15.6.17}$$

where

$$E_{CO} = -\frac{W^2}{6Vz} \tag{15.6.18}$$

is the energy precisely corresponding to the density $n = ½$ and $|E_{CO}(0)| \ll W$ for $V \gg 2t$. At the same time, the CO-gap Δ is given by:

$$\Delta \approx \frac{Vz}{2}\left[1 - 2\delta - \frac{2W^2}{3V^2z^2}(1 + 4\delta)\right]. \tag{15.6.19}$$

The dependence of the chemical potential μ and the total energy E on δ in (15.6.16) and (15.6.17) actually stems from this linear decrease of the energy gap Δ with the deviation from half-filling.

For $n > ½$, the energy of the CO-state starts to increase rapidly due to a large contribution of the Coulomb interaction (the upper Verwey band is partially filled for $n > ½$—that is the difference between $n > ½$ and $n < ½$ on the level of the Green functions in (15.6.7)). In other words, for $n > ½$, contrary to the case where $n < ½$, each extra electron put into the checkerboard CO-state, necessarily has occupied nearest-neighboring sites, increasing the total energy by $Vz|\delta|$. For $|\delta| = n - ½ > 0$, we then have:

$$E_{CO}(\delta) = E_{CO}(0) + \left(Vz - \frac{W^2}{3Vz}\right)|\delta| - \frac{2W^2}{3Vz}\delta^2 + o(\delta^3). \tag{15.6.20}$$

Accordingly, the chemical potential is given by:

$$\mu(\delta) = Vz - \frac{W^2}{3Vz} - \frac{4W^2}{3Vz}|\delta| + o(\delta^2). \tag{15.6.21}$$

It undergoes a jump equal to Vz as $\tau \to 1$. We note that the CO-gap Δ is symmetric for $n > ½$ and $n < ½$ and is given by:

$$\Delta \approx \frac{Vz}{2}\left[1 - 2|\delta| - \frac{2W^2}{3V^2z^2}(1 + 4|\delta|)\right]. \tag{15.6.22}$$

We could make the entire picture symmetric with respect to $n = ½$ by shifting all the one-electron energy levels and the chemical potential by Hartree–Fock type shift $Vz/2$, i.e., defining:

$$\mu' = \mu - \frac{Vz}{2}. \tag{15.6.23}$$

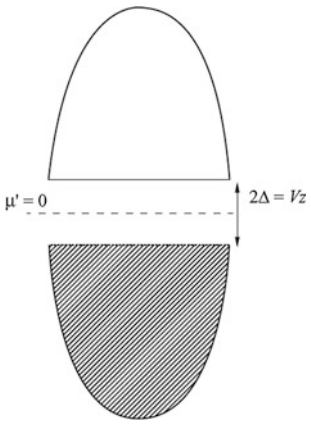

Fig. 15.25 Band structure of the Verwey (Shubin-Vonsovsky) model (15.6.1) at $n = ½$. The lower Verwey band is completely filled. The upper Verwey band is empty. The chemical potential $\mu' = 0$ lies in the middle of the gap with the width 2Δ [8, 39]

In terms of μ' expressions (15.6.16) and (15.6.21) can be written as:

$$\begin{cases} \mu' = -\dfrac{Vz}{2} + \dfrac{W^2}{3Vz} + \dfrac{4W^2}{3Vz}\delta; & n < 1/2, \\ \mu' = \dfrac{Vz}{2} - \dfrac{W^2}{3Vz} - \dfrac{4W^2}{3Vz}|\delta|; & n > 1/2. \end{cases} \tag{15.6.24}$$

Similarly to the situation in semiconductors, we have $\mu' = 0$ precisely at the point $n = ½$, which means that the chemical potential lies in the middle of the gap between lower and upper Verwey bands (see Fig. 15.25). At densities $n = ½ - 0$, the chemical potential $\mu' = -Vz/2$ coincides with the upper edge of the filled (lower) Verwey band.

15.6.2 The Instability of the CO-State with Respect to Phase Separation

We now check the stability of the CO-state. At the densities close to $n = ½$, the dependence of its energy on the charge density has the form illustrated in Fig. 15.26. The figure clearly indicates a possible instability of the CO-state (the energy has a kink for $n \to ½$).

Indeed, the most remarkable implication of (15.6.16–15.6.22) is that the compressibility κ of the homogeneous CO system is negative for the densities different from ½,

$$\kappa^{-1} \sim \frac{d\mu}{dn} = -\frac{d\mu}{d\delta} = \frac{d^2E}{d\delta^2} = -\frac{4W^2}{3Vz} < 0, \tag{15.6.25}$$

where $\delta = ½ - n$. This is a manifestation of the tendency toward the phase separation characteristic of the CO system with $\delta \neq 0$. The presence of a kink in

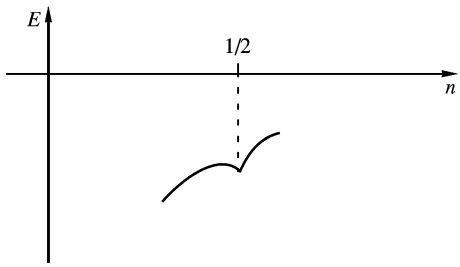

Fig. 15.26 The energy of the CO-state versus charge density for $n \to ½$. The energy has a kink for $n \to ½$ [39]

$E_{CO}(\delta)$ (cf. (15.6.17) and (15.6.20)) implies that one of the states into which the system might separate would correspond to the checkerboard CO-state with $n = ½$, whereas the other would have a certain density n' smaller or larger then ½. This conclusion of [39] resembles that in [61] (see also [66] and [36]), although the detailed physical mechanism is different. The possibility of phase separation in Verwey model (15.6.1) away from $n = ½$ was also reported earlier in [67] for the infinite-dimensional case. In what follows, we focus our attention on the situation with $n < ½$ (underdoped manganites); the case where $n > ½$ apparently has certain special properties—the existence of stripe phases, etc. [35], the detailed origin of which is not yet clear. Let us remind once more that for hole-doped manganites $La_{1-x}Ca_xMnO_3$ we should think in terms of holes. So underdoped $La_{1-x}Ca_xMnO_3$ corresponds to $x < 1/2$, while stripe-formation takes place for $x > 1/2$ in it.

It is easy to understand the physics of the phase separation in our case. As follows from (15.6.22), the CO-gap decreases linearly with the density deviation from $n = ½$. Correspondingly, the energy of the homogeneous CO-state rapidly increases, and it is more favorable to "extract" extra holes from the CO-state, putting them into one part of the sample (for $n < ½$), while creating the "pure" checkerboard CO-state in the other part. The energy loss due to this redistribution of holes is overcompensated by the gain provided by a better charge order.

However the hole-rich regions would not be completely "empty", similarly to pores (clusters of vacancies) in crystals: we can gain extra energy by "dissolving" a certain amount of electrons there. In doing this, we decrease the band energy of the electrons due to their delocalization. Thus, this second phase would be a metallic one. The simplest state of this kind is a homogeneous metal with the electron concentration n_m. This concentration, as well as the relative volume of the metallic and CO-phases, can be easily calculated by minimizing the total energy of the system, the energy of the metallic part of the sample E_m in 3D case is given by:

Fig. 15.27 Complete phase-separation into two large clusters (metallic and charge-ordered). V_m and V_{CO} are the volumes of the two clusters [8]

$$E_m = -tzn_m + c_1 t(n_m)^{5/3} + V(n_m)^2, \tag{15.6.26}$$

where c_1 is a constant.

Minimizing of (15.6.26) with respect to n_m, we find the equilibrium electron density in the metallic phase. For the strong coupling case $V > zt$, we obtain (neglecting a relatively small correction provided by the term with $(n_\mathrm{m})^{5/3}$):

$$n_{m0} \approx \frac{tz}{2V}. \tag{15.6.27}$$

In accordance with this simple treatment, the system with $n_{\mathrm{m}0} < n < ½$ would therefore undergo the phase transition into the CO-phase with $n = ½$ and the metallic phase with $n = n_{\mathrm{m}0}$. For arbitrary n, the relative volumes V_m and V_CO of these phases can be found from the Maxwell construction (see also Fig. 15.27):

$$\frac{V_m}{V_{CO}} = \frac{1/2 - n}{n - n_{m0}} \tag{15.6.28}$$

This implies that the metallic phase occupies the part V_m of the total sample volume V_S given by:

$$\frac{V_m}{V_S} = \frac{1/2 - n}{1/2 - n_{m0}}. \tag{15.6.29}$$

The metallic phase would occupy the entire sample when the total density n is less or equal to $n_{\mathrm{m}0}$.

15.6.3 Nanoscale Phase Separation with Metallic Droplets Inside CO-Matrix

As argued above, the system with a short-range repulsion described by (15.6.1) is unstable with respect to the phase separation for n close but different from ½. The long-range Coulomb forces would, however, prevent the full phase separation into large regions, containing all extra holes, and the pure $n = ½$ CO-region. We can avoid this energy loss by formation (instead of one big metallic phase with many electrons) of the finite metallic clusters with smaller number of electrons. The limiting case would be a set of spherical droplets, each containing one electron. This state is similar to magnetic polarons ("ferrons") considered in the previous Sections of this chapter.

Let us now estimate the characteristic parameters of these droplets. The main purpose of this treatment is to demonstrate that the energy of the state constructed in this way is lower then the energy of the homogeneous state, even if we treat these droplets rather crudely and do not optimize all their properties. In particular, we make the simplest assumption that the droplets have sharp boundaries and that the CO-state existing outside these droplets is not modified in their vicinity. This

state can be treated as a variational one: optimizing the structure of the droplets boundary can only decrease its energy.

The energy (per unit volume) of the droplet state with the concentration of droplets n_d can be written in total analogy with the ferron energy in the double-exchange model [see Sect. 15.3 and Eq. (15.3.8)]. This yields in 3D case:

$$E_{drop} = -tn_d\left(z - \frac{\pi^2 d^2}{R^2}\right) - \frac{W^2}{6Vz}\left[1 - n_d\frac{4}{3}\pi\left(\frac{R}{d}\right)^3\right], \tag{15.6.30}$$

where $E_{CO}(0) = -\frac{W^2}{6Vz}$ is the energy of the CO-state for $n = ½$ ($E_{\mathrm{drop}} = E_{\mathrm{CO}}(0)$ for $n_{\mathrm{d}} = 0$), d—is the lattice constant and R is the droplet (polaron) radius. The first term in (15.6.30) corresponds to the kinetic energy gain of the electron delocalization inside the metallic droplets and the second term describes the CO-energy in the remaining, insulating part of the sample. Minimization of the energy in (15.6.30) with respect to R yields for the optimal polaron radius:

$$\frac{R_{pol}}{d} \sim \left(\frac{V}{t}\right)^{1/5}. \tag{15.6.31}$$

The optimal polaronic energy reads:

$$E_{pol} = -\frac{W^2}{6Vz} - tn_d z\left(1 - C_2\left(\frac{t}{V}\right)^{2/5}\right), \tag{15.6.32}$$

where C_2 is numerical constant.

The critical concentration n_{dc} corresponds to the configuration where metallic droplets start to overlap, i.e., where the volume of the CO-phase (the second term in (15.6.30)) tends to zero. Hence,

$$n_{dc} = \frac{3}{4\pi}\left(\frac{d}{R_{pol}}\right)^3 \sim \left(\frac{t}{V}\right)^{3/5} \tag{15.6.33}$$

Correspondingly in the 2D case $n_{dc} \sim \left(\frac{t}{V}\right)^{1/2}$ and $\frac{R_{pol}}{d} \sim \left(\frac{V}{t}\right)^{1/4}$ (we already used this formula for simple estimates in connection with phase separation in 2D Shubin-Vonsovsky (Verwey) model in Chap. 9).

Actually, one should include the surface energy contribution to the total energy of the droplet. The surface energy in 3D case should be of the order of W^2R^2/V. For large droplets, this contribution is small compared to the term $\sim R^3$ in (15.6.30), it would also be reduced for a "soft" droplet boundary. It is easy to show that even in the worst case of a small droplet (for the order of several lattice constants) with a sharp boundary, R/d acquires the factor $1 - 0.2\,(t/2V)^{1/5}$ related to the surface contribution. Thus, the corrections related to the surface would not exceed about 20 % of the bulk value. That is why we ignore this term below.

Comparing (15.6.17) and (15.6.32) for one-electron droplets we see that for the deviations from half-filling ($0 < \delta \le \delta_{\mathrm{C}} = ½\text{-}n_{\mathrm{dc}}$) the energy of the phase separated state (15.6.32) is always lower that the energy of the homogeneous CO-state

Fig. 15.28 Nanoscale phase separation scenario with an undermelted CO-state within a metallic droplet [8]

(for $n_d = 0$ and $\delta = 0$ the energies (15.6.32) and (15.6.17) coincide). The energy of a droplet state (15.6.32) is also lower than the energy of the fully separated state (15.6.26) obtained by the Maxwell construction from the homogeneous metallic state. Correspondingly, the critical concentration n_{dc} in (15.6.33) is larger then n_{mo} in (15.6.27). There is no contradiction here: in the droplet (polaronic) state which we constructed the electrons are confined within the spheres of the radius R in 3D and even when these droplets start to overlap at $n = n_{dc}$, occupying the entire sample, the electrons by construction, are still confined within their own spheres and avoid each other. In other words, a certain degree of CO-correlations is still present in our droplet state, decreasing the repulsion, and hence the total energy.

Thus the energy of the phase separated state with nanoscale metallic droplets inside insulating CO-matrix corresponds to the global minima of the energy for all $0 < \delta \leq \delta_c$. This justifies our conclusion about the phase separation into CO-state with $n = ½$ and a metallic state with small spherical droplets (see Fig.9.12).

Note that along with one-electron metallic droplets a nanoscale phase separation scenario of the kind shown on Fig. 15.28 can be also organized. Here a metallic droplet is formed by replacing one electron with a hole at the center of a droplet.

Note, however, that the energy of such undermelted CO-state (a "resonance-valence-bond"—RVB-state [75] for the Verwey model) is much more difficult to calculate than that for a one-electron metallic droplet, and this problem will not be considered in this chapter. The nanoscale phase separation with one-electron droplet encountered here resembles that of a strongly interacting Hubbard model close to half-filling (for electron densities $n = 1 - \delta$). The CO-state corresponds to AFM-state in the Hubbard model and the role of nn Coulomb repulsion V plays onsite Hubbard repulsion U. At $n = 1$ in the Hubbard model we have AFM-dielectric (insulating state) due to Mott- Hubbard localization scenario for $U \gg W$ (we discussed it briefly in Chap. 9). Close to half-filling in the limit of $U \gg W$ we have phase separation on small metallic FM-droplets (containing one-hole) inside AFM insulating matrix [73] due to Nagaoka theorem (which predicts FM-transition in the Hubbard model after an addition of one hole to the half-filled AFM-structure in the limit $U \to \infty$) [74].

We would like to emphasize also that for electron density $n > ½$, the compressibility of the CO-state is again negative $\kappa^{-1} = -\frac{4W^2}{6Vz} < 0$, and has the same value as for $n < ½$. As a result it is again more favorable to create a phase-separated state for these densities. However, as already mentioned, the nature of

the second phase with $n > ½$ is not quite clear at present, and therefore, we do not consider this case here.

15.6.4 Phase Separation in the Extended Double Exchange Model (with nn Coulomb Interaction)

In the beginning of the Sect. 15.3 we introduced FM Kondo lattice model (or double exchange model) as a minimal model to describe FM-polarons inside AFM-matrix at small densities $n \ll 1$ (Fig. 15.11) and in almost half-filled case for $x = 1 - n \ll 1$ (Fig. 15.12). To capture an additional possibility of the formation of metallic polarons (we will show that they are actually ferromagnetic also) inside CO-matrix in manganites we should add nn Coulomb repulsion between conductivity electrons to the double exchange model. Then the corresponding Hamiltonian of the extended model reads:

$$\hat{H} = -t \sum_{<i,j>\sigma} c_{i\sigma}^{+} c_{j\sigma} + V \sum_{<i,j>} n_i n_j - J_H \sum_i \vec{S}_i \vec{\sigma}_i + J \sum_{<i,j>} \vec{S}_i \vec{S}_j, \qquad (15.6.34)$$

where we conserved the coefficient V (and not $V/2$) in the second term in (15.6.34) in similarity with (15.6.1). The discussion in Sect. 15.3 shows that we are working in the strong-coupling limit of FM Kondo lattice model $J_H S > W > JS^2$. In the same time as we discussed in Sect. 15.6 we are working in the strong-coupling limit of Verwey model. Thus it is reasonable to consider the following hierarchy of parameters in the extended model:

$$J_H S > V > W > JS^2. \qquad (15.6.35)$$

We emphasize here once more that in manganites, strictly speaking, a correlative radius $r_s \gtrsim 4$ due to large dielectric polarization $\varepsilon \sim (10 \div 20)$, so we are really on the border between weak-coupling perturbative approach (RPA-scheme with $V/t \lesssim 1$ which is valid for $r_s \lesssim 1$) and non-perturbative tight-binding case (for which $r_s \gg 1$ and it is reasonable to assume that $V > t$). In our view, however, the tight binding (strong-coupling) approximation $V > t$ is more preferable since it allows to consider all major phenomena in manganites on a simple qualitative level.

For small electron densities $n \ll 1$ the radius of FM-polaron embedded in the AFM-matrix in the absence of nn Coulomb interaction is given by $R_{pol}/d \sim \left(t/JS^2\right)^{1/5}$ and hence for densities which are far from the percolation threshold $n \ll n_c \sim \left(JS^2/t\right)^{3/5}$ we have the following chain of inequalities (see Fig. 15.29):

$$d/n^{1/3} \gg R_{pol} > d. \qquad (15.6.36)$$

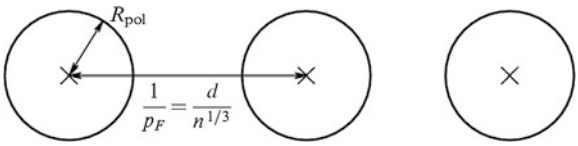

Fig. 15.29 Distribution of conduction electrons in a phase-separated state with FM polarons inside AFM matrix [8]

This chain of inequalities implies that the mean distance between the conduction electrons far exceeds the polaron radius, which in turn is larger than the intersite distance d. (In this Section we will again mostly speak about electrons).

Thus, for FM polarons (ferrons) with one conduction electron per ferron, even the allowance for the strong Coulomb interaction between electrons on neighboring sites does not lead to a charge redistribution. Therefore, upon including the Coulomb interaction, both the energy of the phase-separated state with FM polarons inside AFM matrix and that of a homogeneous state acquire only a Hartree–Fock correction term proportional to $(z/2)Vn^2$, so that the energy difference $E_{\mathrm{pol}} - E_{\mathrm{hom}}$ between the polaron and the homogeneous state remains unchanged, and the global minimum for the energy of the system again corresponds to the phase separated FM polaron/AFM matrix state. The most important point to reemphasize here is that there is only one conduction electron in each ferron. Here lies the main difference between the small-scale phase separation and the large-scale phase separation with a large number of conduction electrons per FM cluster (droplet). Note, however, that within the simplest model (15.6.34) and in the case of large-scale phase separation, the electric charge within an AFM droplet may be made rarefied enough to avoid strong increase in the Coulomb interaction energy. This is likely to be a qualitative explanation of the experiments [30, 35] showing FM droplets, 100–1000 Å across, with a large number of conduction electrons. Note also that the analysis of the large-scale phase separation probably requires considering the elastic energy of the lattice distortions caused by the formation of an inhomogeneous state. Such distortions may make it easier to change the electron density without violating the electroneutrality.

15.6.4.1 Phase Separation for Densities Close to ½

The energy of FM metallic droplet inside CO-matrix (which should be also AFM) for densities close to ½ is given by the combination of the terms typical to FM-polarons inside AFM-matrix (15.3.8) and to metallic polarons inside CO-matrix (15.6.30):

$$E = -tn_d\left(z - \frac{\pi^2 d^2}{R^2}\right) + \frac{zJS^2}{2}\frac{4}{3}\pi\left(\frac{R}{d}\right)^3 n_d - \frac{zJS^2}{2}\left[1 - \frac{4}{3}\pi\left(\frac{R}{d}\right)^3 n_d\right] - \frac{W^2}{6Vz}\left(1 - \frac{4}{3}\pi\left(\frac{R}{d}\right)^3 n_d\right), \tag{15.6.37}$$

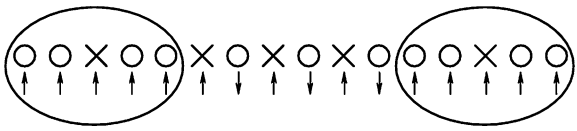

Fig. 15.30 Formation of metallic FM droplets of small radius within a charge-ordered AFM matrix [8]

where n_d is a droplet density. The first three terms in (15.6.37) are identical to the magnetic polaron energy in the double exchange model (15.3.8) but with the electron density n replaced by the droplet density n_d. At the same time the last term in (15.6.37) is identical to the second term in (15.6.30) corresponding to the energy of a homogeneous CO Verwey state. Minimization of the droplet energy (15.6.37) with respect to radius R yields in the 3D case:

$$\frac{R_{pol}}{d} \sim \frac{1}{(t/V + JS^2/t)^{1/5}}. \tag{15.6.38}$$

Note that for $t/V \ll JS^2/t$, we obtain $R/d \sim (t/JS^2)^{1/5}$, and the double exchange result (15.3.9) is reproduced for the metallic droplet radius. In the opposite case $t/V \gg JS^2/t$, we have $R/d \sim (V/t)^{1/5}$, and we arrive to the Verwey model result (15.6.31). Accordingly, the critical concentration for the overlap of metallic droplets is:

$$n_{dc} \sim \left(\frac{t}{V} + \frac{JS^2}{t}\right)^{3/5}. \tag{15.6.39}$$

Physically, minimization of the total energy (15.6.37) with respect to the droplet radius implies that there is only one conduction electron inside the metallic droplet and that this electron is surrounded by FM-ordered local spins. At the same time, outside the droplets we have a CO (checkerboard) arrangement of conduction electrons surrounded by AFM-ordered local spins (Fig. 15.30).

This last result illustrates the main difference between the phase-separated states that are obtained in the extended model (15.6.34) at electron densities $n \to 0$ and $n \to ½$. At low densities ($n \ll 1$), the conduction electron density outside FM polarons is zero and the entire electric charge is contained within metallic droplets. At the same time, at densities close to ½, most conduction electrons are localized in CO-regions outside the metallic droplets.

Finally, the phase diagram of the extended FM Kondo-lattice model with nn Coulomb interaction includes the following regions for $n < 1/2$:

1) For $0 < n \lesssim (JS^2/t)^{3/5}$ the system separates into FM metallic droplets within an AFM insulating matrix.

Recollecting the results of Sect. 15.5 we should have in mind that if we include in the model (15.6.34) additional Coulomb attraction between a conduction electron and Ca(Sr) donor impurity V_{imp} (see (15.5.1)) than the first interval

$0 < n \lesssim (JS^2/t)^{3/5}$, actually is splitted in two: for $0 < n < n_{\mathrm{Mott}}$ we have bound magnetic polarons of de Gennes with extended coats of spin-distortions and for $n_{\mathrm{Mott}} < n \lesssim (JS^2/t)^{3/5}$ we have free FM-polarons (Nagaev-Mott-Kasuya ferrons with rigid boundary) inside AFM-matrix.

2) For $(JS^2/t)^{3/5} \lesssim n \lesssim (t/V + JS^2/t)^{3/5} < ½$ the system is a FM metal. Of course, we must have a certain "window" of parameters to satisfy this inequality. As we already discussed in real manganites we have $t/V \sim 1/2 \div 1/3$ and $JS^2/t \sim 0.1$.

Therefore, the inequality $(JS^2/t)^{3/5} < (t/V + JS^2/t)^{3/5}$ is not necessarily met. Experimental evidence indicates that the desired parameter range exists for $La_{1-x}Ca_xMnO_3$, but definitely not for $Pr_{1-x}Ca_xMnO_3$.

3) Finally, for $(t/V + JS^2/t)^{3/5} \lesssim n < ½$ we have phase separation into metallic FM droplets within an AFM charge-ordered matrix. Note that large Hund-rule exchange J_H between a local spin $\vec{S}$ and $\vec{\sigma}$ can suppress an ideal AFM-structure of local spins inside CO-matrix and promote ferrimagnetism inside it (for total spins $S_{\mathrm{tot}} = S + ½$).

Let us repeat again that in connection to the overall phase-diagram of hole-doped manganites $La_{1-x}Ca_xMnO_3$, presented on Fig. 15.2, we should think in terms of holes describing the regions of PS I, FM-metal, and PS II in the underdoped case ($x < 1/2$).

15.7 Orbital Ferrons

In fact a two-band character of conducting e_g-orbitals (see Figs. 15.6 and 15.7) is important for conductivity electrons in manganites especially close to percolation threshold $x \sim 0.16$. Here the full model, which describes the manganites, is a very complicated Kondo-Hubbard model [76]. The beautiful physics of the phase separation and orbital ordering can be described, however, on the language of a reduced two-band Hubbard model, which neglects double exchange interactions and describes only the essential interactions inside the subspace of two conducting e_g-orbitals.

15.7.1 Two-Band Degenerate Hubbard Model

The two-band model in a most general case was considered in Chap. 10. In manganites we deal with two-band degenerate Hubbard model describing by the Hamiltonian:

$$\hat{H}' = \sum_{\langle n\,m\rangle\ \alpha\beta\sigma} t_{n\,m}^{\alpha\beta}\, c_{n\,\alpha\,\sigma}^{+}\, c_{m\,\beta\,\sigma} + \varepsilon \sum_{m\sigma} n_{m\,\beta\sigma} - \mu \sum_{m\beta\sigma} n_{m\,\beta\sigma} + \tag{15.7.1}$$

where μ is the chemical potential, ε is the energy-shift between the centers of the bands. In our case $\varepsilon = E_{\mathrm{JT}}$ is connected with Jahn–Teller gap. $\{\alpha, \beta\}$—are the two e_{g}-subbands, $< n,\ m >$ are the neighboring sites, $\{\sigma,\ \sigma\ '\}$ are spin projections. Without loss of generality in the degenerate model we can assume $U_1 = U_2 = U' + 2J_{\mathrm{H}} = U$, where strong on-site Hubbard repulsion $U \sim 10$ eV $\gg J_{\mathrm{H}}S \sim 1$ eV $\gg t$. The total number of electrons (in both bands) per site $n_{\mathrm{tot}} = 1 - x$, where we are interested in $x \lesssim x_{\mathrm{C}} = 0.16$. In magnetic oxides $t_1 \sim t_2$. However in other materials such as uranium based HF-compounds (considered in Chaps. 10, 14) and possibly in overdoped cuprates they are different $t_1 \gg t_2$.

15.7.2 Heisenberg-Like Orbital Interaction

The detailed analysis of the two-band degenerate Hubbard model is given in [76, 77]. Here we present a brief sketch of the derivation of the effective model which allows us to get an orbital ferron state. In the strong-coupling case for $U \gg t$ and $x \lesssim 0.16$ we get on 2D square lattice with e_{g}-electrons on $|x^2 - y^2>$ and $|3z^2 - r^2>$-orbitals (see Figs. 15.7 and 15.8) the following effective Hamiltonian:

$$\hat{H}_{eff} = -\sum_{\substack{n,m \\ \alpha,\beta,\sigma}} t_{n\,m}^{\alpha\beta} P_{n\,\alpha\,\sigma}^{+}\, c_{n\,\alpha\,\sigma}^{+}\, c_{m\,\beta\,\sigma}\, P_{m\,\beta\,\sigma} + J \sum_{<n,m>} \vec{\tau}_n\, \vec{\tau}_m. \tag{15.7.2}$$

It is an orbital t-J model. The effective model (15.7.2) is derived from the two-band Hubbard model in [77] by the canonical transformation similar to derivation of the standard t-J model from the one-band Hubbard model in [24]. Pseudospin operators in (15.7.2) $\vec{\tau}_n = \left\{\tau_n^x, \tau_n^z\right\}$, $\tau_n^{x,z} = \frac{1}{2}\sum_{\alpha,\beta,\sigma} c_{n\,\alpha\,\sigma}^{+}(\sigma_{\alpha\beta}^{x,z}) c_{n\,\beta\,\sigma}$ describe an orbital state, $\sigma_{\alpha\beta}^{\mathrm{x,z}}$ are Pauli matrices, quadrupole interaction $J \sim t^2/U \sim (300 \div 400)$ K is analogous to superexchange interaction of AFM-type ($J > 0$) between two orbitals, $P_{\mathrm{m}\sigma\beta}$ are projection operators, excluding double occupation of sites. The Hamiltonian (15.7.2) was firstly proposed by Kugel, Khomskii [42] to describe the orbital ordering in Jahn–Teller systems for $n = 1$. The hopping integrals $t_{\mathrm{nm}}^{\alpha\beta}$ are described by (2×2) matrix (see [41] for more detailed analysis) and read:

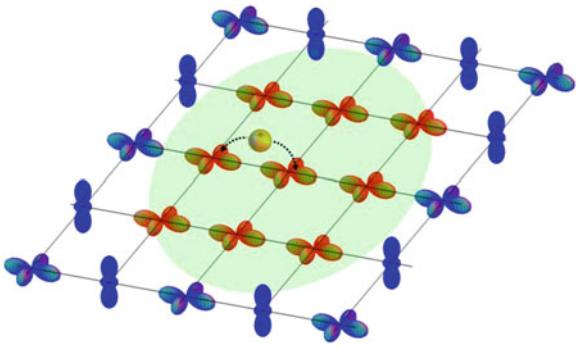

Fig. 15.31 Formation of metallic orbital ferrons inside AFM orbital matrix [41]

$$t_{nm}^{\alpha\beta} = \frac{t_0}{4}\begin{pmatrix} 3 & \mp\sqrt{3} \\ \mp\sqrt{3} & 1 \end{pmatrix}, \tag{15.7.2}$$

where minus (plus) sign corresponds to n-m bond parallel to x (y) axis in [41].

15.7.3 Orbital Ferrons in the Orbital t–J model

In the phase separated sate of the two-band Hubbard model (more precisely of the orbital t-J model) we deal with metallic orbital ferrons inside AFM orbital matrix. The derivation of the optimal radius of metallic orbital ferrons in [41] is exactly equivalent to the derivation of a FM-polaron inside AFM-matrix in 2D square lattice (see Sect. 15.4.3 and Eq. (15.4.7)). Characteristic radius of the droplet: $\frac{R_{pol}}{d} = c_3\left(\frac{t_0\alpha_0^2}{\pi JS^2}\right)^{1/4}$, where $\alpha_0 \approx 3\pi/4$ in the first zero of the Bessel function, (see Fig. 15.31), and c_3 is numerical coefficient connected with the spectrum in Eq. (15.7.2). We can see that inside the circular ferrons we have the same orbitals (say d_{x2-y2}), while outside the ferrons we have alternating order of d_{x2-y2} and d_{3z2-r2} orbitals.

Concluding this Section we can say that we considered free and bound magnetic polarons inside AFM and CO-matrices in 3D and layered manganites and other complex magnetic oxides (cobaltites, nickelates) as well as more exotic (but very beautiful) orbital ferrons inside AFM orbital matrix (inside the matrix with alternating e_g-orbitals in real space) (see the discussion of the overall phase-diagram on the Fig. 15.2 in Sect. 15.2.1).

15.8 Experimental Confirmation of the Overall Phase-Diagram and Phase Separation in Manganites

The phase diagram of manganites discussed in this chapter is in good qualitative agreement both with experiments on nanoscale phase separation in manganites [78–83] and with numerical calculations by Dagotto et al. [64]. Note that real manganites are usually hole-doped, so that experimentally $x = 1 - n$ means the hole concentration. This does not matter much, however, because of the re-entrant character of the phase diagram for $n \to 0$ and $x = 1 - n \to 0$. Nevertheless, the phase diagram of real manganites differs considerably depending on whether it is electron- or hole-doped. The mechanisms of this asymmetry are not yet completely understood. In particular, the asymmetry can be related to the specific features of orbital ordering in manganites and on possible formation, as we have mentioned above, of inhomogeneous states other than droplet structure discussed here, charge- and orbital stripes, for example. To include all these aspects, however, a theory that goes beyond the content of this chapter is needed.

15.8.1 Experimental Confirmation of Nanoscale Phase Separation

Turning now to the experimental confirmation of our results, the beautiful nuclear magnetic resonance (NMR) experiments on $La_{1-x}Ca_xMnO_3$ [78] should be mentioned first. These experiments which employed ^{55}Mn nuclei, provided for the existence of two NMR frequencies in the sample (instead of only one as is typical for a homogeneous state), whose frequencies are naturally attributed to the FM and AFM-domains resulting from the phase separation in manganites. NMR measurements at La nuclei in La-Pr manganites led to the similar conclusion [79].

Further experimental confirmation of phase separation in manganites comes from recent neutron scattering experiments [80, 83]. They showed that in the case of inelastic scattering there are two spin-wave modes, one of which has a quadratic dispersion and corresponds to FM magnons, whereas the other has a linear dispersion and corresponds to magnons in AFM phase.

Note that in elastic neutron scattering experiments the peak intensity $I(q)$ has a Lorentzian shape. The half-width of the peak at low densities $n \sim 0.05$ corresponds to the characteristic polaron radius $R_{\text{pol}} \sim 1/q_0 \sim 10$ Å [80]. At densities n close to ½, the line half-width again corresponds to small-scale phase separation with a characteristic polaron size $R_{\text{pol}} \sim (10 \div 20)$ Å.

Note that similar measurements of the spin wave spectrum in a magnetic field using the AFM resonance technique are interpreted in [84] as favoring some nontrivial compromise between magnetic polaron formation and inhomogeneous spin canting. Probably these experimental results could be explained within a concept of bound magnetic polarons with extended coat of spin-distortions considered in Sect. 15.5.

The further experimental evidence in favor of the polaron picture was obtained by Babushkina et al. [81] who discovered a strongly non-linear current–voltage characteristic in La-Pr manganites close to the phase boundary between the FM and CO-states. This provides indirect evidence for percolative charge transfer [86, 87] naturally activated by the phase separation process. The critical density for the overlap of polarons actually appears as the percolation threshold picture [86].

Finally, the experiments of Voloshin et al. [82] showed a shifted magnetization hysteresis in manganites with the center of the hysteresis loop shifting from the magnetic field $H = 0$ to $H \sim 4$–6 T in the low-density state. The shift appears quite naturally within the polaron picture. To see this note that in a magnetic field the effective Heisenberg exchange is $J_{eff}S^2 = JS^2 - g\mu_B^{el}HS$, where g is the gyromagnetic ratio and μ^{el}_B is the electron Bohr magneton. Therefore the polaron radius $\frac{R}{d} = \left(\frac{t}{J_{eff}S^2}\right)^{1/5}$ increases with the result that in strong magnetic fields the FM-polarons start to overlap at lower densities $n_c(H) < n_c(0) \approx 0.16$.

15.8.2 *Experiments on Large Scale Phase Separation: Formation of Stripes*

Note that, recently, more direct experiments supporting the phase separation scenario have been carried out [30, 85]. In [85] metallic regions inside the insulating matrix were visualized via scanning tunneling microscopy in hole-doped manganites (STM experiments of Mydosh group with "catching" of FM metallic polaron by a needle of ST microscope for $x \sim 0.16$). In [30] experiments on electron-diffraction performed by Cheong's group confirmed checkerboard CO-structure at $x = 0.5$ and also showed the coexistence of metallic FM domains and the insulating CO matrix in underdoped case for $x = 0.4$ in the experiments on dark image electron microscopy. However, both [85] and [30] actually report large scale phase separation, with metallic domains measuring $L \sim (100 \div 200)$ Å in size. Thus, the experiments reported in [85] and [30] neither contradict nor decisively verify the nanoscale polaron picture.

Finally, for $x > 0.5$ Mori et al. [35] showed the formation of stripes in experiments on electron diffraction in overdoped manganites (Fig. 15.32).

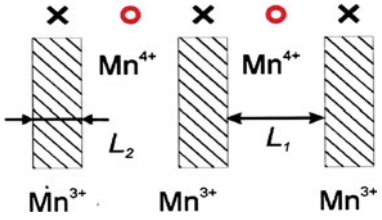

Fig. 15.32 Stripe structure measured by Mori et al. [35] in experiments on electron diffraction in overdoped manganites ($x > 0.5$)

They reported incommensurate charge ordering with the distance between two stripes $L_1 \approx 3\ L_2$, where L_2 is a stripe width. Note that the stripes are static in manganites due to Jahn–Teller effects in contrast with strongly fluctuating stripes in high-T_C compounds.

References

1. Jonker, G.H., van Santen, J.H.: Physica **16**, 337 (1950)
2. Jonker, G.H.: Physica **22**, 707 (1956)
3. Wollan, E.O., Koehler, W.C.: Phys. Rev. **100**, 545 (1955)
4. Jin, S., et al.: Science **264**, 413 (1994)
5. Nagaev, E.L.: Sov. Phys. Uspekhi **39**, 781 (1996)
6. Nagaev, E.L.: Phys. Rep. **346**, 387 (2001)
7. Dagotto, E., Hotta, T., Moreo, A.: Phys. Rep. **344**, 1 (2001)
8. Kagan, M.Yu., Kugel, K.I.: Sov. Phys. Uspekhi **44**, 553 (2001)
9. Khomskii, D.I., Sawatzky, G.A.: Solid State Comm. **102**, 87 (1997)
10. Ramirez, A.P.: J. Phys. Cond. Mat. **9**, 8171 (1997)
11. Coey, J.M.D., Viret, M., von Molnar, S.: Adv. Phys. **48**, 167 (1999)
12. Loktev, V.M., Perelomov, Yu.G.: Sov. Low Temp. Phys **26**, 171 (2000)
13. Emery, V.J., Kivelson, S.A., Lin, H.Q.: Phys. Rev. Lett. **64**, 475 (1990)
14. Emery, V.J., Kivelson, S.A.: Physica C (Amsterdam) **209**, 597 (1993)
15. Zaanen, J., Gunnarson, O.: Phys. Rev. B **40**, 7391 (1989)
16. Castellani, C., di Cesto, C., Grilli, M.: Phys. Rev. Lett. **75**, 4650 (1995)
17. Lorenzana, J., Castellani, C., Di Castro, C.: Phys. Rev. B **64**, 235128 (2001)
18. Nagaev, E.L.: JETP Lett. **6**, 18 (1967)
19. Nagaev, E.L.: JETP **27**, 122 (1968)
20. Kasuya, T., Yanase, A., Takeda, T.: Solid State Comm. **8**, 1543 (1970)
21. Mott, N.F., Davis, E.A.: Electronic Processes in Non-Crystalline Materials. Clarendon Press, Oxford (1971)
22. Krivoglaz, M.A.: Sov. Phys. Uspekhi **15**, 153 (1972)
23. Krivoglaz, M.A.: Sov. Phys. Uspekhi **16**, 856 (1974)
24. Bulaevskii, L.N., Nagaev, E.L., Khomskii, D.I.: JETP **27**, 836 (1968)
25. Brinkman, W.F., Rice, T.M.: Phys. Rev. B **2**, 1324 (1970)
26. Kampf, A., Schrieffer, J.R.: Phys. Rev. B **41**, 6399 (1990)
27. Shraiman, B.I., Siggia, E.D.: Phys. Rev. B **42**, 2485 (1990)
28. Belinicher, V.I., Chernyshev, A.L., Dotsenko, A.V., Sushkov, O.P.: Phys. Rev. B **51**, 6076 (1995)
29. Belinicher, V.I., Chernyshev, A.L., Shubin, V.A.: Phys. Rev. B **56**, 3381 (1997)
30. Uehara, M., Mori, S., Chen, C.H., Cheong, S.-W.: Nature **399**, 560 (1999)
31. Balagurov, A.M., Pomjakushin, V.Yu., Sheptyakov, D.V., Aksenov, V.L., Babushkina, N.A., Belova, L.M., Gorbenko, O.Yu., Kaul, A.R.: Eur. Phys. Jour. B **19**, 215 (2001)
32. Jahn, H.A. Teller, E.: Proc. Roy. Soc. London, Ser A161, 220 (1937)
33. Khomskii, D.I.: Physica B **280**, 325 (2000)
34. Jirák, Z., Krupička, S., Šimša, Z., Dlouhá, M., Vratislav, S.: J. Magn. Mag. Mat. **53**, 153 (1985)
35. Mori, S., Chen, C.H., Cheong, S.-W.: Nature **392**, 473 (1998)
36. Kagan, M.Yu., Khomskii, D.I., Mostovoy, M.V.: Eur. Phys. J. B **12**, 217 (1999)
37. Ogarkov, S.L., Kagan, M.Yu., Sboychakov, A.O., Rakhmanov, A.L., Kugel, K.I.: Phys. Rev. B **74**, 014436 (2006)

38. Kagan, M.Yu., Ogarkov, S.L., Kugel, K.I., Sboychakov, A.O., Rakhmanov, A.L.: J. Phys. Cond. Mat. **20**, 425214 (2008)
39. Kagan, M.Yu., Kugel, K.I., Khomskii, D.I.: JETP **93**, 415 (2001)
40. Kagan, M.Yu., Kugel, K.I., Rakhmanov, A.L., Pazhitnych, K.S.: J. Phys. Cond. Mat. **18**, 10905 (2006)
41. Kugel, K.I., Rakhmanov, A.L., Sboychakov, A.O., Khomskii, D.I.: Phys. Rev. B **78**, 155113 (2008)
42. Kugel, K.I., Khomskii, D.I.: Sov. Phys. Uspekhi **136**, 621 (1982)
43. De Gennes, P.G.: Phys. Rev. B **118**, 141 (1960)
44. Ishihara, S., Inoue, J., Maekawa, S.: Phys. Rev. B **55**, 8280 (1997)
45. Anderson, P.W., Hasegawa, H.: Phys. Rev. **100**, 675 (1955)
46. Pathak, S., Satpathy, S.: Phys. Rev. B **63**, 214413 (2001)
47. Zaanen, J., Oles, A.M., Horsch, P.: Phys. Rev. B **46**, 5798 (1992)
48. Nagaev, E.L.: Physics of Magnetic Semiconductors. Mir Publishers, Moscow (1983)
49. Kagan, M.Yu., Klaptsov, A.V., Brodsky, I.V., Kugel, K.I., Sboychakov, A.O., Rakhmanov, A.L.: Jour. Phys. A: Math. Gen. **36**, 9155 (2003)
50. Kagan, M.Yu., Klaptsov, A.V., Brodsky, I.V., Kugel, K.I., Sboychakov, A.O., Rakhmanov, A.L.: Sov. Phys. Uspekhi **173**, 877 (2003)
51. Itzykson, C., Zuber, J.B.: Quantum Field Theory, McGraw-Hill, NY (1980)
52. Laughlin, R.B.: Phys. Rev. Lett. **60**, 2677 (1988)
53. Fetter, A.L., Hanna, C.B., Laughlin, R.B.: Phys. Rev. B **39**, 9679 (1989)
54. Müeller-Hartmann, E., Dagotto, E.: Phys. Rev. B **54**, R6819 (1996)
55. Berry, M.V.: Proc. Roy. Soc. London, Ser. A, **392**, 45 (1984)
56. Gradshteyn, I.S., Ryzhik, I.M.: Table of Integrals. Series and Products. Academic Press, NY (2000)
57. Verwey, E.: Nature **144**, 327 (1939)
58. Verwey, E., Haayman, P.W.: Physica (Amsterdam) **8**, 979 (1941)
59. Khomskii, D.I.: Preprint No 105. USSR Academy of Sciences, Lebedev Institute of Physics (1969)
60. Mutou, T., Kontani, H.: Phys. Rev. Lett. **83**, 3685 (1999)
61. van den Brink, J., Khaliullin, G., Khomskii, D.: Phys. Rev. Lett. **83**, 5118 (1999)
62. Jackeli, G., Perkins, N.B., Plakida, N.M.: Phys. Rev. B **62**, 372 (2000)
63. Arulraj, A., Biswas, A.K., Raychaudhuri, C.N.R., Rao, P.M., Woodward, T., Vogt, D.E., Cox, A.K., Cheetham W.: Phys. Rev. B **57**, R8115 (1998)
64. Yunoki, S., Hotta, T., Dagotto, E.: Phys. Rev. Lett. **84**, 3714 (2000)
65. Solov'ev, I.V., Terakura, K.: Phys. Rev. Lett. **83**, 2825 (1999)
66. Arovas, D., Guinea, F.: Phys. Rev. B **58**, 9150 (1998)
67. Uhrig, G.S., Vlaming, R.: Phys. Rev. Lett. **71**, 271 (1993)
68. Moritomo, Y., Takeo, M., Liu, X.J., Akimoto, T., Nakamura, A.: Phys. Rev. B **58**, R13334 (1998)
69. Alonso, J.A., Garcia-Munoz, J.L., Fernandez-Diaz, M.T., Aranda, M.A.G., Martínez-Lope, M.J., Casais, M.T.: Phys. Rev. Lett. **82**, 3871 (1999)
70. Shubin, S., Vonsovsky, S.: Proc. Roy. Soc. London **A145**, 159 (1934)
71. Pietig, R., Bulla, R., Blawid, S.: Phys. Rev. Lett. **82**, 4046 (1999)
72. Zhang, F.C., Rice, T.M.: Phys. Rev. B **37**, 3759 (1988)
73. Visscher, P.B.: Phys. Rev. B **10**, 943 (1974)
74. Nagaoka, Y.: Phys. Rev. B **147**, 392 (1966)
75. Anderson, P.W.: Science **235**, 1196 (1987)
76. Zaanen, J., Oles, A.M.: Phys. Rev. B **48**, 7197 (1993)
77. Ishihara, S., Inoue, J., Maekawa, S.: Physica C **263**, 130 (1996)
78. Allodi, G., de Renzi, R., Guidi, G., Licci, F., Pieper, M.W.: Phys. Rev. B **56**, 6036 (1997)
79. Yakubovskii, A., Kumagai, K., Furukawa, Y., Babushkina, N., Taldenkov, A., Kaul, A., Gorbenko, O.: Phys. Rev. B **62**, 5337 (2000)

80. Hennion, M., Moussa, F., Biotteau, G., Rodríguez-Carvajal, J., Pinsard, L., Revcolevschi, A.: Phys. Rev. Lett. **81**, 1957 (1998)
81. Babushkina, N.A., Belova, L.M., Khomskii, D.I., Kugel, K.I., Gorbenko, O.Yu., Kaul, A.R.: Phys. Rev. B **59**, 6994 (1999)
82. Voloshin, I.F., Kalinov, A.V., Savel'ev, S.E., Fisher, L.M., Babushkina, N.A., Belova, L.M., Khomskii, D.I., Kugel', K.I.: JETP Lett. **71**, 106 (2000)
83. Moritomo, Y., Machida, A., Mori, S., Yamamoto, N., Nakamura, A.: Phys. Rev. B **60**, 9220 (1999)
84. Mukhin, A.A., Ivanov, V.Yu., Travkin, V.D., Pimenov, A., Loidl, A., Balbashov, A.M.: Eur. Phys. Lett **49**, 514 (2000)
85. Fäth, M., Freisem, S., Menovsky, A.A., Tomioka, Y., Aarts, J., Mydosh, J.A.: Science **285**, 1540 (1999)
86. Gor'kov, L.P.: Sov. Phys. Uspekhi **41**, 589 (1998)
87. Gor'kov, L.P., Kresin, V.Z.: JETP Lett. **67**, 985 (1998)

Chapter 16
Mesoscopic Transport Properties in the Phase-Separated Manganites

The physics of mesoscopic transport phenomena [1–9] is a very rapidly developing field in the modern condensed-matter physics which is very promising for the applications in small (nano-size) electron devices [5, 12, 13] and very interesting for studying of the quantum interference effects [6, 9, 10, 15] and the quantum effects of localization in dirty or narrow-band (strongly-correlated) metals [11, 16, 17] as well as classical percolation effects in doped semiconductors [14].

16.1 Mesoscopic Transport Properties in Strongly-Correlated Electron Systems

In this chapter we would like to build a bridge between the physics of strongly-correlated electrons [11, 16–18] and the physics of mesoscopic transport phenomena [1–9] studying the transport properties of the CMR-systems. Namely for the CMR-family of materials we will present the simple theory for the tunneling conductivity, magnetoresistance (MR) and $1/f$-noise spectrum [22–28] in the low-doping case [19–24]. In this case as it was shown in Chap. 15, the CMR-systems are in the nano-scale phase-separated state. We will compare the theoretical predictions for transport properties of non-metallic phase-separated manganites with experimental observations in several families of 3D and layered CMR-materials [29–37].

16.1.1 Transport Properties in Non-Metallic Phase-Separated Manganites

In Chap. 15 we considered the formation of nano-scale phase-separated state in different CMR-systems. In particular we studied the formation of small FM-polarons (FM droplets or ferrons) inside AFM, PM or CO-matrices. It is interesting to understand the nature of electron transport in the phase-separated state having in

M. Yu. Kagan, *Modern Trends in Superconductivity and Superfluidity*,
Lecture Notes in Physics 874, DOI: 10.1007/978-94-007-6961-8_16,

mind that small FM-polarons are metallic, while they are embedded in the insulating AFM, PM or CO-matrices. We will consider here the transport mechanism connected with the electron tunneling from one FM-polaron to a neighboring one.

16.1.2 Tunneling Conductivity in the Phase-Separated Manganites

Let us consider an insulating antiferromagnetic sample of volume V_s in electric field E. The total number of magnetic polarons in the volume is N, and thus their spatial density is $n = N/V_s$. As mentioned in Chap. 15, the number of polarons is assumed to be equal to the number of charge carriers introduced by doping. Neglecting the conductivity of the insulating phase, we assume that charge carriers are only located within the droplets. The charge transfer can thus occurs either due to the motion of the droplets or due to electron tunneling. The former mechanism is less effective: indeed, the motion of a droplet is accompanied by a considerable rearrangement of the local magnetic structure, which results in the large effective mass of magnetic polarons. In addition, the droplets are expected to be easily pinned by crystal lattice defects. Thus, it is realistic to assume that the charge transport is essentially due to electron transitions between the droplets.

A magnetic polaron in the ground state contains one electron. As a result of the tunneling process, droplets with more than one electron are created, and some droplets become empty (the lifetime of such excitations is discussed in the end of this section). If the energy of an empty droplet $E(0)$ is taken to be zero, then the energy of a droplet with one electron can be estimated as $E(1) \sim t\, d^2/R_{pol}^2$ (where $R_{\rm pol}$ is the ferron radius). This is essentially the kinetic energy of an electron localized in the sphere of radius R. In the same way, the energy of a two-electron magnetic polaron $E(2) \sim 2E(1) + U$, with U the interaction energy of the two electrons. In all these estimates, we disregarded the surface energy, which as shown in Chap. 15 is expected to be small. Thus, $E(2) + E(0) > 2E(1)$, and the creation of two-electron droplets is associated with the energy barrier of the order of $A \equiv E(2) - 2E(1) \sim U$. It is clear that the interaction energy U of two electrons in one droplet is determined mainly by the Coulomb repulsion of these electrons; hence $A \sim e^2/\varepsilon R_{\rm pol}$, where ε is the static dielectric constant, which in real manganites can be rather large ($\varepsilon \sim 20$). We assume below that the mean distance between the droplets is $n^{-1/3} \gg R_{\rm pol}$ (the droplets do not overlap and we are in non-metallic state far from the percolation threshold [19]). Then, A is larger than the average Coulomb energy $e^2 n^{1/3}/\varepsilon$. Since the characteristic value of the droplet radius R is of the order of 10 Å, we have $A/k_{\rm B} \sim 1000$ K and $A > k_{\rm B}T$ in the case under study. In the following, we assume that the temperature is low, $A \gg k_{\rm B}T$, and we do not consider a possibility of the formation of the droplets with three or more electrons. Even in the case when these excitations are stable, it can be shown that far from the percolation threshold the strong Coulomb interaction suppresses

their contribution to the conductivity giving rise only to the next-order terms with respect to $\exp(-A/k_{\mathrm{B}}T)$.

Let us denote the numbers of single-electron, two-electron, and empty droplets as N_1, N_2, and N_0, respectively. According to our model, $N_2 = N_0$ (number of empty and two-electron droplets coincide), $N = N_1 + 2N_2$, and N is constant. Before turning to conductivity, we evaluate the thermal averages of N_1 and N_2. To this end, we note that the number $P_{\mathrm{N}}^{\mathrm{m}}$ of possible states with m two-electron droplets and m empty droplets equals $C_{\mathrm{N}}^{\mathrm{m}} C_{\mathrm{N-m}}^{\mathrm{m}}$, with $C_{\mathrm{N}}^{\mathrm{m}}$ being the binomial coefficients. Since the created pairs of droplets are independent, we write the partition function [38] in the form:

$$Z = \sum_{m=0}^{N/2} P_N^m \exp(-m\beta), \quad \beta = \frac{A}{k_B T}. \tag{16.1.1}$$

Though the sum can be evaluated exactly and expressed in terms of the Legendre polynomials for arbitrary N, it is more convenient to use the Stirling formula for the factorials [39] and the condition that the sample is macroscopic, $N \gg 1$. Approximating the sum by an integral,

$$Z = \int_0^{N/2} dm \exp\left\{-m\beta - N\ln\left(1 - \frac{2m}{N}\right) + 2m\ln\left(\frac{N}{m} - 2\right)\right\}, \tag{16.1.2}$$

calculating it in the saddle-point approximation, and subsequently evaluating in the same way the statistical average of N_2,

$$\bar{N}_2 = Z^{-1} \sum_{m=0}^{N/2} P_N^m \exp(-m\beta) = -\frac{\partial}{\partial\beta} \ln Z, \tag{16.1.3}$$

we easily obtain:

$$\bar{N}_2 = N \exp\left(-\frac{A}{2k_B T}\right), \tag{16.1.4}$$

$\bar{N}_1 = N - 2\bar{N}_2 = N\left[1 - 2\exp\left(-\frac{A}{2k_B T}\right)\right] = \bar{N}_{1\sigma} + \bar{N}_{1-\sigma}$, where σ is spin-projection of conductivity electron inside the ferron.

Now we calculate the conductivity. Within the framework of the proposed model the electron tunneling occurs via one of the four following processes illustrated in Fig. 16.1.

1. In the initial state we have two droplets in the ground state (with spin-projections of the conductivity electrons σ_1 and σ_2 in them correspondingly), and after tunneling in the final state we have an empty droplet and a droplet with two electrons.

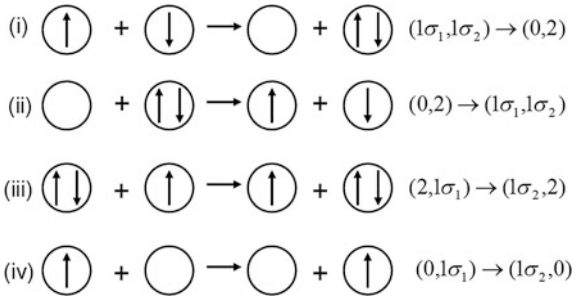

Fig. 16.1 Elementary tunneling processes [22, 23]

2. An empty droplet and a two-electron droplet in the initial state transform into two droplets in the ground state (two droplets with one electron, in the first one spin-projection of electron is σ_1, in the second one—σ_2).
3. A two-electron droplet and a single-electron droplet exchange their positions by transferring an electron from one droplet to the other.
4. An empty droplet and a single-electron droplet exchange their positions by transferring an electron from one droplet to the other.

Note that in the last two cases (3) and (4) σ_1, generally speaking, is not equal to σ_2. In the linear regime, all these processes contribute to the current density j independently, $j = j_1 + j_2 + j_3 + j_4$. The contributions of the first two processes read:

$$j_{1,2} = en_{1,2}\left\langle \sum_i v^i_{1,2} \right\rangle, \tag{16.1.5}$$

where $n_{1,2} = N_{1,2}/V_s$ are the densities of the single- and two-electron droplets, and $\langle \cdots \rangle$ stands for statistical and time averages. The appearance of the factors $n_{1,2}$ reflects the fact that the electron tunnels from a single-electron droplet process (1) or two-electron (2) droplet. The summation in (16.1.5) is performed over all magnetic polarons the electron can tunnel to—one-electron droplets for process (1) and empty droplets for process (2). Finally, the components of the average electron velocity $\langle v^i_{1,2} \rangle$ along the direction of the electric field are obviously found as [40]:

$$\left\langle \sum_i v^i_{1,2} \right\rangle = \left\langle \sum_i \frac{r^i \cos\theta^i}{\tau_{1,2}(r^i, \theta^i)} \right\rangle, \tag{16.1.6}$$

where r^i and θ^i are the electron tunneling length (the distance between the droplets) and the angle between the electric field and the direction of motion, respectively, and $\tau_{1,2}(r^i, \theta^i)$ are characteristic times associated with the tunneling processes. The relation between $\tau_1(r, \theta)$ and $\tau_2(r, \theta)$ can be found from the following considerations. Near the equilibrium, the number of two-electron droplets, excited per unit time, equals to the number of the decaying two-electron droplets. We thus have the detailed balance relation,

$$\frac{\bar{N}_1^2}{\tau_1(r,\theta)} = \frac{\bar{N}_2^2}{\tau_2(r,\theta)}, \tag{16.1.7}$$

where we have taken into account that the probability of the formation of a two-electron droplet is proportional to the total number N_1 of the single-electron states multiplied by the number of available hopping destinations, which also equals N_1. Similarly, the probability of decay of a two-electron droplet is proportional to $N_2 N_0 = N_2^2$. Equation (16.1.7) implies $\tau_2(r, \theta) = \tau_1(r, \theta) \exp(-A/k_B T)$. We write then the conventional expression for the tunneling times [40] in the following form:

$$\tau_{1,2}(r,\theta) = \omega_0^{-1} \exp\left\{\frac{r}{l} \pm \frac{A}{2k_B T} - \frac{eEr\cos\theta}{k_B T}\right\}, \tag{16.1.8}$$

where l and ω_0 are the characteristic tunneling length and magnon frequency, and we have taken into account the contribution of the external electric field to the tunneling probability.

To perform the averaging, we assume that the centers of the magnetic polarons are randomly positioned in space and the average distance $n^{-1/3}$ between them is much larger than the droplet radius R. Both assumptions seem to be perfectly justified far below the percolation threshold. Then the averaged sum in (16.1.5) is essentially the space average of v, multiplied by the number of droplets available for hopping [N_1 for the process (1) and N_2 for process (2)]. Expanding in $eEl/k_B T \ll 1$, we obtain:

$$\left\langle \sum_i v_{1,2}^i \right\rangle = \frac{eE\omega_0}{k_B T} N_{1,2} \exp\left\{\mp \frac{A}{2k_B T}\right\} \left\langle r^2(\cos^2\theta) e^{-r/l} \right\rangle_V, \tag{16.1.9}$$

where

$$\langle \cdots \rangle_V = \frac{1}{V_s} \int \ldots d^3\vec{r}. \tag{16.1.10}$$

In (16.1.9) the electric field is outside the averaging. Rigorously speaking, this means that the characteristic hopping length l is larger than the inter droplet distance $n^{-1/3}$ and our approach is valid only when the droplet concentration is not too small. Substituting (16.1.9) into (16.1.5) and performing the integration, we find:

$$j_{1,2} = \frac{32\pi e^2 E\omega_0 l^5 n_{1,2}^2}{k_B T} \exp\left\{\mp \frac{A}{2k_B T}\right\}. \tag{16.1.11}$$

In processes (3) and (4) the free energy of the system is not changed after the tunneling, and we write the characteristic times as:

$$\tau_{3,4}(r,\theta) = \omega_0^{-1} \exp\left\{\frac{r}{l} - \frac{eEr\cos\theta}{k_B T}\right\}. \tag{16.1.12}$$

The contribution of these two processes to the current is calculated similarly to that of (1) and (2). For process (3) the number of magnetic polarons from which the electron may tunnel is N_2, whereas the number of accepting droplets is N_1. In the same way, for process (4) these numbers are N_1 and $N_0 = N_2$, respectively. Consequently, the factors $n^2_{1,\,2}$ in (16.1.11) are replaced by n_1, n_2,

$$j_{3,4} = \frac{32\pi e^2 E\omega_0 l^5 n_1 n_2}{k_B T}. \tag{16.1.13}$$

From (16.1.11) and (16.1.13) we now obtain the dc conductivity $\sigma = j/E$:

$$\sigma = \frac{32\pi e^2\omega_0 l^5}{k_B T}\left(2n_1 n_2 + n_1^2 e^{-A/2k_B T} + n_2^2 e^{A/2k_B T}\right). \tag{16.1.14}$$

In this subsection we are only interested in the average conductivity; fluctuations lead to the appearance of noise and are considered in Sect. 16.2. Using (16.1.4), we find that all four processes illustrated in Fig. 16.1 give identical contributions to the conductivity; for $A \gg k_B T$ the average conductivity (for which we retain the notation σ) reads:

$$\sigma = \frac{128\pi e^2 n^2\omega_0 l^5}{k_B T} e^{-\frac{A}{2k_B T}}. \tag{16.1.15}$$

We see that the conductivity increases with temperature as $\sigma\,(T) \sim T^{-1}\, e^{-\frac{A}{2k_B T}}$, which is typical for tunneling systems (see, e.g., [40]).

At this point, let us discuss the applicability range of our model. The essence of our picture is the existence of different types of droplets. Only single-electron droplets are stable. Obviously, an empty droplet decays during the time of the order of $1/\omega_0$. On the other hand, following the above discussion, the empty droplet should acquire an electron from neighboring one-electron or two-electron droplets during the characteristic time τ_0, which can be easily calculated based on the following considerations. The probability P per unit time for an empty droplet to acquire one electron can be written as:

$$P = 4\pi\omega_0 \int_0^\infty e^{-r/l}[n_1 + n_2 \exp(A/k_B T)] r^2 dr, \tag{16.1.16}$$

where the terms with n_1 and n_2 correspond to the electron transfer from single- and two-electron droplets, respectively. Performing integration in (16.1.16) and using (16.1.4), we find

$$\tau_0 = \frac{1}{P} = \frac{\exp(-A/2k_B T)}{8\pi\,\omega_0\, l^3 n}. \tag{16.1.17}$$

Just the same estimate can be obtained for the characteristic time of electrons leaving two-electron droplets. For our picture with empty and two-electron droplets to be valid, the following condition must be met: $\tau_0 \ll \omega_0^{-1}$. Thus, our

approach is valid at sufficiently low temperatures, $k_B T \ll A$, and for a not too small droplet density n.

The applicability of our approach also implies that $l > R_{pol}$, $n^{-1/3}$. It is of interest to consider also the case of $l \sim R_{pol}$ and/or low droplet concentrations. In this situation, in usual hopping systems, the conductivity strongly depends on the geometry of current paths [19]. This causes an exponential dependence of conductivity on the carrier concentration. However, our system turns out to be more complicated than those commonly invoked for hopping conductivity. It involves different types of hopping centers giving rise to an unusual geometry of current paths. Therefore, the conventional approaches used for hopping cannot be applied straightforwardly to the analysis of our model at low droplet concentration or at $l \sim R_{pol}$. Despite these complications, we believe that the expression for the conductivity in the case $l \leq n^{-1/3}$ includes the percolation-related factor $\exp\{-\gamma/(n^{1/3} R_{pol})\}$, with γ of the order one [19], though currently we have no rigorous proof of this statement.

The results below for magnetoresistance and noise are insensitive to this factor, and therefore we expect them to be valid in a general case.

16.1.3 Tunneling Magnetoresistance in the Phase-Separated Manganites

As we already discussed, below the percolation threshold when the volume fraction of droplets $n < n_C$, a typical value of A/k_B is mainly determined by Coulomb interaction between two electrons inside the droplet $A \sim e^2/\varepsilon R_{pol}$ and has a typical value of 1000 K. Now we can use this estimate to analyze the magnetoresistance in non-metallic phase-separated manganites. To do that, we use the expression for the radius of the magnetic polaron, obtained in the Chap. 15 $R_{pol} \sim d(t/JS^2)^{1/5}$. Recall once more that here $J \sim 10$ K is an AFM Heisenberg exchange between the local spins $S = 3/2$. It is natural to conclude that in the magnetic field the Heisenberg exchange integral J decreases according to the formula $J(H)S^2 = J(0)S'^2 - g\mu_B^{el}HS$, where μ_B^{el} and g are the electron Bohr magneton and the gyromagnetic ratio, respectively. Consequently, the value of A is decreasing linearly in the experimentally accessible range of magnetic fields, and for the excitation energy we obtain

$$A(H) = A(0)[1 - bH]; \quad b = \tfrac{1}{5}\tfrac{g\mu_B^{el}}{J(0)S}. \tag{16.1.18}$$

It follows now from (16.1.15) that the magnetoresistance is negative and for temperatures $T < A/k_B$ in absolute value reads:

$$|MR| = \frac{\rho(0) - \rho(H)}{\rho(H)} = \exp\left(\frac{A(0) - A(H)}{2k_B T}\right) - 1 = \exp\left(\frac{bHA}{2k_B T}\right) - 1. \tag{16.1.19}$$

For low magnetic fields and not very small temperatures the absolute value of the magnetoresistance (MR) is small, $|\mathrm{MR}| \approx bHA/2k_\mathrm{B}T \ll 1$. In higher fields (but still $bH \ll 1$) the absolute value of magnetoresistance eventually exceeds 1 and behaves in exponential fashion, $|\mathrm{MR}| \approx \exp\{bHA/2k_\mathrm{B}T\}$. Note that for temperatures $T < A/k_\mathrm{B}$ and for typical gyromagnetic ratios $g \sim 2$ the magnetoresistance in our region of doping becomes larger than 1 by absolute value only in relatively high magnetic fields $H \geq 10$ T.

To describe the actual experimental situation (especially at lower fields) in more detail, we need to take into account other important physical mechanisms, in particular, spin-dependent tunneling [22–28].

Effects of spin-assistant tunneling yields nontrivial preexponential factor for the magnetoresistance. The details of the calculations which are rather straightforward you can find in [22]. Here we present the brief sketch of the evaluation of MR (see [27]). The most important is that probability of tunneling depends on the mutual orientation of the electron spin and the magnetic moment of the droplet (see Fig. 16.2). Orientation of the ferromagnetically correlated regions in the external magnetic field H leads to an increase in the transition probability and, hence, to a decrease in resistance with increasing field strength—in agreement with experiment. The conductivity of the system can be represented as $\sigma(H) = \sigma(0) \langle \sum(H) \rangle$, where $\sum(H)$ is the "spin" contribution to the probability of electron tunneling. For this definition, $\mathrm{MR} = \langle \sum(H) \rangle - 1$.

Denoting the effective magnetic moment of the droplet by $M = \mu_\mathrm{B}\, gN_\mathrm{eff}\, S$ (N_eff is a number of local spins in the droplet) and assuming the interaction between the droplets to be negligibly small, we write the Free-energy of the droplet in magnetic field in the following form [41, 42]:

$$U(H) = U(0) - M(H\cos\theta + H_a\cos^2\psi), \tag{16.1.20}$$

where θ is the angle between the applied field $\vec{H}$ and the magnetic moment $\vec{M}$, H_a is the anisotropy field, and ψ is the angle between the anisotropy axis and the direction of the magnetic moment (for the sake of simplicity we consider the case of uniaxial anisotropy). Let $\vec{H}$ be parallel to z-axis, and let the anisotropy axis lie in the (xz) plane and make the angle β with vector $\vec{H}$. In this configuration (see Fig. 16.3):

$$\cos\psi = \sin\theta\sin\beta\cos\varphi + \cos\theta\cos\beta, \tag{16.1.21}$$

Fig. 16.2 Spin-assistant tunneling of electron between two FM-droplets with large magnetic moments $\vec{M_1}$ and $\vec{M_2}$. Angle ν is between $\vec{M_1}$ and $\vec{M_2}$

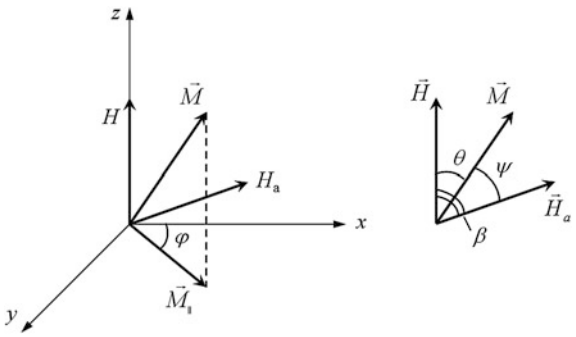

Fig. 16.3 The mutual orientation of the magnetic field $\vec{H}$, anisotropy field $\vec{H}_a$ and magnetic moment of a droplet $\vec{M}$. Angle θ is between $\vec{H}$ and $\vec{M}$, angle ψ is between $\vec{M}$ and $\vec{H_a}$, angle β is between $\vec{H}$ and $\vec{H_a}$, angle φ is between x-axis and projection of $\vec{M}$ on (xy) plane. Magnetic field $\vec{H}$ is parallel to z-axis. Anisotropy field $\vec{H}_a$ lies in the (xz) plane (see [27])

where φ is the angle between the x-axis and the projection of $\vec{M}$ into (xy) plane (see Fig. 16.3).

In the classical limit, a given orientation of vector $\vec{M}$ corresponds to the probability [38, 42]:

$$P(H,\theta,\varphi) \;=\; C(H)\exp\left[\frac{M(H\cos\theta \;+\; H_a\cos^2\psi(\theta,\varphi))}{k_BT}\right], \qquad (16.1.22)$$

where $C(H)$ is the normalization factor. The eigenstates of an electron correspond to conservation of the spin-projection $\sigma = \pm$ ½ onto the effective field direction in a ferromagnetically correlated region. Let an electron interact with Z magnetic moments of local spins S in the droplet. The energy of this interaction is $E_\sigma = -J_{\mathrm{FM}}SZ\sigma$ (where J_{FM} is an effective ferromagnetic exchange interaction). It describes the magnetic interaction between a conduction electron and an effective molecular field generated by ferromagnetically correlated spins in droplet. Since the product $J_{\mathrm{FM}}SZ$ is of the order of the Curie temperature ($T_{\mathrm{C}} \sim 100$ K see Sect. 16.3.3), E_σ is much greater than the energy of interaction between the electron spin and the magnetic field, provided that $H \ll 100$ T. In this case, the effective field direction coincides with the direction of vector $\vec{M}$ and the probability for the electron spin projection to be σ can be written as:

$$P_\sigma \;=\; \frac{\exp(-E_\sigma/k_BT)}{2ch(E_\sigma/k_BT)}. \qquad (16.1.23)$$

Upon transfer from droplet 1 to droplet 2, an electron occurs in an effective field making an angle v (see Fig. 16.2) with that in the initial state, for which:

$$\cos v \;=\; \cos\theta_1\cos\theta_2 \;+\; \sin\theta_1\sin\theta_2\cos(\varphi_1 \;-\; \varphi_1) \qquad (16.1.24)$$

(indices 1 and 2 refer to the droplet number). Then, the work performed for the electron transfer from droplet 1 to droplet 2 is $\Delta E_\sigma = E_\sigma(1-\cos\nu)$. Accordingly, the probability of this transfer is proportional to $\exp(-\Delta E_\sigma/k_B T)$. Taking into account all the probability factors introduced above, the final expression can be written as:

$$\langle \Sigma(H) \rangle = \int_0^{2\pi} d\varphi_1 \int_0^{2\pi} d\varphi_2 \int_0^{\pi} \sin\theta_1 d\theta_1 \int_0^{\pi} \sin\theta_2 d\theta_2 P(\theta_1\varphi_1) P(\theta_2\varphi_2) \sum_{\sigma=\pm 1/2} P_\sigma \exp\left(-\frac{\Delta E_\sigma}{k_B T}\right) \tag{16.1.25}$$

In the high-temperature range, where $k_B T$ is much greater compared to the Zeeman energy $\mu_B^{el} g S N_{\text{eff}} H$ (N_{eff} is a number of local spins in the droplet) and the magnetic anisotropy energy $\mu_B^{el} g S N_{\text{eff}} H_a$, relations (16.1.22–16.1.25) yield in the strongly anisotropic case and low fields ($H \ll 10$ T) [22–25, 27, 28]:

$$|MR| \sim \frac{H^2 H_a}{T^5}, \tag{16.1.26}$$

and in the absence of anisotropy (for $H_a = 0$):

$$|MR| \sim \frac{H^2}{T^2} \tag{16.1.27}$$

.

At higher fields magnetoresistance behaves as:

$$|MR| \sim \frac{H^2}{T} \tag{16.1.28}$$

then goes on a plateau.

Thus for $H \lesssim 10$ T an absolute value of magnetoresistance behaves quadratic in field but temperature dependence of $|\text{MR}| \sim H^2/T^n$ (n running from 1 to 5) is highly nontrivial. Finally in high fields $H \gtrsim 10$ T it grows in exponential fashion with field (see Fig. 16.4) and (16.1.19).

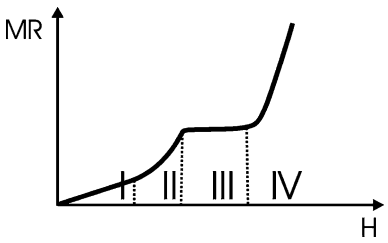

Fig. 16.4 Absolute value of magnetoresistance |MR| in magnetic fields. The different regions I, II, III correspond to quadratic in field behavior $|\text{MR}| \sim H^2/T^n$ with $n = 2$ or 5 in region I, $n = 1$ in region II, $n = 0$ (plateau) in region III. In region IV |MR| grows in exponential fashion with field [22–25, 27, 28]

The low-field regime I for |MR| (see (16.1.26) and Fig. 16.4) is confirmed by experimental observations of several groups for 6 families of 3D (cubic) and layered manganites [30, 32, 33, 35]. We will discuss these results more detaily in the Sect. 16.3.

16.2 1/*f*-Noise Power Spectrum

Almost ten years ago Podzorov et al. [37] reported the observation of giant 1/*f*-noise in perovskite manganites in the phase-separated regime. Generally, systems with distributed hopping lengths are standard objects that exhibit 1/*f*-noise (for review, see [19, 20]). The purpose of this section is to study low-frequency noise within the framework of the model used to calculate the conductivity in subsection 16.1.3 and show that it has, indeed, 1/*f*-form.

Starting from the Ohm's law $U = IL/\sigma S$ [1, 41] (where L and S are the sample length and the cross-section, respectively) and assuming that the measuring circuit is stabilized ($I = const$), we can present the voltage noise at the frequency ω, $\langle\, \delta U^2 \,\rangle_\omega$, in the following way:

$$\left\langle \delta U^2 \right\rangle_\omega = U_{dc}^2 \frac{\left\langle \delta\sigma^2 \right\rangle_\omega}{\sigma^2}, \tag{16.2.1}$$

where U_{dc} is the time-averaged voltage and $\langle \delta\sigma^{\,2} \rangle_{\,\omega}$ is the noise spectrum of the fluctuations of the conductivity.

If we disregard possible fluctuations of temperature in the system, the only source of the fluctuations in our model is those of the occupation numbers n_1 and n_2. Using the conservation law $n_1 + 2n_2 = n$, we find from (16.1.14):

$$\delta\sigma \;=\; \sigma \frac{\delta\, n_2}{\bar{n}_2} [1 \;-\; 2\exp(-A/2k_BT)]. \tag{16.2.2}$$

We thus need to find the fluctuation spectrum $\langle \delta n_2^2 \,\rangle_\omega$. Following the general prescription (see [43]), we recollect that the two-electron droplets decay via process (2) on Fig. 16.1 and the relaxation equation has the form:

$$\delta\, \dot{n}_2 \;=\; -\,\frac{\delta\, n_2}{\tau(r)};\; \tau(r) \;=\; \omega_0^{-1} \exp(r/l \;-\; A/2k_BT), \tag{16.2.3}$$

, where we have neglected the effect of the electric field. The fluctuation spectrum then reads [43]:

$$\left\langle \delta\, n_2^2 \right\rangle_\omega = \left\langle \delta\, n_2^2 \right\rangle_T \left\langle \sum_i \frac{2\tau(r^i)}{1 + \omega^2\tau^2(r^i)} \right\rangle, \tag{16.2.4}$$

where $\langle \delta n_2^2 \,\rangle_{\mathrm{T}}$ is the thermal average of the variation of n_2 squared, and the summation is performed over the "empty droplet—two-electron droplet" pairs,

with r^{i} being the distance between the sites in a pair. Since all such pairs contribute to the noise, the average in (16.2.4) is essentially a spatial integral, with the main contribution coming from short distances,

$$\left\langle \delta n_2^2 \right\rangle_\omega = 8\pi \bar{n}_2 \left\langle \delta n_2^2 \right\rangle_T \int_0^\infty \frac{\tau(r)}{1 + \omega^2 \tau^2(r)} r^2 dr. \tag{16.2.5}$$

Note that (16.2.5) is valid for an arbitrary relation between l and R_{pol}, not necessarily for $R_{\mathrm{pol}} \ll l$.

We are interested below in the frequency range

$$\widetilde{\omega}_0 \exp(-L_s/l) \ll \omega \ll \widetilde{\omega}_0\,, \quad \widetilde{\omega}_0 = \omega_0 \exp(A/2k_BT), \tag{16.2.6}$$

where L_{s} is the smallest of the sample sizes. In this case, with the logarithmic accuracy we obtain for $A \gg k_{\mathrm{B}}T$,

$$\left\langle \delta U^2 \right\rangle_\omega = U_{dc}^2 \frac{\left\langle \delta n_2^2 \right\rangle_T}{\bar{n}_2} \frac{4\pi^2 l^3}{\omega} \ln^2 \frac{\widetilde{\omega}_0}{\omega}. \tag{16.2.7}$$

Thus, in the wide range of sufficiently low frequencies (16.2.6), the noise power spectrum for our system has almost a 1/*f*-form.

The variation $\left\langle \delta n_2^2 \right\rangle_T = V_s^{-2}\left(\overline{N}_2^2 - \left(\overline{N}_2\right)^2\right)$ is easily found in the same way as (16.1.4),

$$\left\langle \delta n_2^2 \right\rangle_T = \frac{\bar{n}_2}{2V_s}. \tag{16.2.8}$$

Combining this with (16.2.7) we write the final expression for the spectral density of noise for $A \gg k_{\mathrm{B}}T$ in the form [22]:

$$\left\langle \delta U^2 \right\rangle_\omega = U_{dc}^2 \frac{2\pi^2 l^3}{V_s \omega} \ln^2 \left(\frac{\omega_0 e^{A/2k_BT}}{\omega} \right). \tag{16.2.9}$$

16.2.1 Discussion Comparison with Experiments

For the further discussion, it is convenient to rewrite (16.2.9) in the form:

$$\alpha_H = \frac{\left\langle \delta U^2 \right\rangle_\omega V_s \omega}{U_{dc}^2} = 2\pi^2 l^3 \ln^2 \left(\frac{\tilde{\omega}_0}{\omega} \right), \tag{16.2.10}$$

where α_{H} is a Hooge constant [19, 20, 43, 44].

It is remarkable that the noise spectrum in our model has a 1/*f*-form up to very low frequencies. This is due to fluctuations in occupation numbers of droplets, associated with the creation and annihilation of extra electron–hole pairs.

This mechanism of 1/*f*-noise is specific for our model and is not present in standard hopping conduction.

Let us estimate the numerical value of the parameter α_H, which is the standard measure of the strength of 1/*f*-noise. This parameter is proportional to the third power of l. Simple estimates (analogous to that presented in the Chap. 15 for ferron radius R_{pol}) reveal that, in general, l is of the order or larger than R_{pol}. Assuming again that the excitation energy is of the order of the Coulomb energy $A \sim e^2/\varepsilon R_{pol}$, taking ω_0 to be of the order of the Fermi-energy inside the droplets (which means $\hbar\omega_0 \sim 300$ K for $n < n_c$), and estimating the tunneling length l as being $l \geq 2\ R_{pol} = 20$ Å, we arrive at the conclusion that the parameter α_H is of the order $\alpha_H \sim (10^{-17} \div 10^{-16})$ cm^3 for $T < A/k_B$ ($T \sim 100 \div 200$ K) and $\omega \sim 1$ Hz $\div$ 1 MHz. This value of α_H is by several orders of magnitude higher than that in the usual semiconducting materials [27]. Such a large magnitude of the noise can be attributed to the relatively low height of the potential barrier A and to the relatively large tunneling length l. Formally, it is also related to the large value of the logarithm squared in (16.2.10).

According to (16.2.9) and (16.2.10), the noise power and the noise parameter (a Hooge constant) α_H are independent of the volume fraction occupied by the droplets. This result is valid in the intermediate range of n, when the droplet density is not too high and not too low. First, we assumed that the droplets are isolated point objects and that the tunneling between the two droplets is not affected by a third polaron. This is only valid provided the droplet density is far from the percolation threshold, $n \ll n_c$. On the other hand, the droplet density must not be too low since the conditions $N, N_1, N_2 \gg 1$ are assumed to be met. Moreover, we neglected the possibilities of the disappearance of a droplet without an electron, the formation of a new droplet due to the electron tunneling, and the decay of two-electron droplets. Thus, the characteristic times of these processes should be longer than the characteristic tunneling time, and the average tunneling distance cannot be too high (see (16.1.17) and the discussion below it).

The above speculations imply that the following set of inequalities should be met, $R_{pol} \ll n^{-1/3} \ll l$, for formula (16.1.15) for the conductivity to be valid. In general, the tunneling length should not be much larger than the droplet radius since just the same physical parameters determine these two characteristic distances. So, these inequalities could not be valid for real physical systems, and it is of interest to consider the situation where $R_{pol}, l \ll n^{-1/3}$, which is beyond the scope of our model. However, some definite conclusions concerning the magnetoresistance and the noise power can be made at present.

First, the factor $\exp(A/2k_BT)$ in the temperature dependence of the conductivity is related to the number of carriers and appears due to the strong Coulomb repulsion of electrons in the droplet. It seems rather obvious that such a factor appears in the formula for the conductivity below the percolation threshold for an arbitrary relation between R_{pol} and l. On the other hand, in contrast to common

hopping systems, a strong 1/*f*-noise in our model results from fluctuations of state occupation numbers. Actually, our result for parameter α_H (16.2.10), only relies on the fact that $\delta\sigma/\sigma - \delta n_2/\bar{n}_2$. As we have mentioned previously (16.2.5), which determines the spectral density of fluctuations of n_2, applies for an arbitrary relationship between R_{pol} and l. It follows then that the value of the parameter α_H for 1/*f*-noise remains approximately the same under the (experimentally relevant) conditions $R_{pol} \sim l$.

Another important point is that we disregard the direct Coulomb interaction between the droplets in comparison with the energy A. This is justified if the gas of the droplets is diluted, $n^{1/3} \gg R_{pol}$. In this respect, we recollect that in standard hopping conduction systems (doped semiconductors) the main mechanism of low-frequency noise is an exchange of electrons between the infinite cluster and nearby finite clusters. In the absence of interactions it leads to the noise power proportional to $\omega^{-\delta}$, with the exponent δ being considerably below 1 [44] To explain 1/*f*-noise in these systems, models involving Coulomb interactions were proposed [45, 46]. These sources of low-frequency noise are thus beyond our discussion. We also did not consider sources of noise different from resistance fluctuations. At least two other types of noise are inevitably present in the system: Nyquist-Johnson (thermal) noise [5], which is a consequence of fluctuation–dissipation theorem, and shot noise due to the discrete nature of electron charge (see [6] and [47] for review). Both these noises are frequency independent (white) at low frequencies. The magnitudes of Nyquist-Johnson, shot, and 1/*f*-noises are governed by absolutely different parameters, and we do not attempt to compare them here, noting only that at low frequencies 1/*f*-noise must dominate.

In our model, we assumed that the number of droplets N is fixed and strictly equal to the number of extra electrons. In actual systems, N can also fluctuate, and this can be an additional source of noise and of 1/*f*-noise, in particular. However, this contribution depends critically on the heights of corresponding energy barriers and can vary for different systems.

As we have already mentioned, the main motivation of our work was the experimental study [37], which observed high 1/*f*-noise power at high temperatures far from the metal–insulator transition. In the same experiment, the noise dropped to much lower levels at low temperatures in the metallic phase. This behavior of the noise power is consistent with the present model since in the metallic phase the electron tunneling contribution to the total conductivity is negligible. In the vicinity of the percolation transition the noise power increases drastically [37]. In this Chapter we do not attempt to describe the system of magnetic polarons close to the percolation threshold. However, we argue that the amplitude of 1/*f*-noise is already large in the phase-separated regime even far from the percolation threshold.

16.3 Experimental Confirmation of the Theoretical Predictions for Tunneling Conductivity

In Sect. 16.1.3 we present a simple model for tunneling conductivity. We consider droplets containing one or two electrons together with empty droplets. The direct generalization of (16.1.15) for the case of the droplets with k, $k + 1$ and $k - 1$ carriers [28] yields for the resistivity:

$$\rho = \frac{k_B T \exp(A/2k_B T)}{128\pi e^2 \omega_0 l^5 k n^2}, \tag{16.3.1}$$

where n is the concentration of ferromagnetic droplets. Electrical resistivity (16.3.1) exhibits a thermoactivative behavior where the activation energy is equal to one half of Coulomb energy A. Expression (16.3.1) provides a fairly good description for the temperature dependence of the electrical resistivity for various manganites. As an illustration, in Figs. 16.5, 16.6, 16.7, 16.8 we present experimental $\rho(T)$ curves for six different materials. Experimental data are plotted for samples reported in [29] by Babushkina et al. in [30] by Fisher et al. in [31] by Zhao et al. in [32] by Wagner et al. The authors of these papers kindly provided us by the detailed numerical data on their measurements. As it could be seen from the figures and their captions, the examined samples differ in their chemical composition, type of crystal structure, magnitude of electrical resistivity (at fixed temperature, the latter varies for different samples by more than two orders of magnitude), and also by their low temperature behavior (which is metallic for some samples and insulating for the others). On the other hand, in the high-temperature range (above the point of ferromagnetic phase transition), $\rho(T)$ exhibits a similar behavior for all the samples, which is well fitted by the relationship $\rho(T) \sim T \exp(A/2k_B T)$ (solid lines in the Figs. 16.5, 16.6, 16.7, 16.8).

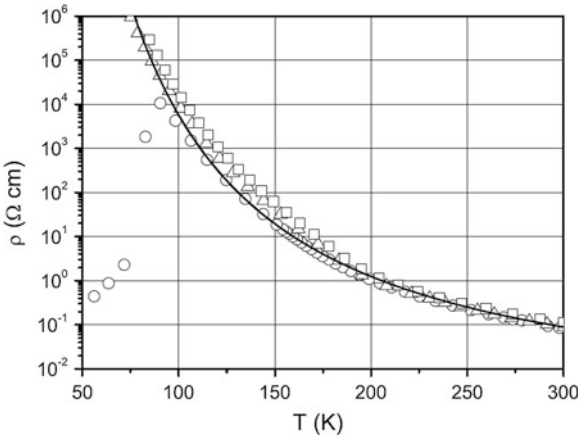

Fig. 16.5 Temperature dependence of the resistivity for $(La_{1-y}Pr_y)_{0.7}Ca_{0.3}MnO_3$ samples [29]. *Squares*, *triangles*, and *circles* correspond to $y = 1$ (with $^{16}O \rightarrow {}^{18}O$ isotope substitution), $y = 0.75$ (with $^{16}O \rightarrow {}^{18}O$ isotope substitution), and $y = 0.75$ (with ^{16}O), respectively. *Solid line* is the fit based on (16.3.1)

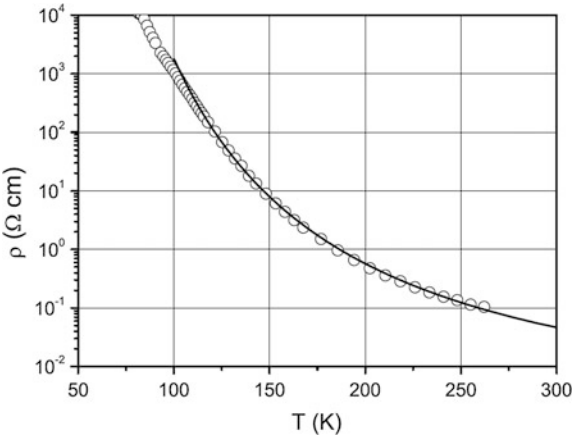

Fig. 16.6 Temperature dependence of the resistivity for $Pr_{0.71}Ca_{0.29}MnO_3$ sample [30]: experimental data (*circles*) and theoretical curve (*solid line*) based on (16.3.1)

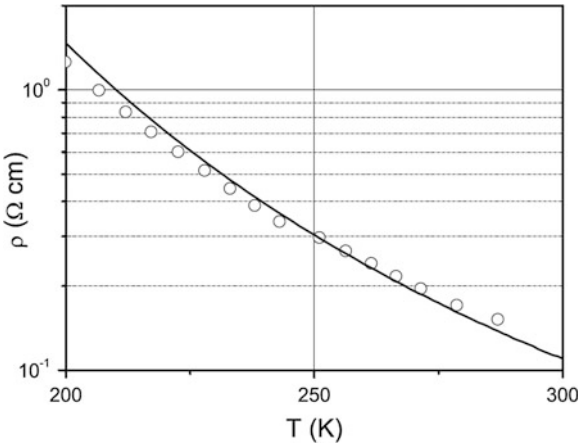

Fig. 16.7 Temperature dependence of the resistivity for a layered manganite $(La_{0.4}Pr_{0.6})_{1.2}Sr_{1.8}Mn_2O_7$ [32]: experimental data (*circles*) and theoretical curve (*solid line*) based on (16.3.1)

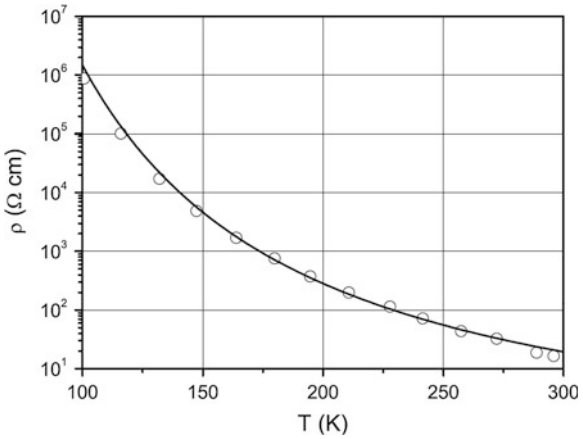

Fig. 16.8 Temperature dependence of the resistivity for $La_{0.8}Mg_{0.2}MnO_3$ sample [31]: experimental data (*circles*) and theoretical curve (*solid line*) based on (16.3.1)

Table 16.1 The coulomb barrier A can be determined with an accuracy of 2–3% and its value lies in the narrow range from 3500 to 3700 K

Samples	A, K	ρ (200 K), Ω·cm	l^5n^2k, cm^{-1}	Data source
$(La_{1-y}Pr_y)_{0.7}Ca_{0.3}MnO_3$*	3650	1.25	2×10^5	Fig. 16.5 (Babushkina et al., 2003)
$Pr_{0.71}Ca_{0.29}MnO_3$	3500	0.57	3×10^5	Fig. 16.6 (Fisher et al., 2003)
$(La_{0.4}Pr_{0.6})_{1.2}Sr_{1.8}Mn_2O_7$	3600	1.5	1.5×10^5	Fig. 16.7 (Wagner et al., 2002)
$La_{0.8}Mg_{0.2}MnO_3$	3700	283	1×10^3	Fig. 16.8 (Zhao et al., 2001)

* The chemical formula for this composition can be written as $(\mathbf{La_{0.4}Pr_{0.6}})_{2\text{-}2x}\mathbf{Sr_{1+2x}Mn_2O_7}$

Based on (16.3.1) and experimental data, one can deduce some quantitative characteristics of the phase-separated state. In particular, the analysis carried out in [32] demonstrated that an accurate estimate for the value of Coulomb energy A can be found by fitting experimental data and using (16.3.1). The data represented in Figs. 16.5, 16.6, 16.7, 16.8 suggest that the Coulomb barrier A can be determined with an accuracy of 2–3 % and its value lies in the narrow range from 3500 to 3700 K (see Table 16.1). As it was mentioned in [22, 32] the characteristic frequency ω_0 in (1) can also vary in a restricted range of $10^{13} \div 10^{14}$ Hz. This estimate might be derived, for example, from the uncertainty principle: $\hbar\omega_0 \sim \hbar^2/2mR_{pol^2}$, where R_{pol} is a characteristic droplet size, and m is the electron mass. Assuming $R_{\text{pol}} \sim$ 1–2 nm [51, 52] one obtains the latter estimate. Note also that these values of a droplet size allow us to find an estimate for the barrier energy A, which is accurate within the order of magnitude. This energy is of the order of $e^2/\varepsilon R_{\text{pol}}$, and substituting permittivity $\varepsilon \sim 10$, we get a value of A consistent with the experimental data.

It is rather difficult to estimate the tunneling length l. However, we can say that in the domain of the applicability of relationship (16.3.1), the length l cannot be much smaller than an interdroplet spacing [22]. In another situation, the behavior of the resistivity would be different. In the quasiclassical approximation, the tunneling length is of the order of the characteristic size for the wave function provided the barrier height is comparable with the depth of the potential well. In our case, the size of the electron wave function is of the order of a ferron size, while the height of the barrier practically coincides with the depth of the potential well. The latter naturally follows from the model of ferron formation considered in Chap. 15. Therefore, it seems reasonable to assume the tunneling length to be of the same order as a ferron size (few nanometers), though, generally speaking, it can differ substantially from R_{pol}.

It is rather nontrivial task to estimate the concentration n of ferrons. In fact, following [32] concentration n could be determined by the dopant concentration x as $n \approx x/d^3$. Yet this approach would bring at least two contradictions. First, even under the moderate concentration of divalent element $x = 0.1$–0.2 the droplets should overlap giving rise to the continuous metallic and ferromagnetic cluster. However, the material could be insulating even at larger concentrations ($x = 0.5 \div 0.6$) [33], at least, in a high-temperature range. Second, as it can be seen

from the experimental data, the relation between a dopant concentration and the conductivity of manganites is relatively complicated—for some materials changing x by a factor of two can change resistivity by two orders of magnitude [32], for other materials $\rho(x)$ exhibits even a nonmonotonic behavior in certain concentration ranges. Note that these discrepancies are essential not only for our model of phase-separation but also for other models dealing with the properties of manganites (e.g., polaronic models [47, 48]). Unfortunately, the authors of [32] do not take into account these considerations when analyzing their results from the standpoint of the existing theories of the conductivity in manganites. The natural conclusion is that the number of carriers, which contributes to the charge transfer processes does not coincide with the concentration of the divalent dopant x. This is particularly obvious in the case of charge ordering when some part of the carriers introduced by doping becomes localized and forms a regular structure [51].

Therefore, using expression (16.3.1) and experimental data, we are able to obtain also the value of the combination l^5n^2k. In Table 16.1, the values of the Coulomb energy A, resistivity ρ at 200 K and, combination l^5n^2k are presented. All estimations were made based on (16.3.1) and the experimental data of Figs. 16.5, 16.6, 16.7, 16.8. Note that whereas the accuracy of the estimate for A is about ± 50 K, the combination l^5n^2k could be estimated only by the order of magnitude (at least, due to the uncertainty in the values of frequency ω_0).

16.3.1 Experiments on Tunneling Magnetoresistance

In [22–25, 27, 28] it was demonstrated that the model of phase separation considered here results in a rather specific dependence of the magnetoresistance MR on temperature and magnetic field. At relatively high temperatures and not very strong magnetic fields, the expression for the magnetoresistance reads [23–25, 27, 28] (see also 16.1.26 and Fig. 16.4):

$$|MR| \approx 5 \times 10^{-3} \left(\mu_B^{el}\right)^3 S^5 N_{eff}^3 Z^2 g^3 J_{FM}^2 \frac{H_a H^2}{(k_B T)^5}, \tag{16.3.2}$$

where μ_B^{el} is electron the Bohr magneton, S is the average spin of a manganese ion, N_{eff} is the number of manganese atoms in a droplet, Z is the number of nearest neighbors of a manganese ion, g is the Lande factor, J_{FM} is an effective exchange integral of the ferromagnetic interaction, and H_{a} is the effective field of magnetic anisotropy of a droplet. The $|\text{MR}| \sim H^{\,2}/T^{\,5}$ dependence was observed in the experiments for a number of manganites in the region of their non-metallic behavior (see [29–31]). The same high-temperature behavior of the magnetoresistance can be obtained by processing the experimental data reported in [32, 35] (see Figs. 16.9, 16.10, 16.11, 16.12).

The value of S depends on the relative content of a trivalent and a tetravalent manganese ions and ranges from 3/2 to 2. Below it is assumed that $S = 2$ for all

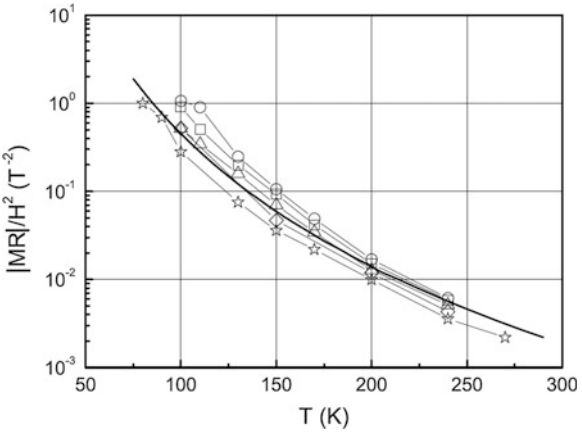

Fig. 16.9 Temperature dependence of $|\mathrm{MR}|/H^2$ ratio for $(La_{1-y}Pr_y)_{0.7}Ca_{0.3}MnO_3$ samples [29]. *Squares, triangles, circles, diamonds*, and *asterisks* correspond to $y = 0.75$, $y = 0.75$ (with 30 % of ^{18}O), $y = 0.75$ (with $^{16}O \rightarrow {}^{18}O$ isotope substitution), $y = 1$, and $y = 1$ (with $^{16}O \rightarrow {}^{18}O$ isotope substitution), respectively. *Solid line* is the fit based on (16.3.2) ($|\mathrm{MR}| \sim 1/T^5$)

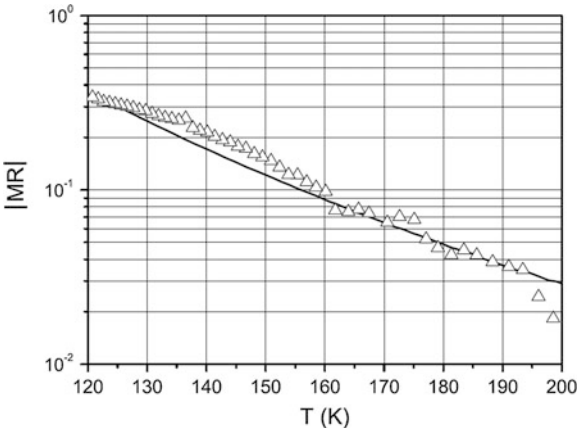

Fig. 16.10 Temperature dependence of the magnetoresistance for $Pr_{0.71}Ca_{0.29}MnO_3$ sample at $H = 2$ T: experimental data (*triangles*) [30] and theoretical curve (*solid line*) based on (16.3.2)

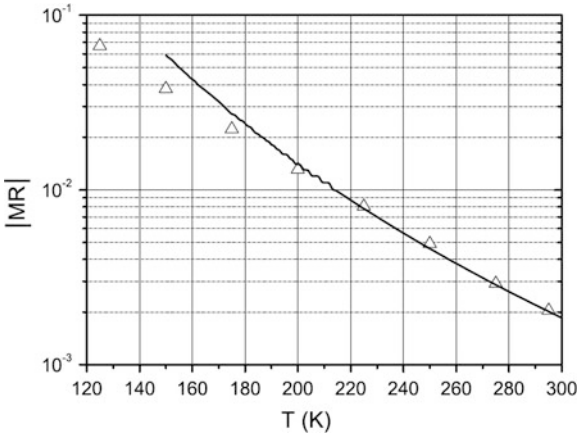

Fig. 16.11 Temperature dependence of the magnetoresistance for $(La_{0.4}Pr_{0.6})_{1.2}Sr_{1.8}Mn_2O_7$ sample (layered manganite) at $H = 1$ T: experimental data (*triangles*) [32] and theoretical curve (*solid line*) based on (16.3.2)

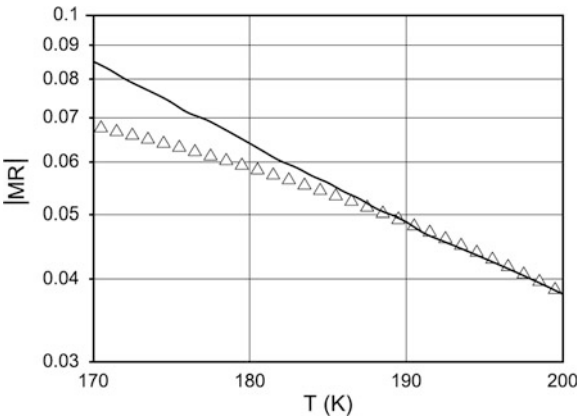

Fig. 16.12 Temperature dependence of the magnetoresistance for $La_{0.8}Mg_{0.2}MnO_3$ sample at $H = 1.5$ T: experimental data (*triangles*) [31] and theoretical curve (*solid line*) based on (16.3.2)

the estimations. Parameter Z in (16.1.30) is, in fact, the number of manganese ions interacting with a conduction electron placed in a droplet. It is reasonable to assume that Z is of the order of the number of nearest-neighbor sites around a manganese ion, i.e. $Z \approx 6$. The Lande factor g is determined from the experimental data. For manganese, g is usually assumed to be close to its spin value 2. The exchange integral J_{FM} characterizes the magnetic interaction between a conduction electron and the molecular field generated by ferromagnetically correlated spins in a droplet. It is this molecular field that produces a ferromagnetic state at low temperatures. Therefore, we can use a well-known relationship $S(S+1)ZJ_{\mathrm{FM}}/3 = k_{\mathrm{B}}T_{\mathrm{C}}$ of the molecular field theory [42] to evaluate the exchange integral (here T_{C} is the Curie temperature). The value of T_{C} is determined from the experiment (based on neutron diffraction or magnetization measurements). For example, in La-Pr–Ca manganites, it is about 100–120 K [49].

The magnetic anisotropy of manganites related to crystal structure of these compounds is usually not too high. This implies that the main contribution to the effective field of a magnetic anisotropy H_{a} stems from the shape anisotropy of a droplet and can be evaluated as $H_a = \pi(1 - 3\bar{N})M_S$, where $\bar{N}$ is the demagnetization factor [42] of the droplet (along the main axis), M_{S} is the magnetic moment per unit volume ($M_{\mathrm{S}} = M/V_{\mathrm{S}}$) of the droplet. Below we assume a droplet to be sufficiently elongated ($\bar{N} \ll 1$) and $M_{\mathrm{S}} = Sg\mu_B^{el}/d^3$. Then $H_{\mathrm{a}} \approx 2$ kOe.

The value of N_{eff} is determined by the size of a droplet and it could be found from the neutron diffraction experiments. However, we are unaware of such measurements performed for the systems under discussion in a wide temperature range. Therefore, N_{eff} is treated here as a fitting parameter. Hence, using (16.1.30) and the above estimates, we can determine the value of N_{eff} from the experimental data on the magnetoresistance (in the range of parameters corresponding to $|\mathrm{MR}| \sim H^2/T^5$). The results are summarized in Table 16.2. In Figs. 16.9, 16.10, 16.11, 16.12, solid curves correspond to the fitting procedure based on (16.3.2). The value of T_{C} was chosen to be equal to 120 K.

Table 16.2 The summarized results for important parameters which determine magnetoresistance in (16.3.2)

Samples	N_{eff}	x	k	Data source
$(La_{1-y}Pr_y)_{0.7}Ca_{0.3}MnO_3$	250	0.3	75	Fig. 16.9 (Babushkina et al., 2003)
$Pr_{0.71}Ca_{0.29}MnO_3$	200	0.29	58	Fig. 16.10 (Fisher et al., 2003)
$(La_{0.4}Pr_{0.6})_{1.2}Sr_{1.8}Mn_2O_7$	250	0.4	100	Fig. 16.11 (Wagner et al., 2002)
$La_{0.8}Mg_{0.2}MnO_3$	265	0.2	53	Fig. 16.12 (Zhao et al., 2001)

As a result, the size of the ferromagnetically correlated regions turns out to be nearly the same at temperatures about 200–300 K for all the compositions under discussion. The volume of these regions is approximately equal to that of a ball with 7–8 lattice constants in diameter. It is natural to assume that within a droplet the number of charge carriers contributing to tunneling processes equals to the number of dopant atoms. Hence, we can write that entering in (16.3.1) $k = N_{\text{eff}}\, x$, where x is the atomic percentage of dopants. The values of x and k are presented in Table 16.2.

16.3.2 Magnetic Susceptibility

The concentration of droplets can be evaluated based on the magnetic susceptibility data, if we assume that the dominant contribution to the susceptibility comes from the ferromagnetically correlated regions. At high temperatures ($k_{\text{B}}T \gg \mu_B^{el} g S N_{\text{eff}} H$, $\mu_B^{el} g S N_{\text{eff}} H_{\text{a}}$), susceptibility $\chi(T)$ can be written as [27, 28]

$$\chi(T) = \frac{n\left(\mu_B^{el} g S N_{eff}\right)^2}{3k_B(T-\theta)}, \tag{16.3.3}$$

where θ is the Curie–Weiss constant [42, 43]. The results of the processing of the experimental data [29–32] are presented in Table 16.3. In Figs. 16.13, 16.14, 16.15, 16.16, the solid curves correspond to the fitting procedure based on (16.3.3). Using these results, we can also estimate the concentration of ferromagnetic phase as $p = nN_{\text{eff}}d^3$. For all the samples, the value of the lattice constant d was taken to be equal to 3.9 Å. Based on the data of Tables 16.1–16.3, it is also possible to find an estimate for the tunneling length l.

Table 16.3 The results of the processing of the experimental data which determine magnetic susceptibility in (16.3.3)

Samples	θ, K	n, cm^{-3}	p	l, Å	Data source
$(La_{1-y}Pr_y)_{0.7}Ca_{0.3}MnO_3$	55	1.8×10^{18}	0.03	24	Fig. 16.13 (Babushkina et al., 2003)
$Pr_{0.71}Ca_{0.29}MnO_3$	105	6.0×10^{18}	0.07	17	Fig. 16.14 (Fisher et al., 2003)
$(La_{0.4}Pr_{0.6})_{1.2}Sr_{1.8}Mn_2O_7$	255	2.5×10^{18}	0.04	19	Fig. 16.15 (Wagner et al., 2002)
$La_{0.8}Mg_{0.2}MnO_3$	150	0.6×10^{18}	0.01	14	Fig. 16.16 (Zhao et al., 2001)

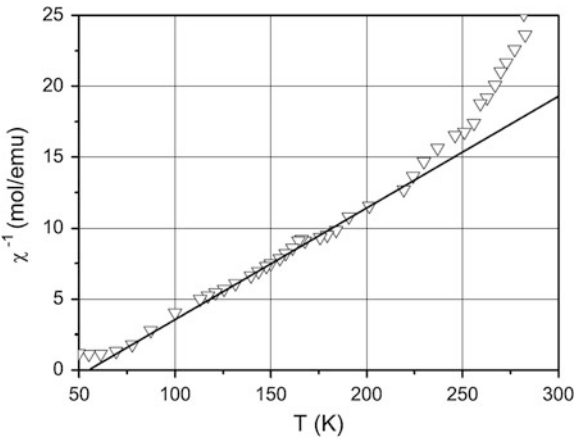

Fig. 16.13 Temperature dependence of the inverse magnetic susceptibility for $(La_{1-y}Pr_y)_{0.7}Ca_{0.3}MnO_3$ sample at $y = 1$: experimental data (*triangles*) [29] and theoretical curve (*solid line*) based on (16.3.3). For the other samples of this group, the behavior of $\chi(T)$ at high temperatures is rather similar to that illustrated in this figure (see [29])

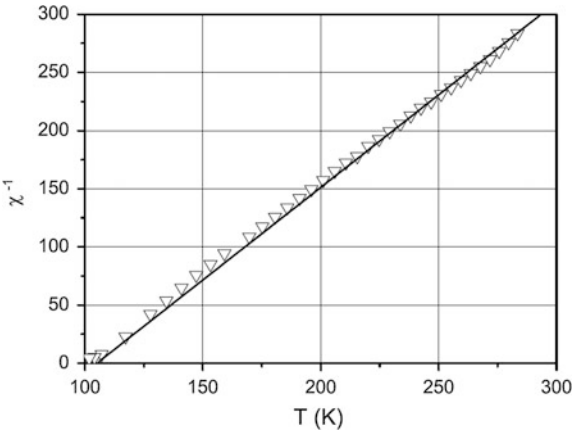

Fig. 16.14 Temperature dependence of the inverse magnetic susceptibility for $Pr_{0.71}Ca_{0.29}MnO_3$ sample: experimental data (*triangles*) [30] and theoretical curve (*solid line*) based on (16.3.3). The sample was porous, its density was assumed to differ by a factor of 0.7 from the theoretical value

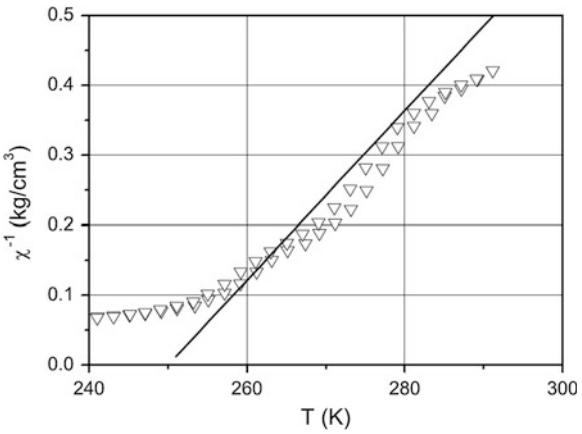

Fig. 16.15 Temperature dependence of the inverse magnetic susceptibility for the sample of $(La_{0.4}Pr_{0.6})_{1.2}Sr_{1.8}Mn_2O_7$ layered manganite: experimental data (*triangles*) [32] and theoretical curve (*solid line*) based on (16.3.3)

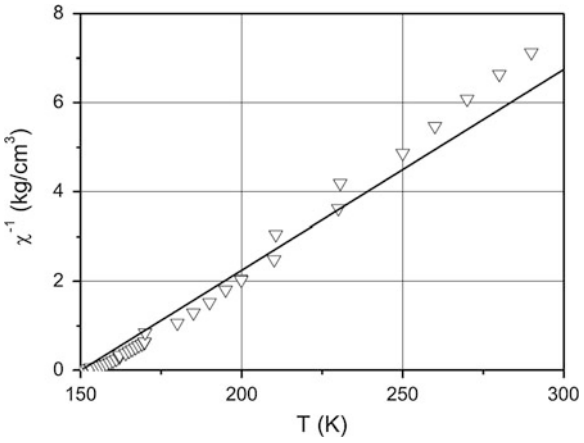

Fig. 16.16 Temperature dependence of the inverse magnetic susceptibility for $La_{0.8}Mg_{0.2}MnO_3$ sample: experimental data (*triangles*) [31] and theoretical curve (*solid line*) based on (16.3.3)

16.3.3 Discussion. The Triple Point in Manganites. Unresolved Questions

To sum up, the analysis performed in the previous sections demonstrates that a simple model of the electron tunneling between the ferromagnetically correlated regions (FM droplets) provides a possibility to describe the conductivity and the magnetoresistance data for a wide class of manganites. The comparison of the theoretical predictions with the experimental data on the temperature dependence of the resistivity, magnetoresistance, and magnetic susceptibility enables us to reveal various characteristics of the phase-separated state such as the size of FM droplets, their density, the number of electrons in a droplet and also to estimate the characteristic tunneling length of the charge carriers. The determined values of parameters appear to be rather reasonable. Indeed, the characteristic tunneling length turns out to be of the order of FM droplet size, the concentration of the ferromagnetic phase in the high-temperature range is substantially smaller than the percolation threshold and varies from about 1 to 7 %.

Note also that the droplets contain 50–100 charge carriers, whereas parameter A deduced from the experimental data is equal by the order of magnitude to the energy of Coulomb repulsion in a metallic ball of $(7 - 8)d$ in diameter. The obtained numerical values for the droplet parameters (characteristic tunneling barrier, size, and tunneling length) are close for manganites with drastically different transport properties.

The large magnitude of the $1/f$-noise in the temperature range corresponding to the insulating state is another characteristic feature of the phase-separated manganites (see experimental results obtained in [37]. In the framework of the model of phase-separation discussed here we get the large value for the Hooge constant α_H in (16.2.10). At temperatures 100–200 K and frequencies 1–1000 s^{-1} we get $\alpha_H = 10^{-16}$ cm^3. This value of α_H is by 3–5 orders of magnitude higher than the corresponding value for semiconductors.

Thus, we have a rather consistent scheme describing the transport properties of manganites under condition that the ferromagnetically correlated regions do not form a percolation cluster. Moreover, the presented approach proves to be valid for a fairly wide range of the dopant concentrations. However, as it was mentioned above, the relation between the concentration of ferromagnetic droplets and the doping level is far from being well understood. If the picture of the phase separation is believed to be applicable, it becomes obvious that not all electrons or holes introduced by doping participate in the transport processes. Below we try to present some qualitative arguments illustrating the possible difference in the effective concentration of charge carriers below and above the transition from paramagnetic to magnetically ordered state.

In the phase diagram of a typical manganite (see [50, 51] and Chap. 15 for a review), one would have the AFM state with FM-phase inclusions in the low-temperature range and at a low doping level. The transition from AFM to FM phase occurs upon doping. At high temperatures, manganites are in the paramagnetic (PM) state. When the temperature decreases, we observe the transition from PM to AFM or FM state depending on the doping level.

Let us consider the behavior of such a system in the vicinity of a triple point. In the AFM phase, radius R_{pol} of a region which one electron converts into FM state can be estimated as $R_{\mathrm{pol}} \sim d(\pi t/2JS^2Z)^{1/5}$ (see [51, 52] and Chap. 15), where J is an AFM exchange interaction between the local spins. For high-temperature PM phase, a radius $R_{\mathrm{pol}}{}^{\mathrm{T}}$ of a region that one electron converts into FM state corresponds to the size of the so-called temperature ferron (see Chap. 15) and equals to $R_{\mathrm{pol}}{}^{\mathrm{T}} \sim d(\pi t/2k_{\mathrm{B}}T\ln(2S+1))^{1/5}$. The critical concentration $x_{\mathrm{C}} \approx 0.15$ of the overlapping of low-temperature ferrons can be derived from the estimate $x_{\mathrm{C}} \sim 3/4\pi\ (d/R_{\mathrm{pol}})^3$, while for the high-temperature ferrons it follows from the estimate $\delta_{\mathrm{C}} \sim 3/4\pi\ (d/R_{\mathrm{pol}}{}^{\mathrm{T}})^3$. Substituting the expressions for the radii of the high- and the low-temperature ferrons to the ratio $x_{\mathrm{C}}/\delta_{\mathrm{C}}$, we obtain the following estimate for this ratio in the vicinity of the triple point corresponding to the coexistence of FM, AFM, and PM phases:

$$\frac{x_C}{\delta_C} \sim \left[\frac{T\ln(2S+1)}{zJS^2}\right]^{3/5} \sim \left[\frac{T_C\ln(2S+1)}{T_N}\right]^{3/5}, \qquad (16.3.4)$$

where T_{C} and T_{N} are the Curie and the Neel temperatures [41, 42], respectively. For the manganites under discussion, we have $T_{\mathrm{C}} \sim T_{\mathrm{N}} \sim (120 - 150)$ K and $\ln(2S+1) \sim 1.6$ for $S = 2$, hence $\delta_{\mathrm{C}} \lesssim x_{\mathrm{C}}$. The sign of this inequality is in agreement with experimental data which imply $\delta \sim (1 - 7)$ %. Thus, we do not have a clear explanation of the charge disbalance in paramagnetic region in spite of the fact that the trend is correctly caught by our simple estimates. Probably, at $x > x_{\mathrm{C}}$ (in real experiments the concentration x can be as high as 50 %), the residual charge is localized in the paramagnetic matrix outside the temperature ferrons. The detailed study of this problem will be a subject of the future investigations.

References

1. Imry, J.: Introduction to mesoscopic physics, 2nd edn. Oxford University Press, USA (2002)
2. Altshuler, B.L., Aronov, A.G.: Electron-electron interaction in disordered conductors. In: Efros, A.L., Pollak, M. (eds.), p 1. North Holland, Amsterdam (1985)
3. Altshuler, B.L., Aronov, A.G., Khmelnitskii, D.E., Larkin, A.I. In: Quantum Theory of Solids. Lifshits, I. M. (eds.), p 130. Mir Publishers, Moscow (1982)
4. Altshuler, B.L., Lee, P.A.: Phys. Today **41**(36) (1988)
5. Beenakker, C.I.M., Bootsma, S.K.: Frontiers in nanoscale science of micron/submicron devices. In: Janho, A.-P., Buzaneva, E.V. (eds.) Kluwer Acad. Publ. (1994)
6. Averin, D.V., Likharev, K.K. In: Altshuler, B.L., Lee, P.A., Webb, R.A. (eds.) Mesoscopic phenomena in solids. Elsevier, Amsterdam (1992)
7. Anderson, P.W. In: Ravello, E.R., Calaniello, E. Lectures on the many-body problem, p. 113. Academic Press, New York (1964)
8. Wegner, F.J.: Zeit. für Physik B Cond. Matt. **25**, 327 (1976)
9. Wegner, F.J.: Zeit. für Physik B Cond. Matt. **35**, 207 (1979)
10. Abrahams, E., Anderson, P.W., Lee, P.A., Ramakrishnan, T.V.: Phys. Rev. B 24, pp. 6783 (1981)
11. Hubbard, J.: Proceedings of Royal Society of London. Series A. **276**, 238 (1963)
12. Mott, N.F.: Metal-insulator transitions, Taylor & Francis, London (1984)
13. Landauer, R.: Localization, interactions and transport phenomena. In: Krämer, B., et al. (eds.) Springer series in solid-state sciences, p. 38. Springer, Berlin (1985)
14. Sklovskii, B.I., Efros, A.L.: Electronic properties of doped semiconductors, vol. 45 in Springer series in solid-state sciences, Springer-Verlag, Berlin (1984)
15. Abrikosov, A.A.: Fundamentals of the theory of metals, North Holland, Amsterdam (1988)
16. E. Fradkin, Field theories of condensed matter systems, Addison-Wesley, 1991
17. Tsvelik, A.M.: Quantum field theory in condensed matter physics, University Press, Cambridge, New York (1998)
18. Auerbach, A.: Interacting electrons and quantum magnetism, Springer (1994)
19. Kogan, Sh: Electronic noise and fluctuations in solids. Cambridge University Press, Cambridge (1996)
20. Dutta, P., Horn, P.M.: Rev. Mod. Phys. **53**, 497 (1981)
21. Tomsovic, S. (ed.): Tunneling in complex systems. World Scientific, Singapore (1998)
22. Rakhmanov, A.L., Kugel, K.I., Blanter, Ya.M, Kagan, M.Yu.: Phys. Rev. B **63**, 174424 (2001)
23. Sboychakov, A.O., Rakhmanov, A.L., Kugel, K.I., Kagan, M.Yu., Brodsky, I.V.: JETP. **95**, 753 (2002)
24. Sboychakov, A.O., Rakhmanov, A.L., Kugel, K.I., Brodsky, I.V., Kagan, M.Yu.: Jour. Phys.: Condens. Matter **15**, 1705 (2003)
25. Kagan, M.Yu., Klaptsov, A.V., Brodsky, I.V., Kugel, K.I., Sboychakov, A.O., Rakhmanov, A.L.: Sov. Phys. Uspekhi **173**, 877 (2003)
26. Kagan, M.Yu., Klaptsov, A.V., Brodsky, I.V., Kugel, K.I., Sboychakov, A.O., Rakhmanov, A.L.: J. Phys. A: Mathematical and General **36**, 9155 (2003)
27. Kugel, K.I., Rakhmanov, A.L., Sboychakov, A.O., Kagan, M.Yu., Brodsky, I.V., Klaptsov, A.V.: JETP **125**, 648 (2004)
28. Kugel, K.I., Rakhmanov, A.L., Sboychakov, A.O., Kagan, M.Yu., Brodsky, I.V., Klaptsov, A.V.: In Physics of spin in solids: materials, methods and applications, Halilov, S.(ed), Kluwert Publishing House, 177 (2004)
29. Babushkina, N.A., Chistotina, E.A., Kugel, K.I., Rakhmanov, A.L., Gorbenko, O.Y., Kaul, A.R. J. Phys.: Condens. Matter **15**, 259 (2003)
30. Fisher, L.M., Kalinov, A.V., Voloshin, I.F., Babushkina, N.A., Kugel, K.I., Khomskii, D.I.: Phys. Rev. B **68**, 174403 (2003)
31. Zhao, J.H., Kunkel, H.P., Zhou, X.Z., Williams, G. Phys. Rev. B 66: 184428 (2002)

32. Wagner, P., Gordon, I., Moshchalkov, V.V., Bruynseraede, Y., Apostu, M., Suryanarayanan, R., Revcolevschi, A. Europhys. Lett. **58**, 285 (2002)
33. Uehara, M., Mori, S., Chen, C.H., Cheong, S.-W.: Nature **399**, 560 (1999)
34. Podzorov, V., Uehara, M., Gershenson, M.E., Koo, T.Y., Cheong, S.-W. Phys. Rev. B **61**, R3784 (2000)
35. Babushkina, N.A., Belova, L.M., Khomskii, D.I., Kugel, K.I., Gorbenko, O.Y., Kaul, A.R. Phys. Rev. B **59**, 6994 (1999)
36. Zhao, J.H., Kunkel, H.P., Zhou, X.Z., Williams, G. J. Phys.: Condens. Matter **13**, 9349 (2001)
37. Podzorov, V., Gershenson, M.E., Uehara, M., Cheong, S.-W. Phys. Rev. B **64**: 115113 (2001)
38. Landau, L.D., Lifshitz, E.M.: Statistical physics, Part 1. Butterworth-Heinemann, Oxford (1999)
39. Gradshteyn, I. S., Ryzhik, J. M. In: Table of integrals, series, and products, Jeffrey, A. (ed.) Academic Press, Waltham (1994)
40. Mott, N.F., Davis, E.A.: Electronic processes in non-crystalline materials. Clarendon Press, Oxford (1979)
41. Landau, L.D., Lifshitz, E.M.: Electrodynamics of continuous media. Pergamon, New York (1984)
42. Smart, J.S.: Effective field theories of magnetism. Saunders, London (1966)
43. Kogan, S.M., Shklovskii, B.I.: Sov. Phys. Semicond. **15**, 605 (1981)
44. Kozub, V.I.: Solid State Commun. **97**, 843 (1996)
45. Yu, C.C.: Physica status solidi (c), Special Issue: 10th Conference on hopping and related phenomena (HRP10), **1**, 25 (2004)
46. Blanter, Y.M., Büttiker, M.: Physics reports **336**, 1 (2000)
47. Jakob, G., Westerburg, W., Martin, F., Adrian, H.: Phys. Rev. B **58**, 14966–14970 (1998)
48. Ziese, M., Srinitiwarawong, C.: Phys. Rev. B **58**, 11519 (1998)
49. Balagurov, A.M., Pomjakushin, V.Y., Sheptyakov, D.V., Aksenov, V.L., Fischer, P., Keller, L., Gorbenko, O.Y., Kaul, A.R., Babushkina, N.A.: Phys. Rev. B **64**, 024420 (2001)
50. Dagotto, E., Hotta, T., Moreo, A.: Phys. Rep. **344**, 1–153 (2001)
51. Kagan, M.Yu., Kugel, K.I.: Sov. Phys. Uspekhi **171**, 577 (2001)
52. Kagan, M.Yu., Khomskii, D.I., Mostovoy, M.V.: Eur. Phys. J. B **12**, 217 (1999)

Conclusions

As I already mentioned in the Introduction, the main target of the present book is to bridge a gap between different communities working in condensed-matter physics and first of all between the low-temperature community and solid-state community. I would like to stress that though the field of condensed-matter physics is not a modern one (it was effectively started in 1950-s, 1960-s) it is far from being complete. It is permanently enriched by the flow of ideas coming from different fields stretching from high-energy physics, atomic physics and quantum optics to biophysics, quantum chemistry and material science. Moreover, there are a lot of unresolved interesting problems in the field.

Let us mention some of them which are the bit close to the content of my book:

1. The search for supersolidity in quantum crystals and the nature of roughening transition on the phase-interface between quantum crystal and superfluid.
2. The problem of quantum melting of the vortex lattice in rapidly rotating Bose-condensates and the possible analogies with the physics of Quantum Hall Effect.
3. The formation of three-particle and four-particle complexes in rotating superfluids and in anion physics.
4. BCS-BEC crossover close to unitarity and the search of Bose-condensation in new materials such as magnons, excitons, polaritons and so on.
5. The search for fermionic and bosonic superfluidity in new systems including 2D and 3D ^{3}He–^{4}He mixtures, new phases of ^{3}He in aerogel, p-wave quantum gases and so on.
6. The problem of chiral anomaly in superfluid ^{3}He-A and the nature of topological phase-transition in unconventional (anomalous) superconductors and superfluids with Dirac nodal points or lines in the superconductive gap, including topological insulators and recently discovered graphene.
7. The nature of superconductivity in high-T_C materials and the nature of anomalous normal state especially in a pseudogap regime. I would say that the powerful support of quantum field theorists is required here.

M. Yu. Kagan, *Modern Trends in Superconductivity and Superfluidity*,
Lecture Notes in Physics 874, DOI: 10.1007/978-94-007-6961-8,

8. Mesoscopic effects in strongly-correlated electron systems including the nature of the heavy mass, anomalous transport properties and nanoscale phase-separation in mixed valence compounds.
9. Different experimental realization of quantum qubits and investigation of quantum noises. Interplay between localization and interaction in the low-dimensional systems.
10. The nature of low-lying magnetic excitations in the low-dimensional magnetic systems on frustrated lattices including spin ice.

There are a lot of other interesting unresolved problems especially on the border between condensed matter and quantum field theory, in mesoscopic physics and localization theory, in quantum turbulence and soft condensed matter, in the physics of amorphous solids and alloys and so on. There are also a lot of important topics which are more close to applications such as nanocomposites and metamaterials, photonics and plasmonics, physics of polymers, and physics of small electron devices.

Thus I would like to encourage the young researches who started their careers in condensed-matter physics to stay in the field and to establish their leadership.

Index

M. Yu. Kagan, *Modern Trends in Superconductivity and Superfluidity*,
Lecture Notes in Physics 874, DOI: 10.1007/978-94-007-6961-8,

D

N

O

P